OCS Study
BOEM 2020-029

Marine Arctic Ecosystem Study (MARES): Moorings on the Beaufort Sea Shelf (2016–2018) and Program Synthesis

September 2020

Authors:
Francis K. Wiese
Carin Ashjian
Matthew Asplin
Keath Borg
Michael Fabijan
David Fissel
Rowenna D. Gryba
Donglai Gong
Rodger Harvey
Peigen Lin
R. McMahon
Natalie Monacci
R. John Nelson
Pam Neubert
Robert Pickart
Shani Rousseau
Kate Stafford
Chris Turner

Prepared under M14PC00008 M17PD00006
By
Stantec Consulting Services Inc.
4500 Daley Dr., Suite 100
Chantilly, VA 20151-3724

US Department of the Interior
Bureau of Ocean Energy Management
Alaska

BOEM
Bureau of Ocean Energy Management

DISCLAIMER

Study concept, oversight, and funding were provided by the US Department of the Interior, Bureau of Ocean Energy Management (BOEM), Environmental Studies Program, Washington, DC, under Contract Number M14PC00008. This report has been technically reviewed by BOEM, and it has been approved for publication. The views and conclusions contained in this document are those of the authors and should not be interpreted as representing the opinions or policies of the US Government, nor does mention of trade names or commercial products constitute endorsement or recommendation for use.

REPORT AVAILABILITY

To download a PDF file of this report, go to the US Department of the Interior, Bureau of Ocean Energy Management Data and Information Systems webpage (http://www.boem.gov/Environmental-Studies-EnvData/), click on the link for the Environmental Studies Program Information System (ESPIS), and search on 2020-029. The report is also available at the National Technical Reports Library at https://ntrl.ntis.gov/NTRL/.

CITATION

Wiese FK, Ashjian C, Asplin MG, Borg K, Fabijan M, Fissel D, Gryba RD, Gong D, Harvey R, Lin P, McMahon R, Monacci N, Nelson RJ, Neubert P, Pickart R, Rousseau S, Stafford K, Turner C. 2020. Marine Arctic Ecosystem Study (MARES): Moorings on the Beaufort Sea shelf (2016–2018) and Program Synthesis. Anchorage (AK): US Department of the Interior, Bureau of Ocean Energy Management. OCS Study BOEM 2020-029. 286 p.

ACKNOWLEDGMENTS

We would like to acknowledge the support provided by the Stantec MARES team: Diane Ingraham, Jeff Green, Cathy Finnie, Wayne Smith, and Melissa Gandy. We would like to also acknowledge COR, Heather Crowley, and the cruise support provided by H. Melling and the crew of the *CCGS Sir Wilfrid Laurier*, and additional field and analysis support provided by James Bartlett, David Billenness, Rick Birch, Ryan Clouston, Ben Garrett, Bronwyn Hobson, Alex Lam, Jeremy Lawrence, Nick Milutinovic, Todd Mudge, Steve Pearce, Max Rosenthal, Ed Ross, Louis Sadava, Dawn Sadowy, Alex Slonimer, Matthew Stone, and Dan Torres.

Contents

List of Figures iv

List of Tables xv

List of Abbreviations and Acronyms xviii

1 Overview 1

1.1 Background 1

1.2 Goals and Objectives 1

1.3 Mooring Program 2017–2018 (Year 2) 2

1.4 Regional Setting 2

1.5 Community Consultation 3

1.6 Permitting 3

2 Methods and Equipment 4

2.1 Mooring Retrieval Activities 4

2.2 Data Management 7

2.2.1 Data Management Workflow 8

2.2.2 Planning and Orientation 8

2.2.3 Raw Data 8

2.2.4 Preliminary Data and Metadata 9

2.3 Quality Assurance/Quality Control (QA/QC) on Year 2 (2017–2019) Data 10

2.3.1 Acoustic Doppler Current Profiler (ADCP) 10

2.3.2 ADCP Backscatter 32

2.3.3 Ice Profiling Sonar (IPS) 35

2.3.4 Conductivity-Temperature Time Series 44

2.3.5 Submersible Ultraviolet Nitrate Analyzer (SUNA) 46

2.3.6 Submersible Autonomous Moored Instrument (SAMI) 51

2.3.7 Acoustic Zooplankton Fish Profiler (AZFP) 51

2.3.8 Passive Acoustic Recorder (AURAL) 54

3 Results 55

3.1 Year 2 55

3.1.1 Physical Oceanography 55

3.1.2 Chemical Oceanography 118

3.1.3 Biological Oceanography 123

3.1.4 Marine Mammals 141

3.2 Seasonal and Interannual Patterns and Variability 142
3.2.1 Physical Forcing Factors 142
3.2.2 Water Column Structure 157
3.2.3 Currents 165
3.2.4 Alongstream Current Velocity and Water Masses 183
3.2.5 Ice 192
3.2.6 Nutrients 207
3.2.7 Zooplankton 211
3.2.8 Fish 216
3.2.9 Marine Mammals 221
4 Conclusions & Recommendations from 2 Years of Mooring Data in the Eastern Beaufort Sea 222
4.1 Physical Oceanography 222
4.1.1 Currents 222
4.1.2 Ice 223
4.2 Chemical Oceanography 224
4.2.1 Nutrients 224
4.2.2 Carbon Dioxide 224
4.3 Biological Oceanography 224
4.3.1 Zooplankton 224
4.3.2 Fish 225
4.3.3 Marine mammals 225
5 Data Synthesis 227
5.1 Overview 227
5.2 Beaufort Sea The Oceanographic Structure and its Impact on the Biological System of the Canadian 227
5.2.1 Introduction 227
5.2.2 Physical Drivers 228
5.2.3 Biological Responses 234
5.3 Seasons in the Canadian Beaufort 243
5.3.1 Introduction 243
5.3.2 Methods 244
5.3.3 Results 244
5.3.4 Discussion 249
5.4 The Importance of Episodic Events 251
5.4.1 Introduction 251
5.4.2 Physical Characteristic of Events 251

5.4.3 System Response to Physical Events 256
5.4.4 Conclusions 261
5.5 New Findings 262
6 Climate Change Considerations and Next Steps 267
7 References 271
A Appendix A: High Resolution Seasons Figures 284

List of Figures

Figure 1. Location of the MARES 2017–2018 mooring array 2

Figure 2. Data coverage of ADCPs during the 2017–2018 deployment period 10

Figure 3. Temporal coverage of the ADCP data at each mooring during the 2017–2018 deployment, extending into 2019 at M1 12

Figure 4. Fraction of data records modified before time-averaging for the (from left to right) M1 300 kHz, M2 300 kHz (upper), M2 300 kHz (lower), M3 QuarterMaster 150 kHz, M3 LongRanger 75 kHz, M4 LongRanger 75 kHz, and M4 QuarterMaster 150 kHz during 2017–2018 deployment, extending into 2019 at M1 17

Figure 5. Fraction of data records modified after time-averaging for the (from left to right) M2 300 kHz (upper), M2 300 kHz (lower), M3 QuarterMaster 150 kHz, M3 LongRanger 75 kHz, M4 QuarterMaster 150 kHz, and M4 LongRanger 75 kHz during 2017–2018 deployment 21

Figure 6. M2 tilt magnitude (top) and water level (bottom) 2017–18 time-series 27

Figure 7. M3 tilt magnitude (top) and water level (bottom) 2017–18 time-series 28

Figure 8. M4 tilt magnitude (top) and water level (bottom) 2017-18 time-series 29

Figure 9. Adjusted delta beta curve correcting sound speed at M2 (above) 30

Figure 10. Adjusted delta beta curve correcting sound speed at M3 (above) 30

Figure 11. Adjusted delta beta curve correcting sound speed at M4 (above) 31

Figure 12. Double quadratic interpolation method used to convert the ice draft time series into a spatial series 32

Figure 13. Example of unedited range and amplitude data measured by an IPS during 2017–2018 deployment, showing a period characterized by sea-ice floes and some range “drop-outs” 39

Figure 14. Example of unedited range and amplitude data measured by an IPS during 2017–2018 deployment, showing a period following the main part of the ice season 39

Figure 15. Data coverage of MicroCATs during the 2017–2018 deployment period 44

Figure 16. Temporal coverage of MicroCAT data at each mooring during the 2017–2018 deployment, extending into 2019 at M1 46

Figure 17. Drift correction curves for internal instrument drift, biofouling, and overall drift for the 2017–2019 deployment at M1 49

Figure 18. Drift correction curves for internal instrument drift, biofouling, and overall drift for the 2017–2018 deployment at M2 49

Figure 19. Temperature time-series as measured by sensors on M1 at various depths during the 2017–2019 deployment 56

Figure 20. Salinity time-series as measured by sensors on M1 at various depths during the 2017–2019 deployment 57

Figure 21. Density time-series as measured by sensors on M1 at various depths during the 2017–2019 deployment 58

Figure 22. Temperature, salinity, and density time-series from CT sensors on M1 and interpolated over the full sampled water depth span during the 2017–2019 deployment 59

Figure 23. Temperature time-series as measured by sensors on M2 at various depths for the top four CTs during the 2017–2018 deployment 60

Figure 24. Temperature time-series as measured by sensors on M2 at various depths for the bottom four CTs during the 2017–2018 deployment 61

Figure 25. Salinity time-series as measured by sensors on M2 at various depths for the top four CTs during the 2017–2018 deployment 62

Figure 26. Salinity time-series as measured by sensors on M2 at various depths for the bottom four CTs during the 2017–2018 deployment 63

Figure 27. Density time-series derived from CT sensor measurements on M2 at various depths for the top four CTs during the 2017–2018 deployment 64

Figure 28. Density time-series derived from CT sensor measurements on M2 at various depths for the bottom four CTs during the 2017–2018 deployment 65

Figure 29. Temperature, salinity, and density time-series from CT sensors on M2 and interpolated over the full sampled water depth span during the 2017–2018 deployment 66

Figure 30. Temperature time-series derived from CT sensor measurements on M3 at various depths during the 2017–2018 deployment 67

Figure 31. Salinity time-series derived from CT sensor measurements on M3 at various depths during the 2017–2018 deployment 68

Figure 32. Density time-series derived from CT sensor measurements on M3 at various depths during the 2017–2018 deployment 69

Figure 33. Temperature, salinity, and density time-series from CT sensors on M3 and interpolated over the full sampled water depth span during the 2017–2018 deployment. The black curves show the depth of each sensor. 70

Figure 34. Temperature time-series derived from CT sensor measurements on M4 at various depths during the 2017–2018 deployment 71

Figure 35. Salinity time-series derived from CT sensor measurements on M4 at various depths during the 2017–2018 deployment 72

Figure 36. Density time-series derived from CT sensor measurements on M4 at various depths during the 2017–2018 deployment 73

Figure 37. Temperature, salinity, and density time-series from CT sensors on M4 and interpolated over the full sampled water depth span during the 2017–2018 deployment. The black curves show the depth of each sensor. 74

Figure 38. Temperature, salinity and density profiles measured at the M1 during recovery in July 2019. 76

Figure 39. Temperature, salinity and density profiles measured at M2 during the recovery in October 2018. 77

Figure 40. Temperature, salinity and density profiles measured at M3 during the recovery in October 2018. 78

Figure 41. Temperature, salinity and density profiles measured at M4 during recovery in October 2018. 79

Figure 42. Daily-averaged ocean currents at M1 over the 2017–2019 mooring array deployment 81

Figure 43. Daily-averaged ocean currents at M2 over the 2017–2018 mooring array deployment 82

Figure 44. Daily-averaged ocean currents at M3 over the 2017–2018 mooring array deployment 83

Figure 45. Daily-averaged ocean currents at M4 over the 2017–2018 mooring array deployment 84

Figure 46. High resolution ocean currents at M2 during an ice-free episode in November 2017 86

Figure 47. High resolution ocean currents at M3 during an ice-free episode in November 2017 87

Figure 48. High resolution ocean currents at M4 during an ice-free episode in November 2017 88

Figure 49. High resolution ocean currents at M4 during an ice-free episode in March and April 2018 89

Figure 50. Top panel: Ice concentration in the vicinity of mooring M1. Bottom panel: Time series of alongstream velocity (color, m/s). Positive is Eastward. The year-long mean vertical structure is shown on the left. 90

Figure 51. Top panel: Ice concentration in the vicinity of mooring M2. Bottom panel: Time series of alongstream velocity (color, m/s). Positive is eastward. The year-long mean vertical structure is shown on the left. 91

Figure 52. Top panel: Ice concentration in the vicinity of mooring M3. Bottom panel: Time series of alongstream velocity (color, m/s). Positive is eastward. The year-long mean vertical structure is shown on the left. 92

Figure 53. Top panel: Ice concentration in the vicinity of mooring M4. Bottom panel: Timeseries of alongstream velocity (color, m/s). Positive is eastward. The year-long mean vertical structure is shown on the left. 93

Figure 54. Sea ice concentration in tenths of coverage in the region of the MARES array as reported by Canadian Ice Services Ice Charts (CIS, 2018) during the 2017–2018 deployment. 94

Figure 55. Horizontal ice speed at M1, M2, M3, and M4 over the 2017–18 deployment 99

Figure 56. Progressive vector diagrams created through integration of the ice velocity time-series for M1 over the full 2017–2019 deployment 104

Figure 57. Progressive vector diagrams created through integration of the ice velocity time-series for M2 over the full 2017–2018 deployment 105

Figure 58. Progressive vector diagrams created through integration of the ice velocity time-series for M3 over the full 2017–2018 deployment 106

Figure 59. Progressive vector diagrams created through integration of the ice velocity time-series for M4 over the full 2017–2018 deployment 107

Figure 60. Time-series of the horizontal extent of ice that transited over the M1, M2, M3 and M4 measurement locations during the 2017–2018 deployment, extending into 2019 at M1 108

Figure 61. M2 draft staircase plot showing min/max and daily mean draft values during the 2017–2018 deployment 112

Figure 62. M3 draft staircase plot showing min/max and daily mean draft values during the 2017–2018 deployment 113

Figure 63. M4 draft staircase plot showing min/max and daily mean draft values, during the 2017–2018 deployment 114

Figure 64. Examples of surface waves propagating through sea ice during April 2, 2018 at M3 117

Figure 65. A spectrogram of the M3 ice draft time-series displayed in Figure 64 117

Figure 66. Lamp time for the SUNA at M2 during the 2017–2018 deployment 119

Figure 67. Comparison of nitrate concentration at M2 during the 2017–2018 deployment 119

Figure 68. Comparison of salinity and normalized nitrate concentration at M2 during the 2017–2018 deployment for a biofouling correction starting from May 13 119

Figure 69. Comparison of salinity and normalized nitrate concentration at M2 during the 2017–2018 deployment for a biofouling correction starting from the start of the deployment 120

Figure 70 Comparison of M1 and M2 quality-controlled nitrate time-series during the 2017-–2018 deployment period 120

Figure 71. Comparison of nitrate concentration and salinity at M1, 2017–2018 121

Figure 72. Comparison of nitrate concentration and salinity at M2, 2017–2018 122

Figure 73. Comparison of nitrate concentration and salinity at M1, 2018–2019 122

Figure 74. Number of hours of daylight over the 2017–2018 deployment 122

Figure 75. Autonomous data from mooring site M1 during the 2016–2017 deployment period and discrete pCO_2 data from September 2017 and July 2019 123

Figure 76. Relative backscatter (upper), mean and 5-day running average mean backscatter for each profile (middle) and daily mean and 5-day running average mean (lower) for M1a during the 2017-2019 deployment 124

Figure 77. Relative backscatter (upper), mean and 5-day running average mean backscatter for each profile (middle) and daily mean and 5-day running average mean backscatter (lower) for the combined data from the upper and lower ADCPs at M2 125

Figure 78. Mean daily water column relative backscatter (Sv) smoothed with 5-day running average (upper) and anomalies from the mean daily water column Sv (lower) for M1 and M2 during the 2017–2019 deployment 127

Figure 79. Quiver Plot of mean daily water column velocities and mean daily backscatter anomaly from M1 (upper) and mean daily water column velocities and daily backscatter anomaly from M2 (lower) during the 2017–2018 deployment 128

Figure 80. Daily mean backscatter anomaly and temperature (upper) and salinity (lower) at mooring M1 130

Figure 81. Daily mean backscatter anomaly and temperature (upper) and salinity (lower) at mooring M2 131

Figure 82. Daily mean backscatter (upper) and backscatter anomaly (lower) plotted as a function of near-bottom temperature and salinity at mooring M1..... 132

Figure 83. Daily mean backscatter (upper) and backscatter anomaly (lower) plotted as a function of near-bottom temperature and salinity at mooring M2..... 133

Figure 84. Daily sums of squares and the backscatter anomalies for M1 and M2 moorings 134

Figure 85. Combined daily sums of squares (Figure 84) plotted as a function of daily bottom water temperature and salinity for mooring M1 (upper panel) and mooring M2 (lower panel)..... 135

Figure 86. Nautical Area Scattering Coefficient (NASC) as a function of time for copepods at site M3 in the Beaufort Sea during 2017–2018 137

Figure 87. Echogram of 200 kHz backscatter (S_v) corresponding to copepods at site M3 in the Beaufort Sea during 2017–2018..... 137

Figure 88. Nautical Area Scattering Coefficient (NASC) as a function of time for adult Arctic cod at site M3 in the Beaufort Sea during 2017/2018 138

Figure 89. Echogram of 38 kHz backscatter (S_v) corresponding to adult Arctic cod at site M3 in the Beaufort Sea during 2017–2018 138

Figure 90. Echogram of 38 kHz backscatter (Sv) corresponding to adult Arctic cod at site M2 in the Beaufort Sea during the 2017–2018 sampling season..... 139

Figure 91. Nautical Area Scattering Coefficient (NASC) as a function of time for the 38 khz frequency at site M2 in the Beaufort Sea during the 2017–2018 season..... 139

Figure 92. Nautical Area Scattering Coefficient (NASC) at 125 kHz as a function of time for juvenile Arctic cod at site M3 in the Beaufort Sea during 2017–2018..... 140

Figure 93. Echogram of 125 kHz backscatter (S_v) corresponding to juvenile Arctic cod at site M3 in the Beaufort Sea during 2017–2018 140

Figure 94. Echogram of 125 kHz backscatter (non-filtered S_v) showing daily migration pattern of juvenile cod and zooplankton at site M3 in the Beaufort Sea, from October 12 to 16, 2017 141

Figure 95. Number of weeks per month with marine mammal detections from October 2017 through September 2018 at M2..... 141

Figure 96. ERA5 surface wind speed (m/s) and direction for 2016–2017 for 70°N 139°W..... 143

Figure 97. ERA5 surface wind speed (m/s) and direction for 2017–2018 for 70°N 139°W..... 143

Figure 98. ERA5 seasonal surface wind speed (m/s) and direction for 2016–2017..... 145

Figure 99. ERA5 seasonal surface wind speed (m/s) and direction for 2017–2018..... 146

Figure 100. ERA5 seasonal surface wind speed (m/s) and direction for October–December 2018 for 70°N 139°W. Directions are expressed as being from (e.g. winds blowing from the east have a 90° direction). 147

Figure 101. (left) Map of the drainage basin of the Mackenzie River and (right) the split of the discharge into the Beaufort Sea via the west and central channels into Mackenzie Bay and to the east via Kugmallit Bay 151

Figure 102. Mackenzie River Daily Discharges for 1973–2011 (Yang et al. 2015) 152

Figure 103. Hydrographs of daily discharges of the Mackenzie River at Arctic Red River, for the Years 2016, 2017, 2018, and 2019 (ArcticGRO discharge dataset (Holmes et al. 2019)) 153

Figure 104. Regional circulation schematic of the Beaufort Sea illustrating connections to adjacent shelves and the Canada Basin (Weingartner et al. 2006) 154

Figure 105. Revised schematic of the circulation of the Chukchi Sea and Western Beaufort Sea from Brugler et al. (2014), including an extended Chukchi shelfbreak jet and the newly-described Chukchi slope current (Corlett and Pickart 2017) 155

Figure 106. Schematic circulation in the vicinity of Mackenzie Canyon, based on the MARES mooring data (yellow stars; Lin et al. 2020) 156

Figure 107. Mean temperature profile using circles connected by a line, and the maximum and minimum temperature profiles using triangles for 2016–17 (blue) and 2017–18 (red) 157

Figure 108. Mean salinity profile using circles connected by a line, and the maximum and minimum temperature profiles using triangles for 2016–17 (blue) and 2017–18 (red) 158

Figure 109. Fall temperature profile using circles connected by a line, and the maximum and minimum temperature profiles using triangles for 2016–17 (blue) and 2017–18 (red) 159

Figure 110. Winter temperature profile using circles connected by a line, and the maximum and minimum temperature profiles using triangles for 2016–17 (blue) and 2017–18 (red) 160

Figure 111. Spring temperature profile using circles connected by a line, and the maximum and minimum temperature profiles using triangles for 2016–17 (blue) and 2017–18 (red) 161

Figure 112. Summer temperature profile using circles connected by a line, and the maximum and minimum temperature profiles using triangles for 2016–17 (blue) and 2017–18 (red) 162

Figure 113. Fall salinity profile using circles connected by a line, and the maximum and minimum temperature profiles using triangles for 2016–17 (blue) and 2017–18 (red) 162

Figure 114. Winter salinity profile using circles connected by a line, and the maximum and minimum temperature profiles using triangles for 2016–17 (blue) and 2017–18 (red) 163

Figure 115. Spring salinity profile using circles connected by a line, and the maximum and minimum temperature profiles using triangles for 2016–17 (blue) and 2017-–8 (red) 164

Figure 116. Summer salinity profile using circles connected by a line, and the maximum and minimum temperature profiles using triangles for 2016–17 (blue) and 2017–18 (red) 164

Figure 117. Compass rose plots of current speed and direction for 2016–17 (left) and 2017–18 (right) for (from top to bottom) M1, M2, M3, and M4 at near-surface depths (5 to 15 m). Directions are expressed as directions towards (e.g. Flow/drift toward the east has a 90° direction). 166

Figure 118. Compass rose plots of current speed and direction for 2016–17 (left) and 2017–18 (right) for (from top to bottom) M2, M3, and M4 at 150 m depth. Directions are expressed as directions towards (e.g. Flow/drift toward the east has a 90° direction). 167

Figure 119. Compass rose plots of current speed and direction for 2016–17 (left) and 2017–18 (right) for (from top to bottom) M3 and M4 at 250 m depth. Directions are expressed as directions towards (e.g. Flow/drift toward the east has a 90° direction). 168

Figure 120. Compass rose plots of current speed and direction at 5 m depth for the M1 site for fall (top), winter (top middle), spring (bottom middle), and summer (bottom) for 2016–17 (left) and for 2017–18 (right). Directions are expressed as directions towards (e.g. Flow/drift toward the east has a 90° direction) 171

Figure 121. Compass rose plots of current speed and direction at the M1 site for all three instances of fall measurements (left) and winter measurements (right) made at 5 m depth for the 2016–17 (top), 2017–18 (middle), and 2018–19 (bottom). Directions are expressed as directions towards (e.g. Flow/drift toward the east has a 90° direction). 172

Figure 122. Compass rose plots of current speed and direction at 10 m depth for the M2 site for fall (top), winter (top middle), spring (bottom middle), and summer (bottom) for 2016–17 (left) and for 2017–18 (right). Directions are expressed as directions towards (e.g. Flow/drift toward the east has a 90° direction) 173

Figure 123. Compass rose plots of current speed and direction at 15 m depth for the M3 site for fall (top), winter (top middle), spring (bottom middle), and summer (bottom) for 2016–17 (left) and for 2017–18 (right). Directions are expressed as directions towards (e.g. Flow/drift toward the east has a 90° direction) 174

Figure 124. Compass rose plots of current speed and direction at 15 m depth for the M4 site for fall (top), winter (top middle), spring (bottom middle), and summer (bottom) for 2016–17 (left) and for 2017–18 (right). Directions are expressed as directions towards (e.g. Flow/drift toward the east has a 90° direction) 175

Figure 125. Compass rose plots of current speed and direction at 150 m depth for the M2 site for fall (top), winter (top middle), spring (bottom middle), and summer (bottom) for 2016–17 (left) and for 2017–18 (right). Directions are expressed as directions towards (e.g. Flow/drift toward the east has a 90° direction) 177

Figure 126. Compass rose plots of current speed and direction at 150 m depth for the M3 site for fall (top), winter (top middle), spring (bottom middle), and summer (bottom) for 2016–17 (left) and for 2017–18 (right). Directions are expressed as directions towards (e.g. Flow/drift toward the east has a 90° direction) 178

Figure 127. Compass rose plots of current speed and direction at 250 m depth for the M3 site for fall (top), winter (top middle), spring (bottom middle), and summer (bottom) for 2016–17 (left) and for 2017–18 (right). Directions are expressed as directions towards (e.g. Flow/drift toward the east has a 90° direction) 179

Figure 128. Compass rose plots of current speed and direction at 150 m depth for the M4 site for fall (top), winter (top middle), spring (bottom middle), and summer (bottom) for 2016–17 (left) and for 2017–18 (right). Directions are expressed as directions towards (e.g. Flow/drift toward the east has a 90° direction) 180

Figure 129. Compass rose plots of current speed and direction at 250 m depth for the M4 site for fall (top), winter (top middle), spring (bottom middle), and summer (bottom) for 2016–17 (left) and for 2017–18 (right). Directions are expressed as directions towards (e.g. Flow/drift toward the east has a 90° direction) 181

Figure 130. Year-long mean vertically-averaged velocity vectors for each mooring, with the standard error ellipses, in 2016–2017 (left) and 2017–2018 (right) 183

Figure 131. Vertical sections of (a) year-long mean alongstream velocity; (b) potential temperature; and (c) salinity, overlain by mean potential density contours (black lines in kg m-3) for 2017–2018 184

Figure 132. Vertical sections of (a) year-long mean alongstream velocity; (b) potential temperature; and (c) salinity, overlain by mean potential density contours (black lines in kg m-3) for 2016–2017 184

Figure 133. Vertical sections of the mean percent occurrence of the water masses across the array for year 1 (left column) and year 2 (right column) 185

Figure 134. Seasonal variation of transports of the shelf current (blue curve) and the shelfbreak jet (red curve) in (a) 2016–2017 and (b) 2017–2018 186

Figure 135. Seasonal variation of water masses within the shelf current in (upper panel) 2016–2017 and (bottom panel) 2017–2018 187

Figure 136. Seasonal variation of water masses within the shelfbreak jet in (upper panel) 2016–2017 and (bottom panel) 2017–2018 188

Figure 137. Seasonal variation of the along-coast wind in (upper panel) 2016–2017 and (bottom panel) 2017–2018, using the ERA5 Data 189

Figure 138. Seasonal variation in ice concentration at m1 in (upper panel) 2016–2017 and (bottom panel) 2017–2018, using the AMSR2 Data 190

Figure 139. Percent occurrence of θ/S values using the mooring array data from the Alaskan Beaufort Sea for (left panel) 2016–2017 and (right panel) 2017–2018 191

Figure 140. Timeseries of 25-day low-passed wind stress curl averaged over Canada Basin in (upper panel) 2016–2017 and (bottom panel) 2017–2018, using the ERA5 Data 191

Figure 141. Compass rose plots of ice drift speed and direction for the M1 site for 2016–17 (left) and for 2017–18 (right). Directions are expressed as directions towards (e.g. Flow/drift toward the east has a 90° direction) 192

Figure 142. Compass rose plots of ice drift speed and direction for the M2 site for 2016–17 (left) and for 2017–18 (right). Directions are expressed as directions towards (e.g. Flow/drift toward the east has a 90° direction) 193

Figure 143. Compass rose plots of ice drift speed and direction for the M3 site for 2016–17 (left) and for 2017–18 (right). Directions are expressed as directions towards (e.g. Flow/drift toward the east has a 90° direction) 193

Figure 144. Compass rose plots of ice drift speed and direction for the M4 site for 2016–17 (left) and for 2017–18 (right). Directions are expressed as directions towards (e.g. Flow/drift toward the east has a 90° direction) 194

Figure 145. Compass rose plots of ice drift speed and direction at the M1 site for fall (top), winter (middle), and spring (bottom) for 2016–17 (left) and for 2017–18 (right). Directions are expressed as directions towards (e.g. Flow/drift toward the east has a 90° direction). 196

Figure 146. Compass rose plots of ice drift speed and direction at the M1 site for all three instances of fall measurements (left) and winter measurements (right) made for 2016–17 (top), 2017–18 (middle), and 2018–19 (bottom). Directions are expressed as directions towards (e.g. Flow/drift toward the east has a 90° direction). 197

Figure 147. Compass rose plots of ice drift speed and direction at the M2 site for fall (top), winter (middle), and spring (bottom) for 2016–17 (left) and for 2017–18 (right). Directions are expressed as directions towards (e.g. Flow/drift toward the east has a 90° direction). 198

Figure 148. Compass rose plots of ice drift speed and direction at the M3 site for fall (top), winter (middle), and spring (bottom) for 2016–17 (left) and for 2017–18 (right). Directions are expressed as directions towards (e.g. Flow/drift toward the east has a 90° direction). 199

Figure 149. Compass rose plots of ice drift speed and direction at the M4 site for fall (top), winter (middle), and spring (bottom) for 2016–17 (left) and for 2017–18 (right). Directions are expressed as directions towards (e.g. Flow/drift toward the east has a 90° direction). 200

Figure 150. Number of keels versus Julian day from top to bottom for M2 2016–17, M3 2016–17, M3 2017–18, M4 2016–17, and M4 2017–18 202

Figure 151. Probability density function of the maximum keel draft (for a 5 m threshold) for 2016–17 (left) and 2017–2018 (right) for M2 (top), M3 (middle), and M4 (bottom) 203

Figure 152. Number of ice keels exceeding a 5 m draft by month at the M3 and M4 sites in each year . 204

Figure 153. Mean ice draft of keels exceeding a 5 m draft by month at the M3 and M4 sites in each year 205

Figure 154. Maximum ice keel draft by month at the M3 and M4 sties in each year 205

Figure 155. Seasonal variation in ice concentration at the two sites which had ice profilers in both years 206

Figure 156. Overlay of nitrate time-series by season for the M1 site 207

Figure 157. Overlay of nitrate time-series by season for the M2 site 208

Figure 158. Minimum 25%, median, 75%, and maximum nitrate concentrations for the fall season 209

Figure 159. Minimum 25%, median, 75%, and maximum nitrate concentrations for the winter season .. 209

Figure 160. Minimum 25%, median, 75%, and maximum nitrate concentrations for the spring season .. 210

Figure 161. Minimum 25%, median, 75%, and maximum nitrate concentrations for the summer season 210

Figure 162. Daily mean relative backscatter (a and c) and standardized relative backscatter (b and d) for the two moorings from the 2016–2017 deployment (a and b) and the 2017–2018/19 deployment (c and d) 212

Figure 163. Daily mean relative backscatter and standardized relative backscatter for the four moorings in the two years, plotted *vs.* day of the year 213

Figure 164. Daily mean relative backscatter and standardized relative backscatter for the four moorings in the two years, plotted *vs.* day of the year. 213

Figure 165. On the left, echogram of 200 khz backscatter (S_v) corresponding to zooplankton at site M3 in the Beaufort Sea, during the 2016/2017 (upper panel) and 2017/2018 (lower panel) season—on the right, corresponding Nautical Area Scattering Coefficient (NASC) as a function of time for zooplankton at site M3 in the Beaufort Sea, during the 2016/2017 (upper panel) and 2017/2018 (lower panel) season 214

Figure 166. Echogram of 125 kHz Backscatter (S_v) showing daily migration pattern at site M3 in the Beaufort Sea, from October 11 to 14, 2016 (upper panel) and from October 12 to 16, 2017 (lower panel) 215

Figure 167. Nautical Area Scattering Coefficient (NASC) as a function of time for adult Arctic cod at site M3 in the Beaufort Sea, during the 2016–2017 (upper panel) and 2017–2018 (lower panel) season..... 217

Figure 168. Echogram of 38 kHz backscatter (S_v) corresponding to adult Arctic cod at site M3 in the Beaufort Sea, during the 2016–2017 (upper panel) and 2017–2018 (lower panel) season..... 218

Figure 169. Echogram of 125 kHz backscatter (S_v) corresponding to juvenile Arctic cod at site M3 in the Beaufort Sea, during the 2016–2017 (upper panel) and 2017–2018 (lower panel) season..... 219

Figure 170. Nautical Area Scattering Coefficient (NASC) at 125 kHz as a function of time for juvenile Arctic cod at Site M3 in the Beaufort Sea, during the 2016–2017 (upper panel) and 2017–2018 (lower panel) season..... 220

Figure 171. Number of weeks per month with marine mammal detections for year 1 (2016–2017) and year 2 (2017–2018) deployment 221

Figure 172. The linkages between biophysical components of the marine ecosystem of the Canadian Beaufort Sea 228

Figure173. The Canadian Beaufort shelf and the Alaskan Beaufort shelf, separated by the Mackenzie Canyon 229

Figure 174. Total monthly duration of upwelling and downwelling conditions at the MARES mooring array between October 2016–2018..... 230

Figure 175. Daily maximum, minimum and mean flows, and standard deviation of the daily Mackenzie River discharges during 1973–2011 (Yang et al. 2015) 232

Figure 176. Along canyon axis salinity and CDOM measurements for an ocean glider in early September 2016 233

Figure 177. Glider observation of Chlorophyll-a fluorescence and dissolved oxygen saturation along the MARES mooring line in early September 2016 235

Figure 178. Marine fish assemblages and associated water mass habitats on the Canadian Beaufort shelf and slope (Majewski et al. 2017) 239

Figure 179. Daylight hours at different latitudes 243

Figure 180. Weekly time series of mooring data collected between October 2016–2018 (see appendix A for higher resolution figures) 246

Figure 181. Configuration of the mooring array in the vertical plane..... 252

Figure 182. (Middle) Timeseries of M3-M4 potential density difference between October 2016 –2018, where periods of canyon upwelling are marked in blue and canyon downwelling in red. Periods of coastal upwelling/downwelling are marked by the light-blue/yellow bars. (Top) The indices of the coastal and canyon upwelling are represented by light-blue bars and blue dots, respectively. (Bottom) The indices of the coastal and canyon downwelling are represented by yellow bars and red dots, respectively..... 253

Figure 183. Along-coast wind (upper-panels, blue), 25-day low-passed wind stress curl in the Canada Basin (upper-panels, red), near-bottom potential density (PD) anomaly on the shelf (lower-panels, blue) and mid-depth PD difference on the slope (lower-panels, red) for (a) coastal and canyon upwelling; (b)

coastal upwelling - canyon downwelling; (c) coastal and canyon downwelling; and (d) coastal downwelling - canyon upwelling. 255

Figure 184. Vertical sections averaged over the composite events for the four scenarios described in the text..... 256

Figure 185. Timeseries of different variables during the September 2017 event 258

Figure 186. Timeseries of different variables during the September 2017 event 260

Figure A-1. Time series plots of (from top to bottom) air temperature, sea ice concentration & marine mammal presence, ice keel # & depth standard deviation, and Mackenzie River discharge of the MARES mooring deployment period..... 284

Figure A-2. Time series plot of alongshore winds with upwelling period highlights, monthly upwelling counts and durations, M3 temperature measurements and M3 salinity measurements. 285

Figure A-3. Time series plots (from top to bottom) of nitrate, chlorophyll-a fluorescence, normalized acoustic backscatter from ADCP, and AZFP NASC zooplankton, juvenile cod, and adult cod. 286

List of Tables

Table 1. Consultation meetings and permits for MARES work in the Canadian Beaufort Sea 4

Table 2. Locations of the MARES 2017-2018 biophysical moorings 4

Table 3. Summary of the recovered moorings that were operated 2017–2018 5

Table 4. Summary of the recovered mooring components at M2, M3, and M4 (2017–2018) 6

Table 5. Summary of the recovered mooring components at M1 (2017–2019) 7

Table 6. Summary of MARES 2017–2019 data size and volume, by platform 9

Table 7. Summary of MARES 2017–2019 data set by instrument and parameter 9

Table 8. Selected 2017–2018 M1 and M2 ADCP configuration parameters 11

Table 9. Selected 2017–2018 M3 and M4 ADCP configuration parameters 11

Table 10. Bin depth referenced to mean sea level as derived from the pressure time-series measured by the pressure sensor onboard the ADCPs at M1 and M2 during 2017–2019 deployment 13

Table 11. Bin depth referenced to mean sea level as derived from the pressure time-series measured by each ADCP during the 2017–2018 deployment 14

Table 12. Count and fraction of data records modified before time-averaging for each ocean current bin for M1 and M2 during 2017–2018 deployment, extending into 2019 at M1. 18

Table 13. Count and fraction of data records modified before time-averaging for each ocean current bin for M3 and M4 during 2017–2018 deployment 19

Table 14. Count and fraction of data records modified after time-averaging for each ocean current bin for M1 and M2 during 2017–2018 deployment, extending into 2019 at M1 22

Table 15. Count and fraction of data records modified after time-averaging for each ocean current bin for M3 and M4 during 2017–2018 deployment 23

Table 16. Summary of edited ice velocity time-series records for the M1 and M2 sites during 2017–2018 deployment, extending into 2019 at M1 25

Table 17. Summary of edited ice velocity time-series records for the M3 and M4 quartermasters during 2017–2018 deployment 25

Table 18. Values used in the derivation of water level time-series for each measurement site during 2017–2018 deployment 26

Table 19. Parameters used in calculation of volume backscattering (Sv) and settings used for each ADCP during 2017–2019 deployment 33

Table 20. Key M2 IPS configuration parameters during 2017–2018 deployment 36

Table 21. Key M3 IPS configuration parameters during 2017–2018 deployment 37

Table 22. Key M4 IPS configuration parameters during 2017–2018 deployment 38

Table 23. Summary of the two main stages of IPS processing (range time-series and ice draft time-series) for M2 during 2017–2018 deployment, giving number of data records having errors that were detected and edited 41

Table 24. Summary of the two main stages of IPS processing (range time-series and ice draft time-series) for M3 during 2017–2018 deployment, giving number of data records having errors that were detected and edited 42

Table 25. Summary of the two main stages of IPS processing (range time-series and ice draft time-series) for M4 during 2017–2018 deployment, giving number of data records having errors that were detected and edited 43

Table 26. Key deployment parameters for the CT sensors used on the M2, M3 and M4 moorings during 2017–2018 deployment, extending into 2019 at M1 45

Table 27. Water sample nitrate laboratory results taken during 2017–2019 48

Table 28. Calibration measurements after instrument recovery 49

Table 29. Flag definitions used in the fully quality controlled time-series of SUNA nitrate results 51

Table 30. Summary of AZFP data collected and analyzed during 2016-2017, and 2017–2018 deployments 52

Table 31. Ice speed statistics (cm/s) by month and for the period of deployment for M1 from 2017–2019 100

Table 32. Ice speed statistics (cm/s) by month and for the period of deployment for M2 from 2017–2018 101

Table 33. Ice speed statistics (cm/s) by month and for the period of deployment for M3 from 2017–2018 102

Table 34. Ice speed statistics (cm/s) by month and for the period of deployment for M4 from 2017–2018 103

Table 35. The horizontal spatial extents of episodes of continuous ice velocity at M2 during the 2017–2018 deployment 109

Table 36. horizontal spatial extents of episodes of continuous ice velocity at M3 during the 2017–2018 deployment 110

Table 37. Horizontal spatial extents of episodes of continuous ice velocity at M4 during the 2017–2018 deployment 111

Table 38. Mean and maximum ice draft values at each site during the full 2017–2018 deployment, extending into 2019 at M1 114

Table 39. M2 draft time series statistics and ice concentrations from 2017–2018 115

Table 40. M3 draft time series statistics and ice concentrations from 2017–2018 115

Table 41. M4 draft time series statistics and ice concentrations from 2017–2018 116

Table 42. Carbon parameters from seawater samples taken at mooring site M1 in 2017 and 2019 123

Table 43. Largest easterly wind-forcing events for 2016–2017 148

Table 44. Largest westerly wind-forcing events for 2016–2017 149

Table 45. Largest easterly wind-forcing events for 2017–2018 149

Table 46. Largest westerly wind-forcing events for 2017–2018 150

Table 47. Summary of general flow characteristics by depth and site 169

Table 48. Summary of the seasonal variability in the currents 182

Table 49. Nitrate statistics by year for the M1 and M2 sites 207

Table 50. Timing and duration of the cryo-seasons during the two MARES study years (highlighted cells indicate major differences between the two years). 245

Table 51. Summary of Currents Trends and Future Projections of Key Physical Attributes 267

List of Abbreviations and Acronyms

ADCP	Acoustic Doppler Current Profilers
ACW	Alaskan coastal water
AMSR2	Advanced Microwave Scanning Radiometer 2
AOOS	Alaska Ocean Observing System
AON	Arctic Observing Network
ARI	Aurora Research Institute
ASL	ASL Environmental Sciences
AU	absorption units
AURAL	Autonomous Underwater Recorder for Acoustic Listening
AW	Atlantic water
AZFP	Acoustic Zooplankton and Fish Profiler
BOEM	Bureau of Ocean Energy Management
BSW	Bering summer water
CDOM	colored dissolved organic matter
CHS	Canadian Hydrographic Service
CRM	Certified Reference Materials
CT	conductivity, temperature
CTD	conductivity, temperature, depth
dB	decibels
DFO	Fisheries and Oceans Canada
DIC	Dissolved Inorganic Carbon
DIW	deionized water
DOI	US Department of the Interior
DVM	Diel Vertical Migration
ECCC	Environment Canada Climate Change
EISC	Environmental Impact Screening Committee
ESP	Environmental Studies Program
ESPIS	Environmental Studies Program Information System
FJMC	Fisheries Joint Management Committee
FSRG	DFO Frozen Seas Research Group
HTC	Hunters and Trappers Committee
IFA	Inuvialuit Final Agreement
IGC	Inuvialuit Game Council
IPS	Ice Profiling Sonar
ISR	Inuvialuit Settlement Region
kHz	kilohertz
JAMSTEC	Japan Agency for Marine Earth Science and Technology
LTSA	long-term spectral averages
MARES	Marine Arctic Ecosystem Study
MWM	melt water / meteoric water
NASC	Nautical Area Scattering Coefficient
NCEI	National Center for Environmental Information

NCEP	National Centers for Environmental Prediction
NOPP	National Oceanographic Partnership Program
NVWW	newly ventilated winter water
OARC	Ocean Acidification Research Center
ONR	Office of Naval Research
QA/QC	quality assurance/quality control
RMSe	root mean square error
RWW	remnant winter water
SAMI	Submersible Autonomous Moored Instrument
SUNA	Submersible Ultraviolet Nitrate Analyzer
TA	Total Alkalinity
TO	task order
TVG	time-varied-gain
UAF	University of Alaska Fairbanks
USARC	US Arctic Research Commission
USCG	US Coast Guard
UW	University of Washington
WCS	Wildlife Conservation Society
WHOI	Woods Hole Oceanographic Institution

1 Overview

1.1 Background

The US Department of the Interior, Bureau of Ocean Energy Management (BOEM) and its partners, Office of Naval Research (ONR), National Oceanographic Partnership Program (NOPP), Shell Oil Company, US Arctic Research Commission (USARC), US Coast Guard (USCG), seek to advance knowledge of the arctic marine ecosystem. The Marine Arctic Ecosystem Study (MARES) arose from increased attention on climate change, energy development, and related sustainability issues in the arctic. Results from this study are intended to inform government, industry, and communities on regulatory needs, operational challenges and resource management, and provide important context for economic development, environmental protection, sustainability of local communities, and health and safety.

The focus area of MARES is the eastern Beaufort Sea shelf from Kaktovik to the Mackenzie Delta coastline to a depth of 1,000 m. The overarching scientific goal of MARES, as initially envisioned, was to increase our understanding of the impact of physical drivers (ocean, ice, atmosphere) on the trophic structure and function of the marine ecosystem on the Beaufort shelf with special attention to the implications on marine mammals and local communities. The intent was to implement an integrated, multidisciplinary study combining retrospective analyses, field studies, modeling, and synthesis spanning atmosphere, ice, physical, chemical, and biological oceanography from benthos to fish, marine mammals, and people.

The MARES program included task orders (TOs) for tagging ice seals with CTD fluorometer tags (TO2; Wiese et al. 2017; Gryba et al. 2019), a glider deployment and benthic sampling in 2016 (TO3; Wiese et al. 2018), and two full years of mooring deployment, the first year from 2016–2017 (TO5), and the second from 2017–2018, with one mooring extending into 2019 (TO4; detailed in Section 2 and 3 below). The results from the first year of the mooring deployment were detailed in Wiese et al. (2019), and some of the data are revisited in this report in Section 3.2 in order to explore seasonal and interannual patterns and variability, as well as their underlying drivers.

1.2 Goals and Objectives

This report constitutes the final report of MARES. According to the TO4 objectives, it documents:

- Retrieval of the moorings redeployed in the eastern Beaufort Sea in October 2017
- Quality assurance/quality control (QA/QC) methodology on Year 2 data (2017–2018)
- Results from the preliminary analysis and interpretation of the data (general characteristics of the data) collected during the second year of deployment

In addition to documenting these Year 2 efforts, this report also refers back to the initial overall program goals and objectives, and provides a first level integration of the findings reported on in previous Task Orders (Section 4 and 5), and:

- Describes seasonal and interannual patterns and variability for different sensors deployed over the length of the program
- Explores some of the drivers behind the observed patterns and variability
- Discusses some of the possible implications of these system characteristics and observed changes in this marine system to indigenous use in Alaska and the Inuvialuit Settlement Region

1.3 Mooring Program 2017–2018 (Year 2)

The 2017-2018 mooring program focused on the recovery and demobilization of the previously deployed moorings (Figure 1) and preliminary data analysis of the newly recovered data. As such, the work described in this section represents a collaborative effort between Stantec, Kavik-Stantec, ASL Environmental Sciences (ASL), the Woods Hole Oceanographic Institution (WHOI), SeaStar Biotech, the University of Washington (UW), the University of Alaska Fairbanks (UAF), AXIOM Data Science, and Fisheries and Oceans Canada (DFO).

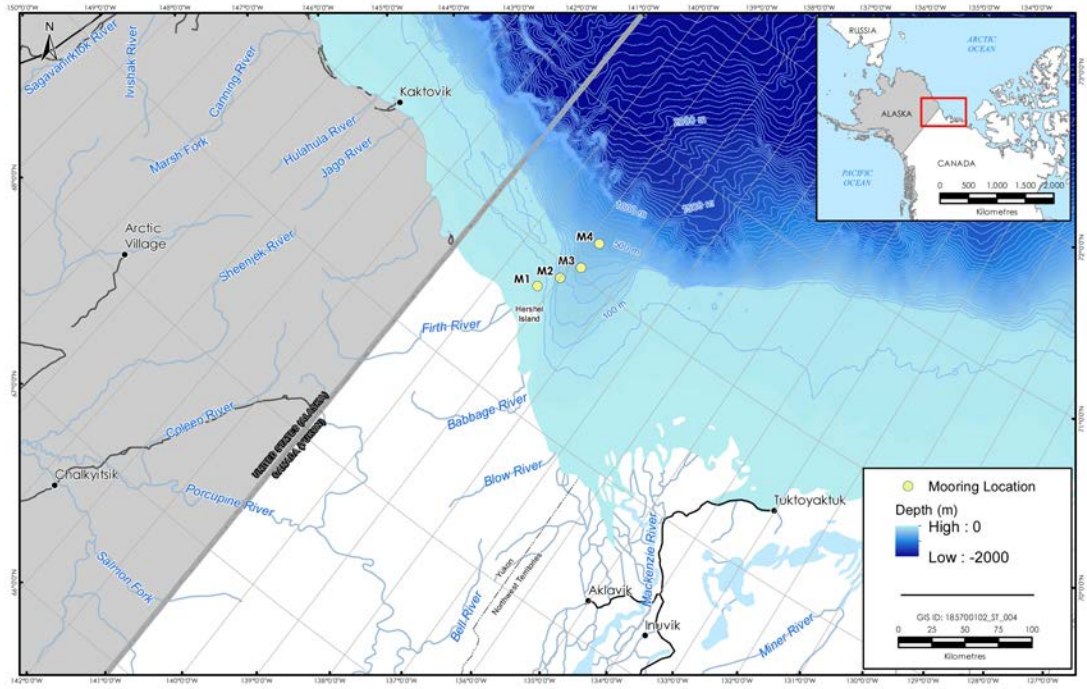

Figure 1. Location of the MARES 2017–2018 mooring array

1.4 Regional Setting

In Canada, the MARES program is entirely within the Inuvialuit Settlement Region (ISR) established in the Inuvialuit Final Agreement (IFA) through the Canadian Federal Government's 1984 *Western Arctic Claims (Inuvialuit) Settlement Act* (Department of Indian and Northern Affairs Canada 1984).

The Environmental Impact Screening Committee (EISC) reviews projects to determine if they meet the IFA definition of development and have the potential for a significant negative environmental impact. The screening process includes feedback from and consultation with the appropriate Inuvialuit co-management bodies (e.g., Fisheries Joint Management Committee [FJMC]), Inuvialuit organizations (e.g., community Hunters and Trappers Committees [HTCs]), and the Inuvialuit Game Council [IGC]), communities, government, and regulatory bodies. Only after this process is complete can permitting agencies issue permits to the project. In addition, research in the Northwest Territories is permitted by the Government of the Northwest Territories through the *Northwest Territories Scientist Act*, administered by the Aurora Research Institute (ARI) which issues the *Northwest Territories Scientific Research Licence*. Issuance of this license requires input from Inuvialuit organizations, government agencies, and project approval from the EISC.

1.5 Community Consultation

EISC and ARI consultation requirements for the MARES program, conducted in the Canadian Beaufort, were met by meeting with the Inuvialuit Game Council that represents the Inuvialuit regionally on wildlife, habitat, and environmental interests, and the local HTCs in the communities of Aklavik, Inuvik, and Tuktoyaktuk that were potentially affected by the program (Table 1). A record of these meetings was included in the EISC and ARI applications.

In 2015 and 2016 Kavik-Stantec Inc. consulted with the IGC and HTCs. The IGC and HTCs did not have any concerns with the program and asked to be updated on the project's progress and results. Consultations in 2017 were conducted to meet ARI permit requirements and update the committees on the project. Stantec submitted a Memo to the IGC on June 9, 2017, which provided requested information on the Alaska Ocean Observing System (AOOS) and data access after completion of the program.

Consultation meetings on the final results were conducted in the first half of 2020. The presentations at these meetings provided a summary of the program results. The IGC were sent the final report and a means to access the project data once publicly available to add to their ISR database.

1.6 Permitting

Stantec and Kavik-Stantec Inc. gathered all necessary permits and permissions as outlined in the contract agreement including applicable permits from the Northwest Territories (ARI) (Table 1).

The MARES program was added to a collaborative agreement between ASL and DFO to conduct oceanographic research in the Canadian Beaufort Sea. The EISC determined that the MARES program did not meet the definition of development, as defined under the IFA, and was therefore not subject to an environmental impact screening. With this approval, the ARI issued a Northwest Territories Scientific Research Licence. This license was renewed annually, with the last renewal in July of 2018.

Table 1. Consultation meetings and permits for MARES work in the Canadian Beaufort Sea

Date	Group	Permit
Consultation Meetings		
2015-12-18	Inuvialuit Game Council	
2016-06-22	Inuvik HTC	
2016-06-23	Tuktoyaktuk HTC	
2016-06-24	Aklavik HTC	
2017-03-17	Inuvialuit Game Council	
2017-04-12	Tuktoyaktuk HTC	
2017-04-13	Aklavik HTC	
2017-04-20	Inuvik HTC	
2020-06-11	Aklavik HTC	
2020-10	Inuvialuit Game Council	
Permits		
2016-08-02	EISC	Project pre-screening approval
2016-08-18	ARI—GNWT	Northwest Territories Scientific Research Licence
2017-01-12	ARI—GNWT	Northwest Territories Scientific Research Licence
2018-07-19	ARI—GNWT	Northwest Territories Scientific Research Licence
NOTES: HTC = Hunters and Trappers Committee EISC = Environmental Impact Screening Committee ARI GNWT = Aurora Research Institute - Government of the Northwest Territories, Canada		

2 Methods and Equipment

2.1 Mooring Retrieval Activities

The MARES 2017–2018 biophysical mooring array was a collaborative effort between Stantec, ASL, WHOI, UAF, SeaStar Biotech, and UW, with vessel support from DFO. The moorings were deployed in the Eastern Beaufort Sea in the region of the Mackenzie Trough (Table 2), at the same locations as the moorings deployed 2016–2017. The inshore mooring, M0 deployed 2016–2017, was not redeployed in 2017–2018.

Table 2. Locations of the MARES 2017-2018 biophysical moorings

Mooring	Operator	Latitude [°N]	Longitude [°W]	Water depth [m]
M1	ASL	69° 46.306´	139° 15.491´	40
M2	ASL	69° 54.528´	138° 59.914´	175
M3	ASL	70° 02.912´	138° 47.295´	300
M4	ASL	70° 15.089´	138° 47.358´	440

The moorings were deployed during Leg 3 of the 2017 *CCGS Sir Wilfrid Laurier* Arctic Expedition. The science team was headed by Dr. Humfrey Melling of Fisheries and Oceans Canada (DFO). The DFO Fresh Water Institute, DFO Frozen Seas Research Group (FSRG), Wildlife Conservation Society (WCS) of Canada, Japan Agency for Marine Earth Science and Technology (JAMSTEC), ArcticNet, and BOEM had research sites along the cruise route. Environment Canada Climate Change (ECCC) was sampling for water and air contaminants along the route, and the Canadian Hydrographic Service (CHS) was doing selective mapping of the bottom bathymetry.

The TO4 mooring array retrieval fieldwork took place during Leg 3 of the *CCGS Sir Wilfrid Laurier's* cruise between September 25 and October 18, 2018. This work was performed by ASL senior oceanographer K. Borg with support from the crew of the *CCGS Sir Wilfrid Laurier*.

During the cruise there was a large tongue of ice blocking passage out of the western Amundsen Gulf. The ice was too heavy for the *CCGS Sir Wilfrid Laurier* to break through on its own.

The presence of the ice blocked access to many sites and caused delays to all programs onboard. For the MARES program, the prolonged ice delay meant there was insufficient time to complete the recovery of all four of the moorings. Moorings M2, M3, and M4 were recovered October 10, 2018, and it was not possible to recover the shallowest mooring, M1.

During the recovery of the moorings, the acoustic releases were first interrogated to confirm the mooring location. Once the ship was suitably positioned, the moorings were released. Once all the gear was observed at the surface, the ship came alongside the mooring. A grappling hook was used to bring the mooring in reach of the derrick's hook, and the mooring was brought on board. The mooring was then disassembled. Large items were put away so that they would not interfere with continued operations, and the instruments were cleaned and inspected. Instrument time checks were performed, and data was downloaded. The initial inspections showed nothing suspect. A summary of the site locations and release times are provided in Table 3.

Table 3. Summary of the recovered moorings that were operated 2017–2018

Mooring	Latitude [N]	Longitude [W]	Water depth [m]	Date [yyyy-mm-dd]	Time [UTC]
M2	69° 54.528´	138° 59.914	175	2018-10-10	20:20
M3	70° 02.912´	138° 47.295´	300	2018-10-10	22:35
M4	70° 15.089´	138° 47.358´	440	2018-10-11	00:44
NOTE: Time is when each mooring was released.					

Table 4 lists the components on each of the moorings and the results of the preliminary inspection of the data logged on the sensors. The physical condition of all sensors was inspected upon recovery and found to be in good working condition. A full diagnosis of the data was carried out as part of the data processing phase for each data set.

Table 4. Summary of the recovered mooring components at M2, M3, and M4 (2017–2018)

Mooring	Equipment	Serial Number	Depth [m]	Start date [yyyy/mm/dd]	End date [yyyy/mm/dd]	Data Size (bytes)	Comments
M2	IPS5	51049	40	2017/09/25	2018/10/11	5,855,377,210	
	SUNA	252	40	2017/09/30	2018/10/11	437,744,224	
	SBE37	11312	40	2017/09/25	2018/10/13	813,004	
	RBR XR-420	17308	57	2017/09/25	2018/10/14	2,076,045	
	300 kHz ADCP	10985	59	2017/10/01	2018/10/12	514,238,426	Loss of upper water column in mid-winter- low backscatter
	RBR Concerto	60176	74	2017/09/25	2018/10/14	9,605,120	
	RBR XR-420	17365	91	2017/09/25	2018/10/14	2,075,916	
	RBR Concerto	60177	109	2017/09/25	2018/10/14	9,596,928	
	RBR Concerto	60175	126	2017/09/25	2018/10/14	9,588,736	
	RBR XR-420	17111	143	2017/09/25	2018/10/14	308,855	
	300 kHz ADCP	6593	162	2017/10/01	2018/10/11	401,727,704	Frequent drop-outs in the mid to upper-water column
	SBE37	11311	162	2017/09/25	2018/10/13	813,066	
	AURAL	93LF	164	2017/10/03	2018/09/28	254,930,784,256	
	AZFP (125/200/400/779 kHz)	55120	166	2017/10/02	2018/10/11	29,720,069,337	
M3	IPS5	51092	52	2017/09/25	2018/10/11	6,742,849,109	
	SBE37	11313	52	2017/09/25	2018/10/13	812,908	
	AZFP	55054	59	2017/09/25	2018/10/11	25,259,178,840	
	QM ADCP	17898	104	2017/10/01	2018/10/12	261,810,159	Minor short-lived data gaps near the surface, mostly in the winter
	SBE37	12282	132	2017/09/25	2018/10/13	812,577	
	SBE37	13596	192	2017/09/25	2018/10/13	812,863	
	SBE37	10754	252	2017/09/25	2018/10/13	812,710	
	LR ADCP	12962	283	2017/10/01	2018/10/12	26,155,248	A few data gaps near-surface.
	AZFP (38Hz)	55088	288	2017/09/30	2018/10/11	22,269,689,578	
M4	IPS5	51089	51	2017/09/25	2018/10/11	6,739,342,906	
	SBE37	13186	51	2017/09/25	2018/10/13	812,654	
	QM ADCP	16157	101	2017/10/01	2018/10/12	261,784,770	Gaps in the upper water column, especially winter.
	SBE37	13689	130	2017/09/25	2018/10/13	812,820	
	SBE37	10755	190	2017/09/30	2018/10/13	812,842	
	SBE37	10756	250	2017/09/30	2018/10/13	812,754	
	LR ADCP	17441	331	2017/10/01	2018/10/12	26,156,694	A few data gaps near-surface.

On October 10, 2018, the *CCGS Louis S. St-Laurent* successfully escorted the *CCGS Sir Wilfrid Laurier* through the worst of the ice, leaving the MARES M1 mooring in place. Once it became clear that M1 would not be recovered, other options for recovering the mooring were investigated. Dr. Robert Pickart of WHOI was planning to be in the area aboard the *USCGC Healy* in early November 2018 and agreed to lead a recovery attempt. Arrangements were also made to ensure as many supporting water samples and CTD casts, which had been planned in conjunction with the initial recovery, would also be completed. A full day attempt was made, but on November 5, 2018, word came that the *USCGC Healy* was unable to reach the M1 site due to heavy ice conditions, leaving the mooring in place until the next open water season.

The mooring at site M1 remained in place until a recovery was planned as part of the *CCGS Sir Wilfrid Laurier* 2019 summer cruise. The M1 mooring was recovered on July 27, 2019 by ASL mooring technician J. Bartlett with support from the crew of the *CCGS Sir Wilfrid Laurier*. Fortunately, there was enough battery power and data storage, so that the majority of the sensors on the mooring continued sampling into 2019, in some instances, adding almost a full additional year of data (Table 5). Unfortunately, the SAMI-CO_2 failed for the entire deployment period and no data were recovered.

Table 5. Summary of the recovered mooring components at M1 (2017–2019)

Mooring	Equipment	Serial Number	Depth (m)	Start Date	End Date	Data Size (bytes)	Percentage of Data Recovered (%)
M1	RBR XR-420	15282	16	2017/10/02	2019/07/27	2,414,476	100
	RBR XR-420	09685	22	2017/10/07	2019/07/27	3,621,263	100
	RBR XR-420	17096	28	2017/10/02	2019/07/27	3,621,341	100
	SBE37	12123	36	2017/10/03	2019/07/27	4,381,585	100
	ADCP	18071	35	2017/10/02	2019/02/11	494,037,099	100
	RBR Concerto	66108	37	2019/07/27	2019/07/27	1,511,424	100
	SAMI	0087	36	2017/10/03	NA	0	0

2.2 Data Management

Key objectives for the MARES data management were to adaptively produce and update a data management plan, oversee data ingestion into the AOOS MARES Research Workspace, and archive and publish data in appropriate locations. With these ends in mind, the data management workflow for TO4 began in 2017, during the initial planning phases for 2017–2018 mooring deployment and be concluded with MARES data sets delivered to BOEM, made publicly available via interactive visualizations in the AOOS Arctic Data Portal (https://portal.aoos.org/old/arctic), and archived in the National Center for Environmental Information (NCEI)[1].

[1] https://www.ncei.noaa.gov/

2.2.1 Data Management Workflow

Data management tasks were divided into three semi-overlapping focuses: planning and orientation; raw data; and preliminary data and metadata.

2.2.2 Planning and Orientation

In the planning and orientation phase of data management tasks, the data management team at Axiom Data Science reviewed deployment plans for the 2017–2018 moorings to understand planned instrumentation, expected data types, and science team responsibility for each mooring and instrument. With this information, Axiom staff updated project data management plans and internal project management notes to be ready to receive data once it had been recovered from the retrieved moorings. Data management personnel hosted several small-group or one-on-one calls and webinars to provide an introduction and orientation to the Research Workspace (Workspace) for MARES scientists and program administrators.

These informational calls reminded science team members how to use and navigate the Research Workspace (the web-based data management platform, described below); and discussed project structure, organization, and individual membership. After mooring retrieval, the data management team hosted additional webinars to reorient project scientists to the Workspace while demonstrating features and reviewing the data handling processes and the management workflow.

The Workspace is a web-based platform developed at Axiom Data Science for collaboratively managing science projects through the entire data lifecycle. It allows research scientists, data managers, and program administrators a secure way to store and organize data within individual projects and research campaigns; to create, share, and execute reproducible numerical workflows; and to generate robust metadata, and to publish finalized data products to custom data catalogs and national data archives. Projects within the Workspace can be shared with selected users, with research campaigns, or with entire organizations. Specific permissions may be set on an individual or group basis. This allows preliminary results and interpretations to be shared by geographically- or scientifically-diverse individuals working together on a project or program before the data are shared with the public, and gives program leads and other stakeholders a front-row view of how their programs are progressing through time. From the beginning, the MARES program has used the Workspace to store, share, track, and document data generated under each Task Order.

2.2.3 Raw Data

Upon return from the mooring retrieval cruise in October 2018, an FTP site was set up from which the data management team ingested the data from the three recovered moorings into the Workspace, where it was organized by mooring and instrument. Notifications were sent to the MARES teams that raw data were now available for QA/QC and preliminary analysis. Raw data from the fourth mooring, M1, were added to the FTP site, ingested by Axiom and uploaded into the Workspace shortly after the mooring was recovered in late-July 2019.

The data from the 2017–2019 moorings and related activities resulted in 31,717 raw data files uploaded into the Workspace (Table 6 and Table 7). These represented biophysical data collected from 39 distinct instruments on the 4 MARES moorings, from CTD casts and water samples acquired during the 2018 mooring recovery and deployment cruises, and from meteorological models of the study area.

Table 6. Summary of MARES 2017–2019 data size and volume, by platform

Platform	Raw Files	Raw Volume (GB)	Preliminary Files	Preliminary Volume (GB)
M1	688	1.633	20	0.138
M2	11991	292.638	180	4.262
M3	18600	54.592	271	4.255
M4	432	7.051	109	4.322
Met Data	6	0.017	6	0.001

Table 7. Summary of MARES 2017–2019 data set by instrument and parameter

Data Type	Parameters	Raw Data Files	Raw Data Volume (GB)	Preliminary Data Files	Preliminary Data Volume (GB)
ADCP	ocean currents	27	3.063	19	1.411
CT	conductivity (salinity), temperature	85	0.094	40	0.15
SUNA	Nitrate	1058	1.211	5	0.004
AURAL	passive acoustic recordings	2161	254.931		0
AZFP	zooplankton, fish profiles	27163	77.264	225	0.078
IPS	sea ice draft, temperature, distance to ice, distance to water	1177	19.339	278	11.252
CTD Casts	temperature, conductivity (salinity), pressure	17	0.01	8	0.001
Water Samples	Nitrate	0	0	1	0
Modeled Met Data	air temperature, atmospheric pressure, wind velocity	12	0	6	0.001

2.2.4 Preliminary Data and Metadata

Members of the MARES science team downloaded raw data from the Workspace to their local workstations to perform quality control processes and begin their analyses. Throughout the preliminary data phase, the data management team remained in contact with MARES scientists to provide reminders about expected data and metadata, to advise on data formatting to meet BOEM requirements, to ensure data sets are ready for long-term preservation, and to review and provide feedback on metadata authored by scientists. Once quality-controlled data were delivered (586 files, see Table 6 and Table 7), the data management team ensured that data sets were documented with descriptive, standards-compliant ISO 19115/19139 metadata. This work ensured that data collected, produced or consolidated through the MARES effort was managed throughout its lifecycle using an established and agreed upon data administration system for storage and organization during the project; and that data will be archived according to BOEM requirements. The data management team also created and maintained a data and metadata inventory to provide the project management team with a status update on data delivery and metadata generation. QA/QC'd data and metadata for the 2017–2019 moorings were delivered to BOEM in October 2019.

2.3 Quality Assurance/Quality Control (QA/QC) on Year 2 (2017–2019) Data

QA/QC of year 1 (2016–2017) data is detailed in Wiese et al. (2019). Although the process was very similar for the 2017-2019 data sets, not all sensors were the same and thus some differences occurred, or some procedures were not necessary at all. For completeness, we provided a full account of the QA/QC procedures for the 2017–2019 data, organized by data type, even if some are equal to those previously reported.

2.3.1 Acoustic Doppler Current Profiler (ADCP)

ADCPs provide precise measurements of both horizontal and vertical components of ocean currents at many levels within the water column (Figure 2). The ADCP instruments measure velocity by detecting the Doppler shift in acoustic frequency, arising from water current or ice movements, of the backscattered returns of four upward transmitted acoustic pulses slanted 20º from vertical. The ADCPs deployed at the four mooring sites differed between mooring locations. The ADCPs at M1 and M2 were 300 kHz ADCPs (RDI Workhorse). One was deployed on a tautline mooring (M1) 9 m off the bottom at 35 m water depth and surveyed the full water column. Two of the instruments were deployed on a tautline mooring (M2) at 58 m and 169 m depth.

At M3 and M4 two ADCPs were used: a 150 kHz Workhorse Quartermaster approximately midway, at 110 m and 97 m, respectively, and a 75 kHz Workhorse Long Ranger at the bottom, approximately at 287 m and 334 m, respectively. The ADCP instruments, operating in conventional water column data acquisition mode with bottom-tracking mode enabled, provided time series measurements of three-dimensional currents and ice velocity.

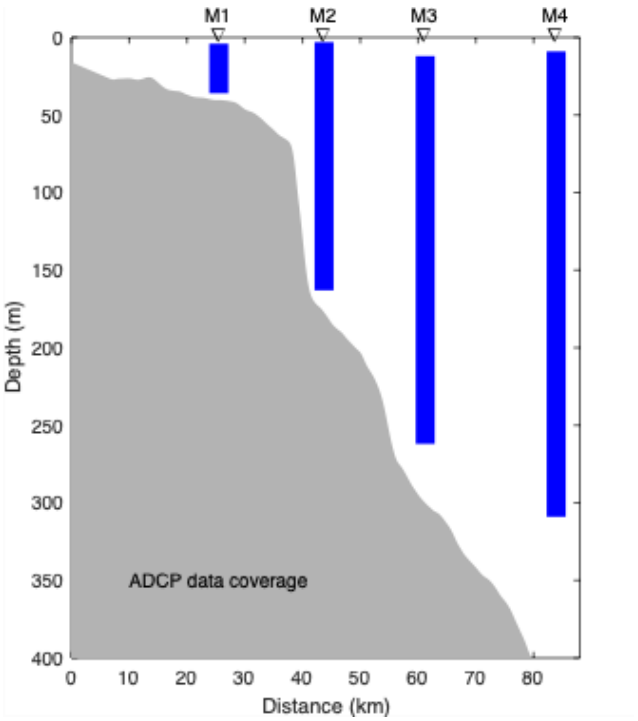

Figure 2. Data coverage of ADCPs during the 2017–2018 deployment period

On recovery of the ADCPs, the actual time and the time read from the instrument clock were recorded to determine clock drift. As is a common occurrence, the instrument clocks drifted slightly over the year-long deployment. The time drift was assumed to occur linearly and was compensated by adjusting the sample interval (Table 8 and Table 9). The instrument depth values were referenced to the mean of the ADCP-measured pressure and converted to depth using water density. The distance to the first bin values (distance from the head of the ADCP to the first acquired current bin) are instrument and configuration dependent and were recorded by each instrument in the raw data file. The total number of ensembles acquired during the deployment was also recorded.

Table 8. Selected 2017–2018 M1 and M2 ADCP configuration parameters

	M1 300 kHz	**M2 300 kHz s/n 6593**	**M2 300 kHz s/n 10985**
Instrument clock drift	13:04 min:sec slow	2:10 min:sec fast	10:06 min:sec slow
Configured sample interval	60 second ensemble (5 pings / ensemble)	60 second ensemble (5 pings / ensemble)	60 second ensemble (4 pings / ensemble)
Sample interval corrected for clock drift [s]	60.090774	59.9998	60.0611
Instrument depth [m]	34.65	169.1	57.5
Bin size [m]	2	4	2
Distance to bin 1 [m]	4.18	6.08	4.19
Raw data value count (ensembles)	717,031	541,412	541,874

Table 9. Selected 2017–2018 M3 and M4 ADCP configuration parameters

	M3 150 kHz Quartermaster 17898	**M4 150 kHz Quartermaster 16157**	**M3 75 kHz LongRanger 12962**	**M4 75 kHz LongRanger 17441**
Instrument clock drift	10:29 min:sec slow	12:03 min:sec slow	1:05 min:sec fast	16:00 min:sec slow
Configured sample interval	150 second ensemble (4 pings / ensemble)	150 second ensemble (13 pings / ensemble)	600 second ensemble (32 pings / ensemble)	600 second ensemble (32 pings / ensemble)
Sample interval corrected for clock drift [s]	150.3365	150.3233	599.9988	600.0177
Instrument depth [m]	110.5	97.2	287	334
Bin size [m]	2	2	16	16
Distance to bin 1 [m]	6.41	6.41	23.62	23.62
Raw data value count (ensembles)	216551	216530	54264	54265

2.3.1.1 Ocean Current Time-Series

The ADCPs at M2, M3, and M4 collected about 372 days of ocean current time-series measurements. As M1 could not be recovered in the fall of 2018, it continued to gather data into February of 2019 when the battery was spent, for a total of 497 days of ocean current time-series measurements (Figure 3).

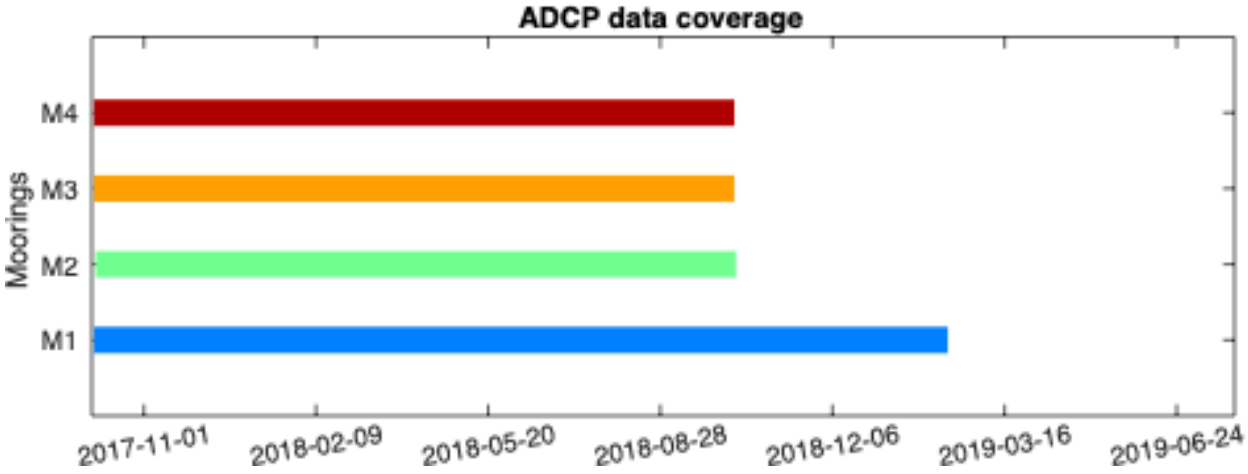

Figure 3. Temporal coverage of the ADCP data at each mooring during the 2017–2018 deployment, extending into 2019 at M1

Current measurements were obtained from near-bottom to near-surface. Table 10 lists the ocean current bin indices and their associated depth for each ADCP at the M1 and M2 sites. Actual depths were determined using the pressure sensor onboard each ADCP. Then a current profile was determined for each ADCP 20-minute average ensemble from the transducer to the center of each bin. Variations in sea surface height (and thus pressure) along with mooring blow-over result in variable depth profiles for each ensemble. Table 10 represents the average depth for each profile throughout the full time series. Actual depths can vary substantially from this table, especially during significant blow-over events.

Table 10. Bin depth referenced to mean sea level as derived from the pressure time-series measured by the pressure sensor onboard the ADCPs at M1 and M2 during 2017–2019 deployment

Bin index	Bin Center Depth [m]		
	M1 300 kHz Workhorse	M2 300 kHz (Upper)	M2 300 kHz (Lower)
30			47.0
29			51.0
28			55.0
27			59.0
26		3.3	63.0
25		5.3	67.0
24		7.3	71.0
23		10.3	75.0
22		13.3	79.0
21		15.3	83.0
20		17.3	87.0
19		19.3	91.0
18		21.3	95.0
17		23.3	99.0
16		25.3	103.0
15		27.3	107.0
14		29.3	111.0
13	6.4	31.3	115.0
12	8.4	33.3	119.0
11	10.4	35.3	123.0
10	12.4	37.3	127.0
9	14.4	39.3	131.0
8	16.4	41.3	135.0
7	18.4	43.3	139.0
6	20.4	45.3	143.0
5	22.4	47.3	147.0
4	24.4	49.3	151.0
3	26.4	51.3	155.0
2	28.4	53.3	159.0
1	30.4	55.3	163.0

NOTE:
Depth is the Center of each Bin; for example, Bin Index 8 for the M2 upper Workhorse spans a Depth of 40.3 to 42.3 m

Likewise, for ADCPs deployed at M3 and M4, combining the results from the LongRanger and Quartermaster on these moorings, current measurements were obtained from near-bottom to near-surface. Table 11 lists the ocean current bin indices and their associated depth for each ADCP at the M3 and M4 sites.

Table 11. Bin depth referenced to mean sea level as derived from the pressure time-series measured by each ADCP during the 2017–2018 deployment

Bin index	Bin Center Depth [m]			
	M3 150 kHz Quartermaster	M4 150 kHz Quartermaster	M3 75 kHz LongRanger	M4 75 kHz LongRanger
46	14.1	-		
45	16.1	-		
44	18.1	-		
43	20.1	6.8		
42	22.1	8.8		
41	24.1	10.8		
40	26.1	12.8		
39	28.1	14.8		
38	30.1	16.8		
37	32.1	18.8		
36	34.1	20.8		
35	36.1	22.8		
34	38.1	24.8		
33	40.1	26.8		
32	42.1	28.8		
31	44.1	30.8		
30	46.1	32.8		
29	48.1	34.8		
28	50.1	36.8		
27	52.1	38.8		
26	54.1	40.8		
25	56.1	42.8		
24	58.1	44.8		
23	60.1	46.8		
22	62.1	48.8		
21	64.1	50.8		
20	66.1	52.8		
19	68.1	54.8		
18	70.1	56.8		
17	72.1	58.8		
16	74.1	60.8		70.4
15	76.1	62.8		86.4
14	78.1	64.8	55.4	102.4
13	80.1	66.8	71.4	118.4
12	82.1	68.8	87.4	134.4
11	84.1	70.8	103.4	150.4
10	86.1	72.8	119.4	166.4

Bin index	Bin Center Depth [m]			
	M3 150 kHz Quartermaster	M4 150 kHz Quartermaster	M3 75 kHz LongRanger	M4 75 kHz LongRanger
9	88.1	74.8	135.4	182.4
8	90.1	76.8	151.4	198.4
7	92.1	78.8	167.4	214.4
6	94.1	80.8	183.4	230.4
5	96.1	82.8	199.4	246.4
4	98.1	84.8	215.4	262.4
3	100.1	86.8	231.4	278.4
2	102.1	88.8	247.4	294.4
1	104.1	90.8	263.4	310.4
NOTE: Depth is the middle of each Bin; for example, Bin Index 8 for the M3 Quartermaster spans a Depth of 91.1 to 89.1 m				

The extracted ADCP time-series were subjected to quality control procedures. The steps in the error detection and removal procedures were as follows:

1. Currents were screened for Correlation < 64, Amplitude < 50 and $V_{Error} > 30$ cm·s^{-1}
2. Current direction time-series was compass corrected using a heading-dependent compass calibration polynomial obtained from performing a dry land compass calibration routine. Also, the magnetic declination for the deployment location was applied to each instrument. This step establishes horizontal motion vectors referenced to geographic (true) north and corrects the data for the inaccuracies of the compass. The resulting current velocity components are herein referred to as V_{East} and V_{North}.
3. Sample interval was adjusted for the observed time drift.
4. Current measurements that were compromised by the obstruction of other components further up the mooring were replaced with flag values.
5. Current measurements determined to be compromised by the water surface and presence of ice were replaced with flag values.
6. Unreasonable first-difference values in the current time-series were automatically identified. Thresholds for each bin were automatically determined using a multiple of the standard deviation of the time-series for the bin after the application of a high pass filter.
7. Values of measured horizontal components of current that had absolute values exceeding an out-of-bound threshold were identified. This threshold is calculated as the rounded maximum of the high pass filtered absolute current speed plus fifty standard deviations plus the mean current speed.
8. All suspect values found in steps 6 and 7 were replaced by linear interpolation.
9. The current time-series was block averaged using a ~20-minute sample interval to reduce standard error but retain enough resolution for the expected timescales of relevant phenomena.
10. The data was visually inspected, and data found to be unreliable based on reduced signal strength and which was inconsistent with the immediately surrounding data was replaced with a flag value of -9999. Modifications in this step were made in both the V_{East} and V_{North} data channels.

The count of records modified in the V_{East} and V_{North} data channels for each current bin up to step 8 is shown in Figure 4 and is listed in Table 12 for M1 and M2 and Table 13 for M3 and M4. At M2 and M4 there is interference that is likely due to the IPS whereas at M3 there is interference that is likely due to the AZFP. Effects on the ADCP data due to interference included drastic direction changes and very high signal strength. Measurements at these depths were replaced with flagged values. In addition, there was a significant amount of data flagged in the shallowest bins of the water column due to the presence of the surface and ice. These processing summaries include data records that were replaced by linearly interpolated values and records that were assigned a value of -9999.

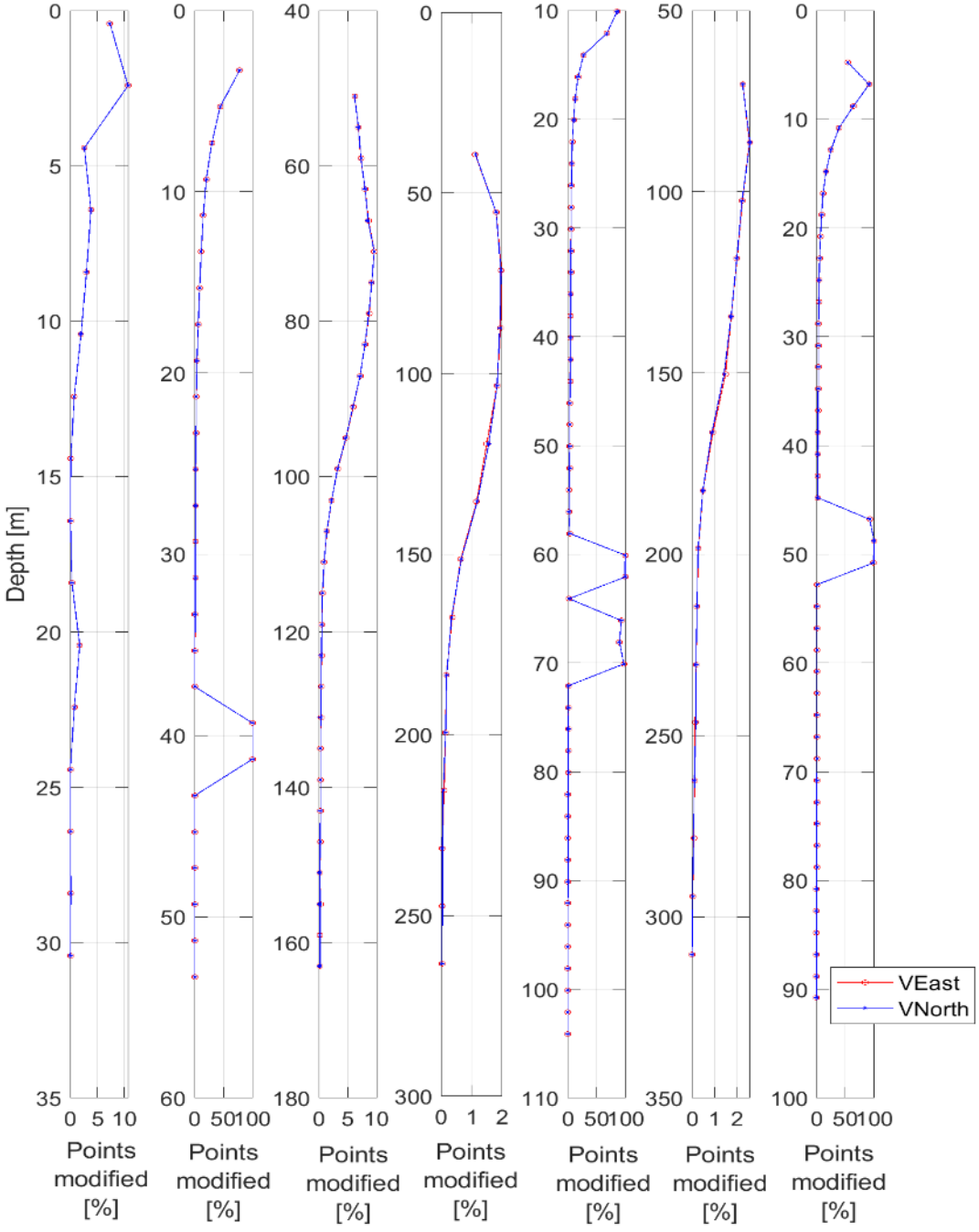

Figure 4. Fraction of data records modified <u>before</u> time-averaging for the (from left to right) M1 300 kHz, M2 300 kHz (upper), M2 300 kHz (lower), M3 QuarterMaster 150 kHz, M3 LongRanger 75 kHz, M4 LongRanger 75 kHz, and M4 QuarterMaster 150 kHz during 2017–2018 deployment, extending into 2019 at M1

Table 12. Count and fraction of data records modified before time-averaging for each ocean current bin for M1 and M2 during 2017–2018 deployment, extending into 2019 at M1.

Bin Index	Count (fraction) of Modified Records					
	M1 300 kHz (upper)		M2 300 kHz (upper)		M2 300 kHz (lower)	
	V_{East}	V_{North}	V_{East}	V_{North}	V_{East}	V_{North}
29			416027 (78%)	416031 (78%)	32921 (6%)	33012 (6%)
28			236336 (44%)	236364 (44%)	36591 (7%)	36533 (7%)
27			158972 (30%)	159095 (30%)	38859 (7%)	38784 (7%)
26			107208 (20%)	107323 (20%)	42765 (8%)	42758 (8%)
25			79891 (15%)	79892 (15%)	45514 (8%)	45829 (9%)
24			61579 (12%)	61458 (11%)	51195 (10%)	51360 (10%)
23			45933 (9%)	45699 (9%)	48916 (9%)	48823 (9%)
22			33376 (6%)	33181 (6%)	46249 (9%)	46545 (9%)
21			21084 (4%)	20884 (4%)	42567 (8%)	42592 (8%)
20			15098 (3%)	14955 (3%)	38071 (7%)	38062 (7%)
19			11822 (2%)	11677 (2%)	31518 (6%)	31801 (6%)
18			9496 (2%)	9392 (2%)	24889 (5%)	25044 (5%)
17			7697 (1%)	7593 (1%)	17119 (3%)	17285 (3%)
16	52402 (7%)	52402 (7%)	6145 (1%)	6104 (1%)	11719 (2%)	11707 (2%)
15	76200 (11%)	76200 (11%)	4979 (1%)	4921 (1%)	7167 (1%)	7294 (1%)
14	18555 (3%)	18555 (3%)	3862 (1%)	3794 (1%)	4710 (1%)	4776 (1%)
13	27270 (4%)	27270 (4%)	3202 (1%)	3117 (1%)	3118 (1%)	3192 (1%)
12	21430 (3%)	21430 (3%)	2227 (<0.5%)	2167 (<0.5%)	2544 (<0.5%)	2609 (<0.5%)
11	14169 (2%)	14169 (2%)	534939 (100%)	534939 (100%)	2267 (<0.5%)	2317 (<0.5%)
10	5272 (1%)	5272 (1%)	534931 (100%)	534931 (100%)	1814 (<0.5%)	1887 (<0.5%)
9	724 (<0.5%)	724 (<0.5%)	1265 (<0.5%)	1200 (<0.5%)	1653 (<0.5%)	1688 (<0.5%)
8	275 (<0.5%)	275 (<0.5%)	827 (<0.5%)	753 (<0.5%)	1270 (<0.5%)	1296 (<0.5%)
7	2195 (<0.5%)	2195 (<0.5%)	614 (<0.5%)	588 (<0.5%)	1349 (<0.5%)	1386 (<0.5%)
6	12430 (2%)	12430 (2%)	501 (<0.5%)	435 (<0.5%)	1217 (<0.5%)	1249 (<0.5%)
5	5408 (1%)	5408 (1%)	361 (<0.5%)	312 (<0.5%)	1059 (<0.5%)	1090 (<0.5%)
4	60 (<0.5%)	60 (<0.5%)	526 (<0.5%)	510 (<0.5%)	765 (<0.5%)	790 (<0.5%)
3	262 (<0.5%)	262 (<0.5%)	-	-	1029 (<0.5%)	1036 (<0.5%)
2	719 (<0.5%)	719 (<0.5%)	-	-	975 (<0.5%)	970 (<0.5%)
1	2 (<0.5%)	2 (<0.5%)	-	-	1014 (<0.5%)	1013 (<0.5%)

Table 13. Count and fraction of data records modified before time-averaging for each ocean current bin for M3 and M4 during 2017–2018 deployment

Bin Index	Count (fraction) of Modified Records							
	M3 150 kHz QuarterMaster		M3 75 kHz LongRanger		M4 150 kHz QuarterMaster		M4 75 kHz LongRanger	
	V_{East}	V_{North}	V_{East}	V_{North}	V_{East}	V_{North}	V_{East}	V_{North}
48	183244 (85%)	183244 (85%)	608 (1%)	604 (1%)	116944 (55%)	116944 (55%)	1216 (2%)	1222 (2%)
47	145048 (68%)	145036 (68%)	973 (2%)	973 (2%)	194800 (91%)	194800 (91%)	1392 (3%)	1380 (3%)
46	58784 (27%)	58776 (27%)	1058 (2%)	1067 (2%)	137402 (64%)	137324 (64%)	1203 (2%)	1213 (2%)
45	38042 (18%)	38029 (18%)	1038 (2%)	1051 (2%)	83333 (39%)	83327 (39%)	1076 (2%)	1081 (2%)
44	27306 (13%)	27293 (13%)	990 (2%)	989 (2%)	53939 (25%)	53944 (25%)	939 (2%)	942 (2%)
43	21440 (10%)	21408 (10%)	843 (2%)	807 (2%)	35747 (17%)	35734 (17%)	768 (1%)	801 (1%)
42	16577 (8%)	16681 (8%)	638 (2%)	628 (2%)	24063 (11%)	24062 (11%)	476 (1%)	500 (1%)
41	14610 (7%)	14664 (7%)	354 (1%)	345 (1%)	18628 (9%)	18630 (9%)	257 (<0.5%)	258 (<0.5%)
40	13241 (6%)	13206 (6%)	182 (<0.5%)	191 (<0.5%)	14263 (7%)	14303 (7%)	143 (<0.5%)	150 (<0.5%)
39	12354 (6%)	12384 (6%)	94 (<0.5%)	90 (<0.5%)	11528 (5%)	11531 (5%)	117 (<0.5%)	118 (<0.5%)
38	11868 (6%)	11823 (6%)	76 (<0.5%)	76 (<0.5%)	9392 (4%)	9395 (4%)	91 (<0.5%)	92 (<0.5%)
37	11524 (5%)	11521 (5%)	32 (<0.5%)	49 (<0.5%)	8315 (4%)	8344 (4%)	88 (<0.5%)	72 (<0.5%)
36	11412 (5%)	11468 (5%)	18 (<0.5%)	14 (<0.5%)	7385 (3%)	7377 (3%)	54 (<0.5%)	56 (<0.5%)
35	11054 (5%)	11061 (5%)	19 (<0.5%)	11 (<0.5%)	6906 (3%)	6918 (3%)	31 (<0.5%)	39 (<0.5%)
34	10633 (5%)	10694 (5%)	10 (<0.5%)	10 (<0.5%)	6442 (3%)	6452 (3%)	10 (<0.5%)	10 (<0.5%)
33	10380 (5%)	10308 (5%)	-	-	6052 (3%)	6040 (3%)	0 (0%)	0 (0%)
32	9483 (4%)	9468 (4%)	-	-	5701 (3%)	5683 (3%)	-	-
31	8927 (4%)	8897 (4%)	-	-	5431 (3%)	5419 (3%)	-	-
30	7913 (4%)	7860 (4%)	-	-	4905 (2%)	4915 (2%)	-	-
29	7475 (3%)	7517 (3%)	-	-	4480 (2%)	4478 (2%)	-	-
28	6721 (3%)	6831 (3%)	-	-	4060 (2%)	4052 (2%)	-	-
27	6205 (3%)	6177 (3%)	-	-	196975 (92%)	196975 (92%)	-	-
26	5509 (3%)	5522 (3%)	-	-	214197 (100%)	214197 (100%)	-	-
25	4815 (2%)	4866 (2%)	-	-	211867 (99%)	211867 (99%)	-	-
24	7365 (3%)	7338 (3%)	-	-	2243 (1%)	2238 (1%)	-	-
23	213399 (100%)	213399 (100%)	-	-	2270 (1%)	2274 (1%)	-	-
22	212791 (99%)	212791 (99%)	-	-	1968 (1%)	1973 (1%)	-	-
21	4201 (2%)	4210 (2%)	-	-	1814 (1%)	1815 (1%)	-	-
20	198497 (93%)	198497 (93%)	-	-	1592 (1%)	1594 (1%)	-	-

Bin Index	Count (fraction) of Modified Records							
	M3 150 kHz QuarterMaster		M3 75 kHz LongRanger		M4 150 kHz QuarterMaster		M4 75 kHz LongRanger	
	V_{East}	V_{North}	V_{East}	V_{North}	V_{East}	V_{North}	V_{East}	V_{North}
19	192233 (90%)	192233 (90%)	-	-	1429 (1%)	1437 (1%)	-	-
18	208013 (97%)	208013 (97%)	-	-	1296 (1%)	1290 (1%)	-	-
17	1796 (1%)	1786 (1%)	-	-	1107 (1%)	1106 (1%)	-	-
16	1572 (1%)	1547 (1%)	-	-	1018 (<0.5%)	1012 (<0.5%)	-	-
15	1344 (1%)	1327 (1%)	-	-	856 (<0.5%)	861 (<0.5%)	-	-
14	1197 (1%)	1187 (1%)	-	-	792 (<0.5%)	796 (<0.5%)	-	-
13	1045 (<0.5%)	1034 (<0.5%)	-	-	620 (<0.5%)	618 (<0.5%)	-	-
12	910 (<0.5%)	918 (<0.5%)	-	-	557 (<0.5%)	551 (<0.5%)	-	-
11	778 (<0.5%)	774 (<0.5%)	-	-	510 (<0.5%)	506 (<0.5%)	-	-
10	668 (<0.5%)	648 (<0.5%)	-	-	357 (<0.5%)	364 (<0.5%)	-	-
9	634 (<0.5%)	620 (<0.5%)	-	-	182 (<0.5%)	181 (<0.5%)	-	-
8	526 (<0.5%)	529 (<0.5%)	-	-	164 (<0.5%)	165 (<0.5%)	-	-
7	488 (<0.5%)	478 (<0.5%)	-	-	144 (<0.5%)	143 (<0.5%)	-	-
6	387 (<0.5%)	387 (<0.5%)	-	-	125 (<0.5%)	125 (<0.5%)	-	-
5	296 (<0.5%)	293 (<0.5%)	-	-	186 (<0.5%)	187 (<0.5%)	-	-
4	229 (<0.5%)	204 (<0.5%)	-	-	-	-	-	-
3	210 (<0.5%)	202 (<0.5%)	-	-	-	-	-	-
2	234 (<0.5%)	220 (<0.5%)	-	-	-	-	-	-
1	259 (<0.5%)	237 (<0.5%)	-	-	-	-	-	-

After the current time-series was averaged to 20-minute intervals there were remaining suspect records near the surface. The values with high associated error velocities and low beam correlation were removed using an ADCP full water column visual editing tool as part of step 10 listed above. The number of records modified in step 10 is shown in Figure 5 and Table 14 for M1 and M2 and in Table 15 for M3 and M4. This processing step was applied to both the V_{North} and V_{East} velocity components, so only the count of vector velocity records is listed for each instrument in Table 14 and Table 15. Table 14 two tables also list the count and fraction of flagged values in both the V_{North} and V_{East} channels of the final quality-controlled time-series. Larger proportions of data required modification at the lower M2 ADCP at 151 m depth (100%) and 71 m depth (65%). These levels of reduced data quality are likely due to interference with elements of the same mooring. The Quartermasters are also missing a higher proportion of data in shallower water due to low signal strength caused by an episodic lack of scatterers such as bubbles and passively moving biology.

Measurements cannot be made without sufficient concentrations of scatterers required to reflect back usable amounts of acoustic energy to the instrument. The LongRangers also contain missing data records due to low concentrations of scatterers in the water column. This occurs mostly during the winter and spring when the ice concentration is high and concentrations of biological scatterers are low.

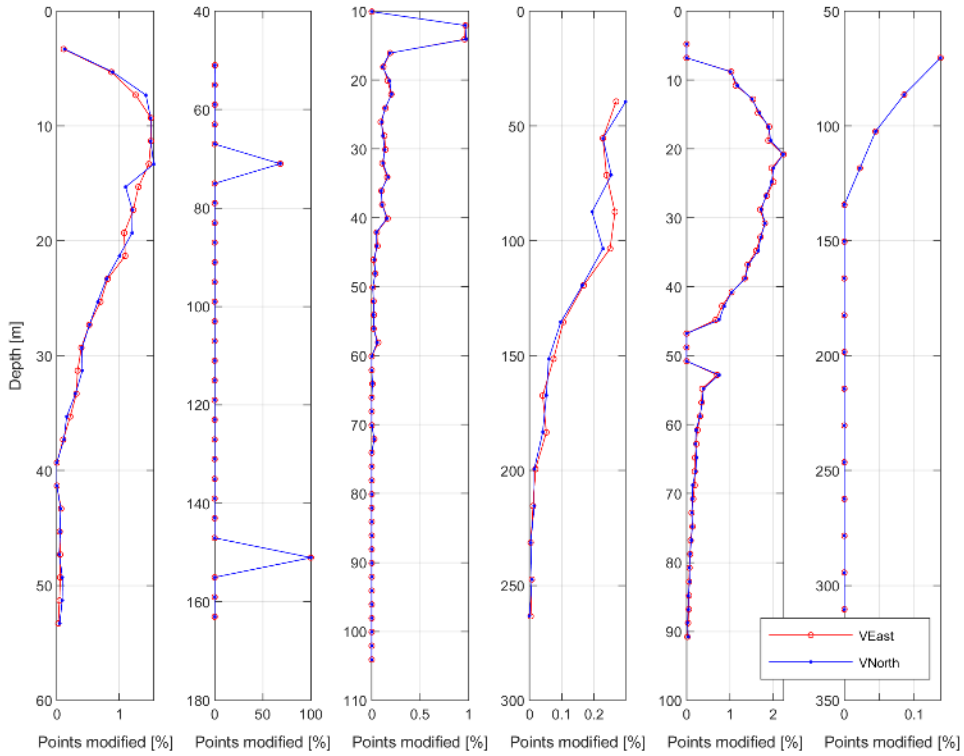

Figure 5. Fraction of data records modified <u>after</u> time-averaging for the (from left to right) M2 300 kHz (upper), M2 300 kHz (lower), M3 QuarterMaster 150 kHz, M3 LongRanger 75 kHz, M4 QuarterMaster 150 kHz, and M4 LongRanger 75 kHz during 2017–2018 deployment

Table 14. Count and fraction of data records modified after time-averaging for each ocean current bin for M1 and M2 during 2017–2018 deployment, extending into 2019 at M1

Bin Index	Count (fraction) of Modified Records					
	M1 300 kHz		M2 300 kHz QuarterMaster (upper)		M2 300 kHz QuarterMaster (lower)	
	V_{East}	V_{North}	V_{East}	V_{North}	V_{East}	V_{North}
29			33 (<0.5%)	29 (<0.5%)	89 (<0.5%)	91 (<0.5%)
28			240 (1%)	234 (1%)	50 (<0.5%)	50 (<0.5%)
27			382 (1%)	338 (1%)	22 (<0.5%)	23 (<0.5%)
26			403 (2%)	404 (2%)	15 (<0.5%)	17 (<0.5%)
25			402 (2%)	404 (2%)	17 (<0.5%)	20 (<0.5%)
24			416 (2%)	395 (1%)	18,277 (65%)	18,262 (65%)
23			295 (1%)	350 (1%)	10 (<0.5%)	10 (<0.5%)
22			324 (1%)	328 (1%)	16 (<0.5%)	16 (<0.5%)
21			323 (1%)	289 (1%)	9 (<0.5%)	11 (<0.5%)
20			268 (1%)	293 (1%)	15 (<0.5%)	15 (<0.5%)
19			213 (1%)	218 (1%)	8 (<0.5%)	8 (<0.5%)
18			175 (1%)	187 (1%)	1 (<0.5%)	2 (<0.5%)
17			140 (1%)	139 (1%)	2 (<0.5%)	2 (<0.5%)
16			108 (<0.5%)	105 (<0.5%)	2 (<0.5%)	2 (<0.5%)
15	23,433 (3%)	23,433 (3%)	109 (<0.5%)	89 (<0.5%)	0 (<0.5%)	0 (<0.5%)
14	16,672 (2%)	16,679 (2%)	80 (<0.5%)	84 (<0.5%)	0 (<0.5%)	0 (<0.5%)
13	10,474 (2%)	10,489 (2%)	42 (<0.5%)	57 (<0.5%)	0 (<0.5%)	0 (<0.5%)
12	6,363 (1%)	6,375 (1%)	30 (<0.5%)	27 (<0.5%)	0 (<0.5%)	0 (<0.5%)
11	3,760 (0.5%)	3,786 (0.5%)	0 (<0.5%)	0 (<0.5%)	0 (<0.5%)	0 (<0.5%)
10	2,039 (<0.5%)	2,094 (<0.5%)	0 (<0.5%)	0 (<0.5%)	0 (<0.5%)	0 (<0.5%)
9	1,259 (<0.5%)	1,317 (<0.5%)	16 (<0.5%)	18 (<0.5%)	0 (<0.5%)	0 (<0.5%)
8	35,669 (5%)	35,669 (5%)	14 (<0.5%)	12 (<0.5%)	0 (<0.5%)	0 (<0.5%)
7	1,867 (<0.5%)	1,898 (<0.5%)	10 (<0.5%)	14 (<0.5%)	0 (<0.5%)	0 (<0.5%)
6	35,309 (5%)	35,309 (5%)	24 (<0.5%)	14 (<0.5%)	0 (<0.5%)	0 (<0.5%)
5	8,513 (1%)	8,523 (1%)	23 (<0.5%)	11 (<0.5%)	0 (<0.5%)	0 (<0.5%)
4	6,782 (1%)	6,811 (1%)	12 (<0.5%)	6 (<0.5%)	26,790 (100%)	26,790 (100%)
3	35,292 (5%)	35,292 (5%)	-	-	0 (<0.5%)	0 (<0.5%)
2	35,518 (5%)	35,518 (5%)	-	-	0 (<0.5%)	0 (<0.5%)
1	213 (<0.5%)	178 (<0.5%)	-	-	0 (<0.5%)	0 (<0.5%)

Table 15. Count and fraction of data records modified after time-averaging for each ocean current bin for M3 and M4 during 2017–2018 deployment

Bin Index	Count (fraction) of Modified Records							
	M3 150 kHz QuarterMaster		M3 75 kHz LongRanger		M4 150 kHz QuarterMaster		M4 75 kHz LongRanger	
	V_{East}	V_{North}	V_{East}	V_{North}	V_{East}	V_{North}	V_{East}	V_{North}
48	0 (<0.5%)	0 (<0.5%)	80 (<0.5%)	72 (<0.5%)	0 (<0.5%)	0 (<0.5%)	37 (<0.5%)	37 (<0.5%)
47	259 (1%)	259 (1%)	61 (<0.5%	61 (<0.5%)	0 (<0.5%)	0 (<0.5%)	23 (<0.5%)	23 (<0.5%)
46	261 (1%)	257 (1%)	68 (<0.5%)	64 (<0.5%)	273 (1%)	277 (1%)	12 (<0.5%)	12 (<0.5%)
45	50 (<0.5%)	51 (<0.5%)	52 (<0.5%)	71 (<0.5%)	315 (1%)	304 (1%)	6 (<0.5%)	6 (<0.5%)
44	30 (<0.5%)	32 (<0.5%)	61 (<0.5%)	67 (<0.5%)	406 (2%)	412 (2%)	0 (<0.5%)	0 (<0.5%)
43	49 (<0.5%)	44 (<0.5%)	44 (<0.5%)	45 (<0.5%)	452 (2%)	443 (2%)	0 (<0.5%)	0 (<0.5%)
42	55 (<0.5%)	54 (<0.5%)	26 (<0.5%)	28 (<0.5%)	509 (2%)	512 (2%)	0 (<0.5%)	0 (<0.5%)
41	37 (<0.5%)	38 (<0.5%)	16 (<0.5%)	20 (<0.5%)	521 (2%)	507 (2%)	0 (<0.5%)	0 (<0.5%)
40	27 (<0.5%)	25 (<0.5%)	14 (<0.5%)	11 (<0.5%)	599 (2%)	601 (2%)	0 (<0.5%)	0 (<0.5%)
39	31 (<0.5%)	36 (<0.5%)	11 (<0.5%)	14 (<0.5%)	539 (2%)	527 (2%)	0 (<0.5%)	0 (<0.5%)
38	36 (<0.5%)	38 (<0.5%)	4 (<0.5%)	5 (<0.5%)	528 (2%)	539 (2%)	0 (<0.5%)	0 (<0.5%)
37	31 (<0.5%)	29 (<0.5%)	4 (<0.5%)	3 (<0.5%)	493 (2%)	498 (2%)	0 (<0.5%)	0 (<0.5%)
36	45 (<0.5%)	43 (<0.5%)	1 (<0.5%)	1 (<0.5%)	463 (2%)	456 (2%)	0 (<0.5%)	0 (<0.5%)
35	26 (<0.5%)	27 (<0.5%)	2 (<0.5%)	2 (<0.5%)	487 (2%)	485 (2%)	0 (<0.5%)	0 (<0.5%)
34	29 (<0.5%)	29 (<0.5%)	0 (<0.5%)	1 (<0.5%)	460 (2%)	458 (2%)	0 (<0.5%)	0 (<0.5%)
33	42 (<0.5%)	44 (<0.5%)	-	-	444 (2%)	432 (2%)	0 (<0.5%)	0 (<0.5%)
32	13 (<0.5%)	14 (<0.5%)	-	-	383 (1%)	379 (1%)	-	-
31	14 (<0.5%)	16 (<0.5%)	-	-	364 (1%)	361 (1%)	-	-
30	7 (<0.5%)	5 (<0.5%)	-	-	279 (1%)	279 (1%)	-	-
29	10 (<0.5%)	10 (<0.5%)	-	-	233 (1%)	220 (1%)	-	-
28	3 (<0.5%)	3 (<0.5%)	-	-	203 (1%)	181 (1%)	-	-
27	5 (<0.5%)	5 (<0.5%)	-	-	0 (<0.5%)	0 (<0.5%)	-	-
26	5 (<0.5%)	6 (<0.5%)	-	-	0 (<0.5%)	0 (<0.5%)	-	-
25	6 (<0.5%)	5 (<0.5%)	-	-	0 (<0.5%)	0 (<0.5%)	-	-
24	15 (<0.5%)	18 (<0.5%)	-	-	201 (1%)	190 (1%)	-	-
23	0 (<0.5%)	0 (<0.5%)	-	-	105 (<0.5%)	97 (<0.5%)	-	-
22	0 (<0.5%)	0 (<0.5%)	-	-	97 (<0.5%)	93 (<0.5%)	-	-
21	2 (<0.5%)	2 (<0.5%)	-	-	83 (<0.5%)	84 (<0.5%)	-	-

Bin Index	Count (fraction) of Modified Records							
	M3 150 kHz QuarterMaster		M3 75 kHz LongRanger		M4 150 kHz QuarterMaster		M4 75 kHz LongRanger	
	V_{East}	V_{North}	V_{East}	V_{North}	V_{East}	V_{North}	V_{East}	V_{North}
20	0 (<0.5%)	0 (<0.5%)	-	-	59 (<0.5%)	67 (<0.5%)	-	-
19	0 (<0.5%)	0 (<0.5%)	-	-	55 (<0.5%)	61 (<0.5%)	-	-
18	0 (<0.5%)	0 (<0.5%)	-	-	62 (<0.5%)	52 (<0.5%)	-	-
17	7 (<0.5%)	7 (<0.5%)	-	-	56 (<0.5%)	50 (<0.5%)	-	-
16	0 (<0.5%)	0 (<0.5%)	-	-	38 (<0.5%)	50 (<0.5%)	-	-
15	0 (<0.5%)	0 (<0.5%)	-	-	36 (<0.5%)	41 (<0.5%)	-	-
14	0 (<0.5%)	0 (<0.5%)	-	-	33 (<0.5%)	31 (<0.5%)	-	-
13	0 (<0.5%)	0 (<0.5%)	-	-	35 (<0.5%)	37 (<0.5%)	-	-
12	0 (<0.5%)	0 (<0.5%)	-	-	29 (<0.5%)	25 (<0.5%)	-	-
11	0 (<0.5%)	0 (<0.5%)	-	-	21 (<0.5%)	23 (<0.5%)	-	-
10	0 (<0.5%)	0 (<0.5%)	-	-	18 (<0.5%)	18 (<0.5%)	-	-
9	0 (<0.5%)	0 (<0.5%)	-	-	19 (<0.5%)	15 (<0.5%)	-	-
8	0 (<0.5%)	0 (<0.5%)	-	-	11 (<0.5%)	15 (<0.5%)	-	-
7	0 (<0.5%)	0 (<0.5%)	-	-	10 (<0.5%)	14 (<0.5%)	-	-
6	0 (<0.5%)	0 (<0.5%)	-	-	6 (<0.5%)	9 (<0.5%)	-	-
5	0 (<0.5%)	0 (<0.5%)	-	-	10 (<0.5%)	5 (<0.5%)	-	-
4	0 (<0.5%)	0 (<0.5%)	-	-	-	-	-	-
3	0 (<0.5%)	0 (<0.5%)	-	-	-	-	-	-
2	0 (<0.5%)	0 (<0.5%)	-	-	-	-	-	-
1	0 (<0.5%)	0 (<0.5%)	-	-	-	-	-	-

2.3.1.2 Ice Velocity

Ice velocity measurements were made with the upper ADCPs at each site using the bottom-tracking feature. The following methodology was used when processing the raw ADCP ice velocity time-series data:

1. Extract the bottom-tracking time-series from the bottom-tracking variable in the raw data file.
2. Time-drift information recorded by the field crew is used to calculate a revised sample interval, assuming a linear time drift of the instrument clock.
3. Average data to ~20-minute sample interval to reduce Doppler noise but keep enough time resolution for expected ice velocity phenomena.
4. Trim to the in-water portion of the deployment.

5. Identify episodes of probable open water and anomalous velocity values in each data record. Use supplemental information to identify these episodes, including IPS time-series, ice charts, satellite imagery as well as instrument-recorded data quality indicators including error velocity, vertical velocity, correlation and echo amplitude. For these episodes, set the values of the horizontal ice velocity components to a flag value of -9999.
6. Identify remaining horizontal ice velocity values exceeding the out-of-bound threshold in absolute value (150 $cm \cdot s^{-1}$).
7. For all suspect values found in steps 5 and 6, the values are replaced by linear interpolation over individual segments with durations of less than one hour. For longer data gaps coincident with significant ice floes recorded by the IPS, construct ice velocity records using upper water column velocities, surface winds, interpolation and smoothing with short-term moving averages. If the ice velocities cannot be reconstructed, then flag the values as unreliable using -9999.
8. Identify sections of higher error velocity and higher velocity variability and apply a moving average filter.
9. Plot the edited ice velocity time-series, evaluate, and repeat editing steps as required.

Table 16 (M1 and M2) and Table 17 (M3 and M4) detail the number of points modified at each site for each ice velocity component. This includes the automatic detection and interpolation of outliers and spikes as well as manual review and adjustment of data.

Table 16. Summary of edited ice velocity time-series records for the M1 and M2 sites during 2017–2018 deployment, extending into 2019 at M1

	M1 300 kHz Workhorse		M2 300 kHz QuarterMaster	
	V_{East}	V_{North}	V_{East}	V_{North}
Automatically despiked	1181	1181	488	279
Smoothed via moving average	5123	5089	306	171
Manually edited and >1 cm/s	3947 (11.1%)	3559 (10%)	1, 129 (4%)	965 (4%)
Total edited	5128 (14.4%)	4740 (13.3%)	1, 923 (7%)	1, 415 (5%)
Flagged	11,393 (32%)	11393 (32%)	12, 401 (46%)	12, 401 (46%)
Total time-series length	35708	35708	26763	26763

Table 17. Summary of edited ice velocity time-series records for the M3 and M4 quartermasters during 2017–2018 deployment

	M3 150 kHz QuarterMaster		M4 150 kHz QuarterMaster	
	V_{East}	V_{North}	V_{East}	V_{North}
Automatically despiked	0	0	0	0
Smoothed via moving average	634	491	387	167
Manually edited and >1 cm·s-1	1,801 (7%)	1,557 (6%)	1,496 (6%)	1,318 (5%)
Total edited	3,977 (15%)	3,729 (14%)	1,883 (7%)	1,485 (6%)
Flagged	11,628 (43%)	11,628 (43%)	11,095 (41%)	11,095 (41%)
Total time-series length	26,801	26,801	26,805	26,805

2.3.1.3 Ice Draft

The ice draft of targets acquired during the mooring deployment were calculated using the quality-controlled versions of target range, pressure at the instrument depth, and instrument tilt. These parameters are necessary to derive the ice draft, d, of a target as follows:

Equation 1

$$d = \eta - \beta \cdot r \cdot \cos\theta$$

where β is a calibration factor called the range correction factor for the actual depth-averaged sound speed through the water column along the sonar beam (see Section 3.1.2.2), r is the range to the target from the IPS, θ is the total instrument tilt, and η is the water level from the IPS sonar transducer to the air-water interface. Note that the sign convention for ice draft is positive downwards, i.e. a draft of +5 m represents an ice feature which extends 5 m below sea level.

The water level is determined as follows:

Equation 2

$$\eta = \frac{P_{IPS} - P_{SLP}}{\rho g} - \Delta D$$

where P_{IPS} is the quality controlled pressure measured by the IPS, P_{SLP} is the sea-level pressure, g is the local acceleration due to gravity, ρ is the depth-averaged density of sea water above the instrument, and ΔD is the distance of the pressure sensor below the acoustic transducer. The depth-averaged density is determined from the CTD casts performed at deployment and recovery of the IPS (see Section 3.1.3). Table 18 lists the values of these parameters used in the processing of the M2, M3 and M4 IPS data.

Table 18. Values used in the derivation of water level time-series for each measurement site during 2017–2018 deployment

Parameter	M2	M3	M4
$\boldsymbol{g}$ [m·s^{-2}]	9.826043	9.826125	9.826242
$\Delta\boldsymbol{D}$ [m]	-0.193	-0.169	-0.169
$\boldsymbol{\rho}$ [kg·m^{-3}]	1023.57	1022.12	1023.44

The total instrument tilt was computed using the pre-processed tilt vector components, θ_x and θ_y, measured by the IPS:

Equation 3

$$\theta = \sqrt{{\theta_x}^2 + {\theta_y}^2}$$

Due to power limitations, the IPS acquired pressure and tilt component observations less frequently relative to the acoustic target measurements. The sampling frequency was carefully selected with a view to minimize the power draw while resolving the anticipated tilt and pressure effects due to mooring motion. The derived water level and total instrument tilt time-series described above was then interpolated to the time sequence of the acoustic target time-series.

If the water level and total instrument tilt time-series do not resolve high-frequency signals, this interpolation can lead to aliasing effects in the derived ice drafts. To minimize these effects, the water level and total instrument tilt time-series were smoothed through episodes of unresolved perturbations. These perturbations were often due to mooring strumming as a result of vortex shedding and high-frequency pressure changes due to surface waves.

The M2 IPS was exposed to some wave events through the fall and early winter which yielded tilts of up to 6 degrees (Figure 6). The pressure record indicates a single major pull down event of up to 3 m which lasted a day and a half starting on November 4, 2017. The M3 IPS only encountered 4 events where the tilt was 4 degrees or larger, and the largest tilts were 6 degrees. There was a single pull-down event of 3–5 m which lasted about 5 days from November 5 to November 10, but which had 3 sub-events (Figure 7). Smaller pull-downs of a 1-2 m were observed in mid-February, early August and early October. The M4 mooring experienced 3 events where the tilts exceeded 4 degrees, one of which reached 11 degrees (Figure 8). This tilt event occurred during an 8.5 m pull-down which started on November 18, 2017 and which was driven by current speeds of up to 80 cm/s. A second pull-down of 6 m occurred in March, 2019.

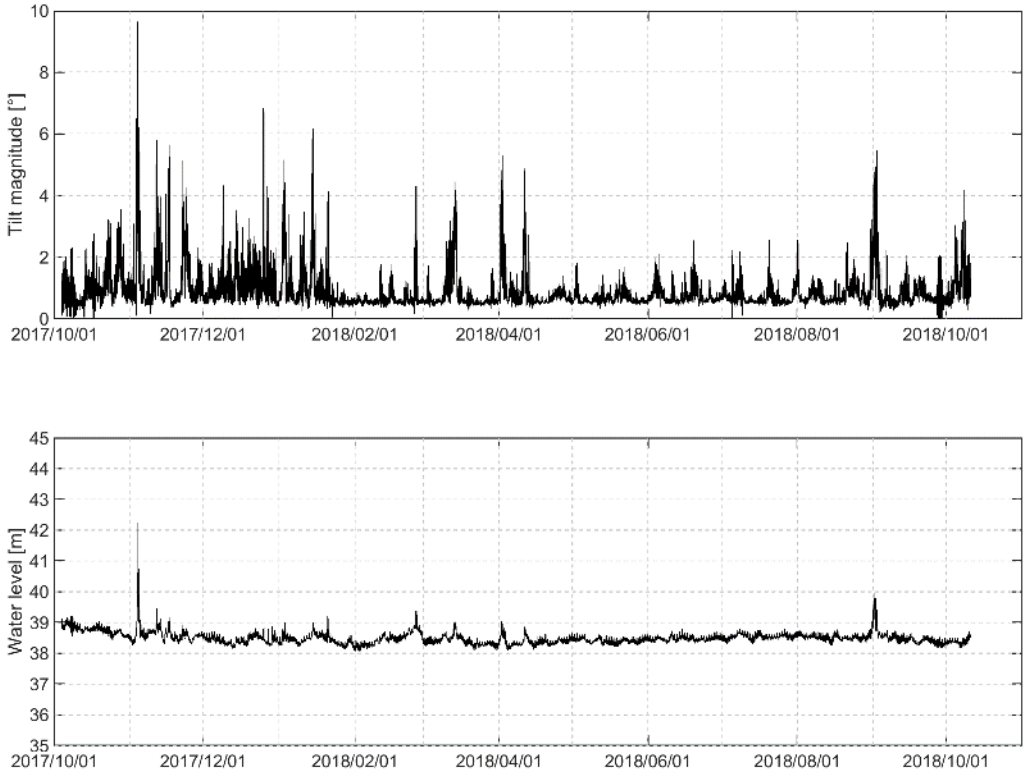

Figure 6. M2 tilt magnitude (top) and water level (bottom) 2017–18 time-series
The measurements at 42 m correspond to a pull-down event which lasted for about a day and a half starting on November 4, 2017.

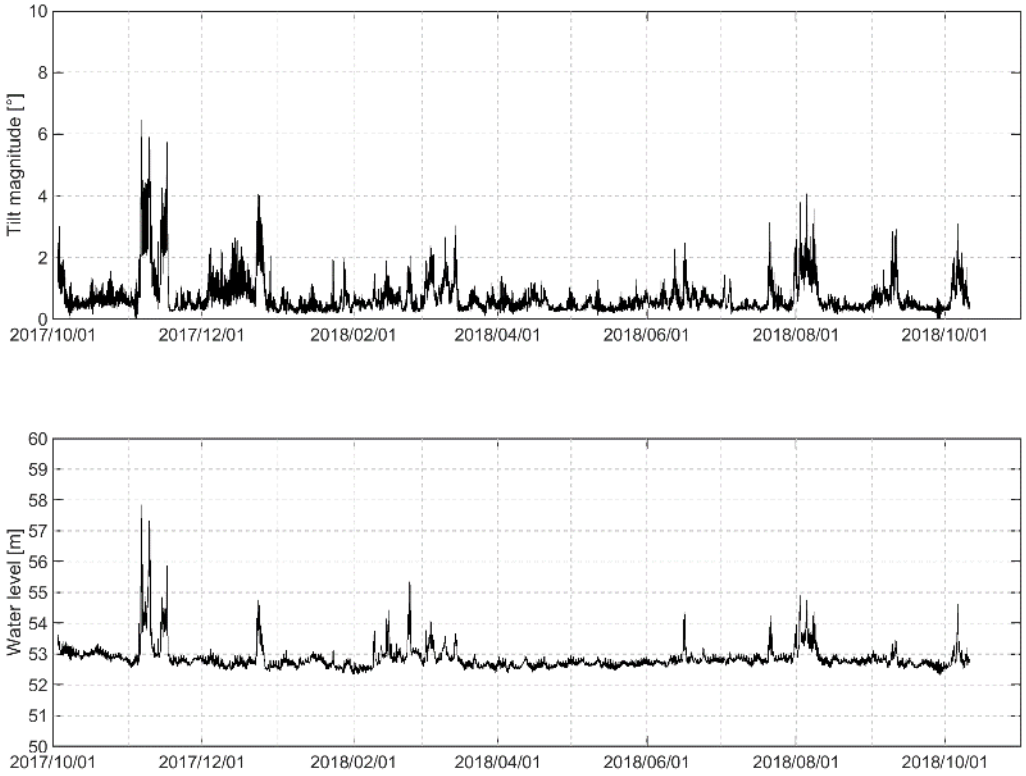

Figure 7. M3 tilt magnitude (top) and water level (bottom) 2017–18 time-series
The main pull-down event lasted 5 days from November 5 to November 10 and was up to 6 m in depth.

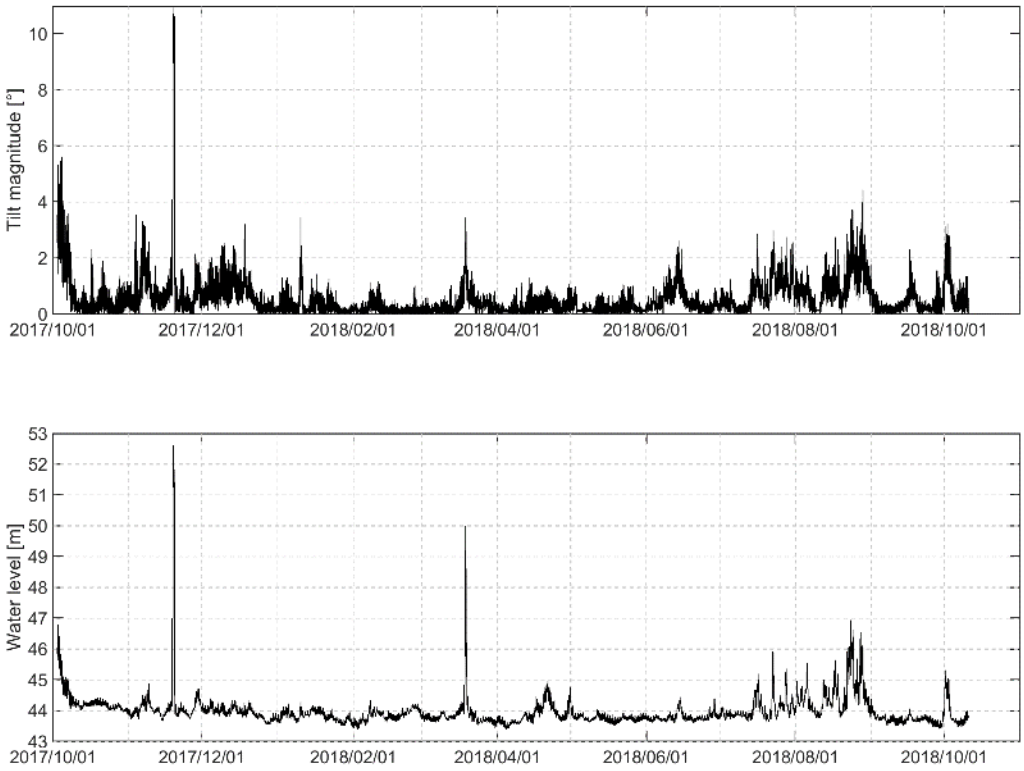

Figure 8. M4 tilt magnitude (top) and water level (bottom) 2017-18 time-series
The 52 m measurements correspond to a pull-down event which lasted 2 days starting on November 18, 2017. The 50 m measurements correspond to a pull-down event which lasted about a day starting on March 18, 2018.

The factor, β, applied to the measured range in Equation 1 represents the ratio of the actual speed of sound to the assumed value. To determine β, open water segments in the range data were selected and β was empirically computed. This process involved several iterations, starting with the coarse seasonal sound speed trends developed in the first pass. Subsequent iterations injected modulations for short- and medium-term fluctuations of the sound speed which can include freshwater inputs, major ocean stratification variations due to upwelling and downwelling, solar irradiance fluctuations leading to air temperature changes and radiative heating of the ice and surface water, and vertical motion of the IPS through stratified water masses during mooring pull-down events. Care must be taken during episodes of potential thin ice and/or surface waves that ice targets within the ice draft time-series are not miscategorized as open water. This requires thorough interpretation of all available evidence including meteorology, ice drift, satellite imagery, sea ice charts, and the ice draft time-series itself. The final β time-series for M2, M3 and M4 are plotted in Figure 9 through Figure 11.

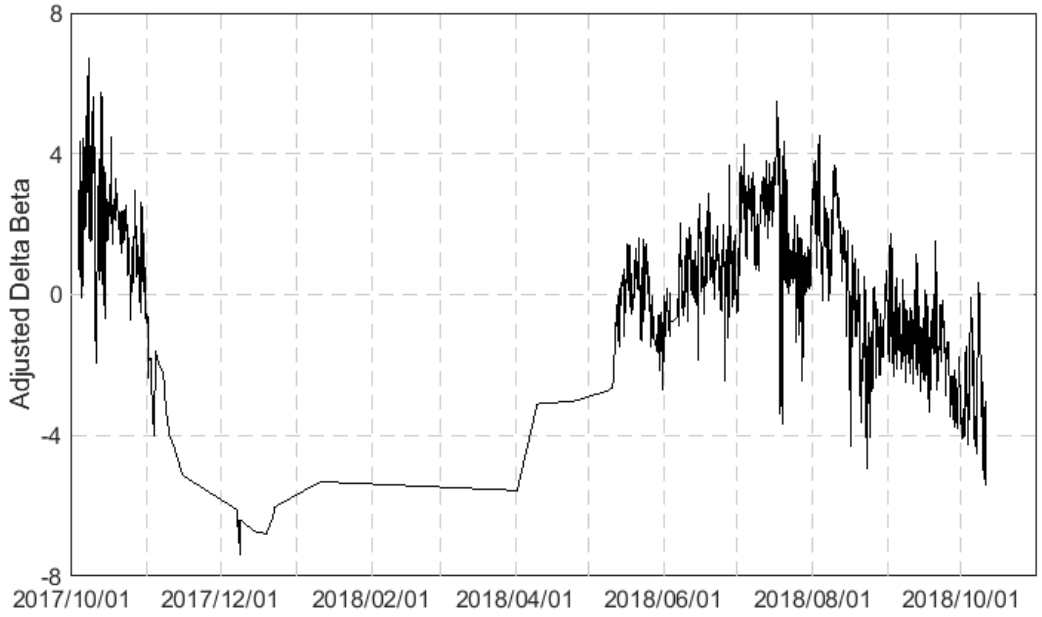

Figure 9. Adjusted delta beta curve correcting sound speed at M2 (above)

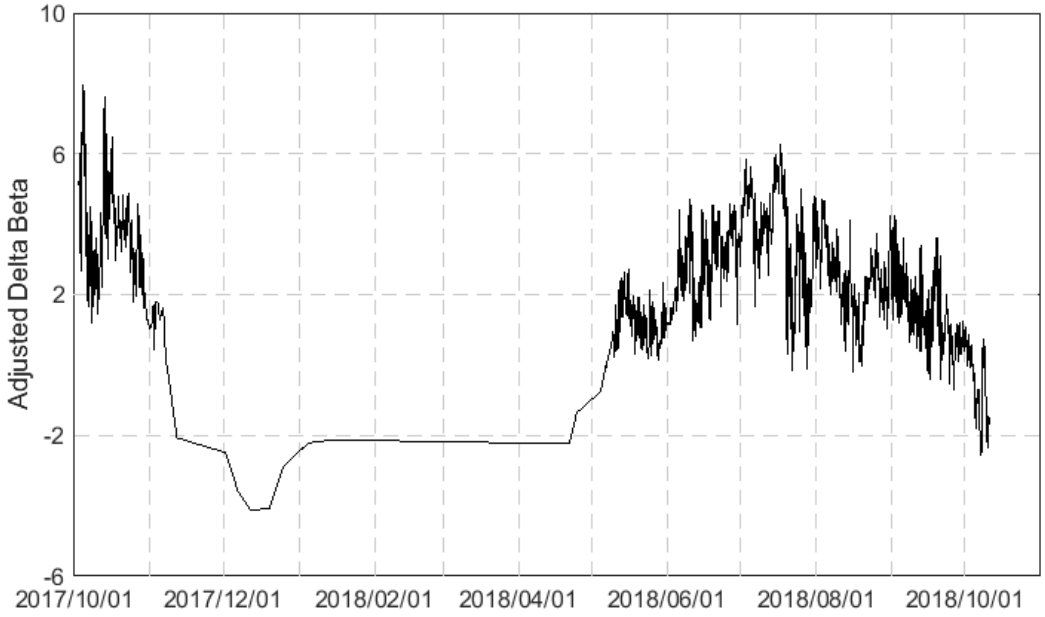

Figure 10. Adjusted delta beta curve correcting sound speed at M3 (above)

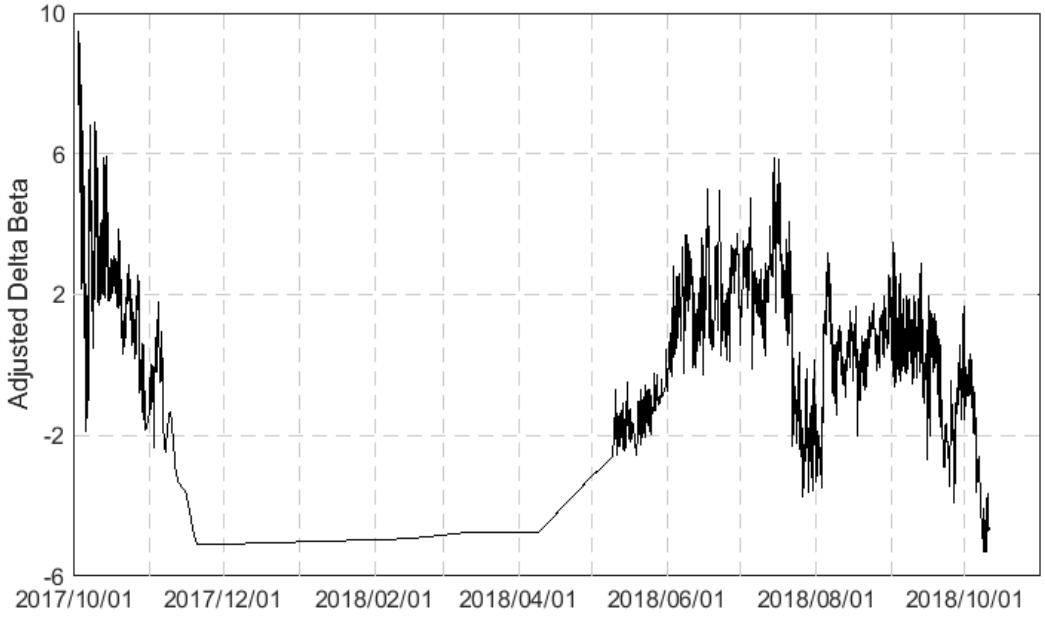

Figure 11. Adjusted delta beta curve correcting sound speed at M4 (above)

These time-series of sound speed correction are notable as they contribute most to the accuracy in the final ice draft time- and spatial-series. As the sound speed time-series are empirically derived, they are influenced by effects in addition to sound speed, for example, bias within the IPS sensors and uncertainty in selection of open water events. The advantage of the empirical approach is that these effects are corrected for; however, caution should be used when interpreting the β time-series for insight into sound speed. The β time-series follow the seasonal trends in air temperature with the highest values occurring in the shoulder seasons—October to November 2017 and mid-May to late-July 2018. The high-frequency fluctuations during these episodes are due to the heat cycling through daylight hours, short-term perturbations due to cold water masses accompanying massive ice features, upwelling of water masses, pulses of freshet, and mooring pulldown through stratified water. Conversely, the β time-series through the winter is relatively constant.

After the ice draft time-series was calibrated for sound speed variations, each record was classified as either ice or open water. The open water records were set to a flag value of -200. Summary statistics of the extent of open water classification in each of the M2, M3 and M4 ice draft time-series are listed in Table 39 through Table 41 in Section 3.1.1.4.3, respectively.

Ice draft time-series were converted to a distance (or spatial) series using the quality-controlled ADCP ice velocity time-series (see Section 2.3.1.3). The cumulative distance was calculated using the east and north displacements for each sample from beginning to end.

The ice draft was sampled at regular time intervals but due to the irregular motion of the ice cover, the resulting distance series was unevenly spaced. To account for this, the distance series was interpolated to regular increments using a double-weighted double-quadratic interpolation scheme:

Equation 4

$$y(x_i) = \frac{Y_1[y(u_{i+2}) - y(u_{i+1})][x_i - x(u_{i+1})] + Y_2[y(u_i) - y(u_{i-1})][x_i - x(u_i)]}{[y(u_{i+2}) - y(u_{i+1})][x_i - x(u_{i+1})] + [y(u_i) - y(u_{i-1})][x_i - x(u_i)]}$$

As shown in Figure 12, the value Y_1 represents the value obtained from a quadratic interpolation using two points to the left and one to the right of x_i and Y_2 represents the interpolated value using two points to the right and, one to the left of x_i. In the figure, the desired regularly spaced interpolation point is x_i, and the measurement locations are given by u_{i-1}, u_i, u_{i+1} and u_{i+2}. The two interpolated values were then averaged using a weighting factor based on the distance between points and on the change in draft between points. The double weighting scheme, shown in Figure 12, was adopted to avoid overshoots in regions of high draft gradients. In order to represent the ice drafts at low ice velocities, the ice draft data were interpolated to 0.10 m distances then block averaged to 1.0 m distances.

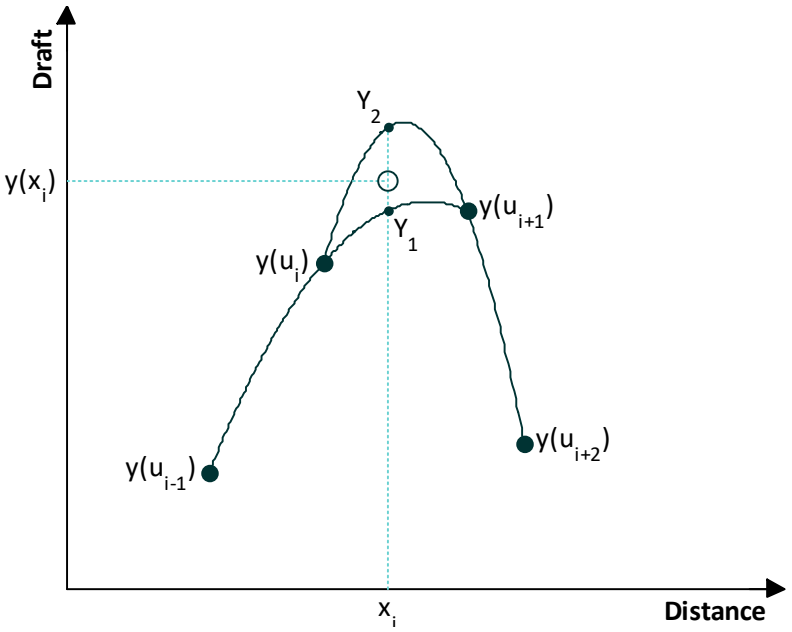

Figure 12. Double quadratic interpolation method used to convert the ice draft time series into a spatial series

2.3.2 ADCP Backscatter

ADCP backscatter analysis focused on the data from the single ADCP at M1 (at 35 m depth) and the two ADCPs at M2 (at 58 m—M2 Upper, and 169 m—M2 Lower depth). Initial processing of the data, including quality control and processing of the velocity data, was conducted as described in Section 2.3.1. Further quality control and processing of the backscatter data was conducted as part of this additional analysis.

All three of the instruments were 300 kHz RDI Workhorse ADCPs. During the year, the depth of the transducers varied slightly as the mooring chain tilted in the prevailing currents. All instruments had beam angles of 20° and were set to a blank interval of 1.76 m. All instruments collected one profile every 1 minute. However, the pulse length, bin length, and number of bins differed between the three ADCPs (Table 19).

Table 19. Parameters used in calculation of volume backscattering (Sv) and settings used for each ADCP during 2017–2019 deployment

ADCP	Bandwidth	C	E_r	a	P_{DBW}	L_{DBM}	q	B	L	D	N
	%	(dB)	(4-beam average)				(Beam Angle, °)	(Blank, m)	(Pulse Length, m)	(Bin length, m)	(# Bins)
M1a	6.25	-151.64	39.5	0.069	14	3.7475	20	1.76	2.37	2	40
M2Upper	6.25	-151.64	42.75	0.069	14	3.7475	20	1.76	2.37	2	35
M2Lower	6.25	-151.64	69	0.069	14	6.2014	20	1.76	4.17	4	29
Source	D.Torres	Mullison	Data	Deines	Mullison	Data	RDI	Data	Data	Data	Data

NOTE: The source of each parameter also is indicated (Deines, 1999; Mullison, 2017; Data from the instrument). Parameters used in the absolute backscatter equation are defined below.

Checking Consistency in Measured Return Signal Strength between Four Beams of Each ADCP

As a first step, the measured return signal strength amplitude (E_r; Mullison 2017) measured for each beam was compared between the four beams of each instrument to ensure that the signal strengths were relatively compatible and that there was no drift or deviation in one of the four beams over the period (~1 year) of the deployment. To do this, the signal strengths for all four beams were plotted together for all of the bins in the profile at 12 evenly spaced times during the deployment period. Some variation between beams was expected. None of the instruments displayed substantial deviations in the signal strengths for the individual beams over the deployment period. As a result, all four beams were included in the average signal strength amplitudes for the deployment. This analysis also identified periods with bad data at the start and end of the record that were collected while the instrument was on deck before and after deployment; these ensembles were removed in subsequent analyses.

Calculation of "Absolute" Backscatter

"Absolute" backscatter was calculated for using measured return signal strength amplitude (counts) from the four beams or each instrument according to the updated equation in Mullison (2017). Mullison (2017) updated the equation of Deines (1999) to include the correct calculation of signal to noise and to be more correct for very low backscatter environments. Accordingly, the equation is:

Equation 5

$$S_v = C + 10\log((T_x + 273.16)R^2) - L_{DBM} - P_{DBW} + 2\alpha R + 10\log(10^{kc(E-Er)/10}-1)$$

Where S_v is the absolute backscatter equation, C is an RDI ADCP model specific constant that depends on the bandwidth used, T_x is the transducer temperature for profile x, k_c is a factor used to convert counts to decibels (dB) that is specific for each beam for each instrument, R is the along-beam range, E is the return strength signal indicator (counts), E_r is the measured return strength in the absence of any signal, L_{DBM} is 10log(pulse length), and P_{DW} is 10logTransmit power. As noted in Table 19, C and P_{DBW} are from Mullison (2017), and α is from Deines (1999), and L_{DBM}, R and E_r are calculated from the data and settings of the instrument. For these data, E_r for each instrument was calculated as the minimum E recorded for the period of the deployment; for all instruments, this minimum was collected from the furthest bin from the instrument (a similar approach was taken using an Acoustic Zooplankton Fish Profiler (AZFP) by Kitamura et al. 2017). As a check, the minimum E was also determined for each beam from bins located below the sea surface; the E_r values from these calculations were very similar to the minima calculated from the entire data set. Values of K_c for each beam for each instrument were obtained from Teledyne. Range (R) was calculated according to equation (3) in Deines (1999) using the blank, bin length, pulse length, beam angle, and bin number. After the absolute backscatter was calculated for each beam, those values were averaged for the four beams.

Despite S_v being termed “absolute backscatter” (Mullison 2017), there remains sufficient uncertainty in the calculation, so that it should still be considered as a type of “relative backscatter”, albeit carefully calculated.

Merging M2 Upper and M2 Lower Data

The data sets from the upper and lower ADCPs on mooring M2 each covered only a portion of the water column, with the lower ADCP data covering 52 m to 164 m and the upper ADCP covering 5 m to 53 m. Comparison of the backscatter at the overlapping depth bins for the profile at each matching time step revealed that the backscatter was consistently greater from the lower instrument than from the upper instrument. Therefore, a correction was applied to the backscatter from the upper instrument by calculating the difference between the backscatter for each profile at the 51 m depth bin and applying that constant correction to the backscatter in the remaining bins of the upper instrument profile. The assumption here is that the correction would not vary with range from the transducer. Since there was only one depth bin for which the data from the two instruments overlapped, it was necessary to accept this assumption. However, since the data are used to analyze temporal and spatial patterns in distributions and the seasonal variation in backscatter within this data, this assumption was acceptable. The two data arrays then were concatenated together. Since the upper instrument collected data in 2-m depth bins while the lower instrument collected data in 4-m depth bins, the data in each profile then were interpolated to 2-m depth bins.

Editing of Spurious Data and Subsampling the Time Periods

Additional editing was conducted for each data set to remove spurious data resulting from backscatter off sea ice, floats suspending instruments shallower on the mooring string than the ADCPs, from sea ice, and from unknown but obvious interference. For each data set (the mean S_v from the four beams), all points at depths shallower than the surface, including a few meters to remove scattering from the surface, were removed. Each profile for each ADCP then was smoothed using a 5-point running average; for depths where a single or several observations had been removed by the blanking (such as for the floats), the smoothing produced a meaningful value. After smoothing, the signature of the floats was still visible in the M2 Upper backscatter at rows 18 , 19, and 25. To remove the signal in bins 18 and 19, the backscatter from bins 17 and 20 were averaged and placed into bin 19 for each profile. Then the backscatter in bins 17 and 19 was calculated and placed into bin 18 for each profile. The backscatter in row 25 was replaced by the average of the backscatter in rows 24 and 26. Similarly, the signal of moored CTD was observed in the M1 data at bins 2 and 3. Averaging of data from bins 1 and 4 were used to correct the bins 2 and 3 data. For both instruments, there also were some very low and some very high values of backscatter in the file that were removed by setting all values of backscatter less than -100 to -100 and all values greater than -55 to -55. For M1, ice generated some very high backscatter signals that also were removed.

The data sets had a profile every minute, making them very large as well as quite variable. To help discern general patterns and for ease of comparison, data were averaged into 30 min averages across the deployment periods.

Mean Backscatter, Velocities, Temperature, and Salinity

To examine changes in water column backscatter and associations of those changes with hydrography and currents, u and v velocities were calculated from the speed and direction data resulting from the initial ADCP processing (Section 2.3.1.1). The daily mean u and v velocities and backscatter then were calculated for each profile. This removed any diel signal in the vertical distribution of backscatter and vertical shear in velocities. Mean daily temperature and salinity from the near bottom CTD on each mooring also was calculated (M1: 36 m; M2: 162 m).

Detecting Diel Vertical Migration (DVM)

Diel vertical migration was detected in a manner similar to the approach of Ashjian et al. (1998, 2002) and following methodology developed for the 2016-2017 MARES moored ADCPs (Wiese et al. 2019). Backscatter at 18 m and at 82 m were used as indicator depths for M1 and M2, respectively. These depths were in the middle of the range of the depth data for each instrument and for some periods showed a daily periodicity in magnitude. The times of each profile in the data was converted to local Alaskan Daylight Time. This placed the time of sunrise and sunset within the 24 hours of a single day for most of the period of the deployment. Times of sunrise and sunset for each day were calculated. For each day in the data records, the time of the data points was adjusted so that the times of sunrise was set to 6 AM and of sunset at 6 PM and noon and midnight remained set, with points in between these four fixed points proportionally adjusted. This adjustment meant that a typical diel signal in the vertical distribution could be approximated using a sinusoidal curve. Also, for each day, the magnitude of backscatter was standardized to the maximum value so that the range varied from 0 to 1. A sinusoid curve was calculated for each 24-hour period, using the cosine function and converting times from that day into degrees from 0 to 360. Both the standardized backscatter and the values of the sinusoid curve were adjusted to share a common range of -0.5 to 0.5. For each day, the deviation of the observed pattern in backscatter from the sinusoid was expressed as the sums of squares of the hourly differences between backscatter and the reference curve:

Equation 6

$$\mathrm{SS}=\sum_{0}^{23}(Sv - Sincurve)^2/(n-1)$$

Good adherence to the sinusoid curve yielded SS values of approximately 0.15 or less.

2.3.3 Ice Profiling Sonar (IPS)

2.3.3.1 Configuration

The IPS instrument is an upward-looking ice profiling sonar, which provides the high-resolution ice thickness, or more correctly, ice draft data required for characterizing the winter oceanic environment. The IPS operates in a pulsed mode with its acoustic beam directed toward zenith. A multi-faceted algorithm (Melling et al. 1995) identifies the target, which may be the underside of sea-ice or the air-water interface. Targets are detected using the range, amplitude and persistence parameters. From this initial selection, up to 5 targets of longest persistence are recorded. Choice of the control parameters must be carried out with a view to minimizing the likelihood that the algorithm will select echoes from sources within the water-column as opposed to the ice under-surface. The ice keel depth is determined from the return travel time of an acoustic pulse (420 kHz; 1.8° beam at -3 dB) reflected off the underside of the sea ice. The return time is converted to an acoustic range value using the average speed of sound in seawater. A pressure sensor (Paroscientific Digiquartz) is used to determine water level changes due to tidal and wind forcing, as well as apparent water level changes arising from depression/tilt of the mooring. A pitch/roll sensor enables correction of instrument tilt effects on the measured target ranges. A temperature sensor provides an estimate of the ambient water temperature near the instrument.

There are three primary concerns when configuring an IPS prior to deployment. Firstly, the sampling scheme for an IPS can be varied throughout a deployment using sampling phases. Each phase spans a set time episode and employs distinct sample intervals for the acquisition of acoustic and ancillary measurements. Secondly, the IPS firmware performs on-board target detection and requires setting of echo amplitude target parameters for each phase. Thirdly, the IPS employs multiple sensors including sonar, pressure, tilt, and temperature. Each sensor has a unique set of calibration coefficients determined during the manufacture and testing of an IPS unit. Table 20 through Table 22 list the key configuration parameters for the IPS units used at M2, M3 and M4, respectively.

Table 20. Key M2 IPS configuration parameters during 2017–2018 deployment

Parameter	Phase					
	1	2	3	4	5	6
Start [yyyy-mm-dd UTC]	2017-09-25	2017-10-15	2017-12-14	2018-03-31	2018-09-01	2018-09-21
End [yyyy-mm-dd UTC]	2017-10-14	2017-12-13	2018-03-30	2018-08-31	2018-09-20	Continuous
Ping interval [sec]	5	1	1	1	5	1
Ancillary interval [sec]	60	10	10	10	60	10
Profile interval [sec]	N/A	60	60	60	N/A	60
Target start amplitude [counts]	10,000	7,000	7,000	7,000	1,0000	7,000
Target stop amplitude [counts]	9,000	6,000	6,000	6,000	9,000	6,000
Minimum persistence [µsec]	62	62	62	62	62	62
Lockout range [m]	1	1	1	1	1	1
Maximum range [m]	60	60	60	60	60	60

NOTE:
Ping interval is the duration between successive acoustic pings; **Ancillary interval** is the duration between successive pressure, tilt, temperature and battery voltage acquisitions; **Profile interval** is the duration between successive storage of the full echo profile corresponding to an acoustic ping; **Target start amplitude** is the threshold that must be exceeded to be considered a target; **Target stop amplitude** is the threshold that defines the end of a target; **Minimum persistence** is the duration between the target start and stop amplitudes that must be exceeded to be considered a target; **Lockout range** and **Maximum range** are the minimum and maximum distances within which acoustic backscatter amplitudes are detected.

Table 21. Key M3 IPS configuration parameters during 2017–2018 deployment

Parameter	Phase					
	1	2	3	4	5	6
Start [yyyy-mm-dd UTC]	2017-09-25	2017-10-15	2017-12-14	2018-03-31	2018-09-01	2018-09-21
End [yyyy-mm-dd UTC]	2017-10-14	2017-12-13	2018-03-30	2018-08-31	2018-09-20	Continuous
Ping interval [sec]	5	1	1	1	5	1
Ancillary interval [sec]	60	10	10	10	60	10
Profile interval [sec]	N/A	60	60	60	N/A	60
Target start amplitude [counts]	10,000	7,000	7,000	7,000	10,000	7,000
Target stop amplitude [counts]	9,000	6,000	6,000	6,000	9,000	6,000
Minimum persistence [µsec]	62	62	62	62	62	62
Lockout range [m]	10	5	5	5	10	5
Maximum range [m]	70	70	70	70	70	70

NOTE:
Ping interval is the duration between successive acoustic pings; **Ancillary interval** is the duration between successive pressure, tilt, temperature and battery voltage acquisitions; **Profile interval** is the duration between successive storage of the full echo profile corresponding to an acoustic ping; **Target start amplitude** is the threshold that must be exceeded to be considered a target; **Target stop amplitude** is the threshold that defines the end of a target; **Minimum persistence** is the duration between the target start and stop amplitudes that must be exceeded to be considered a target; **Lockout range** and **Maximum range** are the minimum and maximum distances within which acoustic backscatter amplitudes are detected.

Table 22. Key M4 IPS configuration parameters during 2017–2018 deployment

Parameter	Phase					
	1	2	3	4	5	6
Start [yyyy-mm-dd UTC]	2017-09-25	2017-10-15	2017-12-14	2018-03-31	2018-09-01	2018-09-21
End [yyyy-mm-dd UTC]	2017-10-14	2017-12-13	2018-03-30	2018-08-31	2018-09-20	Continuous
Ping interval [sec]	5	1	1	1	5	1
Ancillary interval [sec]	60	10	10	10	60	10
Profile interval [sec]	N/A	60	60	60	N/A	60
Target start amplitude [counts]	10,000	7,000	7,000	7,000	10,000	7,000
Target stop amplitude [counts]	9,000	6,000	6,000	6,000	9,000	6,000
Minimum persistence [µsec]	62	62	62	62	62	62
Lockout range [m]	10	5	5	5	10	5
Maximum range [m]	70	70	70	70	70	70

NOTE:
Ping interval is the duration between successive acoustic pings; **Ancillary interval** is the duration between successive pressure, tilt, temperature and battery voltage acquisitions; **Profile interval** is the duration between successive storage of the full echo profile corresponding to an acoustic ping; **Target start amplitude** is the threshold that must be exceeded to be considered a target; **Target stop amplitude** is the threshold that defines the end of a target; **Minimum persistence** is the duration between the target start and stop amplitudes that must be exceeded to be considered a target; **Lockout range** and **Maximum range** are the minimum and maximum distances within which acoustic backscatter amplitudes are detected.

2.3.3.2 Pre-processing

IPS data pre-processing consists of the following steps in accordance with a methodology that has been developed since the 1990s (Fissel et al. 2008; Melling et al. 1995); however, every data set is unique and the general processing procedures outlined below are customized as necessary:

1. Converting raw IPS data from binary form in instrument units to nominal engineering units using the IPS5Extract desktop application. The raw time-series data is plotted, and summary statistics are calculated. These are reviewed for major quality issues including instrument failure, large data gaps, high fractions of anomalous data values, and ice events within the blanking range. Distinct events in the raw data such as the entry into and exit from the water are compared to field notes of the timing of these events to verify consistency with external observations. Events, such as mooring pull-down, that are evident in the range and pressure time-series are compared to verify the internal consistency of the time values associated with each raw data time-series.
2. Correcting the timing characteristics of the IPS data files for the effects of instrument clock time drift. The correction is derived from a comparison of instrument start and stop times with times from an independent clock recorded on start-up and shut-down of the instrument.
3. Automatically correcting for double bounce effects. The acoustic signal transmitted by the IPS can transit the water column multiple times. Under certain deployment conditions, this effect is recorded resulting in range measurements that are too high. If available in the target data, these

records are replaced with more appropriate targets; otherwise, the range value is corrected arithmetically or by linear interpolation.

4. Removing unnecessary data at the start and end of the data record related to out-of-water time before deployment and after recovery.
5. Automated editing of range records associated with no targets. The IPS records the maximum amplitude and corresponding range for every ping regardless of the target detection results. For those pings that do not realize a target, this information can often be used to approximate a target range. All pings that realize a single target with moderate maximum amplitude, defined as the start amplitude plus 10,000 counts, are selected. The range difference between the start amplitude crossing point and the maximum amplitude is calculated for each of these selected targets. The average range difference is computed and is used to correct the range at maximum amplitude for those pings that did not realize a target but whose maximum amplitude exceeded 500 counts. Any gaps remaining after this null target replacement step that are shorter than 10 seconds are linearly interpolated. Figure 13 shows an example data segment containing range drop-outs.

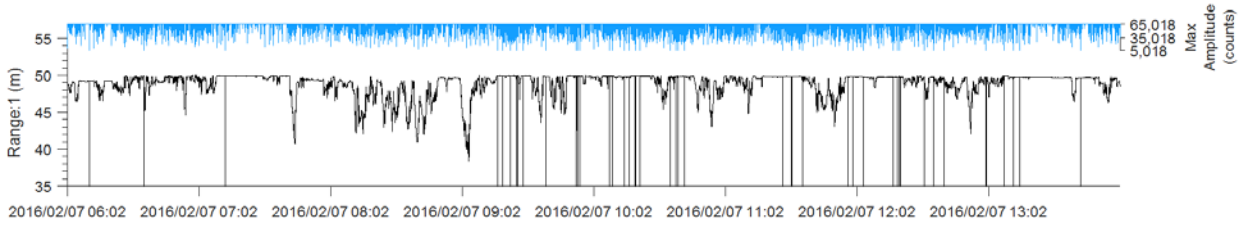

Figure 13. Example of unedited range and amplitude data measured by an IPS during 2017–2018 deployment, showing a period characterized by sea-ice floes and some range "drop-outs"

6. Automated editing of range values considered to be too high. The detection threshold for high range values is calculated as: *instrument depth at high tide + buffer*. The *buffer* value avoids clipping of wave peaks and is determined through a manual review of the raw data.
7. Masking of segments of range data that show evidence of large waves. This prevents the records corresponding to the wave extremes from being identified as spikes in the later automated despiking steps. Figure 14 shows an example data segment containing large waves.

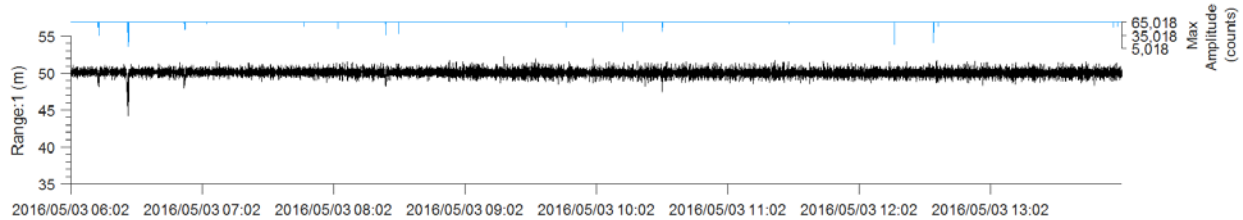

Figure 14. Example of unedited range and amplitude data measured by an IPS during 2017–2018 deployment, showing a period following the main part of the ice season

8. Automated removal of anomalous range and ancillary values based on first-difference values. This includes at least two iterations to remove anomalous features in the range data with lengths of one to four records. The thresholds are refined through trial despiking iterations and reviews of the results. Initial first difference thresholds for the range data is determined through the horizontal distance traveled by the average ice velocity over one IPS range sample interval.

9. Patching of the previously masked segments of range data back into the data record
10. Manually reviewing the edited data for any additional spikes or suspect values. These may include targets within the lockout range and short duration targets due to bubbles associated with strong winds and large waves. The amplitude data is often helpful in classification of range features during this step.
11. Any remaining data gaps in the range, pressure and tilt time-series are reviewed and edited manually.
12. If available, the pressure measured by the IPS when the instrument is vertical and out of the water is compared to coincident and independent measurements of the sea level pressure. The pressure head due to the oil within the IPS pressure sensor must be accounted for. Any resulting offset is applied as a correction to the IPS pressure.

The extent of editing that resulted from the above pre-processing steps is summarized for the M2, M3, and M4 IPS data sets in Table 23 through Table 25, respectively.

Table 23. Summary of the two main stages of IPS processing (range time-series and ice draft time-series) for M2 during 2017–2018 deployment, giving number of data records having errors that were detected and edited

	Phase	1	2	3	4	5	6
	Start date/time [yyyy-mm-dd hh:mm:ss UTC]	2017/10/03 22:37:27.214	2017/10/15 00:00:51.095	2017/12/14 00:02:58.213	2018/03/31 00:06:44.463	2018/09/01 00:12:10.092	2018/09/21 00:12:52.132
	Stop date/time [yyyy-mm-dd hh:mm:ss UTC]	2017/10/15 00:00:50.596	2017/12/14 00:02:57.207	2018/03/31 00:06:43.433	2018/09/01 00:12:09.051	2018/09/21 00:12:47.635	2018/10/11 00:44:00.70
	Sample interval [sec]	5.0001224	1.0000245	1.0000245	1.0000245	5.0001086	1.0000246
Range	**Replaced multiple transit** [# records]	0	0	0	0	0	0
	Replaced null targets [# records]	577	69,500	304,455	136,178	111	1,595
	Interpolated null targets [# records]	0	0	0	0	0	0
	Interpolated out-of-bound [# records]	121	310	1,100	294	14	312
	Interpolated single spikes [# records]	0	1,238	5,867	6,380	0	0
	Interpolated double spikes [# records]	0	108	712	806	0	0
	Interpolated triple spikes [# records]	0	0	33	72	0	0
	Interpolated quadruple spikes [# records]	0	0	4	4	0	0
	Interpolated manually [# records]	0	16	27	101	0	6
Ice draft	**Interpolated manually** [# records]	0	0	0	121	0	0
	Identified open water (0) [# records]	191,076 (100%)	1,407,061 (27.14%)	0 (0%)	4,642,250 (34.89%)	345,589 (100%)	1,505,116 (87.01%)
	Total data [# records]	191,076	5,183,991	9,244,791	13,305,591	345,589	1,729,821
	Identified poor-quality data (-9999) [#records]	0	0	0	0	0	0
	Total edited data [# records]	0 (0%)	45 (<1%)	33 (<1%)	416 (<1%)	0 (0%)	0 (0%)

NOTE:
Distinction is made between those records that have been interpolated and those that have been replaced by other measurement data.

Table 24. Summary of the two main stages of IPS processing (range time-series and ice draft time-series) for M3 during 2017–2018 deployment, giving number of data records having errors that were detected and edited

	Phase	1	2	3	4	5	6
	Start date/time [yyyy-mm-dd hh:mm:ss UTC]	2017/10/02 20:43:27.152	2017/10/15 00:00:57.138	2017/12/14 00:03:20.907	2018/03/31 00:07:36.208	2018/09/01 00:13:43.333	2018/09/21 00:14:30.239
	Stop date/time [yyyy-mm-dd hh:mm:ss UTC]	2017/10/15 00:00:53.636	2017/12/14 00:03:18.952	2018/03/31 00:07:27.204	2018/09/01 00:13:35.433	2018/09/21 00:14:27.739	2018/10/10 22:35:43.512
	Sample interval [sec]	5.0001263	1.0000256	1.0000256	1.0000256	5.0001285	1.0000257
Range	**Replaced multiple transit** [# records]	0	0	0	0	0	0
	Replaced null targets [# records]	287	24,216	67,189	34,747	16	437
	Interpolated null targets [# records]	0	0	0	0	0	0
	Interpolated out-of-bound [# records]	28	28	33	37	0	27
	Interpolated single spikes [# records]	0	1,789	6,976	11,420	0	0
	Interpolated double spikes [# records]	0	120	696	1,350	0	0
	Interpolated triple spikes [# records]	0	12	27	48	0	0
	Interpolated quadruple spikes [# records]	0	4	20	4	0	0
	Interpolated manually [# records]	0	495	1504	2,206	0	0
Ice draft	**Interpolated manually** [# records]	0	41	0	47	0	0
	Identified open water (0) [# records]	209,712 (100%)	1,344,685 (25.94%)	0 (0%)	7,877,055 (59.21 %)	345,601 (100%)	1,722,030 (100%)
	Total data [# records]	209,712	5,184,010	9,244,811	13,305,620	345,601	1,722,030
	Identified poor-quality data (-9999) [# records]	0	0	0	0	0	0
	Total edited data [# records]	0 (0%)	41 (<1%)	0 (0%)	47 (<1%)	0 (0%)	0 (0%)

NOTE:
Distinction is made between those records that have been interpolated and those that have been replaced by other measurement data.

Table 25. Summary of the two main stages of IPS processing (range time-series and ice draft time-series) for M4 during 2017–2018 deployment, giving number of data records having errors that were detected and edited

	Phase	1	2	3	4	5	6
	Start date/time [yyyy-mm-dd hh:mm:ss UTC]	2017/10/02 18:05:26.662	2017/10/15 00:00:55.831	2017/12/14 00:03:13.595	2018/03/31 00:07:19.730	2018/09/01 00:13:13.966	2018/09/21 00:14:00.220
	Stop date/time [yyyy-mm-dd hh:mm:ss UTC]	2017/10/15 00:00:49.833	2017/12/14 00:03:03.570	2018/03/31 00:07:09.691	2018/09/01 00:13:03.925	2018/09/21 00:12:55.209	2018/10/10 20:20:55.606
	Sample interval [sec]	5.0001331	1.0000266	1.0000266	1.0000266	5.0001338	1.0000265
Range	Replaced multiple transit [# records]	0	0	0	0	0	0
	Replaced null targets [# records]	286	17,948	35,846	7,456	29	221
	Interpolated null targets [# records]	0	0	0	0	0	0
	Interpolated out-of-bound [# records]	31	24	28	7	0	14
	Interpolated single spikes [# records]	0	2,275	0	8,937	0	4
	Interpolated double spikes [# records]	0	274	0	1,068	0	0
	Interpolated triple spikes [# records]	0	36	0	0	0	0
	Interpolated quadruple spikes [# records]	0	4	0	0	0	0
	Interpolated manually [# records]	0	3	6,569	863	0	5
Ice draft	Interpolated manually [# records]	0	0	0	496	0	0
	Identified open water (0) [# records]	211,620 (100%)	1,760,006 (33.95%)	0 (0%)	7,414,465 (55.73%)	345,588 (100%)	1,701,174 (99.25%)
	Total data [# records]	211620	5183991	9244791	13305591	345588	1713971
	Identified poor-quality data (-9999) [#records]	0	0	0	0	0	0
	Total edited data [# records]	0 (0%)	9 (<1%)	8 (<1%)	538 (<1%)	0 (0%)	4 (<1%)

NOTE:
Distinction is made between those records that have been interpolated and those that have been replaced by other measurement data.

2.3.4 Conductivity-Temperature Time Series

Time series of temperature, conductivity, and pressure were made by a series of SBE37 MicroCATs, RBR Concertos and RBR XR-420 CT sensors at M1–M4 (Figure 15). Table 26 lists important parameters related to the deployment of each CT sensor on these moorings.

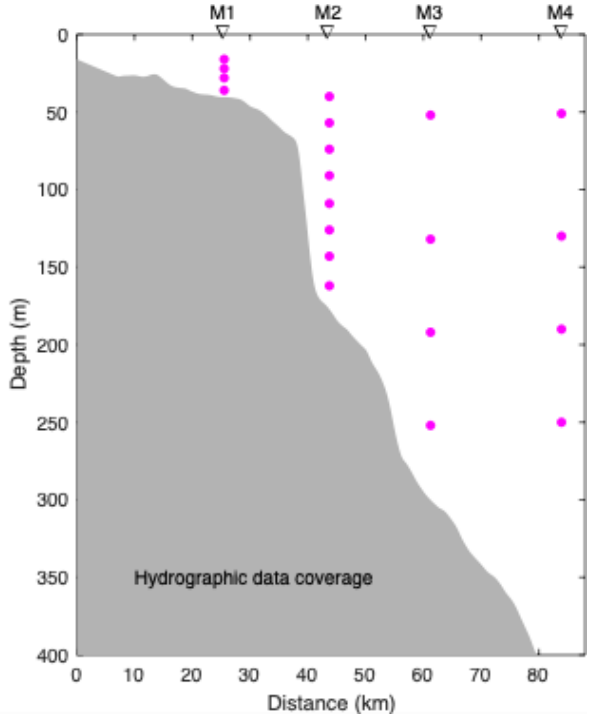

Figure 15. Data coverage of MicroCATs during the 2017–2018 deployment period

Table 26. Key deployment parameters for the CT sensors used on the M2, M3 and M4 moorings during 2017–2018 deployment, extending into 2019 at M1

Mooring	Depth [m]	Measured	Sample Interval [s]
M1	16	Temperature, Conductivity	300
	22	Temperature, Conductivity, Pressure	300
	28	Temperature, Conductivity, Pressure	300
	36	Temperature, Conductivity	900
M2	40	Temperature, Conductivity	900
	57	Temperature, Conductivity, Pressure	300
	74	Temperature, Conductivity, Pressure	300
	91	Temperature, Conductivity, Pressure	300
	109	Temperature, Conductivity, Pressure	300
	126	Temperature, Conductivity, Pressure	300
	143	Temperature, Conductivity, Pressure	2,700
	162	Temperature, Conductivity	900
M3	52	Temperature, Conductivity	900
	132	Temperature, Conductivity	900
	192	Temperature, Conductivity	900
	252	Temperature, Conductivity	900
M4	51	Temperature, Conductivity	900
	130	Temperature, Conductivity	900
	190	Temperature, Conductivity	900
	250	Temperature, Conductivity	900

The measurement data from the CT sensors was subjected to the following quality control steps:

1. Decoding binary data. The data files downloaded from the instruments were converted from their raw format to a .dat/.hdr file pair in scientific units.
2. Correcting the timing characteristics of the CT data files for the effects of instrument clock time drift. The correction is derived from a comparison of instrument start and stop times with times from an independent clock recorded on start-up and shut-down of the instrument.
3. Time-series cropping. The CT measurement data time-series were trimmed to only those times when the instrument was in the water and the mooring was stable on the seabed.
4. Automated anomaly detection and removal. Data spikes based on first-difference thresholds within the measurement data time-series were detected and linearly interpolated.
5. For those CT instruments without pressure sensors, the pressure time-series measured by a nearby instrument on the same mooring was used to add a pressure channel to the salinity and temperature time-series. All pressure time-series were corrected to remove the contribution from sea-level pressure.

The MicroCATs collected data between November 1, 2017 and August 28, 2018 at M2, M3, and M4, and until June 24, 2019 at M1 (Figure 16).

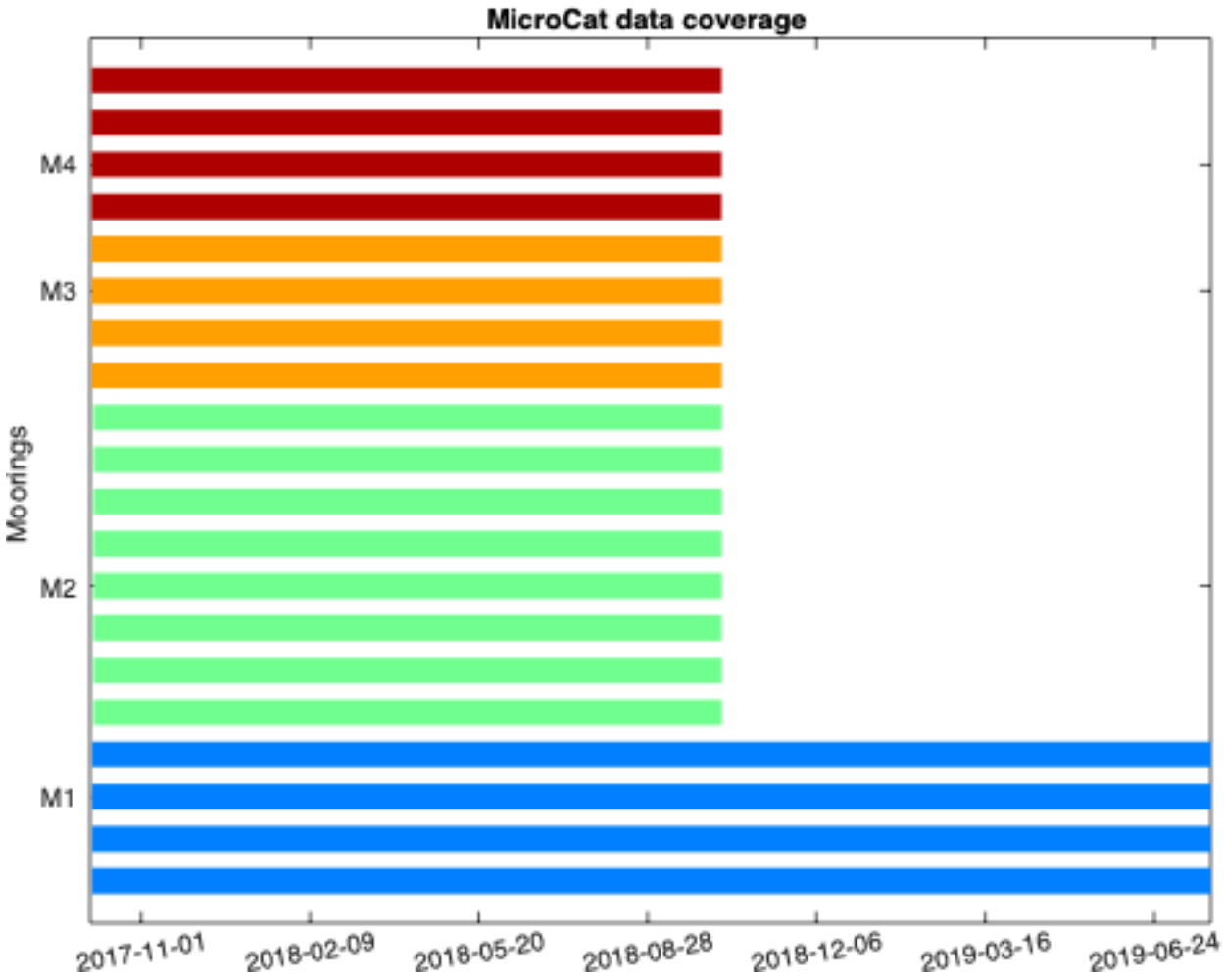

Figure 16. Temporal coverage of MicroCAT data at each mooring during the 2017–2018 deployment, extending into 2019 at M1

2.3.5 Submersible Ultraviolet Nitrate Analyzer (SUNA)

The SUNA instrument is an optical, chemical-free sensor that measures nitrate concentration by detecting the absorption of certain wavelengths across a beam path based on in-situ spectroscopy. The instrument employs a total of 256 wavelength channels. The nitrate processing uses the 217 nm to 240 nm wavelength range, corresponding to 35 of the measured channels. The SUNA instruments housed on the MARES moorings (M1 and M2) used a path length of 5 mm. For the 5 mm path length, the instrument has an accuracy of 4 µM (0.056 $mg \cdot N \cdot L^{-1}$) and a precision of 2.4 µM (0.034 $mg \cdot N \cdot L^{-1}$) in seawater. The instruments were configured to collect data in bursts of five samples, with a sample interval of approximately 2 seconds, and a burst interval of 7200 seconds.

The SUNA gives an estimate of nitrate concentration by applying a multi-variate linear regression. The calculation of the nitrate concentration was determined primarily from four inputs: nitrate, bromide, lamp-temperature, and other absorbing species (other matter that absorbs light outside of the 217 nm to 240 nm band). The instrument also featured adaptive sampling such that extended conditions of high turbidity (or optically dense conditions) result in the lamp integration time being extended beyond the typical duration of 300 to 500 ms. This increase in the lamp-time can prematurely deplete the instrument battery.

The absorbance at the sensor is defined as:

Equation 7

$$A_\lambda = -\log\left(\frac{I_\lambda - I_D}{I_{\lambda,0} - I_D}\right)$$

where I_λ is the detector intensity at wavelength λ for light passing through a sample, $I_{\lambda,0}$ is the detector intensity at wavelength λ for light passing through deionized water (DIW), and I_D is the intensity of the dark spectrum, which is sampled when the lamp is turned off to account for ambient illumination.

If the absorption of the sample is too high for the proxy wavelengths 254 nm and 350 nm (outside the nitrate absorption range), exceeding 1.3 absorption units (AU), then the instrument cannot collect sufficient light to make a measurement, and the model can no longer be used to effectively calculate the nitrate concentration. In that instance, the root mean square error (RMSe) is used to make an estimate of the wellness of the nitrate spectral fit. The RMSe should typically be less than 10^{-3}. If it was higher it may indicate the presence of colored dissolved organic matter (CDOM) that adversely impacts the nitrate estimate.

The lamp and other optical components in the sensor drift with time resulting in changes to the measured nitrate concentration. This drift requires calibration checks be completed with DIW at deployment and again at recovery.

At deployment and recovery, one 500 mL sample from the water column was collected from each site and sent to a lab for analysis to compare to the measurements collected by the SUNA. Samples were stored onboard the ship at -18˚C until the ship returned to port in the fall and the samples could be couriered to the lab. The results from the lab analysis are presented in Table 27. Samples are typically stable for 12 hours in cold and dark conditions (Strickland and Parsons 1960); however, this is a general heuristic for nutrients. Nitrate, on the other hand, tends to be one of the more forgiving nutrients. MacDonald and McLaughlin (1982) investigated the impact of quick freezing and regular freezing, thaw time and light exposure on phosphate, nitrate and silicate. Nitrate was not found to be impacted by quick freezing, and no dependence was found on thaw time, up to a maximum thaw time of 24 hours. Additionally, no dependence was found on exposure to light during the thaw process, for nitrate. Further studies by Fellman et al. (2007) examined the differences in measured dissolved organic nitrogen, dissolved organic carbon, and total dissolved phosphorus between flash freezing (-50˚C) and standard freezer (-7˚C). No significant differences were found between the two temperatures.

Table 27. Water sample nitrate laboratory results taken during 2017–2019

Sample ID	Acquisition date [yyyy-mm-dd hh:mm UTC]	Nitrate concentration [mg·L-1]	Analysis Date [yyyy/mm/dd]
M1D	2017-10-02 23:21	0.066	2017-11-03
M2D	2017-10-03 23:12	<0.050	2017-11-03
M1	2019-07-27 15:30	0.162	2019-11-19
M2	2018-10-11 13:12	0.111	2018-11-20
NOTES: The D in the Sample IDs indicates the sample from the 2017 deployment The detection limit is 0.050 $mg \cdot L^{-1}$			

Test measurements of the instrument in DIW were also collected to help correct for two possible sources of sensor drift. The first is due to biofouling due to biological matter accumulating on the optical sensor. The second is due to internal instrument drift due to changes in the battery voltage and lamp brightness. During the first test measurement the instrument was submersed in DIW prior to cleaning. This measured the combined effects of biofouling and internal error. The instrument was then cleaned, and any biofouling was removed from the lens. During the second test measurement the instrument was submersed in DIW following this cleaning. This measurement recorded the error due to internal instrument drift. The results from the calibration measurements are available in Table 28. The second measurement is compared to the measurements following calibration at deployment where one minute of data was collected in DIW to calibrate the new reference spectrum.

The drift correction curves for M1 and M2 are shown in Figure 17 and Figure 18, respectively. At M2, the instrument drift was significant at 12.986 μM. If the drift correction is not applied properly, there is a chance of seriously skewing the data. With this in mind, a correction was applied that did not begin until there was indication that the biological productivity intensified, as described in Pelerin et al. (2013). A common assumption for fouling corrections is that equipment fouls at a constant rate that begins immediately after the last cleaning and, therefore, represents the starting point for a correction. This assumption is not always valid, particularly when there are wiper malfunctions or episodes of high biological productivity during deployment. It also can be possible to identify the actual start of fouling by using sensor diagnostic data or data statistics. For example, *gradual or abrupt changes in the standard deviation or lamp intensity can be indicative of fouling events*. If the start of a fouling event is identified, corrections can be applied from that date." With this in mind, the date of ice break-up was estimated to be May 13, 2018 from the draft data and used as the reference date for calculating a linear drift correction for biofouling. This precedes evidence in the lamp time which intensifies on May 26, indicating that significant biofouling has already accumulated. This is explored further in Section 3.1.2.

Table 28. Calibration measurements after instrument recovery

Site	Deployment Calibration [µM]	Before cleaning lens [µM]	After cleaning lens [µM]	Difference [µM]
M1	-0.3240	8.151	2.512	5.638
M2	-0.0523	15.356	2.370	12.986

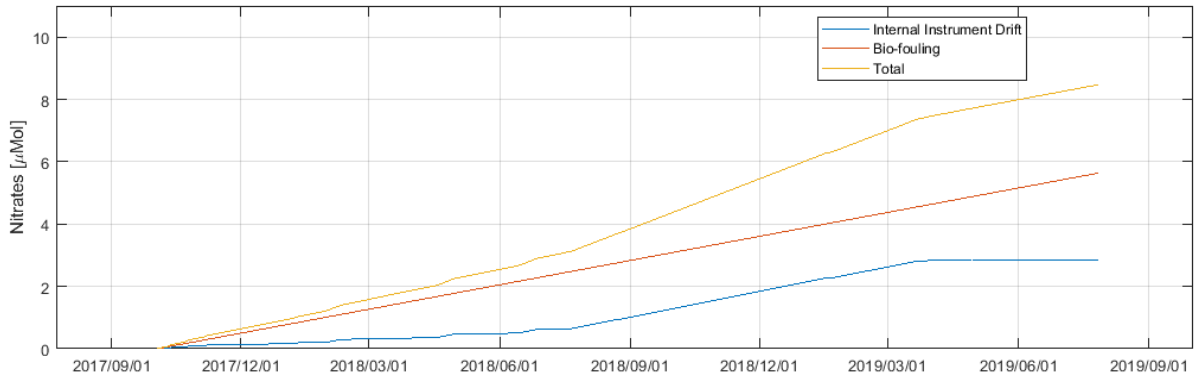

Figure 17. Drift correction curves for internal instrument drift, biofouling, and overall drift for the 2017–2019 deployment at M1

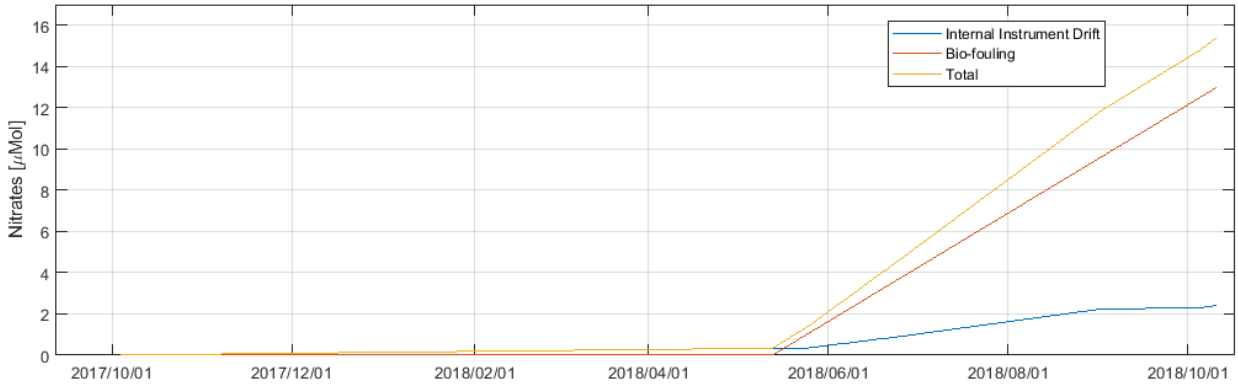

Figure 18. Drift correction curves for internal instrument drift, biofouling, and overall drift for the 2017–2018 deployment at M2

The SUNA data processing consisted of the following steps. The two data sets were somewhat unique requiring customized steps as needed which are described below. Definitions of the flag values used for each site are detailed in Table 29.

1. Extracting raw SUNA data from CSV files to.dat/.hdr format. The raw CSV files were structured into three sections. The first section was in XML format and contained information regarding the instrument and data collection parameters. The next section contained instrument specifics and coefficients. The last section contained the measurements collected by the instrument.
2. Up to five samples were collected per two-hour burst. These were averaged to create an equispaced time-series with a two-hour sample interval.
3. Correcting the sample interval of the data files to account for the effects of instrument clock time drift. The correction was derived from a comparison of instrument start and stop times with coincident readings from an independent clock.
4. Truncating the data files to ensure all data is from a consistent sampling environment. This removed data from times when the instrument was out-of-water and before it had settled to a stable depth.
5. Applying a constant offset in the second column of Table 28 to all data points so that the Deployment Calibration values are shifted to a concentration of 0 μM.
6. Correcting for drift in nitrate values due to biofouling and internal instrument drift using the values collected after instrument recovery. Biofouling was treated as linear for the duration that the instrument was deployed in-water at M1, and linear from May 13 until recovery at M2. Instrument drift depends on the lamp characteristics and on the rate of battery depletion. This instrument drift was non-linear and treated as a function of the lamp time.
7. Interpolating gaps in the nitrate concentration record. Gaps in the data may be due to some factor interfering with proper measurements. Gaps up to 6 records were interpolated. Any gaps exceeding 6 records were flagged as “missing”.
8. Adding a data quality channel and use a flag value of ‘2’ to indicate data exceeding the manufacturer specified thresholds for RMSe (>1 x 10^{-3}) and Absorbance (>1.3 AU). There are some records that neighbor these sections that were also flagged due to suspect values.
9. Interpolating sudden and short-lived changes (spikes) exceeding expected values. A threshold change of 1 μM per hour was used as the limit based on previous studies (Balzano et al. 2012; Simpson et al. 2008; Emmerton et al. 2008). Records that were flagged as problematic in the previous step were excluded from this step.
10. Reviewing the automatically interpolated points and identify any remaining points that look suspect for further interpolation.
11. Indicating data that looks reasonable but that is exceeding manufacturer thresholds for reliable measurements. Some overlap could exist with other data quality values, so a second data quality column was added. This is indicated in the data quality column with a value of '6'. The term ‘reasonable’ is defined as data that is non-noisy and similar to neighboring segments where the instrument thresholds are not exceeded. All indicated sections were also instances where the data was not tracking the trend of the Absorbance values.
12. Custom step for M1. Shifting sections with negative nitrate concentrations into the positive. Any shifted sections were noted in the data quality column with a flag value of “4”. These negative values could result from error due to higher than normal absorbance. It is also possible that the instrument drift and/or biofouling did not occur perfectly linearly. A value of +2.82 μM was used to shift the most negative measurements to a value of 0 μM.

Table 29. Flag definitions used in the fully quality controlled time-series of SUNA nitrate results

Site	Column Number	Flag Value	Definition
M1	10	2	Exceeds manufacturer threshold for absorbance or RMS error.
	11	4	Shifted values by a constant offset to remove negative concentration values.
	11	6	Exceeds manufacturer threshold for absorbance or RMS error, but looks reasonable
M2	10	2	Exceeds manufacturer threshold for absorbance or RMS error.
	11	6	Exceeds manufacturer threshold for absorbance or RMS error, but looks reasonable

2.3.6 Submersible Autonomous Moored Instrument (SAMI)

A Submersible Autonomous Moored Instrument for CO_2 (SAMI-CO2) was deployed at the M1 and M2 mooring sites in the Beaufort Sea. The SAMI-CO2 is a wet-chemical spectrophotometric system, using an indicator dye to determine concentration when CO_2 in the seawater diffuses across a permeable membrane. From October 2016 to September 2017, a SAMI-CO2 sensor was deployed at 36 m water depth at both M1 and M2 sites. From September 2017 to July 2019, one SAMI-CO2 was deployed at water depth 36 m at site M1 but failed during the entire deployment period.

The data consists of temperature data (°C) and partial pressure of carbon dioxide (pCO_2) data (µatm). Upon instrument recovery, the autonomous data was downloaded from the SAMI-CO2 and processed using the software provided by the manufacturer, Sunburst Sensors.

Discrete 200 mL seawater samples were collected upon recovery at sensor sites to validate the autonomous measurements. The seawater samples were analyzed for Dissolved Inorganic Carbon (DIC) and Total Alkalinity (TA) at the Ocean Acidification Research Center (OARC) at UAF. The DIC and TA analyses were performed on a Marianda AIRICA and VINDTA, respectively. These instruments are routinely calibrated using Certified Reference Materials (CRMs) supplied by A.G. Dickson at the Scripps Institute of Oceanography. DIC and TA measurements were then entered in the CO2Calc software (Robbins et al. 2010) to calculate pCO_2 for comparison with the autonomous pCO_2 values, using the equilibrium constants from Millero et al. (2006).

2.3.7 Acoustic Zooplankton Fish Profiler (AZFP)

Data were collected from AZFPs deployed at mooring site M3 in 2016 and mooring sites M2 and M3 in 2017. Table 30. Summary of AZFP data collected and analyzed during 2016-2017, and 2017–2018 deployments summarizes the data collected and depth range of the analysis for both years.

Table 30. Summary of AZFP data collected and analyzed during 2016-2017, and 2017–2018 deployments

Deployment Year	Site	Serial #	Frequencies Analyzed (kHz)	Instrument Depth	Bottom Depth	Analysis Depth Range (m)
2016	M3	55088	38	287	300	112 to 277
2016	M3	55089	125,200	60	300	Surface to 53
2017	M2	55120	38	168	180	Surface to 134
2017	M3	55088	38	287	300	112 to 277
2017	M3	55054	125,200	60	300	Surface to 53

NOTES:
Frequencies shown are those used for the analysis only
Analysis depth range is depth relative to the surface (approximate) converted from the range from the face of the transducer.
The analysis domain was designated to exclude noise from surface bubbles, side-lobes near the transducers, and to account for detection range. Instrument depth and bottom depth are approximate.

The instruments placed at 60m at M3 in the two years (serial numbers 55089 in 2016-2017 and 55054 in 2017-2018) operated at the frequencies 125, 200, 455, and 769 kHz. Only the two lowest frequencies (125 and 200 kHz) were used for the analysis because they were sufficient to discriminate between juvenile Arctic cod and zooplankton. In addition, the 769 kHz did not reach to the surface in either year. The detection range was up to the surface at 125, 200, and 455 kHz in both years, while at 769 kHz, the range was about 20 m in 2016-2017and 12 m in 2017-2018 . Side lobe noise extended to approximately 5–10 m from the transducer at 200, 455, and 769 kHz, while it extended to 12–20 m at 125 kHz.

The deep instrument placed at M3 (serial number 55088 in both years) operated at 38 kHz. The detection range was approximately 175 m. Side lobe noise extended approximately to 35 m from the transducer.

The M2 instrument (serial number 55120) operated at 38, 67, 125, and 200 kHz. The data quality was good at 38 kHz which is suited to detect adult cod. At 67 kHz, strong side-lobe noise appeared as far as 85 m from the transducer. Post-recovery calibration revealed an offset of approximately -9 dB and -25dB for the 125 and 200 kHz, respectively, making the data from these frequencies difficult to trust for comparison and quantitative purposes. As a result, only the 38 kHz was used for further analysis. Side-lobe noise extended to 34 m at this frequency.

All acoustic analyses were performed with Myriax Echoview (version 8.0), R (version 3.5.1), and Matlab (version 8.5). Acoustic data were converted to volume backscattering strength (S_v) as follows:

Equation 8

$$S_v = EL_{max} - \frac{2.5}{a} + \frac{N}{26214a} - TVR - 20logV_{TX} + 20logR + 2\alpha R - 10log\left(\frac{c\tau\varphi}{2}\right)$$

where EL_{max} is the echo level (in dB re 1 µPa) at the transducer that produces full-scale output; N, in counts, is the digital recorded value and is linearly related to the received voltage (v_{in}) after it has been amplified, bandpass filtered, and passed through a so-called ‘’detector’’ whose output is a function of $\log(v_{in}^2)$; a is the slope of the detector response; TVR is the transmit voltage response of the transducer in dB re 1 µPa/volt at 1 m range; V_{TX} is the voltage amplification factor before it is sent out; α is the absorption coefficient, c is the sound speed; and τ is the pulse length. R is the range calculated as $R = ct/2$. $20log\ R + 2\alpha R$ represents the time-varied-gain (TVG) applied to compensate for transmission loss (TL). ϕ, the equivalent beam angle, is approximated by

Equation 9

$$\varphi = 1.4\pi(1 - cos\theta)$$

where θ is half the full -3dB beam angle of the transducer.

The density of targets per unit area is defined as:

Equation 10

$$\rho_a = \frac{NASC}{4\pi \times \sigma_{bs}}$$

where σ_{bs} is the backscattering cross-section (m^2). *NASC*, the nautical area scattering coefficient ($m^2 nmi^{-2}$), is a vertical integration of the volume backscattering strength over the sampled depth:

Equation 11

$$NASC = 4\pi \times 1852^2 \times 10^{\frac{Sv}{10}} \times T$$

T is the vertical extent of the analysis domain, and S_v the mean volume backscattering strength. In this study, we use NASC as an index of abundance, since it is proportional to fish density.

Acoustic noise from several sources was found in the data and was removed prior to analysis. Impulse noise originating from interference with other acoustic instruments on the mooring was removed using the *Impulsive Noise* (IN) algorithm (Ryan et al. 2015) implemented in Echoview. The algorithm was applied on a 5x5 window using a 10 dB threshold, and the thresholded data was replaced by the mean. Noise in the form of large vertical bands from the surface to bottom, that saturated the entire water column, were also present throughout the 2017-2018. The origin of this noise is uncertain. This noise was present at both the M2 and M3 moorings, mostly during the fall, winter and spring months. The noise was removed manually and resulted in a 11.5% and 6.5% data loss at the M2 and M3 moorings, respectively.

Background noise was removed by linear subtraction using Echoview's *Background Noise Removal* algorithm (DeRobertis and Higginbottom 2007). Thresholds for maximum estimated noise were determined empirically and varied depending on instrument and operational frequency. A signal-to-noise ratio of 10 dB specified the acceptable limit for a signal to be deemed distinguishable from noise.

Strong echoes corresponding to ice, as well as bubbles originating from surface waves, were often found near the surface during the analysis of the shallow, multi-frequency echo-sounder data at the M2 and M3 sites. To exclude this noise from the analysis, an exclusion line was generated from the 125 kHz data using Echoview's *maximum* S_v algorithm, using a 2 m offset. The exclusion line was reviewed and corrected manually. Data above this line, as well as data below a 7 m and 34 m distance (M3 and M2 sites, respectively) from the transducer's face, where side lobes had more effect, were excluded from the analysis. When strong side-lobe noise extended beyond the exclusion lines, the corresponding horizontal bands were manually removed.

Acoustic targets were separated into three classes: "zooplankton" (likely to be largely copepods), "Juvenile arctic cod", and "Adult arctic cod". Arctic cod (*Boreogadus saida*) is by far the most abundant

fish in the Beaufort Sea (Benoit et al. 2008). It is possible that mixed in with the *Boreogadus saida* are some *Arctogadus glacialis* individuals but there abundance is not expected to be greater than 1% (Majewski et al. 2017). Adults are found at deeper depths whereas juvenile cod are found in the epipelagic layer (Parker-Stetter et al. 2011; Benoit et al. 2013). It is possible that some detections were due to the presence of *Arctogadus glacialis* which is estimated to be found locally at one percent or less (Majewski et al 2017).

At site M3, the single-frequency, inverted 38 kHz AZFP mounted near the bottom was used to detect adult cod. The shallower multi-frequency AZFP was used to detect juvenile cod and zooplankton in the epipelagic layer. The 125 and 200 kHz frequencies were used to separate the two classes. The data was re-sampled (1 m by 3 minutes) before subtracting data at 200 kHz from data at 125 kHz. A threshold of -1 dB < 125-200 kHz < 1 dB was used for juvenile cod and 125-200 kHz < -4 dB was used for copepod zooplankton (Korneliuss and Ona 2002; Kitamura et al. 2017). Echograms (S_v) and NASC are plotted for are shown for filtered data. Note however, that a certain level of misclassification is inevitable, and the accuracy of this classification is difficult to quantify without the use of trawl and net data for validation.

2.3.8 Passive Acoustic Recorder (AURAL)

An AURAL was deployed at 164 m depth on mooring M2. The AURAL sampled at 16,384 Hz for a useable bandwidth of 10 Hz to 8,192 Hz. Acoustic data were recorded for the first 15 minutes of every hour. Data were examined for non-marine mammal acoustic signatures and those were segregated from the rest. The instrument collected data from October 3, 2017 to September 28, 2018.

Weekly occurrence of all vocal Arctic marine mammal species was assessed by visually examining spectrograms of the acoustic data for species-specific signals each week. If a species was heard at least once during a week, it was considered present. This should be considered a minimum estimate of occurrence of these species, as long periods of time may pass when species are present but not vocalizing. Long-term spectral averages (LTSA) were produced to show how the annual soundscapes changed over season and over time. LTSAs were produced by averaging over 120 s long windows with 20 Hz resolution.

3 Results

3.1 Year 2

3.1.1 Physical Oceanography

3.1.1.1 Temperature, Salinity and Density

The quality-controlled temperatures from M1 are illustrated in Figure 19. Overall, a similar pattern is seen across all the sensors, but with some differences at the shortest time scales. Similarly, salinity is illustrated across the M1 mooring in Figure 20 and density in Figure 21. These measurements are interpolated to provide a contour plot of temperature (top), salinity (middle), and density (bottom) in Figure 22. The pulse of warm (5.5°C) water observed prior to the recovery at the end of July makes the M1 site unique in the M1 time series and compared to other sites, as the other sites were recovered the preceding fall. No temperatures above 1.2ºC were observed during the fall 2016 to fall 2018 time period at any of the sites.

The quality-controlled temperatures from the M2 mooring are illustrated in Figure 23 for the upper water column and in Figure 24 for the lower water column. Similarly, the salinity time-series is shown in Figure 25 and Figure 26, and density is shown in Figure 27 and Figure 28. These measurements are interpolated to provide a contour plot of temperature (top), salinity (middle), and density (bottom) in Figure 29. A particularly warm and salty (~0.5 ºC, ~34.8 psu) intrusion was observed through late November and much of December 2017. This intrusion is likely due to an upwelling event which corresponded to a 66 hour easterly wind event which started on November 21, 2017 and had mean speeds from the east of 4.9 m/s. There are also notable events such as from April 1-4, 2018 in which the mean speeds from west were 6.0 m/s. This short-lived downwelling event drove down the near-bottom temperature and salinity leaving the water column with much reduced temperature and salinity gradients. Other such downwelling events include the event around December 26, 2017, April 12, 2018, April 21, 2018 and September 26, 2018.

The quality-controlled temperatures from the M3 mooring are illustrated in Figure 30 and the quality controlled salinity time-series is shown in Figure 31. The quality-controlled density is shown in Figure 32. These measurements are interpolated to provide a contour plot of temperature (top), salinity (middle), and density (bottom) in Figure 33. The smaller number of temperature sensors at M3 gives it its streaky appearance. The upwelling observed at M2 in December 2017 is also evident at M3. Particularly striking downwelling events include February 21, 2018 and July 22, 2018.

The quality-controlled temperatures from the M4 mooring are illustrated in Figure 34 and the quality controlled salinity time-series is shown in Figure 35. The quality-controlled density is shown in Figure 36. These measurements are interpolated to provide a contour plot of temperature (top), salinity (middle), and density (bottom) in Figure 37. There is still some evidence of the December upwelling event of warm salty water at M4, however, unlike the other sites it is limited primarily to depths below 150 m. Some of the stronger downwelling events at M4 include February 21, 2018 and January 29, 2018,

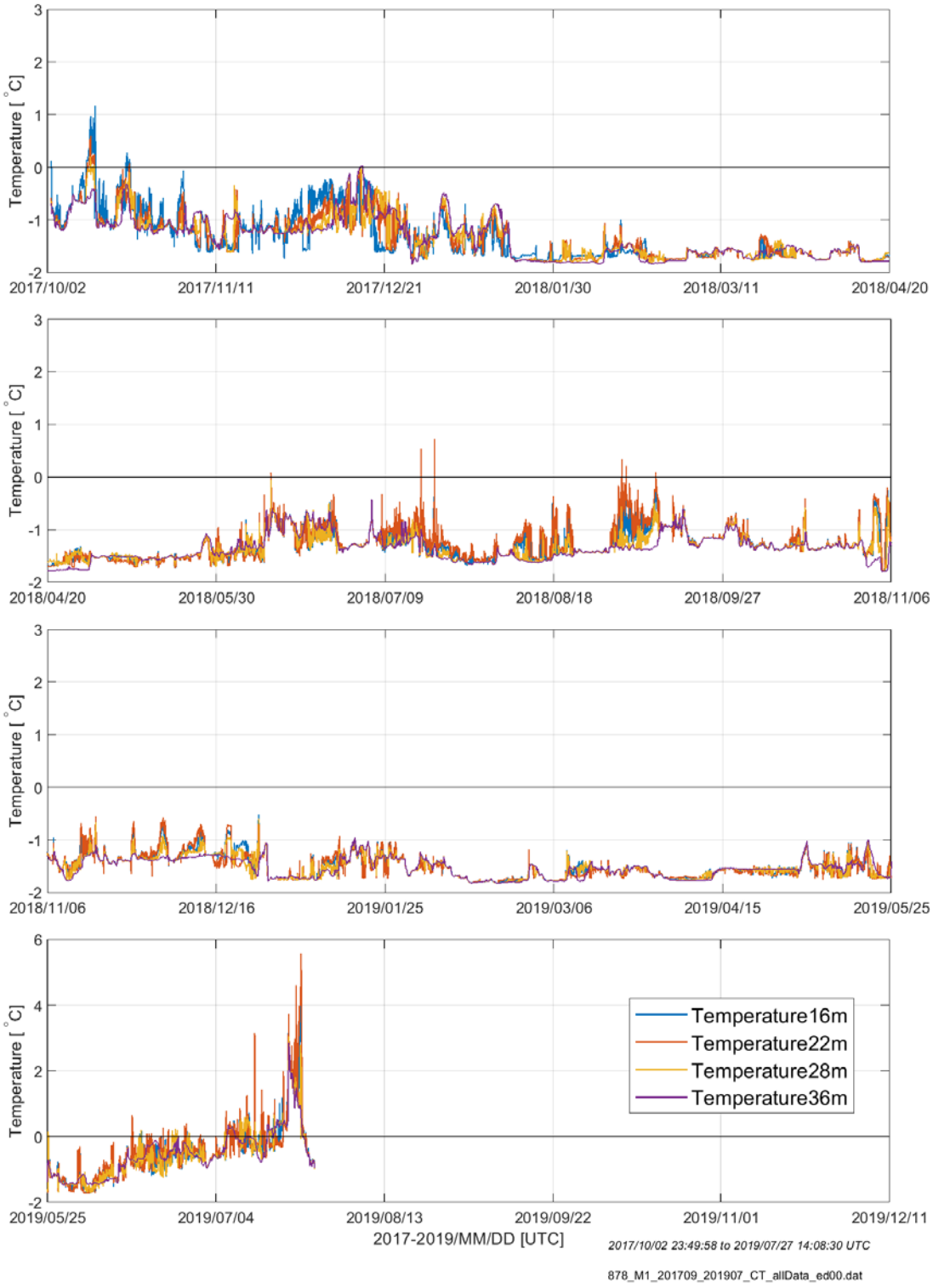

Figure 19. Temperature time-series as measured by sensors on M1 at various depths during the 2017–2019 deployment

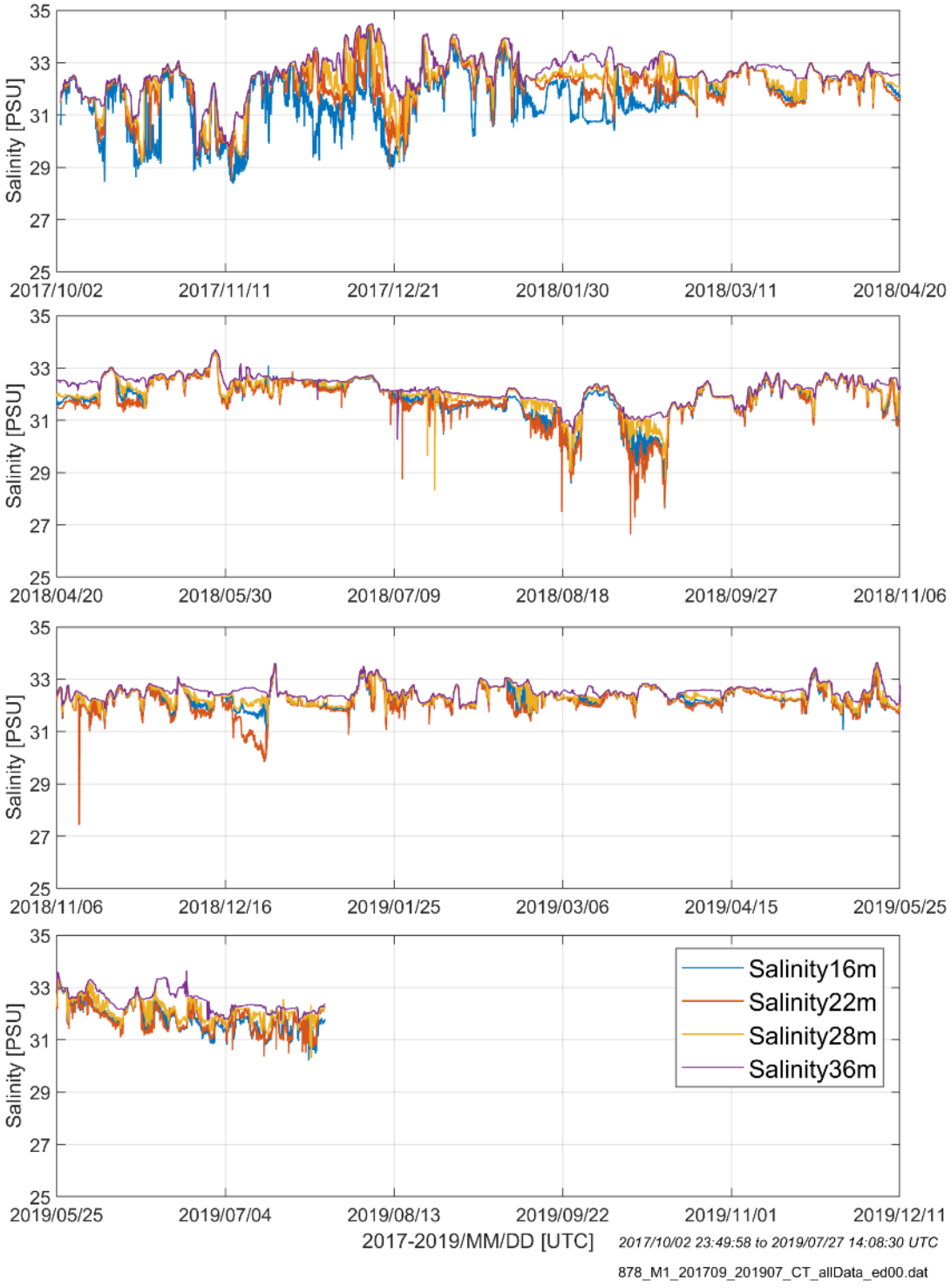

Figure 20. Salinity time-series as measured by sensors on M1 at various depths during the 2017–2019 deployment

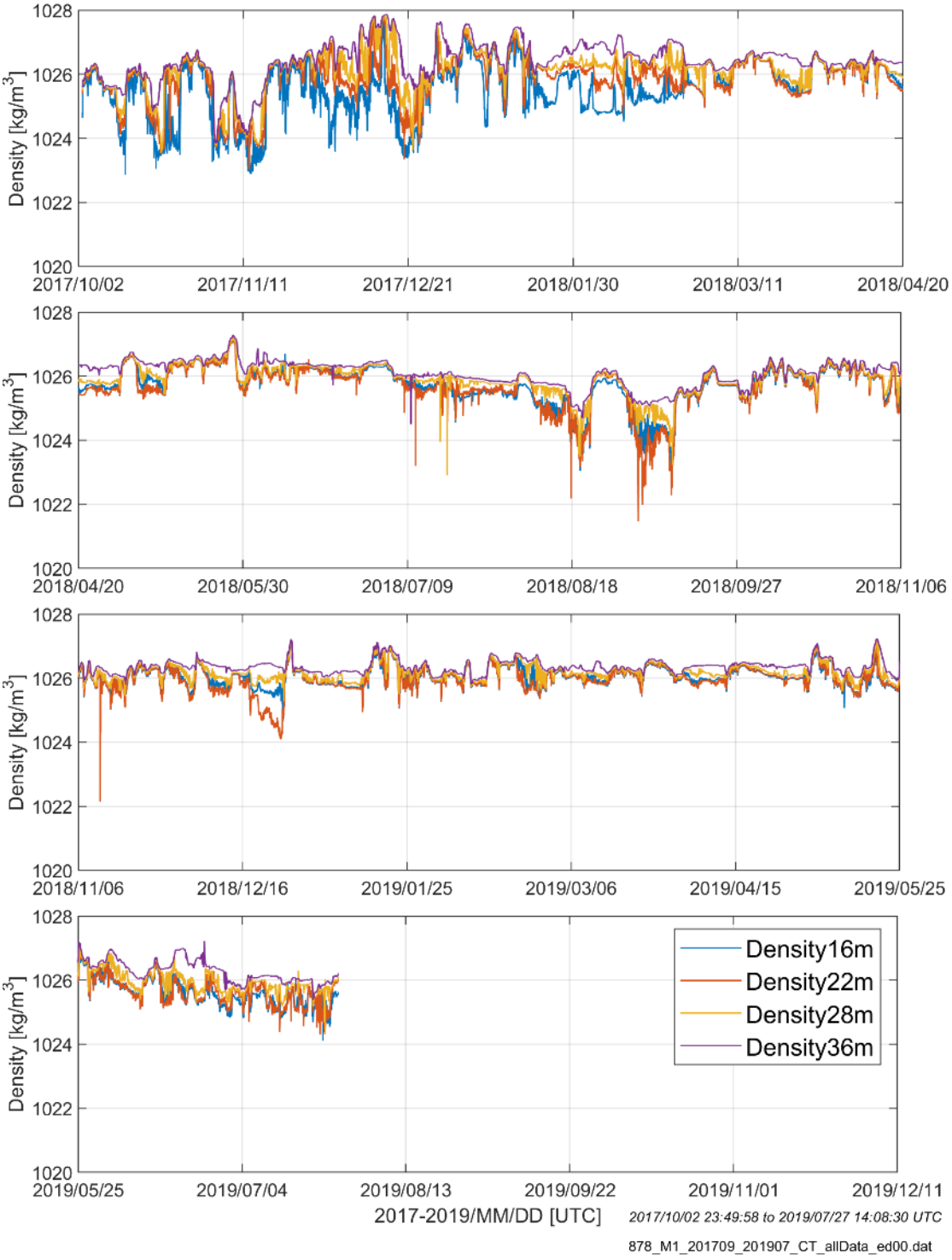

Figure 21. Density time-series as measured by sensors on M1 at various depths during the 2017–2019 deployment

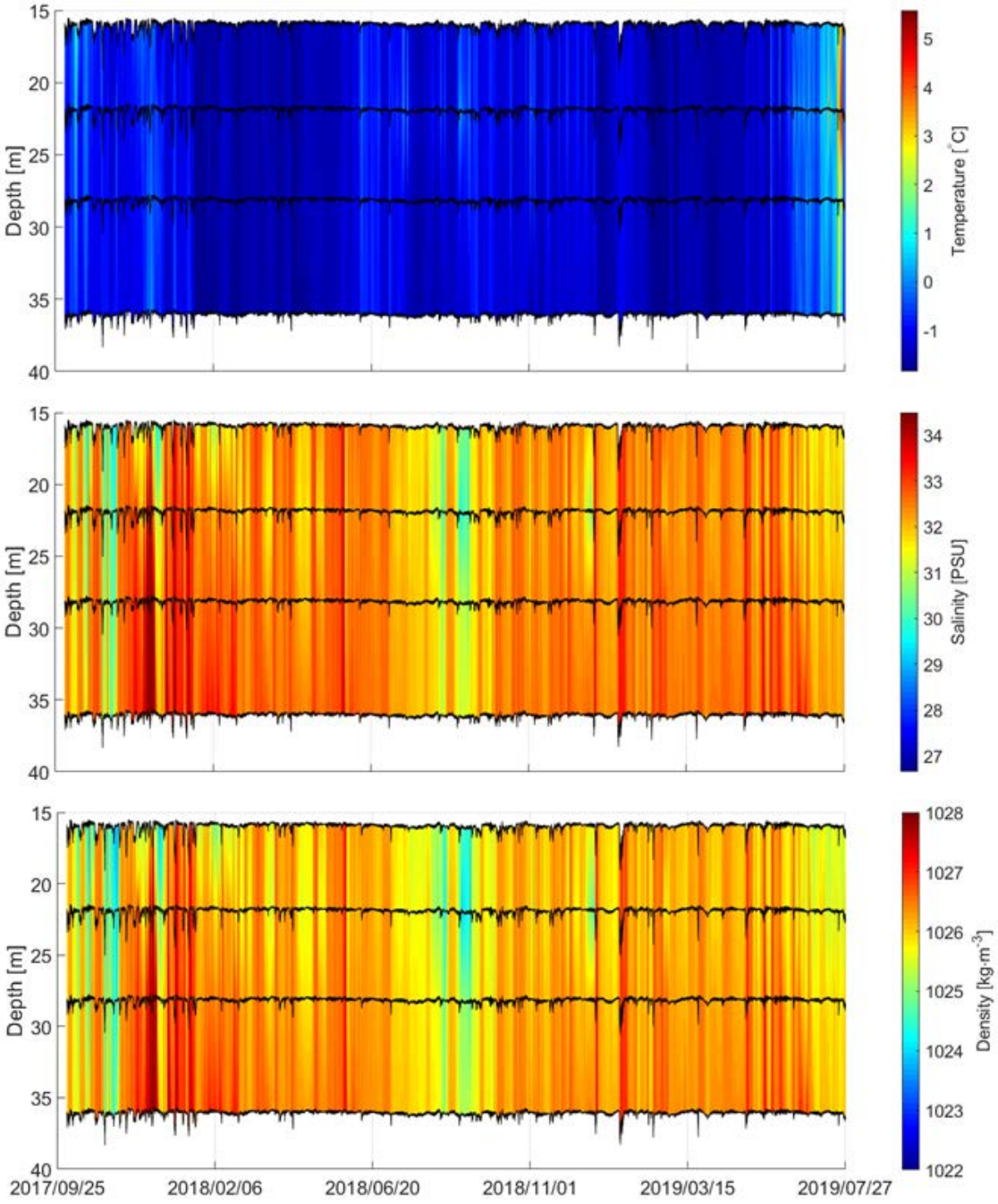

Figure 22. Temperature, salinity, and density time-series from CT sensors on M1 and interpolated over the full sampled water depth span during the 2017–2019 deployment

The black curves show the depth of each sensor.

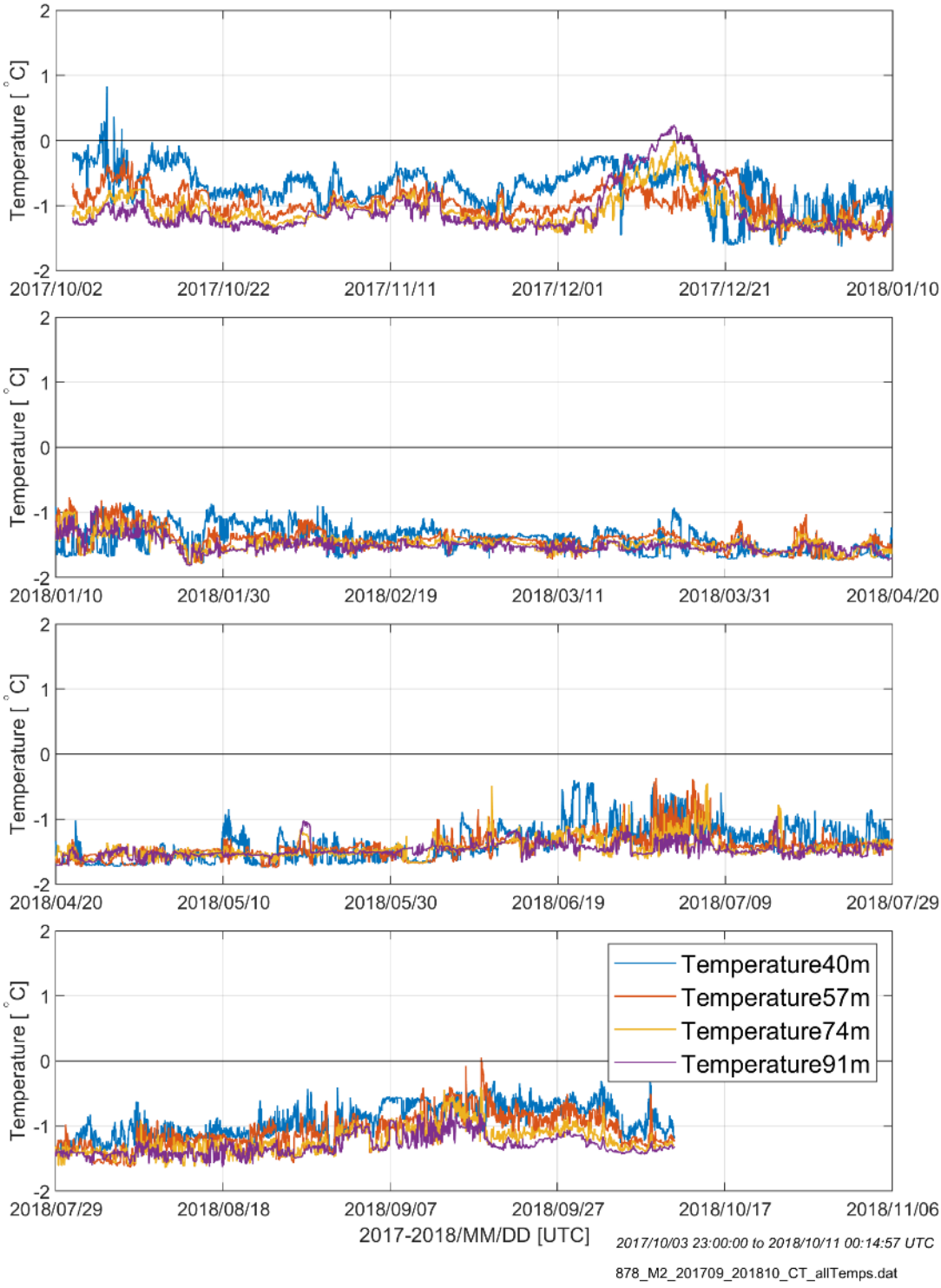

Figure 23. Temperature time-series as measured by sensors on M2 at various depths for the top four CTs during the 2017–2018 deployment

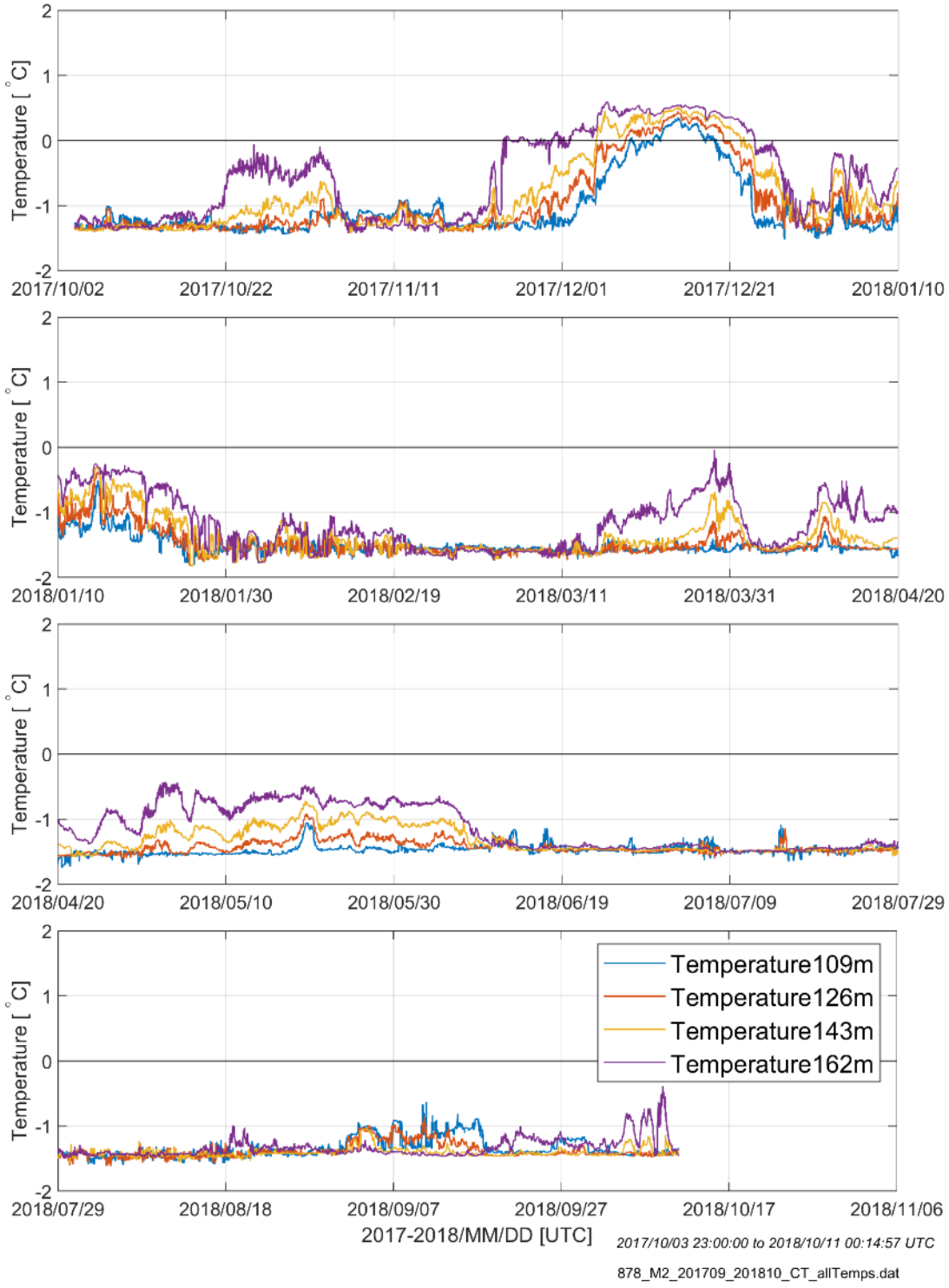

Figure 24. Temperature time-series as measured by sensors on M2 at various depths for the bottom four CTs during the 2017–2018 deployment

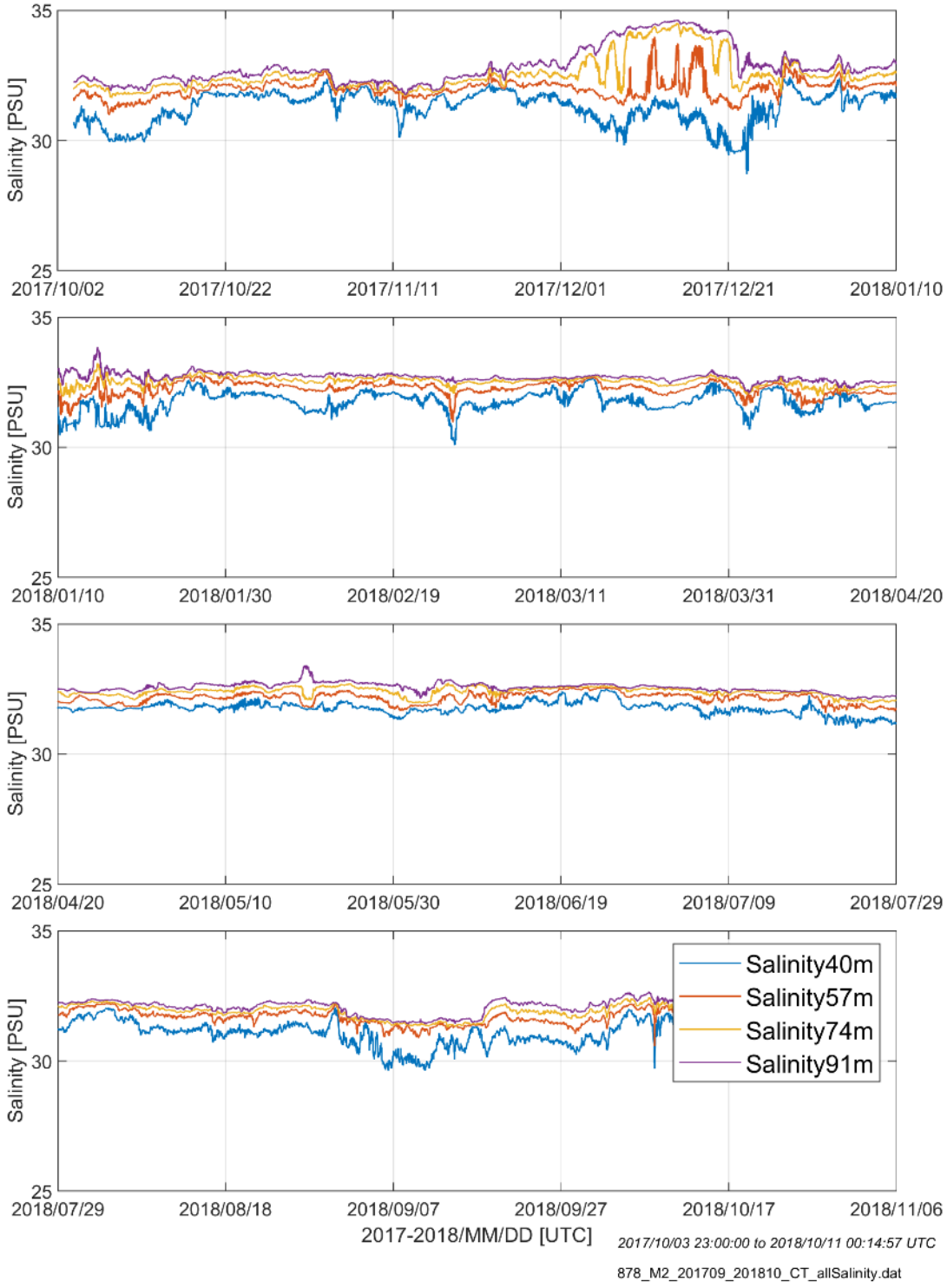

Figure 25. Salinity time-series as measured by sensors on M2 at various depths for the top four CTs during the 2017–2018 deployment

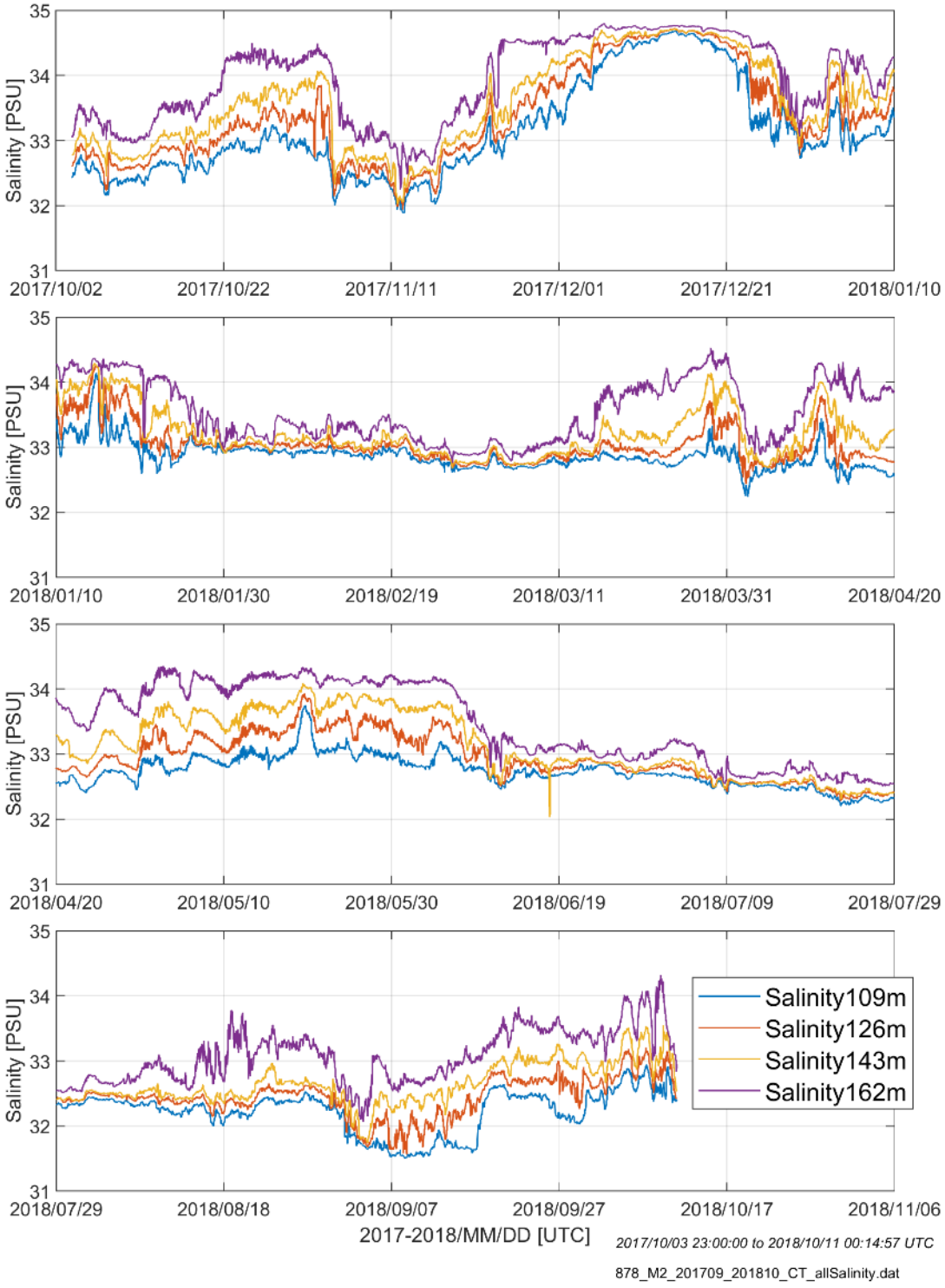

Figure 26. Salinity time-series as measured by sensors on M2 at various depths for the bottom four CTs during the 2017–2018 deployment

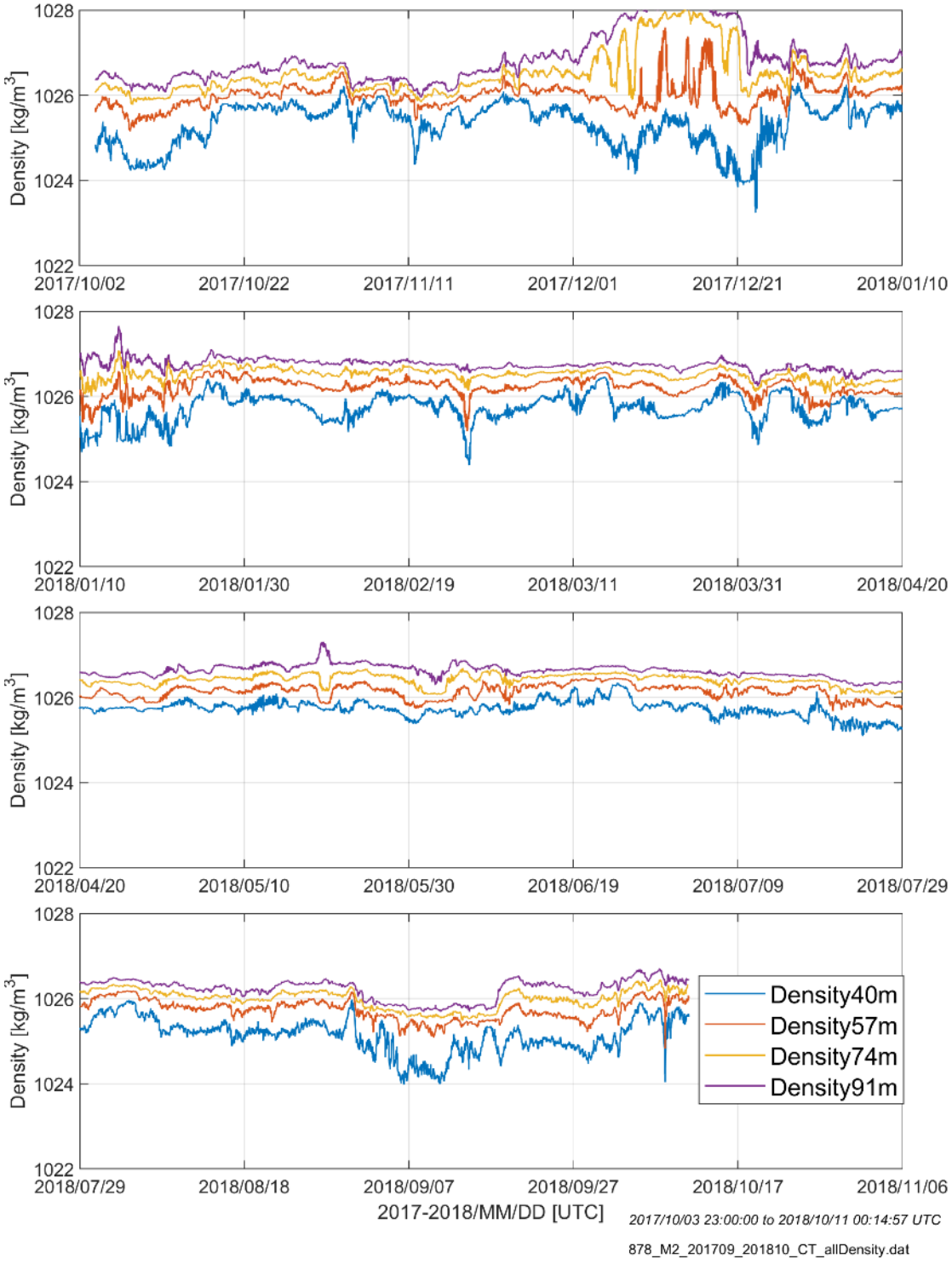

Figure 27. Density time-series derived from CT sensor measurements on M2 at various depths for the top four CTs during the 2017–2018 deployment

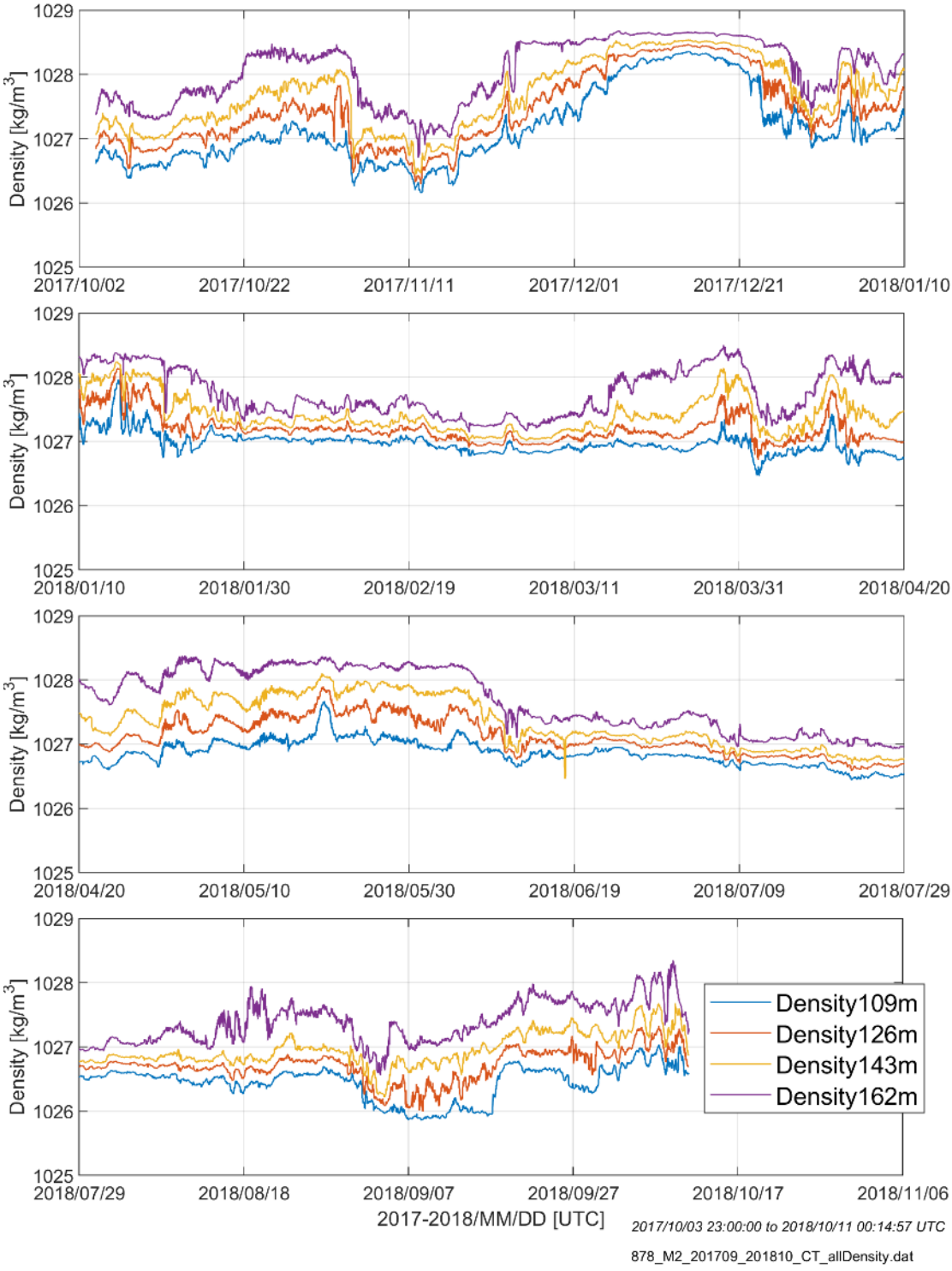

Figure 28. Density time-series derived from CT sensor measurements on M2 at various depths for the bottom four CTs during the 2017–2018 deployment

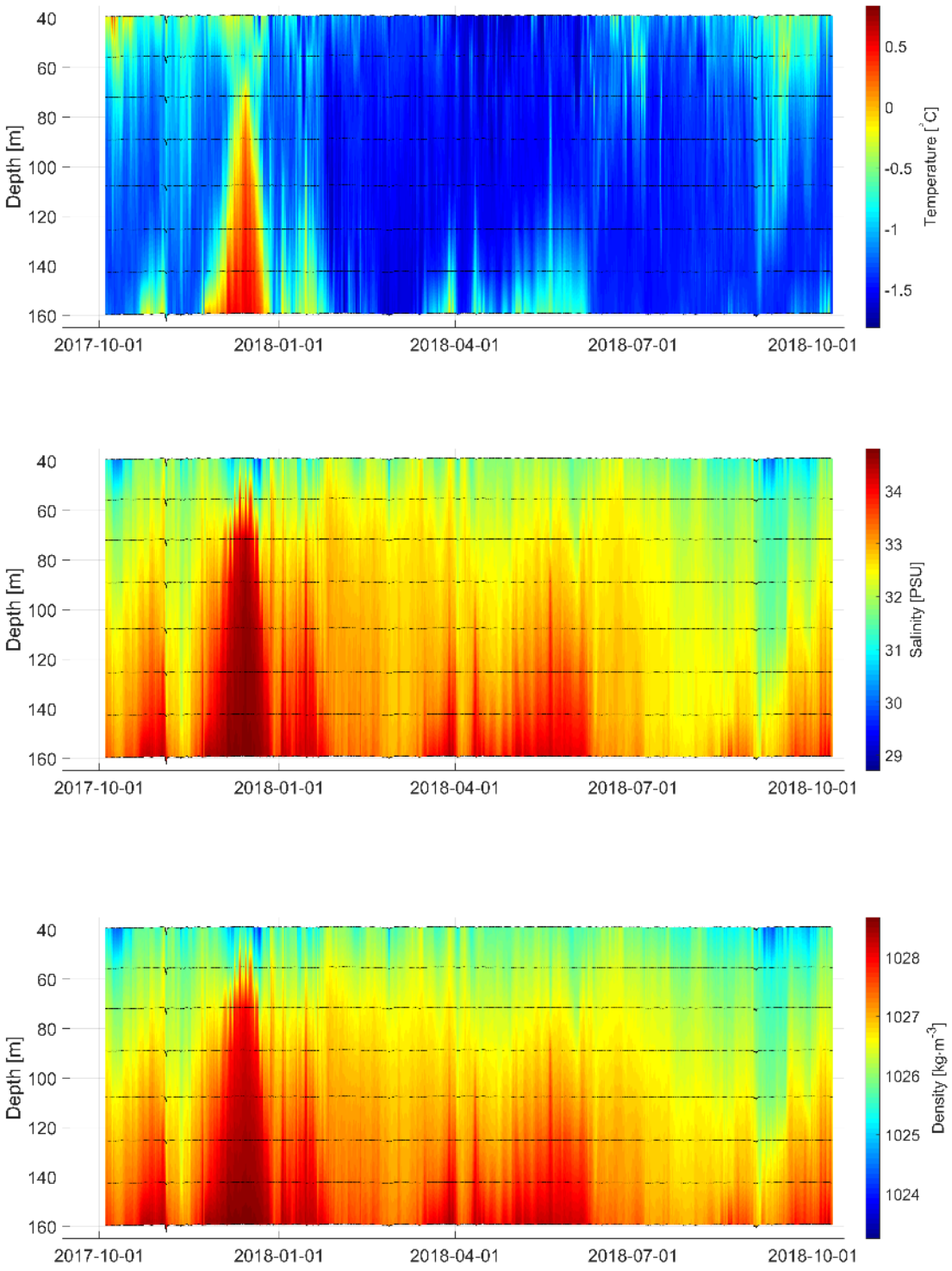

Figure 29. Temperature, salinity, and density time-series from CT sensors on M2 and interpolated over the full sampled water depth span during the 2017–2018 deployment

The black curves show the depth of each sensor.

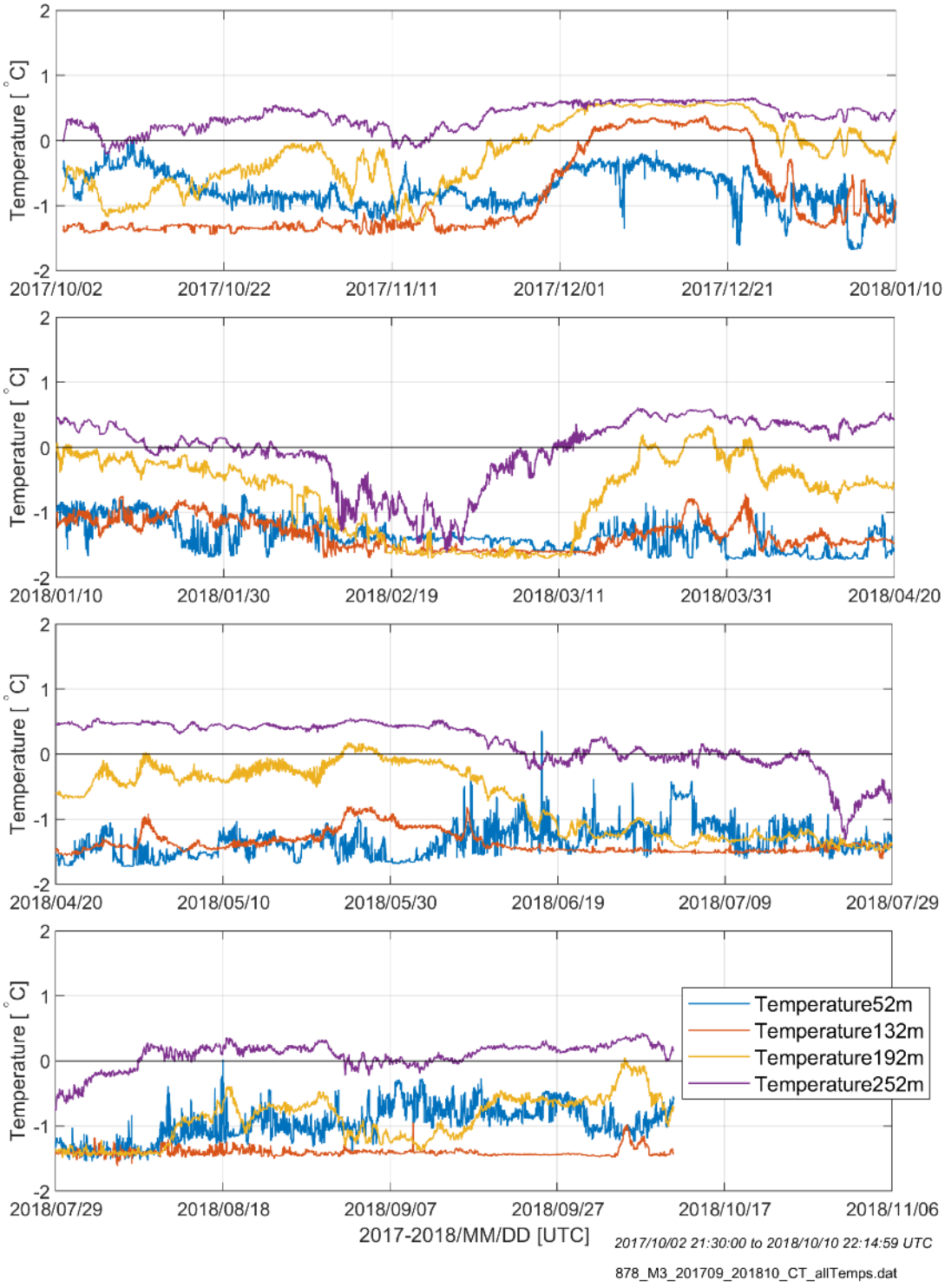

Figure 30. Temperature time-series derived from CT sensor measurements on M3 at various depths during the 2017–2018 deployment

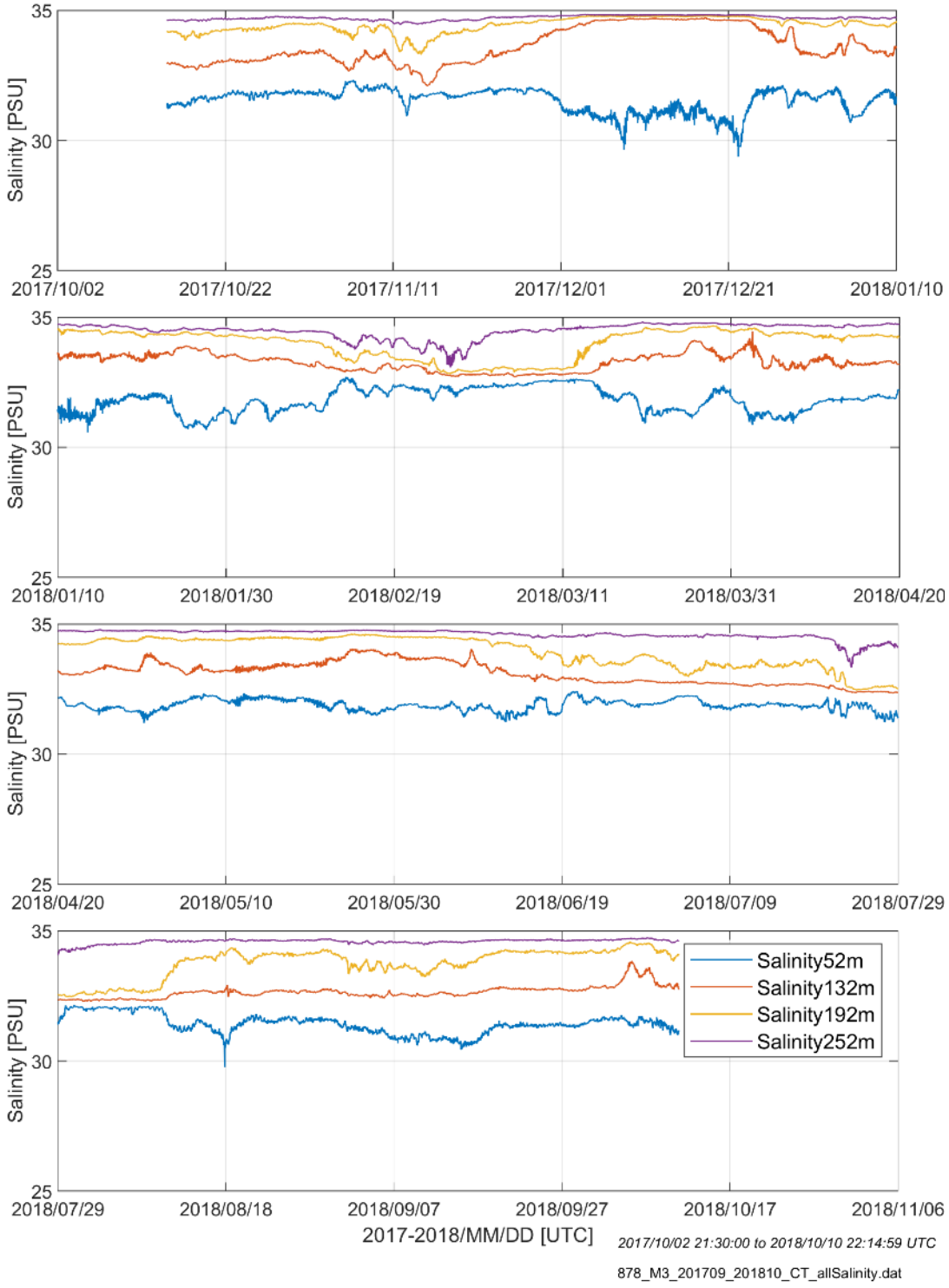

Figure 31. Salinity time-series derived from CT sensor measurements on M3 at various depths during the 2017–2018 deployment

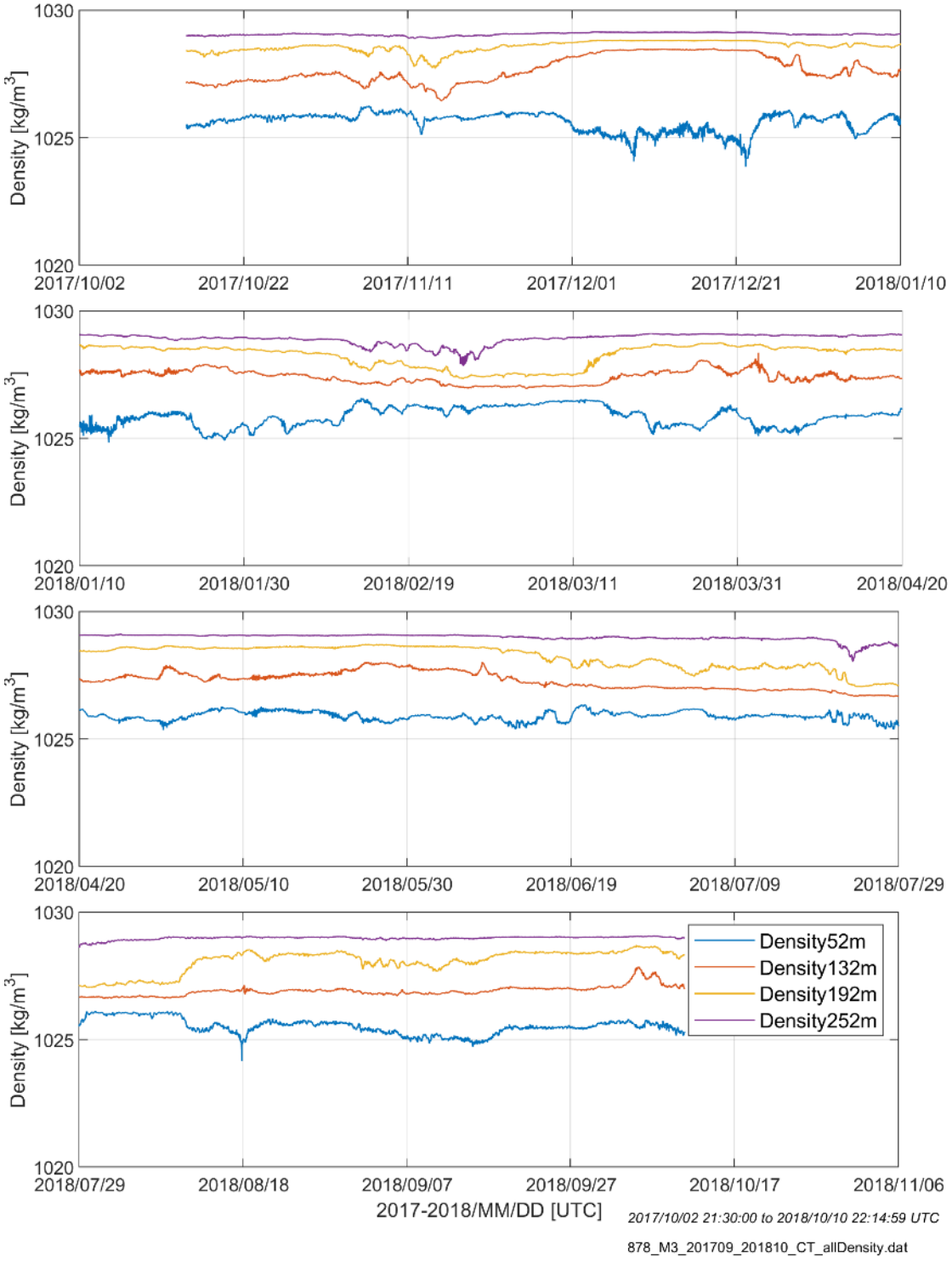

Figure 32. Density time-series derived from CT sensor measurements on M3 at various depths during the 2017–2018 deployment

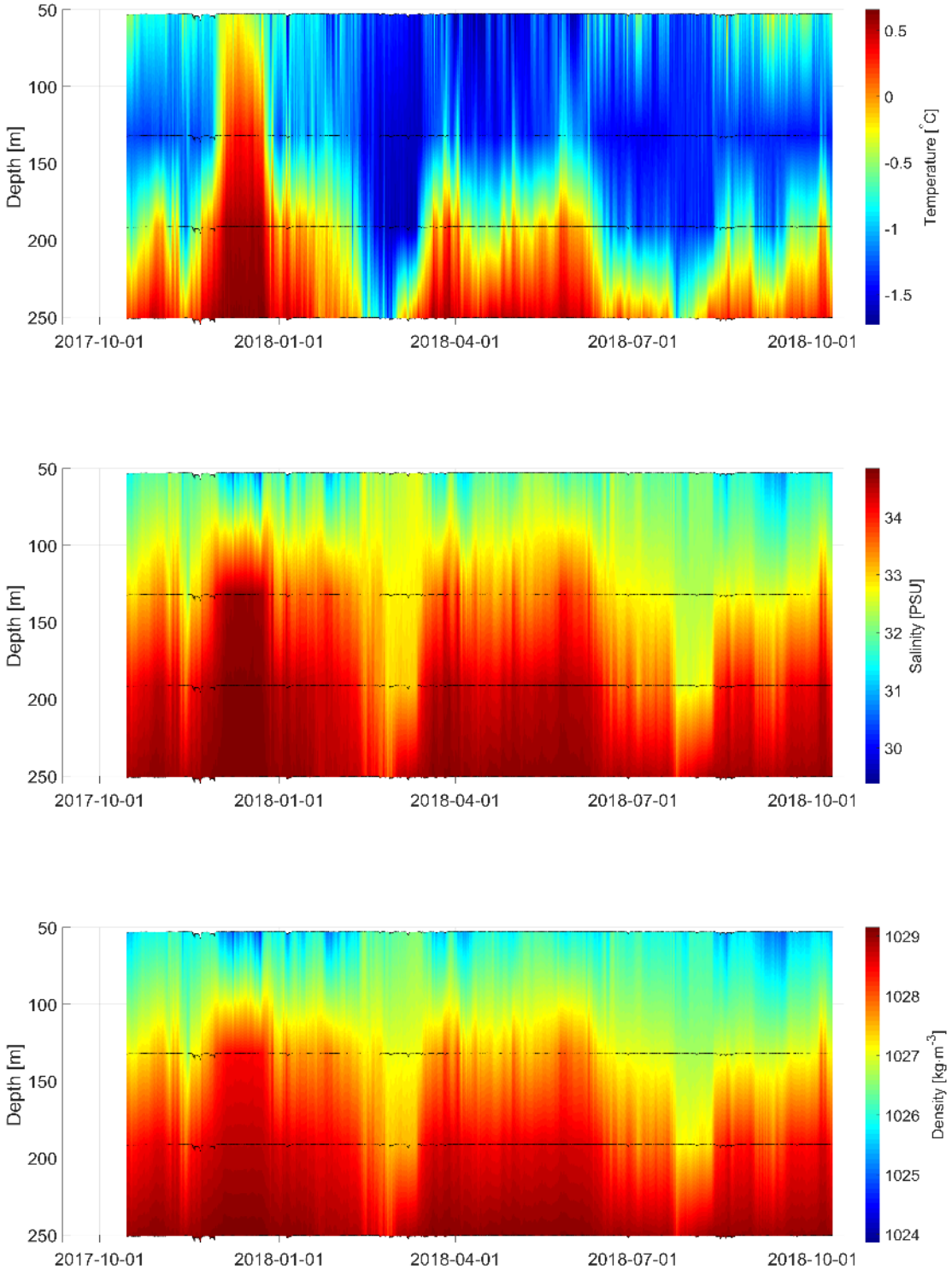

Figure 33. Temperature, salinity, and density time-series from CT sensors on M3 and interpolated over the full sampled water depth span during the 2017–2018 deployment. The black curves show the depth of each sensor.

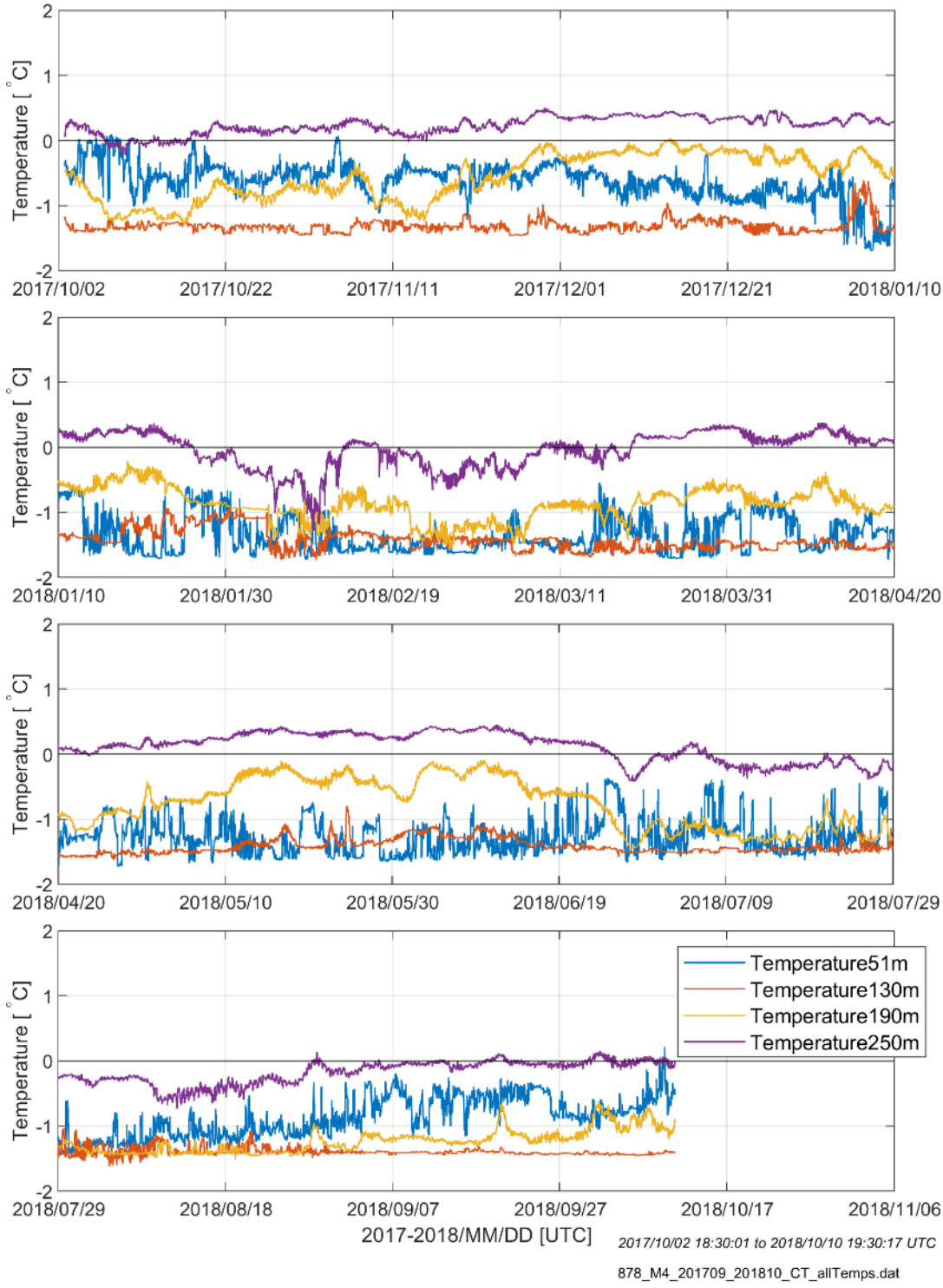

Figure 34. Temperature time-series derived from CT sensor measurements on M4 at various depths during the 2017–2018 deployment

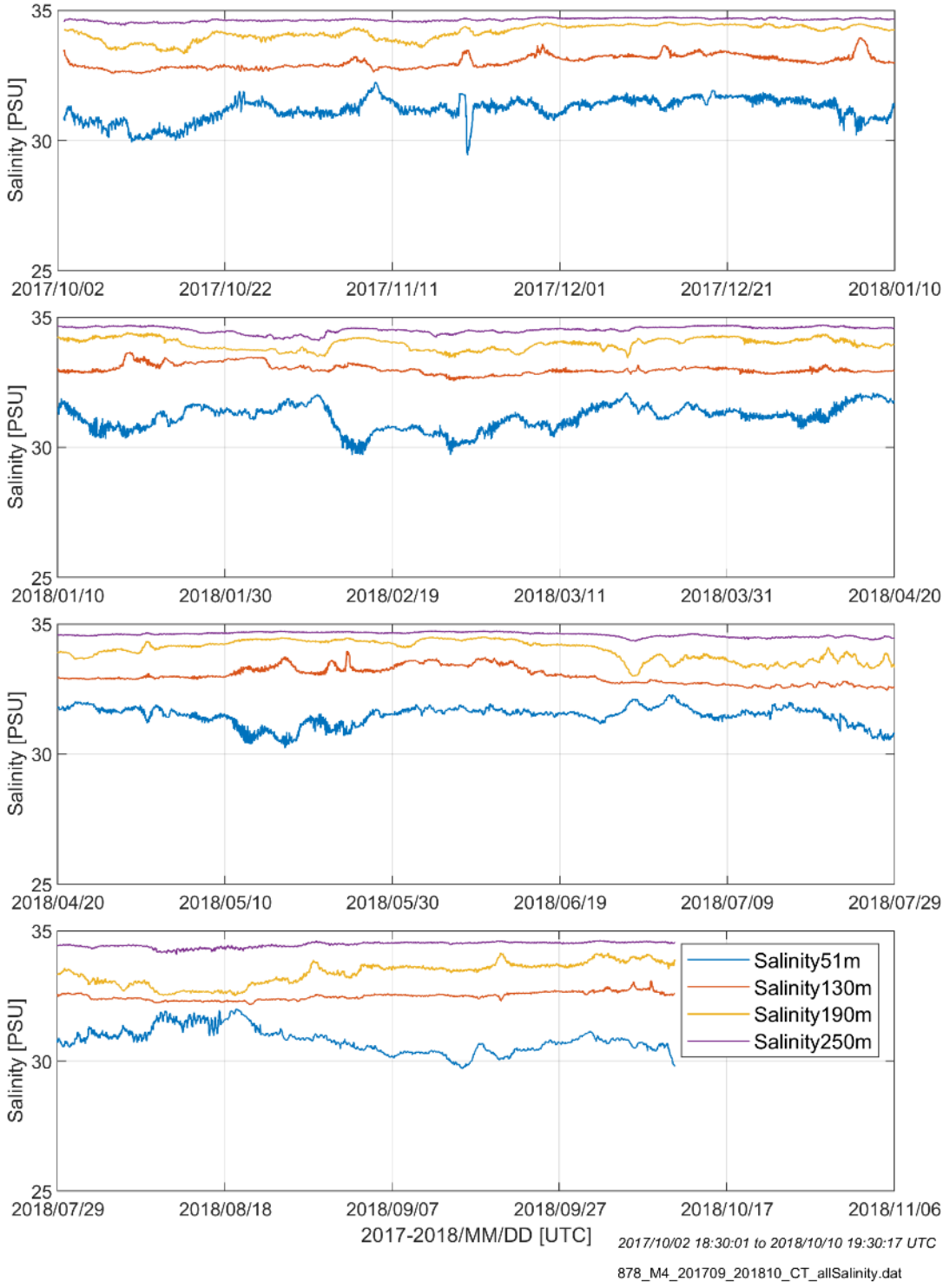

Figure 35. Salinity time-series derived from CT sensor measurements on M4 at various depths during the 2017–2018 deployment

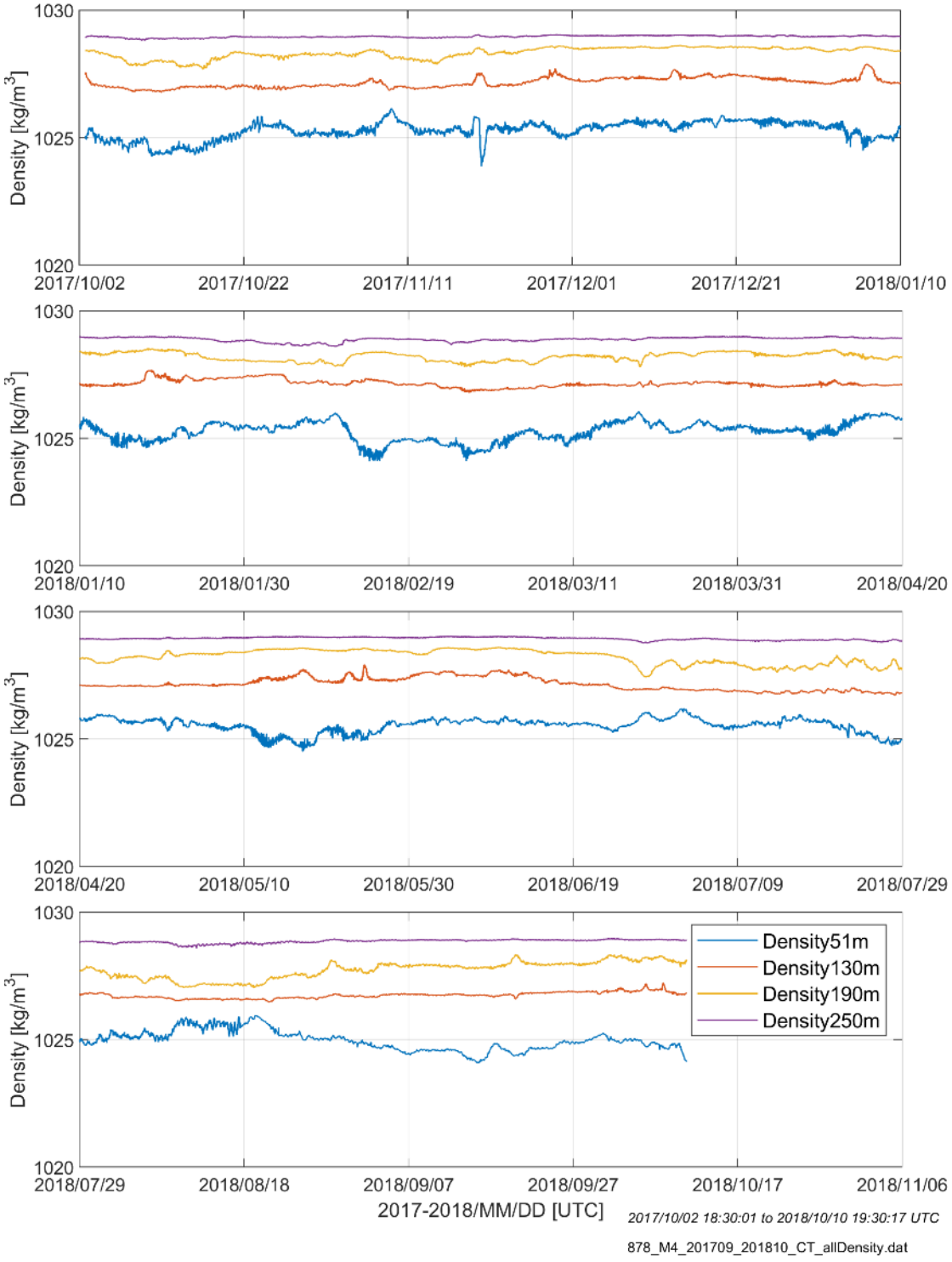

Figure 36. Density time-series derived from CT sensor measurements on M4 at various depths during the 2017–2018 deployment

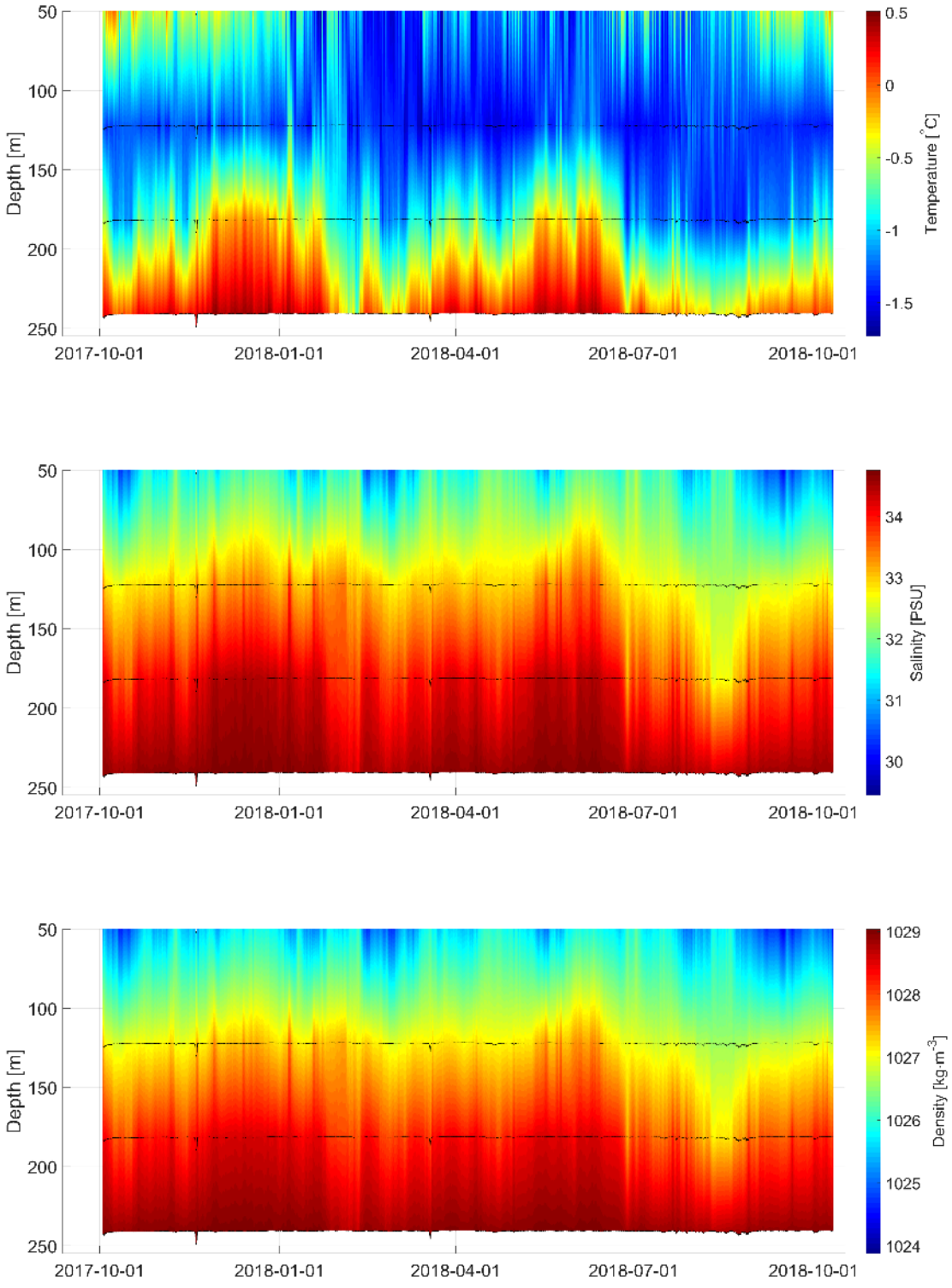

Figure 37. Temperature, salinity, and density time-series from CT sensors on M4 and interpolated over the full sampled water depth span during the 2017–2018 deployment. The black curves show the depth of each sensor.

Temperature, salinity and density profiles were measured at recovery of each mooring. The surface freshening and warming recorded at M1 reflects the late July cast (Figure 38). The warm saline water mass observed at 250 m depth at M3 and M4 is Atlantic Water which occurs at these depths throughout the Arctic Ocean. The casts at M2, M3, and M4 were done in the fall when the surface waters started cooling, and wind events started mixing the upper water column (Figure 39, Figure 40, and Figure 41).

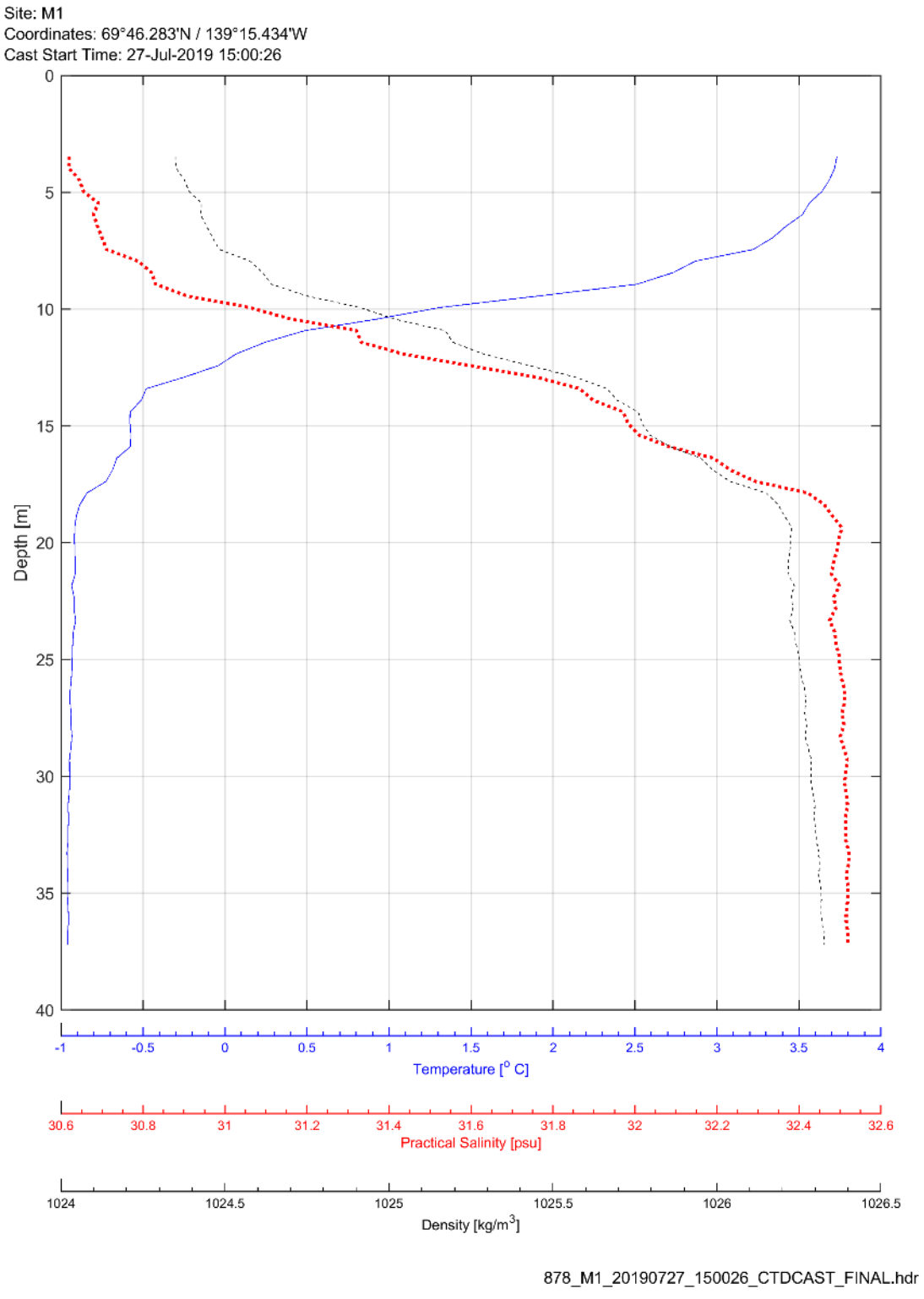

Figure 38. Temperature, salinity and density profiles measured at the M1 during recovery in July 2019.

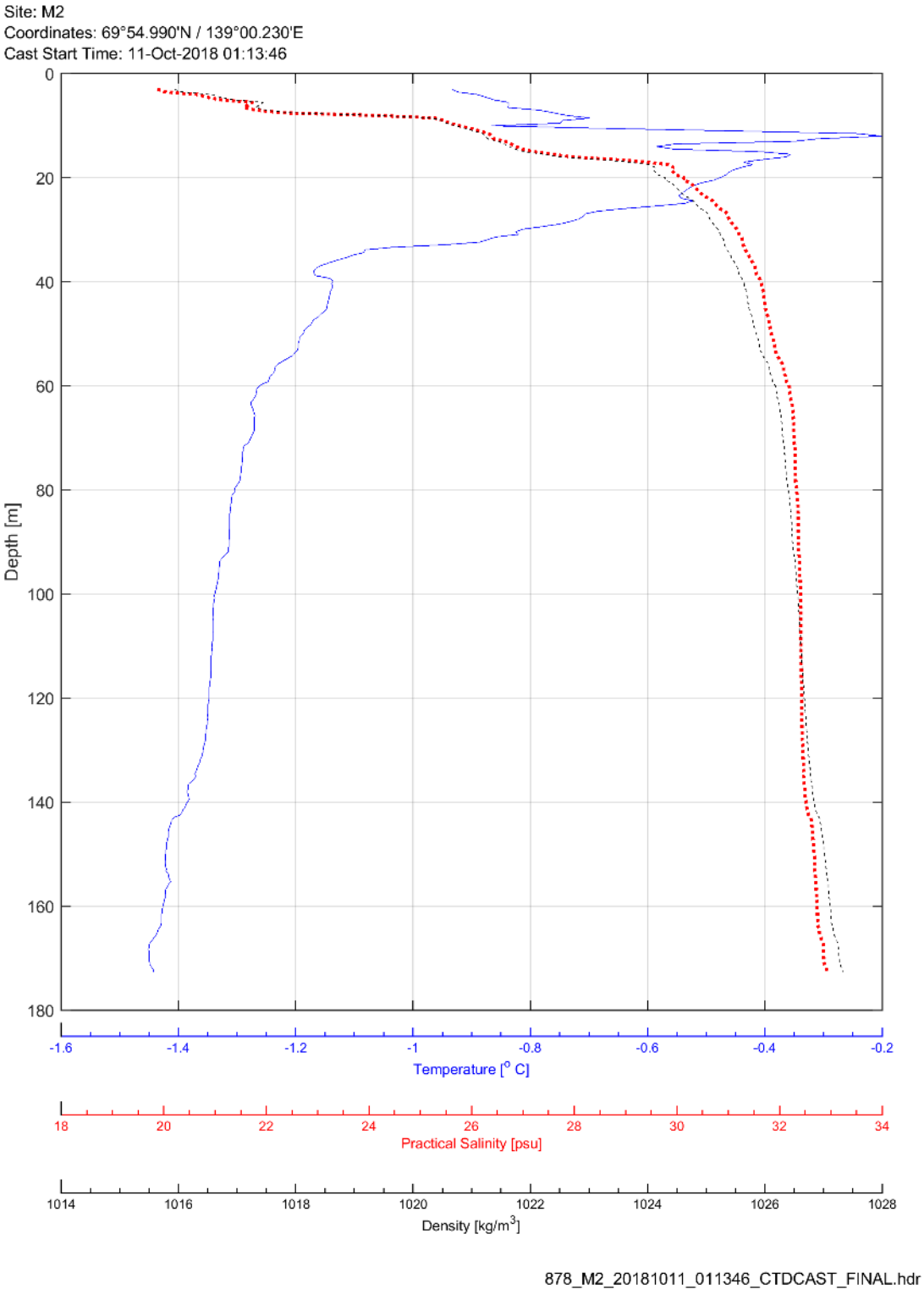

Figure 39. Temperature, salinity and density profiles measured at M2 during the recovery in October 2018.

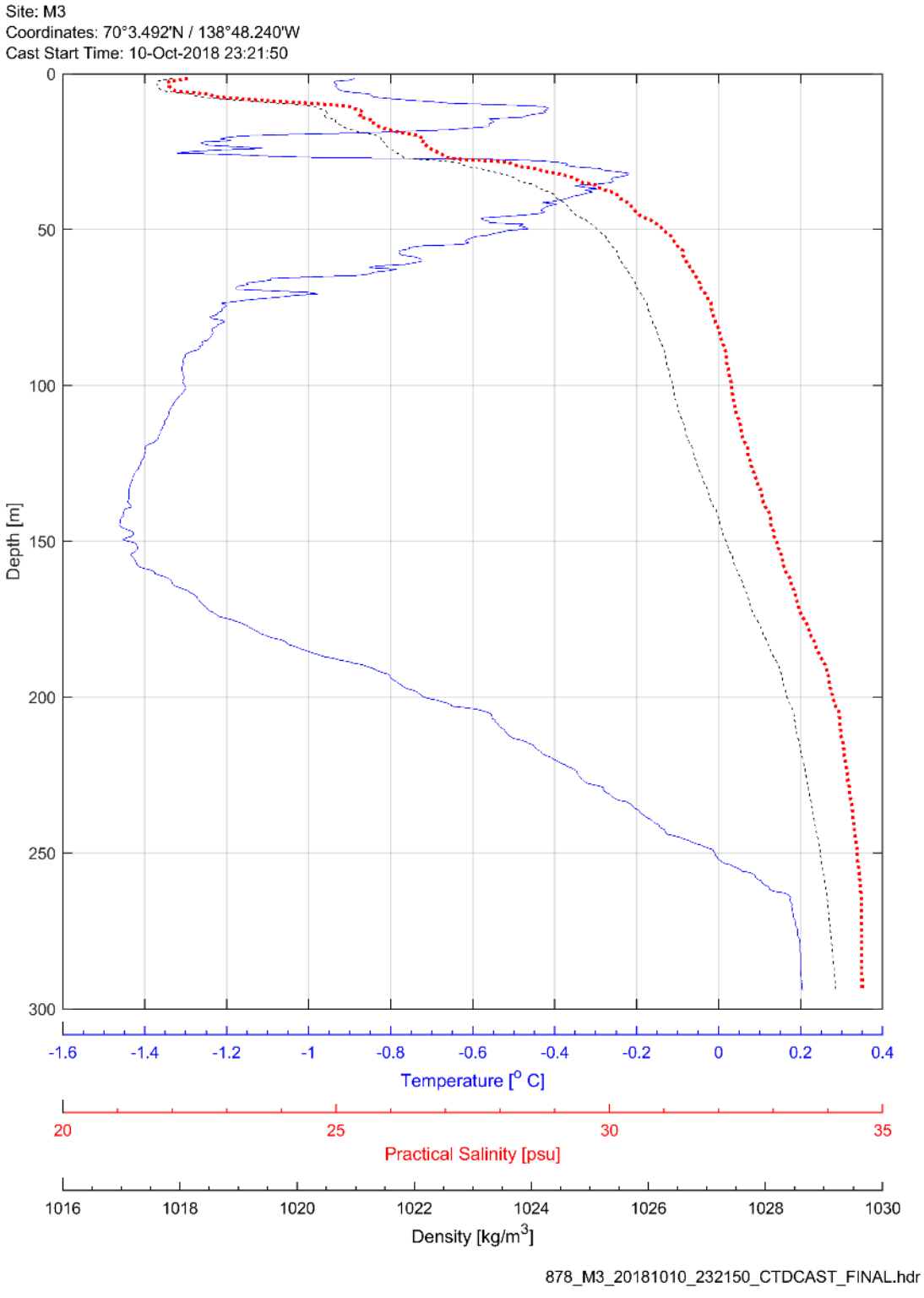

Figure 40. Temperature, salinity and density profiles measured at M3 during the recovery in October 2018.

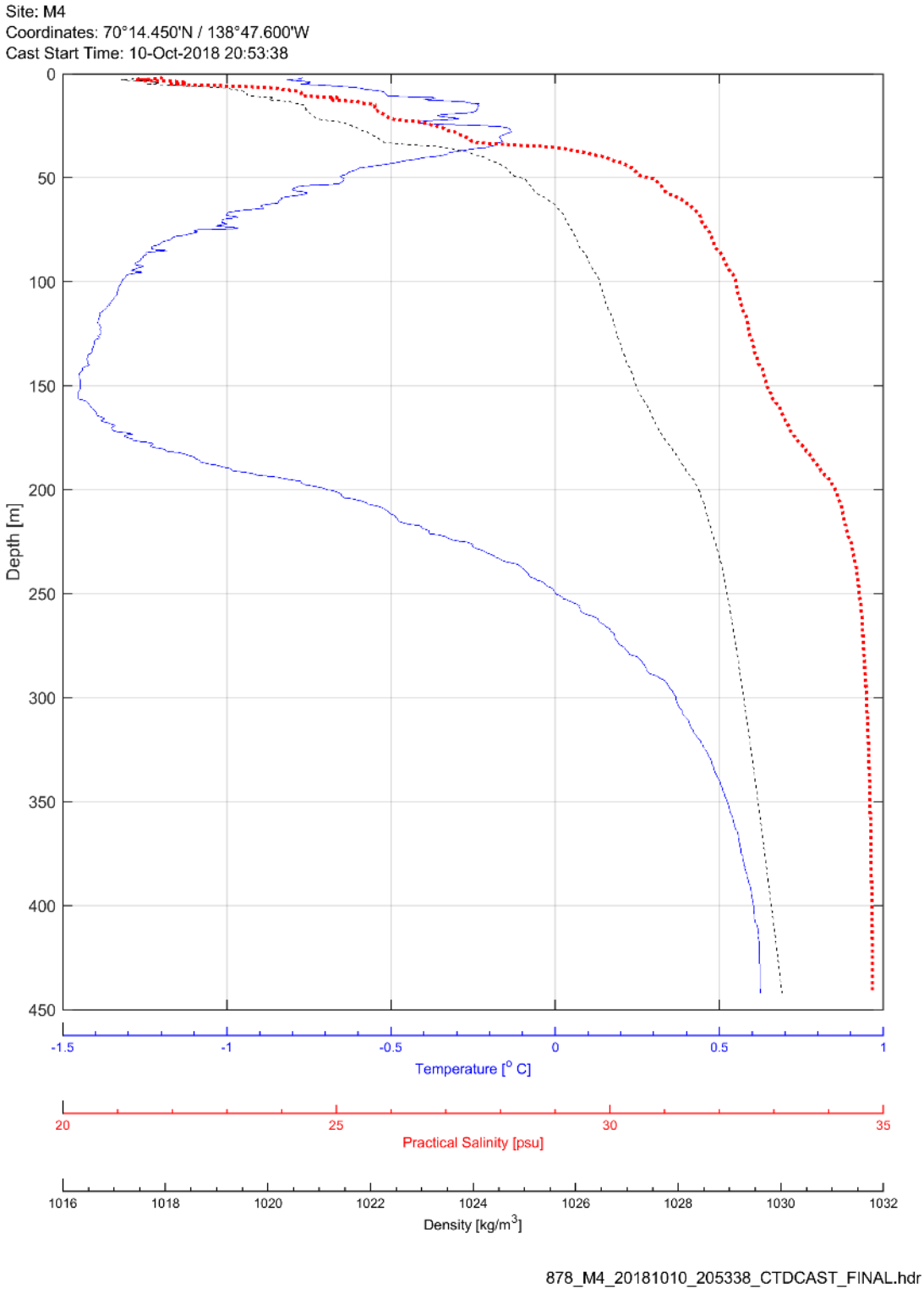

Figure 41. Temperature, salinity and density profiles measured at M4 during recovery in October 2018.

3.1.1.2 Currents

The pairs of quality-controlled ADCP time-series from the three deeper sites provided ocean currents with a depth span of 8 to 164 m at M2, 20 to 264 m at M3, and 16 to 310 m at M4. At M1, the single current meter provided currents between 6 and 30 m depth. The time-series were combined by interpolating to a common time sequence and vector-averaging the ocean current measurement records acquired in overlapping depth bins. The time-series are reported with a 20-minute interval, as described in Section 2.3.1.1 for all four of the sites. The results at this high temporal resolution illustrate many features in the current depth profiles; however, to visualize the time-series over the full deployment, it was necessary to average the currents using a 24-hour window.

The daily-averaged ocean currents at M1, M2, M3, and M4 are plotted in Figure 42 through Figure 45, respectively. The color of each cell in the third and fourth panels shows the ocean current speed and direction. Data gaps in the current time-series are plotted as white cells. There are three regions of data gaps: (1) the blanking distance of the deepest ADCP determines the deepest acquired depth cell, (2) side-lobe effects near the longest range target (either the water/air or water/sea-ice interface) limit the reliability of ocean current measurements near the water column surface, (3) interference with instruments further up the water column, such as the IPS which is frequently blanked out at depths of 40 m (M2) and 50 m (M4), and (4) reduced abundance of biological scatterers in the winter months leads to weakened backscattered acoustic signals, particularly at longer distances. Following up on the results from the 2016-2017 deployments, the LongRanger instruments were deployed using narrowband mode. The narrow band measurements have larger amounts of Doppler noise than the wide band measurements used in 2016-2017 but are able to yield valid measurements even when there are reduced concentrations of scatterers. Overall, changing to narrowband mode increased the data returns for the LongRangers. The top three panels of Figure 42 through Figure 45 show the daily-averaged ocean current speed time-series at near-surface, mid-depth, and near-bottom. The dotted lines on the fourth panel indicate these depths relative to the currents plotted over the full depth span.

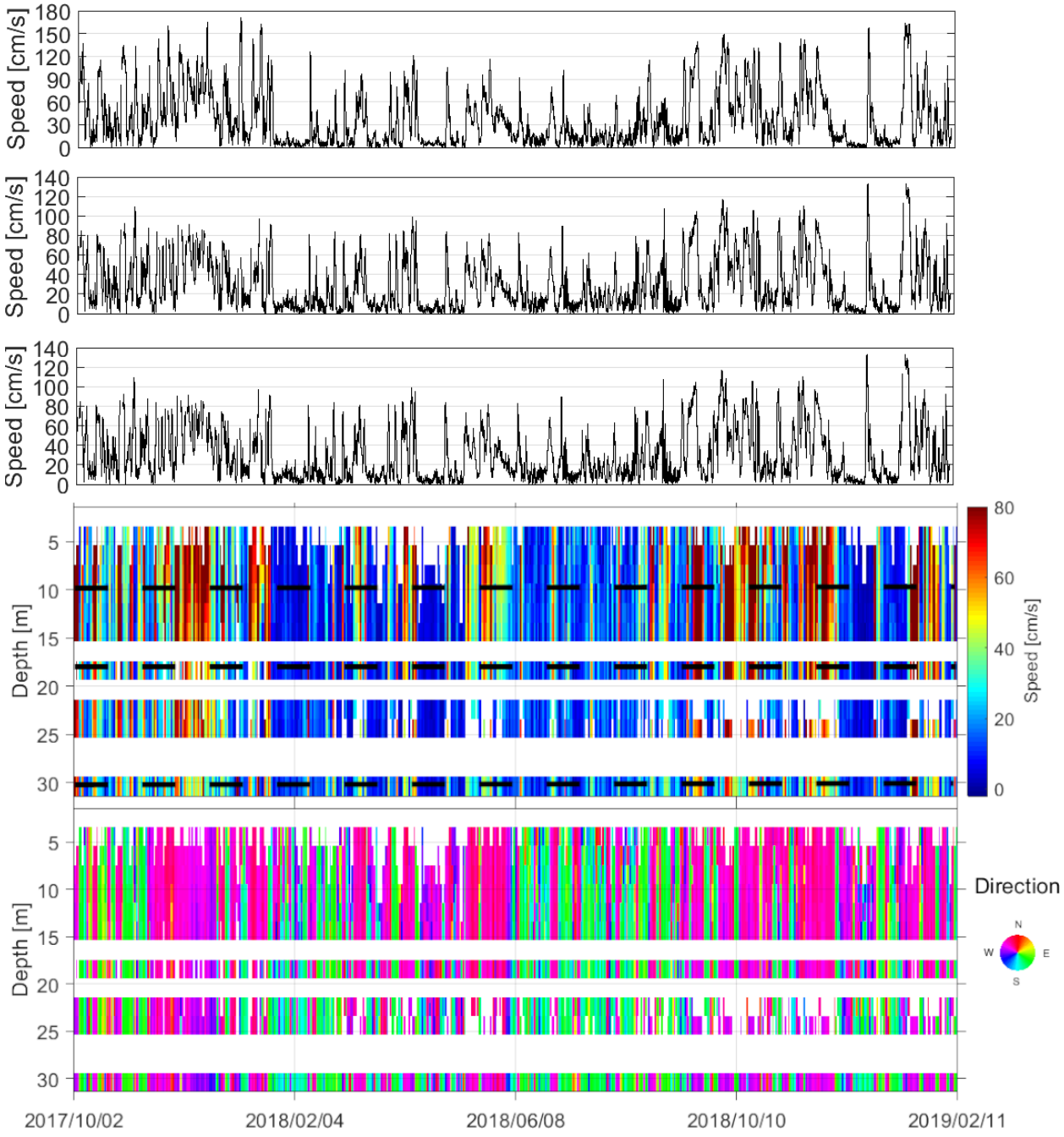

Figure 42. Daily-averaged ocean currents at M1 over the 2017–2019 mooring array deployment
The bottom two panels show the speed and direction (toward) of the ocean currents. The vertical extent spans the nearest reliable surface current depth to the closest bin to the ADCP. The top three panels show the current speed at three depths indicated by the dotted line on the fourth panel: 10, 18, and 30 m. Data gaps are illustrated in white.

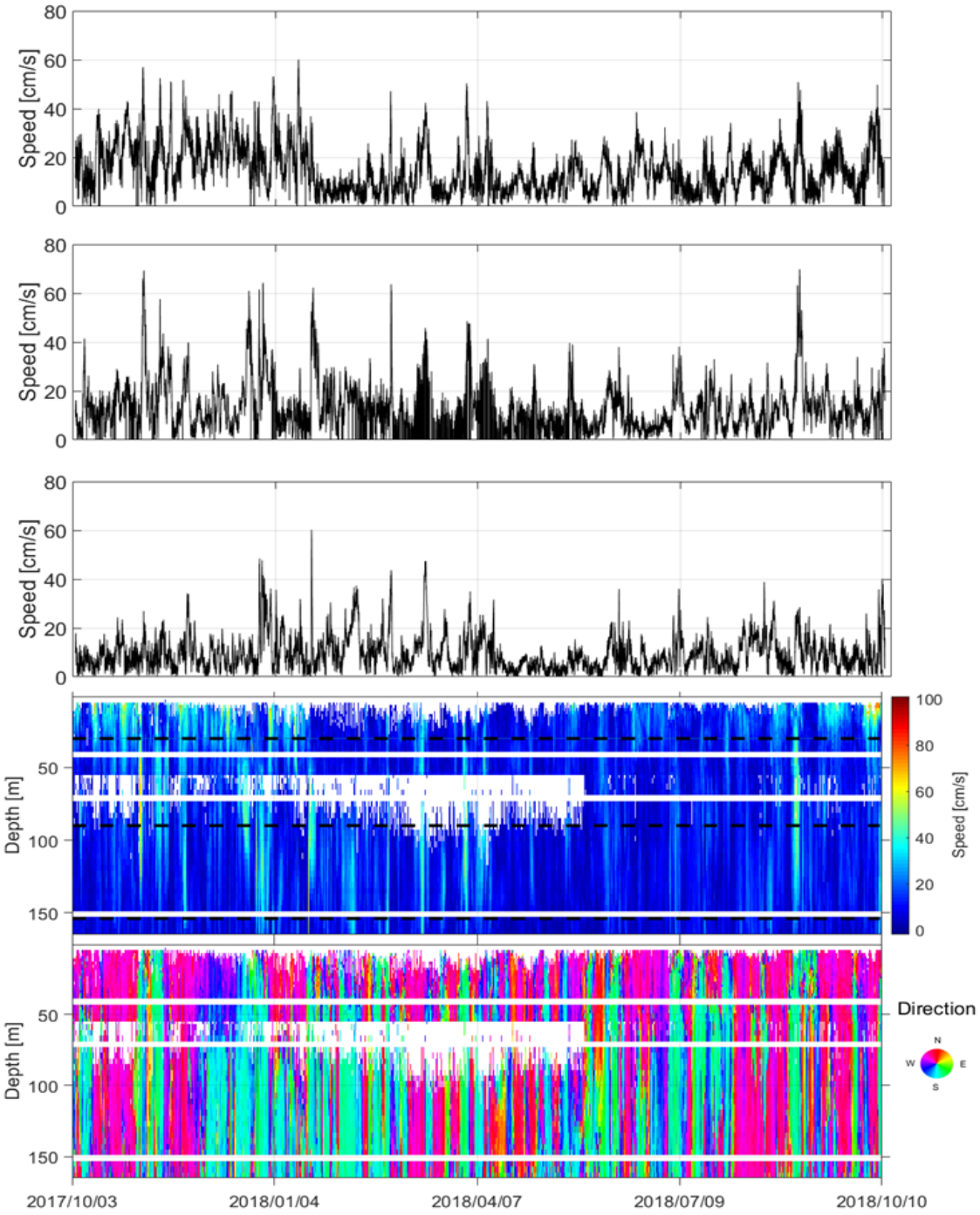

Figure 43. Daily-averaged ocean currents at M2 over the 2017–2018 mooring array deployment
The bottom two panels show the speed and direction (toward) of the ocean currents. The vertical extent spans the nearest reliable surface current depth to the closest bin to the ADCP. The top three panels show the current speed at three depths indicated by the dotted line on the fourth panel: 30, 90, and 154 m. These results were constructed by combining the currents measured from ADCPs moored at two depths. Data gaps are illustrated in white.

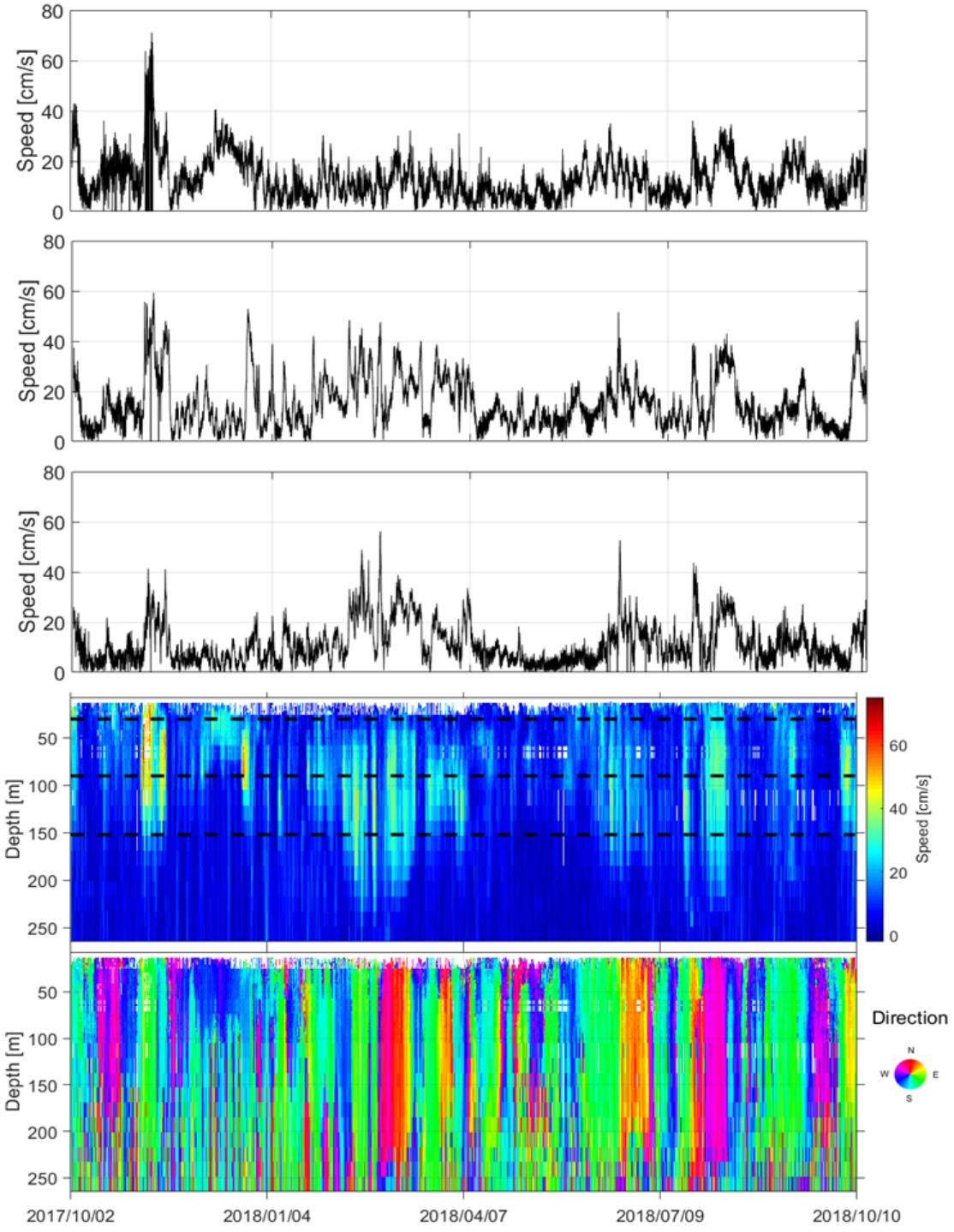

Figure 44. Daily-averaged ocean currents at M3 over the 2017–2018 mooring array deployment
The bottom two panels show the speed and direction (toward) of the ocean currents. The vertical extent spans the nearest reliable surface current depth to the closest bin to the ADCP. The top three panels show the current speed at three depths indicated by the dotted line on the fourth panel: 30, 90, and 152 m. These results were constructed by combining the currents measured from ADCPs moored at two depths. Data gaps are illustrated in white.

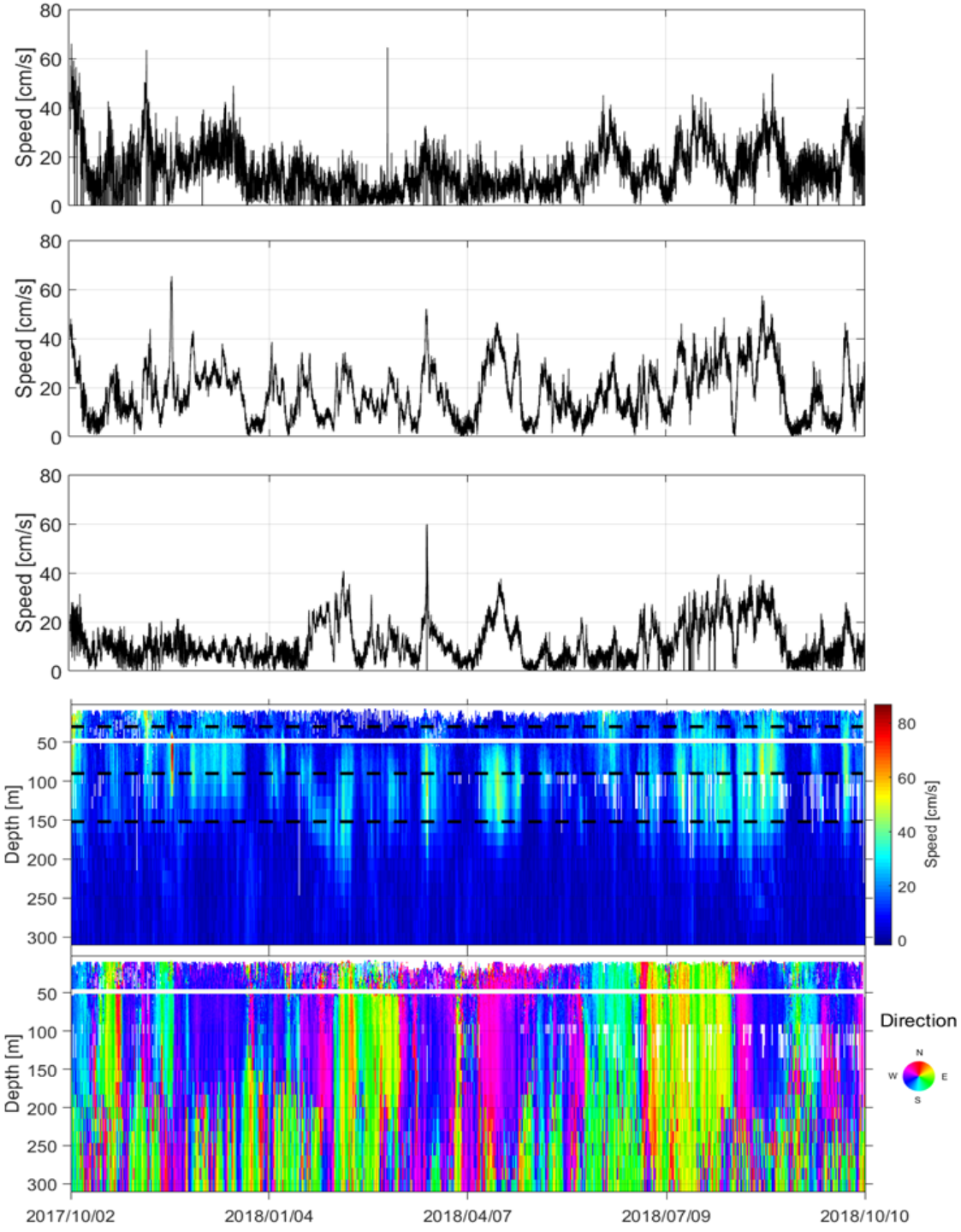

Figure 45. Daily-averaged ocean currents at M4 over the 2017–2018 mooring array deployment
The bottom two panels show the speed and direction (toward) of the ocean currents. The vertical extent spans the nearest reliable surface current depth to the closest bin to the ADCP. The top three panels show the current speed at three depths indicated by the dotted line on the fourth panel: 30, 90, and 152 m. These results were constructed by combining the currents measured from ADCPs moored at two depths. Data gaps are illustrated in white.

The currents at M1 are quite different from the other two sites not only due to their large magnitude, but also their consistency. At sited M2 through M4, there are a handful of events which are at the highest current speeds, and then there is a "gap" in the distribution. For example, at M4 the near-surface currents exceed 50 cm/s in about 4 events. At M1, the currents at around 120 cm/s or larger several times in each season, but with somewhat of a reduction in the winter and spring. The winter and spring seasons at M1 are also notable in that they frequently exhibit small current speeds of less than 30 cm/s. Due to the similarities between the other 3 sites, they will be discussed further.

A common pattern among the M1, M2 and M3 sites is the occurrence of high-speed events which represent the top 10% of the velocity distribution, even during the middle of winter when there is ice present. Ice tends to reduce the direct coupling of the atmosphere to the ocean currents. All three sites had some of their largest events in November, early in the sea ice season when sea ice is rapidly forming in the region. Figure 46 through Figure 48 shows the ice velocities (top panel), NCEP Reanalysis 2 (NCEP, 2019) modeled local wind speed (middle line plot), current speed profile (middle contour plot), and current direction toward (bottom panel) for M2, M3, and M4 respectively during the month of November.

At M2, there is an event which spans from 150 to 30 m depth which reaches speeds in excess of 60 cm/s around November 3, 2017. Events of similar spatial scales, but of smaller magnitude are also seen around November 11 to November 16, 2017, and again from November 22 to November 25, 2017. There is no significant ice cover locally during the strong event at M2, but as it does not reach the surface, it is unlikely to be driven by local winds. The other events occur when ice cover is present. The one event which may be wind driven is characterized by speeds up to 80 cm/s at the surface around November 22, 2017. At M3, there are events which span from 125 to 0 m depth between November 5 and November 10, 2017. There is no significant ice cover during these events and the modeled winds at M3 sometimes reach 10 m/s during this event, however, because some of the strongest currents seem to be around 50 m depth, this event may not actually be driven by the local winds.

Additional events which span from 140 to 40 m depth between November 14 and November 15, 2017 are also evident, but ice is present during these events. At M4, there are elevated current speeds of up to 30 cm/s to depths of 130 m between November 5 and November 9, 2017. Ice of 9+ tenths and up to 1m in draft was observed from November 6 to November 7, 2017 during this event. In spite of the ice, some of the largest current speeds are observed at the surface and may be driven by the local winds. A strong jet with current speeds up to 83 cm/s was observed between November 18 and November 19, 2017 from 35 to 120 m depth. Sea ice was present during this event. Finally, there is a weaker event with speeds up to 40 cm/s from 40 to 120 m depth between November 28 and November 29, 2017. The semi-diurnal banding which is frequently observed at these sites is likely inertial oscillations.

One of the largest events at the M4 site occurred between March 18 and March 19, 2018 at depths between 60 and 180 m. Current speeds of just over 50 cm/s were observed, however, part of the jet was not measured, probably due to low concentrations of scatterers. This drop-out appears as the white patch in Figure 49. A cluster of events occur between April 11 and April 30 between 60 and 160 m depth with speeds reaching up to 45 cm/s. Ice is present through the duration of all of these events, but with the ice drift being < 0.5 cm/s for most of the time between April 19 and April 23, 2018.

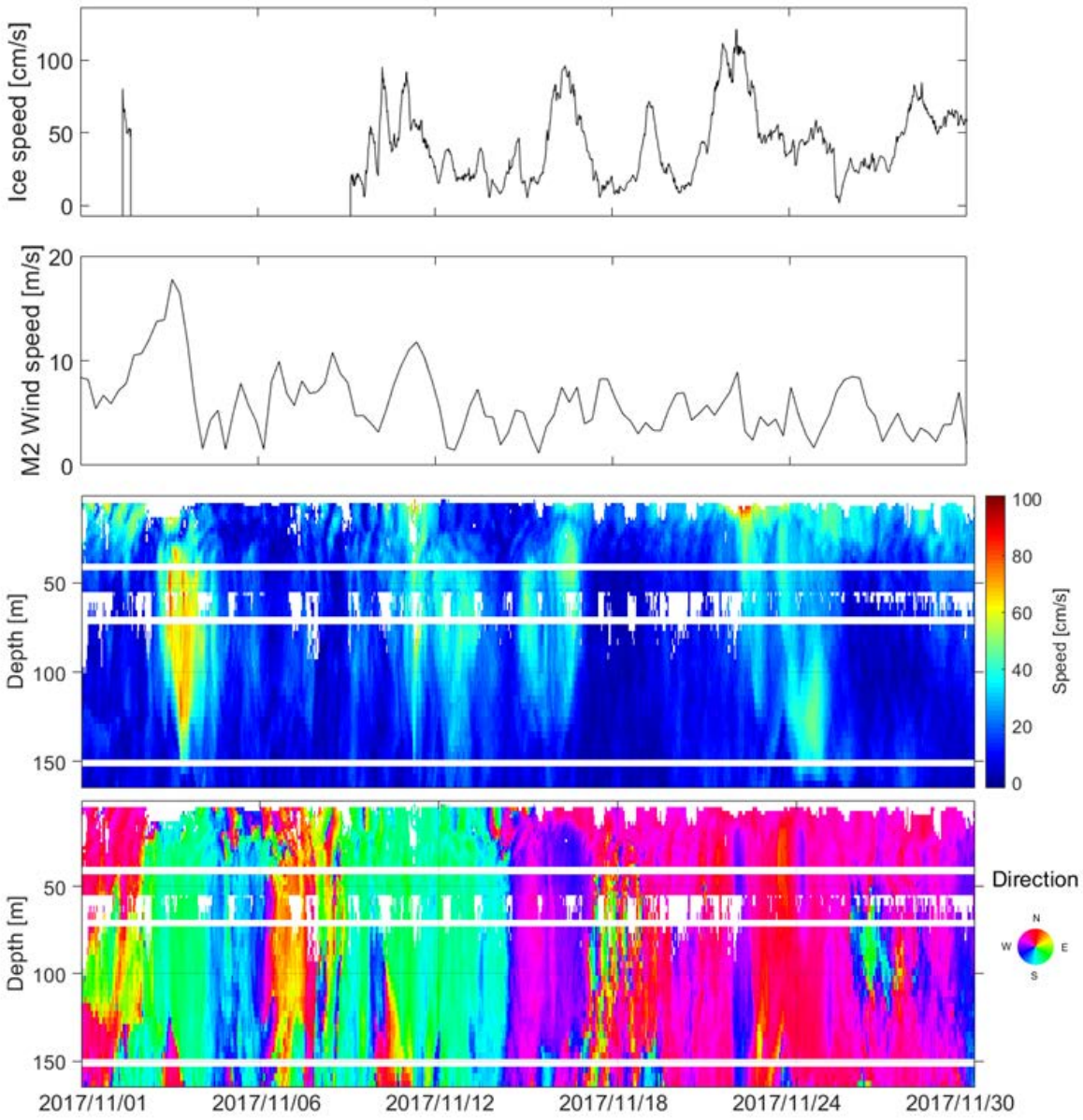

Figure 46. High resolution ocean currents at M2 during an ice-free episode in November 2017
The top two panels show the ice drift speed and NCEP Reanalysis 2 wind speeds at M2. The bottom two panels show the ocean current speed and direction (toward) observed at M2 based on the results of 20-minute intervals over the measured depth span. Low concentrations of scatterers appears as the white patches.

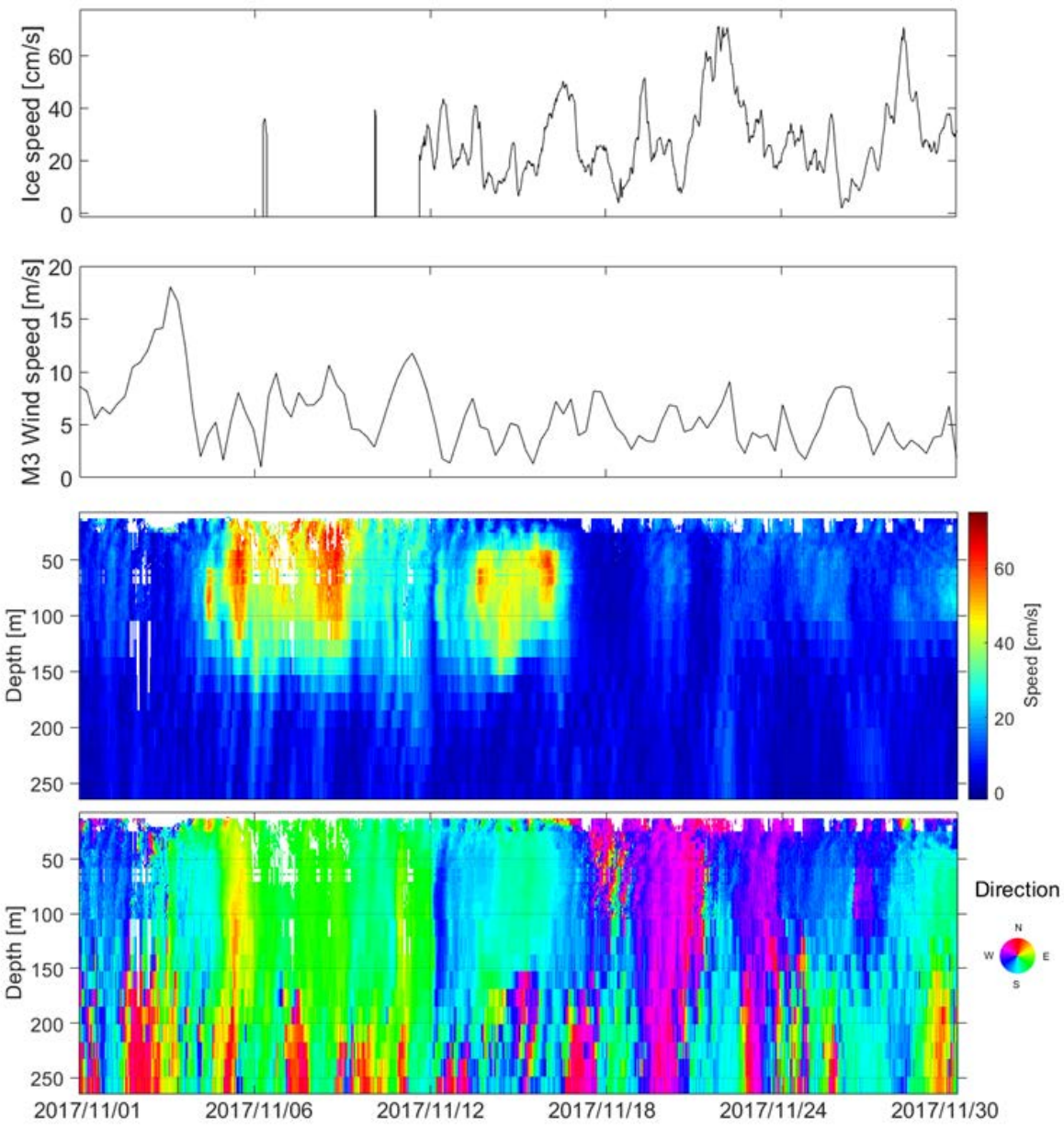

Figure 47. High resolution ocean currents at M3 during an ice-free episode in November 2017
The top two panels show the ice drift speed and NCEP Reanalysis 2 wind speeds at M3. The bottom two panels show the ocean current speed and direction (toward) observed at M3 based on the results of 20-minute intervals over the measured depth span. Low concentrations of scatterers appears as the white patches.

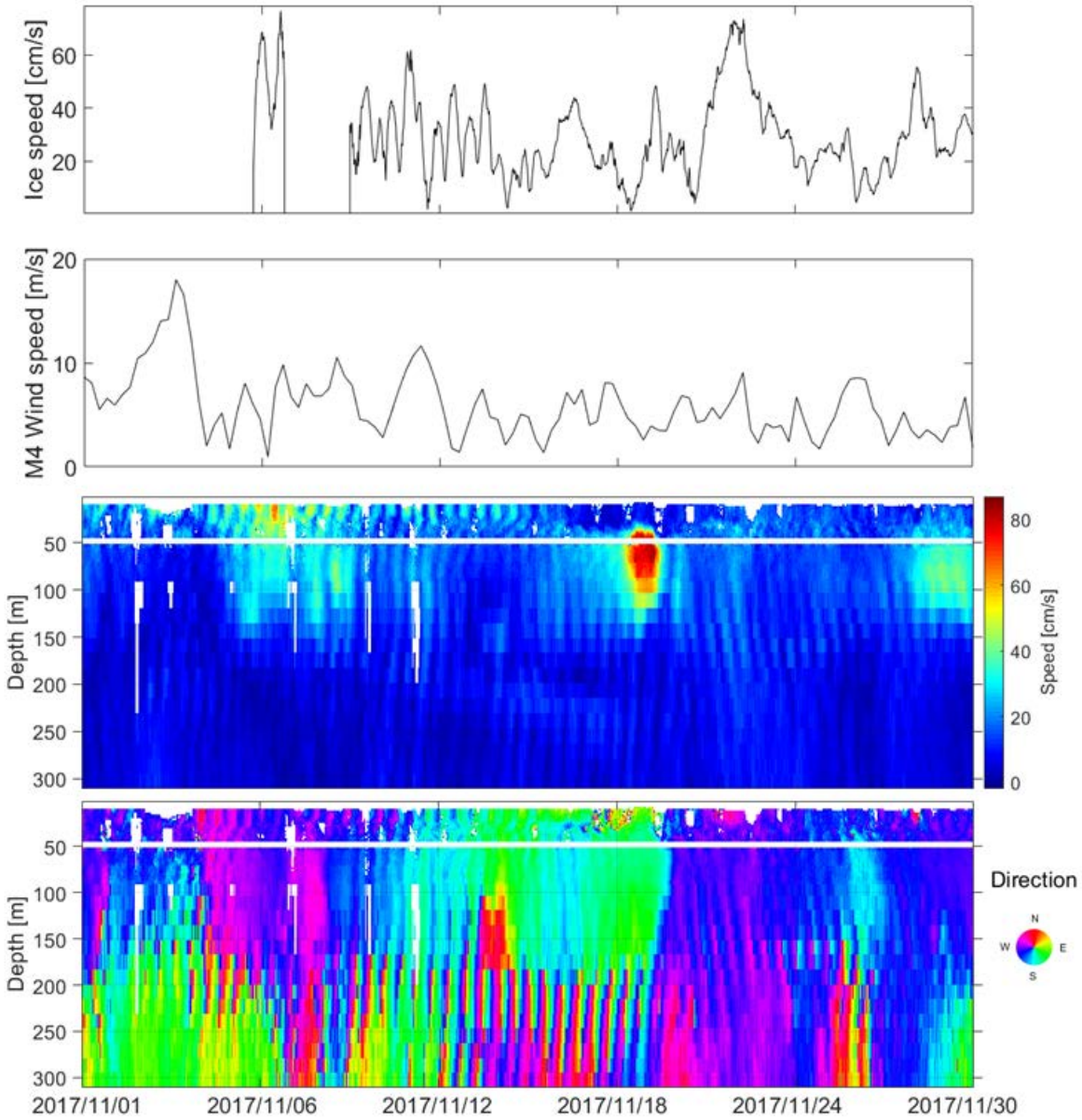

Figure 48. High resolution ocean currents at M4 during an ice-free episode in November 2017
The top two panels show the ice drift speed and NCEP Reanalysis 2 wind speeds at M4. The bottom two panels show the ocean current speed and direction (toward) observed at M4 based on the results of 20-minute intervals over the measured depth span. Low concentrations of scatterers appears as the white patches.

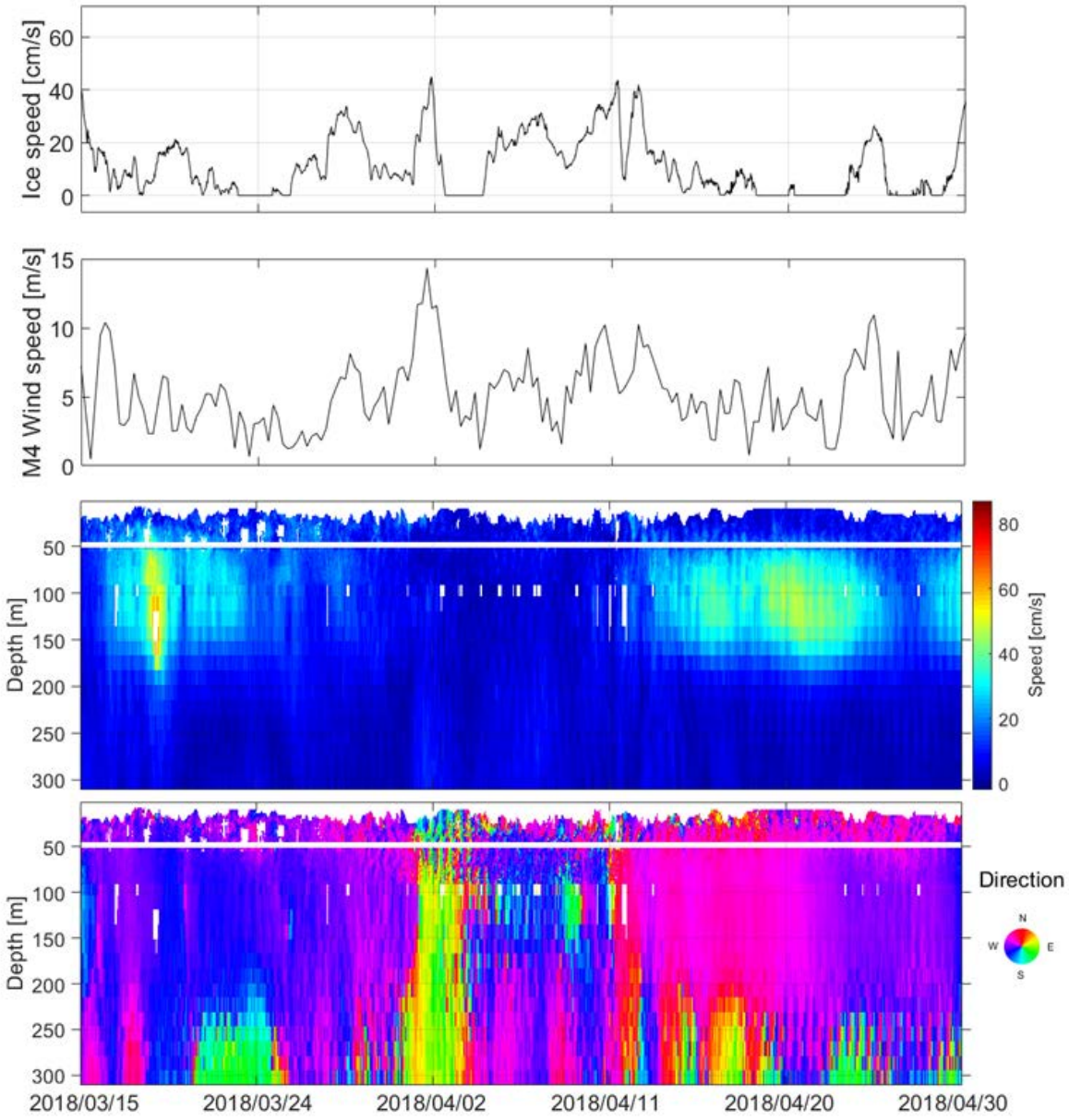

Figure 49. High resolution ocean currents at M4 during an ice-free episode in March and April 2018

The top two panels show the ice drift speed and NCEP Reanalysis 2 wind speeds at M4. The bottom two panels show the ocean current speed and direction (toward) observed at M4 based on the results of 20-minute intervals over the measured depth span. Low concentrations of scatterers appears as the white patches.

3.1.1.3 Alongstream Current Velocity and Water Masses

Figure 50 reveals that there was a strong surface-intensified current flowing toward the west at mooring M1. This is the shelf current identified using the first year of data. The ice concentration in the vicinity of the mooring varied dramatically even during the winter. The open water period in summer was from late June to early October with two short episodes of incursion of sea ice in late July and later in August. Figure 22 demonstrates that the variations of temperature and salinity were vertically coherent. The

relatively warm and salty water that appeared in late November of 2017 is Remnant Winter Water, which then became colder and fresher during the winter months.

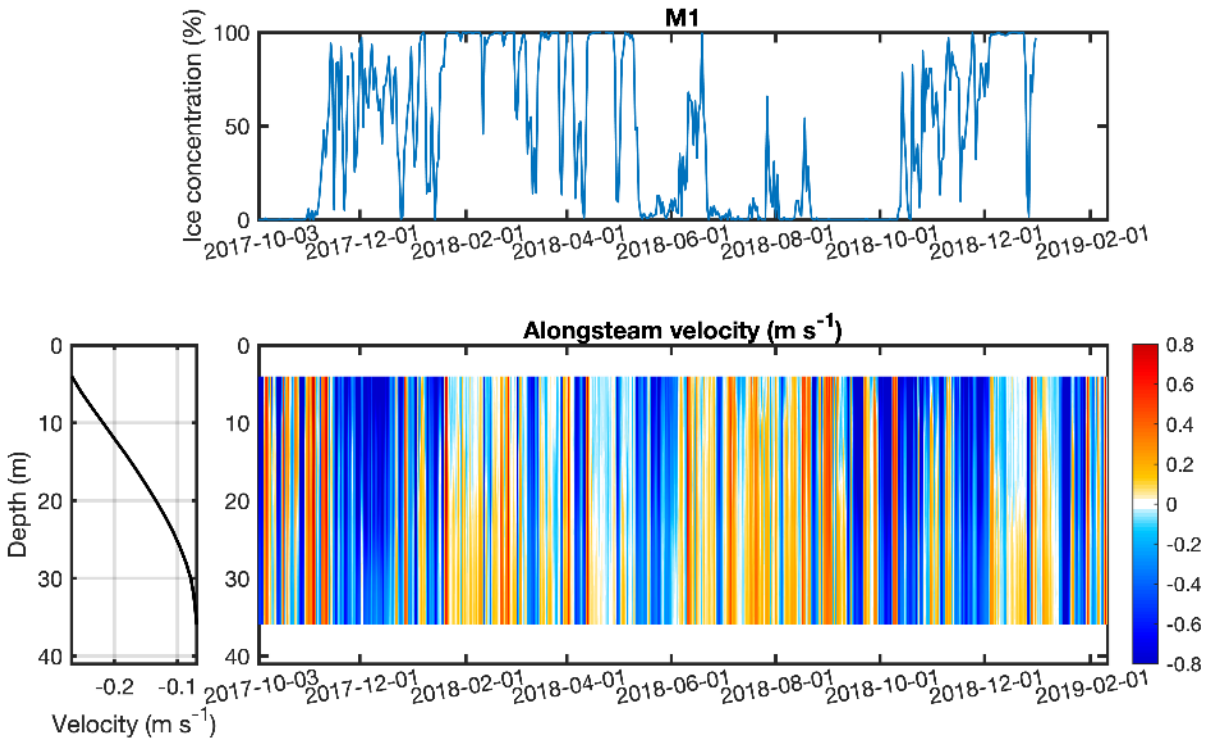

Figure 50. Top panel: Ice concentration in the vicinity of mooring M1. Bottom panel: Time series of alongstream velocity (color, m/s). Positive is Eastward. The year-long mean vertical structure is shown on the left.

The alongstream velocity at site M2 was also surface-intensified and directed westward (Figure 51), similar to M1. As was demonstrated using the year 1 data (Lin et al. submitted), this westward flow is the offshore part of the shelf current. Figure 29 shows that the temperature and salinity at M2 was nearly vertically uniform in late winter and early spring, while there was more stratification in late fall and late spring.

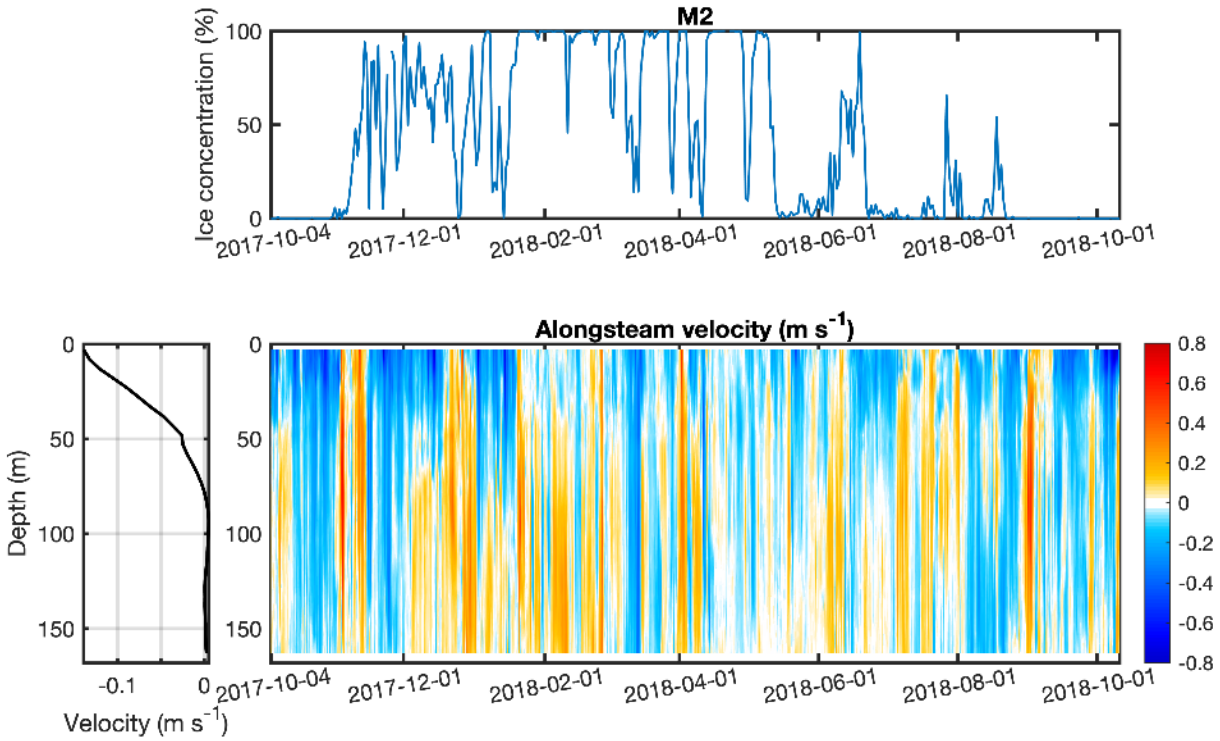

Figure 51. Top panel: Ice concentration in the vicinity of mooring M2. Bottom panel: Time series of alongstream velocity (color, m/s). Positive is eastward. The year-long mean vertical structure is shown on the left.

The alongstream velocity at site M3 was mid-depth intensified flowing to the east (Figure 52). The maximum velocity was ~0.4 m s^{-1} at roughly 100 m depth. The near-surface flow was weakly westward. Figure 33 shows that Atlantic Water was present at depth, while the surface water column was mostly melt water / meteoric water. There were two strong events of cooling and freshening near the bottom of the mooring.

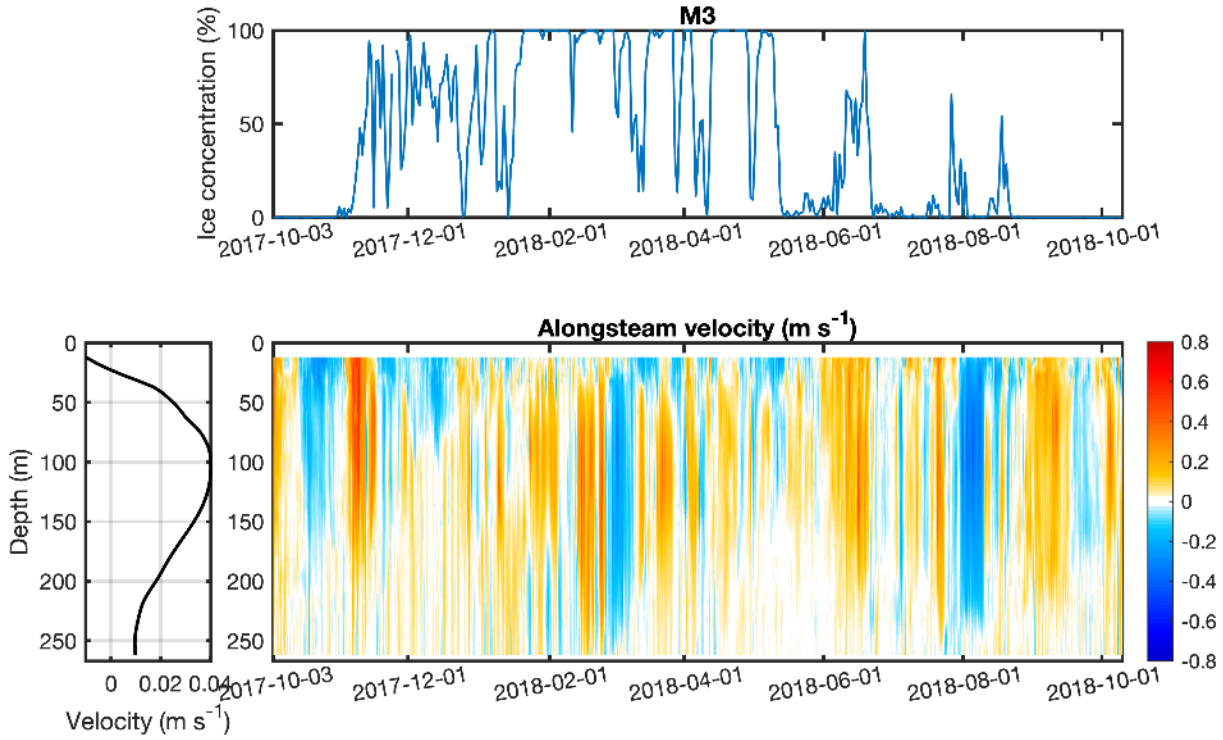

Figure 52. Top panel: Ice concentration in the vicinity of mooring M3. Bottom panel: Time series of alongstream velocity (color, m/s). Positive is eastward. The year-long mean vertical structure is shown on the left.

The alongstream flow at mooring M4 (Figure 53) was mid-depth intensified, but flowing to the west instead of to the east, as it was at mooring M3. The peak speed was close to that of M3. This is consistent with the first-year result that a recirculation is present in the canyon (Lin et al. submitted). In terms of the hydrographic properties, the conditions at M4 (Figure 37) were similar to those at M3 (Figure 33).

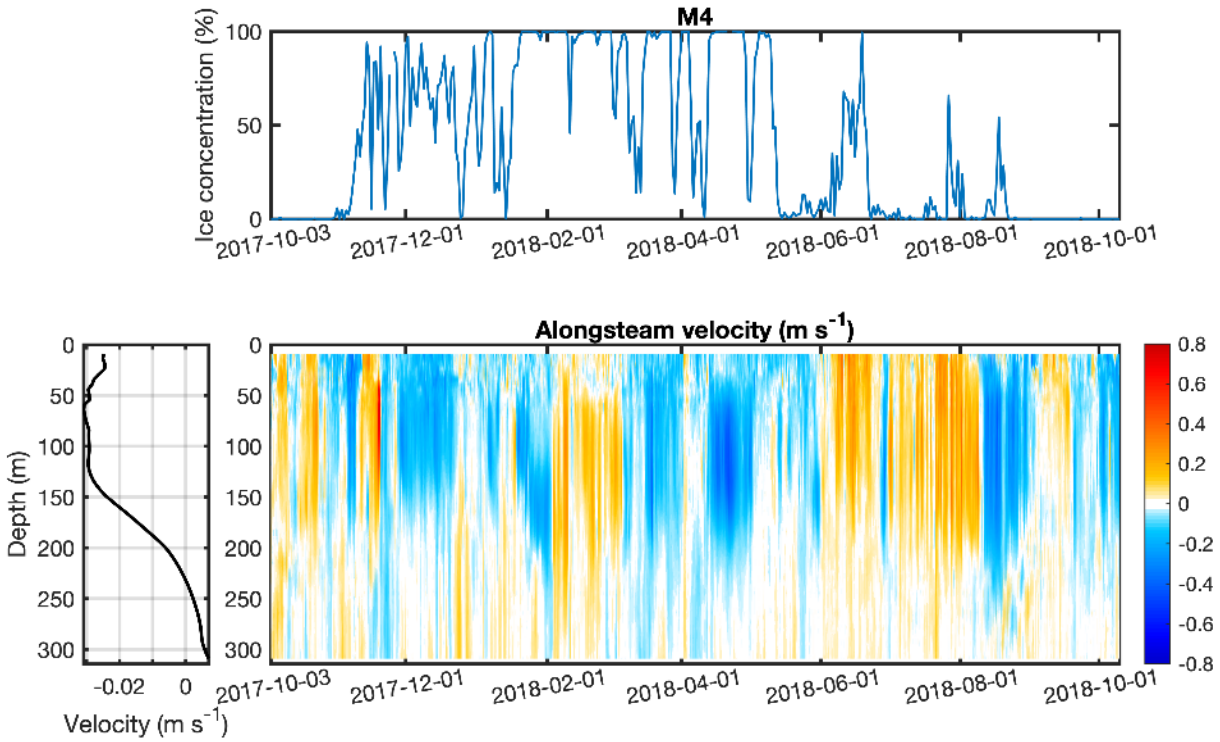

Figure 53. Top panel: Ice concentration in the vicinity of mooring M4. Bottom panel: Timeseries of alongstream velocity (color, m/s). Positive is eastward. The year-long mean vertical structure is shown on the left.

3.1.1.4 Ice

3.1.1.4.1 General Ice Dynamics

Sea ice freeze-up began in the near-shore areas of the Beaufort Sea in mid-October 2017. The entire MARES array was ice covered by early November, and the ice concentrations had reached 9-10 tenths by mid-November (Figure 54). The sea ice concentration remained high throughout the deployment with further evolution of the landfast ice edge until mid-March 2018 where this feature remained at a maximum extent. The regional ice break-up and clearing began in mid-May 2018. The ice motion throughout the deployment expressed many episodes of both appreciable drift and low to zero speeds. Under certain conditions, relative immobility can be indicative of higher internal stresses within the ice pack. Low motion occurred mostly during February, March, and April 2018.

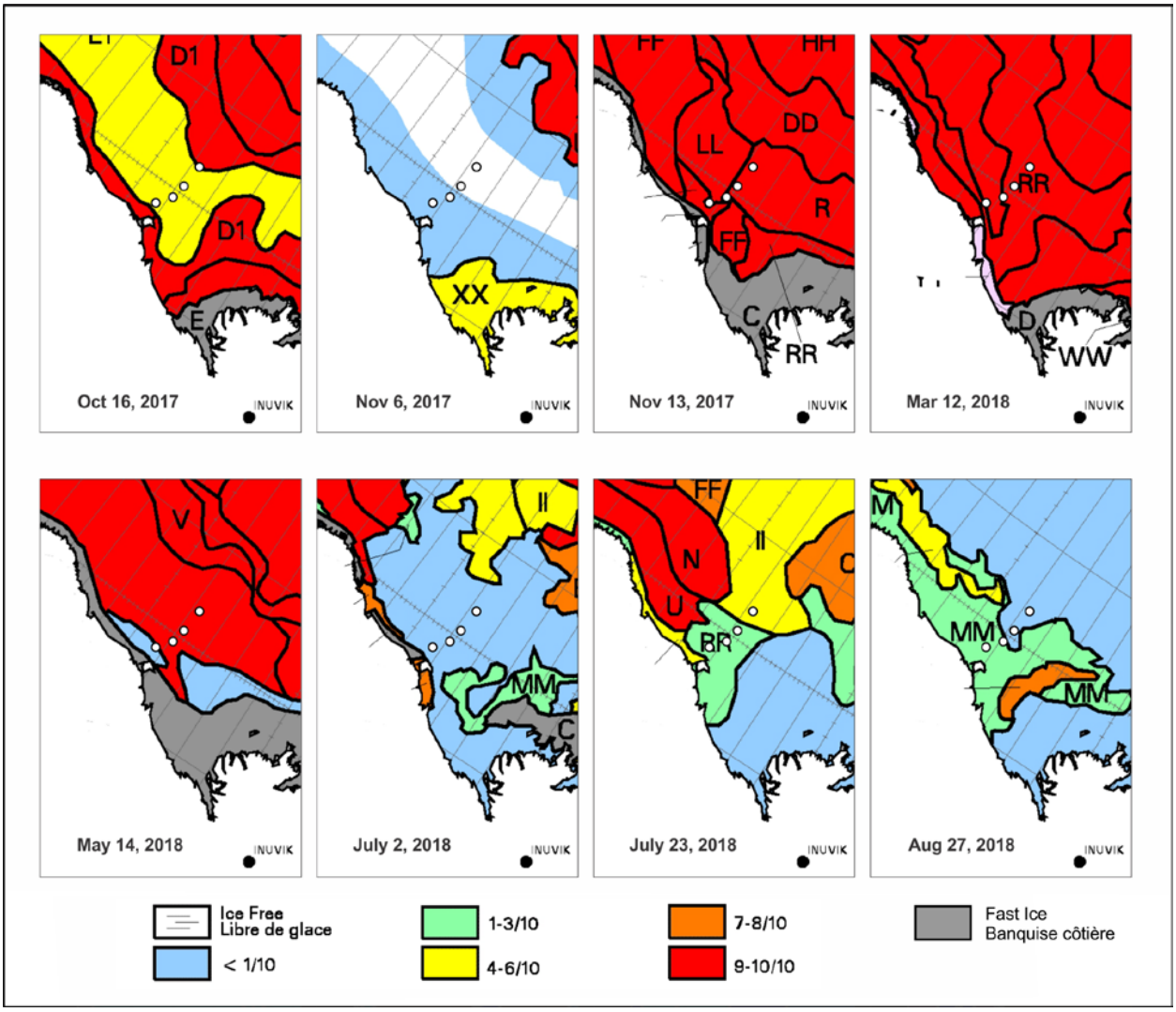

Figure 54. Sea ice concentration in tenths of coverage in the region of the MARES array as reported by Canadian Ice Services Ice Charts (CIS, 2018) during the 2017–2018 deployment.

Selected dates show the seasonal variations which happened in the study area. Grey polygons illustrate regions of landfast ice. The MARES mooring locations are shown by the white circles with black outline.

3.1.1.4.2 Ice Velocity

The ice speed at M1, M2, M3 and M4 is plotted in Figure 55. The mean speed over the full deployment was largest at M1, 46.3 cm/s, followed by M2, 24.7 cm/s. The maximum ice drift speed at M1 was 268 cm/s to the northwest on January 2, 2018. There were 12 instances where ice speed exceeded 200 cm/s at M1. The M2 ice drift speeds reached 147.2 cm/s on January 3, 2018 but exceeded 140 cm/s again on January 14, 2018. The M3 and M4 mean ice drift speeds were 18.8 cm/s and 19.8 cm/s, respectively. These two sites both experienced their maximum ice drift speeds on January 14, 2018: 83.6 cm/s and 85.7 cm/s, respectively. The winds on January 14 reached just under 15 m/s at Herschel Island. NCEP Reanalysis 2 wind results (NCEP, 2019) indicate even stronger winds offshore. Monthly and period of deployment statistics are tabulated for each of the four sites in Table 31 through Table 34.

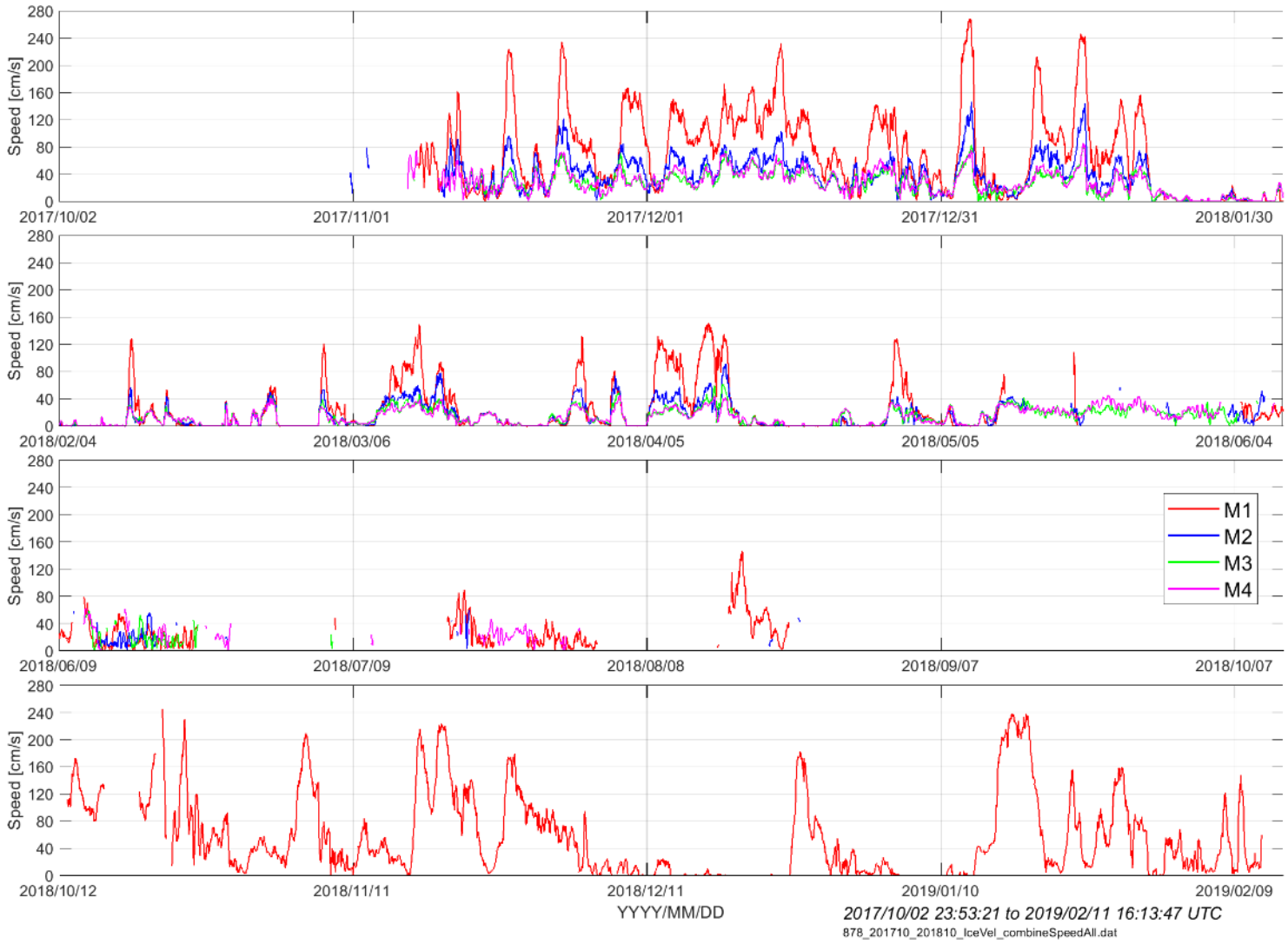

Figure 55. Horizontal ice speed at M1, M2, M3, and M4 over the 2017–18 deployment

Table 31. Ice speed statistics (cm/s) by month and for the period of deployment for M1 from 2017–2019

M1 (cm/s)	Min	1%	5%	25%	50%	Mean	75%	95%	99%	std	Max	# valid	Total #
2017/10/02 2017/10/31	ND	ND	ND	ND	ND	ND	ND	ND	ND	ND	ND	0	2086
Nov-2017	0.02	4.16	9.64	28.01	56.80	72.37	101.34	186.58	222.45	55.77	234.12	1691	2156
Dec-2017	1.16	6.21	11.72	46.30	90.42	87.01	121.97	158.59	218.50	47.59	231.47	2229	2229
Jan-2018	0.00	0.00	0.01	3.03	29.04	59.81	96.84	220.76	255.08	70.03	267.79	2229	2229
Feb-2018	0.00	0.00	0.00	0.03	0.13	8.94	10.37	45.29	111.52	18.93	128.48	2013	2013
Mar-2018	0.00	0.00	0.02	2.32	12.80	26.80	36.90	94.18	127.21	33.20	149.45	2228	2228
Apr-2018	0.00	0.00	0.00	0.22	2.08	32.58	64.37	125.70	144.80	45.66	151.46	2157	2157
May-2018	0.00	0.00	0.13	2.11	8.66	16.44	20.43	61.64	85.60	20.27	108.27	795	2229
Jun-2018	0.31	1.30	3.50	9.99	16.95	19.41	26.58	46.63	62.32	13.01	78.48	1239	2156
Jul-2018	1.05	1.75	3.38	9.69	18.25	23.84	33.39	62.78	84.54	19.17	89.21	732	2229
Aug-2018	1.35	1.90	4.31	11.86	35.24	42.07	58.57	116.12	142.29	34.86	146.43	594	2229
Sep-2018	ND	ND	ND	ND	ND	ND	ND	ND	ND	ND	ND	0	2156
Oct-2018	2.34	3.64	10.20	43.21	84.52	84.12	115.37	173.50	223.57	50.86	245.00	1026	2229
Nov-2018	0.00	1.88	8.00	28.65	60.44	77.89	121.38	200.00	217.95	59.67	223.34	2157	2157
Dec-2018	0.00	0.00	0.00	0.07	3.62	22.48	26.14	88.47	172.58	37.15	181.91	2228	2228
Jan-2019	0.00	0.00	0.01	0.51	19.84	54.23	78.23	216.25	233.67	69.23	238.24	2229	2229
2019/02/01-2019/02/11	0.00	0.03	0.66	9.26	20.49	30.82	44.11	107.48	127.14	30.45	146.83	768	768
2017/10/02–2019/02/11	0.00	0.00	0.02	3.68	23.26	46.31	74.62	156.93	222.45	54.31	267.79	24314	35707

NOTE:
Number of valid ice velocity records and the total number of records is also tabulated. Months with no ice velocities are denoted with flag values ND).

Table 32. Ice speed statistics (cm/s) by month and for the period of deployment for M2 from 2017–2018

M2 (cm/s)	Min	1%	5%	25%	50%	Mean	75%	95%	99%	std	Max	# Valid	Total #
2017/10/03-2017/10/31	3.95	3.95	3.95	15.43	26.14	25.67	37.23	39.13	43.25	11.15	43.25	26	2019
Nov-2017	1.56	6.04	10.86	22.19	40.07	42.76	57.15	89.07	107.84	24.37	121.64	1543	2158
Dec-2017	1.21	6.68	10.69	27.06	42.38	42.57	56.95	76.58	92.60	20.19	103.05	2229	2229
Jan-2018	0.00	0.01	0.01	4.65	23.39	32.35	52.04	104.67	131.93	32.67	147.17	2230	2230
Feb-2018	0.00	0.00	0.00	0.01	0.71	6.85	9.79	32.95	45.94	10.90	56.74	2014	2014
Mar-2018	0.00	0.00	0.00	2.80	9.19	17.26	28.86	51.57	66.55	17.87	77.97	2230	2230
Apr-2018	0.00	0.01	0.01	0.01	3.46	16.18	30.50	56.31	77.82	20.77	91.45	2158	2158
May-2018	0.00	0.00	0.01	4.78	13.94	16.13	26.15	39.51	43.20	13.09	56.85	1104	2229
Jun-2018	0.22	2.57	4.51	9.32	16.23	18.19	22.28	45.21	54.25	11.93	58.26	752	2158
Jul-2018	2.37	2.37	4.67	21.38	38.11	35.30	47.74	58.16	59.81	16.19	59.81	41	2230
Aug-2018	6.13	6.13	6.55	8.92	13.77	17.78	17.01	46.42	49.94	13.09	49.94	35	2230
Sep-2018	ND	ND	ND	ND	ND	ND	ND	ND	ND	ND	ND	0	2157
2018/10/01-2018/10/11	ND	ND	ND	ND	ND	ND	ND	ND	ND	ND	ND	0	721
2017/10/03-2018/10/11	0.00	0.00	0.01	3.30	17.75	24.68	40.40	71.13	104.67	24.74	147.17	14362	26762

NOTE:
Number of valid ice velocity records and the total number of records is also tabulated. Months with no ice velocities are denoted with flag values (ND).

Table 33. Ice speed statistics (cm/s) by month and for the period of deployment for M3 from 2017–2018

M3 (cm/s)	Min	1%	5%	25%	50%	Mean	75%	95%	99%	std	Max	# valid	Total #
2017/10/02 2017/10/31	ND	ND	ND	ND	ND	ND	ND	ND	ND	ND	ND	0	2094
Nov-2017	2.00	4.56	9.12	18.36	25.64	28.17	36.02	57.57	68.21	14.02	71.01	1361	2155
Dec-2017	3.74	5.98	9.78	22.72	33.73	32.99	41.78	57.32	65.23	13.83	74.25	2227	2227
Jan-2018	0.00	0.00	0.00	4.48	16.00	20.82	36.33	54.39	77.92	19.10	83.61	2227	2227
Feb-2018	0.00	0.00	0.00	0.01	1.65	6.73	10.92	26.56	36.31	9.20	44.89	2012	2012
Mar-2018	0.01	0.01	0.03	3.85	9.22	13.85	23.60	35.33	39.21	11.97	47.86	2227	2227
Apr-2018	0.00	0.00	0.00	0.02	6.83	12.75	21.71	40.71	56.83	14.34	61.82	2155	2155
May-2018	0.01	0.03	1.55	12.22	18.86	18.40	24.72	33.29	37.27	9.23	41.77	2100	2227
Jun-2018	0.43	1.05	3.42	8.71	16.06	19.06	24.94	49.43	57.51	13.38	58.49	852	2155
Jul-2018	0.95	0.95	0.95	6.17	12.13	11.82	13.86	20.36	25.49	6.79	25.49	12	2227
Aug-2018	ND	ND	ND	ND	ND	ND	ND	ND	ND	ND	ND	0	2227
Sep-2018	ND	ND	ND	ND	ND	ND	ND	ND	ND	ND	ND	0	2155
2017/10/01 2017/10/10	ND	ND	ND	ND	ND	ND	ND	ND	ND	ND	ND	0	713
2017/10/02 2018/10/10	0.00	0.00	0.01	4.94	17.03	18.79	28.79	47.45	63.30	15.77	83.61	15173	26800

NOTE:
Number of valid ice velocity records and the total number of records is also tabulated. Months with no ice velocities are denoted with flag values (ND).

Table 34. Ice speed statistics (cm/s) by month and for the period of deployment for M4 from 2017–2018

M4 (cm/s)	Min	1%	5%	25%	50%	Mean	75%	95%	99%	std	Max	# valid	Total #
2017/10/02 2017/10/31	ND	ND	ND	ND	ND	ND	ND	ND	ND	ND	ND	0	2102
Nov-2017	0.96	4.19	8.60	18.70	26.16	29.27	37.22	59.52	70.84	14.91	76.55	1607	2156
Dec-2017	1.46	6.58	10.72	22.87	35.55	34.85	45.24	59.06	68.15	14.90	71.21	2227	2227
Jan-2018	0.00	0.01	0.01	6.18	17.84	21.83	34.65	54.46	74.82	18.43	85.65	2227	2227
Feb-2018	0.00	0.01	0.01	0.02	2.43	6.78	10.93	25.84	34.58	8.88	41.73	2012	2012
Mar-2018	0.01	0.01	0.01	4.30	9.59	12.77	21.32	31.32	36.78	10.30	39.52	2227	2227
Apr-2018	0.00	0.00	0.00	0.05	8.37	12.14	21.35	33.70	41.04	12.06	44.93	2155	2155
May-2018	0.00	0.03	1.37	12.08	21.31	20.03	27.89	37.09	42.75	10.61	45.15	2228	2228
Jun-2018	0.09	0.39	2.71	14.44	21.78	25.43	34.45	56.14	61.55	15.42	63.08	520	2155
Jul-2018	0.29	1.57	7.13	16.17	21.68	22.14	29.18	35.89	44.96	8.98	46.08	501	2227
Aug-2018	29.06	29.06	29.06	29.30	31.41	31.62	33.26	35.29	35.29	2.38	35.29	6	2227
Sep-2018	ND	ND	ND	ND	ND	ND	ND	ND	ND	ND	ND	0	2156
2017/10/01 2017/10/10	ND	ND	ND	ND	ND	ND	ND	ND	ND	ND	ND	0	706
2017/10/02 2018/10/10	0	0.01	0.01	6.13	18.05	19.77	29.72	49.4	65.45	15.928	85.65	15710	26804

NOTE:
Number of valid ice velocity records and the total number of records is also tabulated. Months with no ice velocities are denoted with flag values (ND).

The ice flow direction was generally from east to west following the general circulation pattern in the region of the MARES array; however, there were many deviations from this average motion throughout the deployment. The progressive vector diagrams in Figure 56 through Figure 59 illustrate this for each of the sites. In these diagrams, the Eulerian-based ice velocity measurements were integrated and plotted. These diagrams are thus illustrative of the complex ice drift patterns and are not meant to show the true particle path in the Lagrangian sense.

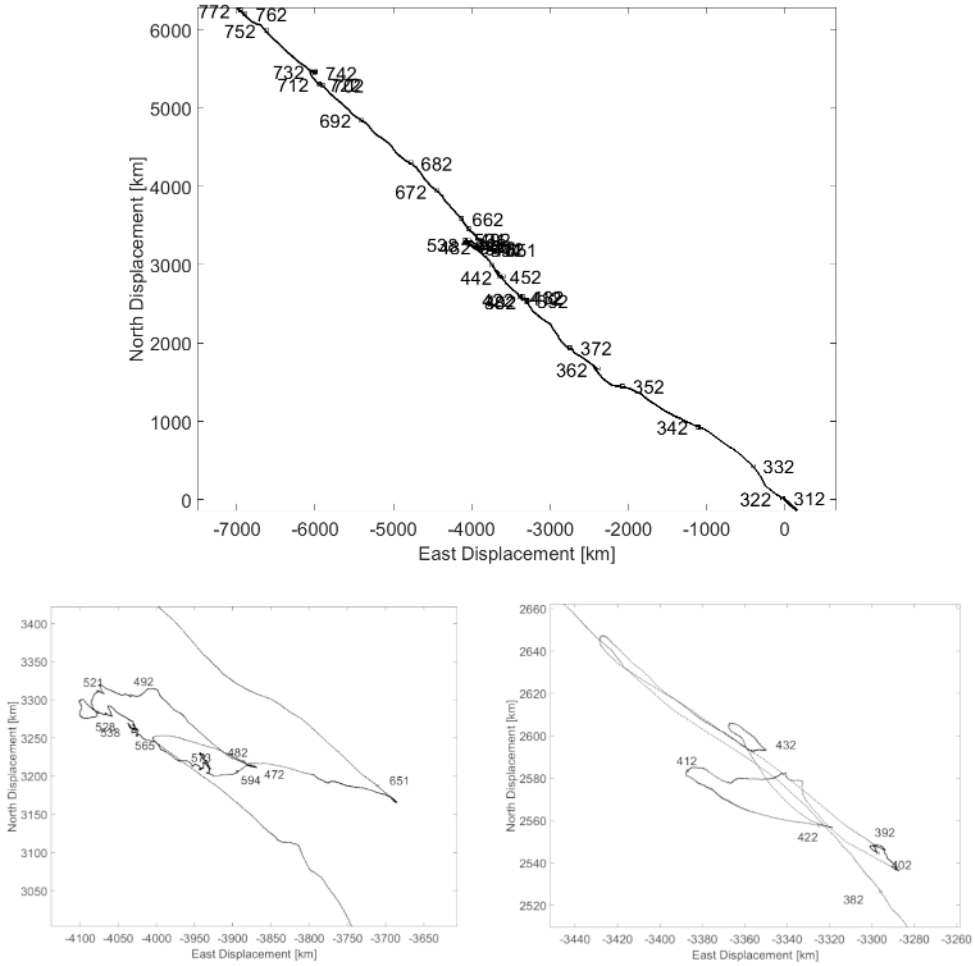

Figure 56. Progressive vector diagrams created through integration of the ice velocity time-series for M1 over the full 2017–2019 deployment

The top panel shows the full deployment period. The lower panels show the most complex sections of the vector. The labels indicate every tenth ordinal day of the year.

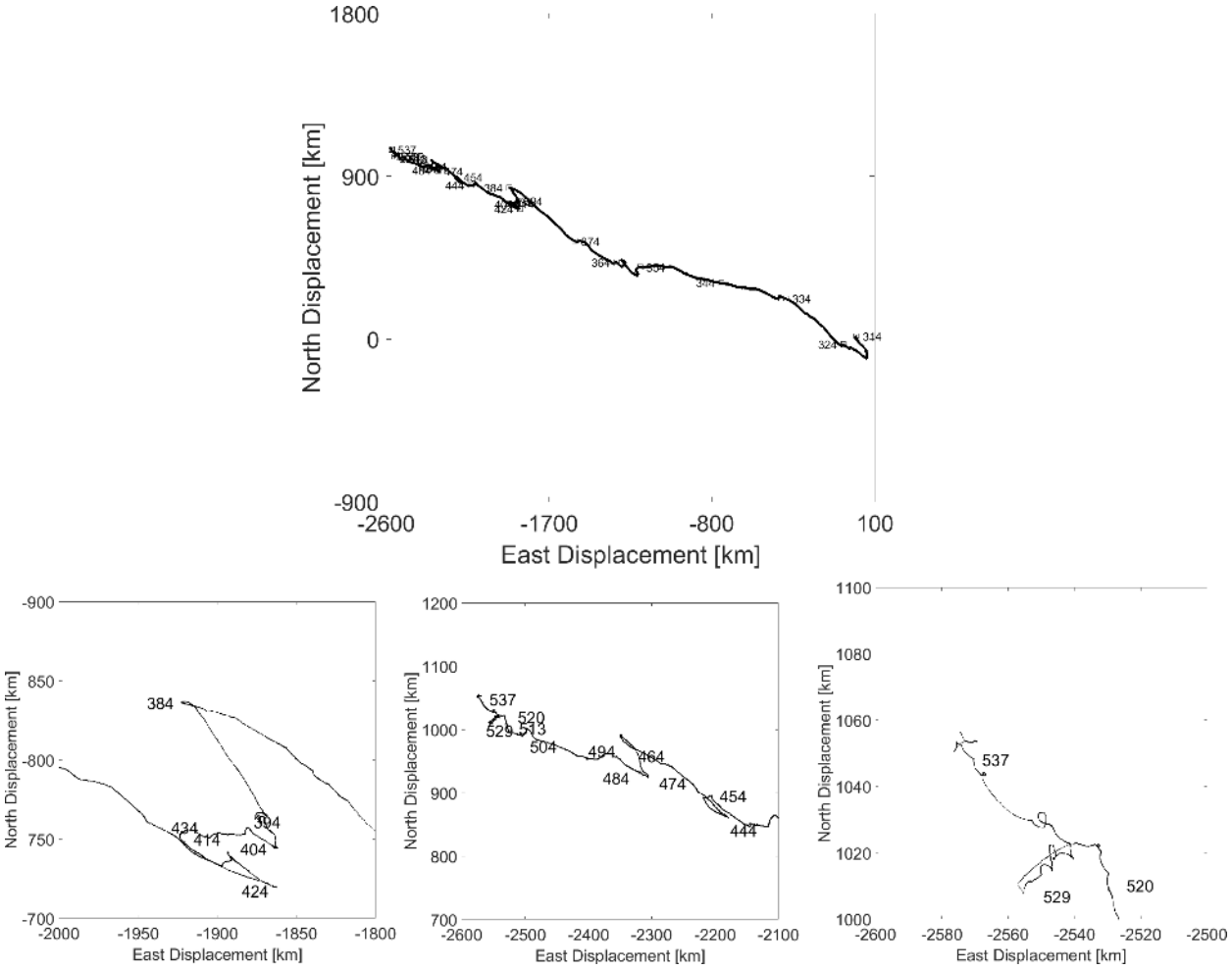

Figure 57. Progressive vector diagrams created through integration of the ice velocity time-series for M2 over the full 2017–2018 deployment

The top panel shows the full deployment period. The lower panels show the most complex sections of the vector. The labels indicate every tenth ordinal day of the year.

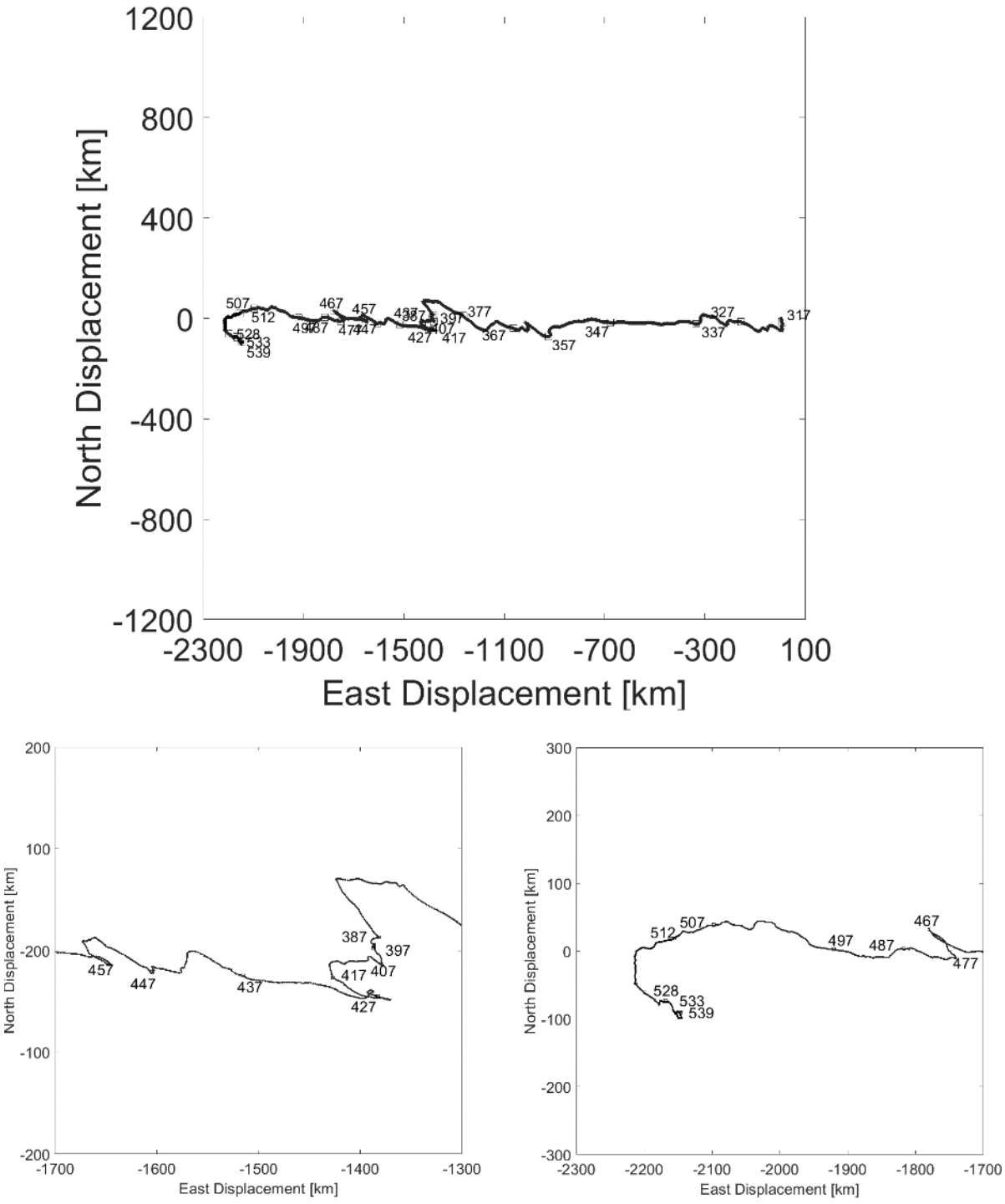

Figure 58. Progressive vector diagrams created through integration of the ice velocity time-series for M3 over the full 2017–2018 deployment

The top panel shows the full deployment period. The lower panels show the most complex sections of the vector. The labels indicate every tenth ordinal day of the year.

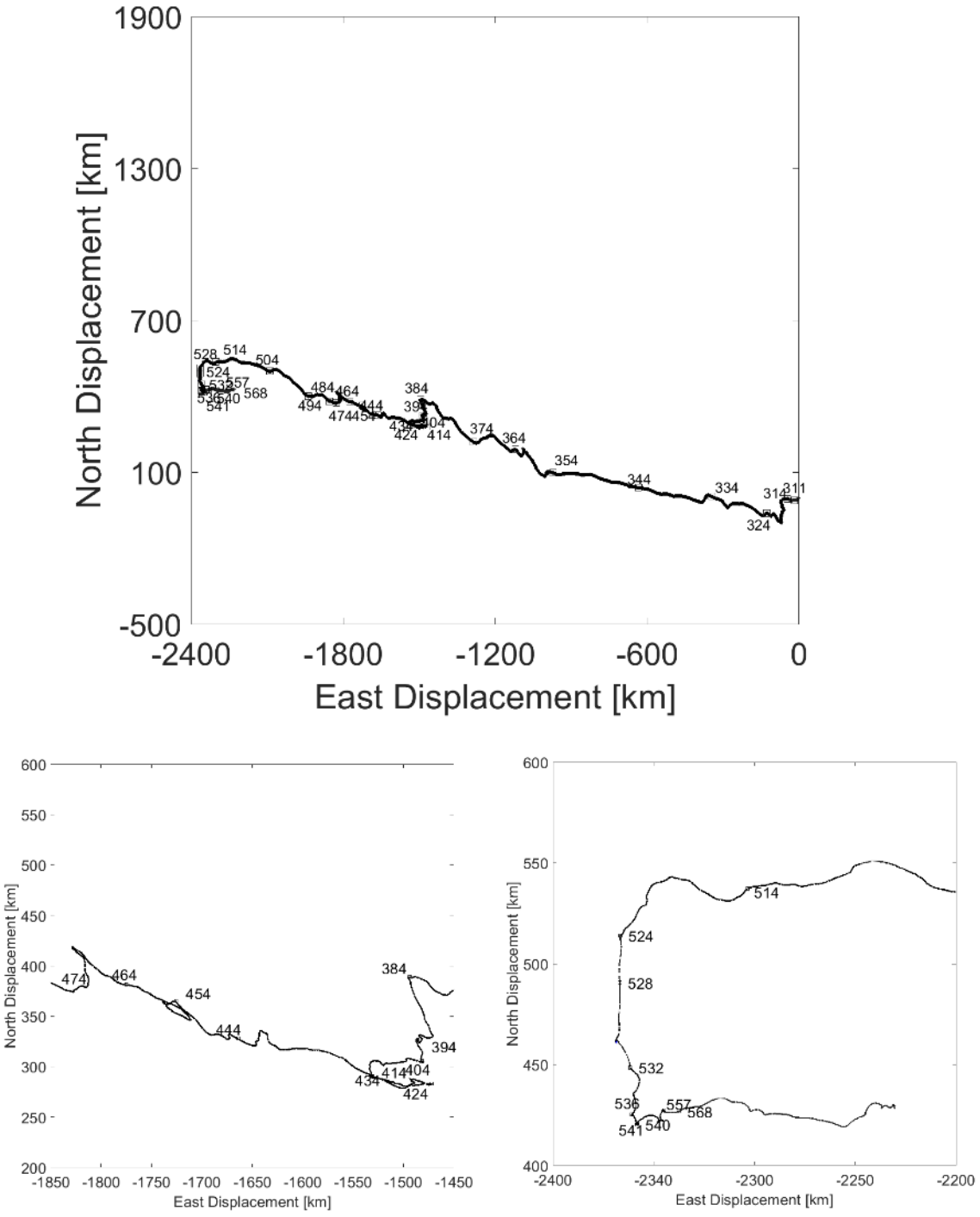

Figure 59. Progressive vector diagrams created through integration of the ice velocity time-series for M4 over the full 2017–2018 deployment

The top panel shows the full deployment period. The lower panels show the most complex sections of the vector. The labels indicate every tenth ordinal day of the year.

The resulting total horizontal distance of ice that transited over each of the sites versus time is plotted in Figure 60. This result is based on the low resolution ice drift time-series, and can thus include the results from M1 where there was no Ice Profiling Sonar. This time-series itself is divided into segments of continuously measured ice velocity. Using the high temporal resolution of the Ice Profiling Sonar, the spatial series can be categorized as ice, open water, or wave and ice. The spatial summarized in Table 35 through Table 37. The total integrated ice distance was 3,976 at M2, 3,222 km at M3, and 3474 km at M4. The total cross-sectional area of ice that transited past M2, M3, and M4 was 3.26, 3.06 and 3.52 km^2, respectively. The break-down by continuous ice section is provided by site in Table 35 through Table 37.

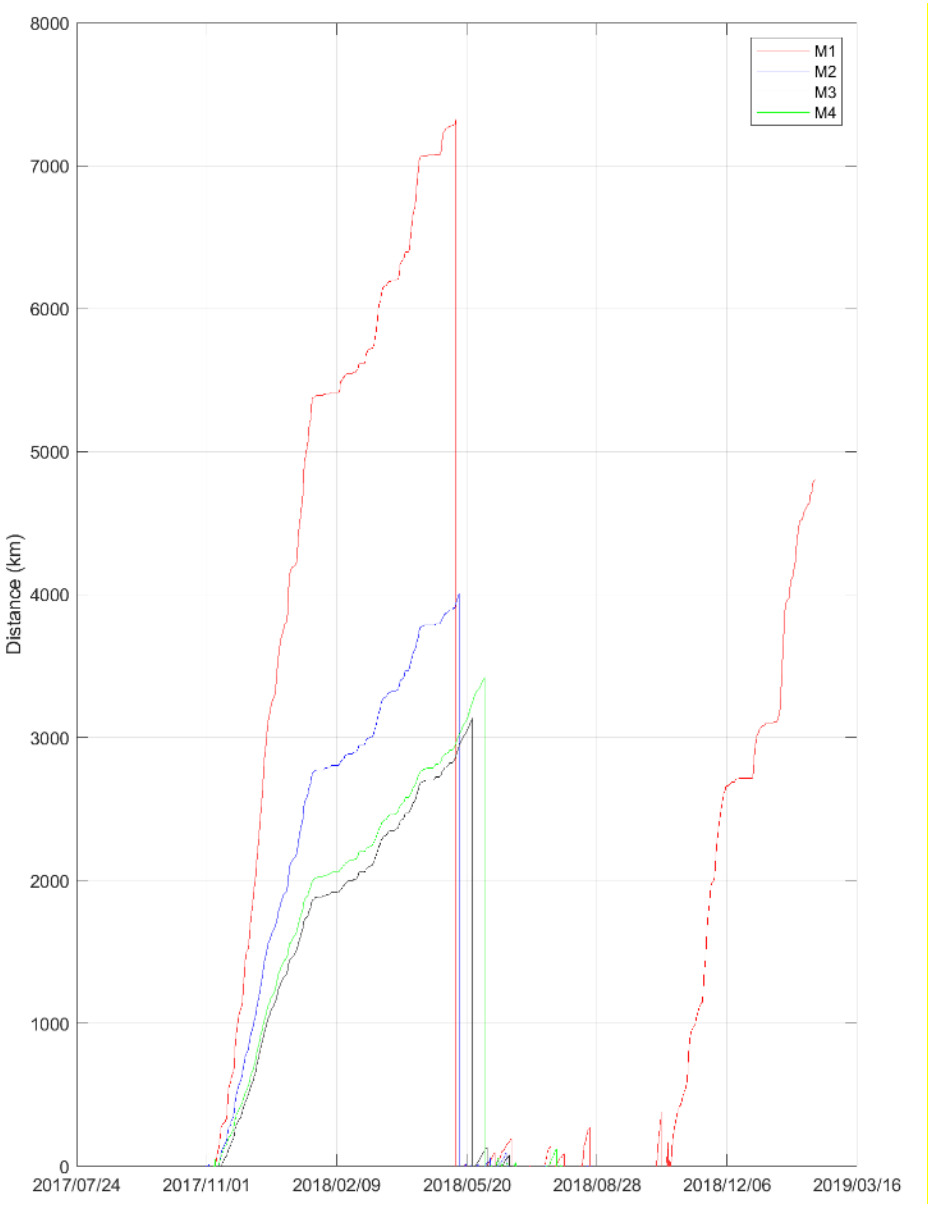

Figure 60. Time-series of the horizontal extent of ice that transited over the M1, M2, M3 and M4 measurement locations during the 2017–2018 deployment, extending into 2019 at M1

Table 35. The horizontal spatial extents of episodes of continuous ice velocity at M2 during the 2017–2018 deployment

Segment	Start Date [yyyy/mm/dd HH:MM:SS UTC]	End Date [yyyy/mm/dd HH:MM:SS UTC]	Horizontal Ice Distance [km]	Total Integrated Ice Distance [km]
1	2017/10/31 14:53:53	2017/10/31 23:33:49	0.951	8.016
2	2017/11/02 09:16:28	2017/11/02 15:56:49	3.325	13.82
3	2017/11/09 20:07:26	2018/05/13 21:58:29	3,828.473	4,005.5
4	2018/05/18 06:24:59	2018/05/19 15:06:51	9.372	18.194
5	2018/05/23 04:52:12	2018/05/23 07:52:19	5.640	5.859
6	2018/05/27 23:59:15	2018/05/28 23:00:28	15.422	16.886
7	2018/06/03 05:28:23	2018/06/07 01:13:53	36.770	59.184
8	2018/06/10 11:18:58	2018/06/10 13:19:01	3.739	4.004
9	2018/06/12 19:22:24	2018/06/19 01:11:24	49.338	94.238
10	2018/06/20 22:14:18	2018/06/21 00:54:24	3.436	3.773
11	2018/06/26 00:21:46	2018/06/26 05:01:54	3.027	3.109
12	2018/07/19 01:15:30	2018/07/19 03:15:34	2.768	3.127
13	2018/07/19 13:36:16	2018/07/19 16:16:18	2.004	2.352
14	2018/07/20 11:37:36	2018/07/20 20:38:05	7.561	11.901
15	2018/08/20 10:23:01	2018/08/20 20:03:23	2.100	4.222
16	2018/08/23 10:27:21	2018/08/23 12:27:24	2.717	3.249

NOTE:
The second last column indicates the horizontal extent for those records in the ice draft spatial-series that correspond to ice only. The last column indicates the horizontal extent for all records in the ice draft spatial-series including open water.

Table 36. horizontal spatial extents of episodes of continuous ice velocity at M3 during the 2017–2018 deployment

Segment	Start Date [yyyy/mm/dd HH:MM:SS UTC]	End Date [yyyy/mm/dd HH:MM:SS UTC]	Horizontal Ice Distance [km]	Total Integrated Ice Distance [km]
1	2017/11/07 01:29:44	2017/11/07 04:50:06	4.055	4.054
2	2017/11/10 18:21:39	2017/11/10 19:21:42	1.379	1.378
3	2017/11/12 05:46:25	2018/05/24 11:08:42	3,048.343	3,133.219
4	2018/05/25 15:12:33	2018/05/25 23:53:37	7.034	8.877
5	2018/05/26 14:15:39	2018/06/04 11:04:04	78.877	131.348
6	2018/06/06 04:49:49	2018/06/06 06:29:56	2.048	2.115
7	2018/06/11 14:27:12	2018/06/13 12:11:46	24.146	46.929
8	2018/06/13 20:34:29	2018/06/13 22:54:42	2.218	2.558
9	2018/06/14 14:56:56	2018/06/14 19:57:32	5.470	7.345
10	2018/06/16 02:21:43	2018/06/21 17:19:36	39.941	76.667
11	2018/06/22 17:02:59	2018/06/23 05:04:31	7.771	11.807
12	2018/07/06 17:28:09	2018/07/06 21:28:33	1.389	1.705

NOTE:
The second last column indicates the horizontal extent for those records in the ice draft spatial-series that correspond to ice only. The last column indicates the horizontal extent for all records in the ice draft spatial-series including open water.

Table 37. Horizontal spatial extents of episodes of continuous ice velocity at M4 during the 2017–2018 deployment

Segment	Start Date [yyyy-mm-dd HH:MM:SS UTC]	End Date [yyyy-mm-dd HH:MM:SS UTC]	Horizontal Ice Distance [km]	Total Integrated Ice Distance [km]
1	2017/11/06 12:40:48	2017/11/07 13:23:53	46.661	46.886
2	2017/11/09 16:10:30	2018/06/02 14:23:43	3,269.992	3,419.420
3	2018/06/07 19:59:59	2018/06/08 00:20:25	3.841	4.037
4	2018/06/11 12:31:22	2018/06/13 09:55:14	20.529	54.155
5	2018/06/14 14:40:55	2018/06/14 16:00:58	1.502	1.718
6	2018/06/15 15:24:05	2018/06/16 04:25:42	13.040	21.058
7	2018/06/19 00:14:32	2018/06/20 07:18:25	23.205	25.800
8	2018/06/23 22:49:46	2018/06/24 00:49:55	1.683	2.535
9	2018/07/10 21:22:08	2018/07/11 01:42:33	16.276	23.751
10	2018/06/24 22:52:54	2018/06/26 13:17:45	2.356	2.355
11	2018/07/19 20:29:49	2018/07/19 22:29:56	1.951	2.220
12	2018/07/20 18:32:41	2018/07/20 20:32:48	1.959	2.034
13	2018/07/21 19:15:52	2018/07/27 20:14:24	67.839	121.257
14	2018/07/30 03:41:41	2018/07/30 17:43:19	2.524	5.497
15	2018/08/01 00:07:23	2018/08/01 02:07:34	1.325	2.280

NOTE:
The second last column indicates the horizontal extent for those records in the ice draft spatial-series that correspond to ice only. The last column indicates the horizontal extent for all records in the ice draft spatial-series including open water.

3.1.1.4.3 Ice Draft and Concentration

The time-series of daily minimum, maximum and mean ice draft measured at M2, M3, and M4 are presented in Figure 61 through Figure 63, respectively. Note that the mean ice draft is computed for ice observations only and therefore does not include a bias due to the presence of open water. The average daily ice draft at M2 was 1.07 m, and the maximum draft of 24.95 m was observed on April 5, 2018. At M3, the average daily ice draft throughout the deployment was 1.02 m. The maximum draft of 24.15 m occurred on March 29, 2018. The average daily ice draft at M4 was 1.14 m and the maximum draft was 24.32 m on April 7, 2018. The mean and maximum ice draft values for the entire deployment for each site are presented in Table 38. More detailed statistics, which include monthly statistics target type, ice concentration and mean and median ice draft are given by site in Table 39 through Table 42.

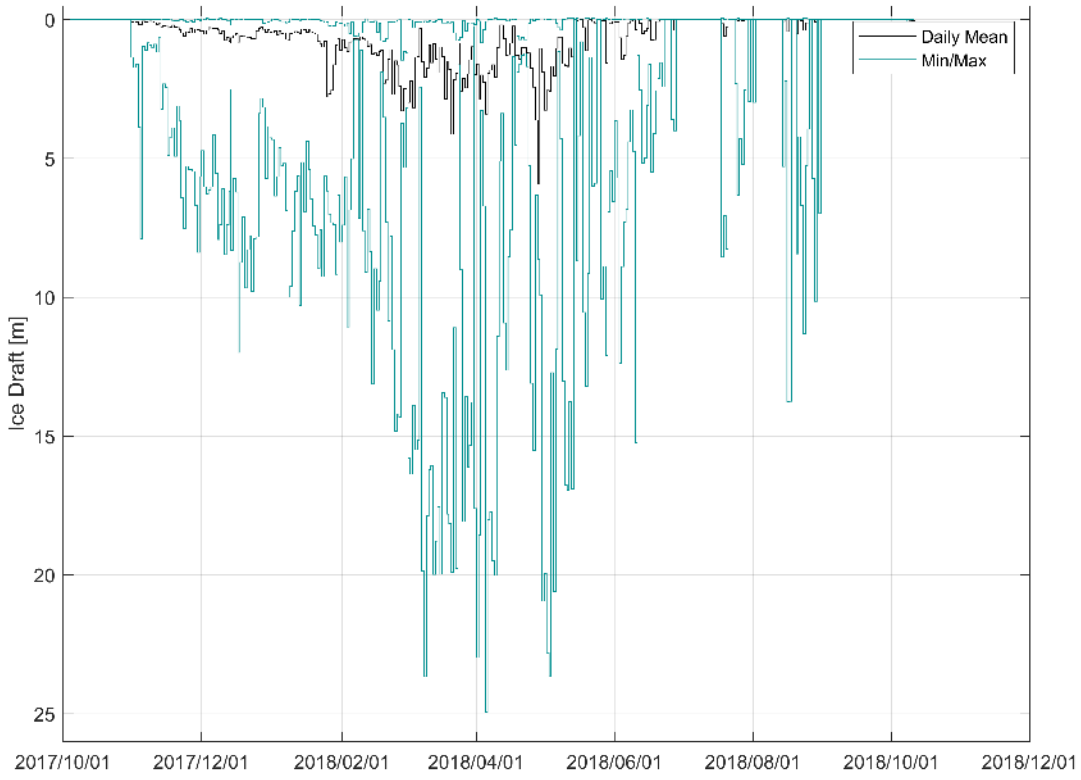

Figure 61. M2 draft staircase plot showing min/max and daily mean draft values during the 2017–2018 deployment

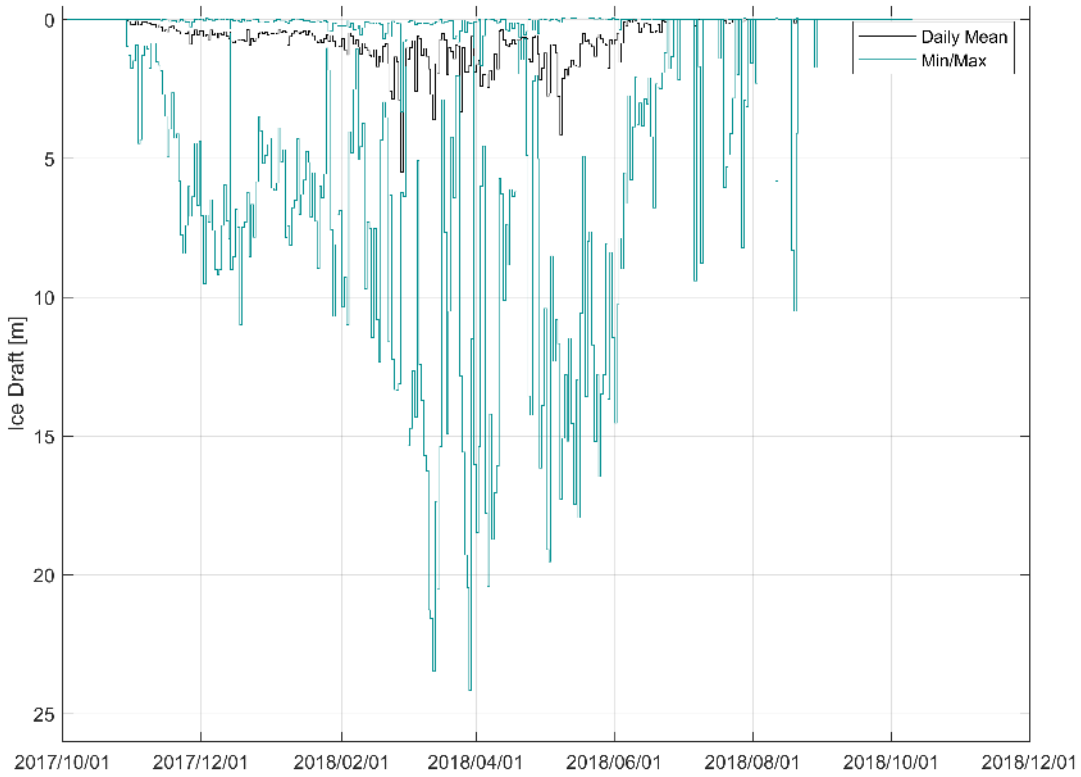

Figure 62. M3 draft staircase plot showing min/max and daily mean draft values during the 2017–2018 deployment

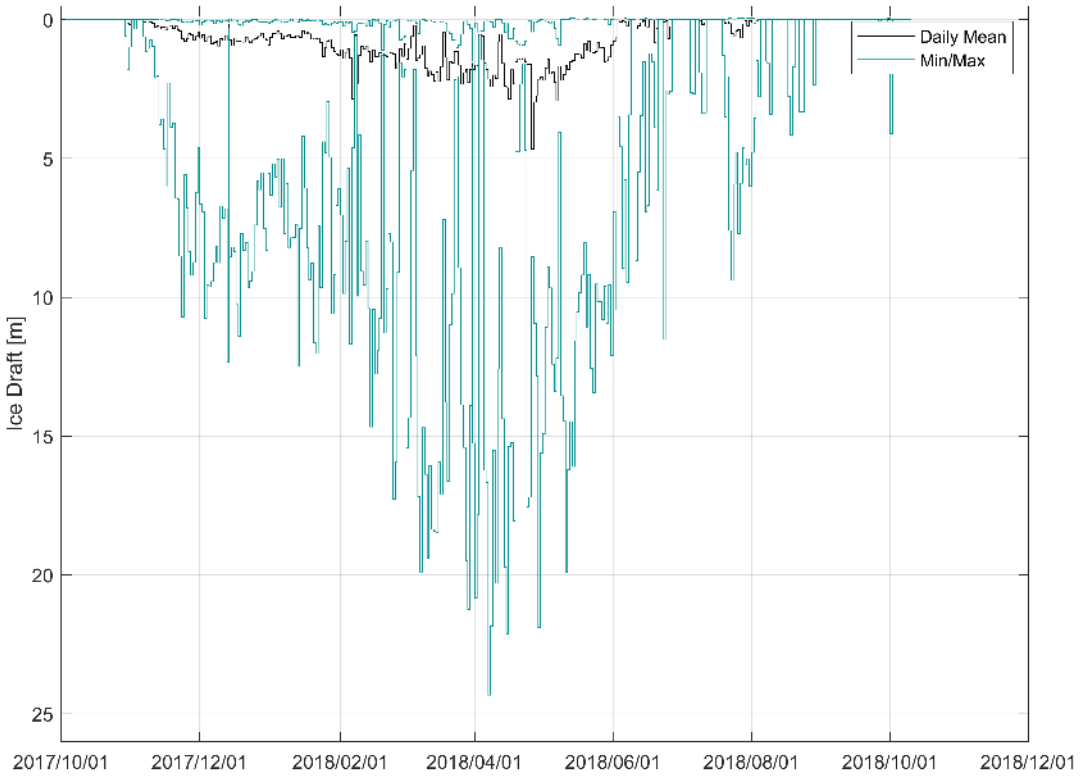

Figure 63. M4 draft staircase plot showing min/max and daily mean draft values, during the 2017–2018 deployment

Table 38. Mean and maximum ice draft values at each site during the full 2017–2018 deployment, extending into 2019 at M1

Site	Mean ice draft (ice-only) [m]	Mean ice draft (all records) [m]	Maximum ice draft [m]
M2	1.07	0.65	24.95
M3	1.02	0.63	24.15
M4	1.14	0.71	24.32

Table 39. M2 draft time series statistics and ice concentrations from 2017–2018

Month	Ice Conc %	Bad Data %	Waves in Ice %	Open Water %	Mean (ice) (m)	Mean (all) (m)	Max (ice) (m)	Median (ice) (m)
October (3)	4.11	0	0	95.89	0.09	0	1.36	0.09
November	99.75	0	0	0.25	0.24	0.24	8.38	0.2
December	100	0	0	0	0.5	0.5	11.99	0.37
January	100	0	0	0	0.82	0.82	10.3	0.44
February	100	0	0	0	1.34	1.34	14.83	0.84
March	100	0	0	0	1.83	1.83	23.66	1.03
April	100	0	0	0	1.69	1.69	24.95	1.07
May	48.04	0	0	51.96	1.7	0.82	23.66	0.98
June	22.25	0	0	77.75	1.21	0.27	15.24	1.04
July	1.51	0	0	98.49	2.35	0.04	8.55	1.99
August	2.28	0	0	97.72	2.59	0.06	13.76	2.01
September	0	0	0	100	0	0	0	0
October (11)	25.93	0	0	74.07	0.03	0.01	0.98	0.02
NOTE: The number in parenthesis indicates the number of complete days of data from any month with partial data.								

Table 40. M3 draft time series statistics and ice concentrations from 2017–2018

Month	Ice Conc %	Bad Data %	Waves in Ice %	Open Water %	Mean (ice) (m)	Mean (all) (m)	Max (ice) (m)	Median (ice) (m)
October (3)	10.73	0	0	89.27	0.13	0.01	1.75	0.12
November	98.45	0	0	1.55	0.32	0.32	8.43	0.28
December	100	0	0	0	0.6	0.6	10.99	0.45
January	100	0	0	0	0.61	0.61	10.68	0.49
February	100	0	0	0	1.49	1.49	13.36	0.89
March	100	0	0	0	1.43	1.43	24.15	0.96
April	100	0	0	0	1.27	1.27	20.41	0.71
May	77.2	0	0	22.8	1.82	1.41	19.52	1.18
June	23.83	0	0	76.17	1.05	0.25	14.52	0.86
July	2.28	0	0	97.72	1.15	0.03	9.41	1.01
August	0.17	0	0	99.83	3.06	0.01	10.5	2.88
September	0	0	0	100	0	0	0	0
October (11)	0	0	0	100	0	0	0	0
NOTE: The number in parenthesis indicates the number of complete days from any month with partial data.								

Table 41. M4 draft time series statistics and ice concentrations from 2017–2018

Month	Ice Conc %	Bad Data %	Waves in Ice %	Open Water %	Mean (ice) (m)	Mean (all) (m)	Max (ice) (m)	Median (ice) (m)
October (3)	9.61	0	0	90.39	0.16	0.02	1.81	0.16
November	82.53	0	0	17.47	0.36	0.3	10.7	0.24
December	100	0	0	0	0.73	0.73	12.33	0.55
January	100	0	0	0	0.71	0.71	12.48	0.52
February	100	0	0	0	1.31	1.31	17.26	1
March	100	0	0	0	1.53	1.53	21.24	1.12
April	100	0	0	0	1.87	1.87	24.32	1.35
May	89.26	0	0	10.74	1.67	1.49	19.92	1.31
June	16.29	0	0	83.71	1.11	0.18	11.52	0.96
July	13.93	0	0	86.07	0.85	0.12	9.39	0.72
August	1.02	0	0	98.98	0.85	0.01	4.77	0.69
September	0.99	0	0	99.01	0	0	1.55	0
October (11)	0.1	0	0	99.9	0.66	0	4.1	0.44
NOTE: The number in parenthesis indicates the number of complete days from any month with partial data.								

3.1.1.5 Waves and Ice

The high sampling frequency and ice draft accuracy enabled observation of episodes of surface waves transiting through the ice pack. As an example, waves of nearly 0.5 m amplitude were observed in the presence of ice at M3 on April 2, 2019 (Figure 64.). The thinnest ice was highly impacted by the waves, but the thickest ice damped out the waves. The two periods of heavier ice appear as red spectra in the spectrogram (Figure 65). The wave dominated sections of the example only reflect the presence of ice in the offset in the mean draft. These sections appear in the spectrograms as higher spectral densities in the upper frequency bands.

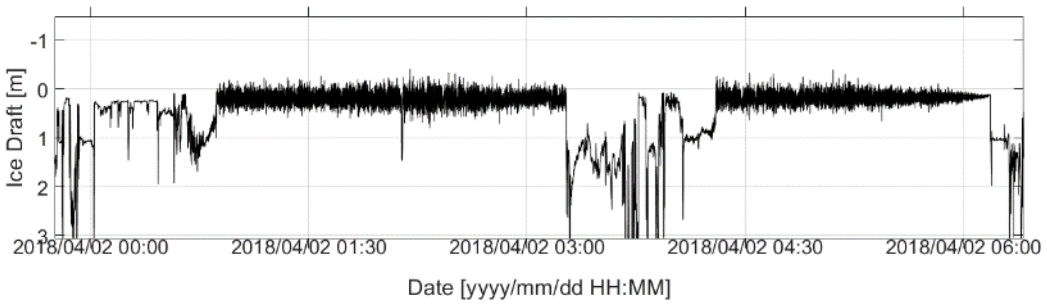

Figure 64. Examples of surface waves propagating through sea ice during April 2, 2018 at M3

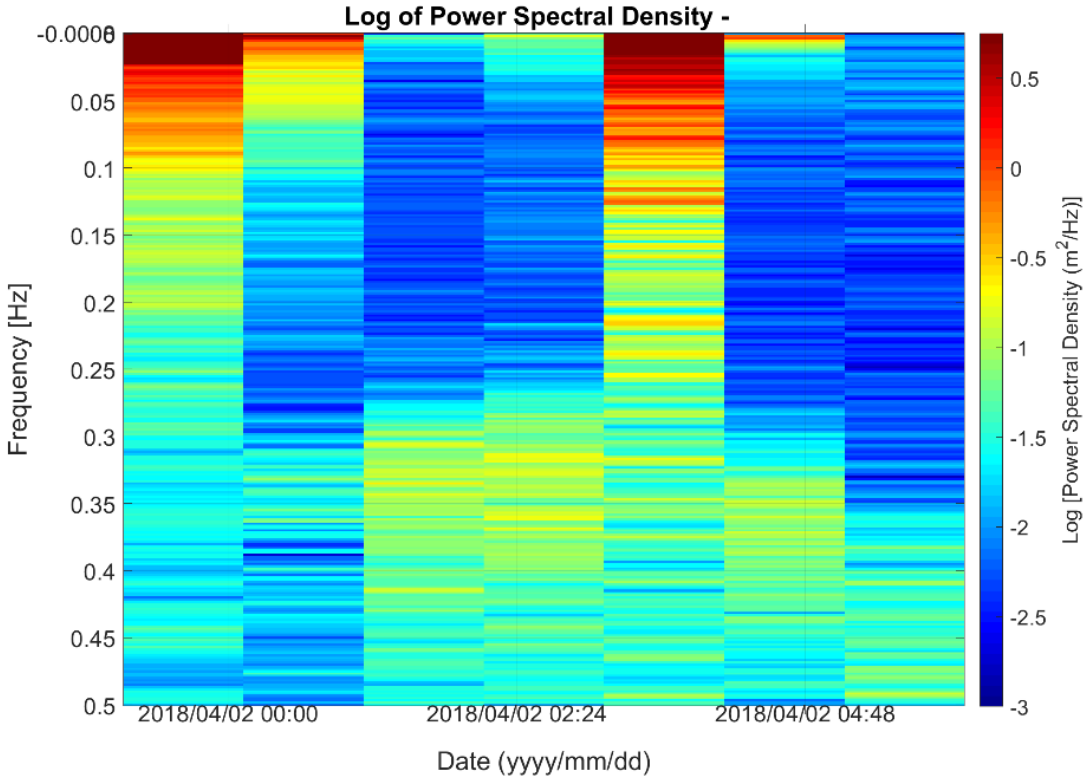

Figure 65. A spectrogram of the M3 ice draft time-series displayed in Figure 64
The color indicates the power spectral density on a log scale.

3.1.2 Chemical Oceanography

3.1.2.1 Nitrates

As mentioned in the methods, the nitrate concentrations are corrected to account for internal instrument drift and drift due to biofouling. Reliable nitrate concentrations were measured from deployment until July 15, 2018. This long data set was possible because the burst interval was reduced from 1 hour to 2 hours from the 2016-17 deployment to the 2017-2018 deployment, preventing the early instrument failure that occurred in 2016-2017. Despite the long deployment, the correction for biofouling was small and consistent throughout, and so the correction was applied from the start of the deployment to be consistent with the previous year of processing. However, it appears that the SUNA at M1 experienced optically dense conditions over brief intervals early in the deployment and intermittently through the rest of the deployment. These conditions led to extended integration time per sample, during which the RMS error and absorbance values exceeded the manufacturer thresholds, deeming those data invalid. Despite exceeding the manufacturer thresholds for RMS error and absorbance values at times, the nitrate sensor often collected stable nitrate values that followed the trend of the salinity measured by the companion CT. During these periods it is possible that the trend of the nitrate values could be useful for interpretation purposes but with the caveat that the actual concentration values may be unreliable.

In the raw data for M1 there were 2,120 (26.6%) records with missing data. In the final quality-controlled time-series, there are 2,064 (26.0%) records with missing data. This decrease in the amount of missing data was accomplished by interpolating across short gaps in the record. In the final quality-controlled time-series, there were 3,140 (39.5%) records identified that exceeded the manufacturer threshold for reliable data. Of these, 1,672 (21.0%) records were identified as being possibly acceptable.

For M2, a sharp change in the slope of the instrument lamp time begins at May 26, which indicates significant fouling issues (Figure 66). From the time-series of ice draft data and satellite imagery, the ice breakup occurred around May 13, which would allow sunlight to penetrate into the water column and drive biological productivity. In Figure 67, the uncorrected nitrate concentration is compared to corrected concentrations where the biofouling correction is applied from the start of the data, and from May 13. The nitrate concentrations corrected from the start of the deployment (red line) have a downward trend over the winter, when concentrations should be stable, and also have many negative values. The nitrates corrected from May 13 (yellow line) have a stable trend over the winter, and fewer issues with negative concentration values. We expect that nitrates will follow the trend of salinity over the winter when there is little biological activity. Figure 68 shows the normalized concentration corrected for biofouling relative to May 13, and Figure 69 relative to the start of the deployment. The correction relative to the start of the deployment deviates substantially from the trend of the salinity over the winter when it is expected to be stable. For these reasons, the biofouling correction was delayed until May 13 when biological activity was expected to actually occur.

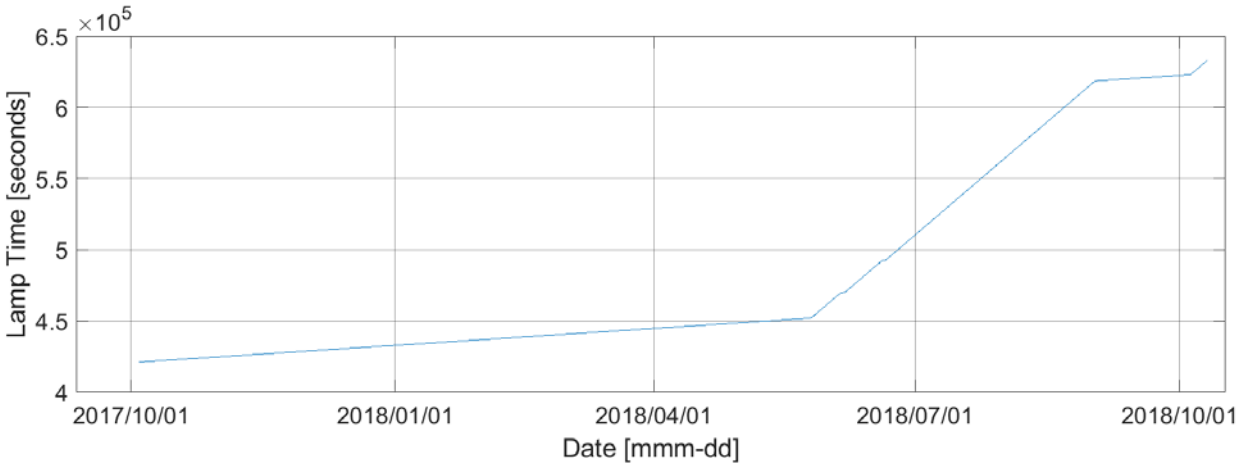

Figure 66. Lamp time for the SUNA at M2 during the 2017–2018 deployment
The slope steepens at May 26 indicating issues with biofouling.

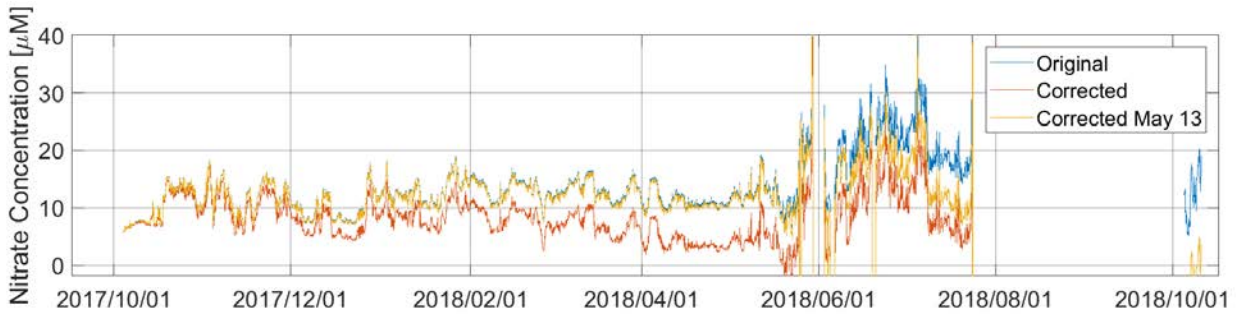

Figure 67. Comparison of nitrate concentration at M2 during the 2017–2018 deployment
The uncorrected concentration is blue, corrected from start is red, and corrected from ice break up is yellow.

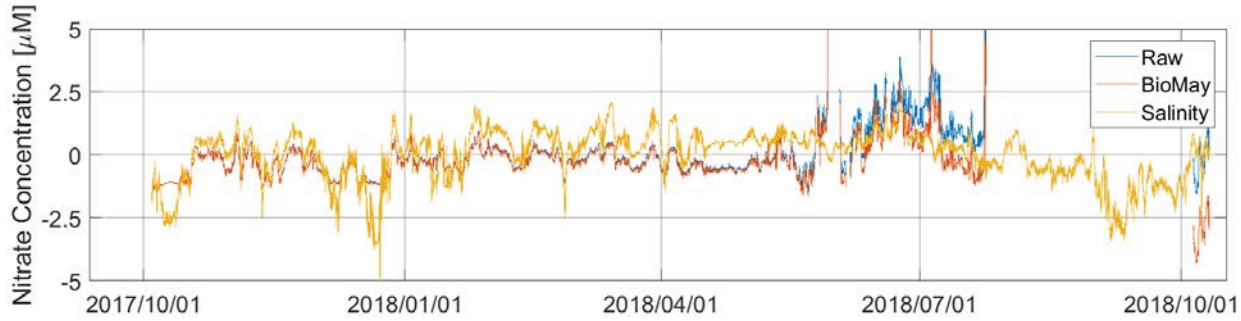

Figure 68. Comparison of salinity and normalized nitrate concentration at M2 during the 2017–2018 deployment for a biofouling correction starting from May 13

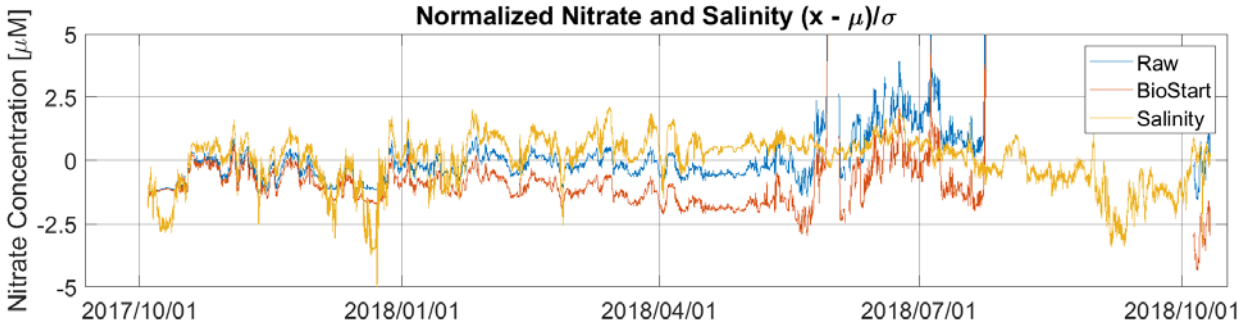

Figure 69. Comparison of salinity and normalized nitrate concentration at M2 during the 2017–2018 deployment for a biofouling correction starting from the start of the deployment

The instrument at M2 was also affected by optically dense conditions, but only towards the end of the deployment. As a result of these conditions much of the data following May 25, 2018 was deemed unreliable, except for two episodes in early June. The quality-controlled nitrate concentration time-series for M1 and M2 are displayed in Figure 70.

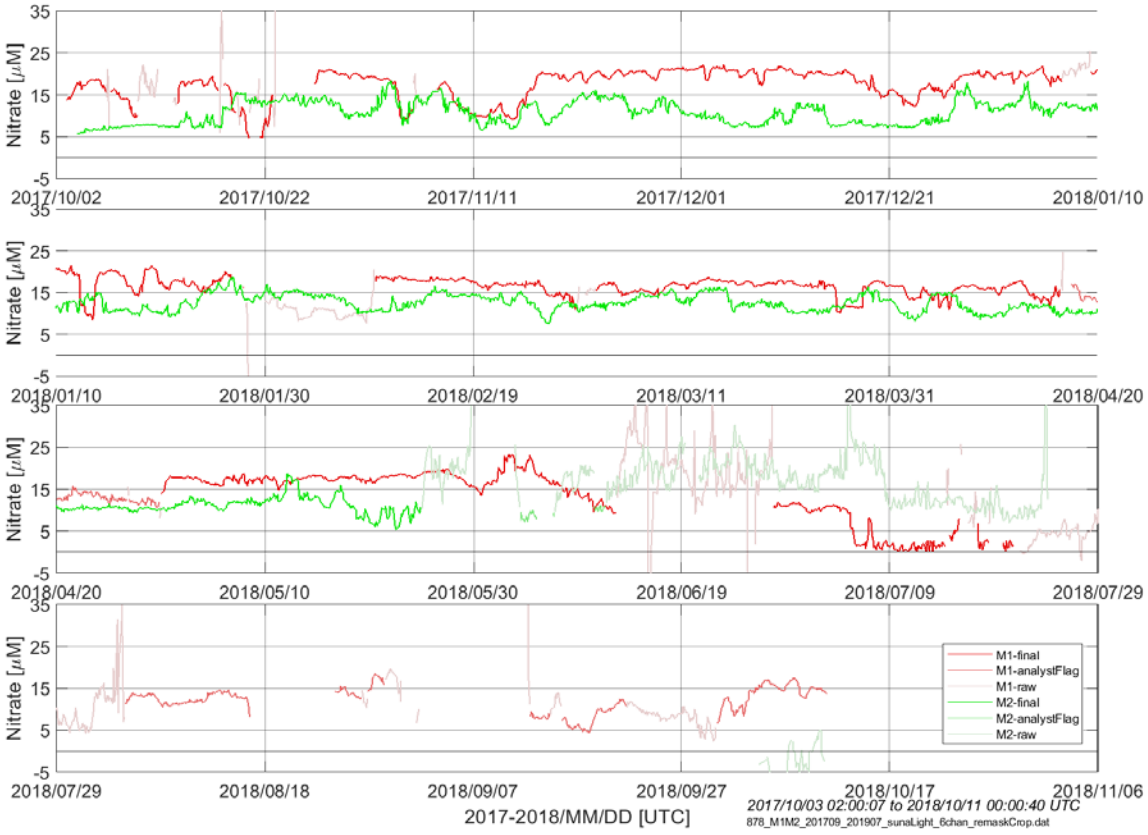

Figure 70 Comparison of M1 and M2 quality-controlled nitrate time-series during the 2017-–2018 deployment period

Low confidence is the raw data, medium confidence includes what was deemed reasonable in spite of QA/QC parameters, and high confidence is the final data which was delivered.

In the raw data for M2 there were 955 (21.1%) records with missing data. In the final quality-controlled time-series, there is 943 (21.1%) records with missing data. As with M1, the amount of missing data was decreased by interpolating across short gaps in the record. In the delivered data, there were 722 (16.2%) records identified that exceeded the manufacturer threshold for reliable data. Of these, 39 (0.9%) records were identified as being possibly acceptable.

The values of high confidence nitrate concentration were between 0.0 to 23.3 µM at M1, and between 5.42 to 18.9 µM at M2. Typically nitrate concentrations are below 20 µM in this region, so the concentrations at M1 were somewhat larger than expected.

During episodes of low (no) biological productivity, the concentration of nitrates generally follows that of biologically inert compounds such as salinity. The salinity is compared to the nitrate concentration in Figure 71 and Figure 72 for the span of the 2017–2018 season at M1 and M2, respectively, and in Figure 73 for M1 over the 2018–2019 season. The salinity has been scaled (de-meaned, divided by standard deviation of salinity, multiplied by standard deviation of nitrate, and added to the mean value of nitrate) to be compared to the nitrate concentration. Productivity usually diminishes when the number of daylight hours decrease, or when ice is present, so we would expect that the trend of nitrate concentration should be relatively consistent during the winter, unless deep water is advected to the upper ocean in the winter, leading to increases in nitrate concentration. The number of daylight hours over the deployment are shown in Figure 74. This trend was observed at M1 and M2 with the nitrates and salinity following a similar trend from October 2017 through to late-May 2018 when the ice break-up occurred, and the high-confidence nitrate concentrations decrease. At M1 during the extended 2018–2019 period, the short-term trends of salinity and medium-confidence nitrate are similar, but the underlying long-term trend in nitrate is disconnected from the salinity trend. This is due to significant error in the nitrate concentrations due to accumulated biofouling following the summer 2018 period.

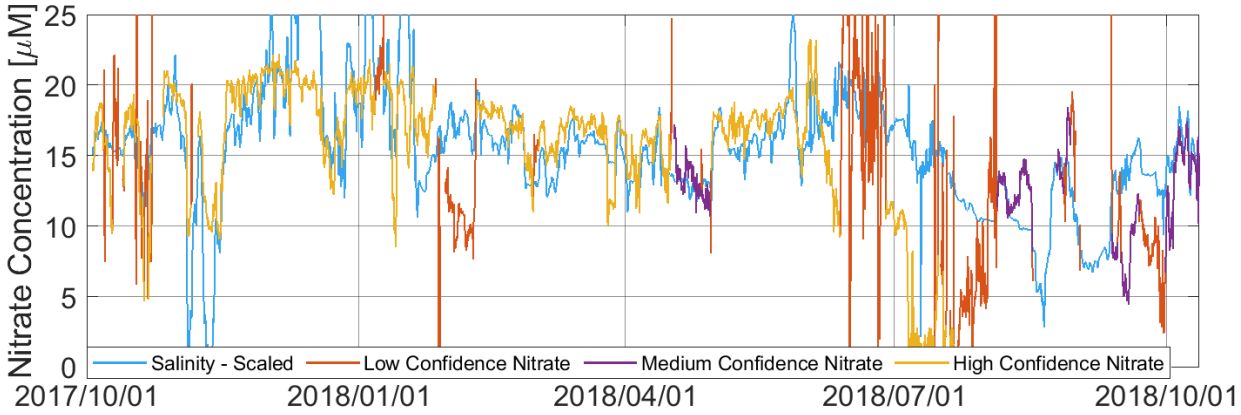

Figure 71. Comparison of nitrate concentration and salinity at M1, 2017–2018
Low confidence is the raw data, medium confidence includes what was deemed reasonable in spite of QA/QC parameters, and high confidence is the final data which was delivered.

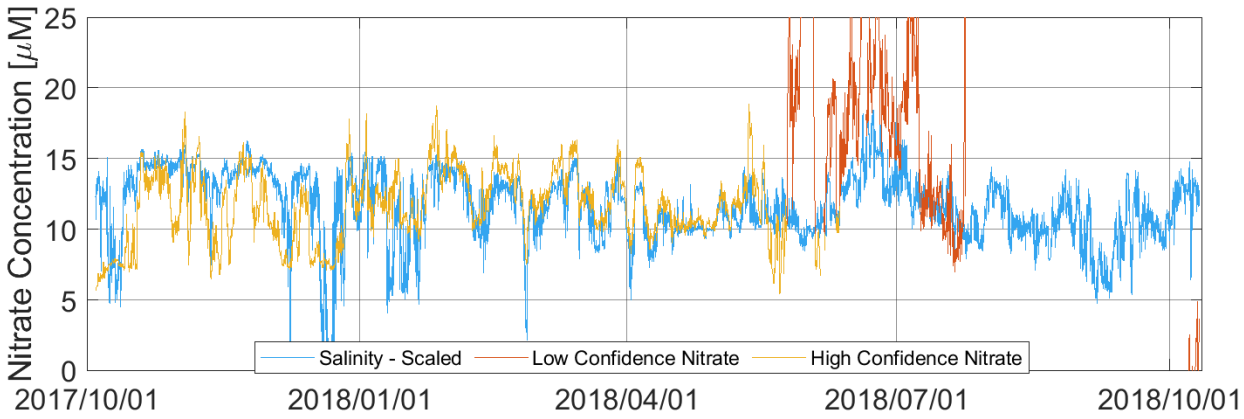

Figure 72. Comparison of nitrate concentration and salinity at M2, 2017–2018
Low confidence is the raw data, medium confidence includes what was deemed reasonable in spite of QA/QC parameters, and high confidence is the final data which was delivered.

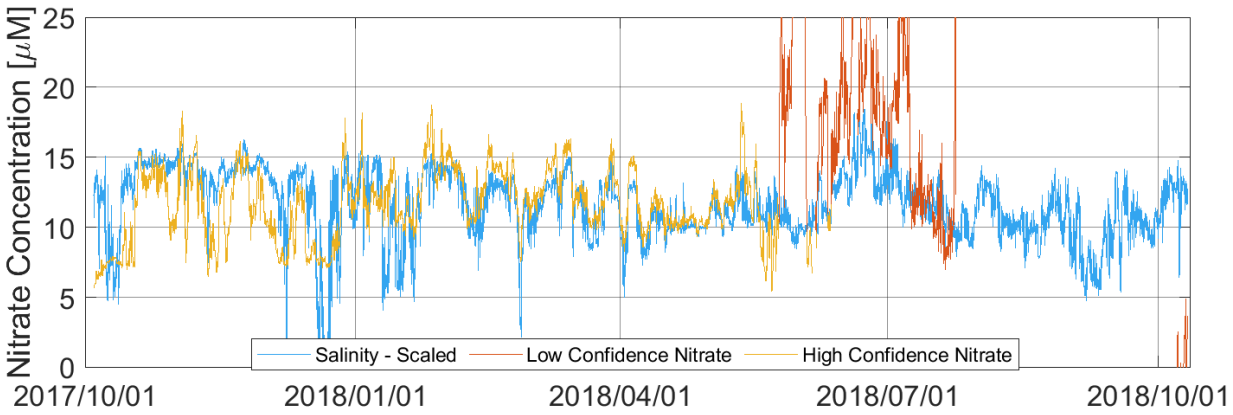

Figure 73. Comparison of nitrate concentration and salinity at M1, 2018–2019
Low confidence is the raw data, medium confidence includes what was deemed reasonable in spite of QA/QC parameters, and high confidence is the final data which was delivered.

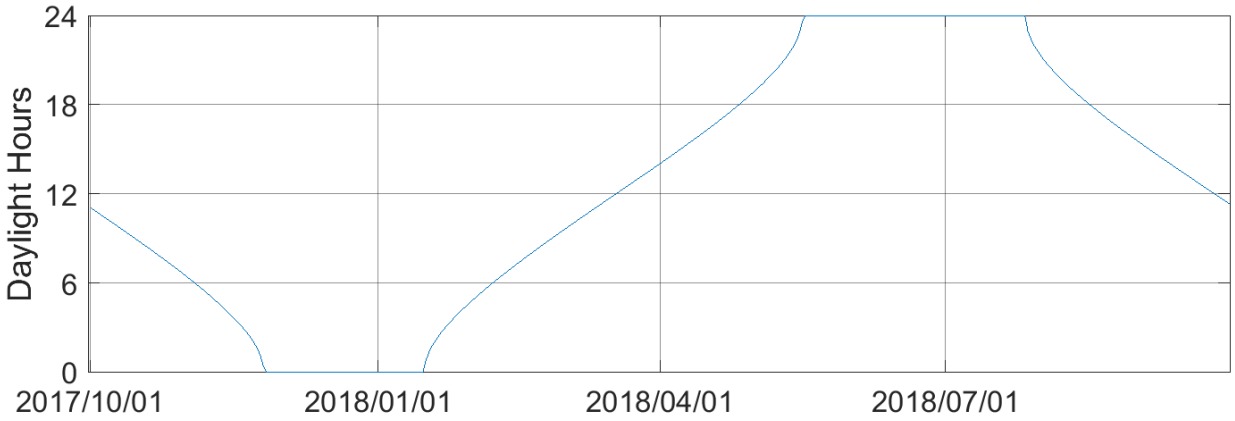

Figure 74. Number of hours of daylight over the 2017–2018 deployment

3.1.2.2 Carbon Dioxide (pCO_2)

The SAMI-CO2 deployed at M1 from September 2017 to July 2019 failed and no autonomous data were recorded. A discrete 200 mL seawater sample was taken at the sensor depth and shown in Table 42.

Table 42. Carbon parameters from seawater samples taken at mooring site M1 in 2017 and 2019

Site	Date (UTC)	Time (UTC)	Depth (m)	Temp (C)	Salinity (psu)	TA (µmol kg^{-1})	DIC (µmol kg^{-1})	pCO_2 (µatm)	$pH_{T,SW}$	Ω_{Ar}
M1	9/27/17	21:00	36	-0.83	31.92	2230.78	2145.75	427.34	7.996	1.11
M1	7/27/19	15:00	36	-0.96	32.52	2243.55	2179.79	517.35	7.919	0.96

The pCO_2 of the seawater sample collected in July 2019 was comparable to the sample collected in September 2017 (Figure 75). This confirms our previous deduction that the autonomous data from the 2016-2017 deployment at M1 were erroneous after April 2017. The autonomous data at M1 before April 2017 averaged 470±48 µatm, shown by the dashed line in Figure 75. The calculated Ω_{Ar} for both seawater samples, September 27, 2017 and July 27, 2019, are near the saturation threshold of $\Omega Ar = 1$ (Table 43.). Seawater undersaturated (i.e. $\Omega<1$) with respect to calcium carbonate ($CaCO_3$) is potentially corrosive to the $CaCO_3$ minerals aragonite and calcite. The emergence of corrosive waters resulting from ocean acidification (OA) may have negative impacts on calcifying organisms (Cross et al. 2018).

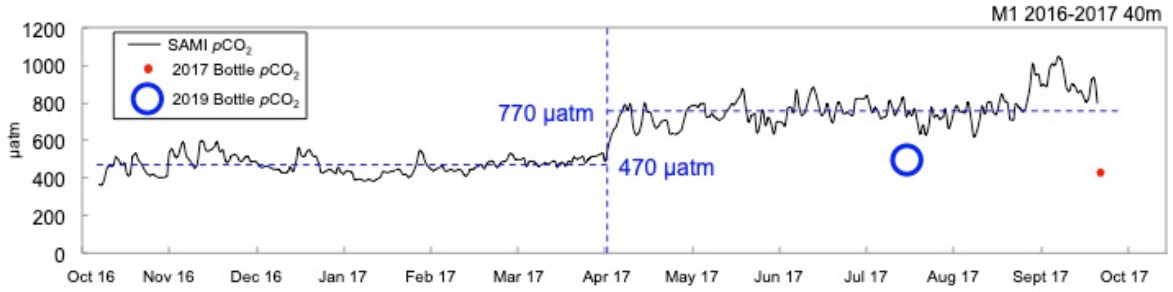

Figure 75. Autonomous data from mooring site M1 during the 2016–2017 deployment period and discrete pCO_2 data from September 2017 and July 2019

3.1.3 Biological Oceanography

3.1.3.1 Zooplankton

ADCP Backscatter

Substantial variation in ADCP relative backscatter was observed throughout the year. Backscatter was greatest near the surface with lower scattering at mid-depth, and lowest backscatter at depth at M1 and M2 (Figure 76).

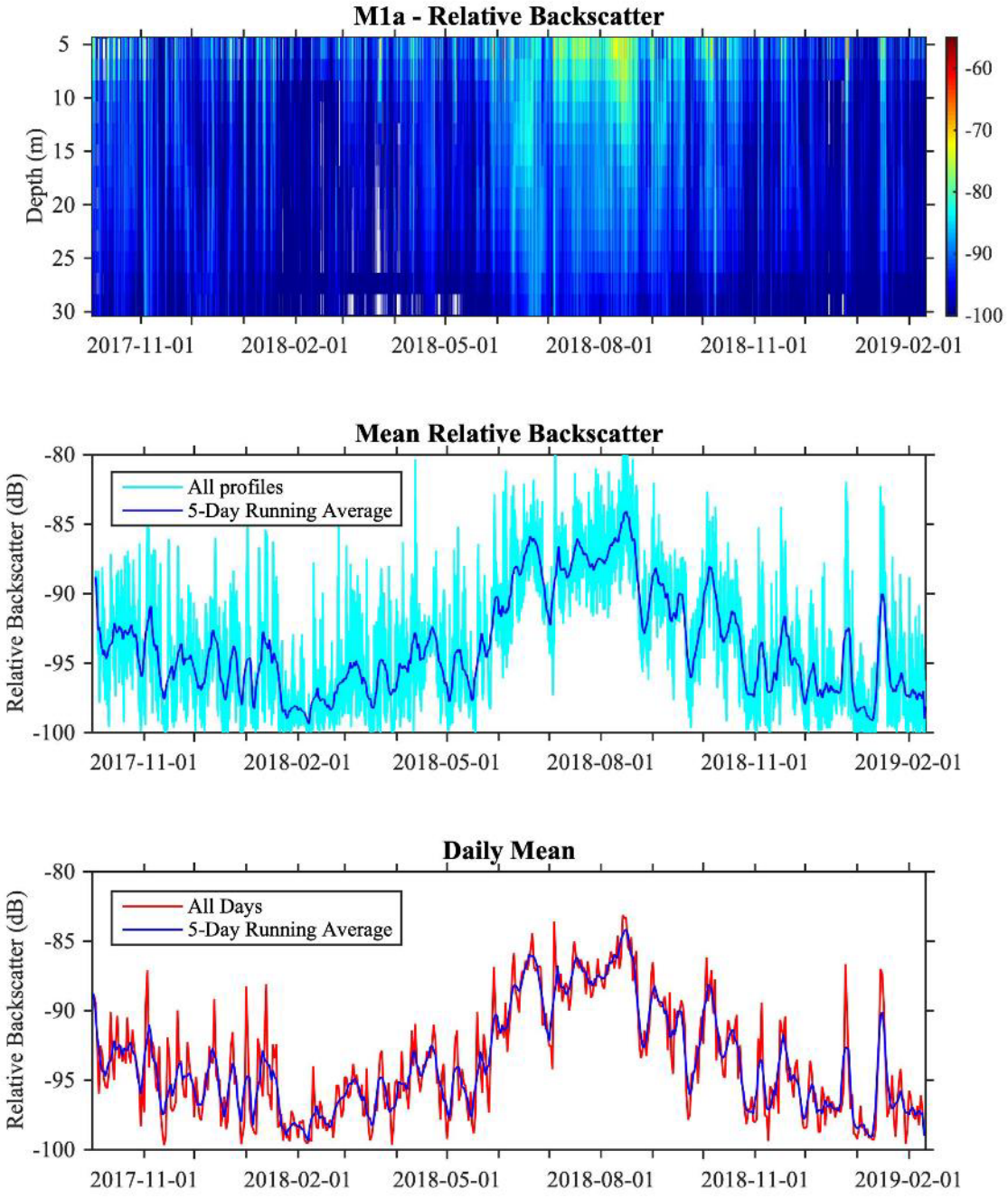

Figure 76. Relative backscatter (upper), mean and 5-day running average mean backscatter for each profile (middle) and daily mean and 5-day running average mean (lower) for M1a during the 2017-2019 deployment

The mean backscatter (middle panel) represented the total variations in water column backscatter over the period of the deployment.

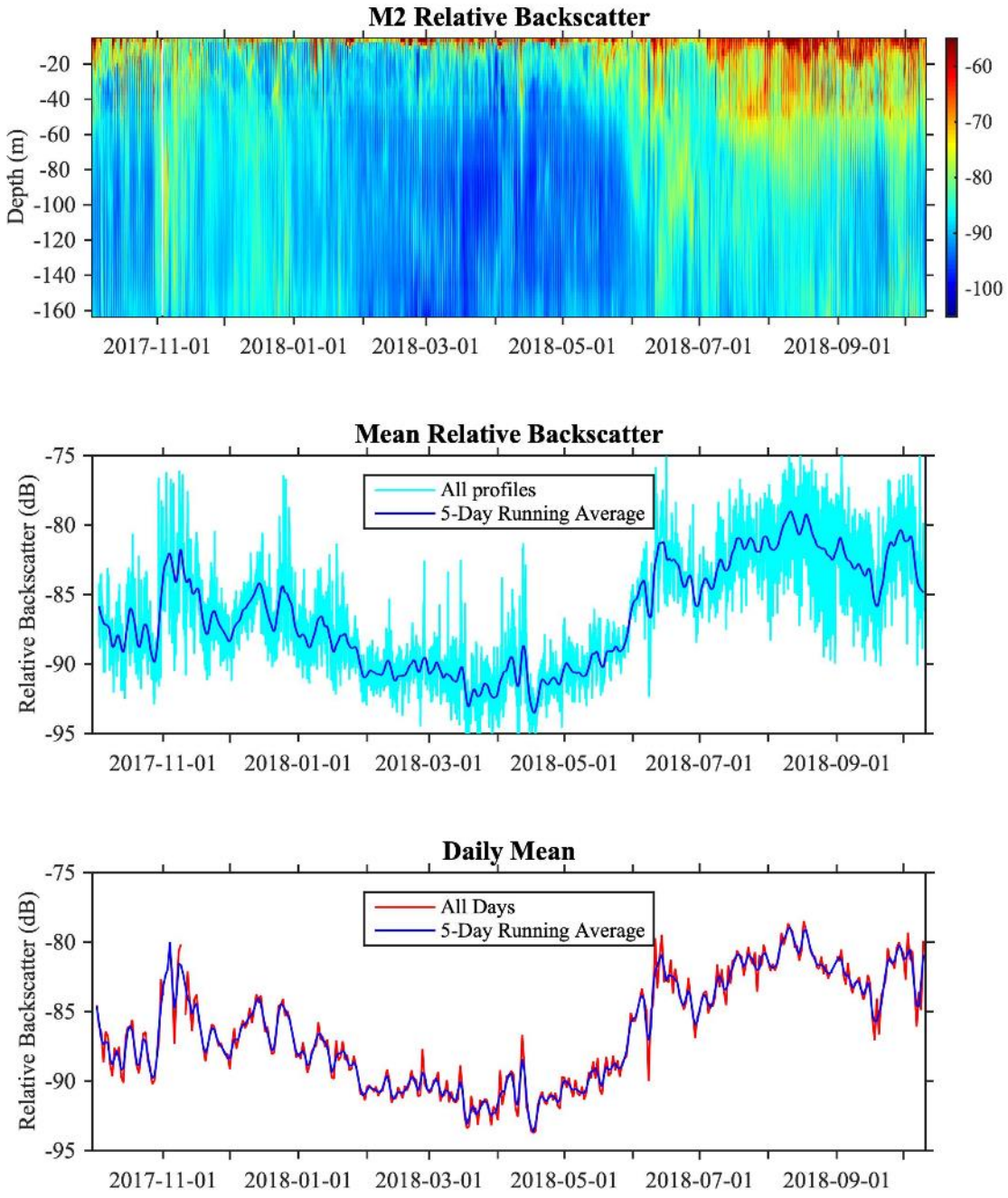

Figure 77. Relative backscatter (upper), mean and 5-day running average mean backscatter for each profile (middle) and daily mean and 5-day running average mean backscatter (lower) for the combined data from the upper and lower ADCPs at M2

The mean backscatter (middle panel) represented the total variations in water column backscatter over the period of the deployment.

Relative backscatter from the two instruments (M1, M2) was compared using the daily mean backscatter data smoothed using a 5-day running mean (Figure 78). The daily anomalies from the mean daily backscatter for the entire records (backscatter anomaly) also were computed and compared. Relative backscatter was greater at the M2 (full water column), moored at 175 m bottom depth, than at M1, located on the shelf at 40 m bottom depth. However, both instruments showed similar trends in backscatter over the period of the deployments, with higher backscatter in early fall (October-November 2017) and summer (June-September 2018) and lowest backscatter in winter-spring 2018 (and 2019). Values were average in late fall ("0" on the anomaly plot) and declined in winter to minima in April and May 2018 after which values increased to maxima in August 2018. Shorter-term maxima and minima were seen throughout the record, most notably in November 2017 for M2. Backscatter (both daily means and anomalies) between M1 and M2 were positively correlated ($r=0.77$ for both, $p<0.01$, $n=374$).

Mean daily water column velocities were compared to the daily mean backscatter anomalies for each mooring (Figure 79). Little association was observed between the velocities and the backscatter anomaly for both moorings ($r<\pm0.1$ between each velocity component (u, v) and Sv for both moorings). By contrast, the u and v components of velocity at each mooring were highly negatively correlated (-0.91 for M1, -0.74 for M2).

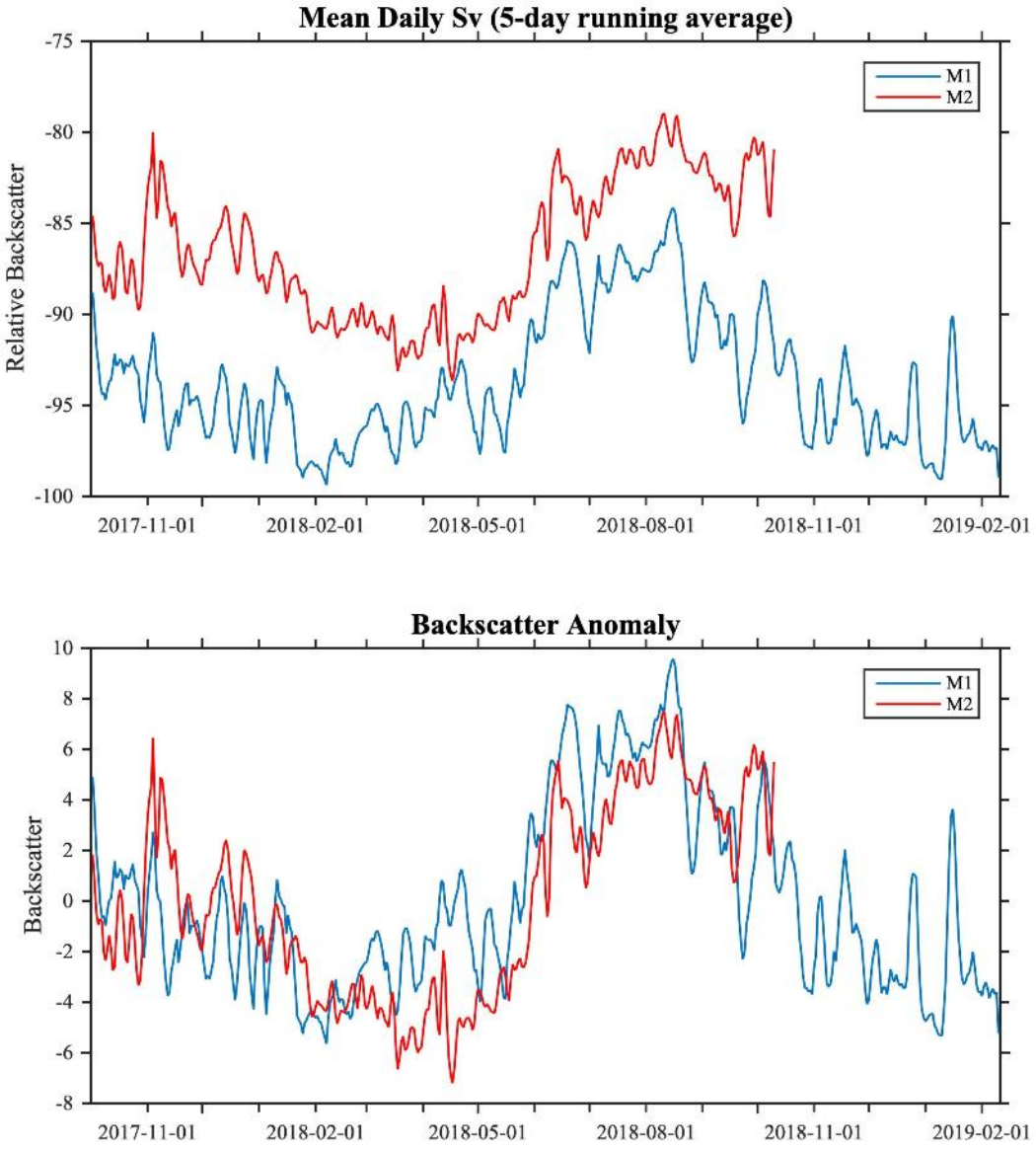

Figure 78. Mean daily water column relative backscatter (Sv) smoothed with 5-day running average (upper) and anomalies from the mean daily water column Sv (lower) for M1 and M2 during the 2017–2019 deployment

Note that the record for M1 extends to February 2019.

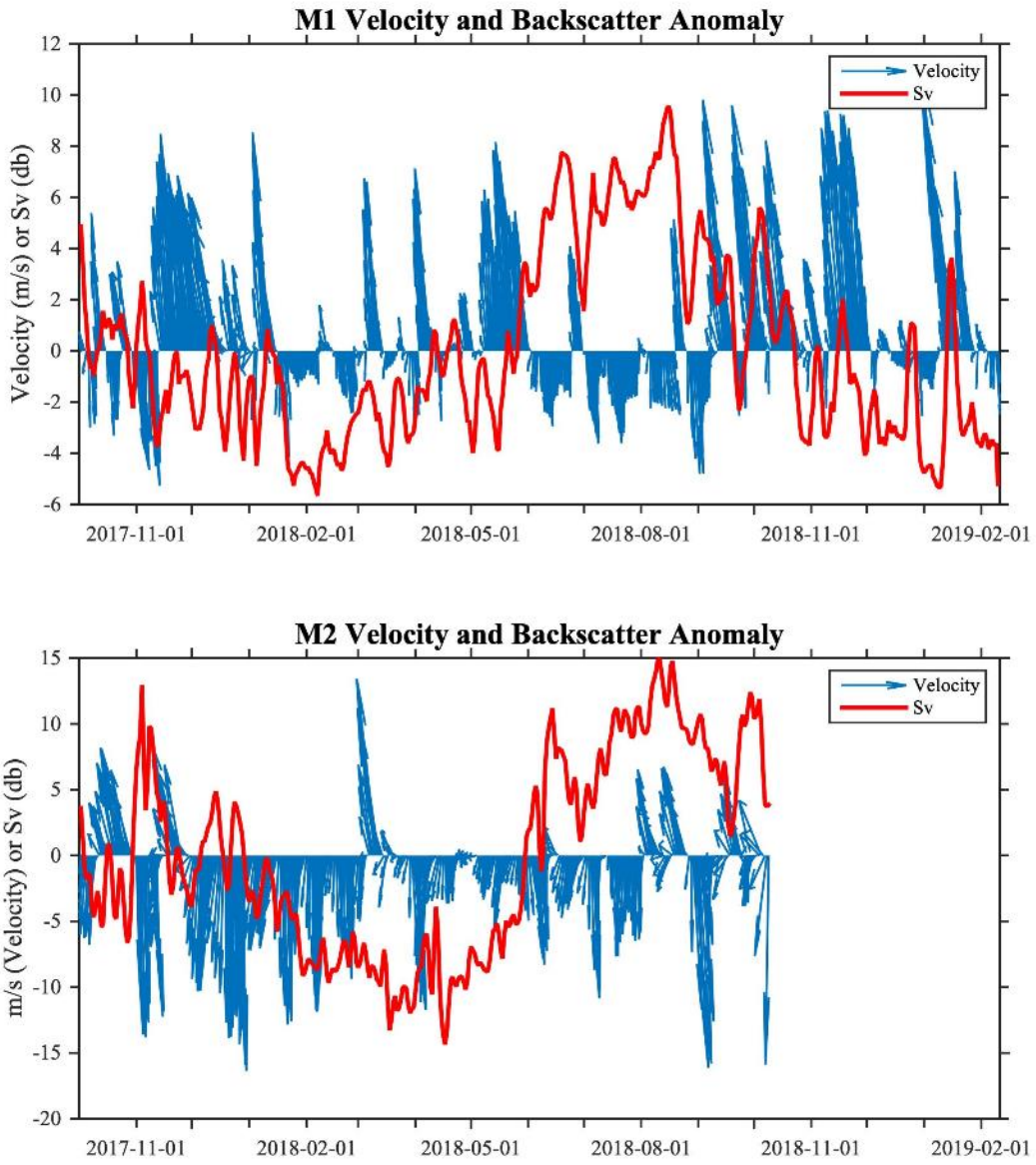

Figure 79. Quiver Plot of mean daily water column velocities and mean daily backscatter anomaly from M1 (upper) and mean daily water column velocities and daily backscatter anomaly from M2 (lower) during the 2017–2018 deployment

All data smoothed with 5-day running mean.

Backscatter anomalies also were compared to the temperature and salinity recorded by the CTD moored near the seafloor on each mooring (Figure 80 and Figure 81). Few associations between trends in temperature and salinity and S_v or between episodic events in temperature, salinity, and S_v were observed, with fairly low correlations (M1: 0.25 and 0.36 for S_v with T and S respectively; M2: 0.19 for S_v with both T and S).

The associations between elevated S_v and water masses were further explored by plotting both mean daily S_v and the daily anomalies of S_v from the data set mean as a function of temperature and salinity from both moorings (Figure 82 and Figure 83). The plots revealed both differences in the water mass composition near bottom at the two sites and that the greatest S_v was associated with different bottom water mass types at the two sites. It is important to remember that the mean S_v is calculated over the water column while the temperature and salinity were measured at near bottom only. Bottom water at the deeper site, M2, all fell along two mixing curves between: (1) warmer, saltier Atlantic type (T>0°C; S>34) water from deep water off of the shelf and cold, fresher Winter Water (T<-1.5°C; S~33); or (2) warmer, saltier Atlantic type (T>0°C; >34) water and a slightly warmer, less saline water mass (T>-1.5°C. ; S<~32.6). Greatest S_v occurred when the bottom water fell along this second mixing curve (Note: Atlantic Water has the greatest density because of its higher salinity). By contrast, bottom water at M1 was much more diverse in TS properties. There were some days with Winter Water; some with properties along a mixing curve with warmer, saltier Atlantic type water; and many with fresher water ranging from -1.8 to -0.5 °C that likely originates from various upper water column or shelf water sources.

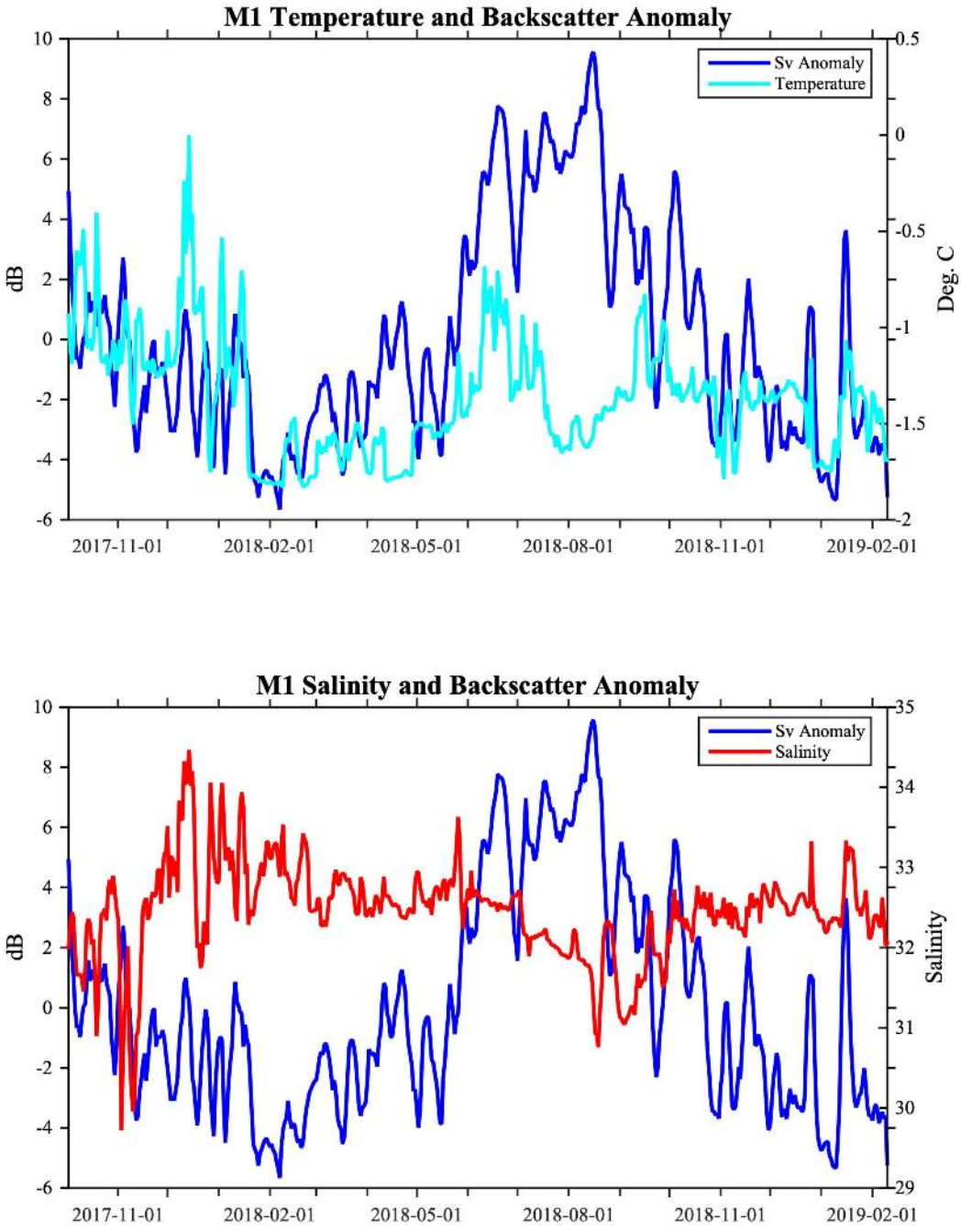

Figure 80. Daily mean backscatter anomaly and temperature (upper) and salinity (lower) at mooring M1

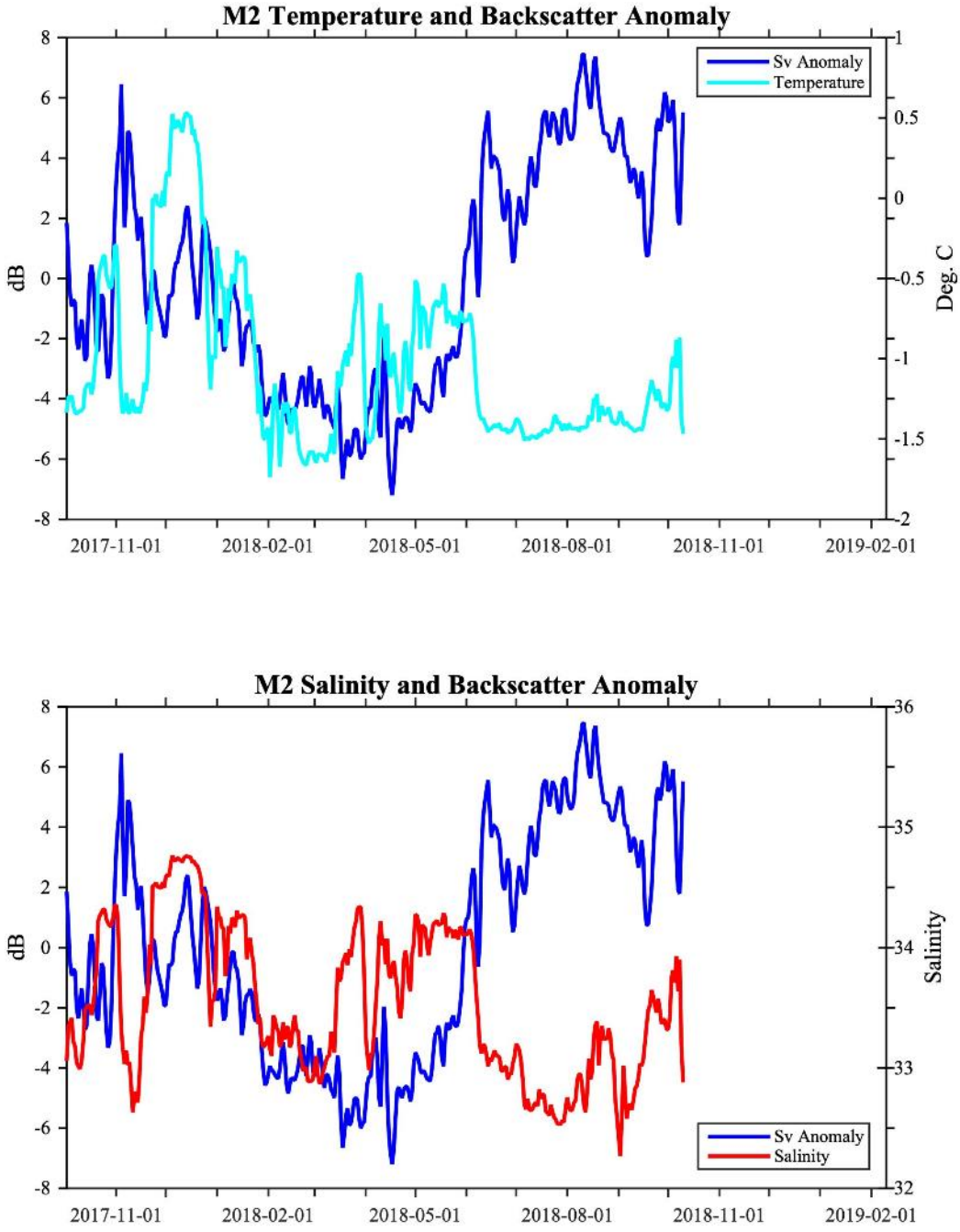

Figure 81. Daily mean backscatter anomaly and temperature (upper) and salinity (lower) at mooring M2

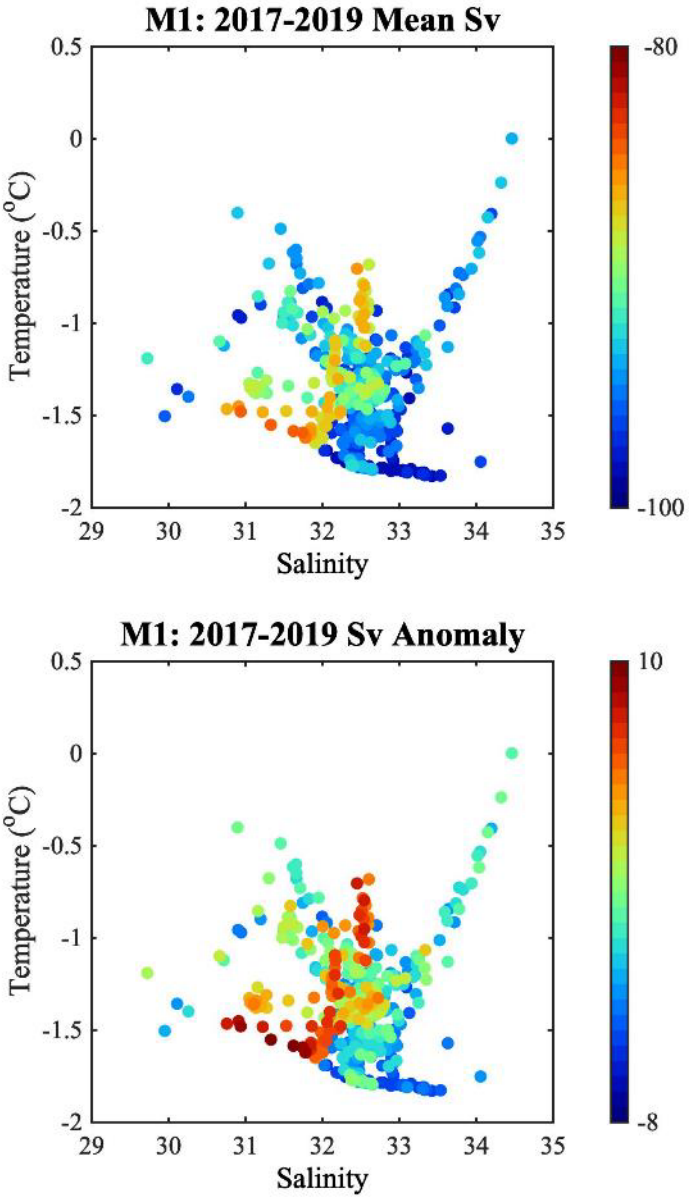

Figure 82. Daily mean backscatter (upper) and backscatter anomaly (lower) plotted as a function of near-bottom temperature and salinity at mooring M1

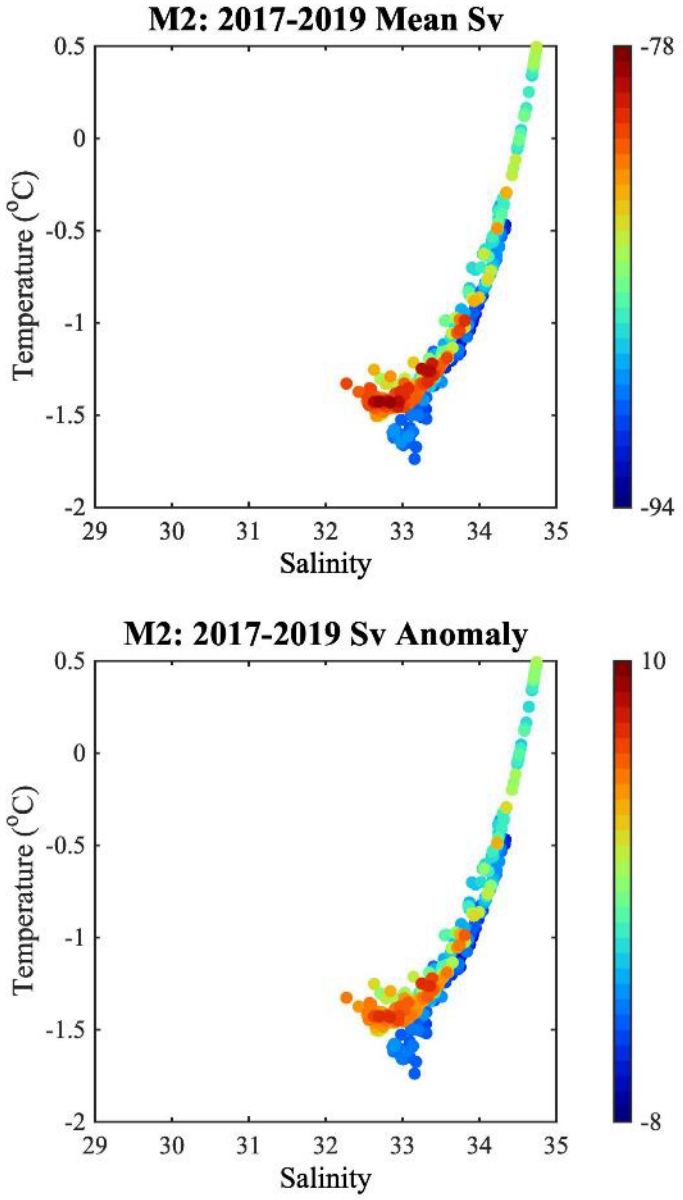

Figure 83. Daily mean backscatter (upper) and backscatter anomaly (lower) plotted as a function of near-bottom temperature and salinity at mooring M2

For detection of diel vertical migration (DVM), the daily sums of squares (SS) were calculated for each record using two different reference sinusoid curves (Wiese et al. 2019). The first pattern had a marked diel signal with migration of backscatter to the near surface during the night hours (centered at midnight) and migration back to depth during daylight (centered at noon). The second pattern, distinct tracks of upward and downward migrating backscatter were associated with times of sunrise and sunset but backscatter during the day at mid-depths was very low, suggesting that the migrating backscatter was located below the instrument, near the sea floor, during the day while backscatter was higher during the night. In contrast to the first pattern, backscatter for these profiles would have a maximum at midnight,

because backscatter was near the surface, and a minimum at noon when most backscatter was deeper. The minimum SS of the two curves for each day was then used to indicate the strength of redistribution of backscatter in the water column. Dates with SS<~0.15 would be characterized by strong DVM. For mooring M1, DVM occurred primarily during the summer (June–August) months, when backscatter was greatest (Figure 84). For M2, the SS was often less than 0.15 but the occurrences were only of a few days in duration. It was notable also that when backscatter was greatest during summer and in November, the SS did not indicate that DVM was occurring.

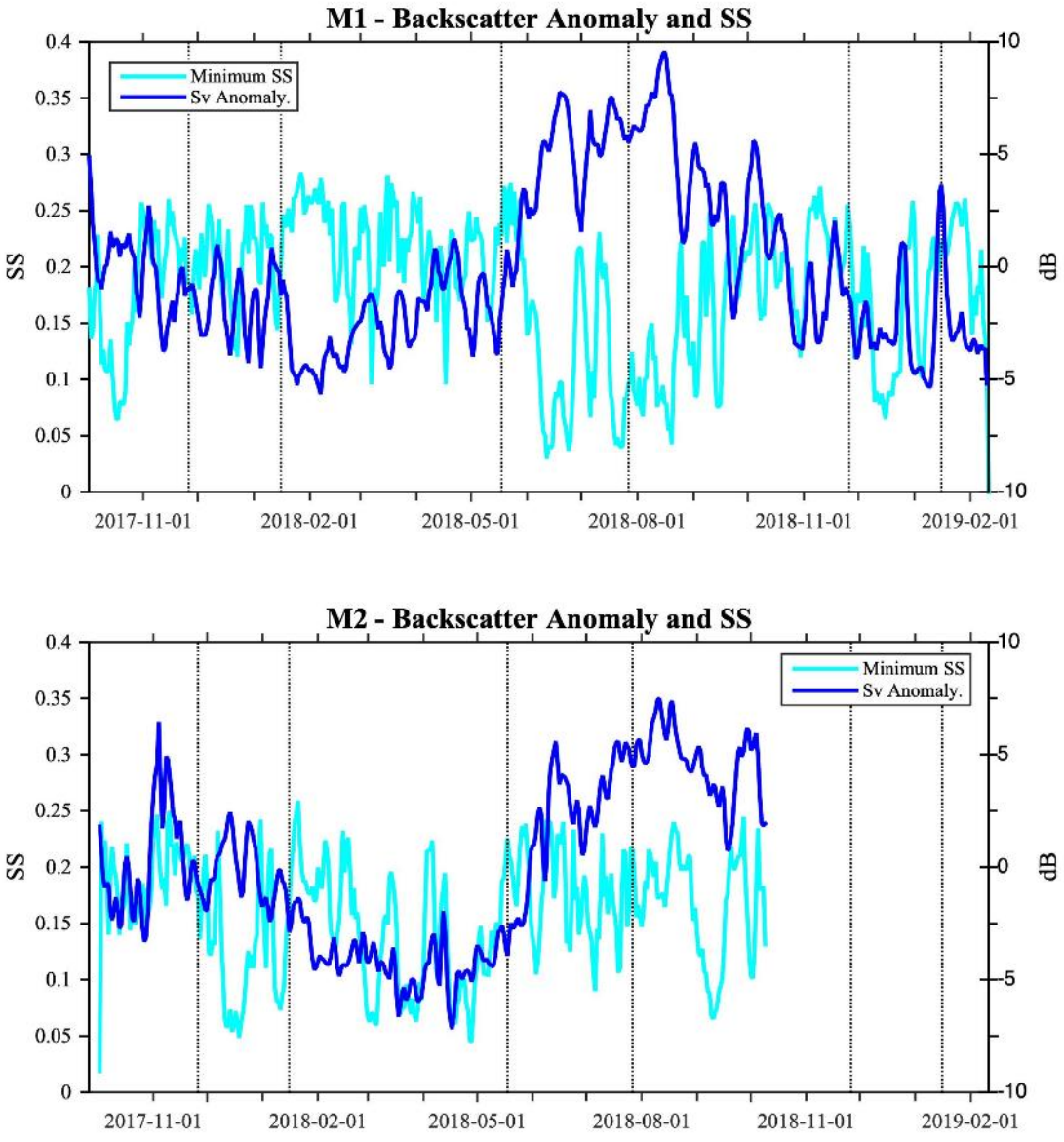

Figure 84. Daily sums of squares and the backscatter anomalies for M1 and M2 moorings
All data smoothed with 5-day running average. Periods of total darkness (Dec.–Mid. Jan.) and total daylight (late May–late Jul.) shown with dotted lines. Periods with strong diel vertical migration have a SS less than ~0.15.

The daily SS were plotted as a function of bottom temperature and salinity to explore if DVM behavior was more or less frequent in different bottom water masses (Figure 85). For M1, DVM was very weak (high SS) when the bottom water appeared to have originated off of the shelf, with TS characteristics along the mixing curve between Winter Water and warmer Atlantic influenced water. By contrast, strongest DVM was observed at M2 when bottom water lay along that mixing curve and weakest DVM occurred when the bottom water did not have the influence of that warmer water, although this was not entirely consistent.

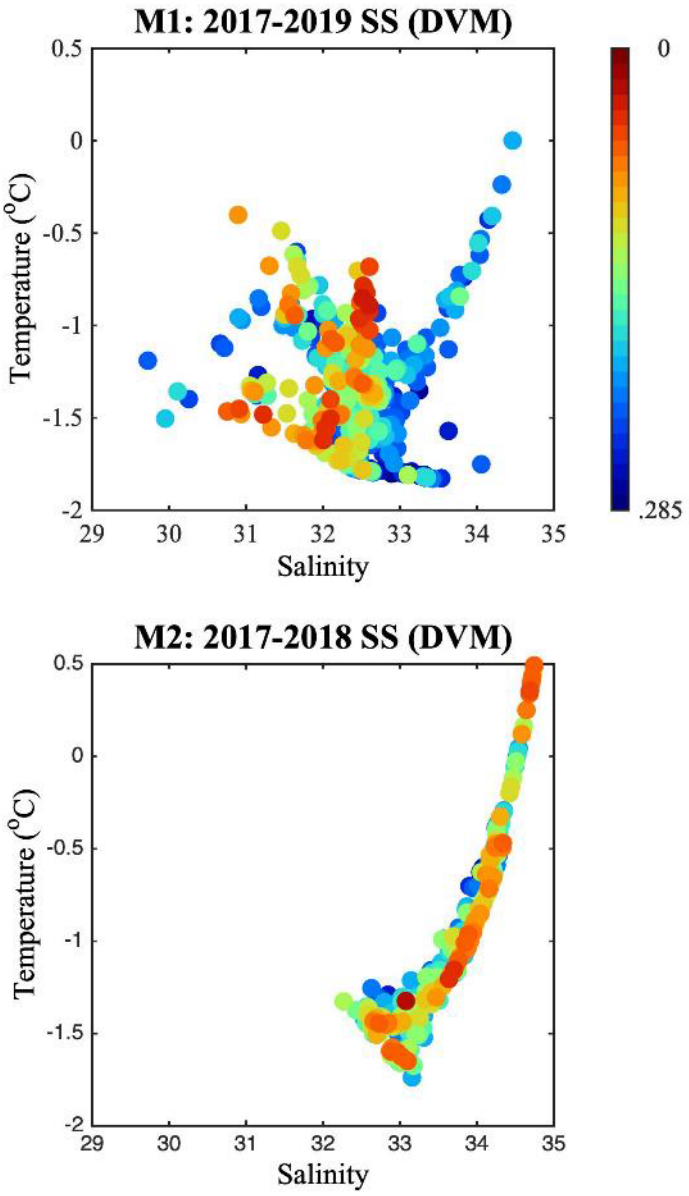

Figure 85. Combined daily sums of squares (Figure 84) plotted as a function of daily bottom water temperature and salinity for mooring M1 (upper panel) and mooring M2 (lower panel)

Beaufort Shelf zooplankton are dominated by copepods in terms of both biomass and abundance (Smoot and Hopcroft 2017) with different regions on the shelf exhibiting different characteristic species compositions. Backscatter should be a better indicator of zooplankton biomass than of zooplankton abundance. Larger copepods such as *C. hyperboreus* and *C. glacialis* usually are present in greater abundance, and thus in biomass, on the outer shelf than in the inner shelf or coastal region although both species can be found across the Beaufort Shelf. The inner shelf and coastal region are characterized by higher abundances but lower biomass of smaller copepods such as *Pseudocalanus* spp. that would be harder to detect with this frequency unless in high biomass such as in a patch. Zooplankton communities over the slope contain both *Calanus* species as well as the offshore Arctic species *Metridia longa, Microcalanus pygmaeus* and *Oncaea borealis* (now known as *Triconia borealis*); of these only *M. longa* might be large enough to contribute to backscatter if present in high enough abundance. Euphausiids or krill (e.g., *T. raschii)* are not a dominant component of the zooplankton community of the Eastern Beaufort Shelf although they can be present in sufficient abundance to provide prey for bowhead whales, based on bowhead whale stomach contents from whales harvested at Kaktovik AK (Lowry et al. 2004). Of these species, *C. glacialis, C. hyperboreus, M. longa,* and *T. raschii* are known as strong diel vertical migrators.

Backscatter at both moorings showed the same seasonal cycle, with greater daily mean water column backscatter (MWCB) observed during the summer and fall and lowest backscatter in late winter to early spring (Figure 79). The lower MWCB during spring may have resulted from a decrease in the abundance of larger zooplankton forms over the winter together with the presence of more abundant smaller forms, either smaller species or smaller life stages resulting from reproduction in late winter (e.g., *C. hyperboreus*) and early spring (e.g., *C. glacialis*), both of which would not scatter sound effectively.

Shorter-term (days-weeks) variability in MWCB also was observed at both moorings, likely driven by episodic physical events. These episodic variations occurred over a time scale of days and must be driven by advection of different populations of plankton, with differing abundances/biomasses, over the sites since these time scales are shorter than the production response time of mesozooplankton at these water temperatures. Many of these short term maxima or minima resulted from a change in MWCB that occurred over the entire water column (Figure 76. Relative backscatter (upper), mean and 5-day running average mean backscatter for each profile (middle) and daily mean and 5-day running average mean (lower) for M1a during the 2017-2019 deployment and Figure 77). The relatively high, significant correlation in MWCB between the two sites ($r=0.77$, $N=374$, $p<0.01$) suggests that common physical events impacted both sites. However, correlations between currents (u and v velocities) and daily bottom water temperature and salinity and peaks in MWCB at both moorings were much lower ($r=0.18$-0.36), although statistically significant because of the high sample size. Examining these associations in TS space suggests that there may be some association between water masses and backscatter, even though this could not be discerned in the daily variations.

As mentioned above, DVM was a regular occurrence on the time scale of days at M2 throughout the year with the possible exception of November, 2017 and occurred fairly consistently during the summer at M1 (Figure 84). A couple aspects of the DVM patterns are remarkable. First, DVM did occur at M2 during the period when the sun did not rise (December-January). Warmer, saltier Atlantic influenced bottom water also was present at M2 during this period (Figure 81), suggesting that movement of deeper, basin water had moved over the mooring site. As for 2018, the occurrence of DVM during this period is puzzling because the known large zooplankton that are strong migrators (*Calanus spp*) should be in diapause during this time. It is possible that the DVM resulted from the presence of euphausiids that do not diapause at depth. Euphausiids are thought to originate in the Bering Sea, thus euphausiids detected at this location would have been advected, perhaps over several years, from their source. At the shallow mooring (M1), DVM was present only during the summer, suggesting that the relative proportion of

vertical migrators in the community was usually low. The regular occurrence of DVM at M1 during summer could have resulted from advective events that temporarily brought greater biomass of the larger, vertically migrating species to that location.

AZFP

Zooplankton

Zooplankton, most likely copepods, were also measured using AZFP at M3. From October 2017 to 2018, the abundance (using the nautical area scattering coefficient, NASC. as a proxy) was moderate throughout the year, with lowest presence in April and May (Figure 86). Peak abundance of zooplankton occurred from June to September 2018. Zooplankton were found throughout the analysis depth domain (surface to 60 m). Diel vertical migration was also evident (Figure 87). Likely both zooplankton and juvenile Arctic cod were moving through the water column to produce this pattern.

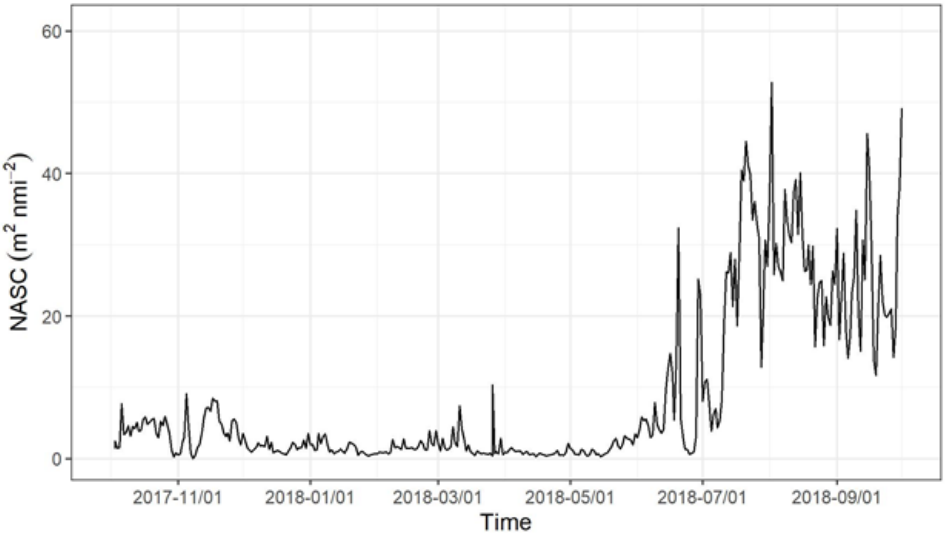

Figure 86. Nautical Area Scattering Coefficient (NASC) as a function of time for copepods at site M3 in the Beaufort Sea during 2017–2018

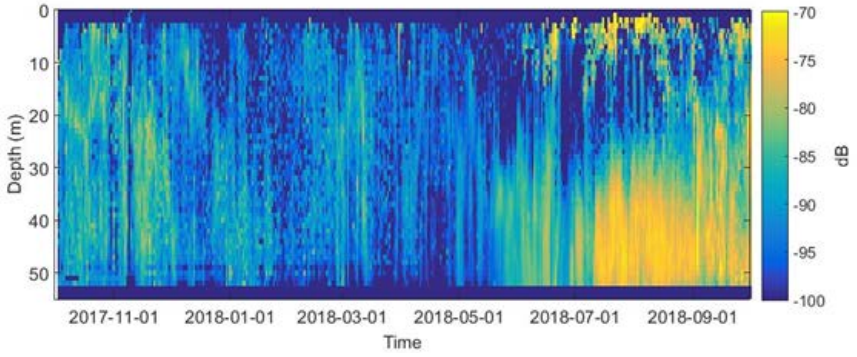

Figure 87. Echogram of 200 kHz backscatter (S_v) corresponding to copepods at site M3 in the Beaufort Sea during 2017–2018

3.1.3.2 Fish

Adult cod

The AZFP frequency of the instruments at M2 and M3 were adequate to detect adult cod. At M3, the bulk of adult cod abundance occurred between September and April, with a peak in October and November of 2017 (Figure 88). A secondary peak in abundance was observed in early March. The abundance remained low from April through July. Most adult cod were found below 200 m depth (Figure 89).

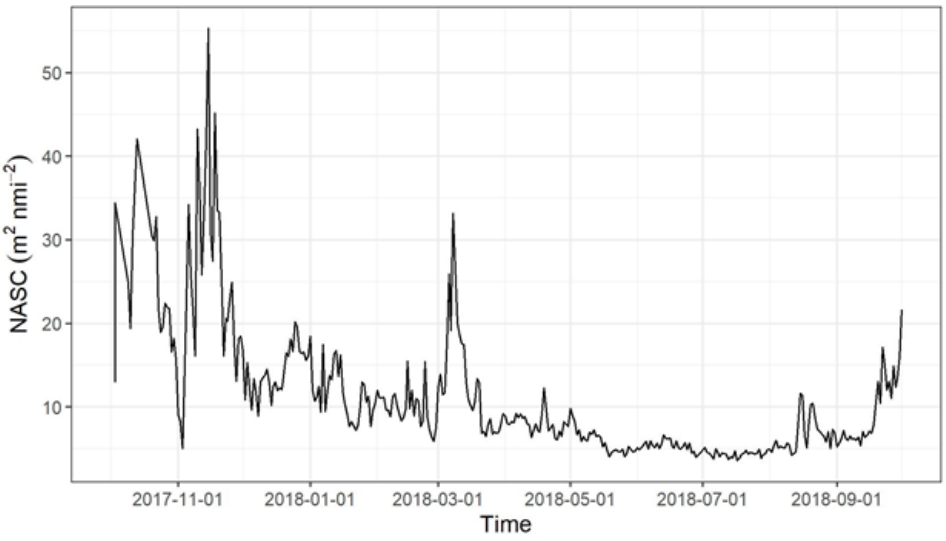

Figure 88. Nautical Area Scattering Coefficient (NASC) as a function of time for adult Arctic cod at site M3 in the Beaufort Sea during 2017/2018

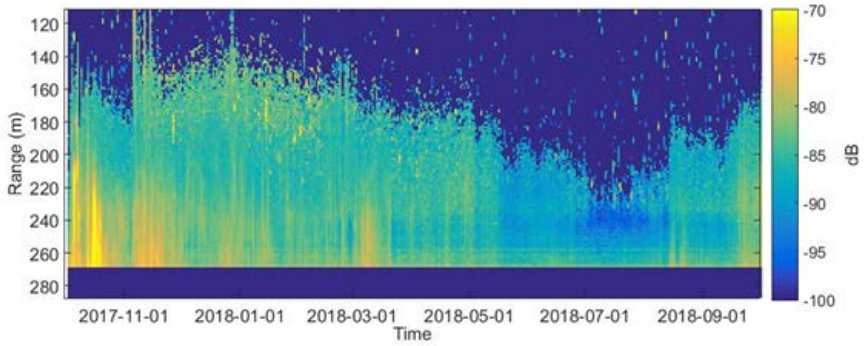

Figure 89. Echogram of 38 kHz backscatter (S_v) corresponding to adult Arctic cod at site M3 in the Beaufort Sea during 2017–2018

Revealing patterns were observed in the echogram time series of the single frequency AZFP at site M2 (Figure 90 and Figure 91). There was a deep layer between 80 and 130 m between late October and February, with a timing similar to the presence of adult cod at depth at site M3. It is likely that the AZFP was only catching the shallowest portion of the adult cod biomass at M2, and that most was in deeper

water. Near the surface, there was a stronger signal in August and September, similar to the juvenile cod detected at site M3.

The acoustic data suggests that the adult cod population was found mostly below 200 m at site M3, while at M2 the upper limit of adult cod was likely detected between 100 and 140 m..

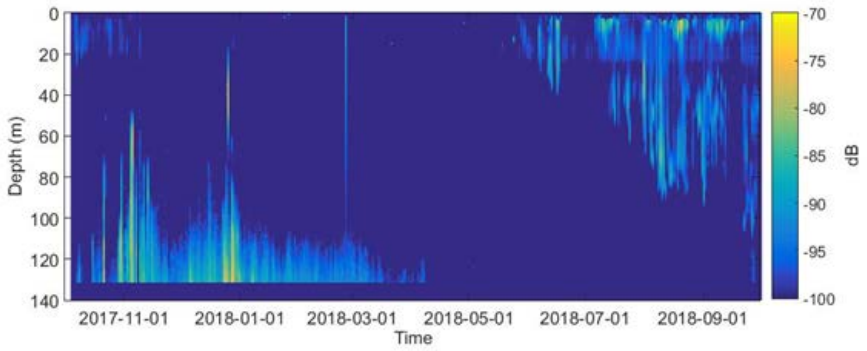

Figure 90. Echogram of 38 kHz backscatter (Sv) corresponding to adult Arctic cod at site M2 in the Beaufort Sea during the 2017–2018 sampling season

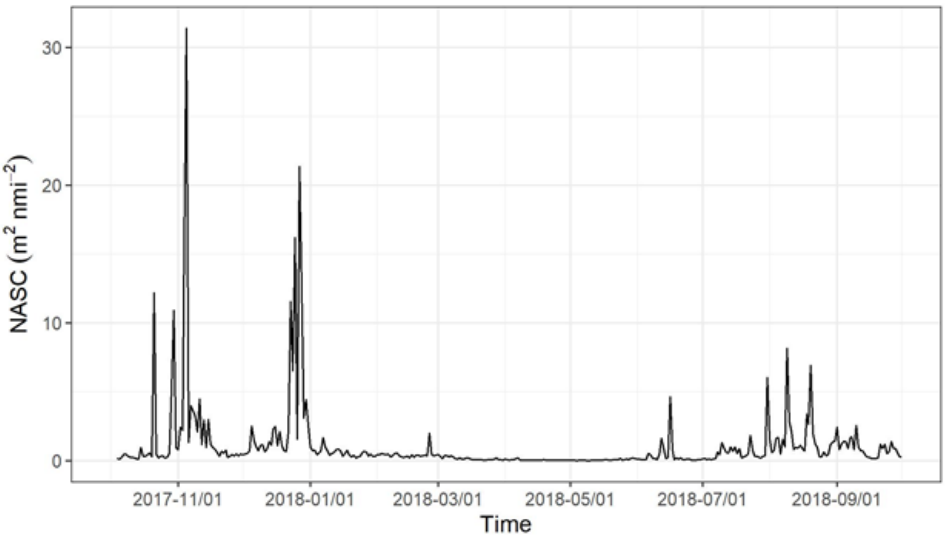

Figure 91. Nautical Area Scattering Coefficient (NASC) as a function of time for the 38 khz frequency at site M2 in the Beaufort Sea during the 2017–2018 season

Juvenile cod

The AZFP frequencies at M3 allowed for the detection of juvenile cod where they were present near the surface from end of May through October, mainly in the upper 40 m (Figure 92 and Figure 93). Juvenile cod were largely absent from the surface layer from November to the middle of May.

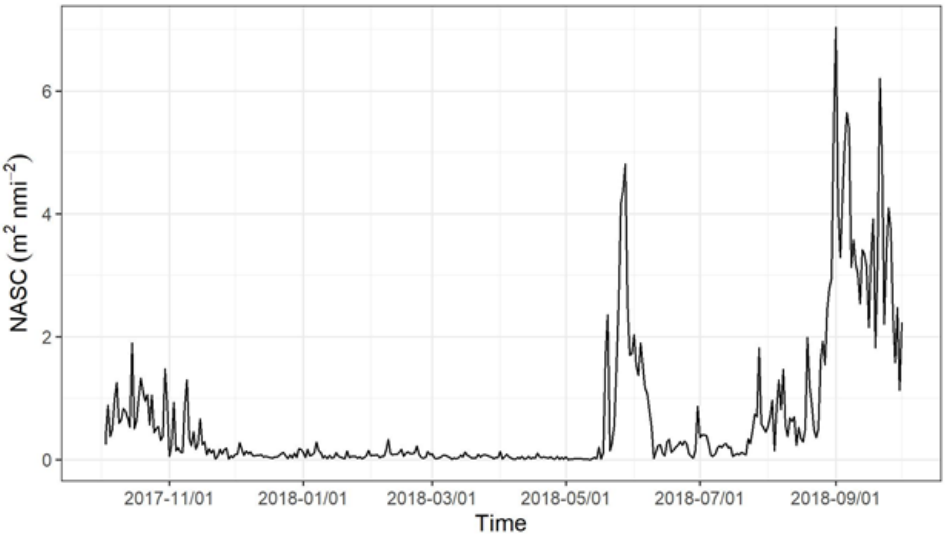

Figure 92. Nautical Area Scattering Coefficient (NASC) at 125 kHz as a function of time for juvenile Arctic cod at site M3 in the Beaufort Sea during 2017–2018

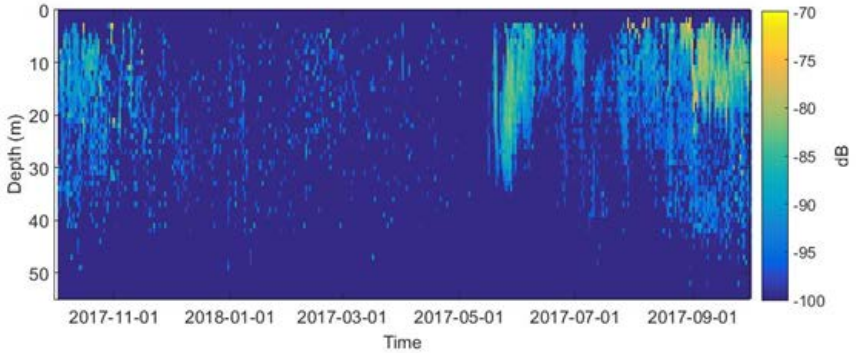

Figure 93. Echogram of 125 kHz backscatter (S_v) corresponding to juvenile Arctic cod at site M3 in the Beaufort Sea during 2017–2018

Diel vertical migration, consistent with findings by Benoit et al 2010, was observed during 2017–2018 (Figure 94. Echogram of 125 kHz backscatter (non-filtered *Sv*) showing daily migration pattern of juvenile cod and zooplankton at site M3 in the Beaufort Sea, from October 12 to 16, 2017).

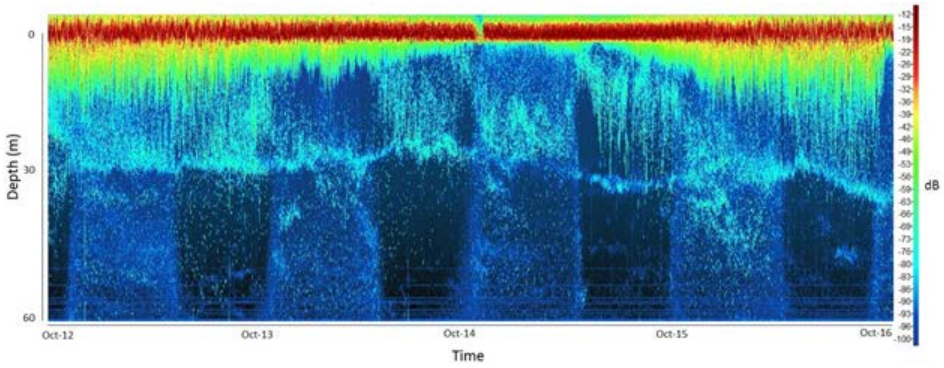

Figure 94. Echogram of 125 kHz backscatter (non-filtered S_v) showing daily migration pattern of juvenile cod and zooplankton at site M3 in the Beaufort Sea, from October 12 to 16, 2017

3.1.4 Marine Mammals

Bearded seals, bowhead whales, and beluga whales were detected by an AURAL located at M2 during the 2017–2018 mooring deployment (Figure 95). Bearded seals were detected consistently in winter and spring (January 2017 through June 2018). Bowhead and beluga whales were detected in the fall of both 2017 and 2018 and through the summer in 2018. No ringed seals were detected.

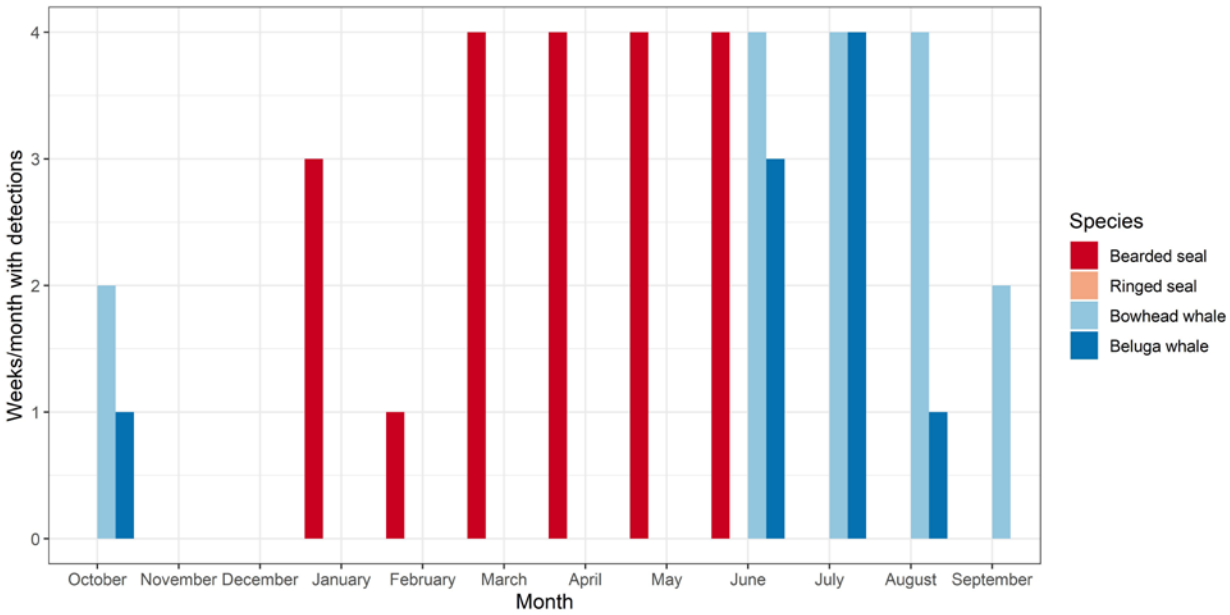

Figure 95. Number of weeks per month with marine mammal detections from October 2017 through September 2018 at M2

3.2 Seasonal and Interannual Patterns and Variability

This section describes some of major large scale physical forcing factors that influence the study region and measured parameters, namely wind, the Mackenzie River, and large scale ocean circulation, and then focuses on a comparison across all mooring data collected as part of the MARES program, between 2016–2019. As such we compare results presented in Wiese et al. (2019) for the 2016–2017 period, with those presented in section 3.1. Where possible and applicable, we derive a sense of mean conditions, major patterns and seasonal signals in the combined data, and also discuss possible regional and local drivers of observed patterns and variability.

3.2.1 Physical Forcing Factors

3.2.1.1 Surface Winds

The interaction of migratory cyclones with quasi-stationary features, such as the Beaufort High, intensify and modify atmospheric surface pressure gradients, thereby causing surface winds. Winds are typically variable from day to day, but can become directionally persistent, intense, and some wind events may be long-lasting in duration. Surface wind forcing is a key physical forcing, where momentum and energy are transferred from pressure-gradient driven atmospheric circulation directly to the ocean-ice surface. During the winter, momentum transfer from the atmosphere to the ice surface may force movement of the sea ice cover, which can cause openings to form in the sea ice cover, known as leads. These leads typically refreeze rapidly but release significant amounts of stored heat energy from the near-surface mixed layer of the ocean to the atmosphere.

To better understand annual and seasonal wind forcing of the ocean-ice surface in the MARES study region, wind data were employed from the new ECMWF ERA5 reanalysis dataset. The ERA5 reanalysis dataset is available from 1950–present, covers a 30 km grid, and provides estimates of a large number of atmospheric, land and oceanic climate variables at hourly and three-hourly intervals. ERA5 data are considered to be fully quality-assured within 3 months of real time. ERA5 replaces the ERA-Interim reanalysis, which stopped being produced on 31 August 2019 (Dee et al. 2020). Surface wind conditions are examined for an ERA5 data grid point (139°W and 70°N), which represents the center of the mooring line. Surface winds are summarized through the use of the speed-direction distribution in the form of compass rose plots for the duration of the deployment. Plots were prepared to align with each deployment period, and are presented annually from 1 October to 30 September for 2016–2017 (Figure 96) and 2017–2018 (Figure 97) respectively. The compass rose plots show the exceedance frequency (radial axis by %) for winds from a particular direction for different wind speed categories on the color bar. Maximum and mean windspeeds are shown for direction on a second radial axis.

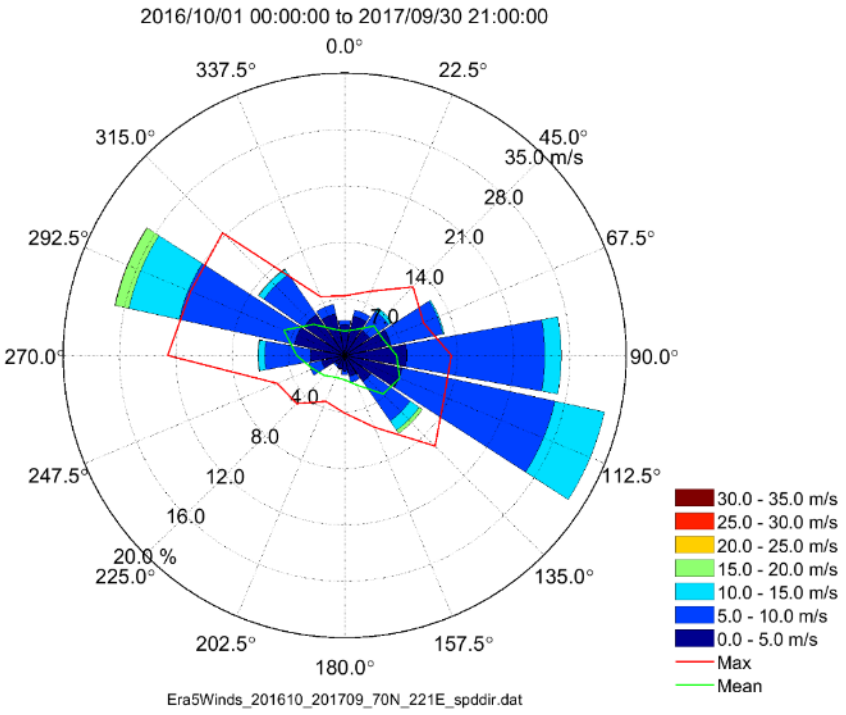

Figure 96. ERA5 surface wind speed (m/s) and direction for 2016–2017 for 70°N 139°W
Directions are expressed as being from (e.g. winds blowing from the east have a 90° direction).

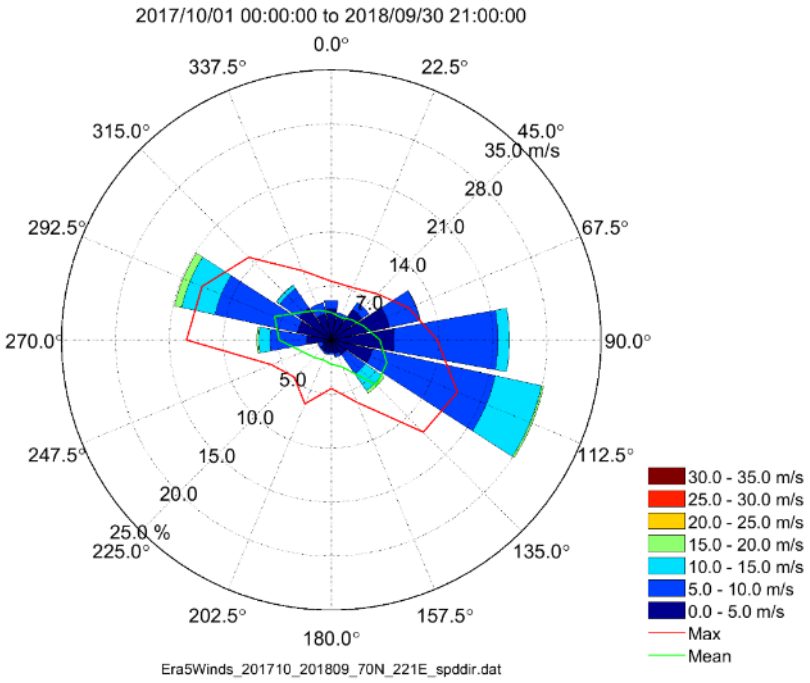

Figure 97. ERA5 surface wind speed (m/s) and direction for 2017–2018 for 70°N 139°W
Directions are expressed as being from (e.g. winds blowing from the east have a 90° direction).

Overall annual wind conditions for both years were dominated by high frequencies of easterlies, east-southeasterlies, or west-northwesterlies. Wind events from these directions were characterized by wind speeds ranging from 5–15 m/s, with some wind events exhibiting winds speeds exceeding >15 m/s, most notably for winds from the northwest. Nominal frequencies were present for wind events from all other compass directions. 1-2% of all events were characterized by wind speeds > 15.0 m/s.

The warming that the Arctic is currently experiencing and the commensurate changes in sea ice extent and volume being observed may be having an impact on the large-scale atmospheric circulation controls on synoptic-scale wind forcing. Moore et al. (2018) describe a collapse of the Beaufort High pressure system that was evident during the winter of 2017 (January–March). This event featured the anomalous reversal of the normally anticyclonic surface winds, and sea ice motion in the western Arctic.
The collapse, as documented, was believed to have been caused by the high frequencies of low-pressure systems entering the Arctic from the North Atlantic, and along the East Siberian Coast. Moore et al. (2018) suggest that thin sea ice cover resulting from an extremely warm autumn (October–December 2016) contributed to the formation of an anomalous thermal low over the Barents Sea, that coincided with a northward shift of the Polar Vortex, thereby permitting the intrusion of cyclones. Sea level pressure, surface winds, and sea ice circulation anomalies in the western Arctic during winter 2017 were at 2-sigma level. Large-scale atmospheric circulation conditions returned to more typical seasonal circulation patterns during 2017–2018; however, they continue to be influenced by the changing Arctic sea ice cover.

On a seasonal scale, large-scale atmospheric circulation features and seasonality of synoptic circulation features drives variability in surface wind characteristics in the Western Arctic. To that effect, we characterized surface winds by months (October–December, January–March, April–June, and July–September) with speed-direction distribution-based compass rose plots for 2016–2017 (Figure 98) and 2017–2018 (Figure 99). October–December 2018 is presented in Figure 100 to cover the end of the 2018 deployment season. The seasonal compass rose plots show the exceedance frequency (radial axis by %) for winds from a particular direction for different wind speed categories on the color bar. Maximum and mean windspeeds are shown for direction on a second radial axis. Wind events were characterized by wind speeds ranging from 5–15 m/s, with some wind events exhibiting winds speeds exceeding >15 m /s. Nominal frequencies were present for wind events from all compass directions. 1–2% of all events were characterized by wind speeds > 15.0 m/s.

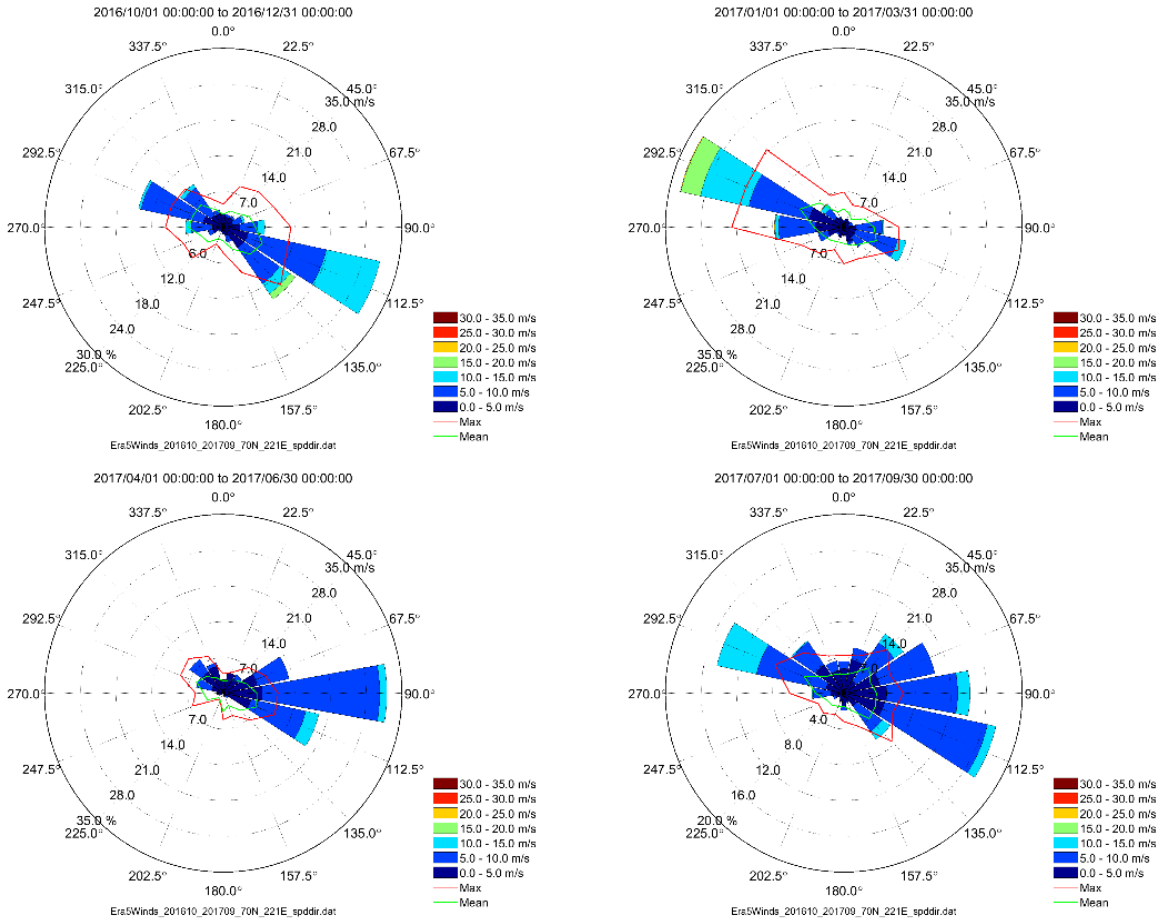

Figure 98. ERA5 seasonal surface wind speed (m/s) and direction for 2016–2017
October–December (top left), January–March (top right), April–June (bottom left), and July–September (bottom right) for 70°N 139°W. Directions are expressed as being from (e.g. winds blowing from the east have a 90° direction).

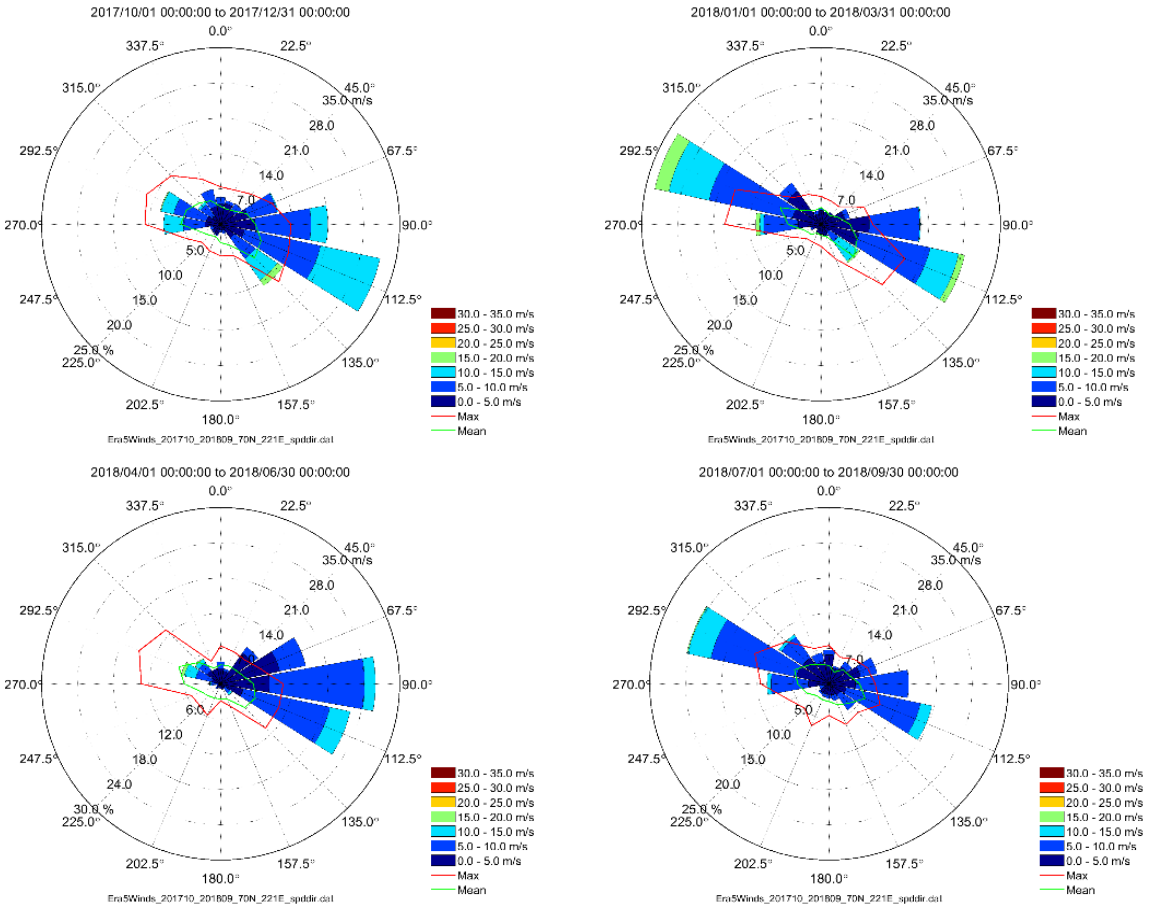

Figure 99. ERA5 seasonal surface wind speed (m/s) and direction for 2017–2018
October–December (top left), January–March (top right), April–June (bottom left), and July–September (bottom right) for 70°N 139°W. Directions are expressed as being from (e.g. winds blowing from the east have a 90° direction).

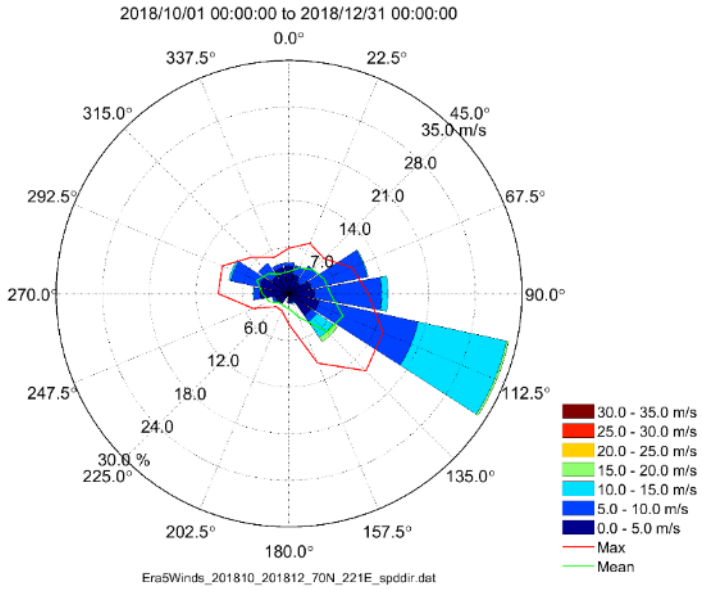

Figure 100. ERA5 seasonal surface wind speed (m/s) and direction for October–December 2018 for 70°N 139°W. Directions are expressed as being from (e.g. winds blowing from the east have a 90° direction).

October – December winds in 2016, 2017, and 2018 were comparable in that they were strongly dominated by east-southeasterlies with wind speeds frequently in excess of 10.0 m/s. These are counterbalanced by less frequent, intense northwesterly wind events, especially in winter, which were likely associated with the passage of a frontal system. The strongest wind events (>15.0 m/s) appeared to occur from the southeast in all three years. East-southeasterly winds in all three years are conducive to oceanic upwelling along the continental shelf where open water is present, and the westward advection of young sea ice types.

January – March winds showed a high degree of variability between 2017 and 2018 and illuminates the anomalous atmospheric circulation patterns during January – March 2017 as described by Moore et al. (2018). The key difference is the relative absence of normally highly frequent east-southeasterly winds during January – March 2017 as compared to 2018, where high frequencies of intense wind events from the west-northwest and east-southeast are noted. This would indicate that less westward ice advection occurred during January – March 2017 than in January – March 2018.

April – June winds characteristics were similar between 2017 and 2018, with a few notable differences. April – June winds were dominated by easterly and east-southerly winds in both seasons, but the frequency of more intense wind events (wind speed > 10 m/s) was greater in 2018 than in 2017. Furthermore, there appeared to be a relatively higher frequency of intense northwesterly wind forcing events in 2018 than in 2017, where winds from this direction tended to be light.

Summer wind forcing (July – September) was characterized in both years with a strong bi-directional pattern (west-northwesterly and east-southeasterly). Wind speeds typically ranged most frequently from 0–10 m/s for both directions, however west-northwesterly winds exceeding 10 m/s were present in both years.

Summer southeasterly wind forcing is particularly important in driving westward advection of summer sea ice away from coastline and driving oceanographic upwelling onto the continental shelf. West-

northwesterly wind forcing drives oceanographic downwelling. Beyond the bi-modal distribution of dominant winds, there were relatively higher frequencies of wind from other directions during July – September than the other seasons, most notably northerly and northeasterly winds.

Synoptic-scale wind events in the Arctic are driven by the interaction of seasonably variable synoptic-scale high pressure features (e.g. the Beaufort High), and migratory cyclones of Pacific, Arctic, and North Atlantic origin following storm tracks into the Arctic Basin (Sepp and Jaagus 2011). The interaction of migratory cyclones with quasi-stationary features, such as the Beaufort High, intensify surface pressure gradients, causing intense surface winds. Some synoptic patterns may support steady wind forcing events that may last up to several days in duration. To explore this further, we conducted an analysis of the ERA5 winds to identify long-lasting wind forcing easterly and westerly wind events that drive sea ice lead formation, and oceanographic upwelling and downwelling events along the continental slope.

Due to the predominance of a bi-directional wind climatology for the study site (east-southeasterly–west-northwesterly), it is desirable to identify persistent wind forcing events for both directions. Wind events were identified by persistence of u-component winds in one direction, or the other for a minimum of 24 hours. A total of 235 events was identified for the period of 01 October 2016 – 31 December 2018 for both easterly and westerly winds. Wind events are ranked by east-west total particle displacement and the largest ten events for easterly and westerly wind forcing events for 2016–2017 and 2017–2018 are summarized in Table 43 to Table 46.

Table 43. Largest easterly wind-forcing events for 2016–2017

Rank (by east-west displacement)	mean_u (m/s)	mean_v (m/s)	Duration (hours)	disp_u (km)	disp_v (km)	Event Start	Event End
1	-5.58	-0.22	321	-6,507	-260	2017-04-27 03:00	2017-05-10 12:00
2	-8.08	1.56	213	-6,283	1,214	2017-04-03 15:00	2017-04-12 12:00
3	-7.90	3.21	207	-5,971	2,428	2016-10-06 21:00	2016-10-15 12:00
4	-4.87	-1.04	321	-5,677	-1,214	2017-06-02 09:00	2017-06-15 18:00
5	-5.65	1.75	240	-4,938	1,529	2016-10-27 15:00	2016-11-06 15:00
6	-8.10	4.13	135	-4,026	2,053	2016-12-14 21:00	2016-12-20 12:00
7	-5.93	0.42	156	-3,394	243	2017-06-26 15:00	2017-07-03 03:00
8	-6.12	2.16	135	-3,042	1,076	2017-01-22 12:00	2017-01-28 03:00
9	-6.59	0.81	111	-2,703	332	2017-07-15 21:00	2017-07-20 12:00
10	-7.47	0.74	84	-2,341	232	2017-06-18 03:00	2017-06-21 15:00

Table 44. Largest westerly wind-forcing events for 2016–2017

Rank (by east-west displacement	mean_u (m/s)	mean_v (m/s)	Duration (hours)	disp_u (km)	disp_v (km)	Event Start	Event End
1	11.65	-4.54	111	4,779	-1,863	2017-02-28 03:00	2017-03-04 18:00
2	8.33	-3.15	96	2,969	-1,124	2017-03-05 03:00	2017-03-09 03:00
3	4.57	-0.89	177	2,961	-577	2017-03-11 18:00	2017-03-19 03:00
4	6.91	-3.04	108	2,760	-1,214	2017-01-09 09:00	2017-01-13 21:00
5	7.29	-3.04	102	2,754	-1,149	2017-02-01 00:00	2017-02-05 06:00
6	5.29	-2.24	111	2,171	-918	2017-02-06 12:00	2017-02-11 03:00
7	13.47	-6.13	33	1,746	-794	2017-01-05 18:00	2017-01-07 03:00
8	6.10	0.39	72	1,646	106	2016-10-20 21:00	2016-10-23 21:00
9	5.11	-1.55	81	1,545	-469	2016-11-23 12:00	2016-11-26 21:00
10	6.31	-4.07	60	1,431	-924	2017-07-03 06:00	2017-07-05 18:00

Table 45. Largest easterly wind-forcing events for 2017–2018

Rank (by east-west displacement)	mean_u (m/s)	mean_v (m/s)	Duration (hours)	disp_u (km)	disp_v (km)	Event Start	Event End
1	-6.96	-0.21	441	-11,122	-332	2017-12-02 12:00	2017-12-20 21:00
2	-5.45	-0.04	384	-7,595	-58	2018-05-01 21:00	2018-05-17 21:00
3	-6.96	0.30	291	-7,362	323	2018-10-10 21:00	2018-10-23 00:00
4	-8.05	4.06	219	-6,437	3,243	2018-09-29 09:00	2018-10-08 12:00
5	-6.69	1.69	261	-6,358	1,606	2018-09-10 15:00	2018-09-21 12:00
6	-7.74	2.65	180	-5,102	1,748	2018-04-04 15:00	2018-04-12 03:00
7	-7.30	4.71	168	-4,497	2,899	2018-01-08 00:00	2018-01-15 00:00
8	-7.33	1.16	165	-4,431	703	2018-11-16 21:00	2018-11-23 18:00
9	-6.68	-0.85	168	-4,114	-526	2018-05-19 00:00	2018-05-26 00:00
10	-5.85	0.72	183	-3,916	482	2018-03-07 21:00	2018-03-15 12:00

Table 46. Largest westerly wind-forcing events for 2017–2018

Rank (by east-west displacement	mean_u (m/s)	mean_v (m/s)	Duration (hours)	disp_u (km)	disp_v (km)	Event Start	Event End
1	8.66	-1.77	159	5,050	-1,034	2018-02-21 00:00	2018-02-27 15:00
2	4.88	-1.06	147	2,636	-572	2018-07-03 15:00	2018-07-09 18:00
3	7.90	-3.98	75	2,217	-1,117	2018-04-12 06:00	2018-04-15 09:00
4	9.25	-4.64	63	2,198	-1,101	2018-01-19 03:00	2018-01-21 18:00
5	5.01	-2.11	117	2,164	-909	2018-08-08 03:00	2018-08-13 00:00
6	8.10	-1.71	60	1,837	-387	2018-08-16 06:00	2018-08-18 18:00
7	6.41	-0.56	75	1,799	-158	2018-06-09 09:00	2018-06-12 12:00
8	8.43	-3.53	54	1,730	-724	2017-11-02 18:00	2017-11-05 00:00
9	8.66	-4.03	51	1,683	-783	2018-09-01 06:00	2018-09-03 09:00
10	6.13	-3.19	72	1,655	-862	2018-02-16 00:00	2018-02-19 00:00

The top ten episodes of very large wind events listed in the Tables above reveal important differences for easterly vs. westerly winds. Large easterly winds have longer durations but somewhat lower peak speeds than the largest westerly wind events. However, the overall displacement within the top 10 wind events is larger for easterly than westerly winds. There is also a notable difference in these largest wind events amongst the seasons. Very large easterly wind events tend to occur most often in the fall and spring, while the very large westerly wind events tend to occur in the winter (especially in 2016–2017) while the remainder can occur in fall, spring and summer.

3.2.1.2 Mackenzie River Discharge

Freshwater discharges from the Mackenzie River into the Beaufort Sea has a profound effect on the oceanography of the upper layer of the receiving oceanic waters. The distance scales of this influence are of the order of hundreds of kilometers. It has recently been shown (Proshutinsky et al. 2019) that 15 to 45% of the total freshwater in the offshore Beaufort Gyre Region of the Arctic Ocean originates from the Mackenzie River. The influence of the Mackenzie River freshwater discharges to total freshwater content on the Beaufort Sea continental margin from Point Barrow to Banks Island is likely much larger.

The Mackenzie River is the largest river flowing into the Arctic Ocean from North America and it is the thirteenth longest river system in the world. It is the longest river system in Canada, and the second largest river in North American (after the Mississippi River). About 90% of the discharge to the ocean is from the Mackenzie River above Arctic Red River (with the balance mostly from the inflowing Peel (7%) and Arctic Red (2%) rivers (Emmerton et al. 2008)) (Figure 101).

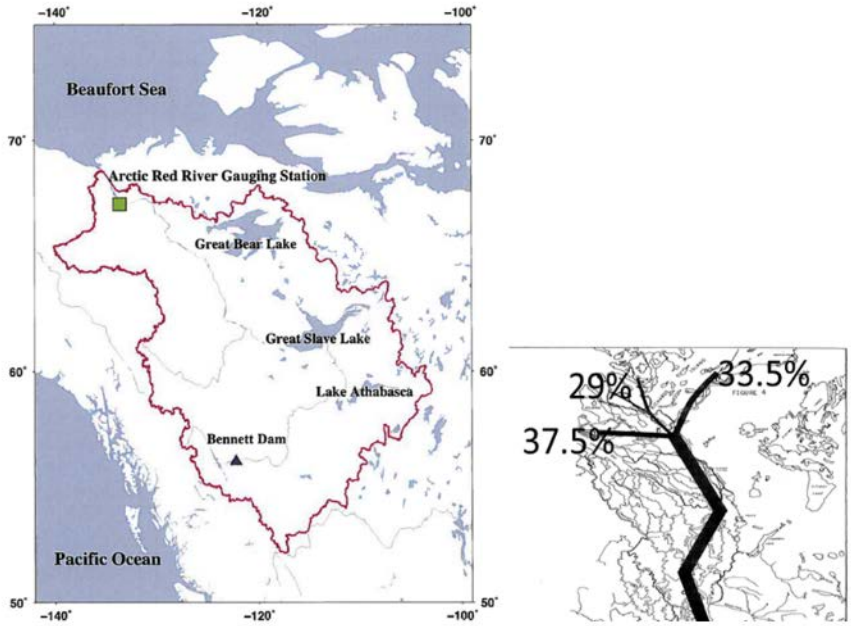

Figure 101. (left) Map of the drainage basin of the Mackenzie River and (right) the split of the discharge into the Beaufort Sea via the west and central channels into Mackenzie Bay and to the east via Kugmallit Bay

The Mackenzie River discharges (Figure 102) have a very pronounced seasonal cycle with four different regimes over the course of a year: (a) low but non-zero discharges (~5,000 m^3/s) during the December to April period, when precipitation in the drainage basin is largely stored as snow rather than as rainfall; (b) the freshet and early summer period when the Mackenzie River discharges attain very high values (~25,000–35,000 m^3/s) ; (c) high to moderate discharges during summer with large variations within each summer period; (d) moderate to low discharges during October and November as the snow season starts within the drainage basin. Yang et al. (2015) show that the Mackenzie River flow regime has changed over the past 4 decades due to climate variation: the advance of snowmelt peak timing by several days; decrease in maximum spring flows by about 3000 m^3/s; and a weak rise of cold season base flows.

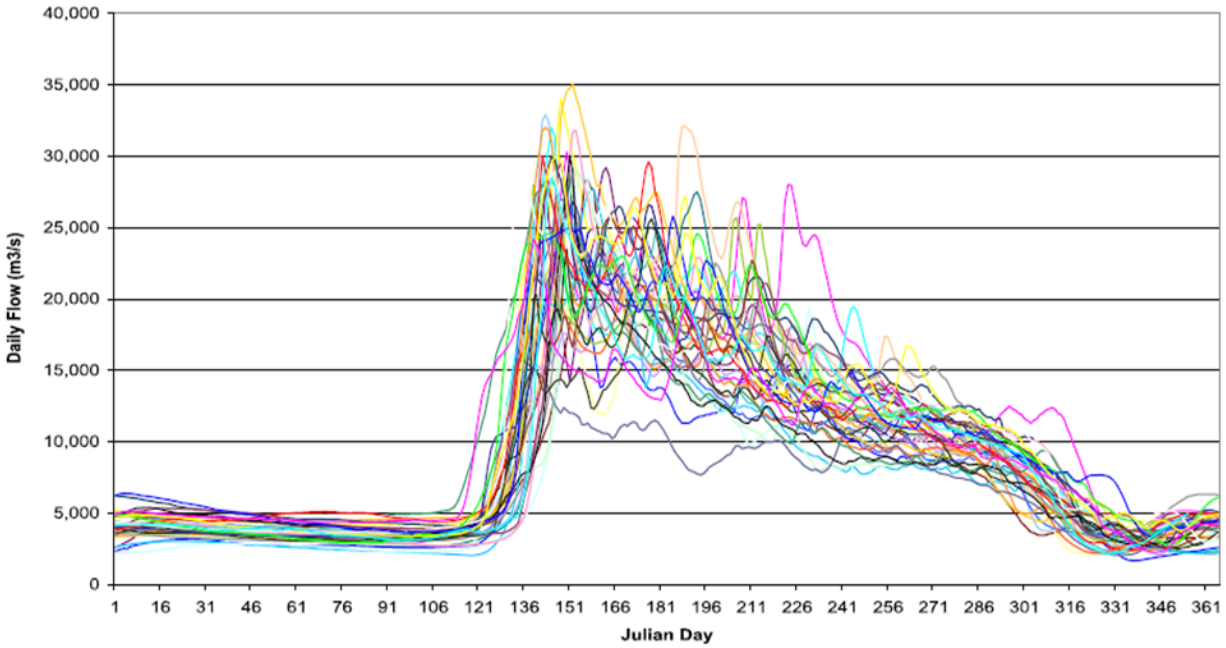

Figure 102. Mackenzie River Daily Discharges for 1973–2011 (Yang et al. 2015)

In late spring (mid-May to June), the release of freshwater into the ocean reaches very high values due to a combination of the freshet conditions of the Mackenzie River discharges and coincident release of accumulated freshwater resulting from the winter discharges beneath the landfast ice (Carmack and Macdonald 2002). The latter contribution takes the form of a "floating freshwater lake (known as Lake Herlinveaux) which contains about 70 km^3 of winter inflow spread over an area of 12 000 km^2 (Macdonald et al. 1995). The release of this freshwater occurs just after freshet as the landfast ice breaks up and disperses in June. The hydrographs of daily Mackenzie River discharge values at Arctic Red River for the years 2016, 2017, 2018, and 2019, during which MARES observations were obtained in the Beaufort Sea, are presented in Figure 103.

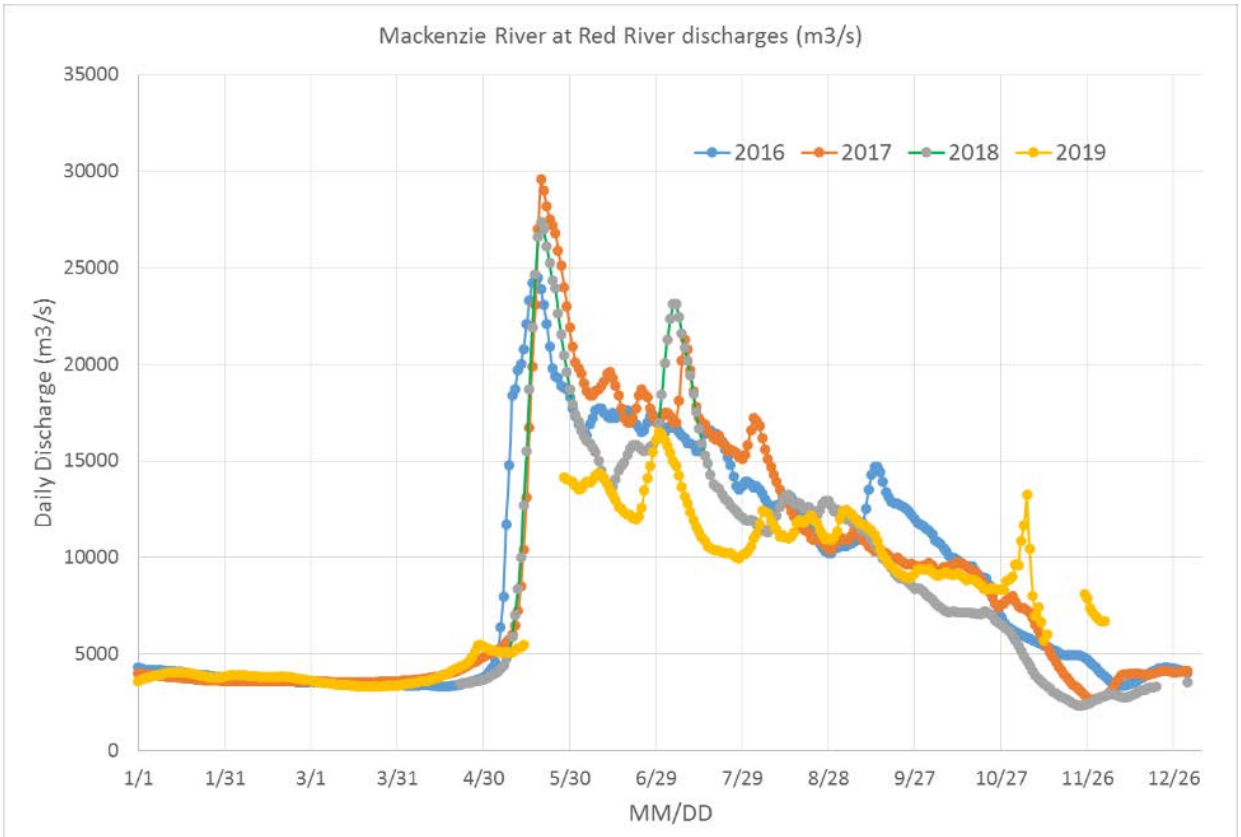

Figure 103. Hydrographs of daily discharges of the Mackenzie River at Arctic Red River, for the Years 2016, 2017, 2018, and 2019 (ArcticGRO discharge dataset (Holmes et al. 2019))

3.2.1.3 Large Scale Ocean Circulation

Transport of water masses between adjoining areas and the study area is potentially important for the temperature-salinity properties, ocean currents, and ice velocities. The general circulation of the Beaufort Sea is shown in Figure 104. An eastward flow of Atlantic Water at water depths in excess of 200 m occurs on the Continental Slope while an episodic eastward flow of Bering Sea Water occurs at the shelf break. A net eastward flow of waters occurs further offshore in the upper layer (Polar Water) of the Beaufort Gyre.

The origin of the episodic eastward shelf break jet is a complex pattern of Pacific Water flowing northward to the Chukchi Sea, shown in Figure 105, results from a bifurcation of the Alaskan Coastal Current which splits into the westward flowing slope current and the eastward flowing Shelfbreak Jet. The origin of the eastward flowing shelfbreak jet downstream of Barrow Canyon is discussed in Pickart 2004 and Nikolopoulos et al., 2009) which in summer is surface-intensified, carrying Pacific summer water while at other times, it is bottom-intensified and transports cold Pacific winter waters. There is evidence of an eastward shelfbreak jet current in the Canadian Beaufort Sea (Kulikov et al., 1998; Forest et al., 2015).

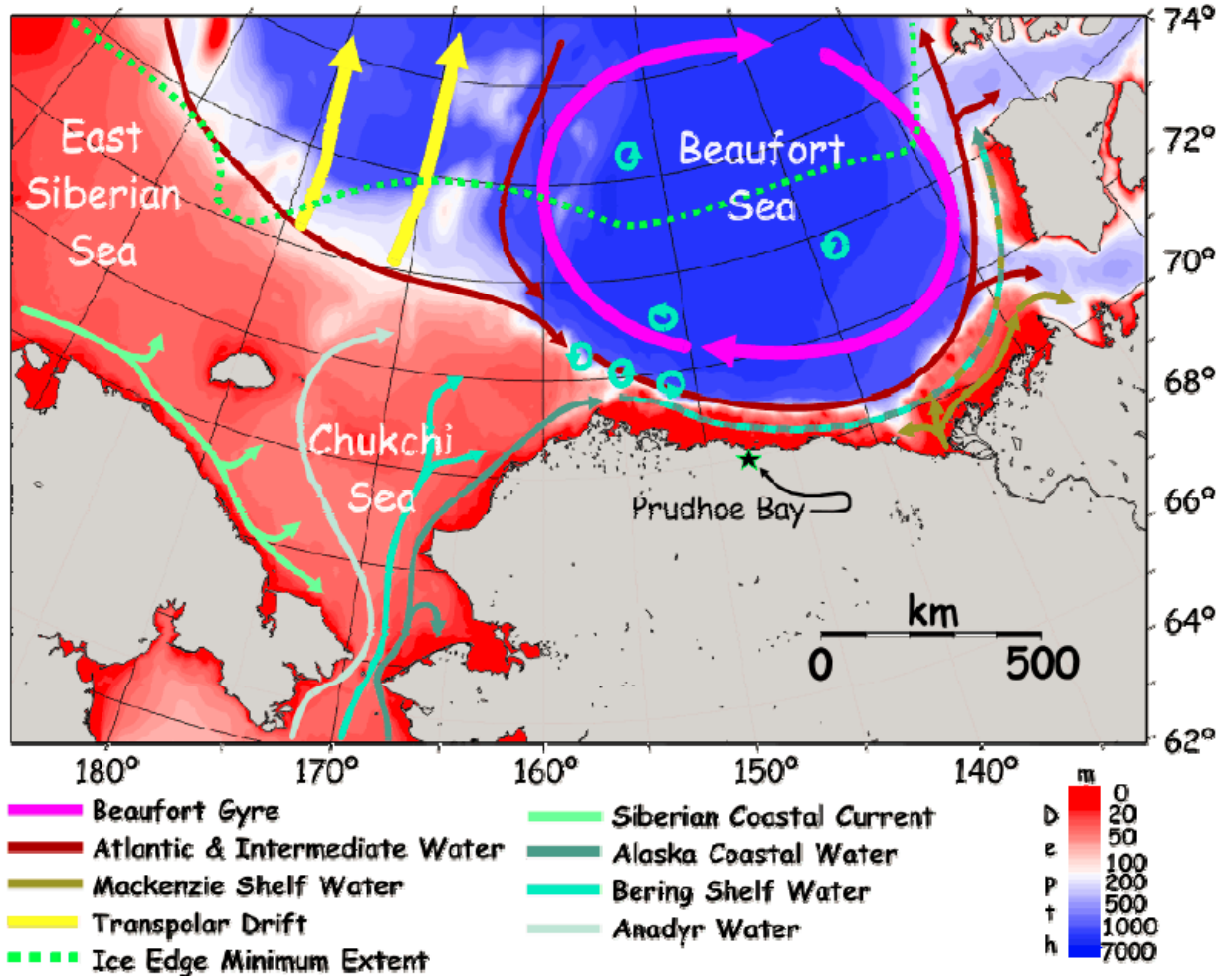

Figure 104. Regional circulation schematic of the Beaufort Sea illustrating connections to adjacent shelves and the Canada Basin (Weingartner et al. 2006)

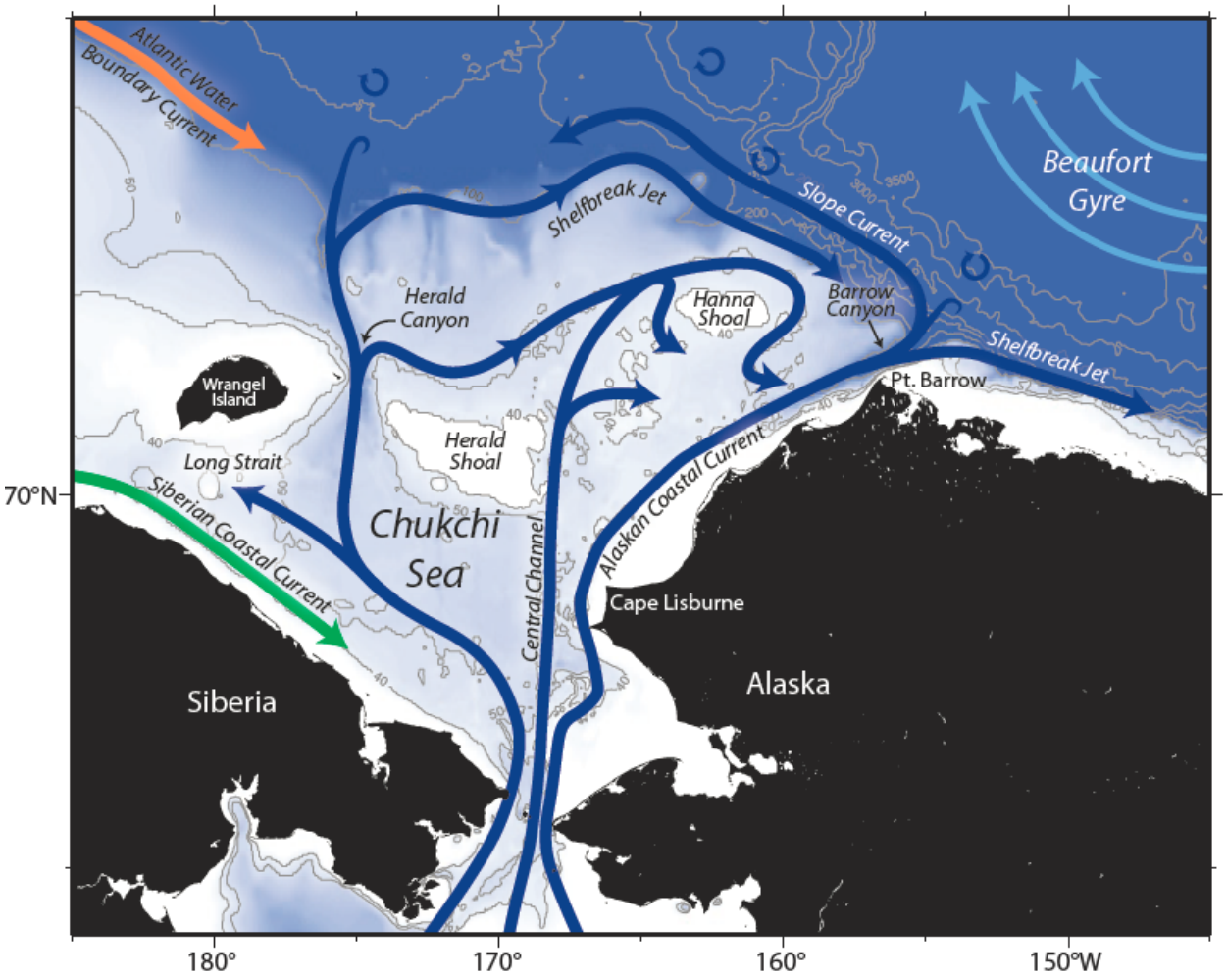

Figure 105. Revised schematic of the circulation of the Chukchi Sea and Western Beaufort Sea from Brugler et al. (2014), including an extended Chukchi shelfbreak jet and the newly-described Chukchi slope current (Corlett and Pickart 2017)

The dynamics of the ocean currents, and the related processes in terms of upwelling and downwelling in relation to water masses, is strongly influenced by the complex special dynamics that occurs in major canyons, specifically the Mackenzie Canyon, which is a major interruption of the continental shelf extending from Alaska to the Canadian Arctic Archipelago.

As discussed in Lin et al. (submitted) in their study of the dynamics of the ocean currents derived in the first year (2016–2017) of the MARES project:

> "Carmack and Kulikov (1998) found that, for a given wind speed, the upwelling in Mackenzie Canyon is 2–3 times stronger than on the adjacent shelf. The downwelling in Mackenzie Canyon was also stronger, though not to the same extent as upwelling. This asymmetry exists because, in the upwelling case, the along-shelf flow opposes the baroclinic wave response and can arrest the waves, leading to a stronger upwelling signal (Allen et al. 2009). Pack ice can also play a role since it is more mobile for easterly winds, and hence the ice-ocean stress is larger (Williams et al. 2006)."

From the MARES mooring measurements of ocean currents, a recirculation was detected within the canyon, which was captured by the two offshore moorings of the array (Figure 106; Lin et al. 2020). It is intensified at mid-depths in the water column and it appears to be independent from the shelfbreak jet. This is consistent with previous modeling work (Hyun 2004) which shows that a current impinging on a dynamically wide canyon gets diverted up the canyon on its upstream flank and subsequently bifurcates after flowing into shallower water (Lin et al. 2020). A portion of the westward flow associated with the southern edge of the Beaufort Gyre appears to get diverted up the canyon, resulting in the recirculation. The dynamics of this recirculation process is supported by the strong correlation with the wind stress curl in the Canada Basin – which drives the gyre – on intra-seasonal timescales (Lin et al. 2020).

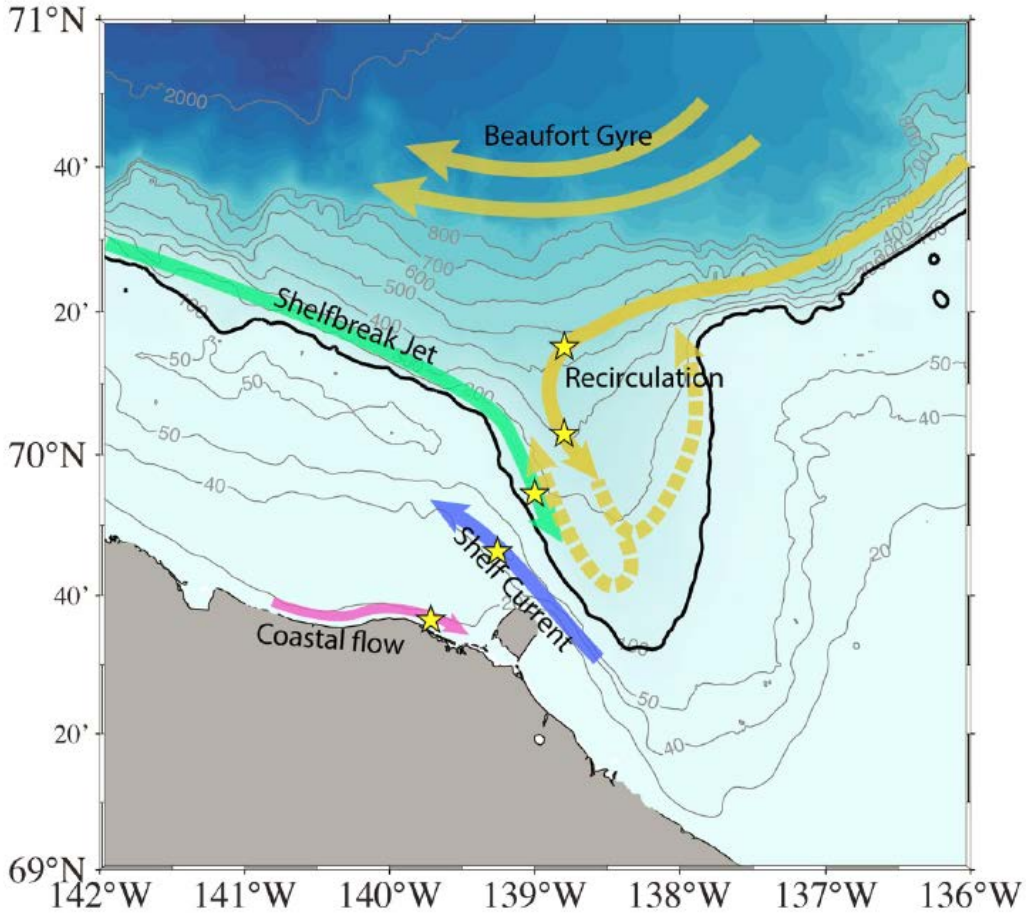

Figure 106. Schematic circulation in the vicinity of Mackenzie Canyon, based on the MARES mooring data (yellow stars; Lin et al. 2020)

The four components of the boundary current system are shown by different colored arrows: the coastal flow, shelf current, shelfbreak jet, and offshore recirculation. The main part of the Beaufort gyre is indicated as well. The dashed yellow arrows denote the deduced bifurcation following the results of Hyun (2004). The mooring indicated by the star closest to shore was only deployed in 2016–2017, while the other moorings were deployed from 2016 to 2018.

3.2.2 Water Column Structure

3.2.2.1 Mean Conditions

The water column structure is examined through plots of the minimum, mean, and maximum of the temperature and salinity profiles over each of the two years. The temperature statistics are presented in Figure 107. These statistics reveal that the average water temperatures at sites M1 and M2 are consistently at or below -1°C, with the minimum temperature at the freezing point temperature of -1.75 °C. There are upward excursions of up to 2 to 4°C closer towards the surface, the amount depending on the site and how close to the surface the measurements were able to get. At sites M3 and M4, the mean water temperatures are somewhat warmer at 50 m depth, at 200 m depth and especially at 250 m depth, but generally remain at or below 0°C.

The salinity statistics are illustrated in Figure 108. The range in salinities tends to be larger in the upper 50 m of the water column in comparison to greater water depths. The salinities, and hence the densities, increase considerably from 31 to 34.5 PSU, with increasing depth, through the upper 200 m to the underlying Atlantic Water with higher salinities greater than 33.64 PSU. In general, the 2017-18 mean salinities are larger in the upper 50 m of the water column near the surface than their 2016–17 counterparts. Overall, the upper 50 m has the highest level of variability over the year and the lowest salinities, through the cold halocline layer (low water temperatures and increasing salinities at 140 m and 200 m), through the Atlantic water mass at 250 m (mean salinity of 34.55, mean temperatures of 0.0°C).

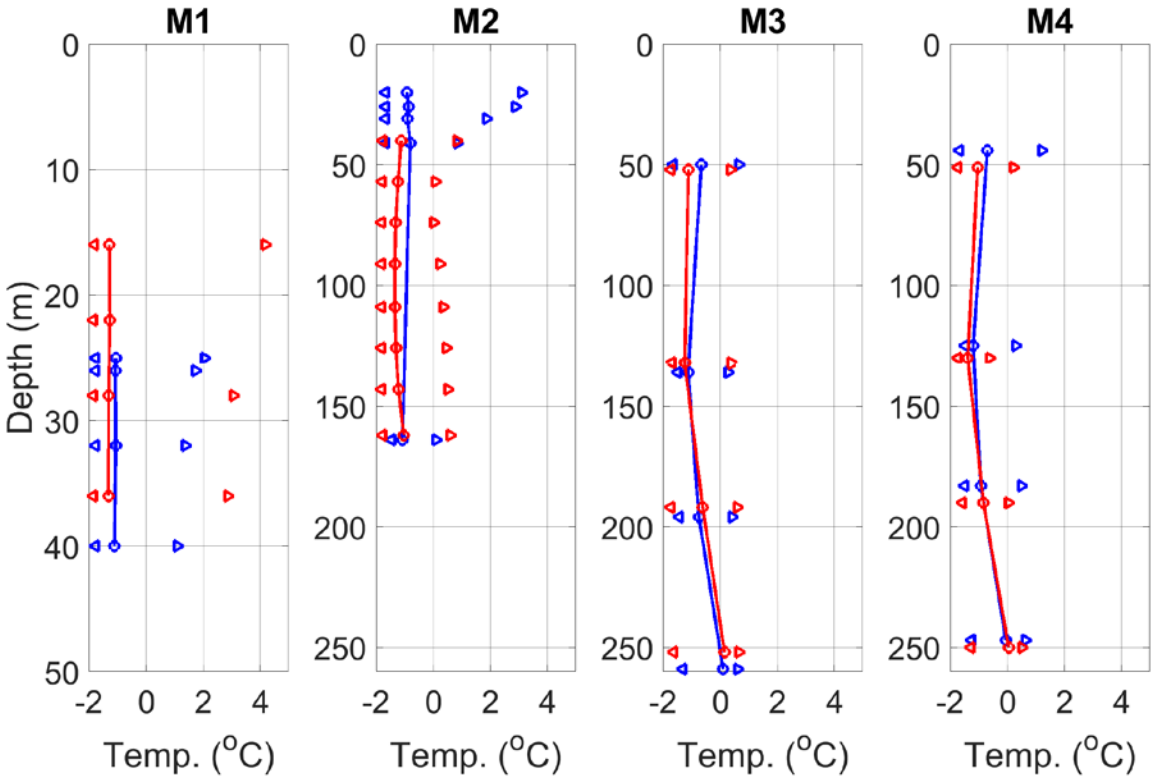

Figure 107. Mean temperature profile using circles connected by a line, and the maximum and minimum temperature profiles using triangles for 2016–17 (blue) and 2017–18 (red)

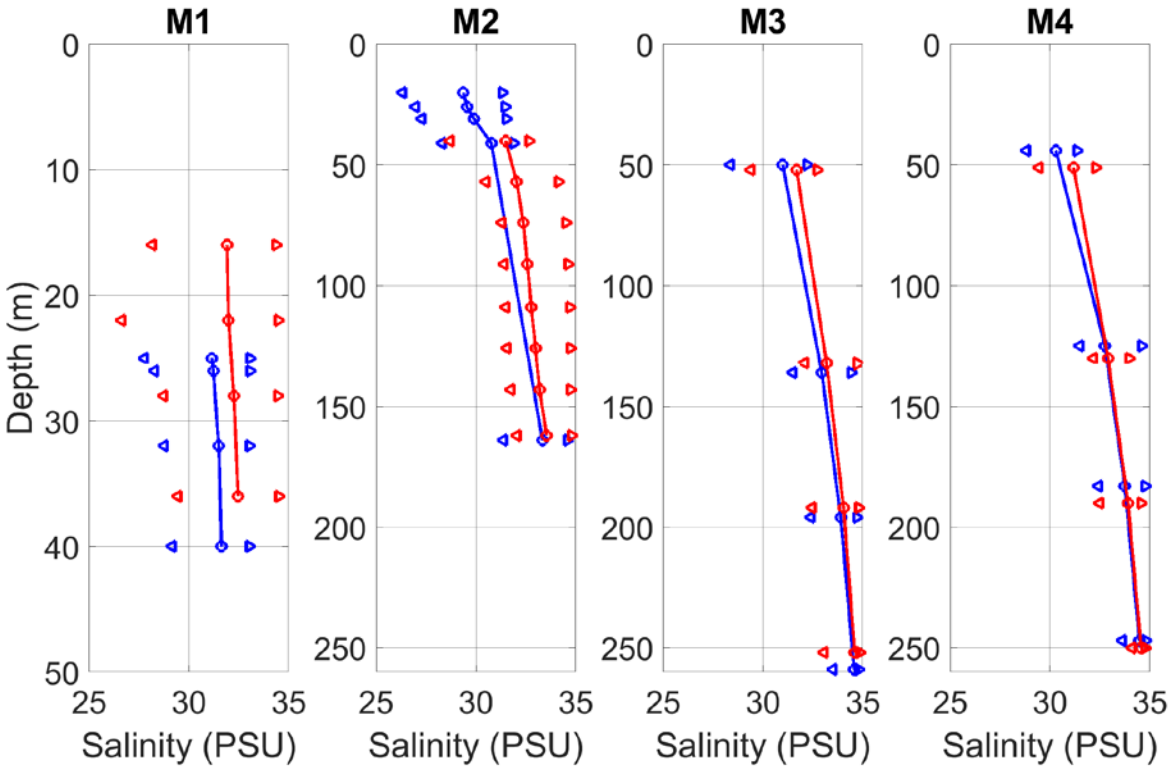

Figure 108. Mean salinity profile using circles connected by a line, and the maximum and minimum temperature profiles using triangles for 2016–17 (blue) and 2017–18 (red)

3.2.2.2 Seasonality

The seasonality of the water column structure is examined through seasonal plots of the minimum, mean, and maximum temperature and salinity. In transitioning from fall (Figure 109) to winter (Figure 110), the near-surface temperatures at M1 and M2 show a reduction in the range of values observed as well a reduction in the mean. Mean temperature values at 40–50 m are lower at the mid-shelf M1 site at -1.2°C by comparison to -0.4°C at site M2 in the fall, and there is a decrease in winter at site M1 and M2 to -1.3 and -1.4 °C, respectively. At depth and at the M3 and M4 sites, there is a smaller reduction in water temperatures from fall to winter. The cooling of the upper portion of the water column reflects the formation of sea ice at the surface which removes heat from the upper water column and can also result in increases in salinity as freezing of sea water extrudes salt into the water column below.

The seasonal differences in water temperature from the first to the second year of observations is rather small at most mooring sites, but in the fall, the water column temperatures below 100–150 m were lower in the first year than the second year by as much as 1°C, especially at site M3, while in winter the year-to-year differences were much smaller but still cooler at 200 m depth by 0.2 to 0.4°C in the first year.

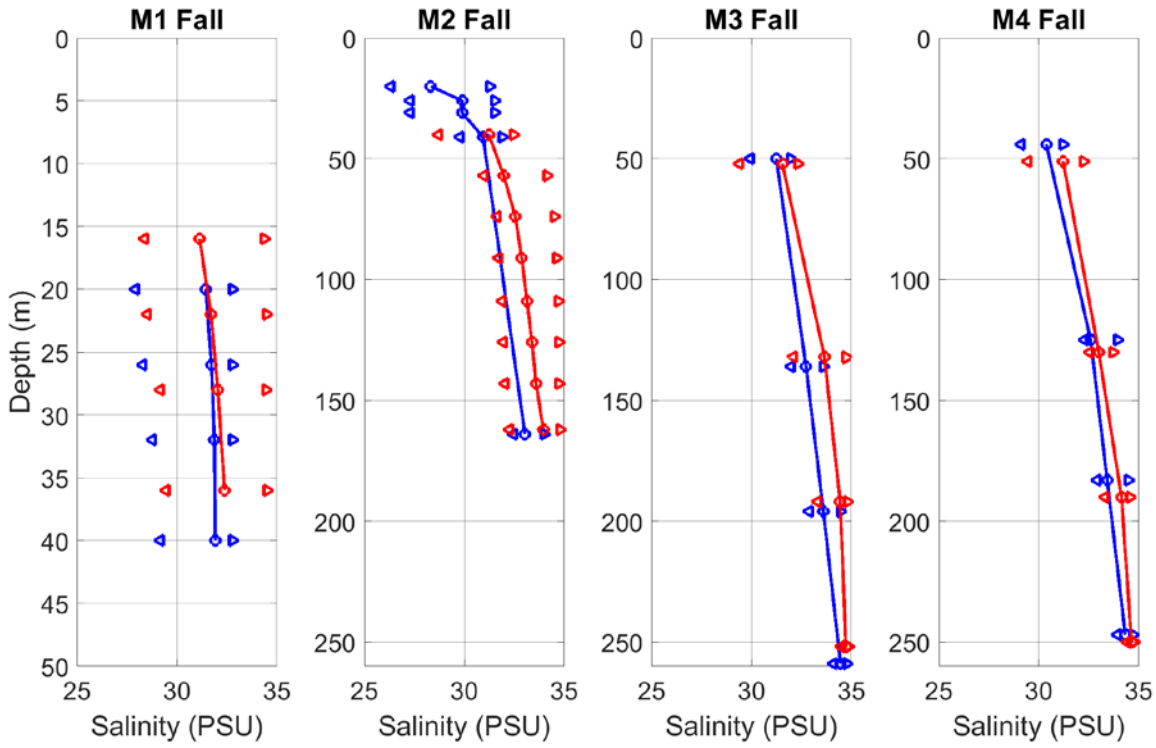

Figure 109. Fall temperature profile using circles connected by a line, and the maximum and minimum temperature profiles using triangles for 2016–17 (blue) and 2017–18 (red)

In transitioning from winter (Figure 110) to spring (Figure 111), the M1 and M2 sites start to expand in the range of values observed towards the surface, but at depth, the range in values at M2 continues to narrow. At M3 and M4, the range in values tends to continue to narrow in the transition from winter to spring. The mean values at these two sites tend not to change significantly in the winter to spring-time period. In the transition from spring (Figure 111) to summer (Figure 112), there are only marginal differences in the temperature statistics at the M1 site. The M2 site shows signs of warming, especially at depths towards the surface. This warming trend towards the surface is also observed at the M3 and M4 sites.

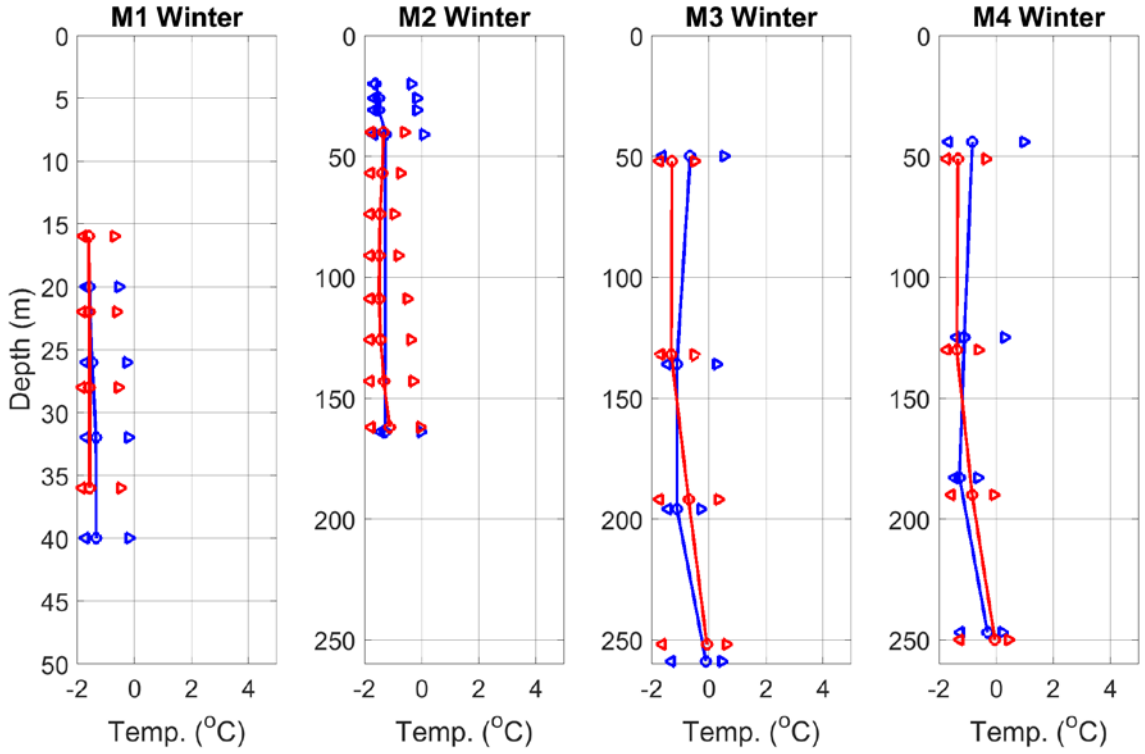

Figure 110. Winter temperature profile using circles connected by a line, and the maximum and minimum temperature profiles using triangles for 2016–17 (blue) and 2017–18 (red)

The year-to-year differences in water column temperature in spring and summer were also generally quite small, and tended to be opposite to that of the fall and winter, with modestly warmer temperatures in the first year in the upper parts of the water column, above 150 m depth, especially at sites M1, M2, and M3 in spring and at all four sites in summer.

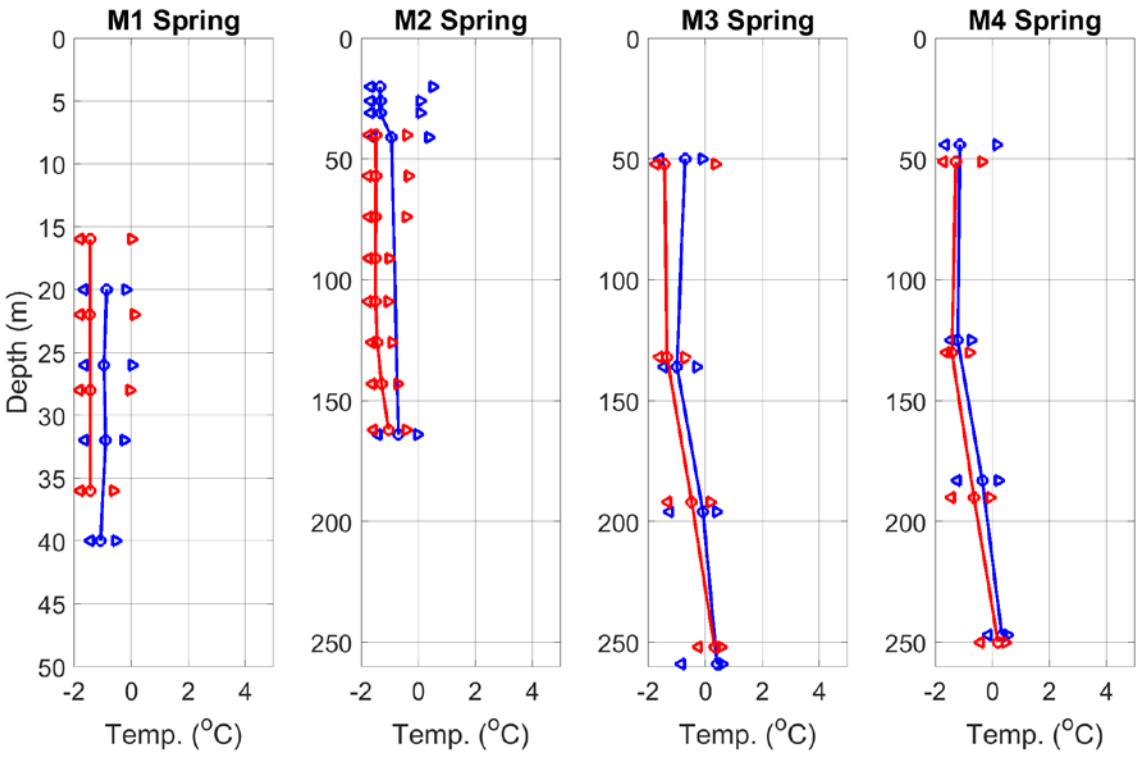

Figure 111. Spring temperature profile using circles connected by a line, and the maximum and minimum temperature profiles using triangles for 2016–17 (blue) and 2017–18 (red)

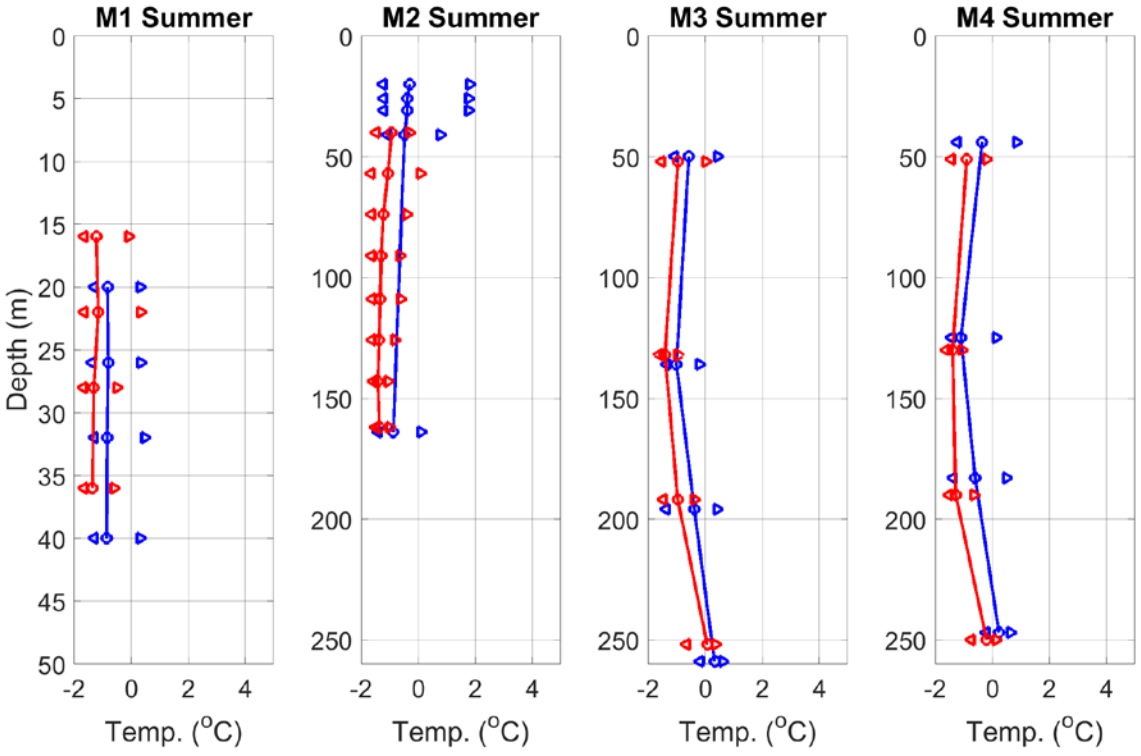

Figure 112. Summer temperature profile using circles connected by a line, and the maximum and minimum temperature profiles using triangles for 2016–17 (blue) and 2017–18 (red)

The salinity statistics profiles are illustrated for the fall (Figure 113) and for the winter (Figure 114). At all four sites there tends to be a reduction in the range of salinities. Changes in the mean tend to be very small, except at the M1 site in winter where the mean salinity seems to be increased at 40 m from 30.9 to 32.9 PSU from the first year to the second year. In the transition to the spring (Figure 115) the M1 site shows some salinification at near-surface levels especially in the first year. At the M2 site, the differences are marginal, but there is a slight freshening in the first year at M3 and a slight salinification at the M4 site, at the 50 m level in the second year. By the summer, the mean salinities at M1 have decreased compared to the spring, in the second year, and there is a larger range in values (Figure 116).

In most cases, the differences between the first year and the second year tend to be larger than those of the seasonal changes within each year at any given mooring site and water depth. The salinities were generally higher in the second year than in the first year especially in winter and spring at sites M1 and M2, above 150 m, and at site M3 in fall, winter, and spring above 200 m. In summer, the year-to-year differences are much smaller, except for a small decrease in salinity at site M4 at mid-depths (130 and 200 m).

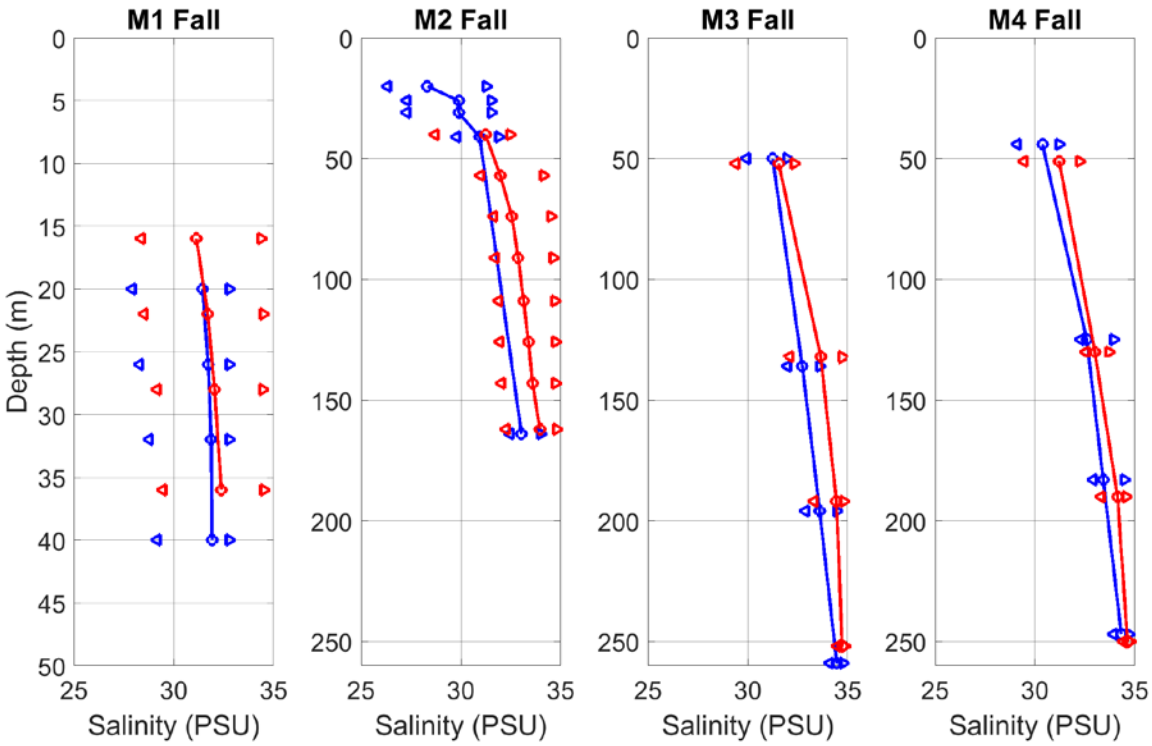

Figure 113. Fall salinity profile using circles connected by a line, and the maximum and minimum temperature profiles using triangles for 2016–17 (blue) and 2017–18 (red)

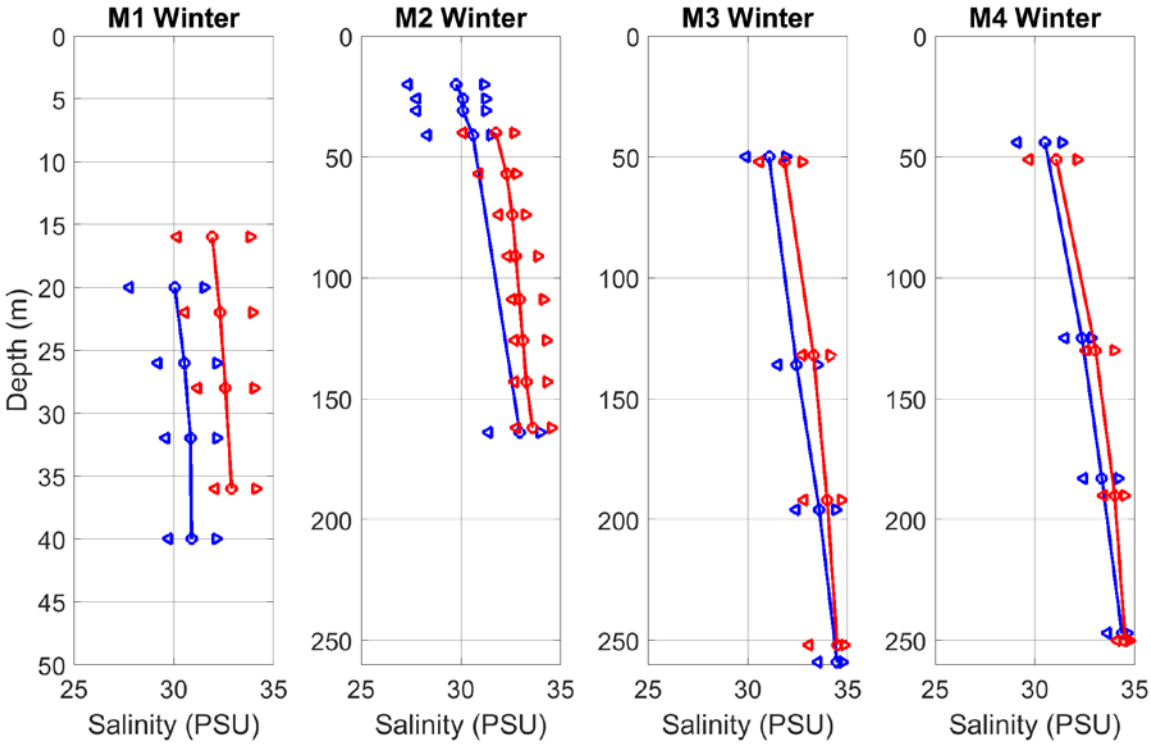

Figure 114. Winter salinity profile using circles connected by a line, and the maximum and minimum temperature profiles using triangles for 2016–17 (blue) and 2017–18 (red)

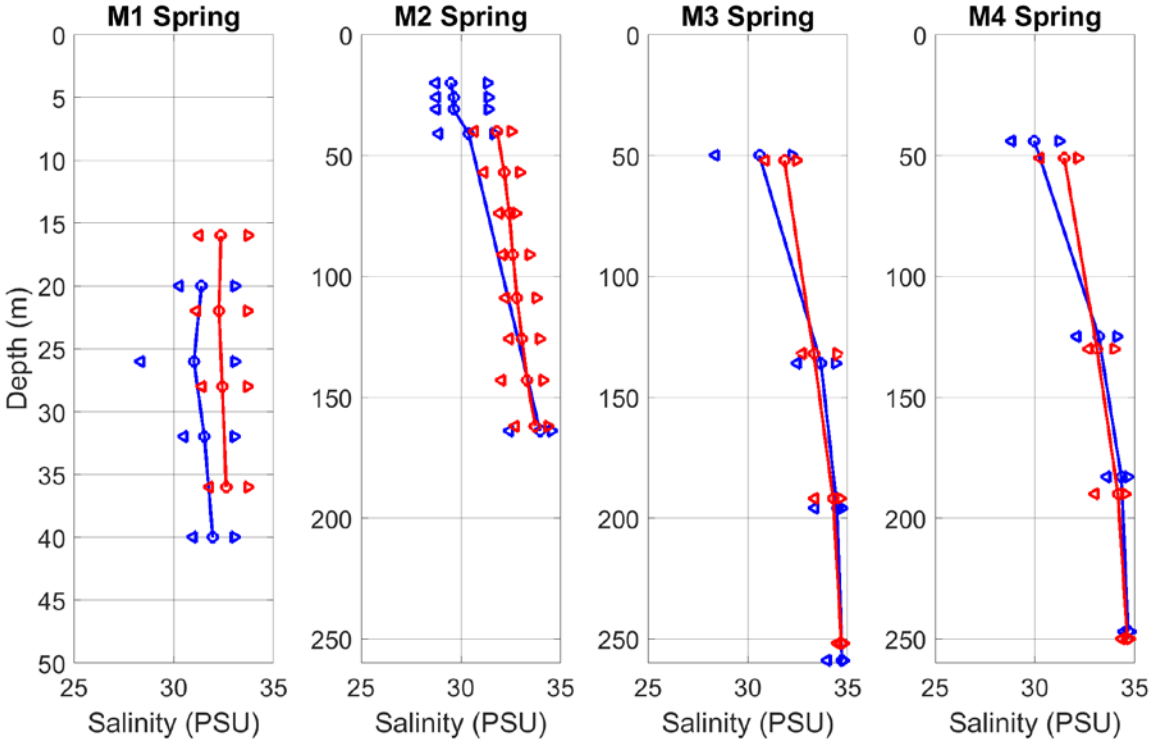

Figure 115. Spring salinity profile using circles connected by a line, and the maximum and minimum temperature profiles using triangles for 2016–17 (blue) and 2017-–8 (red)

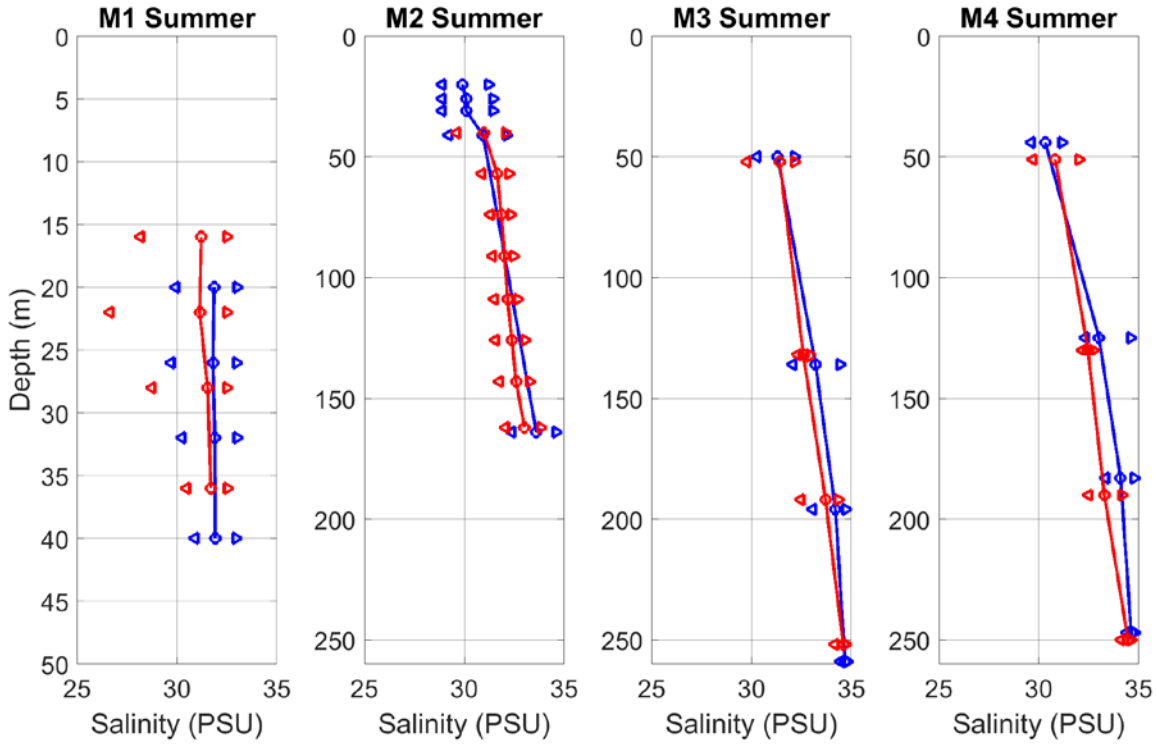

Figure 116. Summer salinity profile using circles connected by a line, and the maximum and minimum temperature profiles using triangles for 2016–17 (blue) and 2017–18 (red)

3.2.2.3 Drivers

The temperatures of the water column, especially in the upper 50 m, are strongly influenced by the cooling of the atmosphere and presence of sea ice in fall and winter and the warming of the atmosphere resulting in the break-up of the sea ice in spring and removal of this ice through much of the summer. For the latter period, direct solar insolation can cause heating of the uppermost portion of the water column. Deeper in the water column, the influence of wind-driven upwelling (bringing colder water at depth closer to the surface) and downwelling (sending relatively warmer water to greater depths) can be important, especially in summer and early fall.

The salinities at any particular depth can be influenced by many drivers. During the open water season, upwelling winds (winds blowing from the east) can draw salty water from depth over the Beaufort Shelf and inner slope. Downwelling events can likewise reduce the salinities at depth. Sea ice can also be a driver of salinity. Starting in the fall when sea ice starts to form, saline brine is rejected during the ice formation process. This brine tends to be dense and will sink down into the water column. This process can continue through the winter. Starting in late spring, solar insolation can start melting the sea ice. This process releases fresh water onto the Beaufort Shelf. Another source of fresh water is the freshet from the Mackenzie River, usually in May/June. However, the lower salinity water due to ice melt and river discharges is largely confined to the uppermost part of the water column, which may be above the

measurement depths that can be obtained from moored instruments. Wind events can further complicate the salinity profiles by mixing this fresh water deeper into the water column. Another influence on salinity is the presence of ocean currents which carry different water masses into the study area, including Pacific water episodically moving eastward at the inner shelf, Polar Water (Timmermans and Marshall, 2020) originating to the north of the Canadian Arctic Archipelago, and water originating in Amundsen Gulf and further eastward which may enter the southeastern portion of the study area.

3.2.3 Currents

3.2.3.1 Mean Conditions

The mean currents are examined using speed-direction distributions in the form of compass rose plots for the entire deployment in this case. The color of each segment denotes its speed interval. The radial length of each segment denotes the proportion of measurements within the illustrated speed and direction interval. The maximum and mean values for each directional sector are illustrated through the second radial scale as the red and green lines, respectively.

Compass rose plots for the near-surface currents are presented in Figure 117. The currents at the M1 site are very large, up to just over 200 cm/s and flow predominantly to the northwest. The near-surface currents at M2 have an even smaller proportion of measurements to the southeast, but the spread in current direction about the northwest direction is greater at M2 than at M1. The current speeds are also much reduced, but still rapid as they can be in excess of 125 cm/s. At the M3 site, the near-surface current speeds are less than 75 cm/s. They tend to be oriented primarily between the northeast through southwest to the southeast directions. The M4 near-surface currents are also less than 75 cm/s but are oriented primarily toward the west-southwest. There are differences between the two mooring years of measurements, with somewhat higher speeds in 2016–2017 *vs.* 2017–2018 especially at sites M1, M2, and M4. At site M3, there are more flows to the NW in 2017–2018 by comparison to 2016–2017.

Compass rose plots for currents at 150 m depth are presented in Figure 118. Across all four sites, the current speeds at this depth are diminished considerably by comparison to the near surface. At the M2 these deeper currents are more bi-directional. At the M3 site, the deep currents are more directional, mostly oriented toward the south-southwest. The directional distribution at the M4 site is very similar between the near-surface and 150 m depth. Between the two mooring years, the currents are generally similar, although a slight shift to more flows to the south-southeast at site M2 and site M3 in 2017–2018 *vs.* 2016–2017 was observed, while there was a shift to more southwest flows in 2017–2018 *vs.* 2016–2017 at M4.

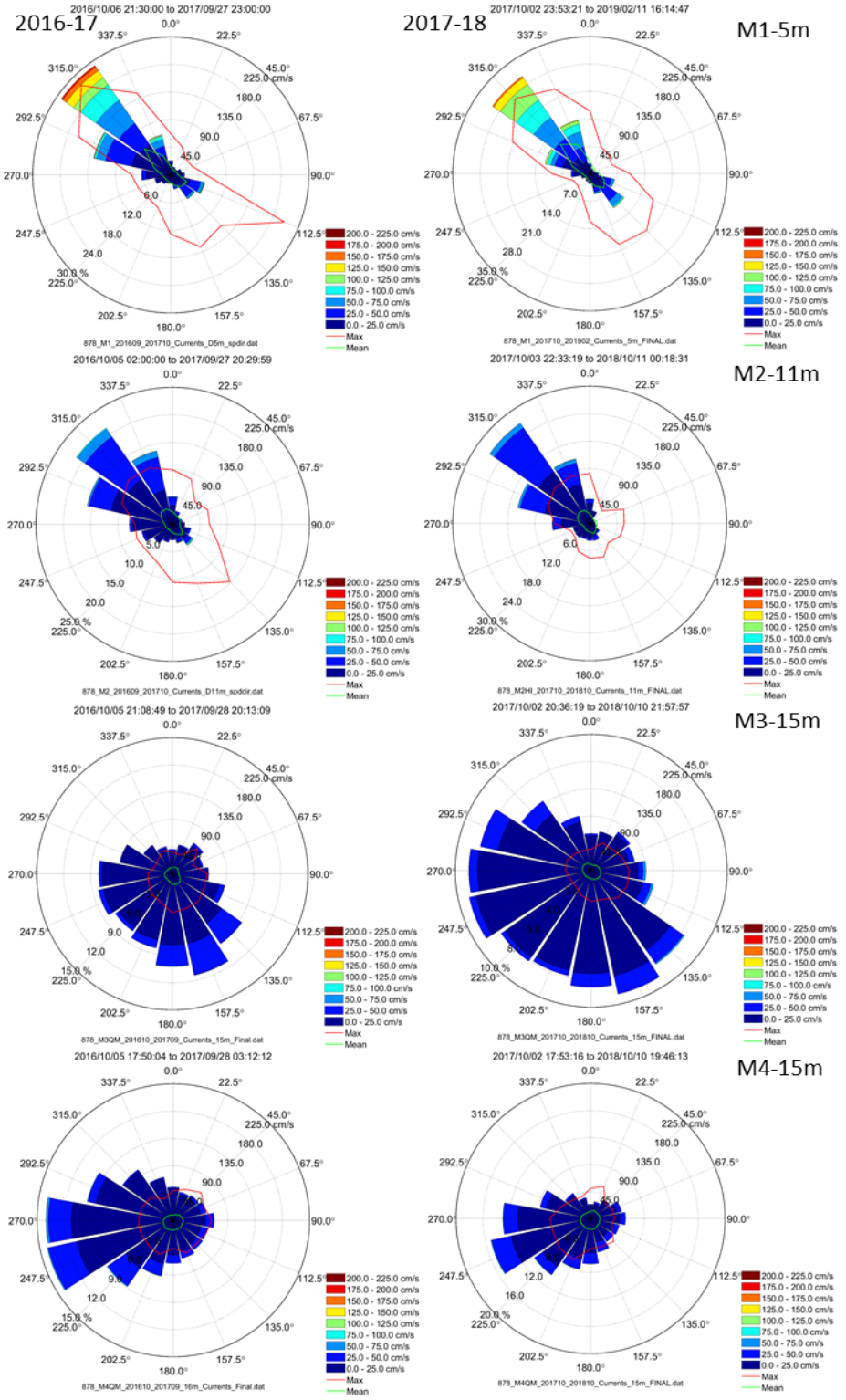

Figure 117. Compass rose plots of current speed and direction for 2016–17 (left) and 2017–18 (right) for (from top to bottom) M1, M2, M3, and M4 at near-surface depths (5 to 15 m). Directions are expressed as directions towards (e.g. Flow/drift toward the east has a 90° direction).

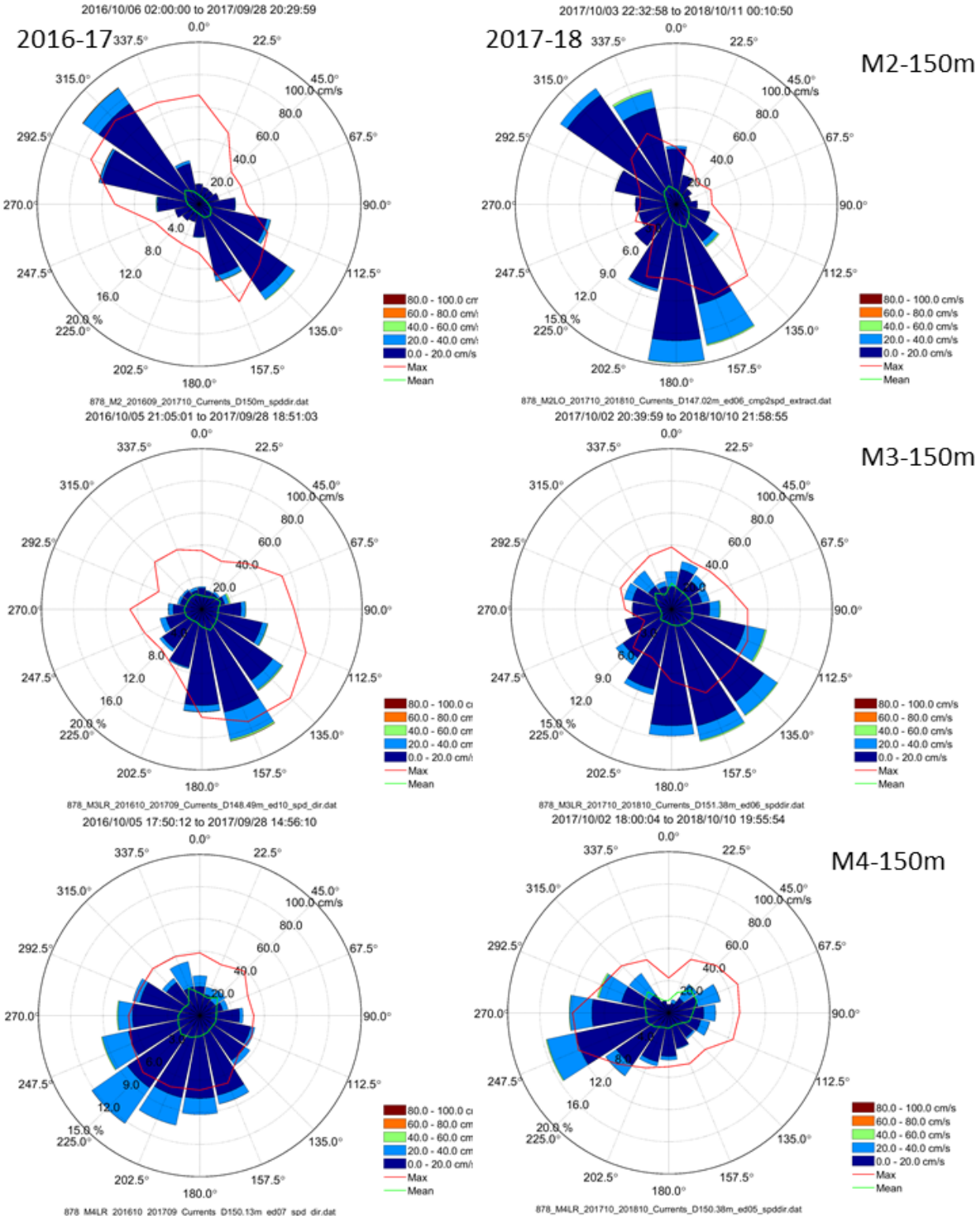

Figure 118. Compass rose plots of current speed and direction for 2016–17 (left) and 2017–18 (right) for (from top to bottom) M2, M3, and M4 at 150 m depth. Directions are expressed as directions towards (e.g. Flow/drift toward the east has a 90° direction).

Compass rose plots for 250 m depth are illustrated in Figure 119. The current speeds at this depth dropped by a factor of two or more compared to the 150 m depth. The M3 direction distribution included more observations with flow to the south-southwest at 250 m. The M4 direction distribution was more bimodal to the east and to the west, but with a significant proportion of off-axis observations. The current distributions at 250 m are quite similar between the two years, although some more flows to the south-southeast were observed at M3 in 2017–2018 *vs.* 2016–2017, and larger speeds to the west were observed in the second year at M4 compared to year 1.

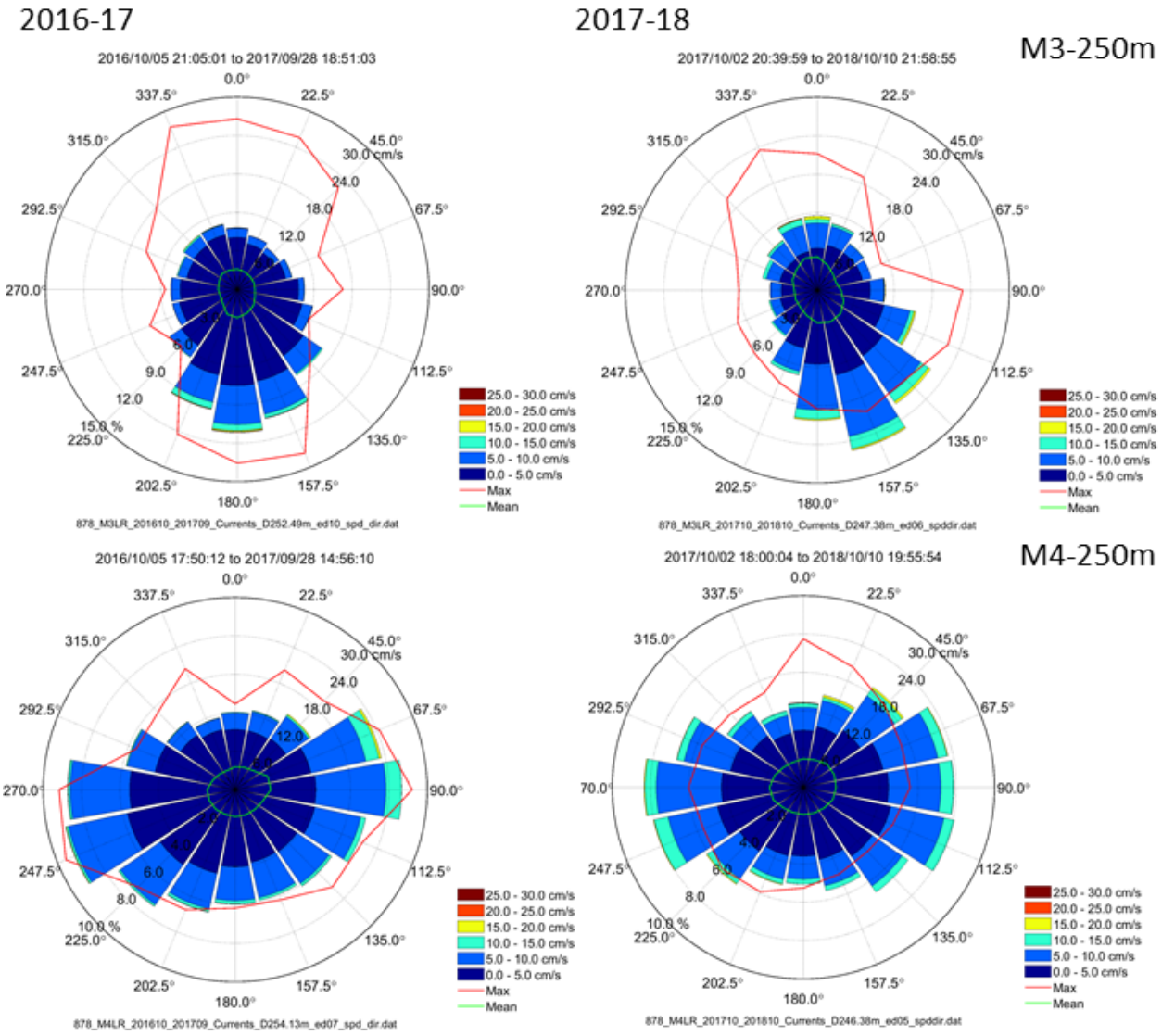

Figure 119. Compass rose plots of current speed and direction for 2016–17 (left) and 2017–18 (right) for (from top to bottom) M3 and M4 at 250 m depth. Directions are expressed as directions towards (e.g. Flow/drift toward the east has a 90° direction).

The general characteristics of the flows are summarized in Table 47.

Table 47. Summary of general flow characteristics by depth and site

Depth	Site	Comment
Near Surface	M1	Speeds > 200 cm/s, predominant NW flow
	M2	Speeds > 125 cm/s, more spread in NW flows
	M3	Speeds < 75 cm/s, flows NW and counterclockwise to SE
	M4	Speed < 75 cm/s, flow primarily to WSW.
150 m	All Sites	Diminished speeds compared to near-surface; mostly < 20 cm/s with largest speeds of ~ 40 cm/s
	M2	Flow is more bi-directional than near-surface
	M3	Flow is more directional than near-surface – to the S-SE
	M4	Similar character to the near-surface
250 m	All Sites	Diminished speeds compared to the 150m currents by a factor of 2 or more, generally < 5 cm/s.
	M3	Increased proportion of flows to the NW, but SE flow is still dominant
	M4	Bi-modal flow, but significant off-axis flow.

Direct impact of surface winds is limited to near-surface currents, with much larger speeds especially at site M1. The influence appears to be smaller at sites M3 and M4 in the near surface level and at all sites at depth. Even for near-surface currents at M1 and M2 there are some differences, most notably the much larger current speeds at M1 which would appear to be more related to an amplification of the near-surface current response to wind forcing given the spatially uniform surface winds. Site M2 currents have a more pronounced dominance of the northwestward currents than would be expected from the more bi-directional southeasterly vs. northwesterly winds, which indicates that other factors in addition to direct wind forcing must be in play here. At 150 m depth, sites M2 and M3 have more southeastward flows consistent with episodic eastward flows of Pacific water at these mid-depth levels. Current speeds at site M3 and M4 at 250 m depth are much reduced from those at shallower depths at all sites.

3.2.3.2 Seasonality

The seasonality of the near-surface currents at the four sites is examined using compass rose plots, as introduced in Section 3.2.3.1. For the near-surface currents at M1, some of the fastest current speeds are observed in the fall. The orange sector and large light blue sector in the fall panel of Figure 120 indicate that these fast events were most often directed towards the northwest. The winter of 2016-17 and the summer of 2017–18 are distinct in that they have a large proportion of southeastward current measurements at a site which predominantly has flow to the northwest. As the M1 site was not recovered at the same time as the other sites, there is an additional fall and winter season of current measurements which are examined in the context of the 2016–17 and 2017–18 seasons (Figure 121). The southeastward flow in the fall of 2018 and the winter of 2019 are particularly small, with larger speeds to the northwest, as compared to the preceding 2 years.

At site M1, the fall surface winds exhibit seasonally large occurrences of southeasterly winds, parallel to northwestward near-surface currents, so wind driven forcing appears to be important in this season. Similarly, the winter surface winds exhibit more northwesterly winds which is consistent with more southeastward near-surface currents, especially in 2016–2017, which again is consistent with the distribution of near-surface currents at site M1. Similarities between the spring and summer surface winds for the two different years are also apparent with the near-surface M1 currents.

The seasonality of the near-surface currents at the M2 site is illustrated in Figure 122. Currents in excess of 120 cm/s to the southeast are observed in the winter of 2016–17, though they account for 5% or less of the observations at this site. A storm on January 5–6, 2017 with wind speeds from the northwest of 25 m/s at Pelly Island and 35 m/s at Herschel Island are responsible for the majority of these observations. Currents of over 1 m/s toward the southeast are also observed in the summer of 2016–17 due to northwesterly winds of 15 m/s at Pelly Island which briefly push the currents in excess of 100 cm/s. Such energetic events are not observed in the 2017–18 season. In general, the fall is the most energetic season for near-surface currents.

The seasonality of the near-surface currents at the M3 site is illustrated in Figure 123. The strong directionality observed at M1 and M2 breaks down further offshore and the current directions vary more widely. Near-surface currents at M3 were also strongest in the fall in 2017-2018, similar to M1 and M2. In 2016–17, however, winter near-surface currents are strongest with 0.78% of their observations in excess of 60 cm/s, followed by summer, with 0.62% of observations above 60 cm/s.

The seasonality of the near-surface currents at the M4 site is illustrated in Figure 124. The currents tend to be more directional than the M3 currents, but not as directional as the M1 and M2 currents. Overall, the strongest currents are observed in the fall, though there is a larger proportion (5.5%) of observations in the 45–60 cm/s interval in the summer of 2016–17 summer.

For sites M2, M3, and M4, the seasonal directional distributions of currents, even at near-surface levels, are quite different than the equivalent seasonal surface wind distributions, so linkages between surface wind forcing and the ocean currents at these sites are not readily apparent from comparisons of directional distributions.

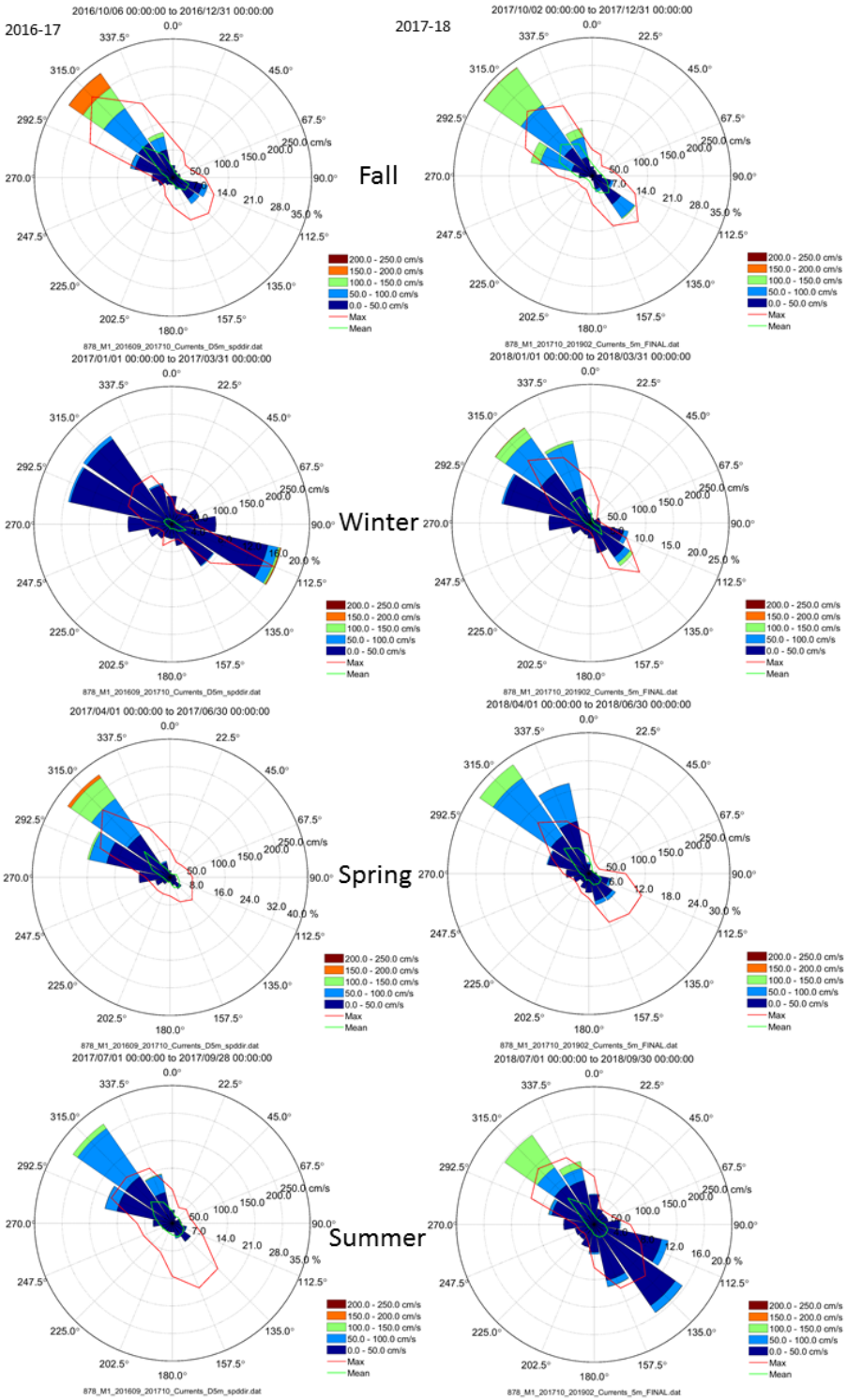

Figure 120. Compass rose plots of current speed and direction at 5 m depth for the M1 site for fall (top), winter (top middle), spring (bottom middle), and summer (bottom) for 2016–17 (left) and for 2017–18 (right). Directions are expressed as directions towards (e.g. Flow/drift toward the east has a 90° direction).

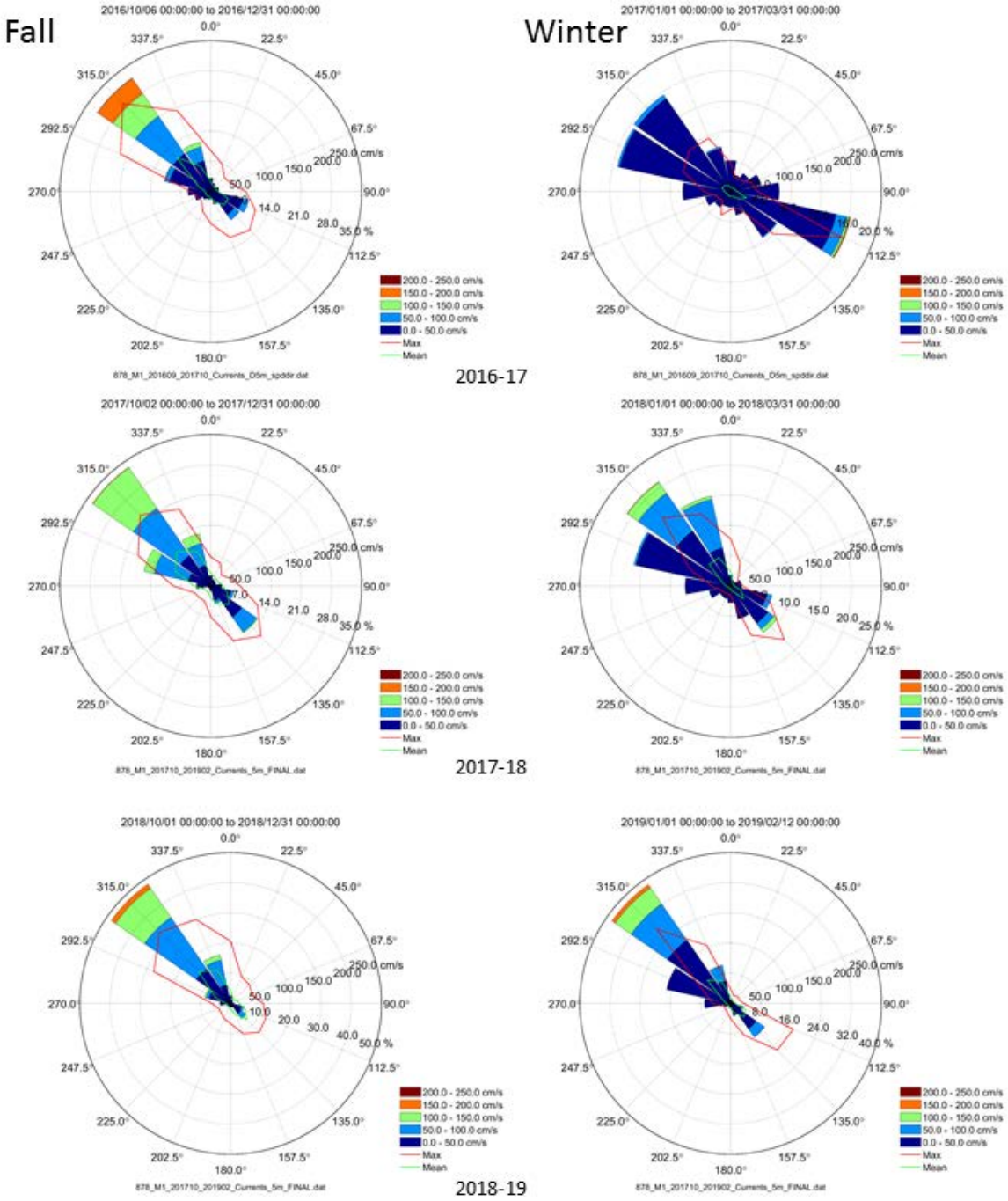

Figure 121. Compass rose plots of current speed and direction at the M1 site for all three instances of fall measurements (left) and winter measurements (right) made at 5 m depth for the 2016–17 (top), 2017–18 (middle), and 2018–19 (bottom). Directions are expressed as directions towards (e.g. Flow/drift toward the east has a 90° direction).

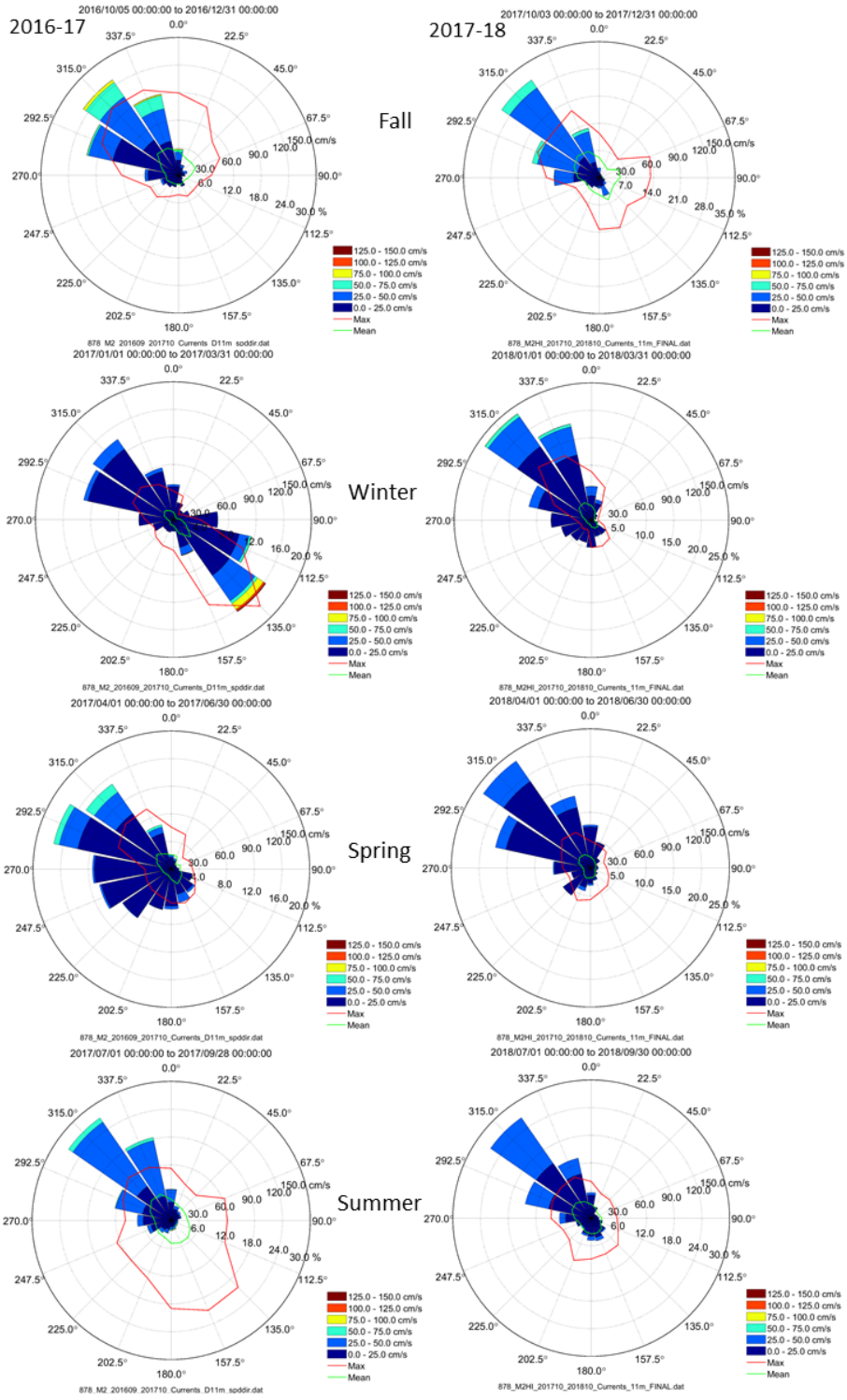

Figure 122. Compass rose plots of current speed and direction at 10 m depth for the M2 site for fall (top), winter (top middle), spring (bottom middle), and summer (bottom) for 2016–17 (left) and for 2017–18 (right). Directions are expressed as directions towards (e.g. Flow/drift toward the east has a 90° direction).

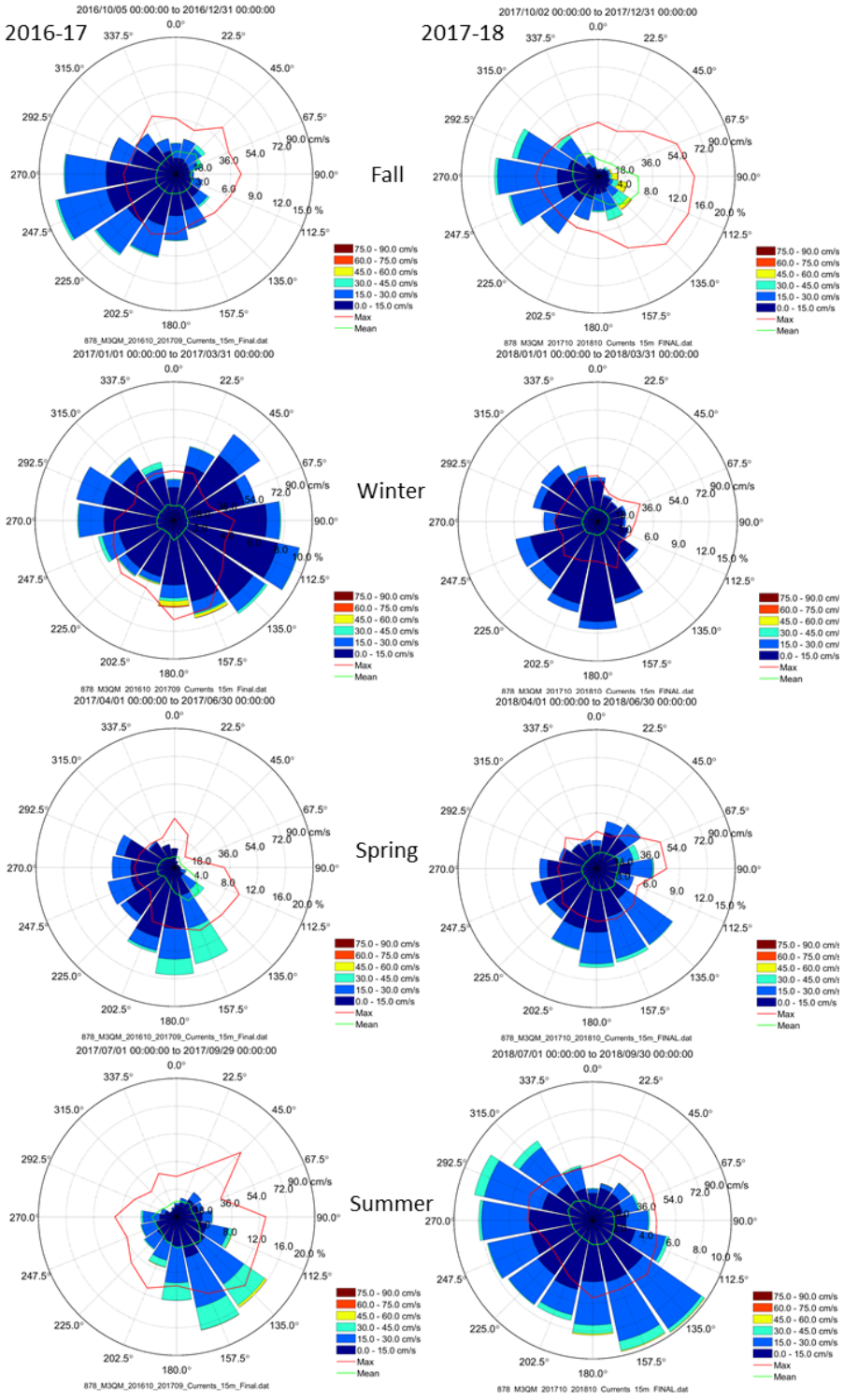

Figure 123. Compass rose plots of current speed and direction at 15 m depth for the M3 site for fall (top), winter (top middle), spring (bottom middle), and summer (bottom) for 2016–17 (left) and for 2017–18 (right). Directions are expressed as directions towards (e.g. Flow/drift toward the east has a 90° direction).

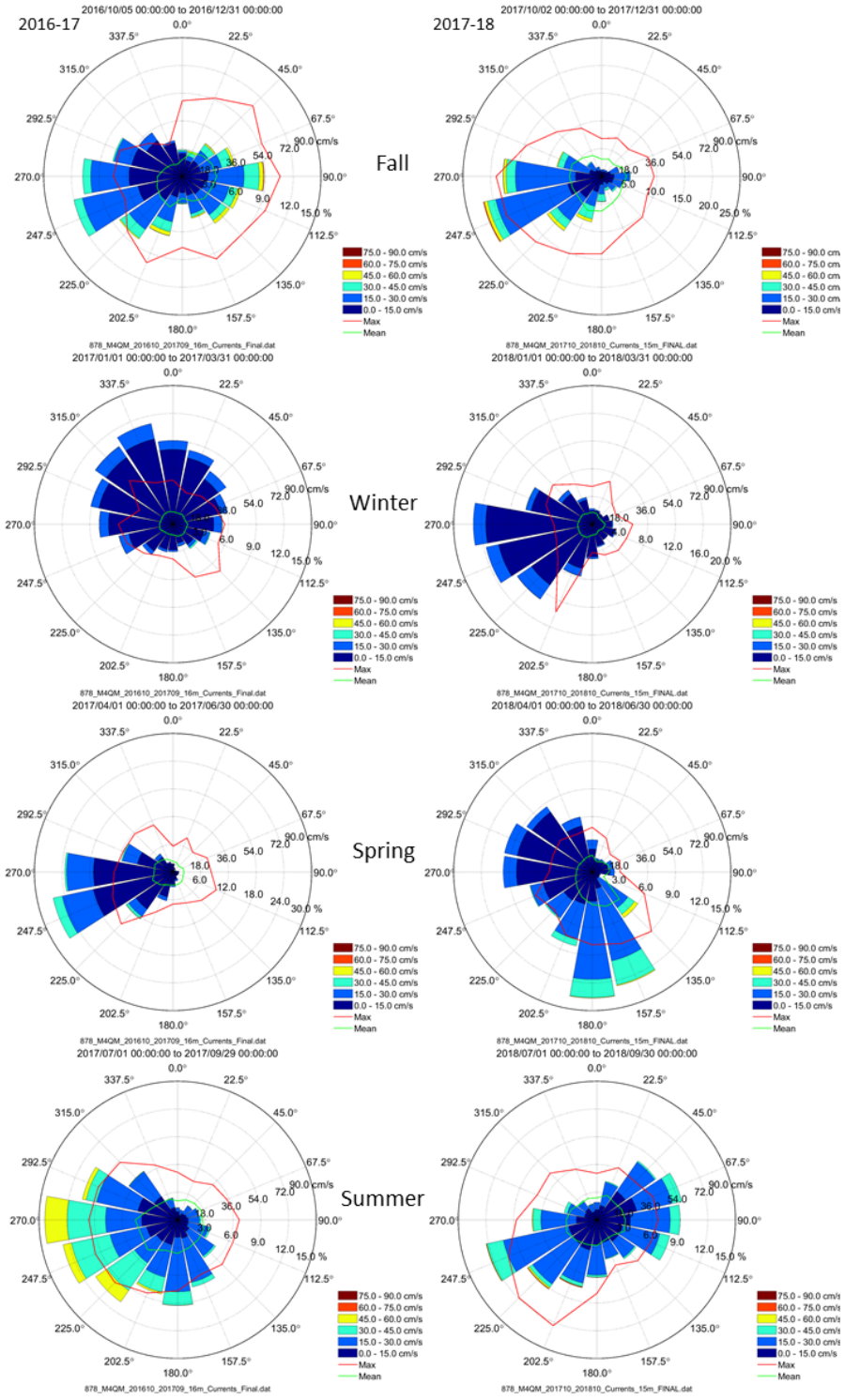

Figure 124. Compass rose plots of current speed and direction at 15 m depth for the M4 site for fall (top), winter (top middle), spring (bottom middle), and summer (bottom) for 2016–17 (left) and for 2017–18 (right). Directions are expressed as directions towards (e.g. Flow/drift toward the east has a 90° direction).

The seasonality of the 150 m currents at M2 is illustrated in Figure 125. The speeds are reduced compared to the near-surface. In each of the seasons, especially in fall, there is a much stronger component towards the south east as compared to the near-surface, except for the spring of 2018 when there is a large proportion of currents directed toward the south.

The seasonality of the 150 m currents at M3 is illustrated in Figure 126. In general, the speeds are reduced compared to the near surface. In the fall the currents are directed more towards the south and the southeast than the near-surface currents which are directed more towards the west. In the winter of 2016–17, the currents tended to be much more directional at 150 m depth. In the winter of 2017–18 the currents tended to favor currents to the southwest. In the spring of 2017, the currents are directed primarily towards the south southeast, whereas at the near-surface the currents showed a little more flow towards the northwest. This predominance towards the south east was retained in the spring of 2018. In the summer of 2017, the 150 m currents show the same predominance of flow toward the southeast observed at the near surface. In the summer of 2018, the 150 m currents show the same transformation to directional flow observed at the near surface, but the directionality becomes even stronger at the 150 m level.

The seasonality of the 250 m currents at M3 is illustrated in Figure 127. There is a further reduction in speed at this depth compared to the waters above. The currents at 250 m depth continue to show a bias towards the south and southeast, but they tend to have a small but still significant counterflow to the northwest. The summer of 2018 still has flow towards the north, but it is the only season in which the proportion of observations in this direction did not increase compared to the 150 m depth.

The seasonality of the 150 m currents at M4 is illustrated in Figure 128. Generally, the current speeds are reduced compared to the near-surface and in the fall, there is generally strong resemblance between the 150 m depth and near-surface currents. But in the fall of 2016, the 150 m currents are almost all in the southwest quadrant. In the winter season, there is a trend towards more directional flow at 150 m compared to the near surface. In the spring the 150 m currents are mostly in the southwest quadrant. In the near-surface, the currents are directed towards the west in 2017, and along a northwest-southeast axis in 2018. In the summer of 2017, the currents are directed in a 90-degree cone toward the south at 150 m depth, but in a similarly sized cone directed towards the southwest at the near-surface. In the summer of 2018, the currents are bidirectional at both depths, but the directional distribution is somewhat narrower at the 150 m depth.

The seasonality of the 250 m currents at M4 is illustrated in Figure 129. There is a further reduction in current speeds compared to the 150 m level. Overall, the directional distributions are very broad, especially in the summer and fall. Exceptions include the winter which shows bidirectional flow along the east-west axis and the spring of 2017 which has flow mostly in the southeast quadrant.

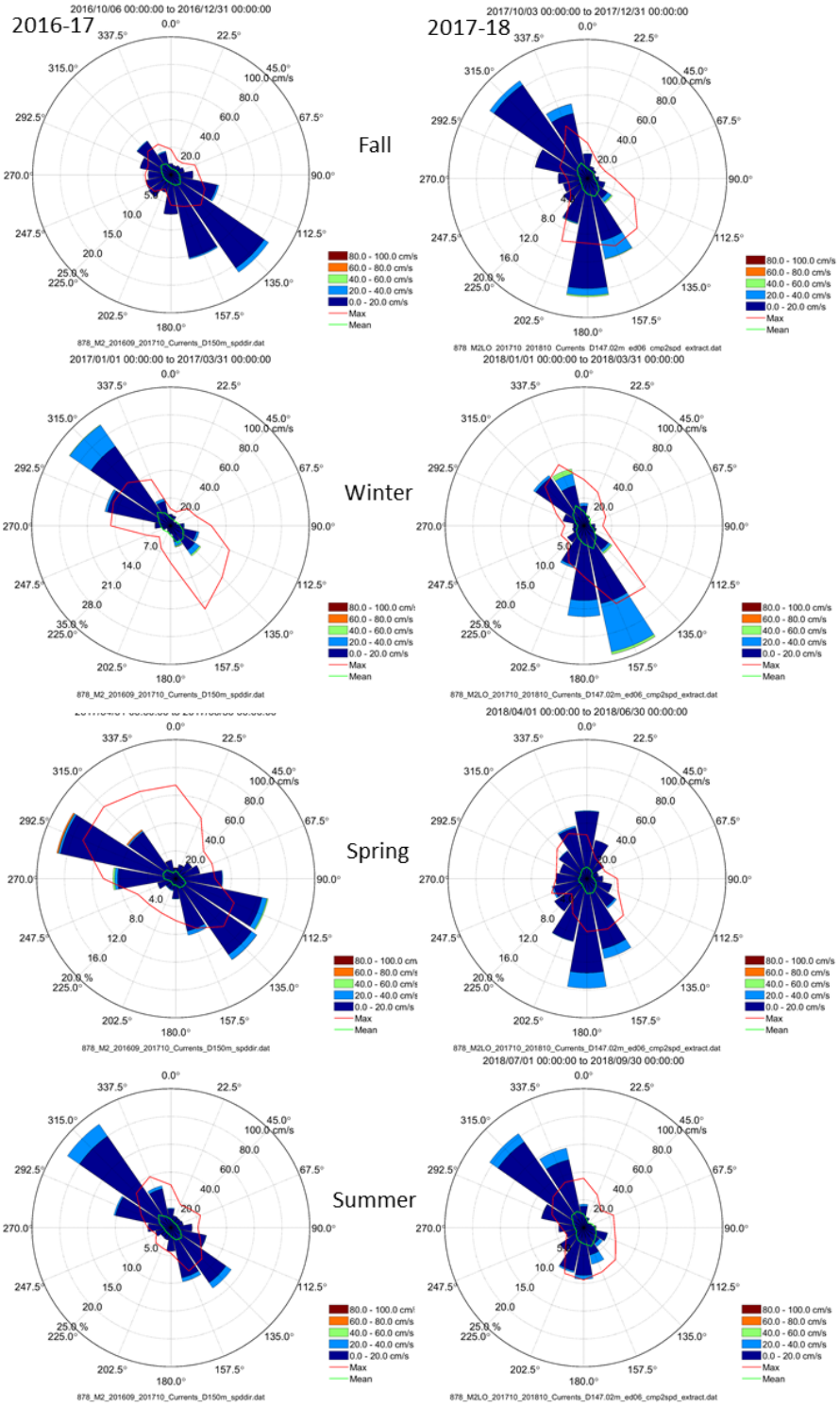

Figure 125. Compass rose plots of current speed and direction at 150 m depth for the M2 site for fall (top), winter (top middle), spring (bottom middle), and summer (bottom) for 2016–17 (left) and for 2017–18 (right). Directions are expressed as directions towards (e.g. Flow/drift toward the east has a 90° direction).

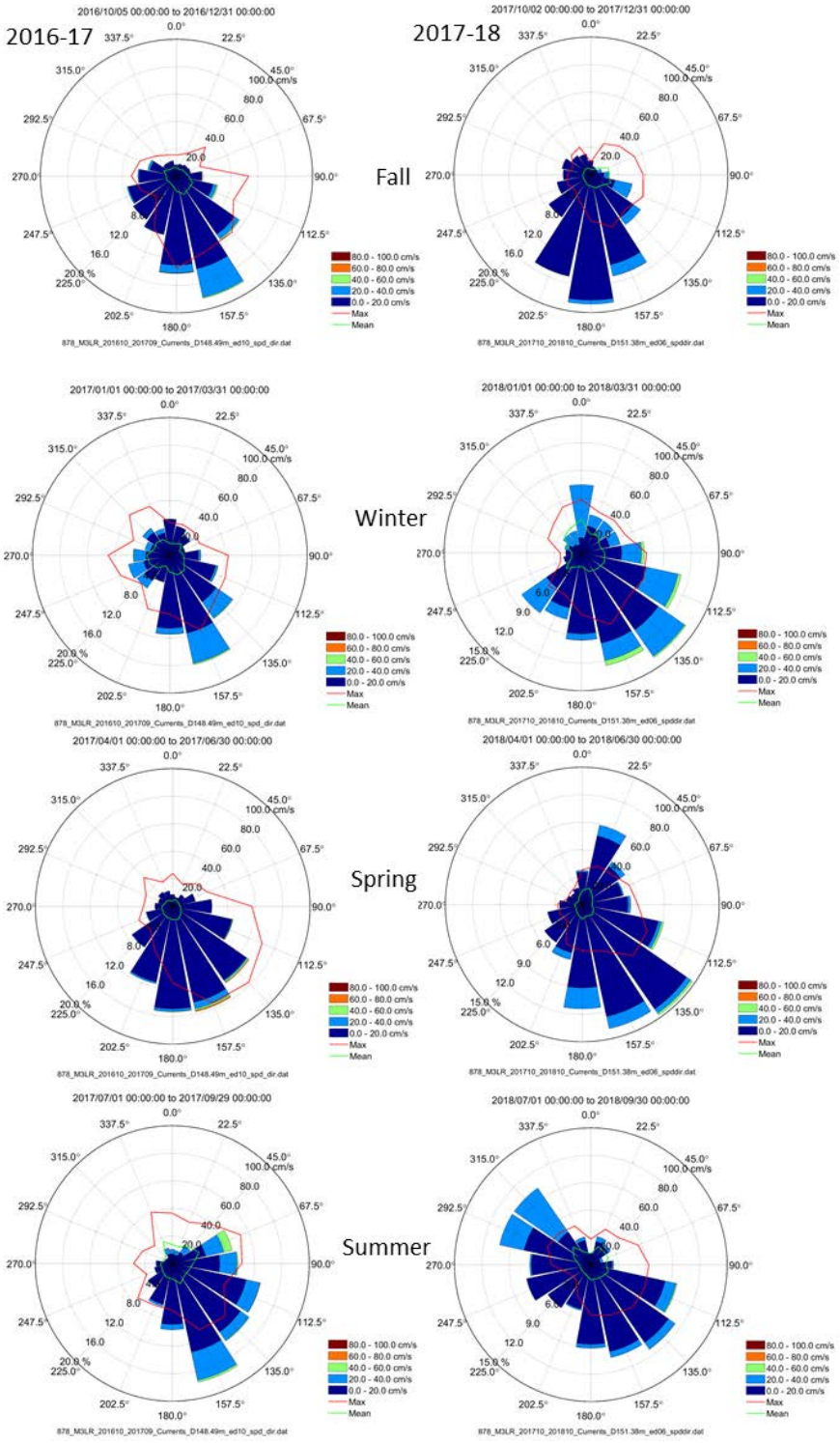

Figure 126. Compass rose plots of current speed and direction at 150 m depth for the M3 site for fall (top), winter (top middle), spring (bottom middle), and summer (bottom) for 2016–17 (left) and for 2017–18 (right). Directions are expressed as directions towards (e.g. Flow/drift toward the east has a 90° direction).

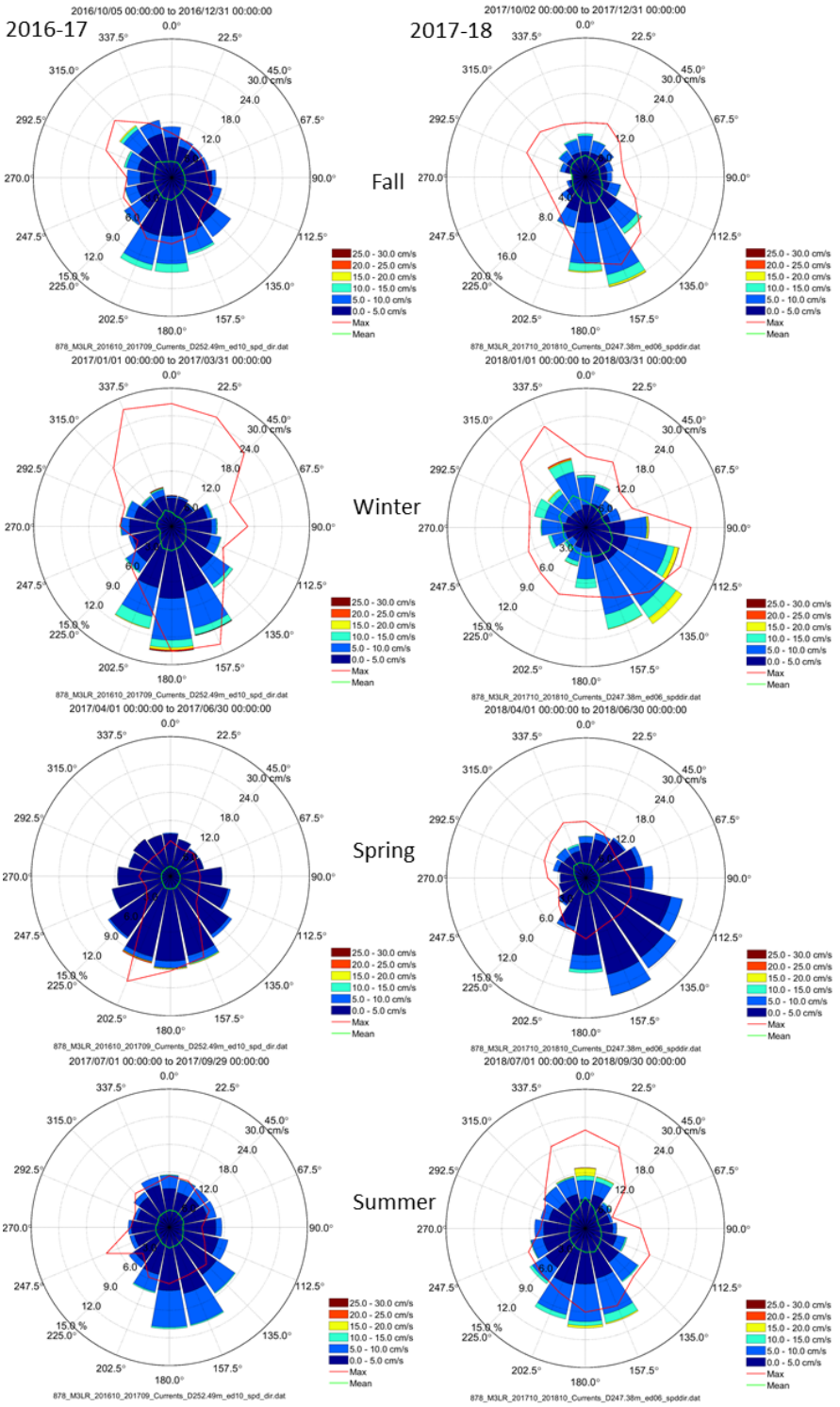

Figure 127. Compass rose plots of current speed and direction at 250 m depth for the M3 site for fall (top), winter (top middle), spring (bottom middle), and summer (bottom) for 2016–17 (left) and for 2017–18 (right). Directions are expressed as directions towards (e.g. Flow/drift toward the east has a 90° direction).

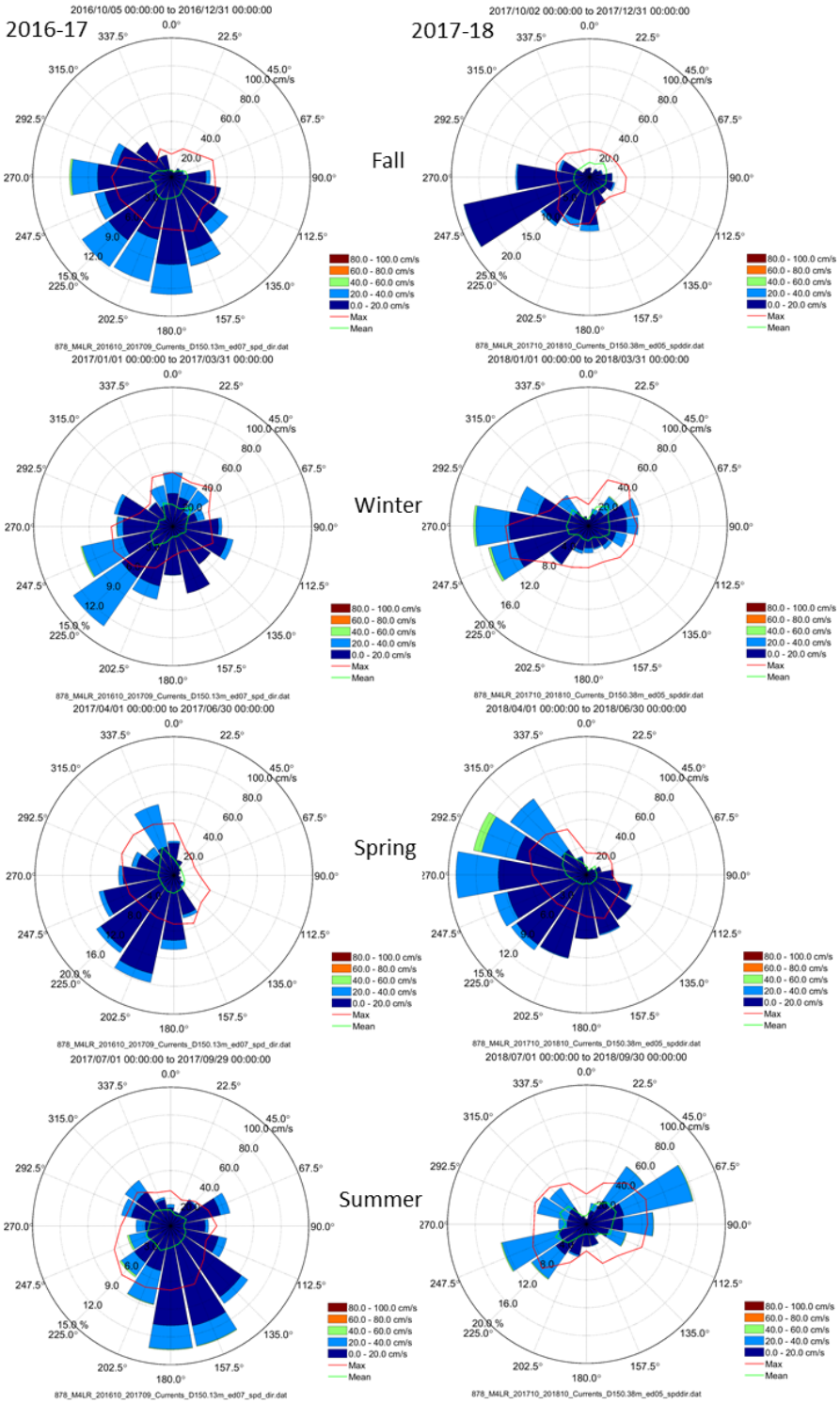

Figure 128. Compass rose plots of current speed and direction at 150 m depth for the M4 site for fall (top), winter (top middle), spring (bottom middle), and summer (bottom) for 2016–17 (left) and for 2017–18 (right). Directions are expressed as directions towards (e.g. Flow/drift toward the east has a 90° direction).

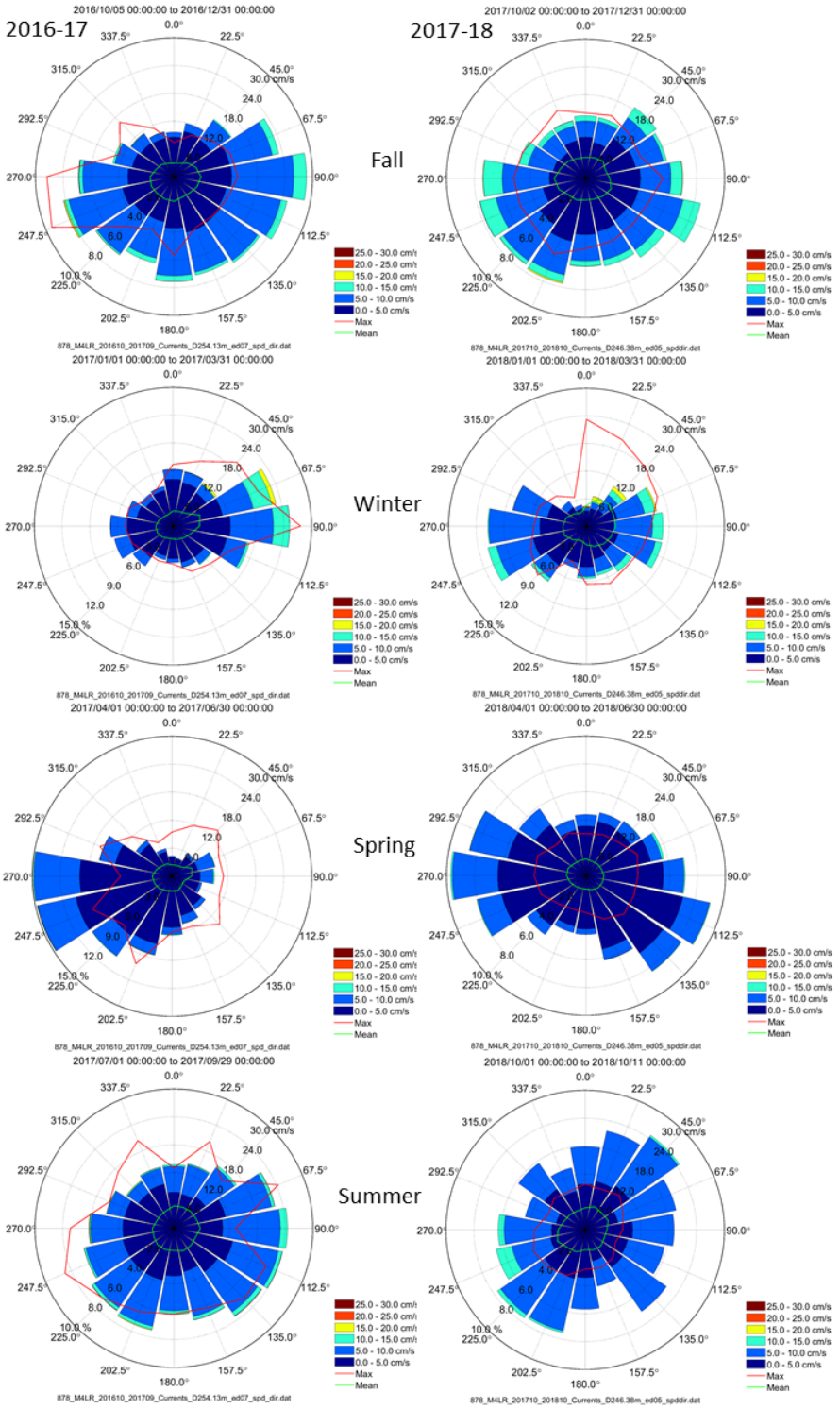

Figure 129. Compass rose plots of current speed and direction at 250 m depth for the M4 site for fall (top), winter (top middle), spring (bottom middle), and summer (bottom) for 2016–17 (left) and for 2017–18 (right). Directions are expressed as directions towards (e.g. Flow/drift toward the east has a 90° direction).

A summary of the seasonal variability in the currents is provided in **Error! Not a valid bookmark self-reference.**Table 48.

Table 48. Summary of the seasonal variability in the currents

Depth	Site	Comment
Near Surface	All Sites	The near-surface current distribution is quite different from the wind directional distribution
	M1	Fast flows to the NW in the fall Unusual SE flows in winter 2016-2017 and summer 2017-2018 Smallest SE flows in fall 2018 and winter 2019
	M2	The fall is generally the most energetic season, with some exceptional events • A single storm responsible for SE currents > 120 cm/s in winter 2016-2017 • A single storm responsible for SE currents > 100 cm/s in summer 2016-2017
	M3	The directionality of the near-shore sites breaks down offshore Strongest currents in the fall Winter 2016-2017 has 0.8% observations in excess of 60 cm/s Summer 2016-2017 has 0.6% observations in excess of 60 cm/s
	M4	Directionality is intermediate between the near-shore sites and M3 Strongest currents in the fall 5.5% of currents are 45-60 cm/s in the summer of 2016-2017
150 m	All Sites	Reduced speeds compared to the near-surface
	M2	Compared to the near-surface, the flows tend to be directed more to the SE, except in spring 2018 where there is a large proportion of flows to the south
	M3	Fall flows are more to the S and SE compared to near-surface westerlies Winter 2016-2017 has more directional flows Winter 2017-2018, SW currents are favored Spring 2017, SSE currents are favored, but changes to SE for Spring 2018 Summer 2016-2017 favored flows to SE, switching to bi-directional flow in summer 2017-2018
	M4	Fall 2016, currents predominantly in the SW quadrant More directional flow in winter than in near-surface Spring currents predominantly in the SW quadrant Summer 2017, flows spread in a cone around S direction Summer 2018, bidirectional flows NE/SW
250 m	All Sites	Reduction in current speeds compared to 150 m
	M3	Bias of flow to the S and SE with small counterflow to the NW Summer 2018, only season where proportion of N flows did not increase over the 150 m counterparts
	M4	Summer and fall direction distributions are very broad Winter shows bidirectional flow along the east-west axis Spring 2017 shows flow mostly in the SE quadrant

3.2.3.3 Drivers

The ocean currents are driven by many factors including winds, sea ice presence, Mackenzie River discharges, stratification of the water column and larger scale ocean currents which originate from the west and the east. The near-surface currents are predominantly wind driven, especially at sites M1 and M2. Even at depth, synoptic wind events are a major influence on the ocean currents through upwelling and downwelling events associated with episodes of strong and prolonged easterly and westerly wind events, respectively; however, the linkages are more complex between surface winds and ocean currents at mid-depth and deeper levels. Currents at the MARES mooring sites are also influenced by complex canyon dynamics in the Mackenzie canyon which interacts with the currents flowing over the outer shelf and slope waters (see Section 3.2.4).

3.2.4 Alongstream Current Velocity and Water Masses

3.2.4.1 Mean Conditions

Figure 130 shows the year-long mean vertically-averaged velocity vectors (upper 260 m), along with the standard error ellipses, at each site for the two years. Analogous to the first-year result (Lin et al. submitted), the strong shelf current at M1 stands out flowing to the northwest. The recirculation within the canyon is present in both years (evident by current direction at M3), although not as strong in year 2. Another change in year 2 is the stronger westward depth-averaged flow at M2.

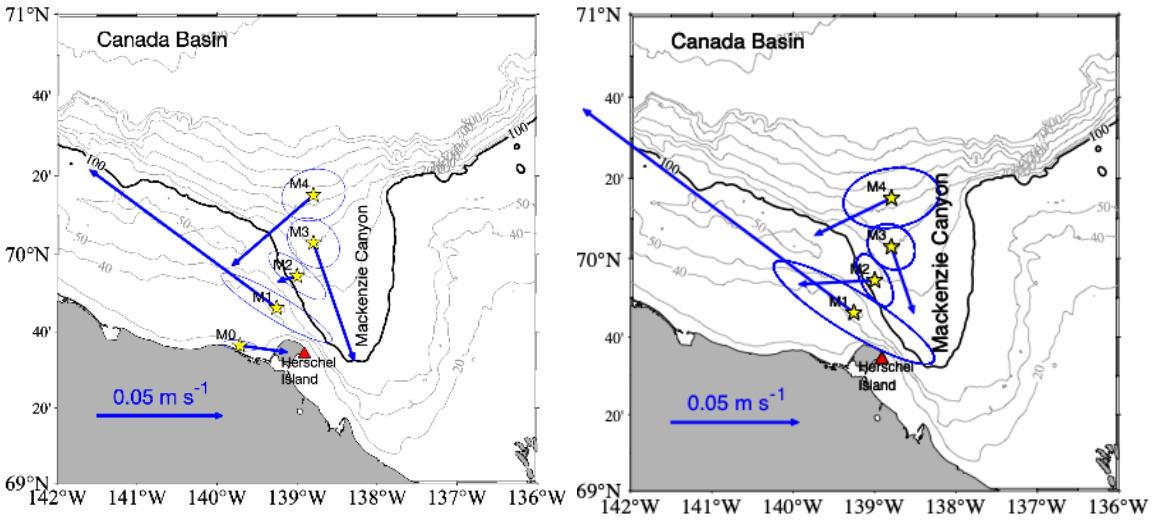

Figure 130. Year-long mean vertically-averaged velocity vectors for each mooring, with the standard error ellipses, in 2016–2017 (left) and 2017–2018 (right)

Bathymetric contours are in meters; the 100-m isobath at the rim of Mackenzie Canyon is highlighted by the thick contour. The red triangle marks the location of the Herschel Island meteorological station.

The year-long mean vertical sections of alongstream velocity for year 2 are shown Figure 131. This reveals the surface-intensified, westward-directed shelf current in the upper 50 m centered at mooring M1. The velocity at M2 on the upper slope has a two-layer structure: westward flow near the surface and eastward flow at mid-depth. Farther offshore, the alongstream flow has a dipole-like structure with equal but opposite mid-depth intensified flow (centered near 100 m depth) at M3 and at M4 within the canyon. This is referred to as the recirculation in the canyon.

Comparing these mean sections to year 1 (Figure 132), one sees that the recirculation is weakened in the second year, and the water above 150 m is colder and saltier in year 2.

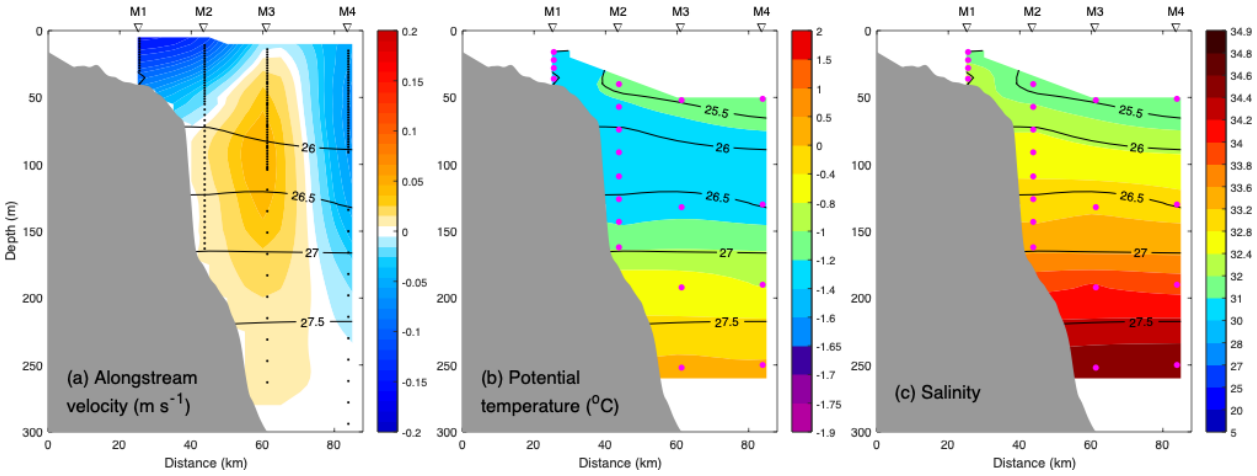

Figure 131. Vertical sections of (a) year-long mean alongstream velocity; (b) potential temperature; and (c) salinity, overlain by mean potential density contours (black lines in kg m-3) for 2017–2018

The black dots in (a) are the ADCP data points. The magenta dots in (b) and (c) show the location of the MicroCATs.

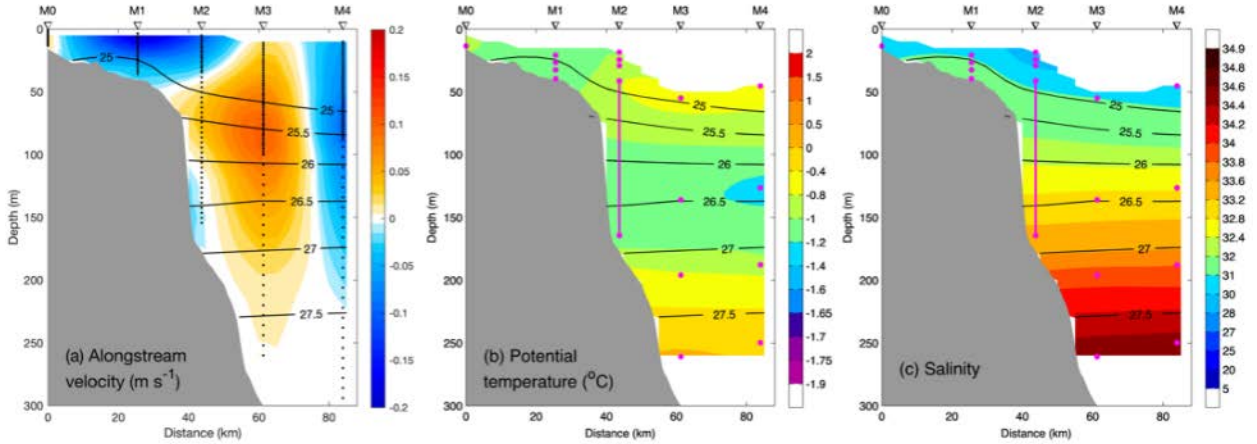

Figure 132. Vertical sections of (a) year-long mean alongstream velocity; (b) potential temperature; and (c) salinity, overlain by mean potential density contours (black lines in kg m-3) for 2016–2017

The black dots in (a) are the ADCP data points. The magenta dots in (b) and (c) show the location of the MicroCATs.

The percent presence of different water masses in the vertical plane was computed using the full year of data for each of the two years (Figure 133). In both years there was little-to-no Alaskan coastal water (ACW), and Atlantic water (AW) was present only below 150 m. In year 1, only a very small amount of Bering summer water (BSW) was found in the upper 50 m, while there was no signal of this water mass in year 2 (although the BSW was mainly present at mooring M0 in year 1, which was not re-deployed the second year). The newly ventilated winter water (NVWW) was more prevalent seaward of the shelfbreak in year 2. The remnant winter water (RWW) was the primary water mass present from about 70–200 m in both years but extended onto the shelf in year 2. It largely replaced the sea ice melt water / meteoric water (MWM) in the upper layer (shallower than about 70 m) that was present in year 1.

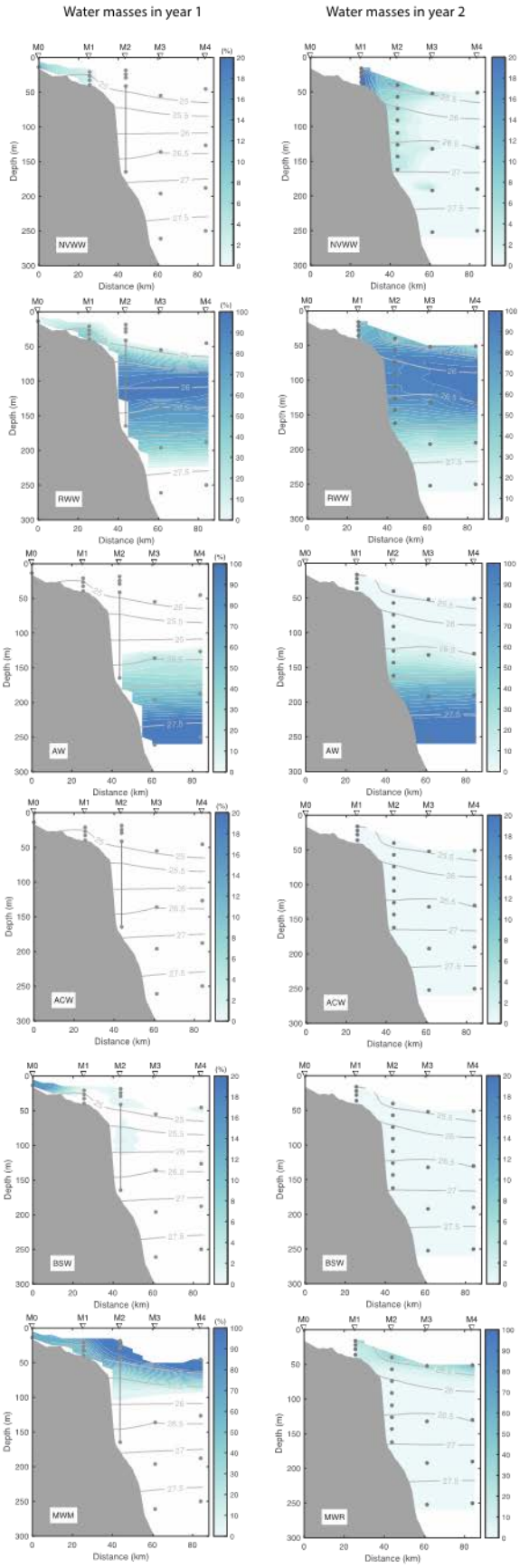

Figure 133. Vertical sections of the mean percent occurrence of the water masses across the array for year 1 (left column) and year 2 (right column) ACW = Alaskan coastal water; BSW = Bering summer water; NVWW = newly ventilated winter water; RWW = remnant winter water; AW = Atlantic water; and MWM = sea ice melt water / meteoric water.

3.2.4.2 Seasonality

Figure 134 compares the seasonally-varying transport of the Shelf Current and the Shelfbreak Jet between the two years. We note that, without mooring M0 in the second year, the transport value of the Shelf Current for year 2 is less robust (we used linear extrapolation towards the coast). Despite this, it is clear that the seasonal variation of the Shelf Current is quite different in the two years. The transport peaks in April in year 1, versus December in year 2. This is consistent with simultaneous peaks in easterly along-coast wind in the two years, further confirming that the Shelf Current is predominantly wind-driven. The Shelf-break Jet displays no consistent seasonality, with generally weak eastward and westward flow. Its peak eastward transport occurs in December in both years, with a smaller peak in early summer (June in year 1; July in year 2). Besides the local forcing, we also addressed the influence of upstream. Using the mooring data in the Alaskan Beaufort Sea, we demonstrated that the variation of the Shelfbreak Jet transport is correlated with upstream with a 55 hours delay. It is consistent with the phase speed of shelf waves.

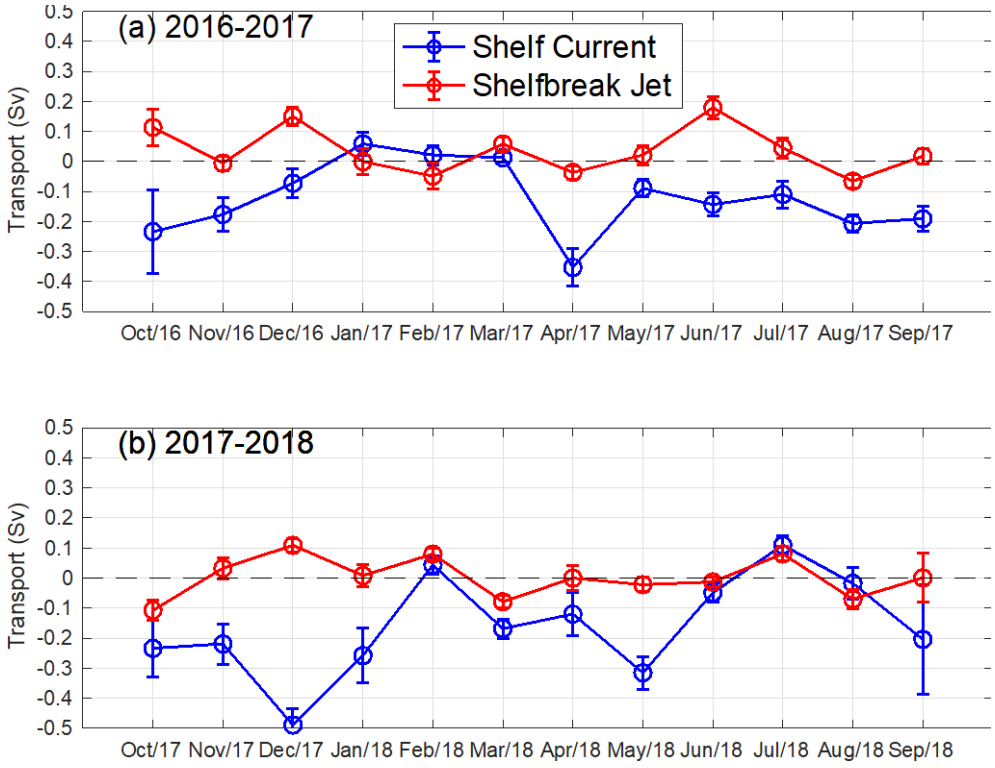

Figure 134. Seasonal variation of transports of the shelf current (blue curve) and the shelfbreak jet (red curve) in (a) 2016–2017 and (b) 2017–2018

As noted above (Figure 133), the water mass composition of the boundary current system is significantly different in the two deployment years. Within the Shelf Current, the dominant water mass in year 1—the sea ice MWM—was no longer present from January–July in year 2 (Figure 135). The current instead advected winter waters, i.e. NVWW and RWW. The BSW showed up in the summer months of year 1, while is negligible in year 2. With regard to the Shelfbreak Jet, in year 1 it advected varying amounts of MWM and RWW, whose presence varied out of phase throughout the year (Figure 136). By contrast, RWW was the dominant water mass in year 2, accounting for over 80% of the water advected by the jet.

The presence of MWM was minimal in year 2. Interestingly in year 2, Atlantic water (AW) and NVWW appeared in December and April, respectively, water masses that were both absent in year 1. BSW is not found in the Shelfbreak Jet throughout the two years, except for a little pulse in January of year 1.

The occurrence of the former was due to a strong upwelling event, while the occurrence of the latter was due to a strong downwelling event.

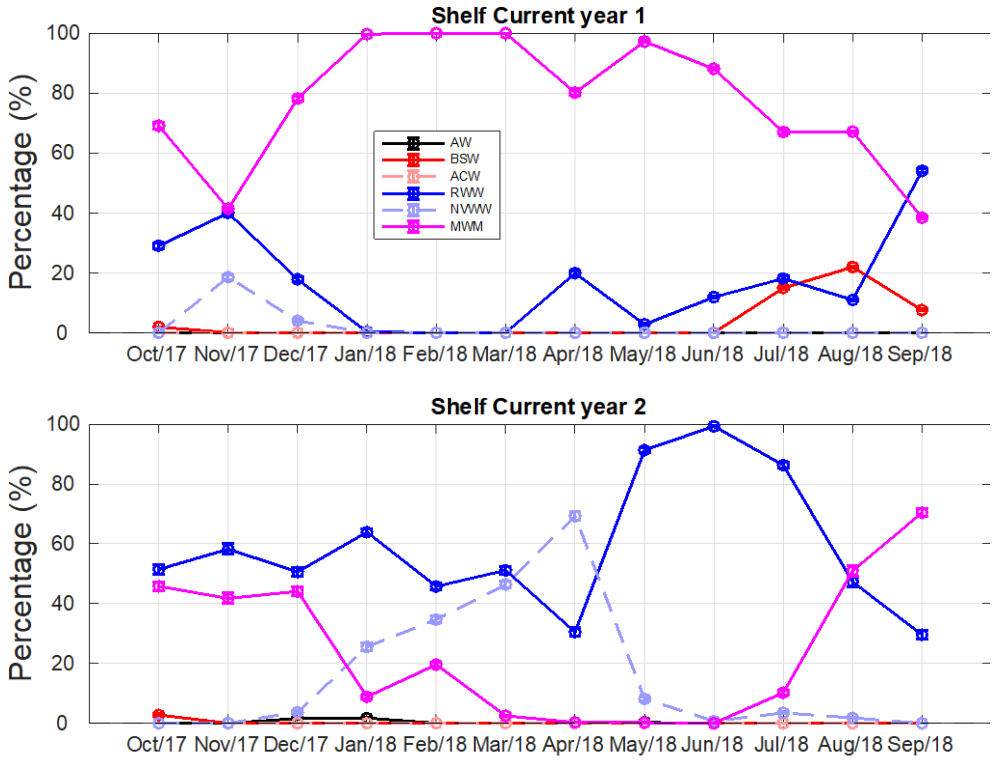

Figure 135. Seasonal variation of water masses within the shelf current in (upper panel) 2016–2017 and (bottom panel) 2017–2018

ACW = Alaskan coastal water; BSW = Bering summer water; NVWW = newly ventilated winter water; RWW = remnant winter water; AW = Atlantic water; and MWM = sea ice melt water / meteoric water.

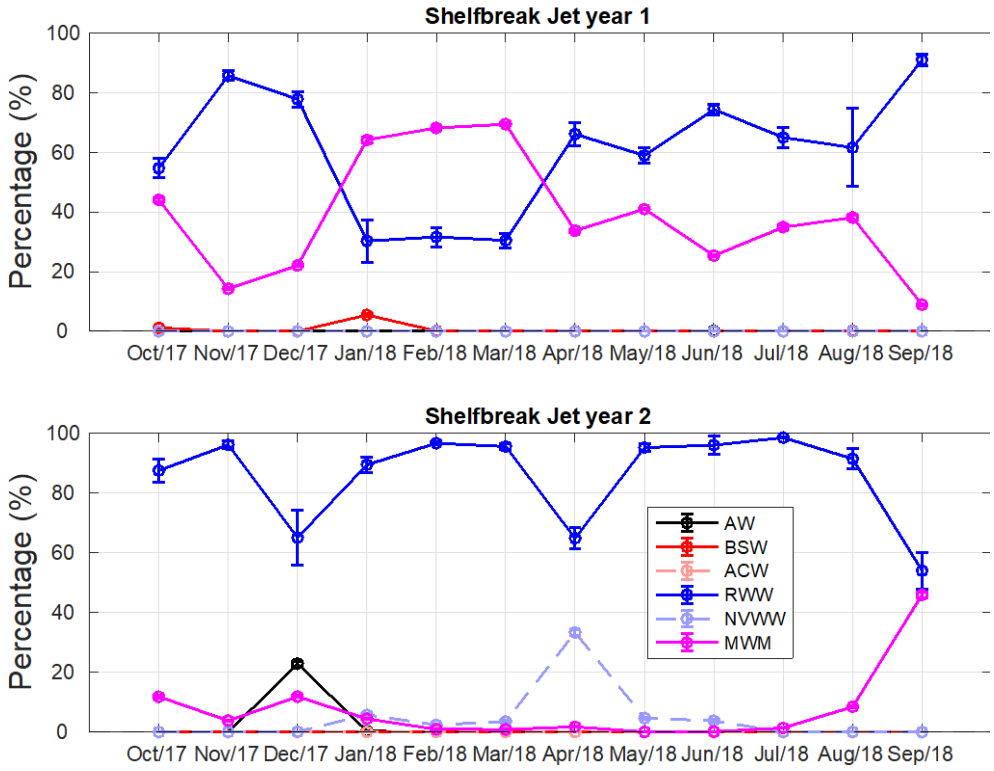

Figure 136. Seasonal variation of water masses within the shelfbreak jet in (upper panel) 2016–2017 and (bottom panel) 2017–2018

ACW = Alaskan coastal water; BSW = Bering summer water; NVWW = newly ventilated winter water; RWW = remnant winter water; AW = Atlantic water; and MWM = sea ice melt water / meteoric water.

3.2.4.3 Drivers

We now consider differences in some of the pertinent physical drivers between the two years, in an effort to explain some of the year 1 *vs.* year 2 variations in currents and water masses. Figure 137 presents the monthly mean along-coast wind for the two years. Averaged over the year, the wind was weakly out of the east for each deployment. While there was significant month-to-month variability over the course of each year, there was no consistent seasonal cycle between the two years. Notably, however, there is significant correlation between the along-coast wind and the Shelf Current in both years, further confirming that the current is predominantly wind-driven. Recall that the transport of the Shelf Current peaks in April in year 1, versus December in year 2 (Figure 134). This is consistent with simultaneous peaks in the along-coast wind in the two years (Figure 137).

The wind-current correlation is stronger in year 2 than in year 1, which we attribute to ice cover. Figure 138 shows the monthly mean ice concentration at mooring M1 from Advanced Microwave Scanning Radiometer 2 (AMSR2). The ice concentration was close to 100% during the months of January–March in year 1, while this was true only in February of year 2. Therefore, it can be expected that there were more time periods of nearly immobile ice in year 1. Consequently, the wind-driven response of the water column would be reduced due to internal ice stresses resulting from the highly consolidated pack ice. Note in Figure 134a that the transport of the Shelf Current was nearly zero during January–March of year 1, despite the fact that the along-coast winds were strongly out of the west (Figure 137). This helps explain the reduced correlation between the wind and the Shelf Current in year 1.

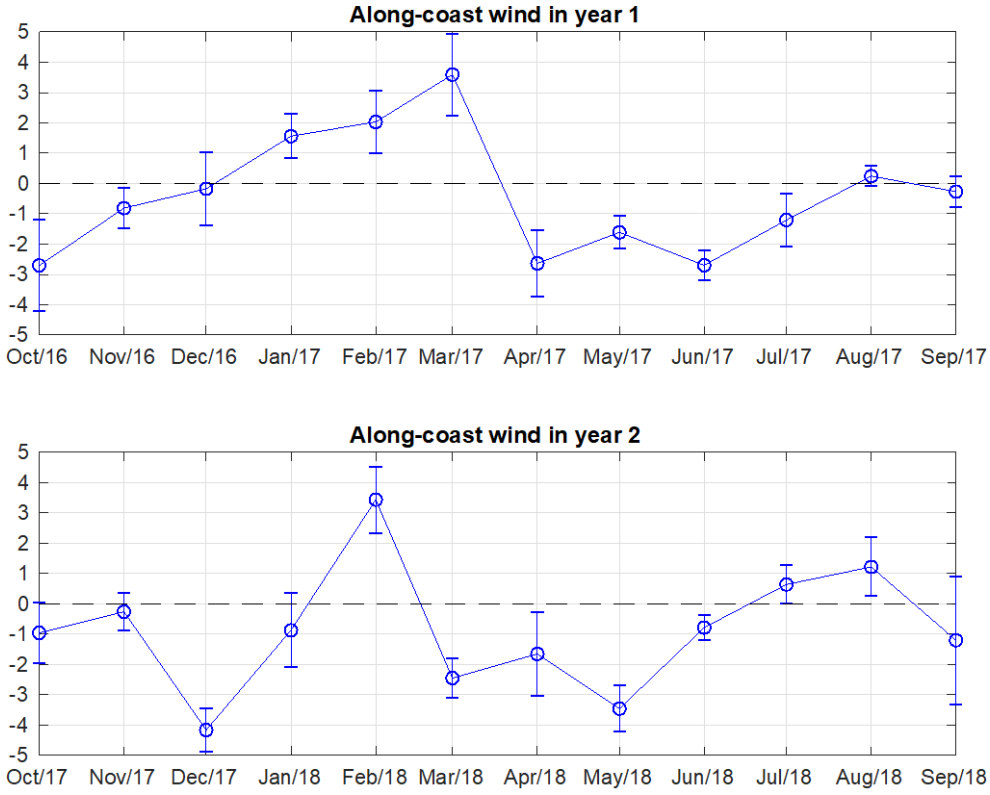

Figure 137. Seasonal variation of the along-coast wind in (upper panel) 2016–2017 and (bottom panel) 2017–2018, using the ERA5 Data

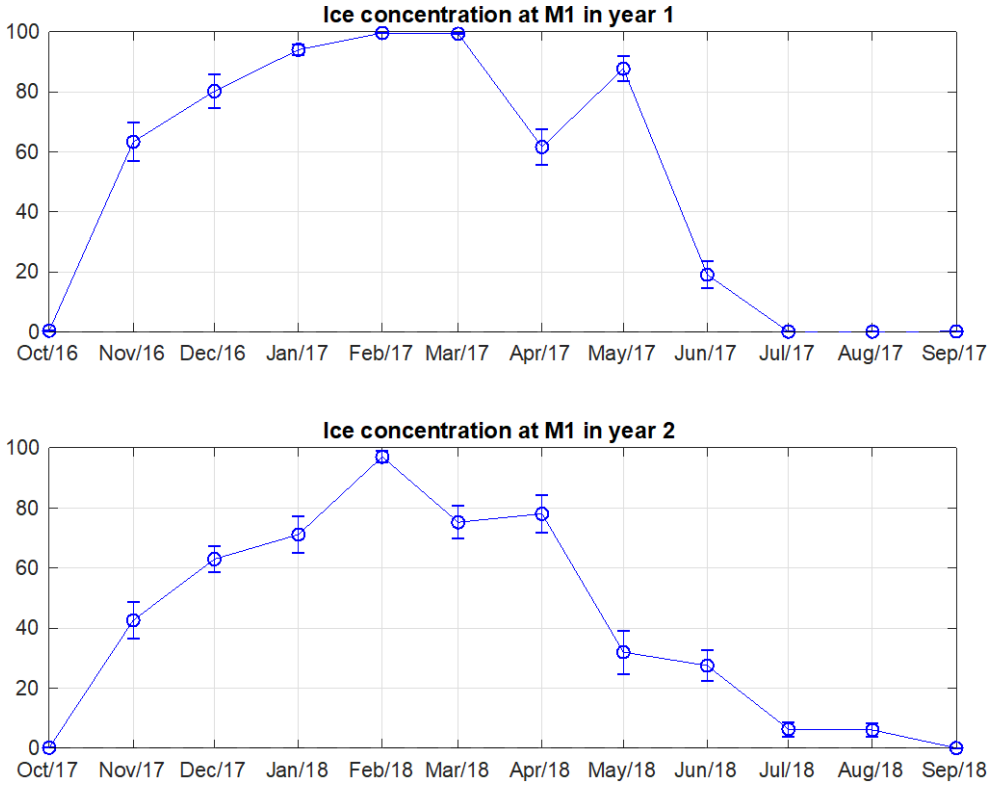

Figure 138. Seasonal variation in ice concentration at m1 in (upper panel) 2016–2017 and (bottom panel) 2017–2018, using the AMSR2 Data

With regard to the substantial difference in water mass presence in the two years, we diagnose the upstream condition in the Alaskan Beaufort Sea using contemporaneous timeseries from the Arctic Observing Network (AON) mooring deployed in the core of the Shelfbreak Jet at 152°W. Figure 139 shows the potential temperature/salinity (θ/S) diagrams for the two years. Notably, there was a large amount of NVWW present in year 2 in the Alaskan Beaufort Sea, but barely any in year 1. In contrast, MWM had a greater occurrence in year 1 than in year 2. These differences are consistent with the water mass occurrences documented in the MARES moorings for the two years (Figure 135, Figure 136). In particular, more NVWW was present seaward of the shelfbreak in year 2, while more MWM was present in the upper layer in year 1. This suggests that the upstream condition (conditions to the west of the study area) can strongly affect the water masses in the vicinity of Mackenzie Canyon.

In addition to the upstream condition, changes in the water masses between the two years was also likely the result of local shelf-basin interactions, i.e., upwelling and downwelling. For instance, AW was only measured at the array in December of year 2. That particular month had the strongest easterly winds over the two year period, which would drive intense coastal upwelling. Furthermore, that month was characterized by large negative wind stress curl over the Canada Basin (Figure 140). As previously determined, this results in a stronger recirculation at moorings M3 and M4, which also drives water up the canyon.

Further work is required to investigate these aspects of the response in Mackenzie canyon to the variable physical drivers.

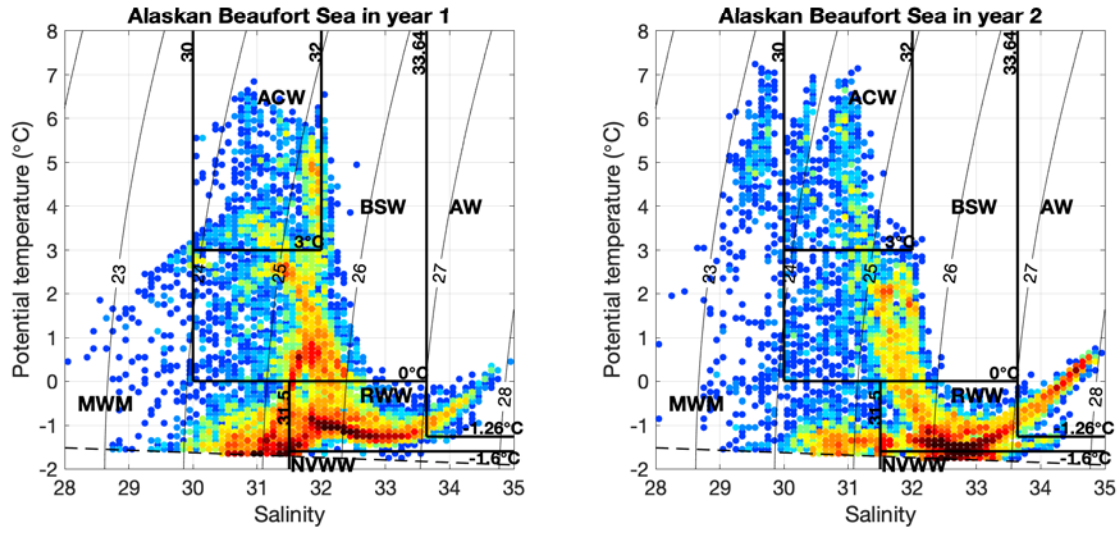

Figure 139. Percent occurrence of θ/S values using the mooring array data from the Alaskan Beaufort Sea for (left panel) 2016–2017 and (right panel) 2017–2018

Data from http://aon.whoi.edu/

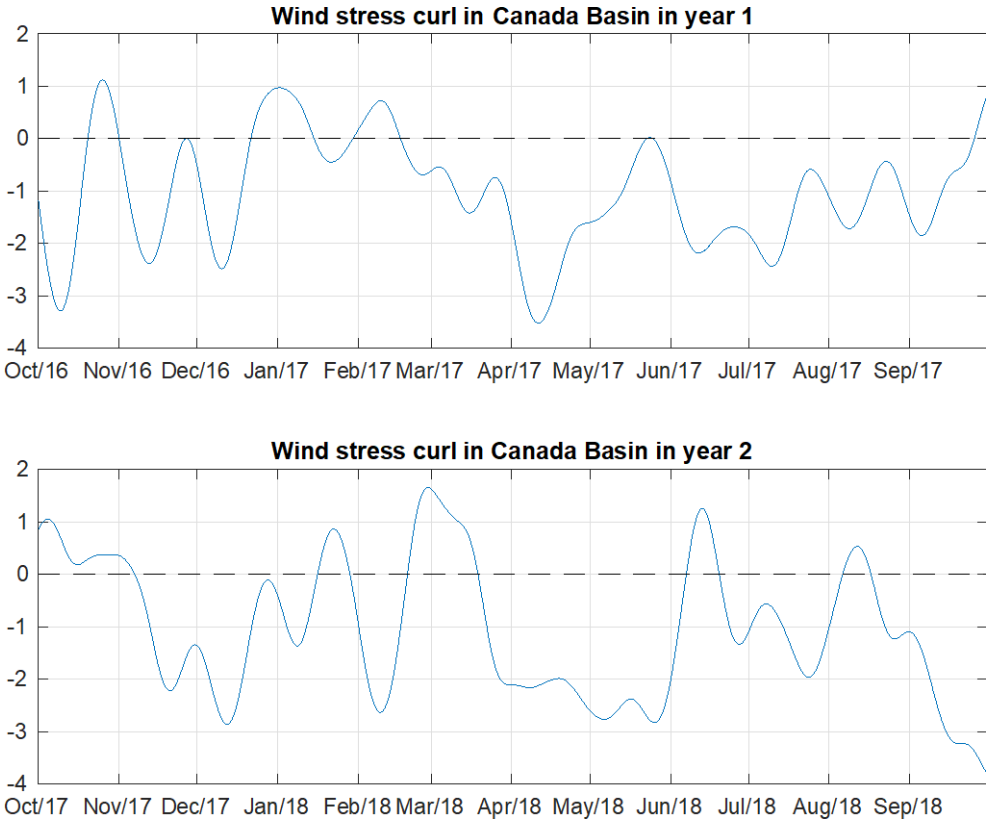

Figure 140. Timeseries of 25-day low-passed wind stress curl averaged over Canada Basin in (upper panel) 2016–2017 and (bottom panel) 2017–2018, using the ERA5 Data

3.2.5 Ice

3.2.5.1 Ice Velocity

Ice drift is examined using compass rose plots which show the speed and direction joint frequency distribution for the entire deployment. In the following figures, the color of each segment denotes its speed interval. The radial length of each segment denotes the proportion of measurements within the illustrated speed and direction interval. The maximum and mean values for each directional sector are illustrated through the second radial scale as the red and green lines, respectively.

3.2.5.1.1 Mean Conditions

The mean ice drift for each ice season (November to June) at M1 (Figure 141) tends to be bi-directional: westerly-northwesterly and easterly-southeasterly. Ice velocities are dominated by flow to the west northwest in the first year and are aligned more to the northwest in the second year with reduced eastward movement in year 2. The ice speeds are very large at site M1, especially in the second year, when there is a larger proportion of observations in the 200-250 cm/s speed interval, and the maximum increases up to nearly 268 cm/s from about 221 cm/s in year 1. There is a considerable similarity in the directional distributions of the surface winds with those of ice motion at site M1, including a greater dominance of northwesterly ice drift and southeasterly winds in the second year *vs.* the first year.

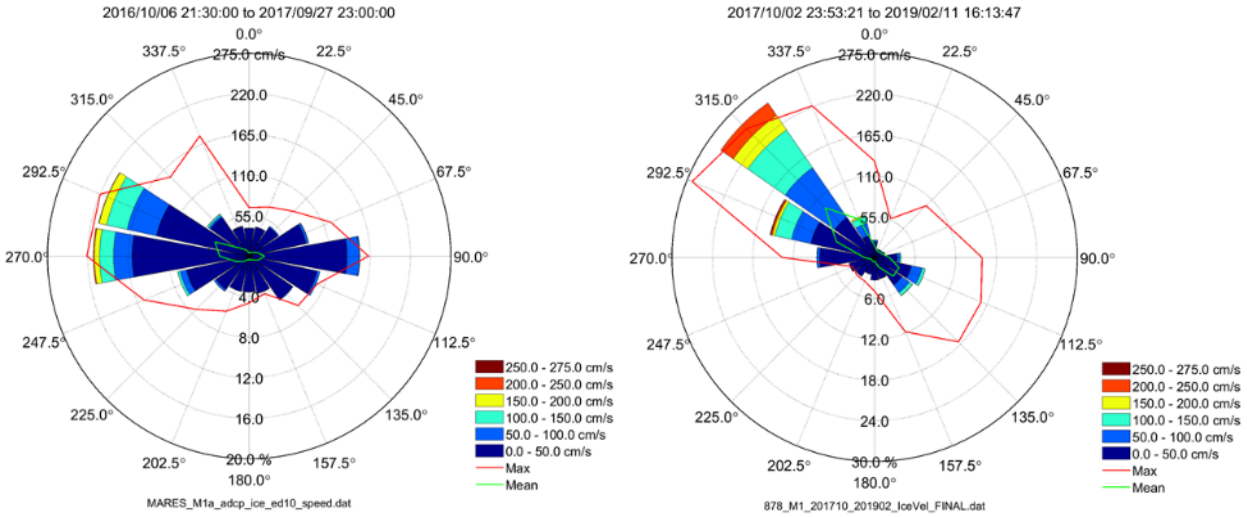

Figure 141. Compass rose plots of ice drift speed and direction for the M1 site for 2016–17 (left) and for 2017–18 (right). Directions are expressed as directions towards (e.g. Flow/drift toward the east has a 90° direction).

The ice drift at M2 (Figure 142) also tended to be bi-directional, with dominant ice drift being flows to the west in the first year and to the west northwest in the second year. In the second year there is a larger proportion of observations in the 200–250 cm/s speed interval, and the maximum increases up to nearly 275 cm/s.

At M3, the first year ice drift was not as highly directional as at M1 and M2, though there is some preference for drift to the west-northwest (Figure 143). In the second year the ice drift became much more directional, with a strong preference for flow to the west. Ice speeds at site M3 are noticeably reduced by

comparison with sites M1 and M2. At site M3, the average (peak) speeds are 12 cm/s (127 cm/s) in the first year and 19 cm/s (84 cm/s) in the second year.

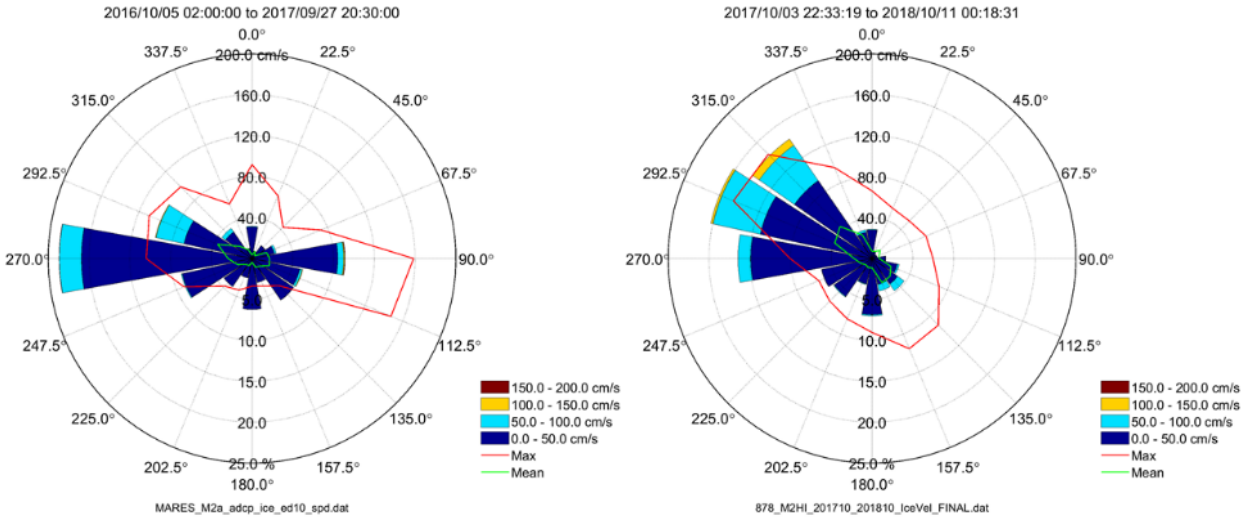

Figure 142. Compass rose plots of ice drift speed and direction for the M2 site for 2016–17 (left) and for 2017–18 (right). Directions are expressed as directions towards (e.g. Flow/drift toward the east has a 90° direction).

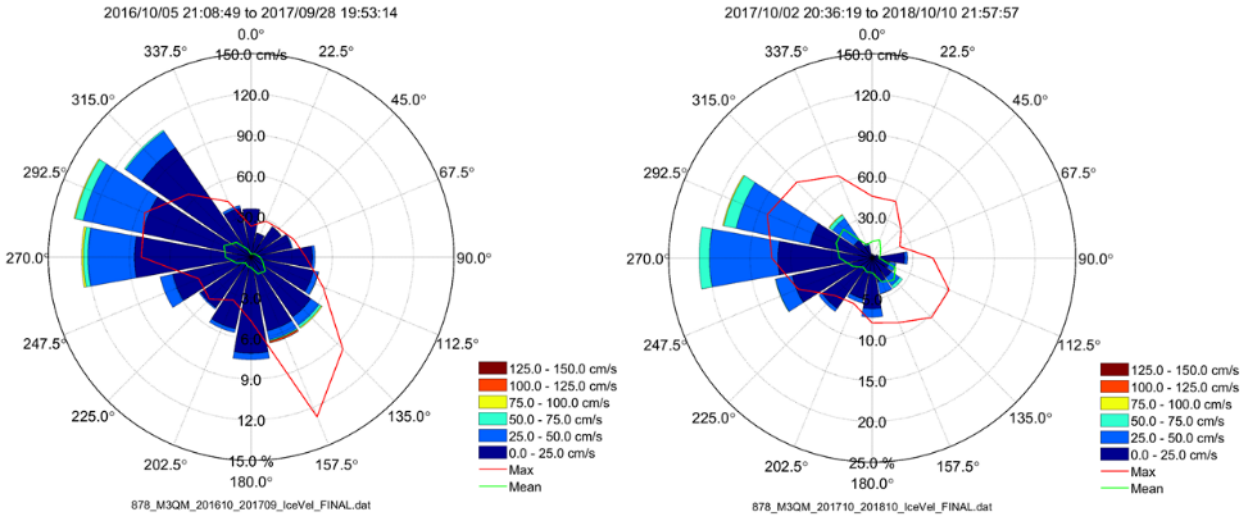

Figure 143. Compass rose plots of ice drift speed and direction for the M3 site for 2016–17 (left) and for 2017–18 (right). Directions are expressed as directions towards (e.g. Flow/drift toward the east has a 90° direction).

Ice drift at M4 was dominated by flow to the west northwest in both years, though there is a greater proportion of ice movements to the southeast in the first year and a larger spread in directions in the second year (Figure 144). The ice speeds at site M4 are quite similar in magnitude to those of site M3 and much reduced from those measured at sites M1 and M2.

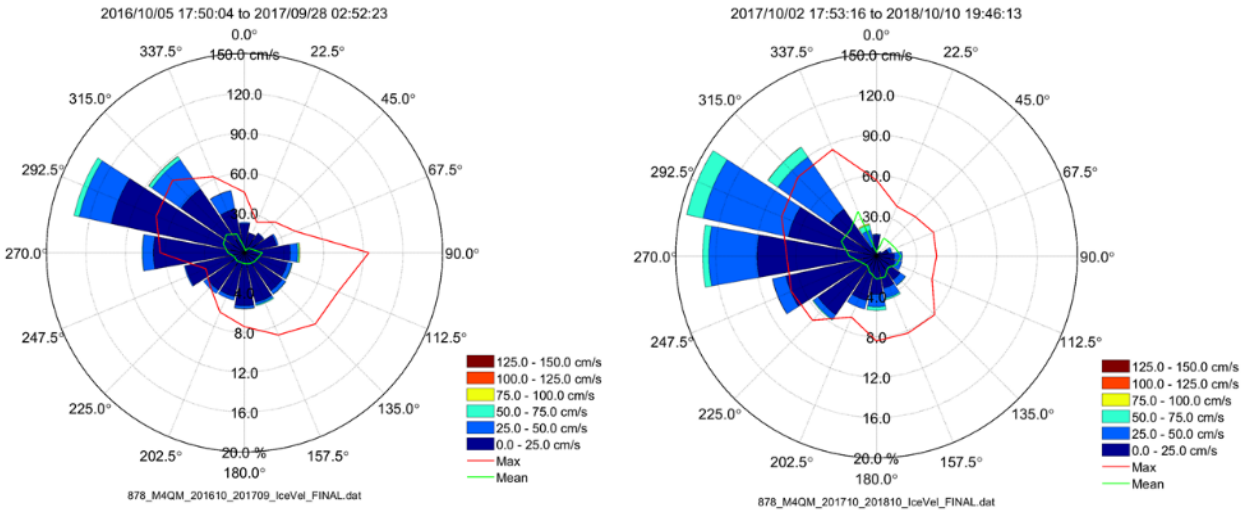

Figure 144. Compass rose plots of ice drift speed and direction for the M4 site for 2016–17 (left) and for 2017–18 (right). Directions are expressed as directions towards (e.g. Flow/drift toward the east has a 90° direction).

At sites M2, M3, and M4, the more dominant ice drifts to the northwest in the second year, 2017–2018 *vs.* the first year 2016–2017 which may, in part, be related to a greater dominance of winds from the southeast in the second year. However, in the second year, the dominance of northwesterly ice drift is very pronounced by comparison to relative distributions of the surface winds between the southeast and northeast.

3.2.5.1.2 Seasonality

The seasonality of the ice drift at the four sites is examined using compass rose plots, as already introduced in the previous section. Seasonal compass rose plots, are limited to the fall, winter, and spring seasons as there are very few ice velocity measurements available in summer when largely open water conditions prevail throughout the region. The seasonality for the M1 site is illustrated in Figure 145. Overall, the fall and winter show a marked increase in drift speeds in year two. As was previously shown in monthly ice speed statistics in Table 31 for site M1, the mean and maximum ice speeds for year 2 attain the highest values in the fall of 2017 (November and December), extending into January 2018 with a peak speed of nearly 268 cm/s. In the remainder of the winter, and into the early spring months, ice speeds are reduced due to extended intervals in which the ice motion is very low. These intervals can be attributed to large internal ice stress. As the ice concentrations generally decrease later in the spring, the ice becomes more mobile (Figure 55). The spring of 2017 (year 1) shows a larger proportion of moderate to high-speed ice drifts (> 150 cm/s). As in the annual results, the year 2 ice drifts are oriented more to the northwest.

The M1 site instruments were left in the water longer than any of the other sites, which gives us an opportunity to observe all of a third fall season, and large proportion of a third winter season. Figure 146 shows how the proportion of high-speed drift in fall and winter continues to increase in the third season (even more red than in the second season), but the increase is not as marked as between the first and second seasons. Similarly, the directions in the third season are more comparable to the second season (to the northwest).

Figure 147 illustrates the seasonal ice drift speeds and directions at the M2 site, which tend to be lower than those at site M1 but are still relatively large compared to sites M3 and M4. The largest change in drift direction is in the winter. In the first year the drift is generally aligned east/west, but in the second year the drift is predominantly towards the northwest with very little eastward movement. The ice drift in the winter of 2018 has the largest proportion of high ice drift speeds (> 100 cm/s) while in the previous winter the ice drift speeds are much lower. This drift, to the northwest in the winter of 2018, may be related to greater proportion of winds from the southeast in this winter by comparison to smaller numbers in the previous winter.

The seasonal patterns in ice drift for the M3 site are illustrated in Figure 148. In both years, the high ice drifts were moderate (50–75 cm/s), and the largest proportion of moderate ice drift speeds occurred in the fall. The ice drifts are dominated by movements to the west and northwest in all seasons/years, except in the 2016–17 winter season when the movements were approximately equally split between northwest and southeast and some large ice speeds of up to 120 cm/s occurred to the south-southeast. This difference in the winter ice drifts direction can be readily related to the difference in surface wind distributions for the two years.

The seasonal patterns in ice drift for the M4 site illustrated in Figure 149, are very similar to those of site M3. The largest ice drifts are moderate speeds (50–75 cm/s), and the largest proportion of moderate ice drifts occur in the fall. In winter and spring, the ice speeds tend to be smaller at 0–50 cm/s. Except for the winter of 2017, which shows bidirectional flow, the remaining seasons show flow mostly towards the west-northwest to northwest. Like site M3, the difference between the two years in winter cannot be readily related to differences in the surface wind directional distributions.

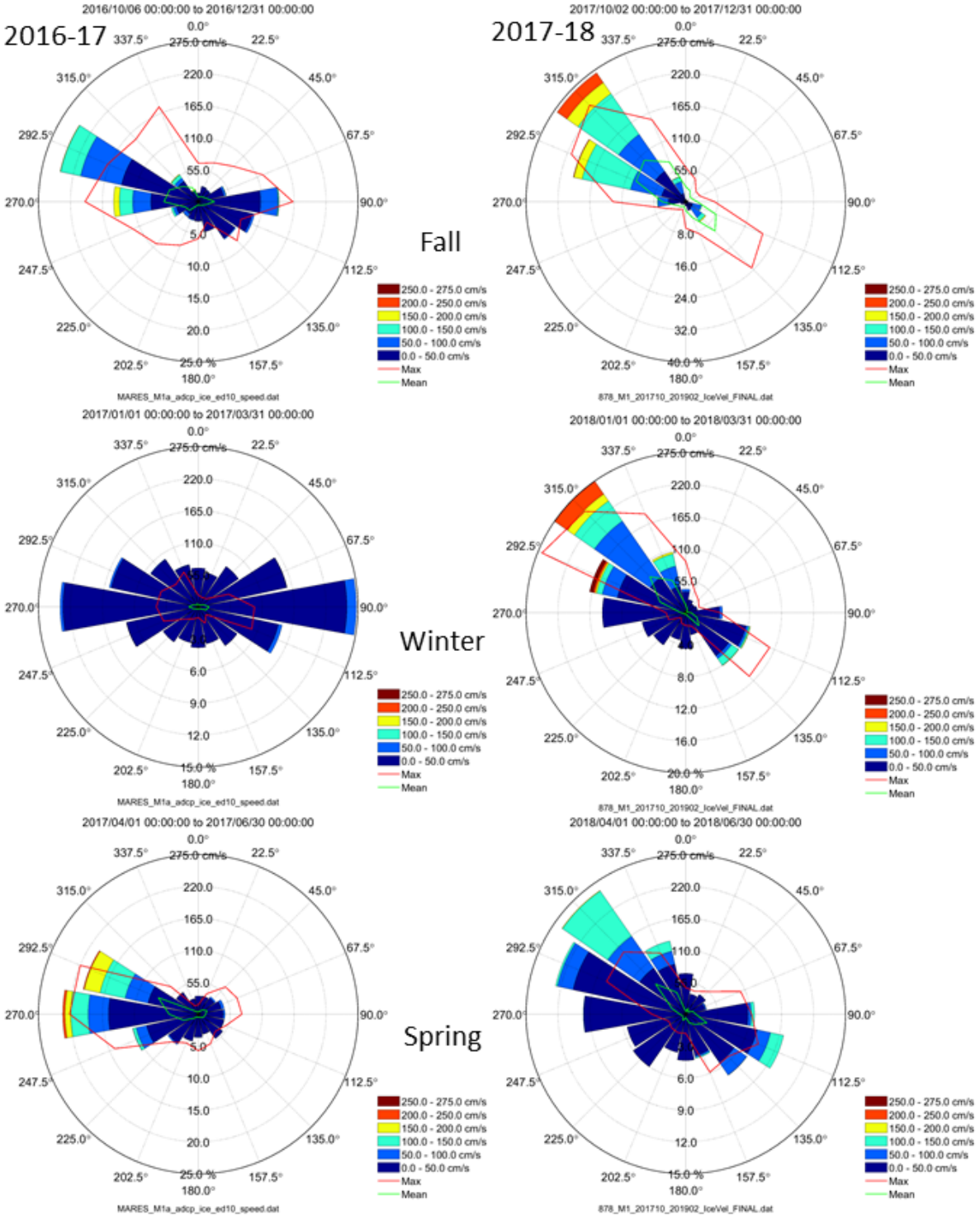

Figure 145. Compass rose plots of ice drift speed and direction at the M1 site for fall (top), winter (middle), and spring (bottom) for 2016–17 (left) and for 2017–18 (right). Directions are expressed as directions towards (e.g. Flow/drift toward the east has a 90° direction).

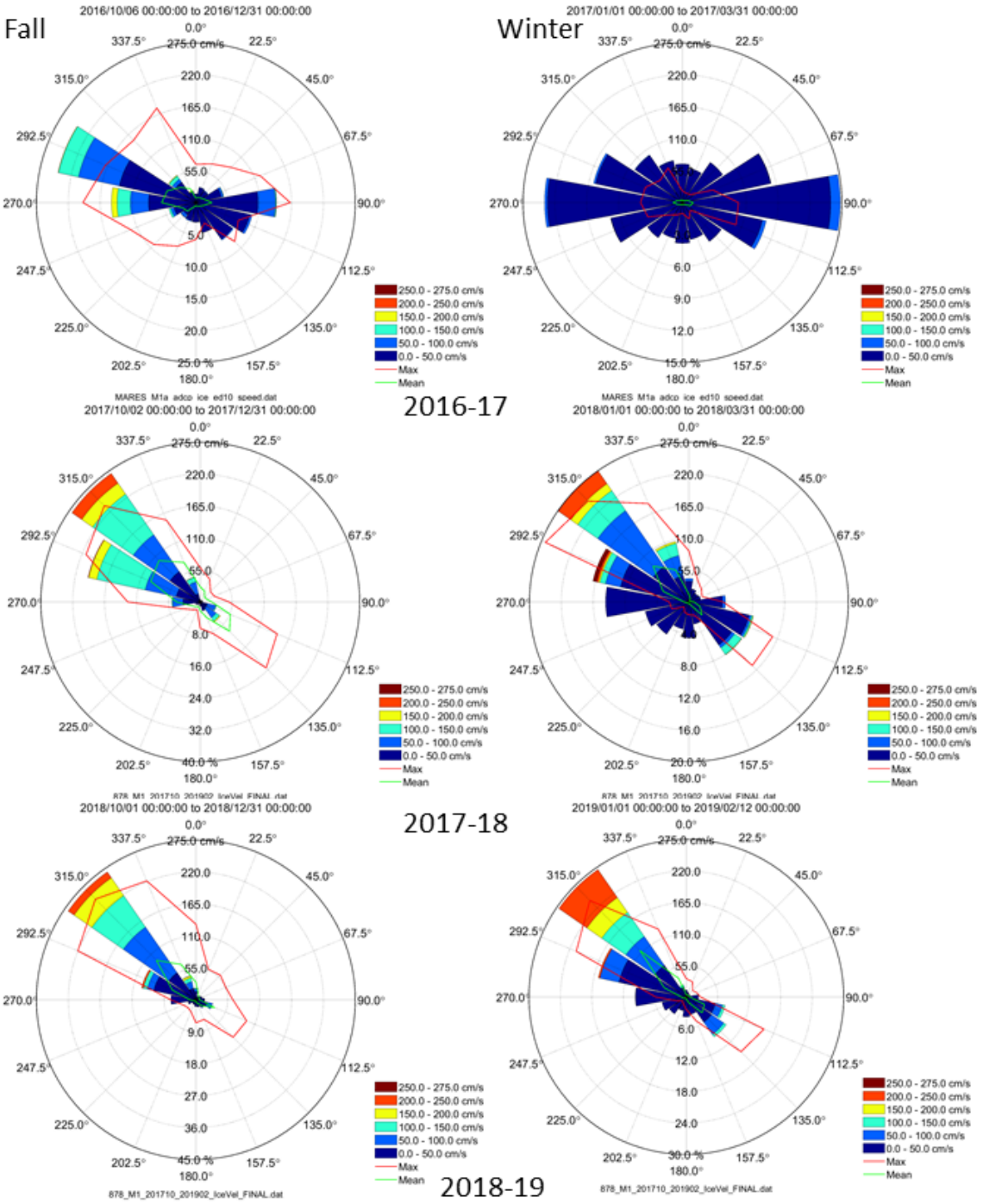

Figure 146. Compass rose plots of ice drift speed and direction at the M1 site for all three instances of fall measurements (left) and winter measurements (right) made for 2016–17 (top), 2017–18 (middle), and 2018–19 (bottom). Directions are expressed as directions towards (e.g. Flow/drift toward the east has a 90° direction).

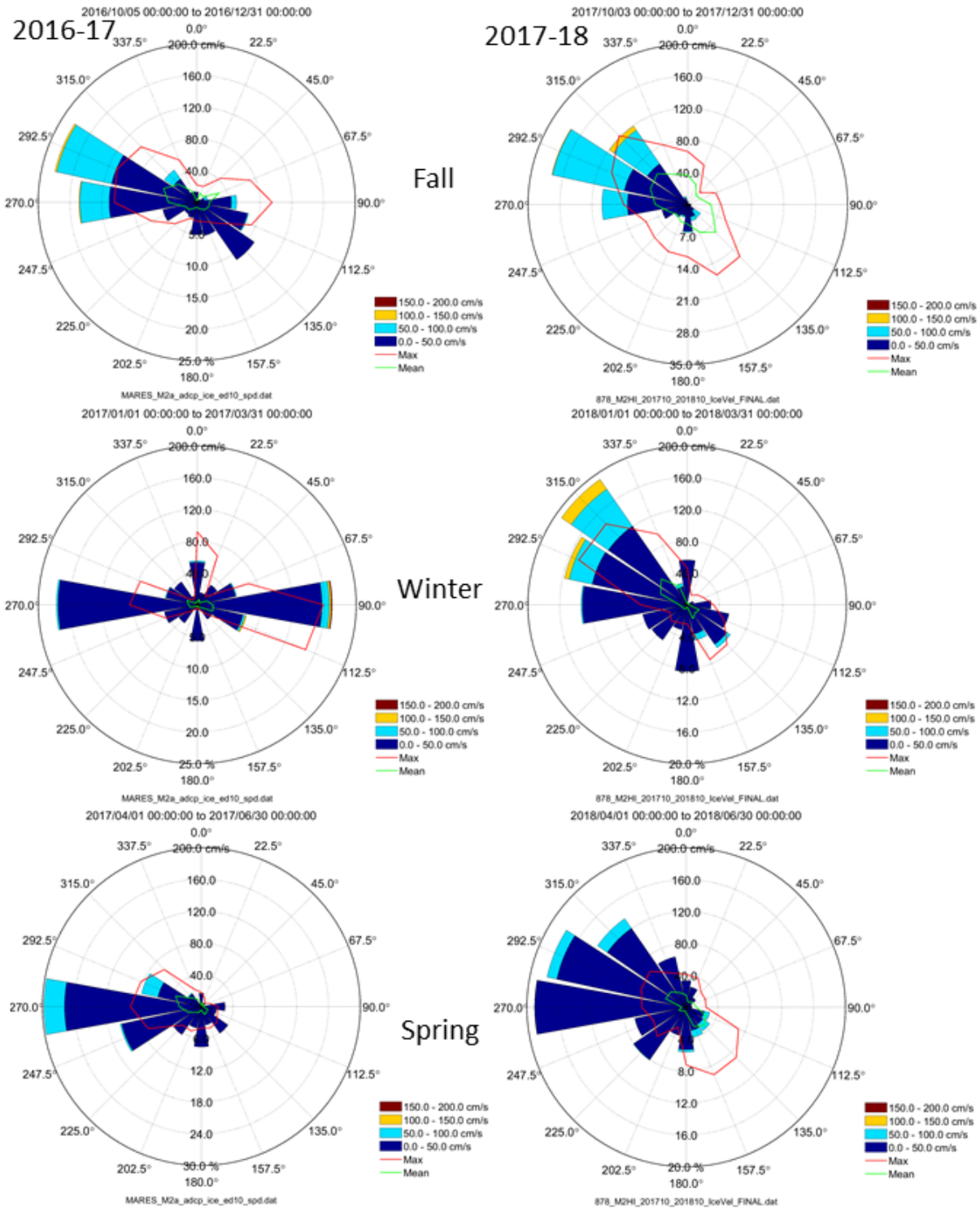

Figure 147. Compass rose plots of ice drift speed and direction at the M2 site for fall (top), winter (middle), and spring (bottom) for 2016–17 (left) and for 2017–18 (right). Directions are expressed as directions towards (e.g. Flow/drift toward the east has a 90° direction).

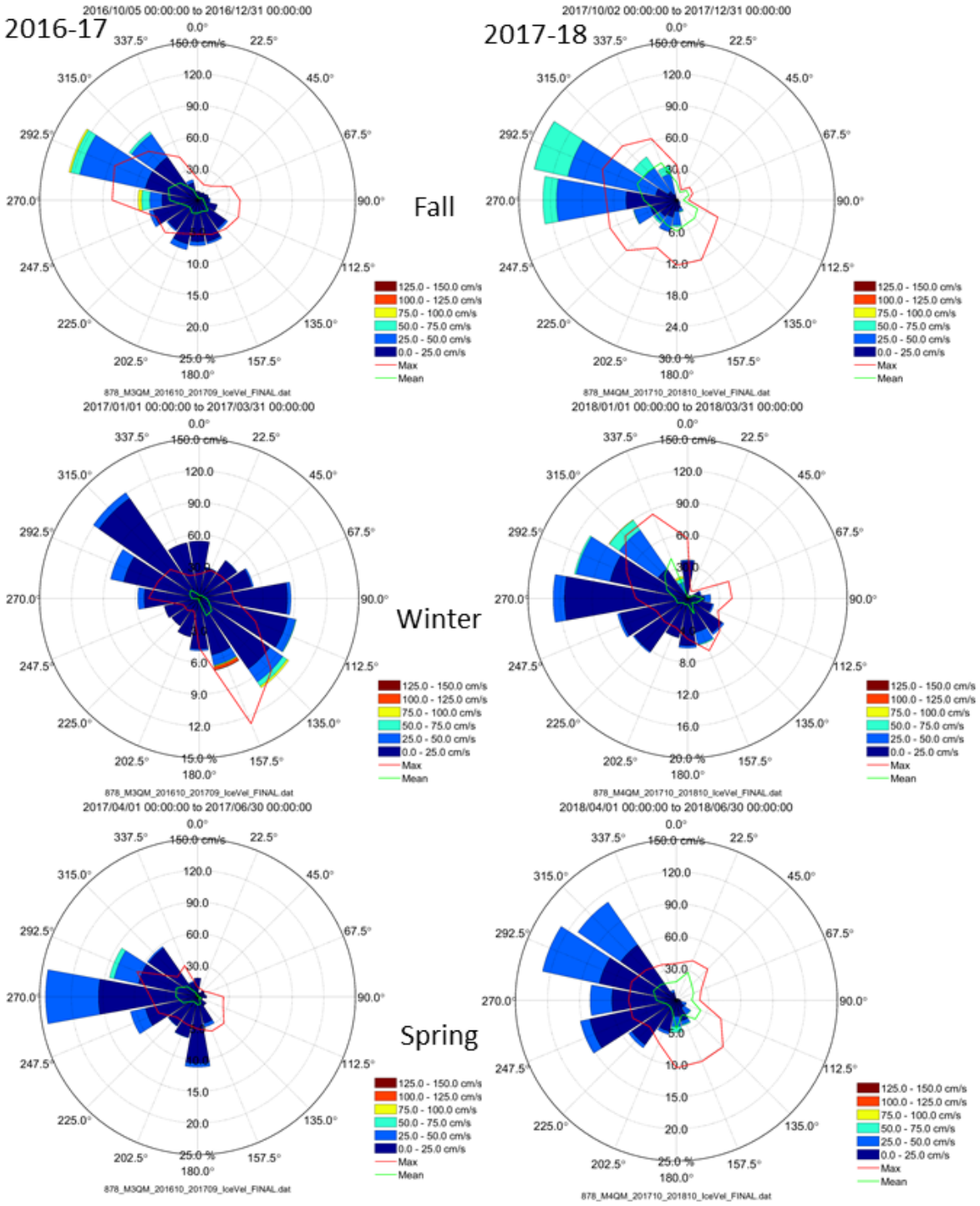

Figure 148. Compass rose plots of ice drift speed and direction at the M3 site for fall (top), winter (middle), and spring (bottom) for 2016–17 (left) and for 2017–18 (right). Directions are expressed as directions towards (e.g. Flow/drift toward the east has a 90° direction).

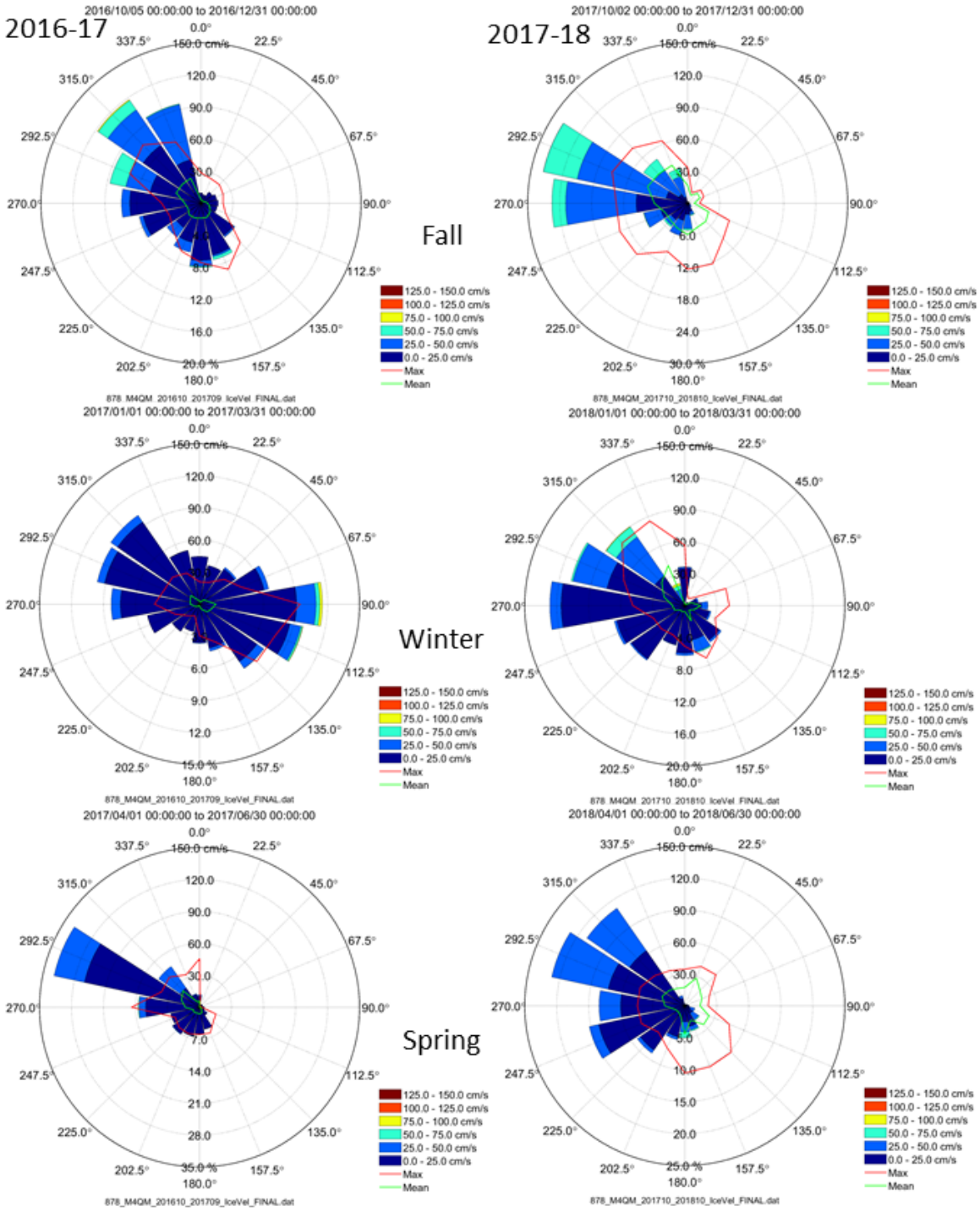

Figure 149. Compass rose plots of ice drift speed and direction at the M4 site for fall (top), winter (middle), and spring (bottom) for 2016–17 (left) and for 2017–18 (right). Directions are expressed as directions towards (e.g. Flow/drift toward the east has a 90° direction).

Overall, the seasonality is somewhat different among the four measurement sites in that at sites M3 and M4, the largest ice drifts occur in the fall and are reduced in winter and spring, which occurs in both years. However, at both sites M1 and M2, large ice speeds also occurred in other seasons: At site M1, large ice speeds towards the northwest were present in the winter of 2017–18 and 2018–19, while at site M2, large ice speeds occurred in the spring of 2016–17 especially to the west.

3.2.5.1.3 Drivers

Ice drift is forced within the constraints of physical boundary conditions (e.g. ice floe geometry, fast ice edge) by a combination of the near-surface currents and the wind forcing, with the latter being the most important. In winter and early spring, higher ice concentrations and the associated internal ice stress act to resist the wind forcing and reduce the ice speeds for extended intervals of near-zero ice speeds.

For inshore waters just beyond the landfast ice zone, episodic reduction and partial clearing of sea ice due to the formation of coastal flaw leads greatly reduces the effects of internal ice stress. This was clearly illustrated by large ice speeds in April and May 2017 and discussed in Fissel et al. (2019).

The dominance of northwesterly ice drifts at all mooring sites in spring appears to be related to the overwhelming dominance of winds blowing from the east and southeast in spring, which is more pronounced than in any other season. However, the sea-ice conditions in terms of concentrations, ice thicknesses and openings or fractures of the sea cover in the form of leads in the ice, can modulate the response of ice drift to wind forcing. The change in ice cover and leads/fractures is related to the seasonal development of the ice cover as a result of earlier conditions in late fall and winter.

3.2.5.2 Ice Draft and Concentration

3.2.5.2.1 Mean Conditions

The mean monthly ice drafts generally grow from November to December and attain values exceeding 1 m from January/February until June (see Table 39, Table 40, and Table 41 for 2017–2018). Statistics of number of keels observed per day at the 5 m threshold (light blue), 8 m level (medium blue), and 11 m threshold (dark blue) for each of the sites which had an ice profiling sonar over the two seasons are illustrated in Figure 150. The peaks in the keel counts tend to occur from February through to early May with over 200 keels, at the 5 m threshold, passing in a single day at M2 2017–2018 and M3 2016–2017. The largest number of ice keels exceeding 5 m ice draft occur at site M3 in 2016–2017 and at site M2 (available only in 2017–2018) while the number of large ice keels is smaller at site M4 in both years.

Probability density functions of the maximum draft, exceeding a 5 m ice draft threshold, are given for the 3 sites with IPS units for each of the two ice seasons in Figure 151. These large ice keels occur somewhat more frequently at site M2 (2017–2018 only) and at site M3 in both years with lesser numbers at site M4 in both years. The very largest ice keel was measured at site M3 and M4 in 2016–2017 with maximum values of 26.32 and 26.59 m *vs.* maximum observed ice keels of 24.95 m, 24.15 m and 24.32 m in 2017–2018 at sites M2, M3, and M4 respectively (Table 38).

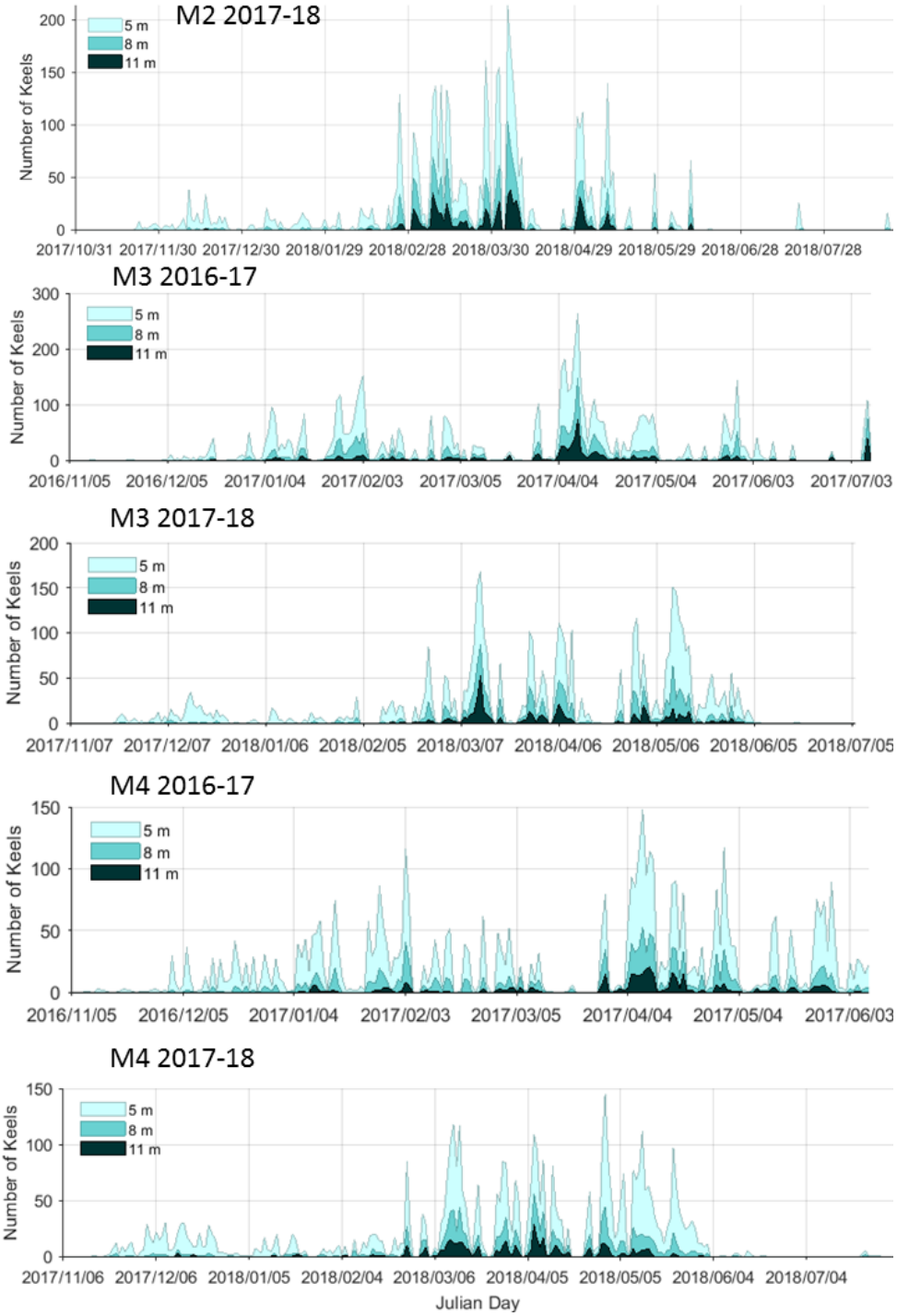

Figure 150. Number of keels versus Julian day from top to bottom for M2 2016–17, M3 2016–17, M3 2017–18, M4 2016–17, and M4 2017–18

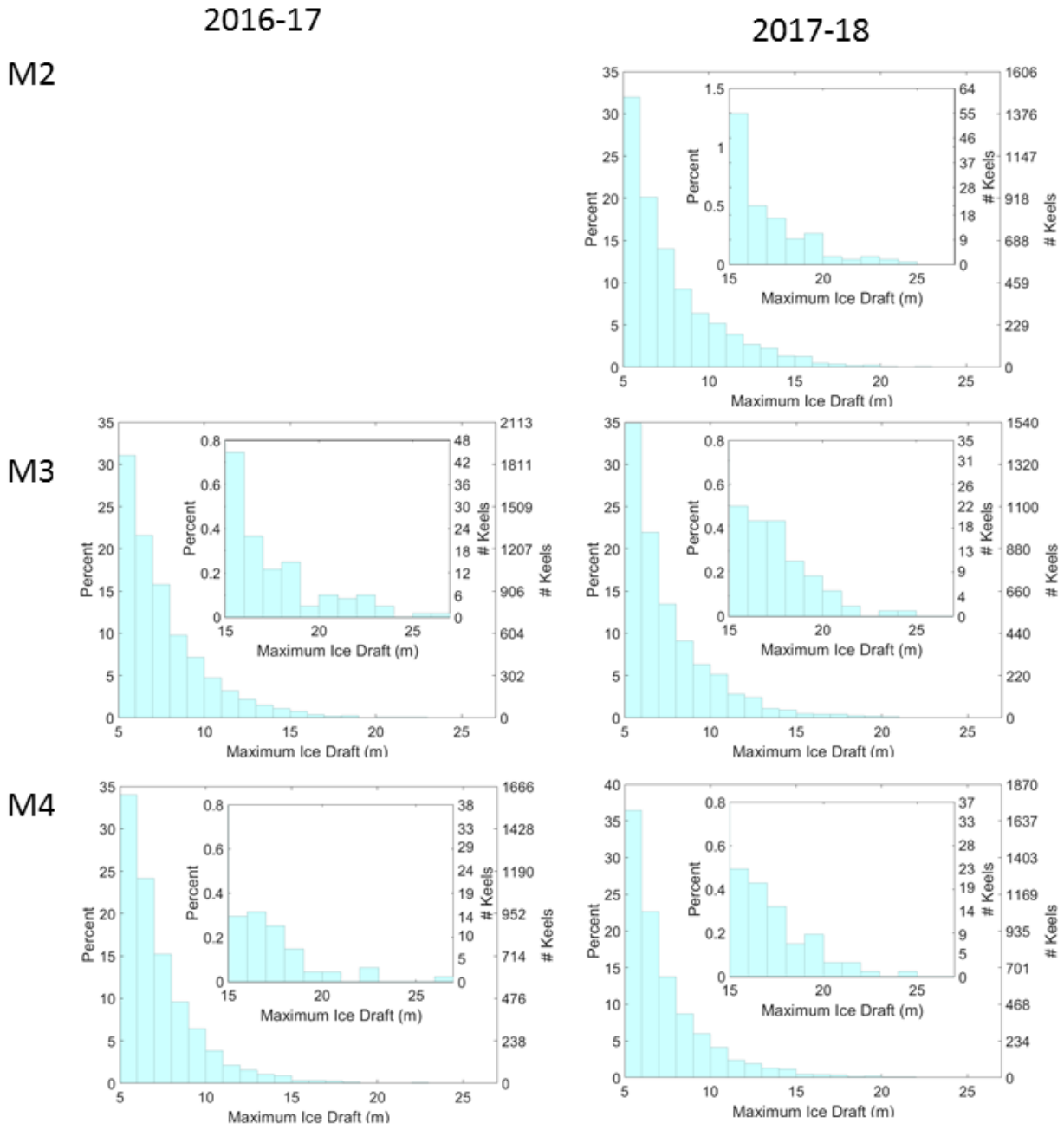

Figure 151. Probability density function of the maximum keel draft (for a 5 m threshold) for 2016–17 (left) and 2017–2018 (right) for M2 (top), M3 (middle), and M4 (bottom)
The insets zoom into the probability densities at the largest draft values.

As ice concentration is highly seasonal, but also shows high degrees of variability, the mean ice concentrations are not discussed. More is said about ice concentrations in the seasonality section below.

3.2.5.2.2 Seasonality

The seasonal variations in ice draft can be examined using the spatial-series of ice draft. This variability has been examined for the M3 and M4 sites which had ice profiling sonars in both years, and it is first examined via the number of keels which exceeded a 5 m threshold observed by month (Figure 152). There is a high degree of correlation between each of the sites measured in a given year, largely driven by thermal forcing, as well as by westerly winds which drive the sea-ice towards the coastline causing keel formation events in shallower waters through stamukhi formation (Wadhams, 2000). During the local maxima, there tended to be more keels observed in the 2016–17 ice season than in the 2017–18 ice season, however, the main peak in spring starts earlier and ends later in the 2017–18 ice season.

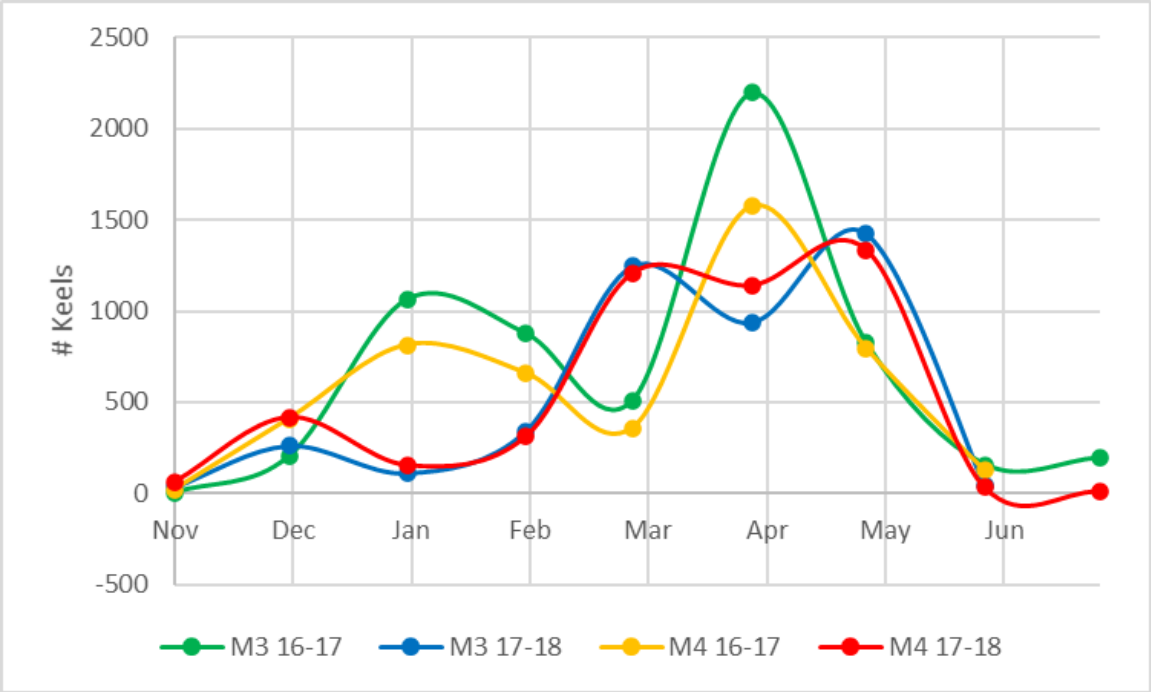

Figure 152. Number of ice keels exceeding a 5 m draft by month at the M3 and M4 sites in each year

The seasonal variability can also be examined through the mean ice draft of keels which exceeded the 5 m threshold (Figure 153), and through the maximum ice draft statistic (Figure 154). Over-all the thickest ice is observed in the late winter and early spring. Excluding M4, which is in the deepest water and has the lowest internal ice stresses, the maximum drafts were around 22–26 m.

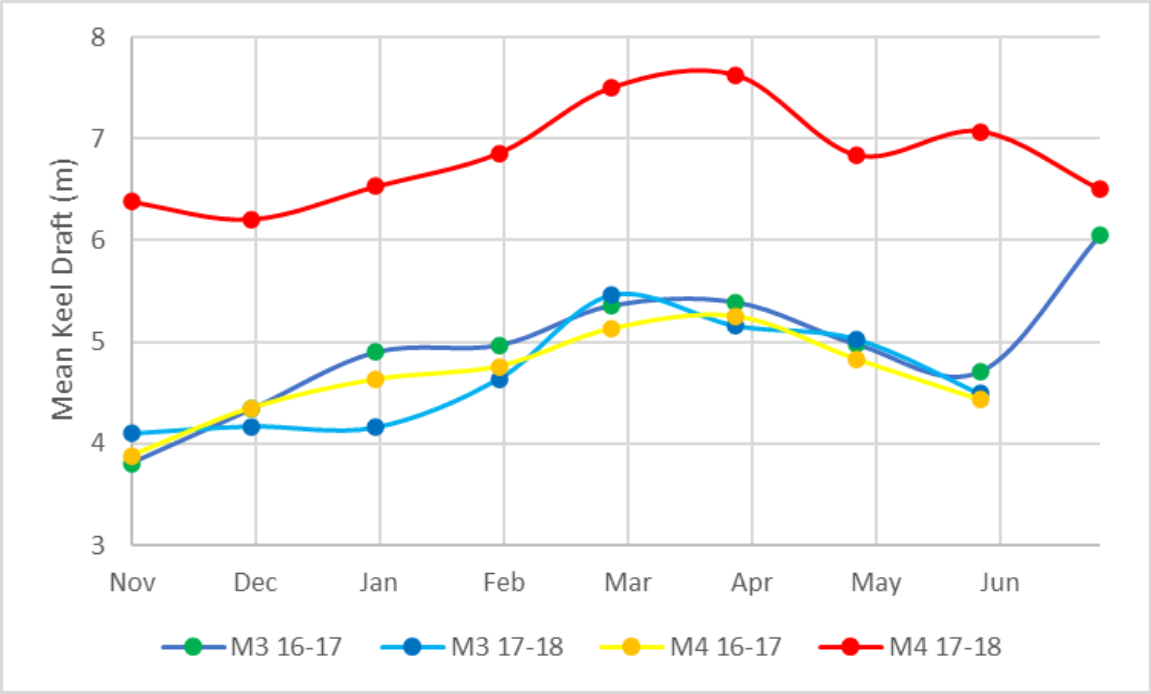

Figure 153. Mean ice draft of keels exceeding a 5 m draft by month at the M3 and M4 sites in each year

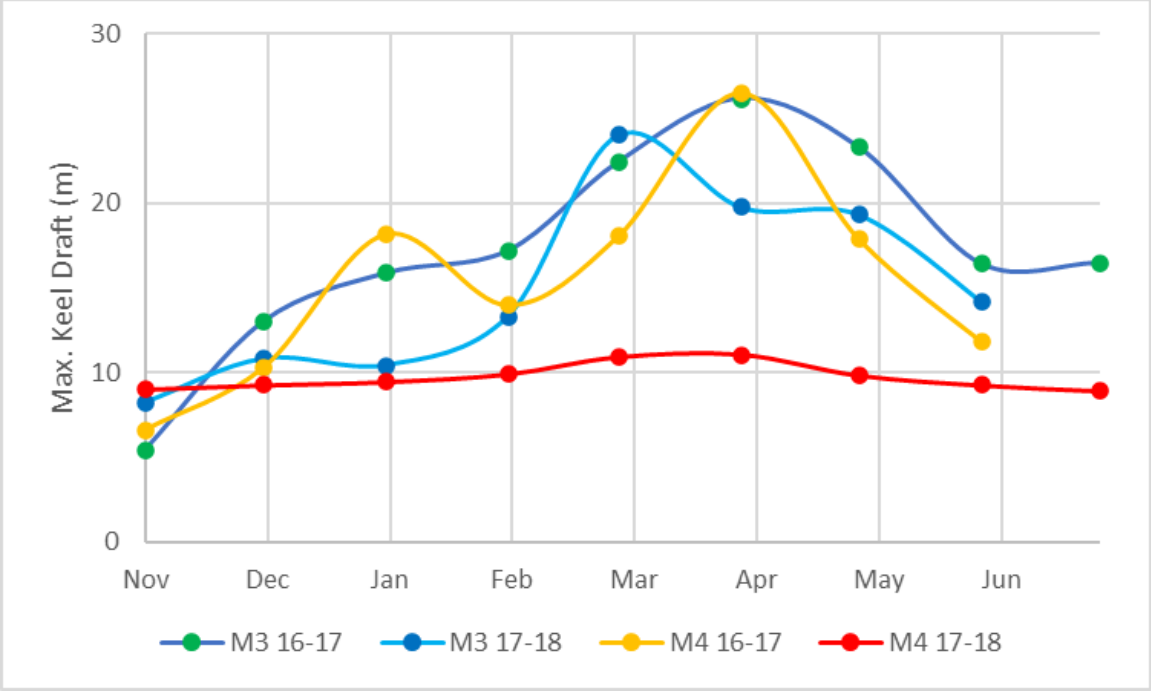

Figure 154. Maximum ice keel draft by month at the M3 and M4 sties in each year

Ice concentration is highly seasonal, as illustrated in Figure 155. During the study period, the development of sea ice at M3 and M4 started in October and November due to the cooling air temperatures and remained until March/April (non-withstanding wind events that may cause temporary leads). In spring (March–May), the combination of westerly winds and warming air temperatures caused ice concentrations to diminish and ice to melt, leading to an open-water season between June and October. Variations in these forcing factors causes changes such as the lingering of the sea-ice as observed in the 2017–18 year.

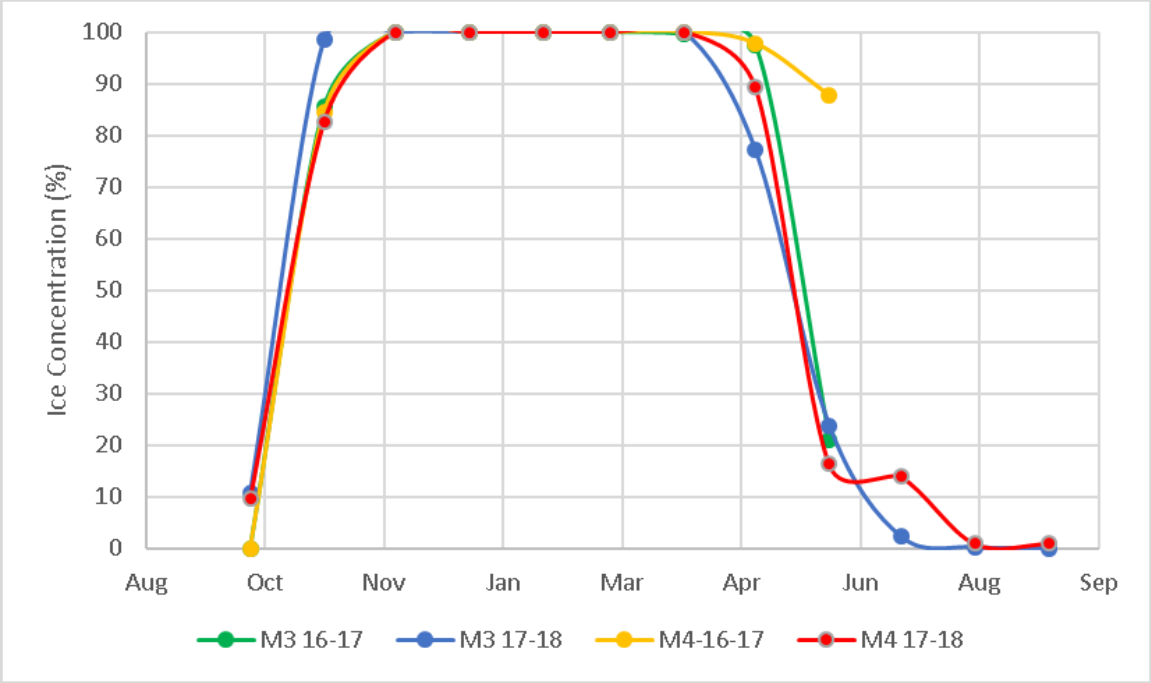

Figure 155. Seasonal variation in ice concentration at the two sites which had ice profilers in both years

3.2.5.2.3 Drivers

Ice draft is a result of both thermodynamic and dynamic processes. As would be expected, air temperatures need to be consistently cold enough to allow ice formation to occur in fall and winter, which is readily achieved in the high latitudes of the Beaufort Sea where the sun sets in November and rises again in February. This high degree of seasonal cooling in fall and winter and seasonal warming in spring and summer is the main determinant of the average sea ice drafts. Deep keels, however, are created by dynamic processes including the collision of individual ice floes with one another. Especially strong winds from the west can drive the sea ice against the coast under which conditions very deep ice keels can be formed. When the winds reverse and blow from the east, the ice is driven away from the shore and this creates leads which can refreeze and then be used to build up additional keels during the next westerly wind event. As spring arrives and air temperatures start to warm, the leads stop refreezing and there is a net reduction in the ice cover concentrations and ultimately in heating of the partial amounts of open water leading to the melt of the sea ice cover. As a result, we see more and deeper ice keels present in late winter and spring. Larger occurrences of deep keels tend to occur in years with more directionally variable winds.

3.2.6 Nutrients

3.2.6.1 Mean Conditions

Yearly nitrate concentration at M1 and M2 are summarized in Table 49. Concentrations for the extended period for M1 into 2019 are not included as they were considered unreliable after June 2018 (see Section 3.1.2.1).

Table 49. Nitrate statistics by year for the M1 and M2 sites

	Min (µM)	Mean (µM)	Std dev. (µM)	Max (µM)
M1 2016–17	0.62	13.86	3.72	29.48
M2 2016–17	2.48	8.39	1.91	17.18
M1 2017–18	0.04	15.65	4.32	23.27
M2 2017–18	5.42	11.57	2.51	18.86

3.2.6.2 Seasonality

The moored nitrate sensors on the M1 and M2 moorings allow the seasonal changes in nitrate to be monitored. No nitrate sensors were deployed at the other moorings. Figure 156 illustrates the nitrate concentration over the course of a year at the M1 site and Figure 157 illustrates the M2 counterpart. The nitrate concentrations can vary episodically, but the range in values by season tend to be similar across each of the years sampled at each site, respectively.

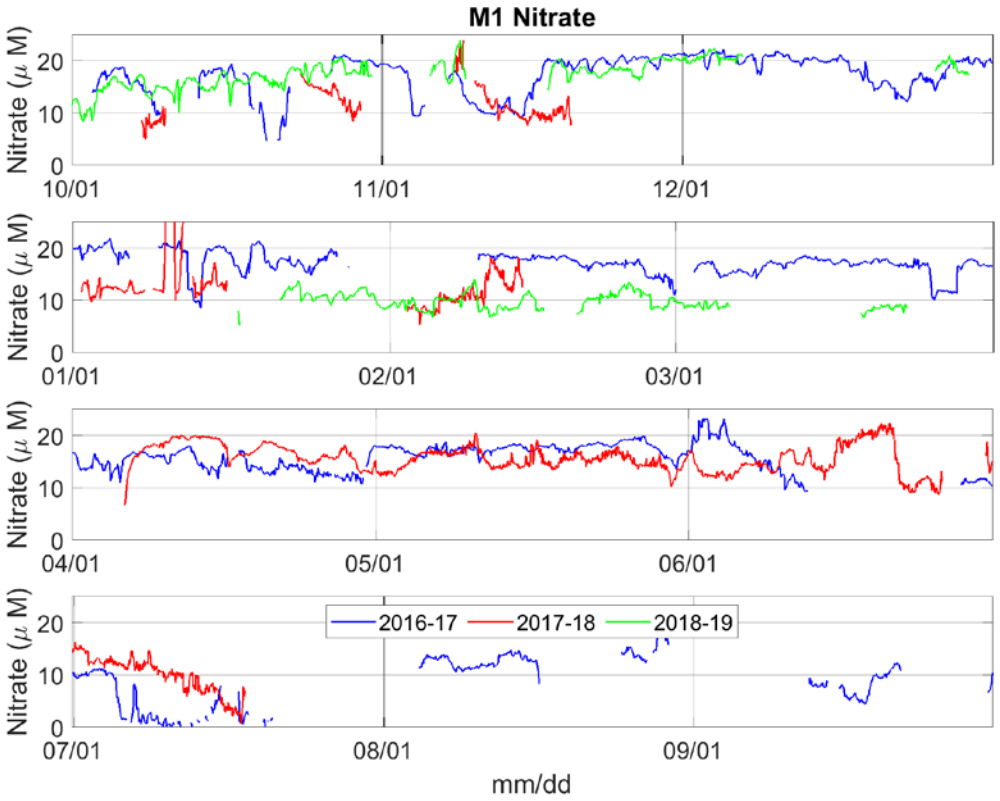

Figure 156. Overlay of nitrate time-series by season for the M1 site

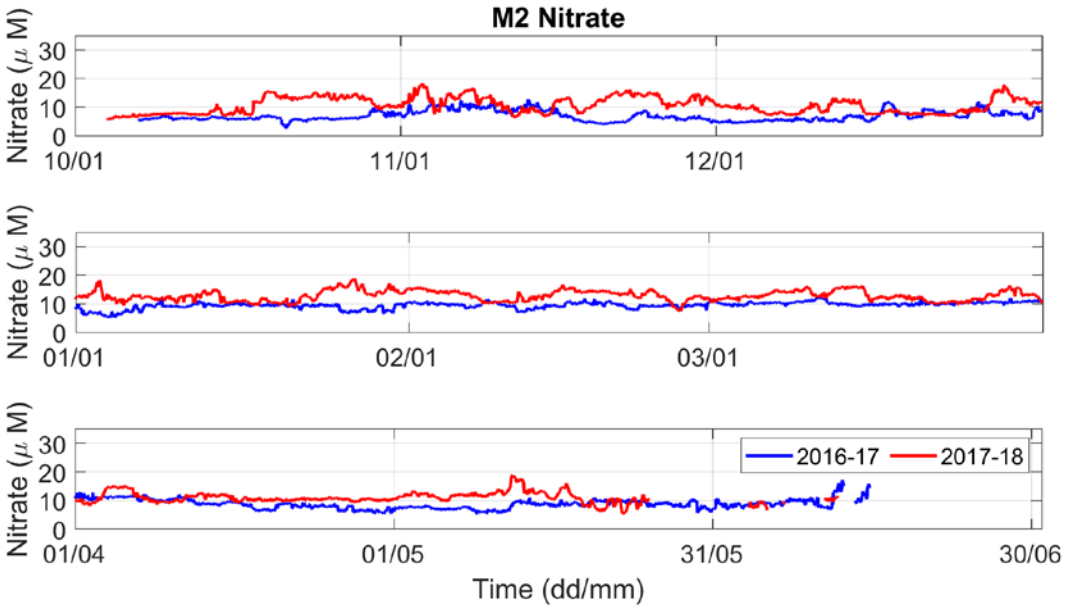

Figure 157. Overlay of nitrate time-series by season for the M2 site

To further show the variability, the minimum, 25 percentile, median, 75 percentile, and maximum values are shown by season in Figure 158 through Figure 161. In general, the M2 nitrate concentration percentile levels are smaller than at M1. At each of the sites, there tends to be very little year-to-year variability in the percentile levels, less than 5 µM, for the spring and summer seasons. The M1 site seems to have the most variability in nitrate concentrations in the fall and winter seasons compared to M2. Most notably is the much smaller nitrate values in the fall of 2016-17 versus the other two fall seasons, or the particularly large nitrate values in the spring of 2017-18.

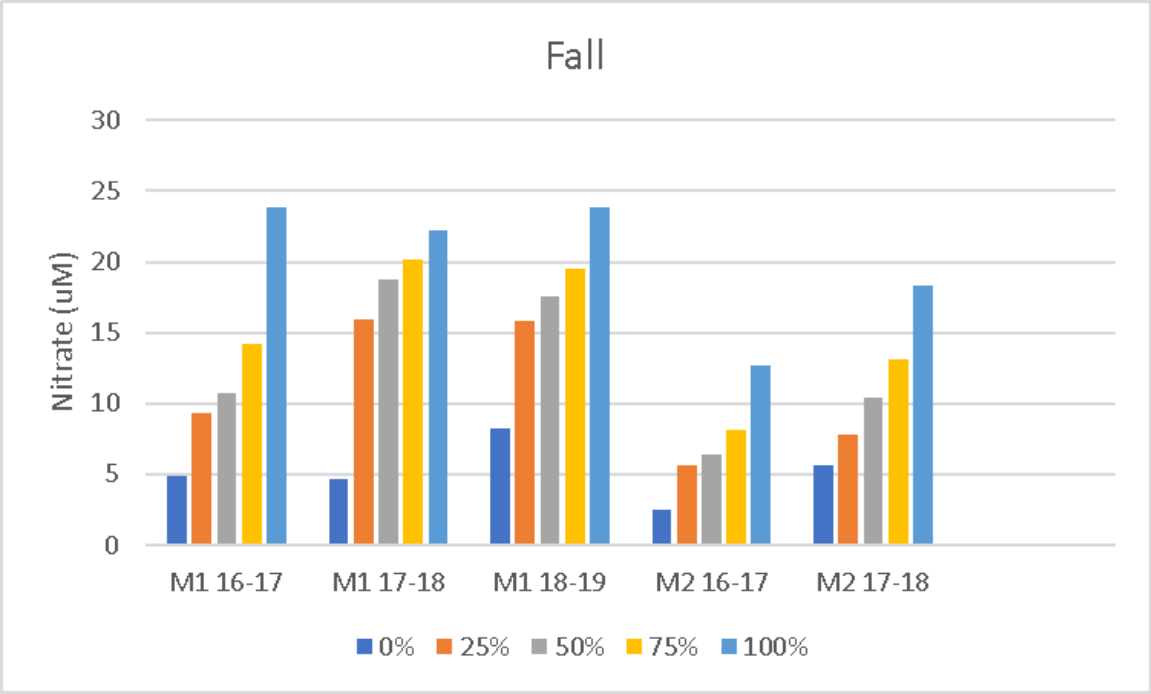

Figure 158. Minimum 25%, median, 75%, and maximum nitrate concentrations for the fall season

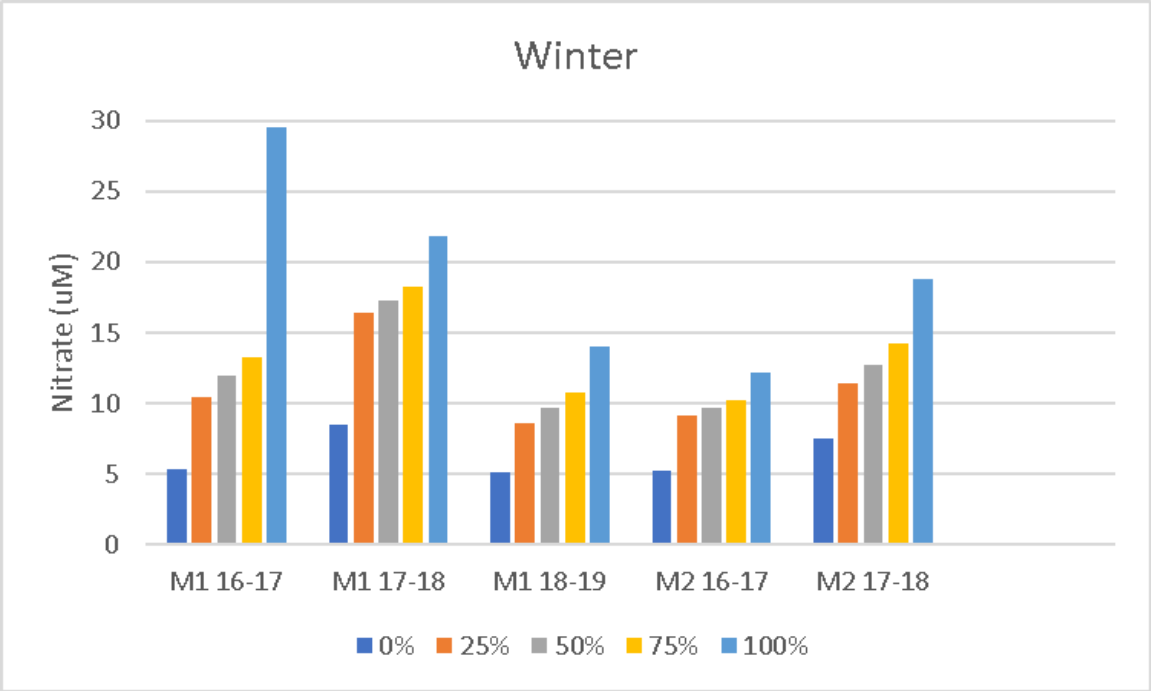

Figure 159. Minimum 25%, median, 75%, and maximum nitrate concentrations for the winter season

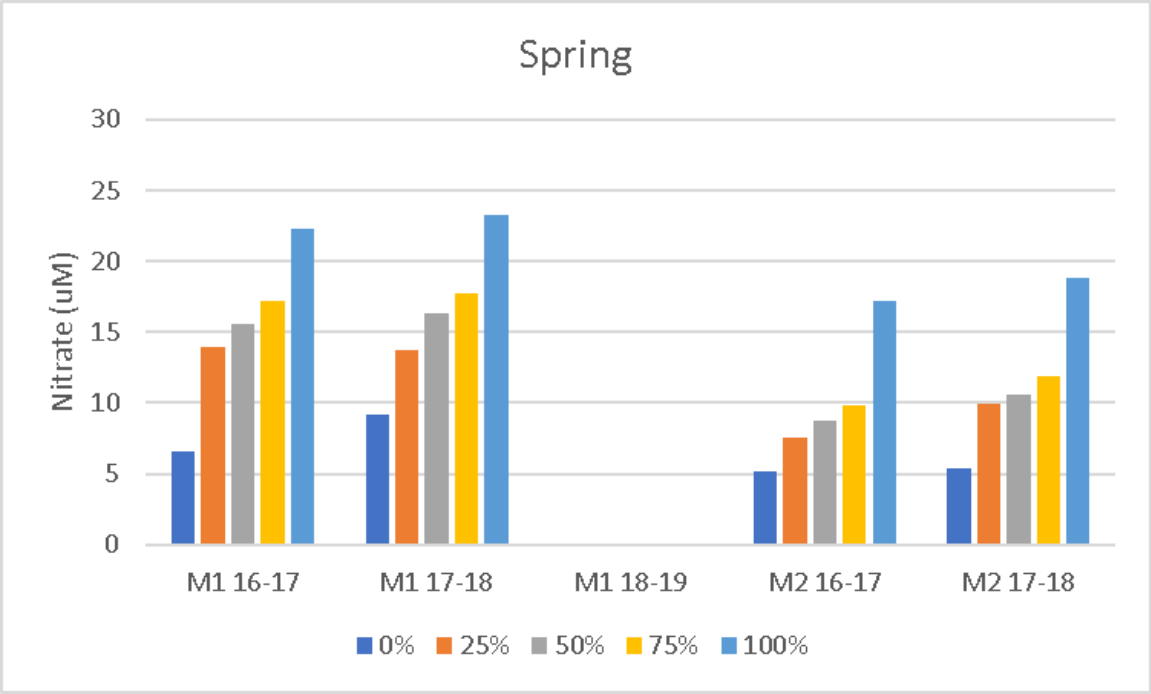

Figure 160. Minimum 25%, median, 75%, and maximum nitrate concentrations for the spring season

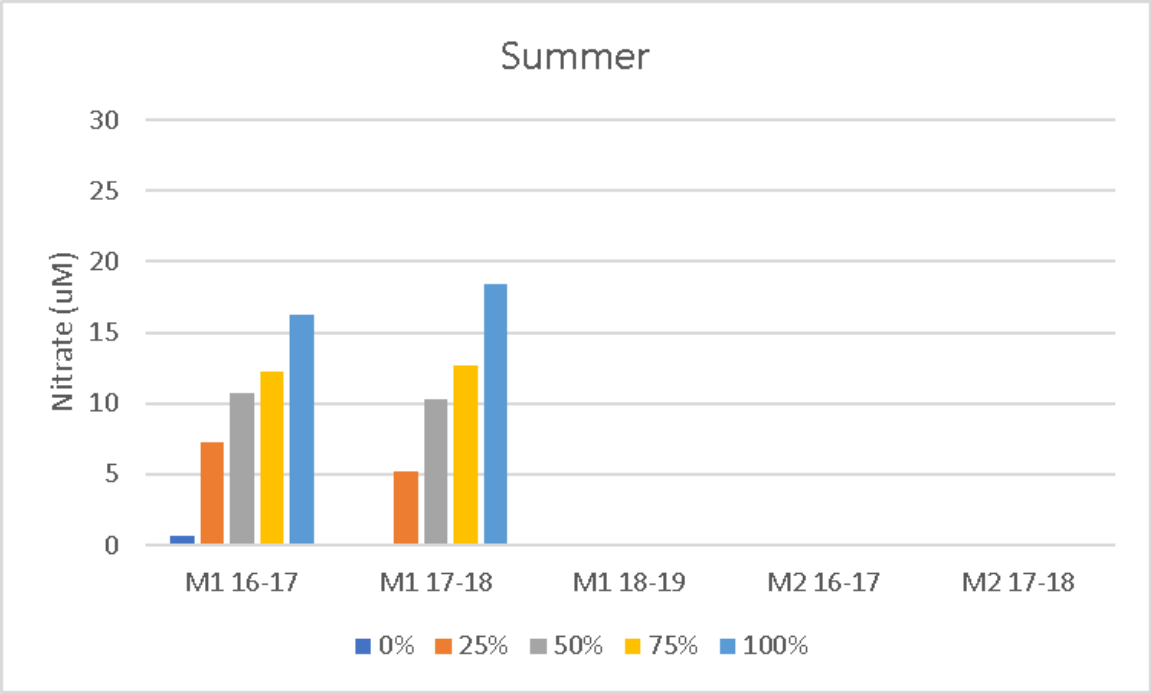

Figure 161. Minimum 25%, median, 75%, and maximum nitrate concentrations for the summer season

3.2.6.3 Drivers

Nitrate concentrations are driven by availability and the demand on this nutrient. Nitrogen on the shelf stems from freshwater input (primarily in spring and summer), sediment resuspension (primarily by storms in fall), and upwelling events during the open water season. Nitrates are primarily used by sea ice algae and phytoplankton in the spring and summer when the light returns and the ice melts. This pattern is evident at both M1 and M2, where nitrates stay high during the fall and winter, start getting drawn down starting in April, and get replenished again starting in October. Although only available for year 1, the timing of plankton blooms as evident in the fluorometer data presented in Wiese et al. (2019) concurs well with this phenology.

3.2.7 Zooplankton

3.2.7.1 Seasonality and Interannual Variability—ADCP

Relative ADCP backscatter data from ADCPs on moorings M1 and M2 for the two deployment periods (2016–2019) were compared to identify a seasonal cycle in relative backscatter. For each record, daily mean relative water column backscatter was calculated. Because different backscatter was observed between each of the two moorings and between years, the daily mean relative backscatter in each record was standardized to a range of 0–1, with 0 being the minimum value and 1 being the maximum value observed in each record in each year (Figure 162). The standardized daily mean relative backscatters were then smoothed using a 7-day running mean. Direct comparison of the four records by the day of the year (Figure 163) revealed a similar cycle but with considerable shorter term variability. Therefore, the standardized relative backscatter was smoothed using a 21-day running mean to better observe the seasonal cycle (Figure 164).

Lowest backscatter was observed for all records during April-May of the two years except for M1 in year 2 when the minimum occurred in early February. Following those minima, backscatter increased dramatically and somewhat coherently (within ~2 weeks) from early May to mid-June in both years for all four records and continued to increase in July and August. The spring increase started 1–2 weeks earlier at M1 than at M2. The earliest increase was seen at M1 in 2016–2017 (year 1). At M2, the increase occurred during the same weeks in the two years. Backscatter started to decline in all four records in mid-August of both years.

Patterns between the four records were much less coherent in terms of the relative magnitude of backscatter present at each mooring during October–May. This was particularly true for the records from M1 for which backscatter was greater in October through May 2016–2017 than in 2017–2018. This might have resulted from greater advective loss or mortality of scatterers from the shelf in the second year or from greater survival or advective input of scatterers in the first year. Backscatter during November 2018–February 2019 at M1 was similar to that observed in the previous year. For M2, it was interesting that the greatest backscatter for 2016–2017 occurred on the first date of the record; this might have been an aberration except that backscatter was still relatively high for a number of following days (Figure 162 and Figure 163). Backscatter at M2 was lower during year 2, similarly to what was seen at M1, with the exception of mid-November to January when the records showed biomass was approximately equivalent.

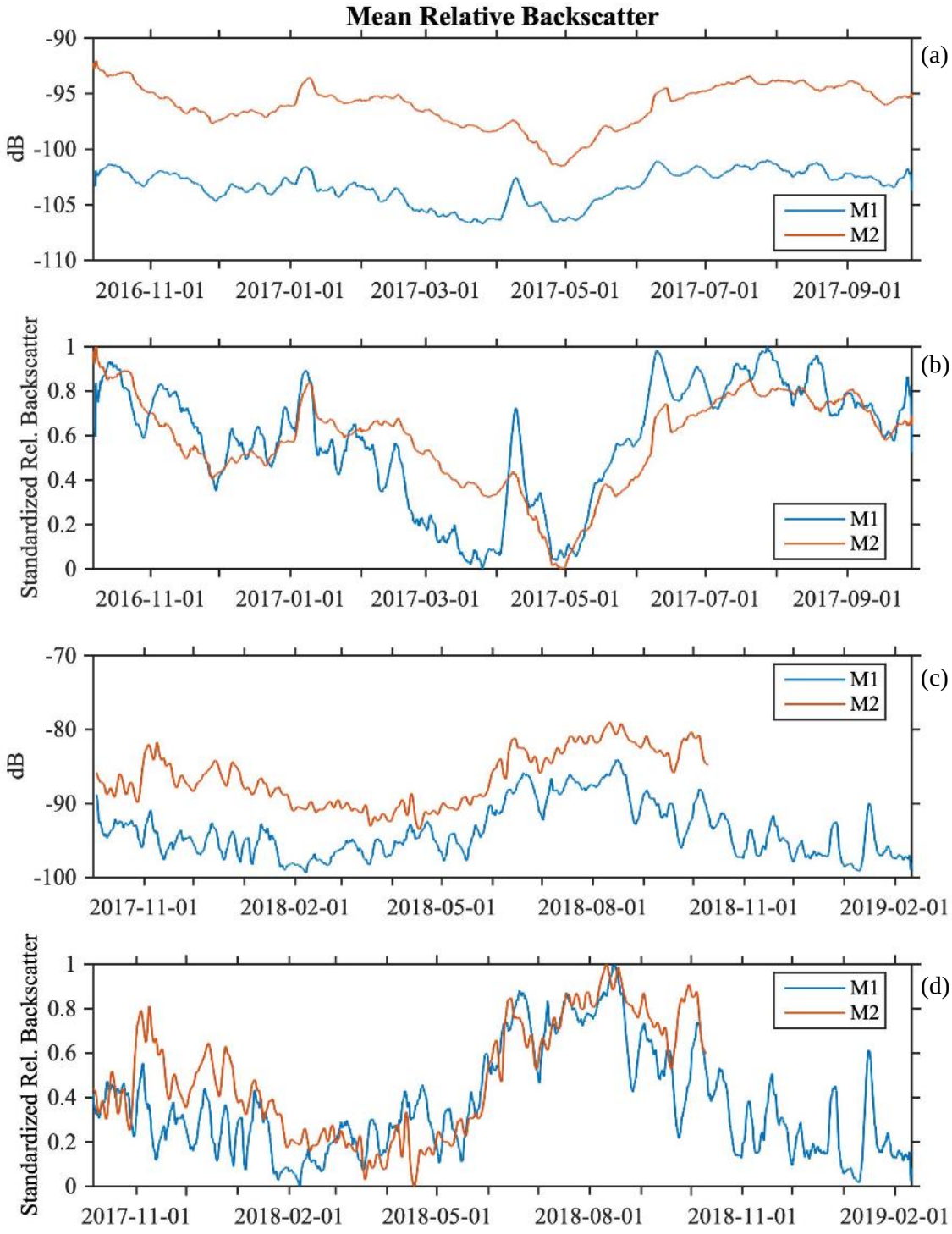

Figure 162. Daily mean relative backscatter (a and c) and standardized relative backscatter (b and d) for the two moorings from the 2016–2017 deployment (a and b) and the 2017–2018/19 deployment (c and d)

Data smoothed using a 7-day running mean.

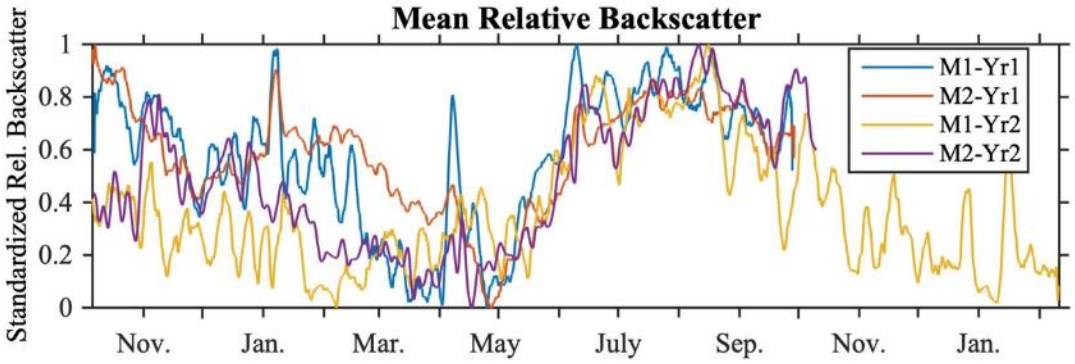

Figure 163. Daily mean relative backscatter and standardized relative backscatter for the four moorings in the two years, plotted *vs.* day of the year
Data smoothed using a 7-day running mean. Yr1=2016-2017; yr2=2017-2018/19.

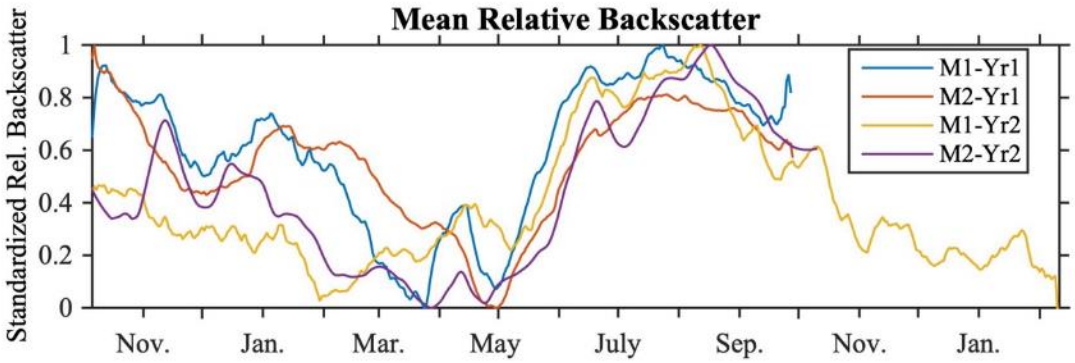

Figure 164. Daily mean relative backscatter and standardized relative backscatter for the four moorings in the two years, plotted *vs.* day of the year.
Data smoothed using a 21-day running mean. Yr1=2016-2017; yr2=2017-2018/19.

3.2.7.2 Seasonality and Interannual Variability—AZFP

The abundance of zooplankton differed between the two sampling seasons. From October 2016 to 2017, the abundance was moderate throughout the year, with lowest presence in April and May, with increased abundance in October and the end of February, and a more consistent presence between July to October (Figure 165). In year 2, zooplankton abundance was low all year except for the July to October period during which abundance was higher than in the corresponding period the previous year.

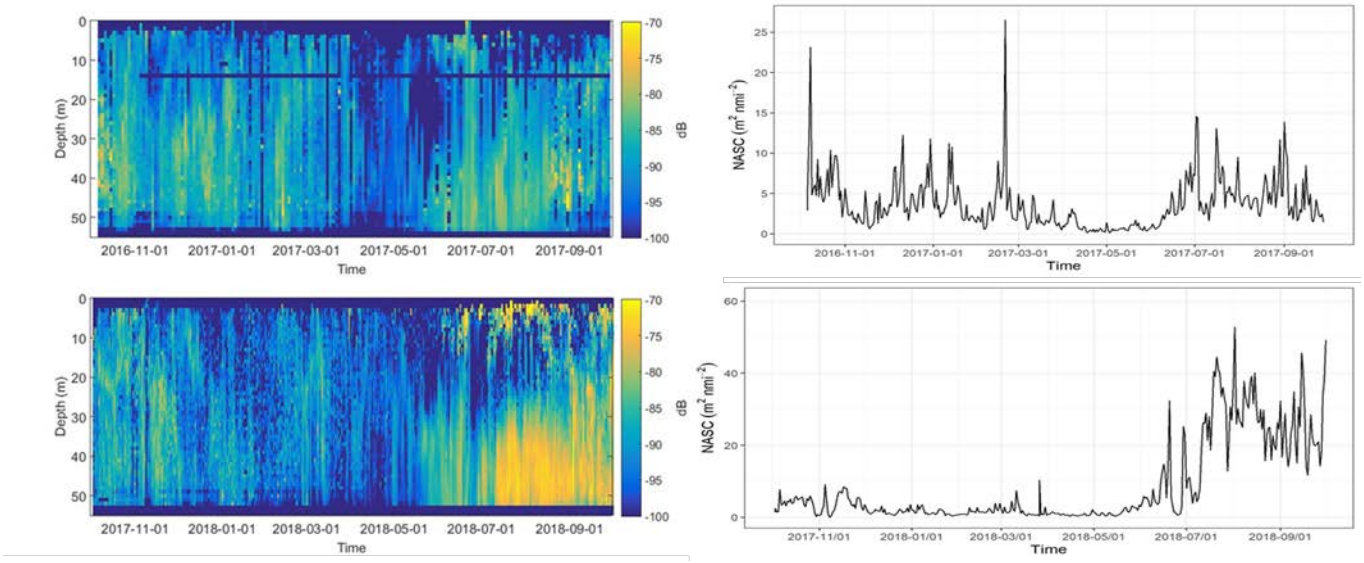

Figure 165. On the left, echogram of 200 khz backscatter (S_v) corresponding to zooplankton at site M3 in the Beaufort Sea, during the 2016/2017 (upper panel) and 2017/2018 (lower panel) season—on the right, corresponding Nautical Area Scattering Coefficient (NASC) as a function of time for zooplankton at site M3 in the Beaufort Sea, during the 2016/2017 (upper panel) and 2017/2018 (lower panel) season

Note the different scales of the y-axis.

Diel vertical migration was observed during both sampling seasons (Figure 166). Copepods and juvenile cod likely both contributed to the diel vertical migration pattern observed (Benoit et al. 2010).

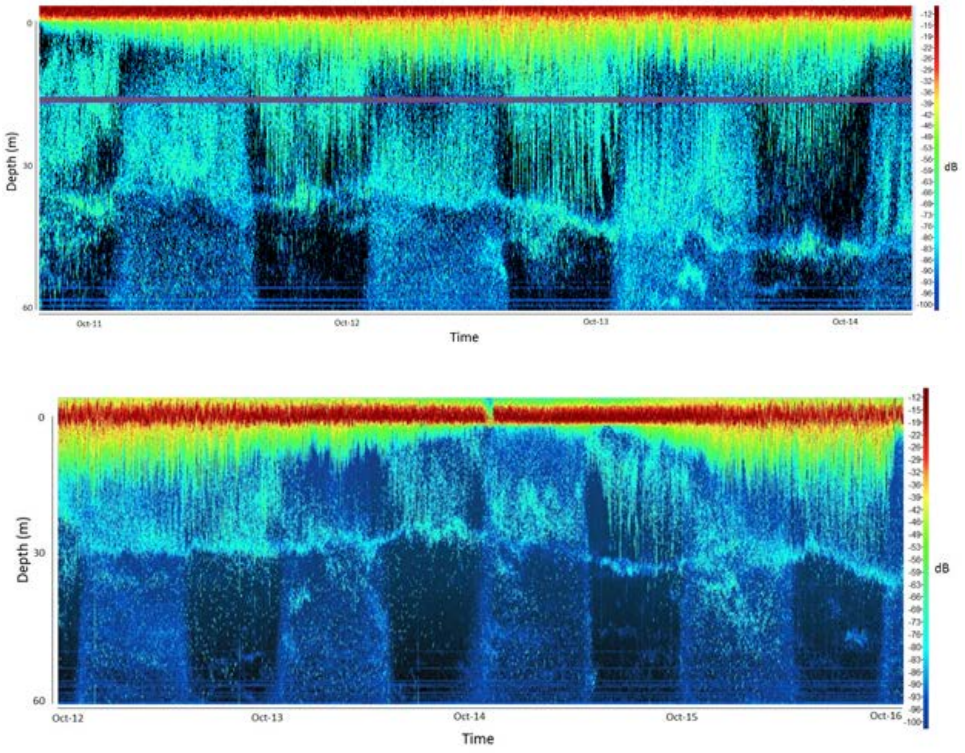

Figure 166. Echogram of 125 kHz Backscatter (S_v) showing daily migration pattern at site M3 in the Beaufort Sea, from October 11 to 14, 2016 (upper panel) and from October 12 to 16, 2017 (lower panel)

3.2.7.3 Drivers

As observed in 2016–2017, the observed backscatter patterns were consistent with there being different zooplankton communities at the shallow inner shelf site (M1) *vs.* the deeper outer shelf site (M2). Lower backscatter was observed throughout the year at M1 than at M2, suggesting that the zooplankton community at M1 contained lower abundances and biomass of large copepods such as *C. glacialis* that would scatter sound effectively, and higher abundances of smaller, more neritic species such as *Pseudocalanus* spp., while the zooplankton community at M2 was composed of larger, more oceanic species including both *Calanus* species.

The dramatic, near cohesive increases in backscatter during May–July (also seen at M3 with the AZFP) coincided with the productive period on the Beaufort Shelf, when sea ice is retreating, ice algal and water column primary production is initiated, and secondary production is ongoing. It also coincides with the cessation of diapause at depth of the large, overwintering *Calanus* spp. that are found along the shelf and slope of the Beaufort Sea. These animals migrate into the upper water column during the spring to exploit the spring primary production and could be more available for advection onto the shelf that time. Reproduction and growth of many zooplankton species also is ongoing during this period, likely contributing to the elevated backscatter. The less cohesive and varying declines in backscatter during the late fall and winter at the four locations may reflect differing advective regimes and events between years and locations, as well as potentially differing sea ice conditions.

It is possible also that zooplankton composition at these sites could be influenced by Mackenzie Water moving westward across the shelf. In the Smoot and Hopcroft (2017) study, Mackenzie Water was characterized by the presence of small, brackish copepod species such as *Eurytemora* spp. and *Limnocalanus macrurus* as well as cnidarians; these small copepods would not effectively scatter the sound from the ADCPs. The near-bottom temperature and salinity characteristics quantified by the CTDs on the moorings do not show low salinities (and warmer water in summer) that would indicate the presence of Mackenzie Water, although it could have been present in the upper water column above the depth of the CTDs. It would be useful to compare patterns in backscatter and DVM with a categorization of water mass evolution that includes a greater portion of the water column. Further comparisons with physical and biological drivers during the overall program synthesis will help identify potential physical and biological mechanisms influencing these patterns.

3.2.8 Fish

3.2.8.1 Seasonality and Interannual Variability

Adult cod

From October 2016 to 2018, the bulk of adult cod abundance occurred between September and April (Figure 167). As discussed above the majority of "adult cod" backscatter is from *Boreogadus saida* with potentially some *Arctogadus glacialis* mixed in at no more than 1% relative to B. saida. The highest abundance was observed at the beginning of December 2016. The following year, the highest abundance occurred in October and November of 2017. A second smaller peak in abundance at M3 was observed in early March of both years. The abundance remained low from April through July. Most adult cod were found below 200 m depth (Figure 168).

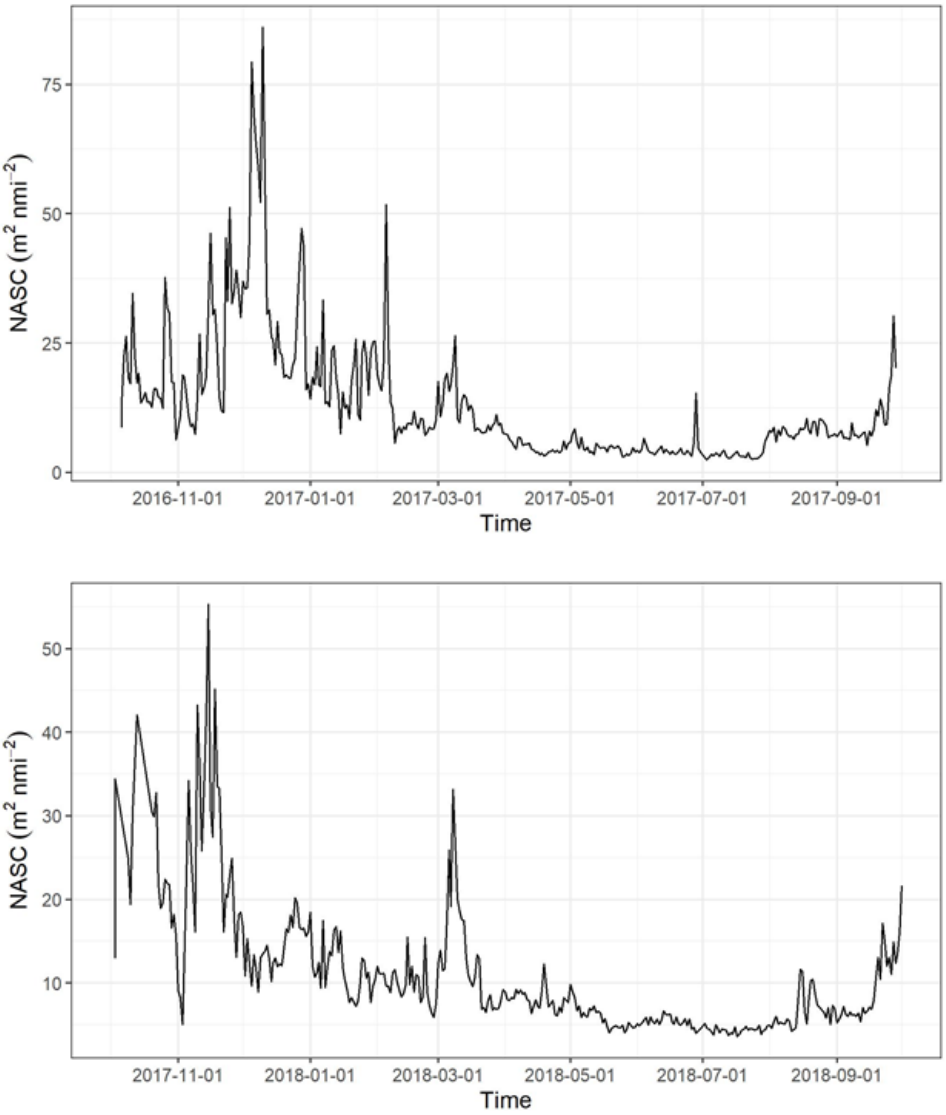

Figure 167. Nautical Area Scattering Coefficient (NASC) as a function of time for adult Arctic cod at site M3 in the Beaufort Sea, during the 2016–2017 (upper panel) and 2017–2018 (lower panel) season

Note the different scales of the y-axis.

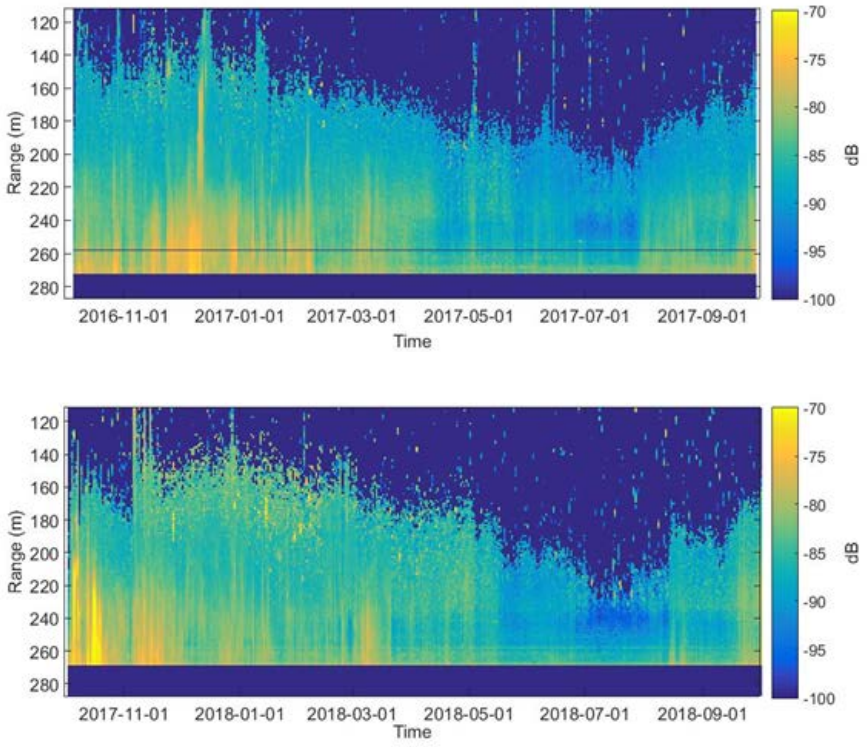

Figure 168. Echogram of 38 kHz backscatter (S_v) corresponding to adult Arctic cod at site M3 in the Beaufort Sea, during the 2016–2017 (upper panel) and 2017–2018 (lower panel) season

Juvenile cod

Juvenile cod were present near the surface at M3 from end of May through October in both years, mainly in the upper 40 m (Figure 169). Juvenile cod were present in higher numbers during the 2016–2017 sampling season, with a NASC 25 times higher than during the 2017–2018 sampling season (Figure 170). The temporal pattern was similar during both sampling season, with a local peak from the end of May to mid-June, and the bulk of the biomass observed from July to October. A similar pattern was found at site M2.

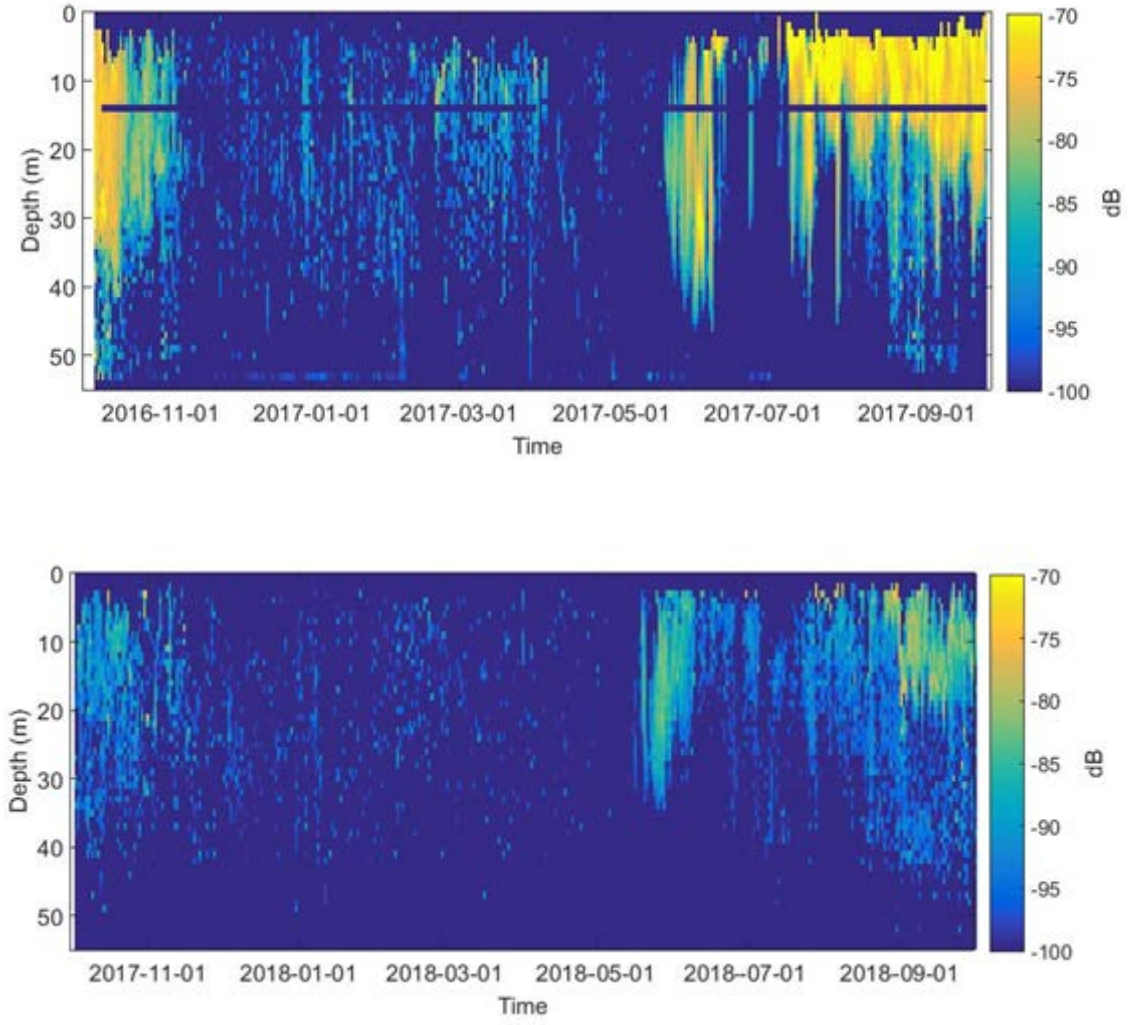

Figure 169. Echogram of 125 kHz backscatter (S_v) corresponding to juvenile Arctic cod at site M3 in the Beaufort Sea, during the 2016–2017 (upper panel) and 2017–2018 (lower panel) season

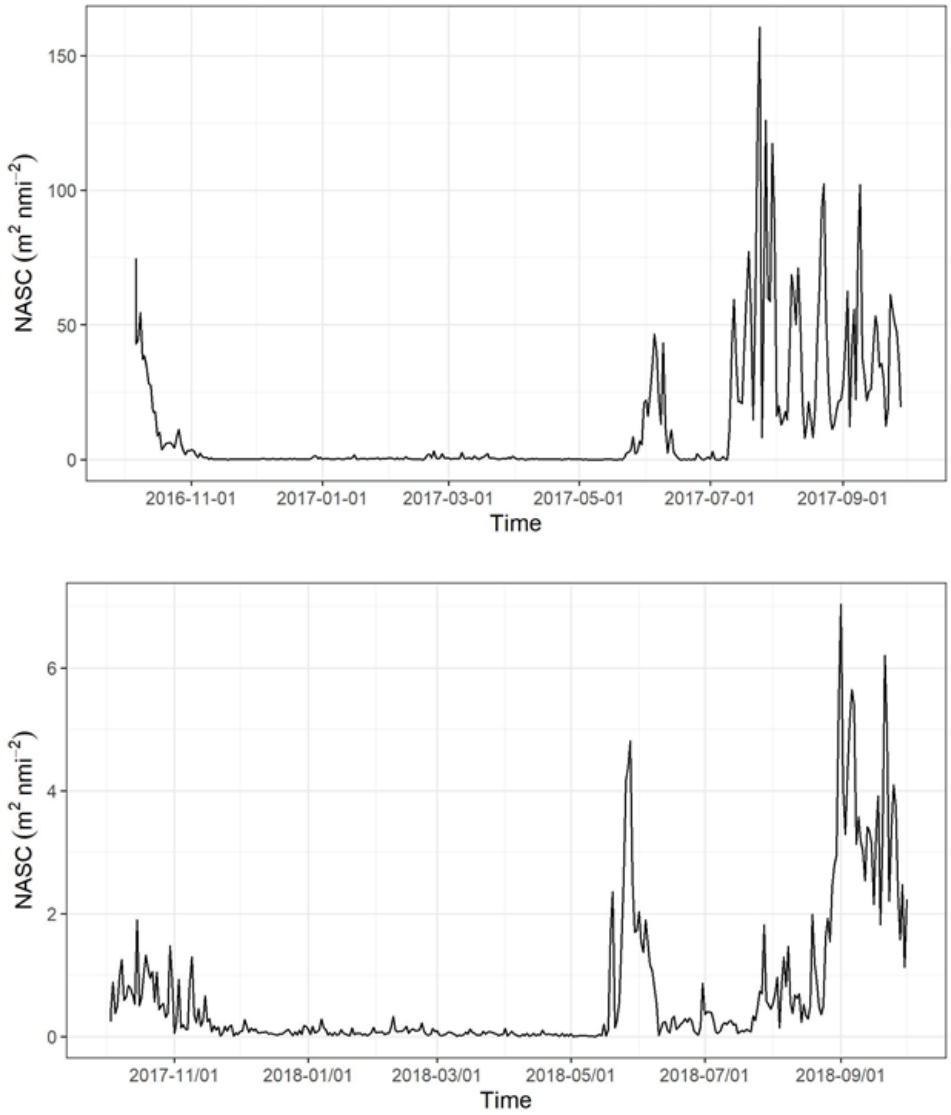

Figure 170. Nautical Area Scattering Coefficient (NASC) at 125 kHz as a function of time for juvenile Arctic cod at Site M3 in the Beaufort Sea, during the 2016–2017 (upper panel) and 2017–2018 (lower panel) season

Note the different scales of the y-axis.

3.2.8.2 Drivers

Although it is difficult to know the specific cues juvenile and adult Arctic cod are following, the patterns we observe over the two years of study are consistent with what is known about the life history of the species. Spawning of Arctic cod occurs in early spring under the ice and eggs drift for two to four months before hatching (Graham and Hop 1995). Newly hatched individuals feed to a large degree on early stage calanoid copepods. Our observations of juvenile cod near the surface from the end of May to October is consistent with young of the year cod foraging where zooplankton are feeding on primary production (both ice associated and planktonic). Young of year fish may be high in the water column in order to avoid predation by older cod. In the fall, most young of the year individuals move deeper in the water column (Geoffroy et al. 2016; Majewski et al. 2015). or into the pack ice (Gradinger and Bluhm 2004;

Melnikov and Chernova 2013; David et al. 2016). The ontogenic shift to deeper water is reflected in our observation of greatest presence of adult cod below 200 m from September to April at M3. These observations beg the question as to where the adult cod observed at M3 are found from May to August.

3.2.9 Marine Mammals

3.2.9.1 Seasonality and Interannual Variability

Bowhead whales and beluga whales were detected during the year 1 (2016–2017) and year 2 (2017–2018) deployment periods (Figure 171). Both species were detected in the summer and fall during both deployment periods but were detected 2 months earlier in year 1 than in year 2. Both species also remained 2 months longer into the winter in year 1 compared to year 2.

Bearded and ringed seals were both detected in the first year of deployment, but no ringed seals were detected in year 2 (Figure 171). In year 1, bearded seals were detected in the fall and through to the summer. Unlike year 1, bearded seals were not detected in the fall and winter of year 2 and were only detected in 6 months of year 2.

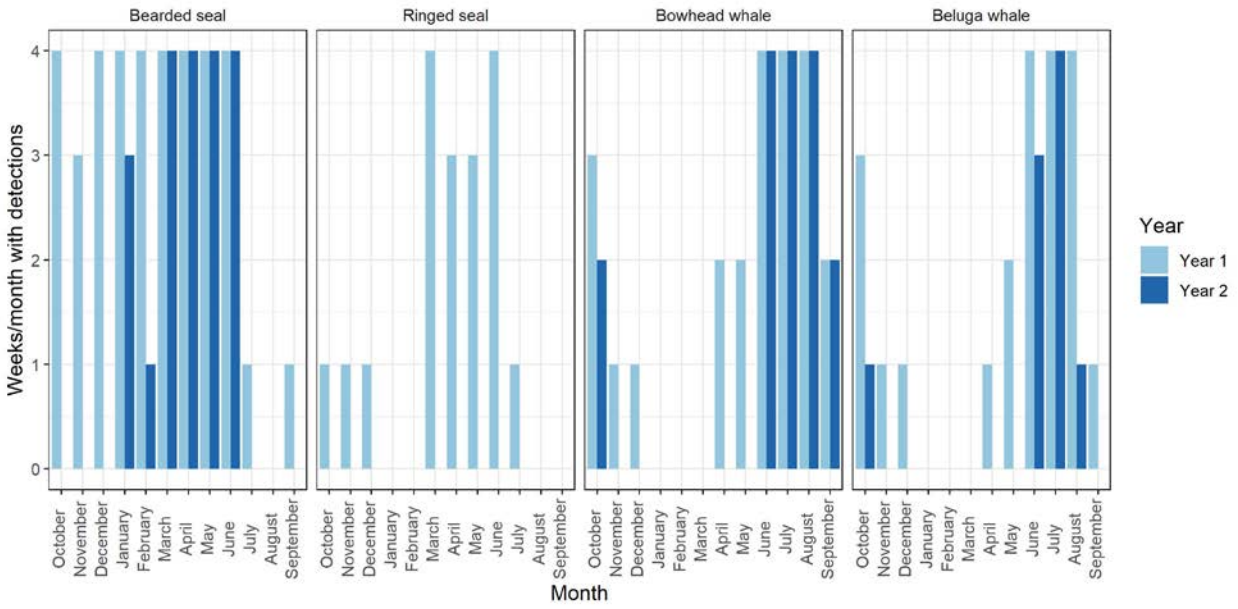

Figure 171. Number of weeks per month with marine mammal detections for year 1 (2016–2017) and year 2 (2017–2018) deployment

3.2.9.2 Drivers

The seasonal detections of bowhead and beluga whales is likely a reflection of the migratory patterns for these species, although the lack of detections of a species do not indicate absence. Bowhead whales migrate into the eastern Beaufort Sea for summer feeding (Moore and Laidre 2006, Harwood et al. 2017). Typically, the migratory route in the spring is farther offshore then the fall migration (Quakenbush et al. 2013), which may be reflected in the lower numbers of detections in the spring in y1 and the lack of detections in spring of year 2. The differences in fall/winter detections may be associated with differences in ice conditions, as bowhead whales will occupy inner shelf areas when ice conditions are light and will frequent deeper waters in heavy ice conditions (Treacy et al. 2005). Similarly, the variation in beluga

detections may be associated with variations in habitat selection, although more likely to be associations with habitat feature related to their prey rather than sea ice concentrations (Hauser et al. 2017).

The shortened duration of bearded seal detections in year 2, from January to June, compared to October to July in year 2, may be due to differences in ice formation and retreat. MacIntyre et al. (2013) found that peaks in bearded seal call detections were strongly associated with increased sea ice concentrations and decreased calls after breeding season in June. Potential differences in ice formation and duration between years should be explored to determine if similar associations are observed here.

The absence of ringed seal detections in year 2 was surprising as we would anticipate some calls throughout the deployment period. Interannual variation in ringed seal vocalizations have been noted in other multi-year studies (e.g., Jones et al. 2014), but not a complete absence in one year.

4 Conclusions & Recommendations from 2 Years of Mooring Data in the Eastern Beaufort Sea

4.1 Physical Oceanography

4.1.1 Currents

4.1.1.1 Findings

- The first extensive measurement study of ocean currents to the west of the Mackenzie Canyon reveal very large wind driven currents on the shelf.
- Over the continental slope, extending into the Mackenzie Canyon, complex patterns of currents occur at greater depths with a large response to wind-driven upwelling over the slope and a recirculation of water movements within the Mackenzie Canyon which may be related to wind forcing over the adjoining portions of the Canada Basin.
- Episodic currents are also present on the shelf edge and inner slope which can result in eastward transport of water of Pacific origin.
- The near-surface currents in the uppermost 5 to 20 m of the water column are heavily influenced by wind forcing combined with the effect of the discharge of the Mackenzie River and sea ice melt in late spring and summer and sea ice formation in fall and winter. The mooring data does not well resolve the currents in the uppermost portion of the water column, but satellite imagery and glider data sets can be used to augment the analysis of this important layer.
- In the year 2 deployment, although the inner-shelf mooring M0 was no longer deployed as it was in Year 1 (2016–2017), the mooring array M1-M4 revealed the main boundary current system: 1. The Shelf Current, surface-intensified and flowing westward; 2. the Shelfbreak Jet, bottom-intensified and flowing eastward; and 3. the recirculation in the canyon.
- The Shelf Current was stronger in year 2 (2017-2018) than in year 1 (2016–2017), while the recirculation was slightly weaker. The biggest discrepancy between the two years was the mean flow at mooring M2 on the upper slope, which was significantly stronger in year 2 due to a weakening of the Shelfbreak jet.
- There were large differences in the hydrographic fields between the two years. The water was significantly colder and saltier in upper 150 m in year 2 (less melt water/meteoric water and more winter waters). This is likely associated with changes in the strength of the boundary currents.

4.1.1.2 Recommendations

Further analysis of the very extensive MARES oceanographic data sets will yield additional understanding of detected ocean currents, which in turn will illuminate the large scale oceanography within the continental margin of the Beaufort Sea, especially in the vicinity of the Mackenzie Canyon. As such, it will be informative to compare the hydrography and circulation in the vicinity of Mackenzie Canyon in 2016–2017 versus 2017–2018 and explore the factors that may have led to any differences observed.

Both upwelling and downwelling in the vicinity of Mackenzie Canyon are relatively common. Using the two-year data set we can study wind-driven coastal upwelling/downwelling, as well as the recirculation-driven upwelling in the canyon; this includes the atmospheric forcing, the modulation of the response due to sea ice, and the biological ramifications.

A follow-up measurement program can now be better designed for further investigation of the Mackenzie Canyon ocean dynamics and its effects on shelf edge and inner slope transports along the Alaskan Beaufort Sea to the west and on the Mackenzie Shelf to the east.

4.1.2 Ice

4.1.2.1 Findings

- The direct measurements of sea ice from the MARES moorings, from Sept. 2016 through to the early part of 2019, reveal a very dynamic regime of sea ice motion.
- Sea ice motion is largely wind driven but also influenced by the seasonal effects of internal ice stresses developed in winter and early spring as the sea ice thickens and becomes more concentrated. The internal ice stress inhibits ice motion, but it exhibits a high degree of spatial and temporal variability.
- Another important contributor to sea ice dynamics is associated with the highly variable openings or fractures in the sea ice cover due to large scale leads including those far offshore, and the episodic occurrences of large coastal flaw leads just offshore of the coastline and landfast ice. The widespread and extended occurrence of these openings contributed to very energetic ice motion in the spring of 2017 in contrast to the more normal ice motion encountered in the spring of 2018 which appears to be associated with lesser openings and fractures in the sea ice cover.

4.1.2.2 Recommendations

- Further analysis of the very extensive MARES sea ice data sets, including ice motion and ice drafts, along with wind data sets and satellite imagery data on the surface sea ice features, will yield further understandings of the sea ice regime in this area.
- Further monitoring of the sea ice regime is required due to the large amount of interannual variability and the changing sea ice conditions that have and are occurring over decadal time scales.

4.2 Chemical Oceanography

4.2.1 Nutrients

4.2.1.1 Findings

Nitrate was found to vary on episodic and seasonal scales. Overall, the nitrate concentrations reached a minimum over the summer months when nitrate consumption of organisms such as sea ice algae and phytoplankton are most active. Starting in the fall and carrying on into the darkness of winter, the nitrate concentrations are renewed.

4.2.1.2 Recommendations

To get better sense of spatial variability and the influence of physical and other drivers, future studies should attempt to deploy sensors across the entire shelf.

4.2.2 Carbon Dioxide

4.2.2.1 Findings

Unfortunately, we had significant sensor error from the SAMI pCO2. The Ocean Acidification Research Center (OARC) at the University of Alaska Fairbanks (UAF) is currently working with the manufacturer, Sunburst Sensors, to eliminate malfunctions that are possibly related to pressure changes in the internal membrane during air shipment.

While we had great difficulty with our SAMI-CO2 sensors, it is notable that the useful data collected in year 1 show a $CaCO_3$ undersaturation with respect to aragonite in this region. The Beaufort Sea is a known OA hotspot where cooler water temperatures and unique biochemistry preconditions the system to be sensitive to increased anthropogenic CO_2 (Cross et al. 2018 and Bates and Mathis, 2009). Biological impacts from OA may have significant implications to an ecosystem that is already experiencing ocean change.

4.2.2.2 Recommendations

In the future, we recommend a suite of sensors be deployed together. These packages may include a Seabird SeaCAT with T, S, and dissolved oxygen sensors. The oxygen data can be useful when interpreting recovered pCO_2 data. In circumstances where other biogeochemical parameters are wanted to study carbon cycling or ocean acidification, a moored pH sensor is also deployed. When pCO_2 and pH data are both collected, the user may calculate total alkalinity, dissolved inorganic carbon, and calcium carbonate saturation states. Future deployment of this kind in this region would help determine the ecosystem impacts of observed values over time.

4.3 Biological Oceanography

4.3.1 Zooplankton

4.3.1.1 Findings

- The dramatic, near cohesive increases in zooplankton abundance during May-July coincided with the productive period on the Beaufort Shelf, when sea ice is retreating, ice algal and water column

primary production is initiated, and secondary production is ongoing. It also coincides with the cessation of diapause at depth of the large, overwintering *Calanus* spp. that are found along the shelf and slope of the Beaufort Sea.

- The less cohesive and varying declines in zooplankton abundance during the late fall and winter may reflect differing advective regimes and events between years and locations as well as potentially differing sea ice conditions.
- DMV signals were present for zooplankton and juvenile cod. For mooring M1, DVM occurred primarily during the summer (June–August) months, when backscatter was greatest. At M2, DVM was a regular occurrence on the time scale of days throughout the year with the possible exception of November 2017. That DVM occurred even when the sun did not rise (December-January) is remarkable.

4.3.1.2 Recommendations

Future studies in this region would benefit from greater water column coverage of AZFPs working in the higher frequencies such that zooplankton taxa could be better characterized. The ADCP provides a very useful picture of patterns and trends and this could be well augmented by having greater information regarding the taxa detected.

Further comparisons with physical and biological drivers will help identify potential physical and biological mechanisms influencing patterns in abundance, timing and behavior.

4.3.2 Fish

4.3.2.1 Findings

- Juvenile cod were present near the surface from end of May through October, mainly in the upper 40 m. DMV was detected (see above) which likely in part was due to movement of juvenile cod..
- The bulk of adult cod abundance was detected between September and April. The abundance remained low from April through July. Most adult cod were found below 200 m depth.
- The AZFP observations made here well describe the emerging understanding of the life history of Arctic cod in the Beaufort Sea; young of the year cod are found high in the water column during spring and summer and appear to migrate to deeper waters in the fall.

4.3.2.2 Recommendations

Greater spatial coverage such that migration of young of the year and adult cod could be monitored across the shelf would be desirable. From our observations we do not have information as to where the adult cod observed at M3 are in spring in summer. A study designed to determine this would contribute greatly to understanding the of the life history of Arctic cod of the region.

4.3.3 Marine mammals

4.3.3.1 Findings

- Two cetaceans, bowhead whales and beluga whales, and one phocid, bearded seal, were detected in 2017–2018.
- Ringed seals were not detected in 2017–2018 but were detected in the previous year.
- Bowhead and beluga whales were detected in the summer and fall.
- Bearded seals were detected in late winter through the summer.

4.3.3.2 Recommendations

The deployment of additional AURALs to form an array would allow for the localization of animals and potentially estimates of number of animals vocalizing. This would allow for broadscale understanding of where these animals are vocalizing and potentially what habitat they are using. For bearded seals, which have increased vocalizations during breeding season, this would provide much needed insights into preferred habitat. Additionally, marine mammal satellite tagging would be beneficial to gain insights into habitat use, as there has been limited tagging in this region. This would allow for finer scale understanding of habitat use and influence of the Mackenzie on these species and their prey.

5 Data Synthesis

5.1 Overview

The full benefit of interdisciplinary multi-year work, as carried out under MARES, is realized by consolidating all project results to understand the relationships across the different spatial and temporal parameter measures. This is especially true in marine environments, like the Beaufort Sea, that have inherently complex interactions within and among abiotic and biotic drivers and variables, and the people that depend on the health of this ecosystem.

Initially, MARES included the development of a system conceptual framework and a substantial modeling effort that would have served as a broader synthesis for all the information collected since the summer of 2016. In the absence of support for those activities, a more focused synthesis meeting was funded and held in the fall of 2019 in Seattle, WA. The following sections serve as the report for this synthesis meeting, illustrating a first level of integration of MARES data, and focusing on three integration scales:

- ***Broad Scale***: describing the general system characteristics and identifies the main system-wide abiotic drivers and its consequences for the biological components of the ecosystem.
- ***Seasonal Scale***: describing the general seasonal cycle in the eastern Beaufort Sea based on general system knowledge and illustrated by the MARES data.
- ***Event Scale***: describing the relationship between physical, chemical, or biological events and illustrating the importance of event scale drivers to the overall system dynamics.

5.2 The Oceanographic Structure and its Impact on the Biological System of the Canadian Beaufort Sea

5.2.1 Introduction

Broad scale processes in the Beaufort Sea are governed by large scale and regional physical drivers. These drivers are linked together, and to the marine biological components of the broader region within the western Arctic Ocean (Figure 172). The strength of each of the driver and linkages between them dictate the broad scale and systematic processes present in the Beaufort Sea.

Here, we describe the main broad scale physical drivers, their linkages, and their influence on the general chemical and biological components in this region.

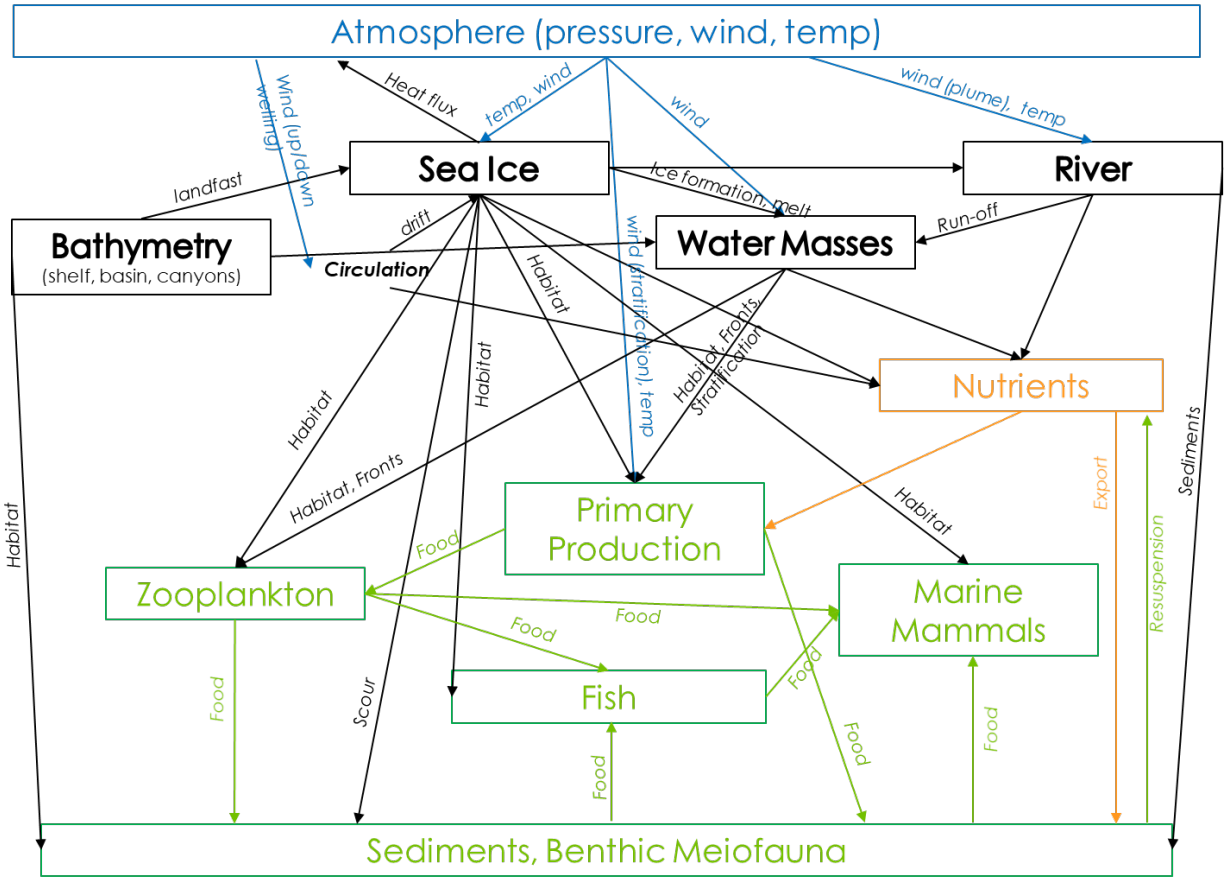

Figure 172. The linkages between biophysical components of the marine ecosystem of the Canadian Beaufort Sea

Blue=atmospheric drivers, black=abiotic drivers, orange=nutrients, green=biological.

5.2.2 Physical Drivers

The physical drivers include both dynamic drivers and fixed components. Dynamic drivers in the Beaufort Sea include winds, freshwater inputs (e.g., Mackenzie River), and sea ice formation and movement. The dynamic drivers interact with each other either in synergistic or antagonistic ways, determine circulation patterns and water mass distribution, and are in turn influenced by fixed components such as bathymetry. In the MARES region, the eastern Beaufort Sea, bathymetry, particularly the Mackenzie Canyon, persistent and episodic winds, and the Mackenzie River, are the main physical drivers that impact sea ice, nutrients, water masses, and the rest marine ecosystem.

5.2.2.1 Bathymetry

The bathymetry of the Beaufort Sea has a profound influence on the oceanographic processes on regional and local scales. The continental margin of the Beaufort Sea extends from 157W at Barrow Canyon, extending eastward to 125W, spanning a distance of over 1200 km (Figure173). The Mackenzie Canyon at 138W interrupts and separates the Alaskan Beaufort Shelf from the Canadian Beaufort Shelf, which are very different in their geometry. The Alaskan Beaufort Shelf extends to water depths of about 75 m with a reasonably uniform width of about 65 km (Williams and Carmack 2015). The width of the Canadian Beaufort Shelf increases to more than 130 km due to deposition of sediments over past millennia from the Mackenzie River. The shelf ends at 125W with the deep water of the Amundsen trough that extends into

Amundsen Gulf. The Mackenzie Canyon allows deep water to approach within 20 km of the Yukon coastline. The steep shelfbreak bathymetry on the western wall of the Mackenzie Canyon can cause the shelfbreak jet to accelerate significantly (>0.6 m/s) over a very narrow region. This has transport implications for the Mackenzie River plume water in this part of the Mackenzie Canyon. The Barrow, Mackenzie and Amundsen Canyons are the major bathymetric features defining the Alaskan and Canadian Beaufort Sea Shelf. Other minor canyons also traverse the continental shelf including the Kugmallit Valley (Williams et al. 2008), Garry Trough, and the Tingmiark Valley but these bathymetric features are notably shallower and narrower than the three major canyons.

A major dynamic feature of submarine canyons is canyon-induced upwelling and downwelling. In the Northern Hemisphere, a right bounded flow (with coast to the right) is would lead to canyon downwelling. On the other hand, a left bounded flow would result in canyon upwelling (Klinck 1996). Although the external drivers for canyon upwelling and downwelling are sometime the same as for coastal upwelling and downwelling (e.g. winds), canyon upwelling and downwelling is an ageostrophic phenomenon that mainly depends on the direction of the flow (Allen and Hickey 2010; Zhang and Lentz 2017). The magnitude of upwelling depends on the canyon geometry (Spurgin and Allen 2014). The Mackenzie Canyon is generally considered a dynamically wide canyon where the flow should remain largely geostrophic. However, the steep bathymetry on the western wall and the shape turn at the eastern tip of the canyon can lead to non-geostrophic flows in and around the canyon.

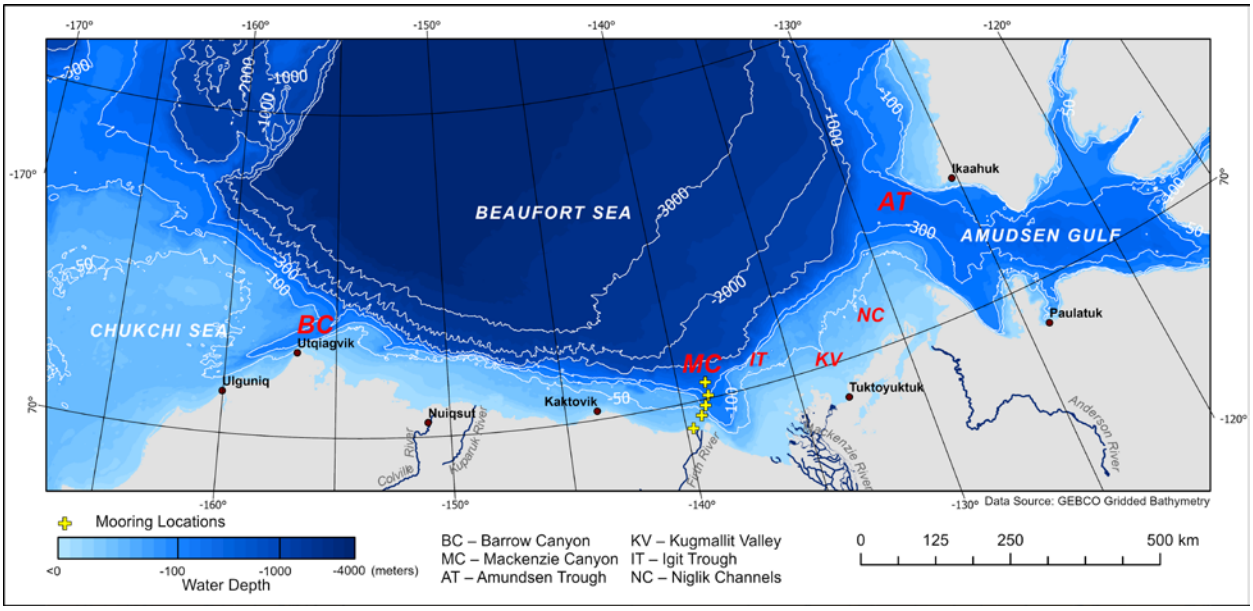

Figure173. The Canadian Beaufort shelf and the Alaskan Beaufort shelf, separated by the Mackenzie Canyon

Both the Canadian and eastern portion of the Alaskan Beaufort Sea shelves are strongly influenced by the discharge of the Mackenzie River (see also Section 1.2.2.3 below) while the western Alaskan Beaufort shelf is influenced by the seasonally warm and fresh Alaskan Coastal Current that contains outflow from the Yukon River (Williams and Carmack 2015) and flows along the shelf break, intruding upon the shelf itself under upwelling conditions (Okkonen et al. 2009). The flow of increasingly warm and fresh Pacific waters entering the Chukchi Sea through Bering Strait has been increasing recently (Serreze et al. 2019; Woodgate 2018). A portion of these waters flow eastward inside the Beaufort shelf break jet (Lin et al. 2016), aided by large scale winds, especially the westerly/downwelling wind patterns which drive the bottom intensified shelf-break jet as far east as the entrance to Mackenzie Canyon (Lin et al. 2020) and

even further east off the Mackenzie shelf-break (Dmitrenko et al. 2018). The downwelling results in a flow, driven by the pressure gradient, that enhances the shelf break currents. Instabilities in the shelf-break jet can spawn eddies observed in the Canadian Beaufort (Carmack and Kulikov 1998) and along the Alaskan north slope (Manley and Hunkins 1985; Spall et al. 2007).

The role of bathymetry on sea ice is a direct connection in the shallow waters (< 20 m) which is the limiting water depth for the presence of landfast ice. There is also an indirect connection through the effect of bathymetry on the circulation in the upper layer of the ocean which in turn affects the movement of sea ice.

5.2.2.2 Wind

The strength and direction of the prevailing winds has a large effect on surface transport as well as upwelling and downwelling. Upwelling and downwelling occurs frequently in Beaufort Sea (Pickart et al. 2009; Dmitrenko et al. 2018; Lin et al. 2019; Foukal et al. 2019;) and these wind-driven dynamics are major controllers of biological productivity and distribution of water masses. Upwelling takes place during episodes of strong easterly winds and results in a westward and offshore (upper layer) movement of the water which can open leads in winter and clear the sea surface of ice in late spring and summer. When fast ice is in place, Ekman pumping generates upwelling at the floe edge. In the winter under easterly winds, clearance of ice to the offshore promotes rapid cooling of upwelled water and new ice growth. Ice clearance in spring and summer promotes warming of upwelled water via insolation with the possibility of subsequent freshening if ice happens to drift back into the warmed water and melt.

Its counterpart, downwelling, is associated with westerly winds and it results in eastward movement of water with a shoreward component in the upper layer. With strong westerlies, ice and surface water move towards shore, causing crushing of the nearshore ice into ridges, thickening it and establishing high surface albedo. Partially isolated from insolation, and in contact with ice, surface waters stay cool into the summer under a predominant westerly spring-time wind scenario. It has been argued that, over the past two decades, easterly wind episodes have been dominant over westerly (Wood et al. 2013; Proshutinsky et al. 2019), but westerly wind episodes still occur, and these can be dominant in some years. Using mooring data from the Alaskan Beaufort Sea during the period 2002-2004, Foukal et al. (2019) found that downwelling conditions occurred a bit more often than upwelling conditions. During the two years of MARES mooring deployment, the opposite was true: coastal upwelling occurred 29% percent of the time, while coastal downwelling occurred 20% of the time (Figure 174).

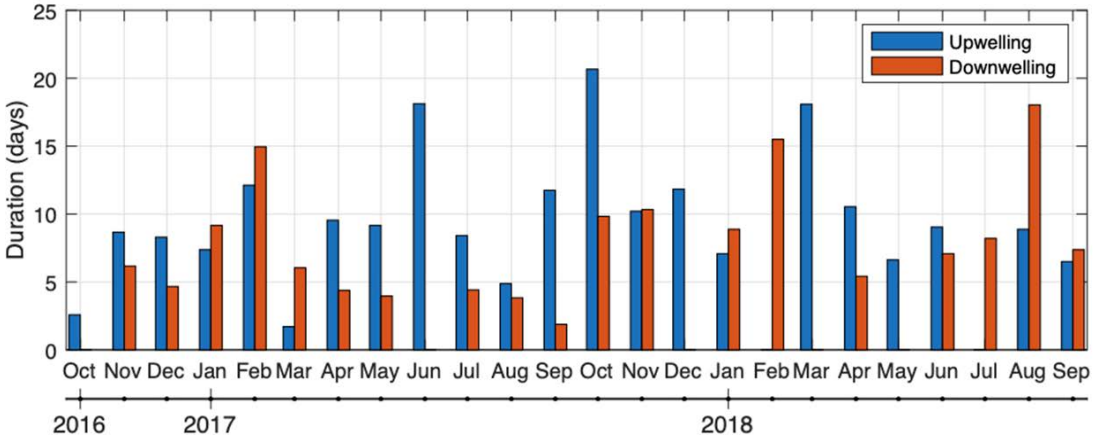

Figure 174. Total monthly duration of upwelling and downwelling conditions at the MARES mooring array between October 2016–2018

The upwelling process brings nutrient rich waters from depth up to the euphotic zone in the upper layer, especially along the continental shelf edge and continental slope over the full width of the Beaufort Sea (Mundy et al. 2009; Tremblay et al. 2011; Pickart et al. 2013; Kirillov et al. 2016). Wind-forced upwelling events may also drive re-suspension of organic and inorganic materials along the Beaufort Sea coastline (Mucci et al. 2008), and nutrients are also supplied by the Mackenzie River runoff. The supply of nutrients (Macdonald et al. 1987) is critical to high levels of primary productivity due to the depletion of these nutrients through the initial 'bloom' of phytoplankton in newly formed open water areas (see Section 1.3) (Parsons et al. 1988; Carmack et al. 2004; Lavoie et al. 2009). In Mackenzie Canyon, upwelling is enhanced by 2-3 times over that in areas off the continental shelf edge (Carmack and Kullikov 1998; Muchaca and Allen 2018; Muchaca 2019), resulting in very high levels of primary productivity in these inshore waters.

5.2.2.2.1 Wind and Sea Ice

Barber et al. (2012a, b) synthesized results from the 2007–2008 International Polar Year Circumpolar Flaw Lead System Study. These results included information from western science, and traditional knowledge collected from surveys of residents of Inuvialuit coastal communities in the Canadian Beaufort Sea on changing coastal sea ice conditions and local characteristics. They noted that sea ice conditions observed near communities and traditional hunting areas are strongly controlled by the interaction of strong winds with existing areas of open water (autumn) or cracks in the ice (winter). This has been observed even during times when ice is not normally prone to cracking (i.e. January–March). Anticyclonic atmospheric forcing tends to promote the development of the largest leads via strong easterly winds over the Alaskan and Canadian coastal areas. Petty et al. (2016) found an amplified response of the Beaufort Gyre ice circulation to wind forcing, especially during the late 2000s. Anticyclonic ice drift increased between 1980 and 2010 across all seasons, with the strongest trend in autumn, associated with increased ice export out of the southern Beaufort Sea (into the Chukchi Sea). In spring and summer, the ice drift curl amplification was mainly observed between 2007 and 2010. Between 2010 and 2013, anticyclonic wind and ice circulation seemed to weaken again, suggesting nonlinear ice interaction feedbacks (e.g., a weaker, more mobile sea ice pack), enhanced atmospheric drag, and/or an increased role of the ocean.

Timing of the opening of the spring flaw lead system along coastal areas in the southern Beaufort Sea may also be changing (e.g., Barber et al. 2012a, b), particularly along the Alaska coastline. Wind-forcing of the late winter sea ice (March/April) induces clockwise motion in the Beaufort sea ice gyre, causing internal stresses leading to widespread break-up of the winter sea ice cover, despite the sea ice extent and thickness at or near their seasonal maximums. Following the 2007 sea ice minimum, there is little remaining multiyear pack ice in the Western Beaufort and Chukchi Seas to 'hold back' sea ice (e.g. Stroeve et al. 2011), therefore momentum transfer from the atmosphere to the sea ice is more effective at moving the sea ice. This process may be priming the southern Beaufort Sea, particularly along the Alaska coastline for earlier break-up (Babb et al. 2019) and promote opportunities for additional light and heat transfer into the water column. Mid-winter fracturing events with widespread leads have been observed since 2013 and identified within the MARES study period (particularly in the spring of 2017, see Section 3.1.2.4 in Wiese et al. 2019). Sea ice leads forming during these events rapidly refreeze in a process that releases stored heat from the mixed layer of the ocean below (Smith et al. 2018), and results in brine expulsion from the formation of young sea ice. There is a potential implication for sea ice dynamic processes where mid-winter leads containing young sea ice may be forced to close by a change in wind direction, thereby creating pressure ridges through rafting and rubbling processes along floe edges. This would promote the development of sails and keels (Melling and Riedel 1995), which could increase atmospheric-sea ice drag (increase momentum transfer to the sea ice from the atmosphere), and

subsequently transfer this momentum to the mixed layer of the ocean, directly below the sea ice through movement of keels through the water column (e.g. Skyllingstad et al. 2003).

5.2.2.3 Mackenzie River

The Mackenzie River, as the largest river flowing into the Arctic Ocean from North America, has a profound influence on the oceanography of the Beaufort Sea. Unlike all other North American Arctic rivers, discharges occur year-round with peak values during freshet in late May and June, followed by reductions through the summer months, and further reductions in autumn (Figure 175). Comparatively low, but significant, discharges continue from January to early May, much of which accumulates beneath the coastal landfast sea ice on the Mackenzie shelf.

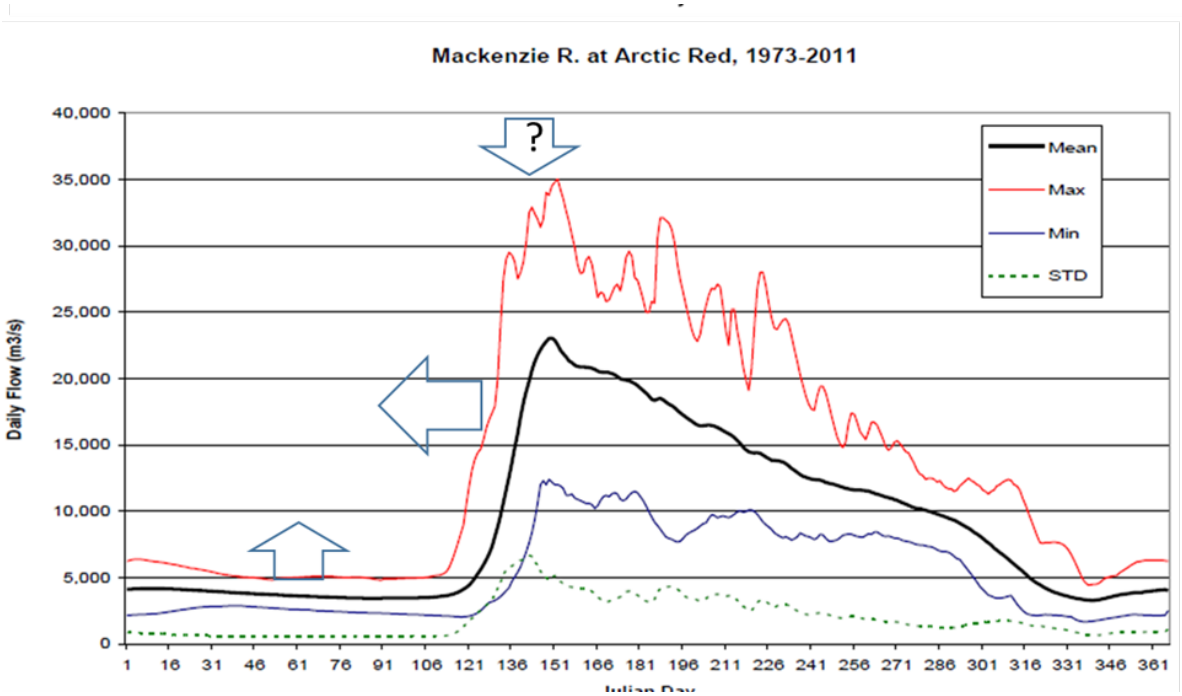

Figure 175. Daily maximum, minimum and mean flows, and standard deviation of the daily Mackenzie River discharges during 1973–2011 (Yang et al. 2015)

The possible long-term trends in the annual hydrograph are shown by the large arrows. Changes in the max daily flow rates are unclear.

Other rivers, including the Colville, Kuparak, and Anderson Rivers also drain directly into the Arctic Ocean, while the Yukon River drains into the Bering Sea and then enters the Arctic Ocean through Bering Strait, and contributes freshwater to the Beaufort Sea Shelf. The total combined discharge directly draining into the western Arctic shelves (332 km^3/d) of other rivers is comparable to the total Mackenzie River discharge (288 km^3/d) while the Yukon River discharge (206 km^3/d) is about 70% of that of the Mackenzie River.

In spring when the system has had time to recharge and nutrient concentrations are high, the fresh water from the Mackenzie River is confined by sea ice. This results in a small area near the coast of very thick freshwater which is exposed to light. The initial flooding of the landfast ice in coastal areas results in a profound change to the physical habitat for seals and polar bears. The ongoing injection of freshwater then leads to the break-up of the landfast ice and the expansion of the large amounts of stored freshwater into a much larger open water area over the Mackenzie Canyon and beyond.

This River-derived freshwater results in a highly stratified upper layer and acts to insulate the deeper ocean water from the atmosphere. Once the landfast ice barrier is been breached, the river plume is subject to prevailing winds. Easterly winds result in a substantial portion of the Mackenzie River freshwater being transported offshore and to the west (Thomson et al. 1986). Some of the freshwater is captured in the deep waters of the Beaufort Gyre where it was the largest source of freshwater within the Gyre from 2004 to 2014 under the predominately easterly wind regime of that time (Proshutinsky et al. 2019). The fate of Mackenzie freshwater transported to the east under the influence of westerly winds is to flow directly into and through the Canadian Arctic Archipelago (Fichot et al. 2013). Under certain conditions, although not entirely well-defined, the Mackenzie River plume is also seen directly advected offshore (Figure 176). The detached plume can mix with surrounding water masses through energetic wind events, affecting the upper water column density structure and freshwater budget in the Eastern Beaufort Sea. The residence time of freshwater moving to the west into the Beaufort Gyre is much longer (11+/- 4 years; https://www.whoi.edu/page.do?pid=66638) compared to a few years-time to traverse the Canadian Arctic Archipelago to the east. In all cases, the ultimate destination of the freshwater is into the North Atlantic Ocean.

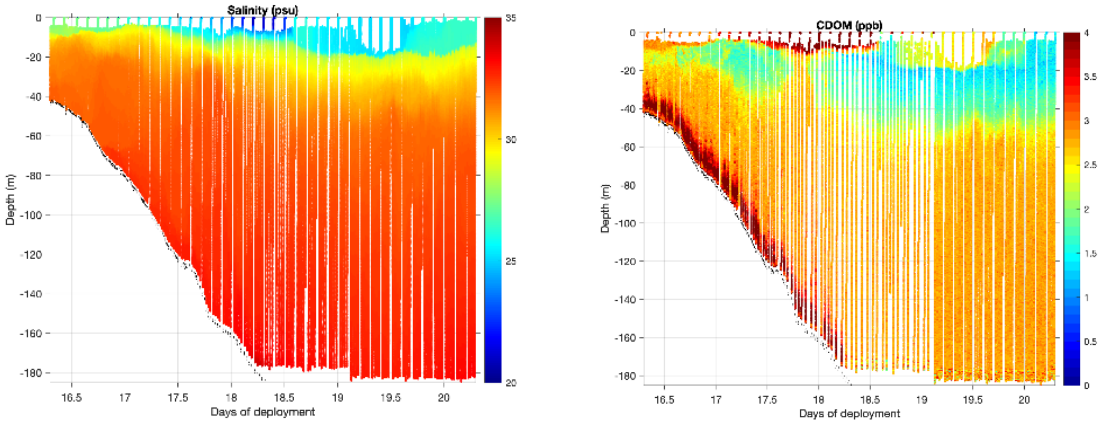

Figure 176. Along canyon axis salinity and CDOM measurements for an ocean glider in early September 2016

Low salinity and high CDOM waters in the upper water column indicate Mackenzie River plume water.

5.2.2.3.1 The Mackenzie River and Sea Ice

In the area of the Mackenzie River discharge the "latent heat in the river water advances the melting of ice by perhaps as much as two months in the delta, and by lesser amounts away from the river mouth" (Carmack and Macdonald 2002). The role of the heat derived from the warm Mackenzie River water on melting sea ice in late spring and early summer has been documented by Nghiem et al. (2014) for the summer of 2012. This source of heat into the Beaufort Sea has gotten more effective in melting sea ice due to the thinning and increased mobility of the sea ice which has been occurring in recent decades (Nghiem et al. 2014). Combined with the observed warming of the waters of the Mackenzie River discharge and earlier onset of freshet, the Mackenzie shelf area has exhibited a distinct trend towards lower ice concentrations in late spring (e.g., June 4) since 2000 to the present (Fissel et al. 2020). This reduction in overall ice concentrations from typical values of > 80% to about 30% over this twenty year period, reflects earlier breaching of the landfast sea ice in Mackenzie Bay leading to an expansion of the areas offshore in the westernmost part of the Mackenzie shelf that is exposed to the warm Mackenzie River water.

5.2.2.4 Connectivity of Canadian and Alaskan Beaufort

The MARES study has improved our understanding of the transports and pathways of freshwater, ice breakup and clearing and ocean water properties over the continental margin of the Alaskan and Canadian Beaufort Sea.

While the Alaskan and Canadian (Mackenzie) shelves are physically separated by the presence of the Mackenzie Canyon, they are closely interconnected through the presence of large scale atmospheric circulation features, (i.e., winds), the movement of the sea ice cover, and the transport of ocean water properties (temperature, salinity, nutrients, sediments, dissolved organic matter, etc.). Given the general dominance of winds blowing from the east over winds blowing from the west through much of the year, the Canadian Beaufort Sea including the Mackenzie Canyon can be considered "upstream" of the Alaskan Beaufort Sea, in terms of transport of upper layer water properties including freshwater from the Mackenzie River (reduced salinities) and nutrients upwelled in Mackenzie Canyon under easterly winds. At the continental shelf and along the inner continental slope, there are episodic occurrences of enhanced eastward transport of water properties below the upper layer, due to a persistent eastward shelf current and the eastward Alaskan Beaufort Shelfbreak jet (Lin et al. 2016; 2020), which carries Pacific water properties into the Canadian Beaufort Sea continental margin.

5.2.3 Biological Responses

Biological responses to physical drivers in the eastern Beaufort Sea are highly seasonal and have highly variable maxima depending on the links to and strength of physical drivers present. Links to the physical drivers can be direct (e.g., phytoplankton response to ice melt) or indirect (e.g., marine mammal presence in response to plankton). The upper trophic level marine ecosystem exhibits nonlinear responses to changes in the physical system. Here we described the general biological responses to physical drivers according to trophic levels in this system but leave the detailed seasonal analysis to Section 1.3.

5.2.3.1 Primary and Secondary Productivity

Light and nutrient availability underpin primary productivity in the Arctic (Tremblay et al. 2015; Ardyna et al. 2017). In the Beaufort Sea nutrients originate from the Mackenzie River, from the shelf-break jet transporting Pacific water from the west, and from wind-driven upwelling events (see Section 1.4) (Tremblay et al. 2015; Macdonald et al. 1987). Ocean currents also introduce nutrients, detritus, and plankton rich water from the boreal Atlantic and Pacific oceans (Wassmann et al. 2015). The seasonality of primary productivity is the combined result of nutrient availability and photosynthetically active radiation (PAR) penetration into the water column, which is mediated by sea ice thickness and snow cover on the ice.

In the spring (during ice cover), productivity (e.g., pelagic algae blooms and ice algae) is highest near the sea ice edge where PAR can penetrate, and nutrients are released from the ice melt (Horvat et al. 2017). Carmack et al. (2004) estimate spring productivity at about 10 mg of carbon per meter squared per day (C m^{-2} d^{-1}). In late July, productivity peaks reaching about 200 C m^{-2} d^{-1} because of increased PAR penetration and nutrient availability (Carmack et al. 2004). Productivity continues to be high into the fall when increased wind-driven mixing brings nutrients back into the photic zone. Typically, primary productivity is highest near the sea surface and generally decreases exponentially with water depth (Carmack et al. 2004). The interplay between light and nutrient availability can result in ephemeral hotspots of primary productivity that are relied on by higher trophic levels (Ardyna et al. 2017).

In coastal waters of the southeastern Beaufort Sea, the recent increase of southeasterly winds and decrease in sea ice cover have promoted the upwelling of nutrients to the surface layer through the summer season,

resulting in increased total production by microalgae (Tremblay et al. 2011). Beyond the continental shelves, another observed and projected consequence of the rapidly melting sea ice cover in the western Arctic is a decrease in the salinity and increase in the temperature of the surface waters offshore in Canada Basin (McLaughlin and Carmack 2010). A warmer and fresher surface layer is less dense making it more difficult to mix with the cold, saline, dense and nutrient-rich waters of deeper layers. The end result is a limitation of nutrient replenishment by wind mixing and a reduction of microalgal production that can cascade throughout the food web.

Subsurface primary producers appear to play a significant role in the eastern Beaufort Sea during the open water season. Glider observations near the Mackenzie Canyon found a persistent layer of sub-surface chlorophyll maximum near depth of 50 m off the shelf and elevated chlorophyll-a concentration throughout the water column at depths below 10 m on the continental shelf (Figure 177). This subsurface primary production is consistent with the elevated dissolved oxygen concentration throughout the upper water column down to a depth of 60m.

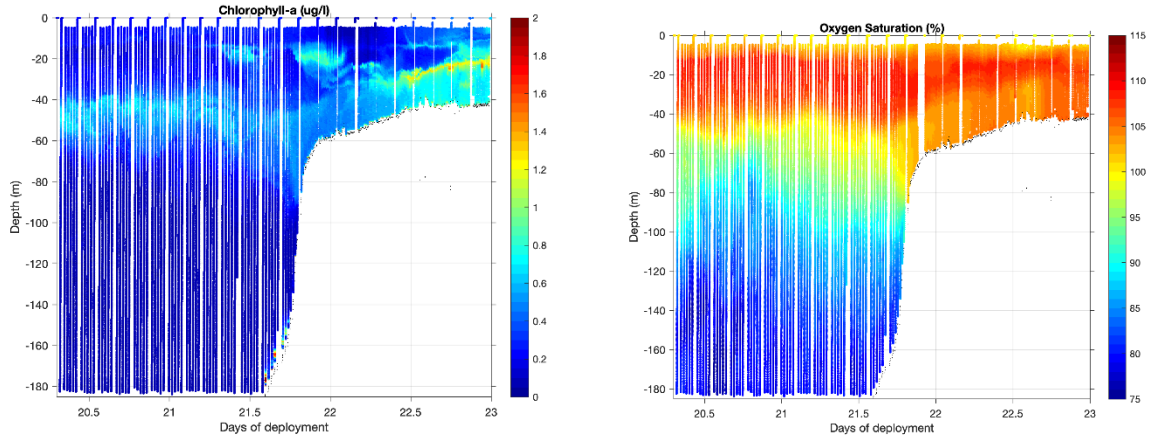

Figure 177. Glider observation of Chlorophyll-a fluorescence and dissolved oxygen saturation along the MARES mooring line in early September 2016

Subsurface chlorophyll-a maximum was seen at 50 m off the shelf break and at depths below 10 m on the continental shelf.

The traditional paradigm of Arctic productivity predominantly occurring at the ice edge (and not below it) has recently been challenged. Massive sub-ice blooms have recently been observed in the Chukchi sea (e.g., Mundy et al. 2009; Arrigo et al. 2012; Horvat et al. 2017), indicating fundamental changes in our understanding of the system, and how it might be affected by climate change. The extent of sub-ice phytoplankton blooms has likely been underestimated by ~ 30% (Horvat et al. 2017) and warrants further study.

The upper water column (0 – 60 m) is highly stratified due to the large freshwater volumes, as described above. The effect of the stratification is to inhibit vertical mixing in the uppermost surface layer of the ocean, limiting primary productivity locally due to nutrient limitation. However, given the dominance of wind forcing of the ocean upper layer, the Mackenzie River plume area where the high freshwater and high stratification occurs is mobile, extending to the west and moving offshore under the dominant easterly winds, and extending to the east and more confined to inshore waters under the less frequent but still important westerly wind events. Westerly winds also cause the ice to converge along the coast in the Canadian Beaufort Sea, further constraining primary production due to light limitation.

Phytoplankton blooms are critical events for Arctic marine food webs because they create a pulse of primary productivity that is used by zooplankton (Søreide et al. 2010) and benthic secondary producers (Renaud et al. 2007; Waga et al. 2019). For example, Campbell et al. (2009) report that for the Chukchi Sea approximately 44% of primary productivity is consumed by micro- or mesozooplankton, while the remaining 56% is either exported further offshore or transported to the sea floor.

While zooplankton diversity in the Canadian Arctic has not been fully characterized (372 species identified thus far), the number of species in the Arctic rivals that identified in western (481 species) and eastern (381 species) Canada. Calanoid copepods (suborder copepoda) dominate the Arctic species richness chart with approximately 40–50% of the total number of species belonging to this suborder (Archambault et al. 2010). In the Canada Basin, surveys found that copepods made up approximately 90% of zooplankton abundance and more than 80% of biomass (Rutzen and Hopcroft 2018). In the Canadian Beaufort, 44–81% of zooplankton abundance and 52–71% of biomass was comprised of *Calanus glacialis*, *Calanus hyperboreus*, *Metridia longa*, *Oithona similis, Triconia borealis*, *Microcalanus pygmaeus*, and *Pseudocalanus* sp. (Smoot and Hopcroft 2017) with *C. glacialis* and *C. hyperboreus* dominating (>75%) biomass. Community structure was most strongly related to temperature and salinity in the upper 200 m, suggesting that future changes in the physical environment may lead to changes in the distribution of zooplankton communities in the Beaufort Sea. Euphausiids, or krill, are relatively rare in the eastern Beaufort Sea, based on analyses of bowhead whale stomach contents, but are more abundant in the western Beaufort Sea near Pt. Barrow (Lowry et al. 2004) and are not endemic but rather are advected there from the Bering Sea (Berline et al. 2008). The acoustic instruments (AZFP, ADCP) used to estimate zooplankton abundance in this study are more effective at sensing the larger bodied zooplankton (e.g., *Calanus* spp., euphausiids). The much smaller zooplankton (e.g., *Oithona* sp., *M. pygmaeus, Pseudocalanus* spp.) are not expected to be detected by the frequencies used.

Zooplankton life histories (phenologies) are often synchronized to that of phytoplankton. This means that zooplankton population dynamics can be influenced by factors that act on phytoplankton. For example, disruptions in sea ice breakup and the spring melt directly affect the timing of phytoplankton blooms and, therefore, can indirectly affect zooplankton due to timing mismatch between their phenologies and the timing of primary production (Huntley et al. 1983; Søreide et al. 2010; Rutzen and Hopcroft 2018; Dezutter et al. 2019). For example, Dezutter et al. (2019) showed that a disruption to sea ice breakup in 2012 caused a mismatch in peak abundance of herbivorous zooplankton and phytoplankton productivity. The large *Calanus* spp. follow a life history that includes an obligate overwintering diapause (similar to hibernation) at depth (>200 m) in the slope and basin regions, with upwards migration in spring timed to exploit the annual increase in ice algal and phytoplankton production (Falk-Petersen et al. 2009). These animals follow multiple year life cycles, reproducing during the productive season and overwintering at one or two different stages of maturation, depending on their longevity (2–3 years).

The large bodied *Calanus* spp. are a high-quality food source for many fish, birds, and marine mammals because of their high fat content (which is in the range of 50–70% lipids by dry mass) (Conover 1988; Falk-Petersen et al. 2009; Kjellerup et al. 2015). Accordingly, zooplankton productivity can influence the population dynamics of numerous other Arctic species (Bradstreet and Cross 1982; Cobb et al. 2008; Falk-Petersen et al. 2009; Kjellerup et al. 2015). For example, five zooplankton “hotspots” in the eastern Beaufort Sea, driven by oceanographic conditions such as temperature, salinity, depth, and upwelling events, are important foraging grounds for bowhead whales during August and September (Harwood et al. 2017):

- waters near to Cape Parry
- Cape Bathurst
- Tuktoyaktuk Peninsula
- Mackenzie River estuary

- near Herschel Island

5.2.3.2 Benthos

The benthic marine ecosystem plays a key role in arctic marine ecosystems as it supports nutrient cycling and energy transfer processes, and is important habitat for fish, invertebrates (Welch et al. 1992; Renaud et al. 2007; Conlan et al. 2008; Merkel et al. 2012, Nelson 2013), and feeding grounds for marine mammals such as bearded seals (Grebmeier et al. 2015). Benthic macrofaunal assemblages in the Arctic are highly variable and influenced by a suite of abiotic factors. In general, two major gradients of benthic community composition have been established: 1) in the onshore-offshore axis (driven largely by ice scour, salinity, and depth), 2) in the east-west axis (driven largely by productivity and substrate characteristics) (Cobb et al. 2008). At a finer resolution, salinity and sea bottom temperature were the most important covariates identified by Cusson et al. (2007) for determining overall community composition. However, depth was the strongest positive predictor of species richness (Cusson et al. 2007). Ice scour is also linked to invertebrate abundance and diversity and favours organisms capable of rapidly colonizing disturbed sediments (Cobb et al. 2008). Overall, taxonomic diversity is generally high in shelf and slope areas and tends to be more variable inshore (Conlan et al. 2008).

Benthic communities use approximately 60% of new annual carbon production, which highlights the strong ecological connection between pelagic and benthic communities (Renaud et al. 2007; Conlan et al. 2013). At the MARES benthic sampling locations, abundances of surface deposit feeders dominated the meiofaunal population across the four stations. Surface deposit feeders graze on available sources of organic matter near the sediment-water interface (Rhoades and Germano 1982). Foraminifera was the most abundant taxa, with increasing abundance toward greater depth. Harpacticoid copepods and diatoms were the second most abundant taxa with their maximum abundances occurring at the mid-shelf stations. The major taxonomic groups that were most abundant did not account for greatest calculated biomass; Sipunculida and Bivalvia outweighed copepods and diatoms, while small Foraminfera provided significant contribution to the biomass calculation (wet and dry weight). Abundances of non-protist, non-algal related organisms were low, however there were 23 Families of Polychaeta and 19 Families of Crustacea identified from the samples. Carbon used by benthic species, from lower trophic levels, eventually provide feeding opportunities to higher trophic levels (e.g., bearded seals, and spectacled eider (*Somateria fischeri*)) (Conlan et al. 2013). The strength of pelagic-benthic coupling seems to decrease as depth increases (Roy et al. 2014).

The Mackenzie River water can have very high values of turbidity and suspended sediments, especially during the high discharges of the freshet from late May through much of the summer. These suspended sediments (72 Mt/yr.) settle out of the plume and are deposited on the seabed. The location of where these sediments are deposited depends on large part on the winds; historically, the largest deposition levels have been found close to shore (56%) and on the middle-shelf (20%) of the Shelf, especially along the wide Mackenzie Shelf to the east of the Mackenzie Delta (Hill et al. 1991; Osborne and Forest 2016).

While terrestrial inputs are large, primary production in the water column and on ice results in significant inputs of marine derived materials to surface sediments. During this study, benthic meiofauna showed high diversity and abundance at mid-shelf stations, particularly station M3 (McMahon et al. in press). Meiofauna abundances were dominated by surface deposit feeders and filter feeders that feed off sinking organic fluxes. This contrasted with the shallowest station (M1) which received the largest terrestrial inputs but showed the lowest abundance of meiofauna and may be the result of the low fresh detrital matter deposited as well as ice scouring which could limit the community (Urban-Malinga et al. 2005). The overall meiofaunal population appears more diverse and higher in abundance at stations where there was evidence of greater marine derived organic materials reaching surface sediments. Results from the meiofaunal population combined with information from isotopes, amino acids, and lipid biomarkers

suggest that despite the large amounts of eroded terrestrial organic material delivered by the Mackenzie River to the adjacent shelf (e.g., Ouyang 2003; Ni et al. 2008), the arrival of labile marine organic material reaching underlying sediments largely drives benthic populations (McMahon et al. in press).

Ice formation retention of Mackenzie flow and resulting increase in primary production beyond the shallow delta may explain why mid-shelf stations show higher amounts of organic carbon, diatom markers, diatom frustules, and benthic grazer communities than the in-shore areas. Offshore of the natural ice blockade of the Makenzie River outflow seasonal sea ice breakup first occurs near the shore-lead seaward of the stamukhi before the below water ice has thawed to release Mackenzie River water. When this break up occurs, released nutrients allow strong phytoplankton blooms to occur at the mid shelf. Carbon fluxes to the sediment increase as the conditions become more favorable for phytoplankton production with Mackenzie River runoff flowing over these mid-shelf areas, increasing nutrients in a time when sufficient light is available for increased primary production (Forest et al. 2007, 2013).

In addition to ice driven retention of waters, resuspension and upwelling/downwelling events are also important as dispersion agents to increase benthic meiofaunal populations at M3 and M4. During the MARES mooring deployment period, between one and five upwelling events occurred almost every month of year, lasting, on average, between one and two weeks. This suggests that shelf transport is a regular event, agreeing with previously observed resuspension events from similar areas of the Mackenzie Canyon and shelf (Forest et al. 2015, Forest et al. 2016). Such transport events could bring nutrients onto the shelf and lead to increases in primary production and subsequent meiofaunal populations as detrital carbon reaches sediments. The Mackenzie region also experiences frequent downwelling events that have the potential to move sediments from shallow waters to the shelf edge. Osborne and Forest (2016) concluded that 78% of the sediments deposited beyond the shelf edge are the direct result of bottom resuspension in shallower waters moved offshore by downwelling and storm events. Evidence from specific organic markers including amino acids reflecting degradation (i.e., GABA) increase in sediments at offshore stations as material is repeatedly resuspended and transported across the shelf as degradation proceeds. Such resuspension events can explain the short-term primary production fuel needed to support benthic populations at the station M3 and M4. These short term and repetitive physical processes would contribute to increased meiofaunal populations where algal and terrestrial carbon inputs compete.

Along Hershel Island near station M1, the stamukhi, or rubble ice zone, occurs in which land-fast ice meets and joins the annual and multi-year sea ice (Macdonald and Carmack 1991). During the winter months, this stamukhi ice pack reaches the seafloor, effectively blocking any interaction of the Mackenzie River runoff with shelf waters and scouring the sediment surface (Carmack and Macdonald 2002). During the winter, this ice-flaw lead (or polynya) that borders the sea ice and the stamukhi, frequently breaks up and causes new ice formation that leads to brine rejection (Macdonald and Carmack 1991). This brine rejection causes downward convection in the shallow water column and may explain why specific steroidal ice algal markers (e.g., 24-ethylcholest-5,24(28)enol and 24-ethylcholest-5-enol) are higher in sediments at station M2. Downward convection could increase sedimentation of released ice algae that thrives in the low winter light to the underlying sediments. One might speculate this new production would be common for zones associated with shore leads where nutrients are upwelled like those observed mid-shelf region of the Mackenzie shelf seen as increased meiofaunal populations in the mid-shelf areas (Renaud et. al 2007).

5.2.3.3 Fish

Fish distribution and abundance is influenced by the quality and distribution of their preferred habitat, which, for pelagic species is associated with different water mass properties, and for benthic fish with physical and biological characteristics on the sea floor. As such their occurrence in time in space is an integration of all the abiotic and biotic drivers and variables elaborated on in this section thus far. During

MARES, fish occurrence, in particular arctic cod, was only evaluated indirectly through the AZFPs on moorings M2 and M3. There, their abundance patterns were highly seasonal and are further elaborated on Section 1.3. In general terms, however, marine fish assemblages in the Beaufort Sea have been described in detail by Majewski et al. (2017) and shown to be associated by water mass habitats (see Section 3.2.4.1 in main report for a description of observed water masses at the mooring sites) which are directly linked to bathymetry (Figure 178), and thus also susceptible to upwelling and downwelling events on the Canadian Beaufort shelf and slope (Niemi et al. 2019). In addition, the presence of anadromous fish is also related to brackish water found along the coastline of the Beaufort Sea. For example, arctic cisco hatch in the Mackenzie River, migrate west along the coast in a brackish corridor to the Colville River, where they mature, and then return to the Mackenzie Delta (Gallaway et al. 1983). Although this was not investigated during MARES, knowledge of these drivers is important, as "this complex migration pattern is intimately linked to the supply of freshwater and its distribution in coastal waters, which is partly controlled by the ice" (Carmack and Macdonald 2002) and winds (Fechelm and Fissel 1987).

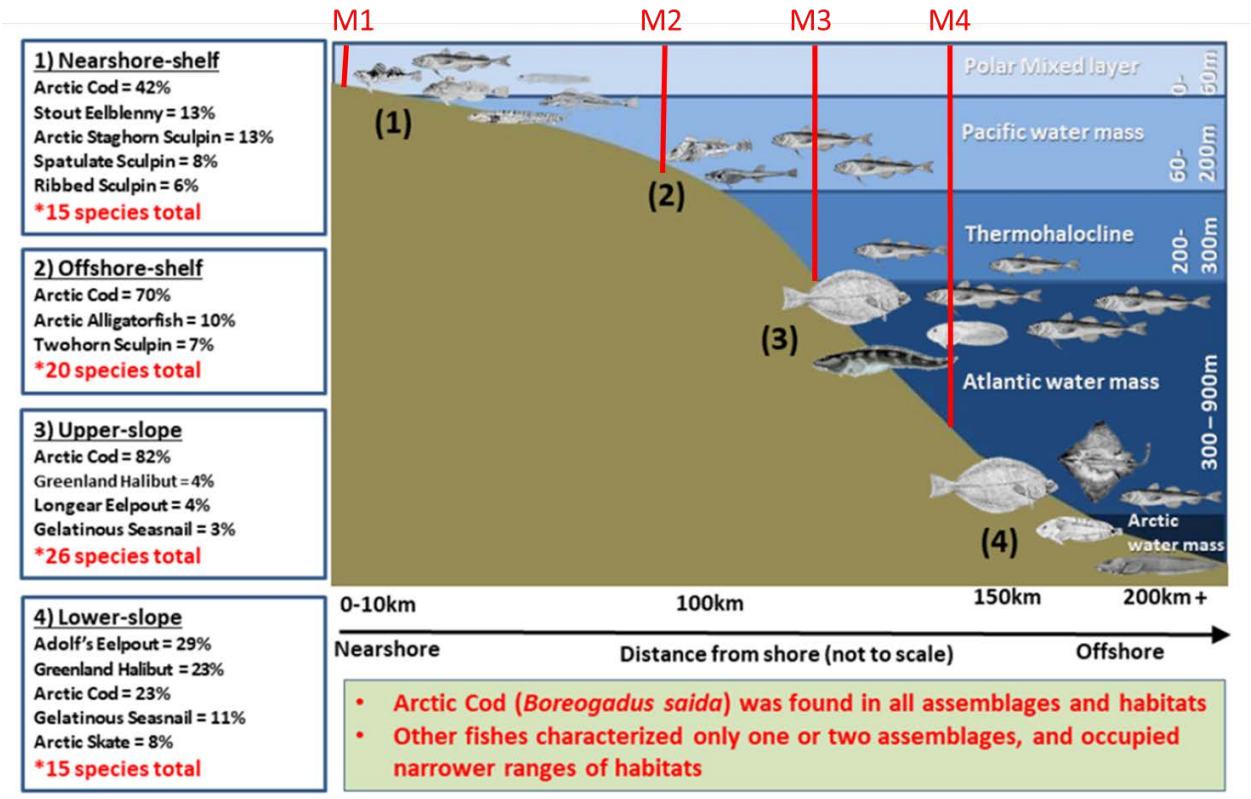

Figure 178. Marine fish assemblages and associated water mass habitats on the Canadian Beaufort shelf and slope (Majewski et al. 2017)

The locations of the MARES moorings are shown in relation to the water mass habitats (in red).

5.2.3.4 Marine Mammals

Marine mammals in the southeastern Beaufort Sea, in the region around the MARES moorings include beluga whale (*Delphinapterus leucas*), bowhead whale (*Balaena mysticetus*), ringed seal (*Phoca hispida*) and bearded seal (*Erignathus barbatus*), and polar bear (*Ursus maritimus*) with other species such as killer whales (*Orcinus orca*), narwhal (*Monodon Monoceros*), and gray whales (*Eschrichtius robustus*), considered infrequent visitors (Cobb et al. 2008). Beluga and bowhead whales are seasonal migrants to the MARES study area and their presence is closely linked to sea ice. Ringed seals, bearded seals and

polar bear are present year-round although seasonal movements from the region have been observed (Cobb et al. 2008, Kelly et al. 2010, Yurkowski et al. 2016).

During the MARES study, we detected beluga and bowhead whales, and ringed and bearded seals, and we focus our discussion on these four species. The timing of the detections of these species are driven by physical and biological factors, with ice and prey being of primary importance.

5.2.3.4.1 Beluga whale

Beluga whales are seasonal migrants to Canada's Western Arctic, occupying their summer range in the southeastern Beaufort Sea and Amundsen Gulf during the open water season (Allen and Angliss 2013; Harwood and Smith 2002; Hauser et al. 2014, Moore et al. 2000). This seasonal presence was reflected in the detections of beluga whales in the MARES study area with detections from April to December inclusive (Figure 180, Figure A-1).

Beluga whale habitat selection in the Beaufort Sea is influenced by features such as ice, depth, slope, temperature, and proximity to bathymetric features (e.g., Hauser et al. 2017; Loseto et al. 2006). These features together promote and guide beluga distributions in the Beaufort Sea, regional productivity, foraging opportunities, and protection from predators (e.g., Higdon et al. 2006; Laidre et al. 2006).

Spring sea ice conditions are important determinants of the timing and movement of beluga into the Beaufort Sea and subsequent aggregations in the Mackenzie River estuary (Fraker 1979a,1979b; Huntington et al. 1999). Sea ice is an essential habitat for beluga in the spring (Hornby et al. 2016), when beluga seem to select areas with heavy ice concentrations (8/10-10/10) and 200–500 m water depths (Asselin et al. 2011a, b). They seem to particularly prefer ice edges, known are regions of high productivity during early spring ice melt where they feed on their main prey, arctic cod (Asselin et al. 2011a, b), and also benefit from protection from weather and/or predators (e.g., killer whales) (Asselin et al. 2012; Heide-Jørgensen et al. 2010). When spring is characterized by unusually low ice concentrations, such as during the IPY-CFL project in spring 2008, belugas may use fast ice and coastal regions instead (Asselin 2011a, b).

Beluga are mostly observed in shallow water during the summer season (i.e., in depths less than 50 meters) (Barber et al. 2001; Hornby et al. 2016; Loseto et al. 2006). Core areas where beluga tend to congregate in July and August have been identified extending from the Mackenzie River Delta and along the Tuktoyaktuk Peninsula to the entrance of Liverpool Bay, in Viscount Melville Sound and Amundsen Gulf in early summer, near the Mendeleev Ridge in late summer, and along the Beaufort Slope throughout the summer. (L. Loseto, pers. comm, Hauser et al. 2014). During late July and early August, beluga whales travel back and forth from the Mackenzie Estuary to deeper waters off the coast, moving along the continental shelf from Herschel Island to around Cape Bathurst (Harwood et al. 1996; Harwood and Kingsley 2013; Richard et al. 2001). During this time, their distribution becomes broad and is characterized by small groups dispersed across the shelf and offshore waters of the Beaufort Sea (Harwood and Kingsley 2013). They are more frequently observed over the continental slope (201–2000 m) and in ice cover that was 0-10% and 71-100% (Moore et al. 2000).

Beluga seem to prefer warm sea surface temperatures (>2°C) and a mid-to-high chlorophyll concentration, which are indicative of enhanced local productivity and/or upwelling (Hornby et al. 2017). Size related dietary studies suggest that larger sized beluga preferred offshore arctic cod whereas smaller sized beluga feed on prey in near shore habitats that included near shore arctic cod (Loseto et al. 2009). Whalen et al. (2019) has shown that belugas seem to prefer sandy shoal habitat in the estuary and may use it to rub on and scrape off molting skin, thus supporting the hypothesis that beluga may come to the estuary during the annual molt. Similarly, Scharffenberg et al. (2019) has shown that movement of

belugas within the estuary is influenced by temperature, salinity, and wind speed and that individuals move farther into the estuary during periods of cold oceanic influxes.

5.2.3.4.2 Bowhead whale

Bowhead whales typically migrate to the southeastern Beaufort Sea in early summer and begin their migration west in late fall and early winter (Moore and Laidre 2006, Moore et al. 2000). The migratory patterns of bowhead whales were likely reflected in the MARES detections of this species, with detections from April through December (Figure 180, Figure A-1).

The migration of bowhead whales (Bering-Chukchi-Beaufort Sea population) into the Canadian Beaufort Sea in early summer is related to the clearing of continuous sea ice cover (Braham et al. 1984, Moore and Laidre 2006), although it is possible for bowheads to navigate through ice covered areas (George et al. 1989). Their summer and fall distributions in the region are primarily related to depth (e.g., Moore et al. 2000), and abundance and distribution of zooplankton (Thomson et al. 1986).

In the Alaskan Beaufort Sea in July and August, and near the near the MARES study area, bowhead whales were more frequently observed on the continental slope (201–2000 m) and selected ice cover of 0–10% and 41–70% (Moore et al. 2000). In September and October, bowheads were associated with the inner shelf waters when ice was moderate to light, and outer shelf and slope during heavy ice conditions (Moore 2000). Whales near Mackenzie Bay and Herschel Island were primarily in water <100m deep (Mate et al. 2000). While present in the area near Herschel Island and Mackenzie Bay in fall, subadult bowhead whales exhibited localized movements and staggered departure during their westward migration (Mate et al. 2000; Quakenbush et al. 2012).

Bowhead whales feed on crustacean zooplankton such as euphausiids and copepods as well as on epibenthic organisms (mysids and gammariid amphipods) (Lowry et al. 2004). The annual variability in bowhead whale sightings, and the spatial distribution of bowhead whales is related to the abundance and distribution of zooplankton (Thomson et al. 1986). The whales are present in aggregations, which are known to occur mainly in the shallow, shelf waters when oceanographic conditions promote concentration of their zooplankton prey (Harwood et al. 2017). Harwood et al. (2017) found that “the Mackenzie Shelf aggregations [of bowhead whales] are located in an area strongly influenced by the brackish water plume of the Mackenzie River and adjacent to Yukon coastal waters, which are particularly productive during periods of easterly winds that promote strong upwelling (Thomson et al. 1986)”. The presence of major fronts within the Mackenzie River plume waters and other rivers on the Beaufort Shelf can provide an aggregating mechanism for concentrating zooplankton abundance (Thomson et al. 1986; Okkonen et al. 2018) which attracts feeding bowhead whales. Bowhead whale feeding in summer has been observed along the continental slope, during low ice conditions, suggesting they may be taking advantage of upwelling events that result in increased prey availability (Christman et al. 2013).

5.2.3.4.3 Ringed seal

Ringed seals are present year-round in the eastern Beaufort Sea, although some individuals migrate from the region in the fall (Harwood et al. 2012; Yurkowski et al. 2016). MARES detections of ringed seals occurred throughout the year, although were absent in January, February, August, and September (Figure 180, Figure A-1). During winter and spring ringed seals have relatively small home ranges within the landfast ice (<1 km^2) and but can range extensively in summer (Kelly et al. 2010). Key habitat for seals is closely associated with sea ice and prey availability (Cobb et al. 2008).

Sea ice is likely the primary influence on ringed seal distribution (Burns et al. 1985), although water depth, location relative to ice edge, snow depths, and ice deformation have been shown to influence seal density in the Beaufort Sea (Frost et al. 2004). Ringed seals are associated with sea ice year-round, and highest densities of breeding adults are found on landfast ice in winter and spring (Burns et al. 1985). In the Alaskan Beaufort Sea in late May – early June, densities of ringed seals tended to be greatest at water depths between 5m and 35m, on flatter, less deformed ice nearest to the fast ice edge (Frost et al. 2004). Sea ice is used by ringed seals during the molting period in spring and early summer to haul out on (Burns et al. 1985). Changing sea ice and water temperatures affect the distribution and availability of ringed seal prey, which subsequently affect diet, body condition, productivity, and survival of ringed seal pups (Crawford et al. 2015). Reducing sea ice cover alters key habitat for feeding, breeding, and resting, ultimately reducing survivorship (Moore and Huntington 2008; Harwood et al. 2012).

Ringed seals feed on pelagic and semi-demersal fish and invertebrates in the water column, but they are widely adaptable in their feeding habits (McLaren 1958). Aggregations of ringed seals in the southeastern Beaufort Sea observed in late summer and earlier fall were associated with areas with high zooplankton production (Harwood and Stirling 1992), with prey concentrations a result of upwelling or bathymetry (Harwood et al. 2012). Prey may also influence the location of breeding habitat, selected during ice formation through to breakup (Kelly et al. 2010).

5.2.3.5 Bearded seal

Bearded seals can be found in the Beaufort Sea year-round although most individuals will migrate ahead of sea ice formation in fall and return in summer (Burns et al. 1985). Densities of bearded seals are lower in the eastern Beaufort Sea then the western Beaufort Sea (Burns and Frost 1979). MARES detections of bearded seals occurred year-round, with the exception of August (Figure 180, Figure A-1), and are generally found near the Tuktoyaktuk Peninsula year-round (Hartwig 2009). Their distribution is primarily influenced by sea ice and benthic productivity.

Bearded seals are generally solitary animals (Cobb et al. 2008; Kovacs 2016) but use vocalizations for breeding and to mark territories (MacIntyre et al. 2013). They are primarily found on sea ice in areas of shallow water (less than 200m), due to the high productivity of benthic organisms in these waters (Cobb et al. 2008; Smith 1981) as they are primarily benthic feeders (Burns and Frost 1979, Burns and Frost 1979). They primarily feed on bivalve molluscs, crabs, shrimps, sculpins and occasionally saffron or Arctic cod (Burns and Frost 1979). Although they are primarily benthic foragers, in the Chukchi Sea juveniles are known to follow fish up some of the rivers in the fall (Cameron et al. 2018). TLK holders noted that seals follow fish up the West Channel of the Makenzie River and into the delta and spend long periods of time welling in freshwater, such as in Coney Lake, and may overwinter in freshwater parts of the delta (IMG Golder and Golder Associates 2011).

During summer in the Eastern Beaufort Sea bearded seals are primarily associated with shallow water (< 100m) and areas with open leads (Stirling et al. 1977). In winter they will avoid areas of thick ice, preferring areas with leads and polynyas, and will use the ice in spring for pupping and molting (Burns et al. 1985, Burns and Frost 1979). Information related to bearded seal associations with ice come primarily from the Chukchi and Bering Seas. Juvenile bearded seals (<2 years) selected areas near the ice edge (or areas of 15% concentrations) and areas with 50-60% ice concentrations (Breed et al. 2018). Cameron et al. (2018) found that juvenile bearded seals had increased probability of use with increasing ice concentrations, up to ice concentrations of 80%. Bearded seals are primarily found in open water during ice-free periods, although some individuals may be associated with the pack ice (Cobb et al. 2008).

5.3 Seasons in the Canadian Beaufort

Early studies of the oceanography of this part of the Beaufort Sea have described the "extraordinary spatial and seasonal variations in ice cover, temperature, light, freshwater, turbidity, and currents of the (Canadian) Beaufort Sea (which) define unique places or times critical to marine life" (Carmack and Macdonald 2002). Here we describe two years in the eastern Bering Sea and focus on seasonal patterns from physics and geo-chemistry to biology, considering the relationships among the measured parameters to examine structure and function of this marine ecosystem.

5.3.1 Introduction

The ecosystem of the Beaufort Sea is seasonally driven by the high-latitude solar cycle which at the latitude of Tuktoyaktuk (69.45 N) has the sun setting at the end of November to emerge again in mid-January, with continuous sunlight between early June and mid-July and August (Figure 179). Outflow of the Mackenzie River is also a highly seasonal influence on the Beaufort Sea, typically peaking in mid-May (Figure 175). The effects of solar input, and the input of nutrients and freshwater from Mackenzie River outflow are powerful, highly seasonal abiotic drivers that are in turn moderated by clouds, snow, ice, and wind, to shape the biology of the system. Prevailing currents and upwelling conditions are additional important aspects of the system that are influenced by seasonally and by broad scale drivers (see Section 1.2) and occur episodically on daily and weekly time scales (see Section 1.4). Taken together, broad scale regional conditions, the annual cycle of the major abiotic drivers, and the episodic events, result in the seasonal cycle of the ecology of the Beaufort Sea.

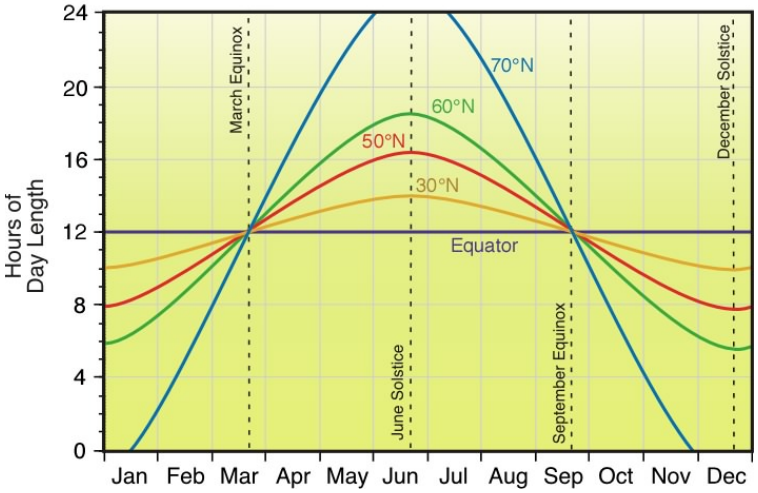

Figure 179. Daylight hours at different latitudes
MARES study was conducted around 70 N.

Our goal is to describe the seasonal cycle of drivers and the corresponding responses of the ecosystem over the course of two years. We recognize that the base parameters such as temperature and salinity have direct effects on the biology of the system that we measure here (such as abundance), and also indirect effects (such as metabolic rate) which are important, but outside of the scope of this project. The largest amplitude of seasonal variation of the primary drivers is seen in light, air temperature, Mackenzie River runoff, and sea ice coverage; additionally, temperature and atmospheric pressure differences throughout the year drive large scale and seasonal wind patterns (see Section 1.2). These abiotic drivers interact with each other, and together, directly, or indirectly, influence the abundance, distribution, and timing of biological communities. Here we focus on characterizing the biology by phytoplankton

(fluorescence), zooplankton, juvenile and adult cod abundance/biomass, and marine mammal occurrence (see also Figure 172). Our aim is to deepen our understanding of the workings of the Beaufort Sea seasonal cycle as well as provide a basis for further hypothesis-driven investigation.

It is recognized that describing seasonal cycles from two years of data in a system that has large inter-annual variability in the physical environment and its main drivers (especially in ice and winds), is fraught with caveats. Given that this is the first synoptic year-round high-resolution data collection of its kind in this region, however, we see this at a first step towards a more comprehensive future analysis.

5.3.2 Methods

To examine the seasonal cycles and infer ecosystem relationships, we created weekly time series of MARES mooring data collected between October 2016 and October 2018 (or early 2019 for M1 data; see main report for details on mooring locations and instruments).

The time series data were plotted in Julia and the Plots.jl library. With the exception of air temperature, wind, and potential density plots, the seasonal time series plots were generated using either weekly or monthly averaged data. For air temperature at Herschel Island, daily climatological mean was computed using all available data between 1994 and 2020. The actual daily mean data for the MARES is overlaid on top of the climatological mean. The shaded region represents +/- 2 standard deviations.

Daily mean water column relative acoustic backscatter data from the ADCPs were smoothed with a 7-day filter and standardized to the total range of values within the record for each instrument and each year that minimum values were converted to “0” and maximum values were converted to “1”. This brought out the intra- and inter-annual patterns without biasing interpretation due to potential differences in relative backscatter between instruments. Examination of the patterns in relative backscatter prior to standardization revealed that the Year 2 values were greater than the Year 1 values, although different instruments used in the two years reducing our confidence in the comparison. Note, however, that the AZFP data showed a similar interannual difference.

Recognizing the critical influence of sea ice in structing this marine ecosystem, we divided the year into 4 ice seasons as follows:

Ice Season: Sea ice cover in the region (Figure 180) is 100%

Spring Transition: Sea ice cover in the region is decreasing and between 99-25%

Open Water Season: Sea ice cover in the region is below 25%

Fall Transition: Sea Ice cover in the region is increasing and between 25-99%

5.3.3 Results

The weekly time-series of MARES mooring data starting in October 2016 and ending in September 2018 are plotted in Figure 180 (See Figure A-1 to Figure A-3 for high resolution plots). Below we describe the seasonal cycle based on the framework of the four ecosystem phases based on the annual cryo-cycle. We then examine the potential relationships between physical drivers (e.g., ice, temp, wind) and response variables (e.g., biomass of zooplankton) to elucidate the function of the annual cycle of the Beaufort Sea/Makenzie River canyon ecosystem.

As noted, a fundamental aspect of the high latitude Beaufort Sea ecosystem is the substantial interannual variability. This is noted *a priori* with the intrusion of migratory Arctic cyclones into the Western Arctic

and the collapse of the Beaufort High during Winter 2016–2017 (e.g., Moore et al. 2018). This event affected ocean-sea ice dynamic and thermodynamic processes over the study site. As a result, the ice regimes differ in the two years, affecting the duration of the spring transition and the length of the open water season (Table 50 and Figure 180).

Table 50. Timing and duration of the cryo-seasons during the two MARES study years (highlighted cells indicate major differences between the two years).

Season	Start	End	Duration (days)	Duration (weeks)
Fall transition	10/15/2016	11/15/2016	31	4
Ice	11/15/2016	4/20/2017	156	22
Spring transition	4/20/2017	6/15/2017	56	8
Open water	6/15/2017	10/15/2017	122	17
Fall transition	10/15/2017	11/10/2017	26	4
Ice	11/10/2017	5/1/2018	172	25
Spring transition	5/1/2018	8/1/2018	92	13
Open water	8/1/2018	9/15/2018	45	6

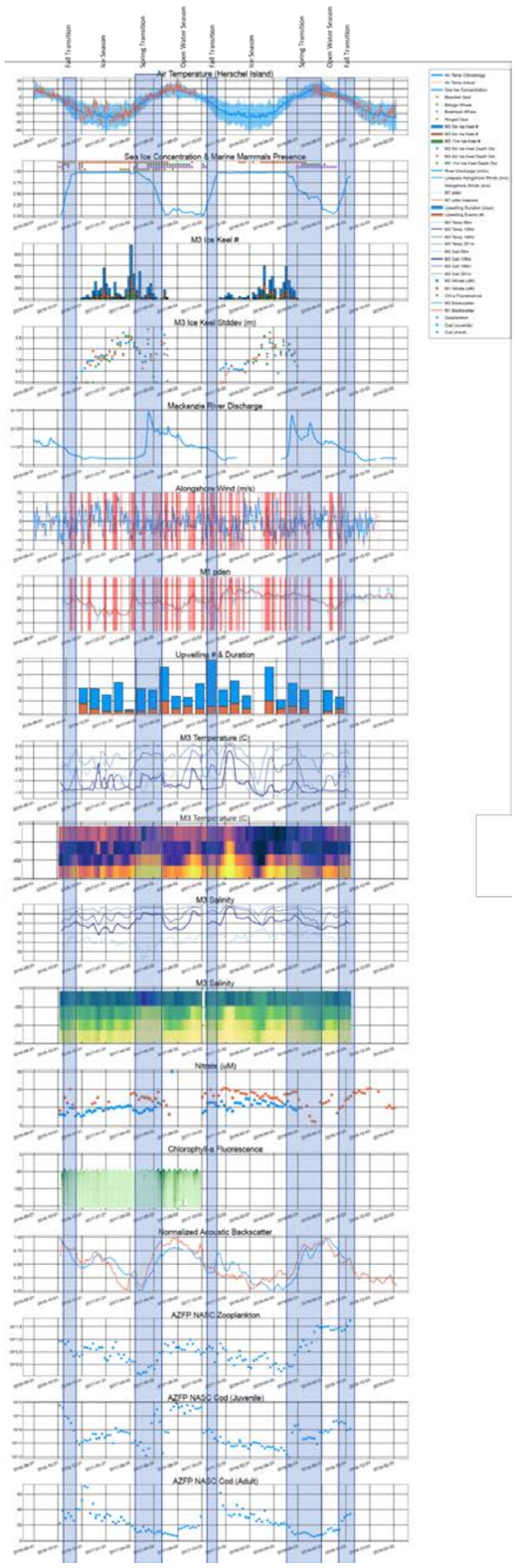

Figure 180. Weekly time series of mooring data collected between October 2016–2018 (see appendix A for higher resolution figures)

Shaded areas indicated the timing of the seasons.

5.3.3.1 Ice Season

The ice season starts around mid-November and lasts for over six months, typically until late April. Ice keels not seen during ice formation became increasingly common by mid-winter, peaking in the latter third of this time-period in early to mid-spring. During the ice season, flows from the Mackenzie River declined, to reach a minimum in early December and remain relatively low but constant with a winter flow of 5000 m^3/s (which is still a major input compared to most other Arctic rivers in the summer).

During this time surface alongshore winds were generally strong with episodic wind events (easterly vs. westerly). Despite the ice cover, several prolonged upwelling events were observed in both years lasting on average around 1 week, perhaps in part facilitated by the large number of ice keels transferring energy into the water column. Predominant ice drift direction was towards the west-northwest at all mooring sites. In general, the alongshore upwelling winds did not exhibit a clear seasonal signal and upwelling events were found throughout the year. Nitrates were observed to be variable but generally increasing across the ice season (especially in 2016–2017) as nutrients replenish during the winter months when primary production is at its minimum.

Air temperatures varied but remained between -7 and -30^{o}C, and water temperature at M3 below 55 m ranged between -1.5 and 0.5^{o}C. At 55 m temperatures showed a consistent decline from -0.5 to -1^{o}C until May but were up to 1 degree colder during the second winter. Water temperatures at 136 m, 196 m and 261 m were highly variable driven by upwelling and downwelling events with no discernable seasonal pattern. Likewise, salinity during in ice season did not show any appreciable trends and the water column below 55 m at M3 remained stratified throughout.

With no discernable phytoplankton presence during ice season at the depth measured (below 50 m), it is perhaps not surprising zooplankton biomass estimated by AZFP and ADCP declined throughout the ice-covered season. The only exception was an uptick in early January 2017 observed in the AZFP and ADCP data, coincident with the same observation in the fluorescence data at M2. Juvenile cod also declined at the beginning, then stayed constant or even increased in January and March (perhaps due to an episodic event), to then decline again to reach its minimum during the spring transition when ice cover is around 75% (see below). Adult cod biomass, on the other hand, peaked early in the ice season and then showed a steady decline the remainder of the time. Bearded seals were heard throughout the ice seasons and in in the first year only, ringed seals, bowhead and beluga were also detected at the beginning and end of this period.

5.3.3.2 Spring Transition

A detectable decline (break up) in ice coverage signals the beginning of the spring transition. Breakup was observed to begin in late-April to early May, when the days are already 19h long, but mean air temperatures are still below -10^{o}C. Although past their peak numbers, hundreds of ice keels were still detected in May and June. By early June, the sun does not set anymore, air temperatures reached 0^{o}C and ice cover was at 60-75%. After early June, ice dynamics over the moorings proceeded differently in the two years even though air temperatures were comparable. In spring 2017, ice coverage declined to persistently below 25% by mid-June, the entire spring transition period lasting approximately 8 weeks. In 2018, however, the decline was slower, taking 13 weeks and not reaching ice cover below 25% until the beginning of August. As the ice melted back in June, water temperature declined 2^{o}C at all depths at M2, with a steeper decline in the first year, matching the faster sea ice melt.

During this time Mackenzie River discharge peaked, increasing sharply from its minimum of 5000 m^3/s in early May to 30,000 m^3/s 2 weeks later. At M3 in the first year (2017) a strong freshening signal was

observed at 55m in May likely due to a combination of river water and ice melt. In late June, below 55m, temperature declines were also observed. In the second year (2018) the freshening river runoff signal was not seen at 55m. This could be due to the delay in ice melt observed. A salinity decrease at deeper depth was also observed during the ice melt back in the second year, but like the spring transition, was slower and drawn out. Wind speeds during this time are less than during the ice season, and variable in direction. Both years had several upwelling events which combined lasted between on forth to one third of the total spring season.

Nitrate concentrations are at or close to their highest observed levels at the beginning of the spring transition period, having been replenished from upwelling and or riverine output over the fall transition and ice periods. As light penetrates the water column during ice breakup, fluorescence increases (likely both from ice algae and ice edge phytoplankton bloom), nitrate concentrations start to drop sharply, reaching minimum concentrations at different times in both years, but each time right at or shortly after the end of the spring transition.

The increase in phytoplankton associated with ice break up also marks a sharp increase in zooplankton biomass (represented by backscatter from the ADCP and AZFP) in both years of the study, from its lowest levels in early May to its maximum levels by the beginning of open water season (i.e., end of June in 2017 and early August in 2018). Although the timing of the peak matched the end of the spring season and beginning of the open water season in both years, the slower ice melt in the spring of 2018 may have provided better growing conditions or less predation by juvenile cod, resulting in markedly higher zooplankton abundance or biomass during the second year, as seen in the acoustic zooplankton estimates. Juvenile cod biomass matches the timing of increase of their zooplankton prey, being close to their peaking at the same time at the end of the respective spring transition seasons. Adult cod were observed to continue their decline first observed at the onset of ice formation. This decline continued through the end of the spring transition. The spring transition period in 2017 was marked by the presence of bearded seal, bowhead whale, ringed seal, and beluga whales, although no ringed seals were heard during the second year, and bowhead and beluga were no heard until a month after the start of breakup.

5.3.3.3 Open Water Season

This time period is defined by the absence of ice cover (defined as below 25%). Air temperatures are above freezing, reaching up to 20^{o}C in August, but water temperatures below 55 m remain at or below freezing, and sometimes dropping below freezing at the beginning of the season after several prolonged upwelling events. Winds were predominantly positive (towards the east), particularly in the summer of 2017, resulting in up to five upwelling events per month, lasting several days each. The upwelling events helped to replenish some of nutrients levels that were depleted by the spring/early open water season bloom. The upwelling events also punctuated the otherwise stable salinity measurements (see Section 1.4 for discussion of the importance of these episodic events). River run-off decreased to between 30-60% of its spring maximum. Chlorophyll-a concentrations continued to increase, and a subsurface chlorophyll-max could clearly be seen throughout the open water season at depth of 50 m extending to 150 m. A second phytoplankton pulse was observed at the end of the open water season (in September 2016 and 2017) extending down to 80 m, coincident with temperature and salinity increases.

Zooplankton biomass that increased during the spring continued to increase early in the open season, taking advantage of the growing phytoplankton bloom. Although numbers started to decline towards the end of this season, a slight uptick was seen in late September, coincident with that second plankton bloom. Despite the much shorter open water season in 2018, zooplankton abundance was higher than in 2017. Conversely, juvenile cod, which also reach their peak during this season, had much higher abundances in 2017. This suggests that zooplankton growth may be facilitated by a long spring transition

or shorter open season, or that juvenile cod thrive during faster transition and thus create higher top down pressure on zooplankton in those years.

Adult cod biomass was comparable between years and having reached its lowest levels at the end of the spring transition, started to increase again through the open water season. All four species of marine mammals were present during this time of year, and all were heard at some point at the MARES moorings during the open water season in the first year, but no ringed seals were heard in 2018.

5.3.3.4 Fall Transition

During the fall transition, days grew shorter and air temperatures dropped below freezing. Sea ice returned quickly to this region, taking 4 weeks to increase from 25% to 100% ice cover by mid-November; by which time, the sun is about to set for the winter. Ice keels were not observed during the fall transition phase and river runoff approached its minimum. Winds became stronger again and more westerly, although some significant upwelling events were still observed, especially in November of 2017.

Besides onset of ice formation and entry into the fall transition season, biotic and abiotic conditions in fall are potentiated by the proceeding summer. In general water temperatures seemed to increase slightly at the beginning of the season, but generally remained below 0˚C, whereas salinity remained stable and clearly stratified. Higher winds and some punctuated upwelling events started to replenish the nutrient levels drawn down by the primary producers during the spring transition and open water season. The fall transition phase signaled the end of the main productive period of the Beaufort Sea. Although substantial chlorophyll-a amounts are still detected in the water column during the fall transition phase, they are remnants of the open-water bloom being advected downwards.

In this part of the Beaufort Sea, the metazoan zooplankton are typically made up large calanoid copepods tend to dominate biomass while smaller copepods such as *Oithona similis* and *Pseudocalanus* sp. dominate numerically (Smoot and Hopcroft 2017). Zooplankton biomass measured at the MARES moorings by the ADCP and AZFP generally continued to decline during this transition season, although the AZFP detected an increase in the fall of 2018. This decline is likely to be a regular feature in the functioning of the zooplankton community in this area, resulting from ontogenetic migration to depths below the transducers at the mooring sites. This is coupled with the same migration from the upper water column at locations further offshore, limiting re-supply of zooplankton onto those depths on the shelf/slope due to horizontal advection. Recall that the acoustic instruments are effective primarily at sensing the larger-bodied zooplankton such as *Calanus* spp. and euphausiids and that euphausiids, originating in the Bering Sea, are only rarely transported as far to the east along the Beaufort Shelf as the study area. The smaller zooplankton may persist but are unlikely to be sensed with the instrumentation. Juvenile cod biomass also decreased in the fall transition period coincident with the decline in biomass of zooplankton. In contrast, an increase in observed adult cod biomass was observed, perhaps in part to young of the year cod recruiting into the adult cod population after a summer of feeding and rapid growth. Although all marine mammal species were heard during the fall transition in 2016, none were detected in 2017 and 2018.

5.3.4 Discussion

The observations that we report here confirm and extend what we know about the Beaufort Sea ecosystem seasonal cycle, particularly when in the context of the cycle of ice. The presence and timing of ice coupled with the wind and the influence of the Mackenzie River control the biological processes in this region.

One of the most powerful result from this study is a deeper understanding of the effects of wind and an increase in the awareness of the importance of this primary driver. At an annual scale, alongshore winds appear variable with no consistent seasonal pattern but, embedded in this annual record are episodes in which the direction and timing of the spring-time winds have a powerful influence. Semi-sustained westerlies prior to break up and over the summer in 2018 led to a late sea ice retreat, an icy summer, and Ekman transport of ice shoreward. Spring and summer westerlies pushed the Mackenzie River plume away from the mooring array into the Canadian archipelago, likely reducing the overall freshwater input to the Beaufort Gyre during this time. Under a prevailing spring and summer westerly system, ice is slow to clear from the shore and we speculate that the spring bloom is protracted. In turn, this influences the growth of taxa that feed directly or indirectly on this freshly produced carbon.

Alternatively, easterlies are critical for upwelling nutrients, plume transport to the west, and for clearing out the ice in spring and creating flaw leads in the winter. Easterly prevailing winds in spring and summer, as seen in 2017, created a shorter spring transition, and an earlier and longer open water season. This resulted in greater solar warming of the water, stronger stratification, and potentially support of an earlier, explosive, and short-lived phytoplankton bloom.

Interestingly, in the easterly dominated spring (2017) the biomass of juvenile cod was observed to be higher than the westerly dominated spring (2018). Biomass of zooplankton observed followed the opposite pattern, with zooplankton production apparently promoted by the cool icy protracted summer season in 2018. Besides the effect on ice cover, the easterly winds push the plume west, providing nutrients and heat across the MARES array. Western transport of the plume may also promote rapid ice clearing to the west. Earlier warming of the surface waters may have accelerated the growth of juvenile cod in the summer of 2017, “accelerating” cohort hatching and growth (see Bouchard and Fortier 2011). This “accelerated” cohort may have then more effectively grazed down zooplankton; explaining why we observed a lower zooplankton biomass in summer 2017. Conversely, when westerlies dominate, the cooler, icier waters promote a prolonged bloom and delayed hatching and slower growth of cod.

Further work on the impact of wind could lead to a yearly forecast measure for this marine ecosystem. Directional long-term trends in these winds could subsequently shed light into the future productivity in the region and its downstream impacts to the Alaskan Beaufort Shelf. Given the importance of winds at shorter temporal scales, episodic events that punctuate the above described seasons are further investigated below.

5.4 The Importance of Episodic Events

5.4.1 Introduction

Wind-driven coastal upwelling and downwelling are important mesoscale processes along the shelf of the Beaufort Sea that lead to shelf-basin exchange of water masses affecting biogeochemical properties (Pickart et al. 2011; 2013). Upwelling is driven by easterly winds and can be intensified when there is partial ice cover, due to the ice-ocean stress (Schulze and Pickart 2012; Lin et al. 2020). In contrast to upwelling, downwelling is driven by westerly winds and fluxes near-bottom water off the shelf, which is able to ventilate the halocline in the Canada Basin (Foukal et al. 2019). In the Mackenzie canyon, upwelling and downwelling have been commonly observed seaward of the shelfbreak, which is not wind-driven (e.g., Macdonald et al. 1987; Dmitrenko et al. 2018). The MARES mooring data has led to the identification of a persistent recirculation in the canyon that appears to be the result of interaction of the southern limb of Beaufort Gyre and the canyon topography (Lin et al. 2020). This flow is associated with the Mackenzie Canyon upwelling/downwelling investigated by the above studies. Lin et al. (2020) demonstrated that the low-frequency variation of the recirculation is correlated with the wind stress curl in the Canada Basin, which drives changes in the Beaufort Gyre.

5.4.2 Physical Characteristic of Events

We identify coastal upwelling (downwelling) as periods corresponding to positive (negative) near-bottom potential density anomaly relative to the 30-day lowpass timeseries at mooring M1 (Figure 181), when easterly or westerly winds blow. We define a coastal upwelling/downwelling index as the integrated potential density anomaly over the event (Figure 182). For canyon upwelling, Carmack and Kulikov (1998) used the effective depth, i.e. the isohaline displacement from offshore to onshore, to quantify upwelling. In this study, canyon upwelling (downwelling) is identified as periods corresponding to positive (negative) potential density difference between M3 and M4 in the depth range 80-250m (the core of the recirculation). Positive values mean that the isopycnals slope upwards toward the head of canyon, namely canyon upwelling, while negative values represent canyon downwelling. Our criterion is comparable to that employed by Carmack and Kulikov (1998). We then defined a canyon upwelling/downwelling index as the integrated density difference over the event (Figure 182), in analogous fashion to the coastal index. We consider only pronounced canyon events when the absolute potential density difference exceeds 0.1 kg/m^3.

The timeseries of the coastal and canyon upwelling/downwelling events, and the associated index for each type, are shown in Figure 182. Over the two-year period, there is more upwelling than downwelling in both the coastal region and canyon, particularly in the second deployment year. Note that both types of events occur throughout the year, which is consistent with the conditions in the Alaskan Beaufort Sea reported by Lin et al. (2019).

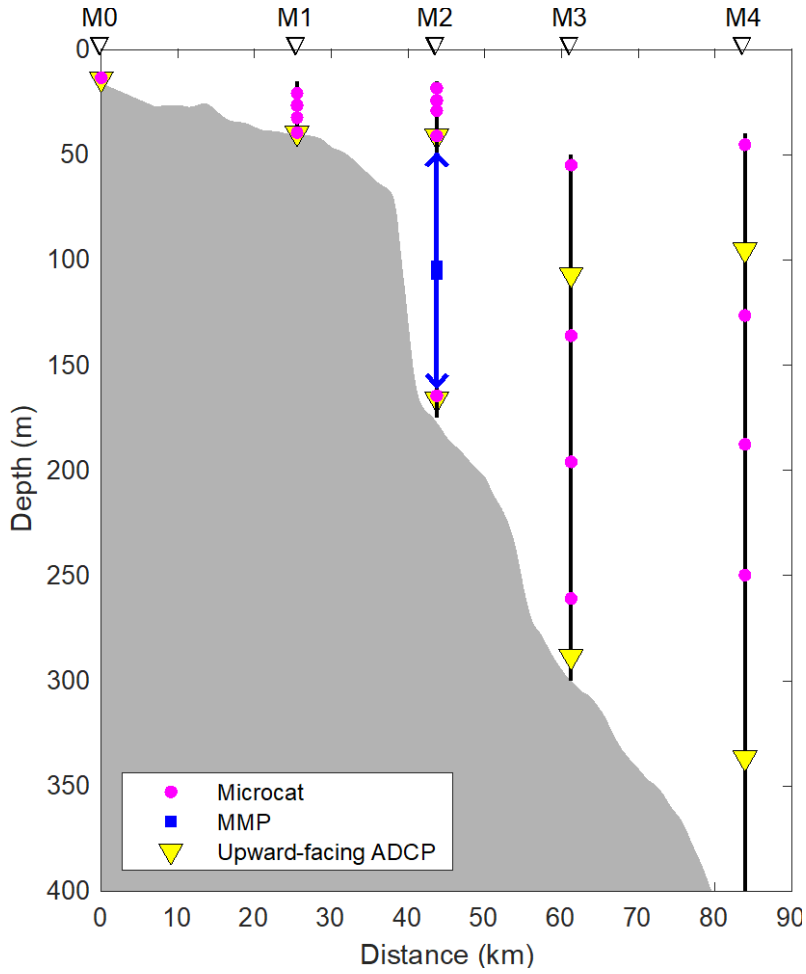

Figure 181. Configuration of the mooring array in the vertical plane
The legend shows the different scientific instruments used: MicroCATs, a McLane moored profiler (MMP), and upward-facing acoustic Doppler current profilers (ADCPs).

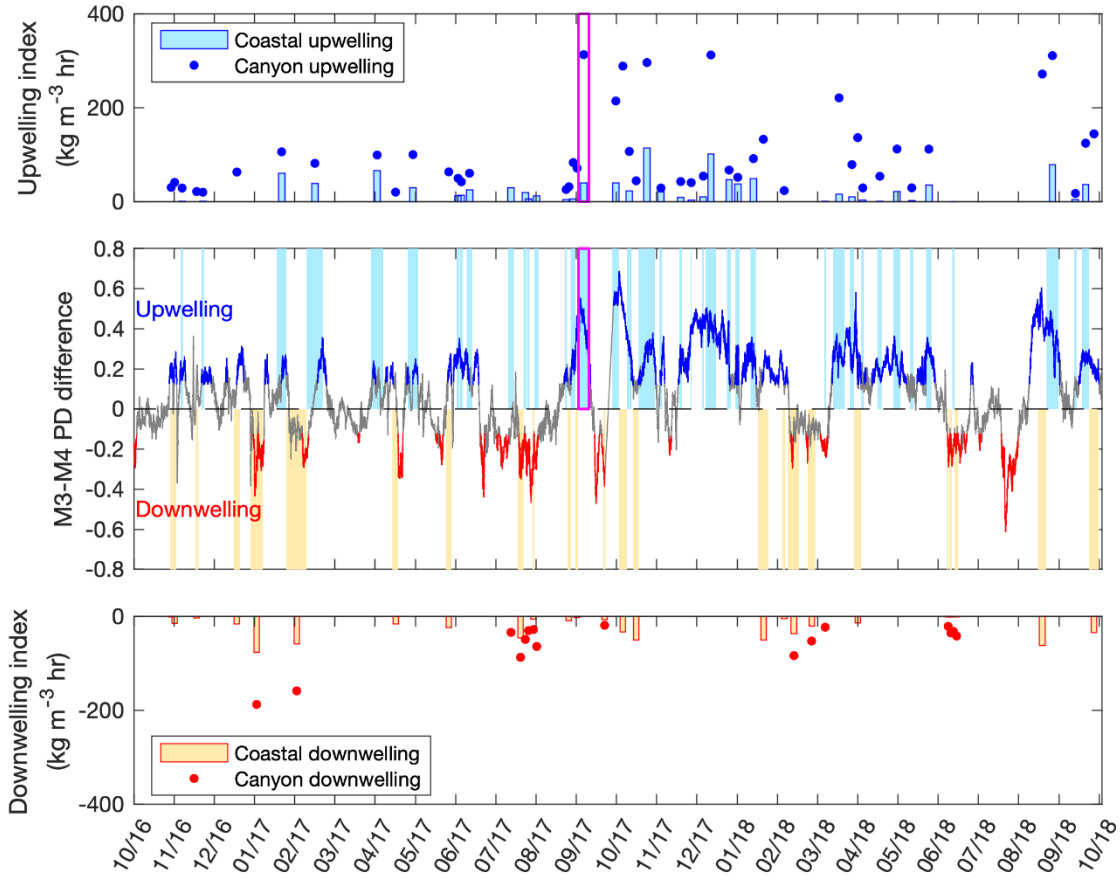

Figure 182. (Middle) Timeseries of M3-M4 potential density difference between October 2016 – 2018, where periods of canyon upwelling are marked in blue and canyon downwelling in red. Periods of coastal upwelling/downwelling are marked by the light-blue/yellow bars. (Top) The indices of the coastal and canyon upwelling are represented by light-blue bars and blue dots, respectively. (Bottom) The indices of the coastal and canyon downwelling are represented by yellow bars and red dots, respectively.
The specific upwelling event investigated in detail in this chapter is marked by the magenta rectangle in the top two panels.

We considered four scenarios (event types): (a) simultaneous coastal and canyon upwelling (33 events); (b) coastal upwelling coincident with canyon downwelling (6 events); (c) simultaneous coastal and canyon downwelling (10 events); and (d) coastal downwelling coincident with canyon upwelling (15 events). For each case we constructed a composite event by normalizing the time axis from the beginning of the event (time = 0) to the end of the event (time = 1) and averaging the events together. Since there is a delayed response between atmospheric forcing and hydrography, we also considered the time-period just prior to and after the event. In each case, the beginning/end times were dictated by the coastal event. As noted above, the canyon events are driven by the wind stress curl over the Canada Basin, which varies on longer timescales than the wind stress along the coast that forces the coastal events. As such, there can be multiple coastal events during the time period of a single canyon event.

Figure 183 shows the composite timeseries of wind forcing (along-coast wind and basin wind stress curl) and density response (near-bottom density anomaly on the shelf and mid-depth density difference on the

slope) for the four scenarios. On average, the wind intensifies prior to the event and peaks around 5 m/s close to the onset of the event in all of the scenarios. This is consistent with the wind threshold of coastal upwelling/downwelling in the Alaskan Beaufort Sea (Schulze and Pickart 2012; Lin et al. 2019; Foukal et al. 2019). There is a lagged response of the coastal upwelling/downwelling to the along-coast wind: the shelf density response peaks in the normalized time 0.4-0.6. For the canyon, Figure 183 reveals that the wind stress curl over the Canada Basin is negative when there is canyon upwelling, and near-zero when there is canyon downwelling. This is consistent with the results reported in Lin et al. (2020), who found that increased negative wind stress curl results in stronger westward flow impinging on the canyon, which leads to a stronger recirculation and enhanced up-canyon flow.

The velocity and hydrographic responses for each of these scenarios are effectively depicted by vertical sections averaged over the duration of the composite events (Figure 184):

(a) Coastal and canyon upwelling (Figure 184a). This is the dominant scenario, with a total of 33 events over the 2 years. The mean alongstream section reveals that the shelf current centered at M1 flow towards the west (i.e., large negative velocity), while there is a cross-stream Ekman cell (offshore flow in the upper layer and onshore flow in the bottom layer). Within the canyon, the alongstream velocity reveals the recirculation (positive at M3 and negative at M4), with large onshore cross-stream flow. This is consistent with the recirculation structure shown in Lin et al. (2020). Not surprisingly, the isopycnals slope upward towards the shelf in the vicinity of the shelfbreak, although deeper in the water column the isopycnal tilt is much less pronounced. On average, the secondary circulation brings warmer, saltier water up to the shelf.

(b) Coastal upwelling – canyon downwelling (Figure 184b). The velocity and hydrographic signatures on the shelf and shelfbreak do not change significantly from case (a), except that the shelf current is weaker, and less-salty water is upwelled. Again, there is a cross-stream Ekman cell on the shelf. The dominant change occurs in the canyon. In this scenario there is eastward flow at both M3 and M4, and downslope flow at M3. Accordingly, the isopycnals on the continental slope are deflected downward progressing onshore, in contrast to scenario (a).

(c) Coastal and canyon downwelling (Figure 184c). In this scenario the velocity on the shelf is reversed to east, and there is a downwelling cross-stream Ekman cell with onshore flow in the upper layer and offshore flow in the bottom layer. This results in nearly level isopycnals in the vicinity of the shelfbreak. The canyon flow is largely the same as scenario (b), while there is a stronger downward isopycnal tilt over the slope progressing onshore.

(d) Coastal downwelling – canyon upwelling (Figure 184d). This situation is less straightforward in terms of the water column response. The alongstream velocity on the shelf at M1 is reversed, but immediately offshore at mooring M2 the alongstream flow is still westward in the upper layer. This is understandable in that the along-coast winds favor reversal of the shelf current, while the basin-averaged wind stress curl does not. Interestingly, there is no Ekman cell on the shelf where the flow is directed offshore from top to bottom, while over the slope the flow is directed onshore. As a result, the isopycnals are nearly level over the slope.

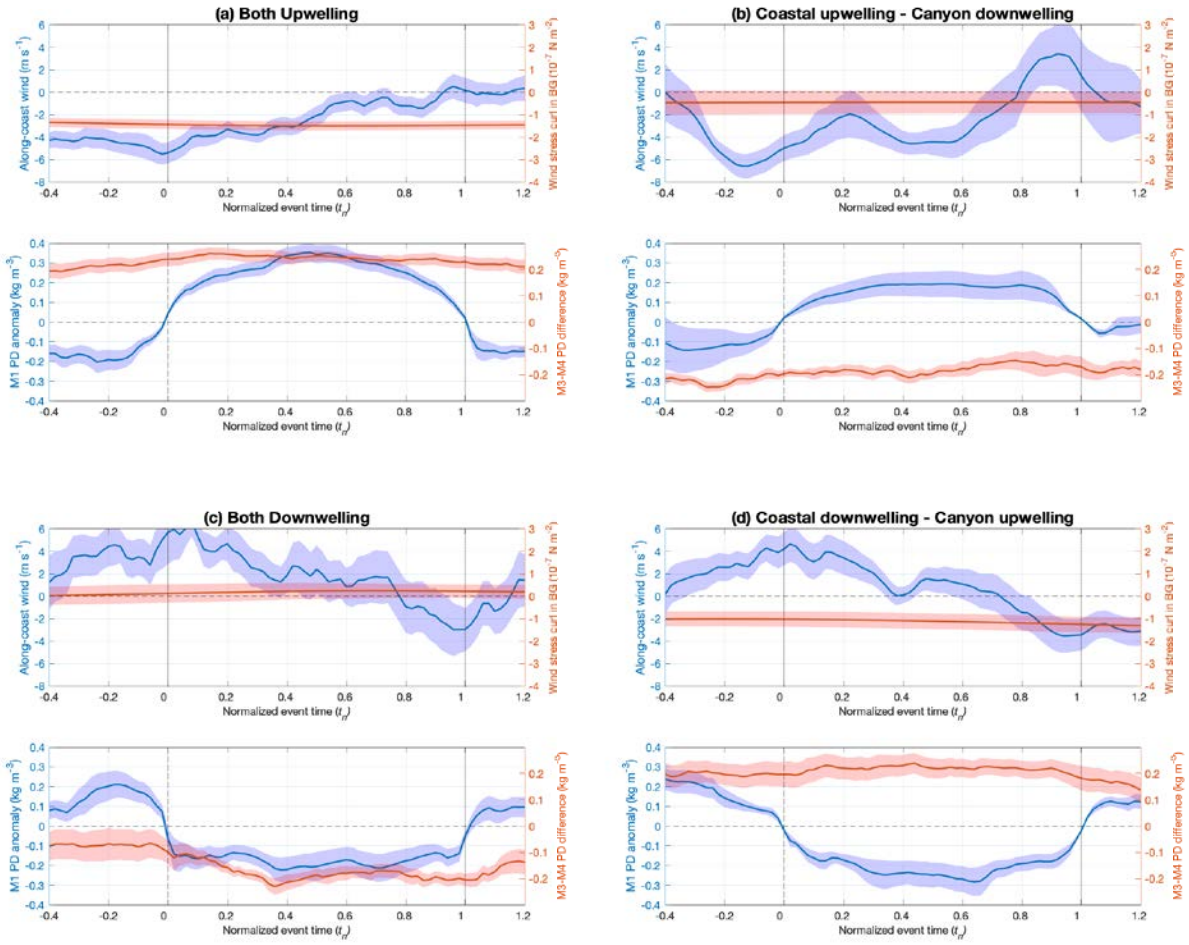

Figure 183. Along-coast wind (upper-panels, blue), 25-day low-passed wind stress curl in the Canada Basin (upper-panels, red), near-bottom potential density (PD) anomaly on the shelf (lower-panels, blue) and mid-depth PD difference on the slope (lower-panels, red) for (a) coastal and canyon upwelling; (b) coastal upwelling - canyon downwelling; (c) coastal and canyon downwelling; and (d) coastal downwelling - canyon upwelling.
The shading represents the standard error.

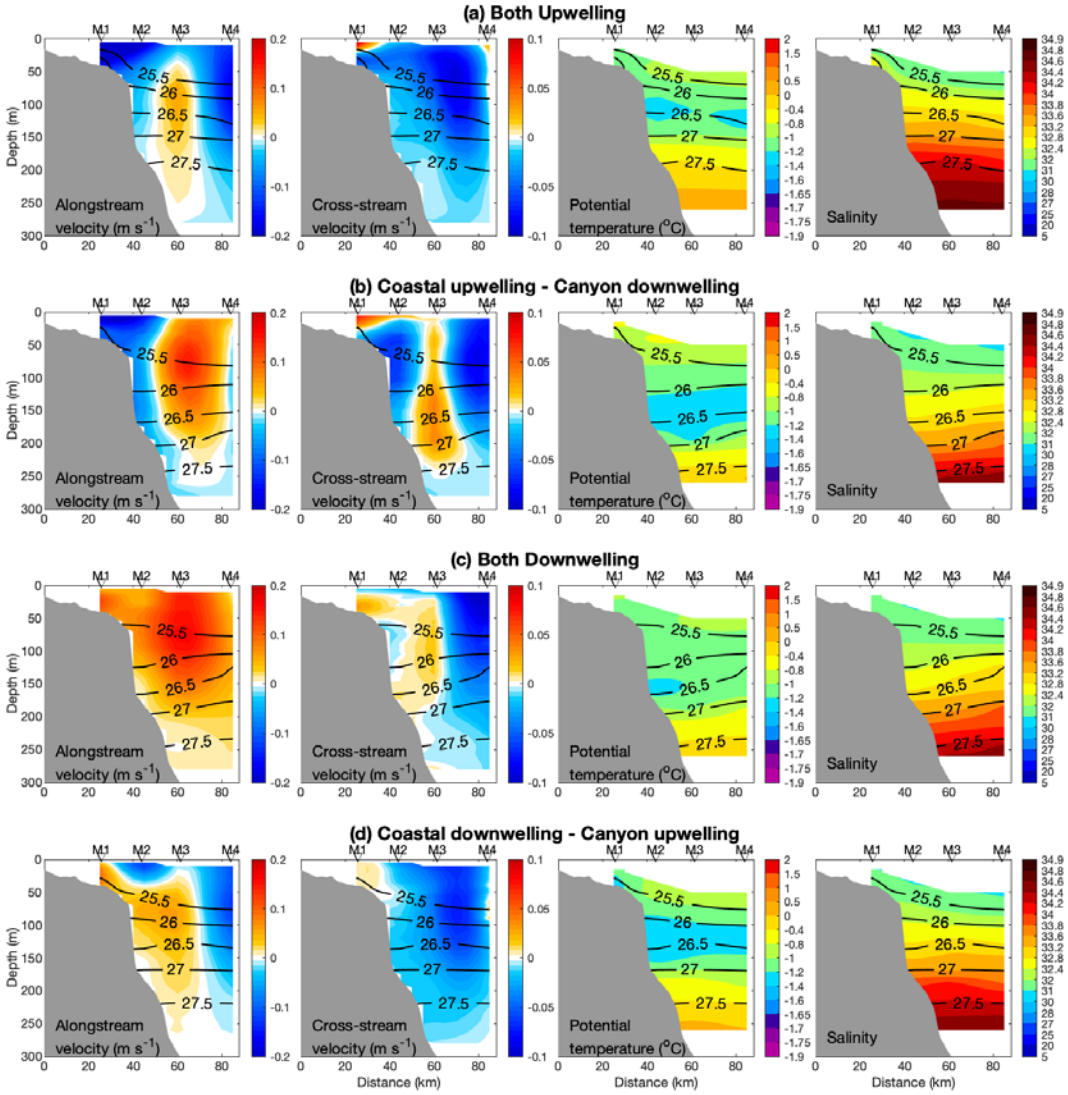

Figure 184. Vertical sections averaged over the composite events for the four scenarios described in the text.

The columns are alongstream velocity, cross-stream velocity, potential temperature, and salinity, with potential density contours (kg m^{-3}) overlaid. (a) coastal and canyon upwelling; (b) coastal upwelling - canyon downwelling; (c) coastal and canyon downwelling; and (d) coastal downwelling - canyon upwelling.

5.4.3 System Response to Physical Events

To gain insight into the importance of these wind-driven episodic events on the broader marine system, we carried out a case study focused on one particular event in September 2017 (see Figure 182). This event was chosen because it was a combined coastal and canyon upwelling event, suggesting that any responses may therefore be easier to detect, and because it occurred during the open water season, thus removing any confounding issues due to ice. Furthermore, the high-resolution McLane moored profiler (MMP) was operational during this time, providing additional variables such as turbidity and fluorescence that were not available in year 2.

The event, as identified, lasted between September 7 and September 15, 2017. To investigate system responses driven by this upwelling event, hourly data were compiled across the physical, chemical, and biological measurements taken by the MARES moorings during this time (Figure 185 and Figure 186). The along-coast wind was obtained from both the Herschel Island weather station and from the ERA-5 reanalysis product (Figure 185a). The two timeseries agree well with each other except for some high-frequency variability near the end of the event. The along-coast wind is mainly upwelling-favorable for the first half of the event (until Sep 12), with considerable fluctuations thereafter.

During the first half of the event, the velocity at M1 shows the canonical upwelling situation: an intensified westward-flowing shelf current and cross-stream Ekman cell with offshore flow in the surface layer and onshore flow at depth (Figure 185b and 185c). The dynamics become more complex during the second half of the event, after Sep 11, during which time the flow rotates anticyclonically. We suspect that the current rotation is associated with the variable wind. The spectral energy density reveals that both the wind and current have two significant peaks at 21 hrs and 45 hrs, respectively. The correlation between the two fields is supported by the significant wavelet coherence in the 20-50 hrs period (not shown). The hydrography has a lagged and prolonged response to the wind and current during this time, showing the presence of upwelled warm and salty water until Sep 14, extending several days beyond the relaxation of the Ekman cell.

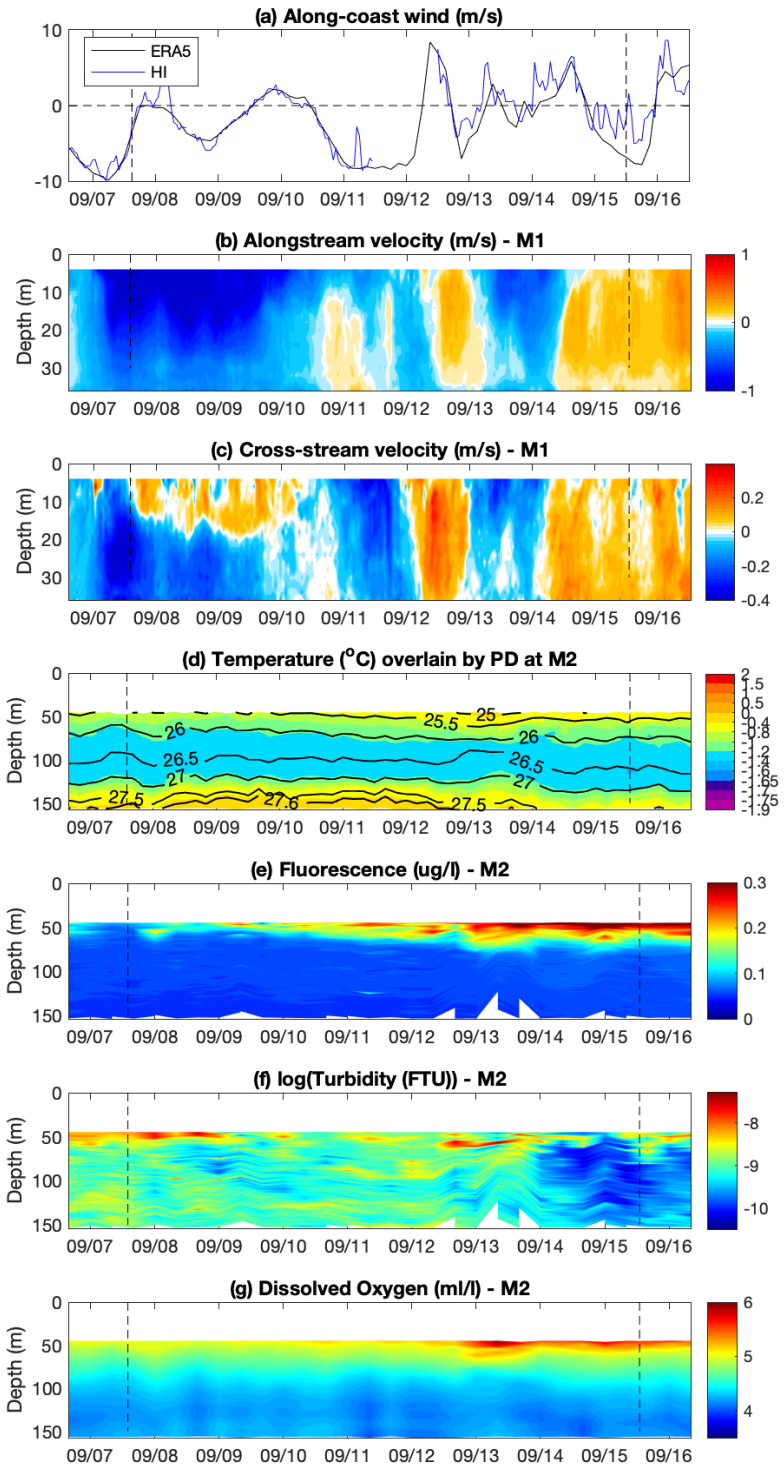

Figure 185. Timeseries of different variables during the September 2017 event
(a) along-coast wind (m/s) from Herschel Island weather station (blue curve) and ERA-5 (black curve); (b) alongstream and (c) cross-stream velocities at M1 (m/s); (d) temperature (°C) overlain by potential density contours; (e) Fluorescence (μg/l); (f) Turbidity (log(FTU)); (g) Dissolved Oxygen (ml/l). The vertical black dashed lines denote the range of the event.

The fluorescence, turbidity and dissolved oxygen were measured by the MMP at M2, which extends from 50 to 150 m depth in the vicinity of the shelfbreak (Figure 181). The fluorescence at those depths was very low until Sep 11 when a signal appeared below 50 m and continuously deepened and strengthened until the end of the event (Figure 185e). The dissolved oxygen showed a similar signal (Figure 185g). We suspect that this pattern is related to the upwelling circulation. The upwelled water is high in nitrate, which can spur local production on the Beaufort shelf even in mid- to late-September when there is less sunlight (Pickart et al. 2013). During the first part of the event, the secondary circulation advects water towards the surface in the vicinity of the shelfbreak, which tends to keep the water trapped there. This in turn would promote phytoplankton growth, which was probably occurring above the depth of the MMP. After several days one would expect a signal in fluorescence and oxygen to develop which would deepen in time. The penetration of this signal to depth was likely aided by the collapse of the Ekman cell. Note that the fluorescence/oxygen signal appeared in the MMP record shortly after the Ekman cell spun down (compare Figures 185c and 185e).

The measurements from the ADCP and the AZFP allow us to investigate associated signals for zooplankton and fish (Figure 186). As the upwelling develops, the backscatter signal is enhanced, particularly at M1, and subsequently weakens again towards the end of the event (Figure 186b). In the upper layer, at the M2 site, there is also a backscatter intensification, though not as pronounced (Figure 186c). The zooplankton enhancement is also apparent in the data from the AZFP farther offshore at M3 (Figure 186f). This could be interpreted as either an advection of zooplankton to the mooring sites or possibly some enhanced growth in the zooplankton population in response to the primary production occurring during/after the initial upwelling signal.

Information gathered by the AZFP at M3 is probably most strongly influenced by the canyon upwelling. It measured adult cod in the deep part of the water column and juvenile cod and copepods in the upper layer, quantified by the nautical area scatter coefficient (NASC, m^2/nmi^2). Copepods (Figure 186f) and juvenile cod (Figure 186e) show an enhanced signal in the upper 20 m, and between 30-40 m, respectively, immediately after the onset of the event. Inspection of the full timeseries over the duration of the array deployment reveals that such high NASC patches for zooplankton and juvenile cod are generally associated with upwelling, indicating that this one event is not unique. We suggest that during these events the phytoplankton are fluxed offshore, which attracts the copepods and juvenile cod in the upper layer. It is important to note, however, that the MARES mooring array is unable to resolve the 3-dimensional circulation, hence these signals could also be originating from upstream.

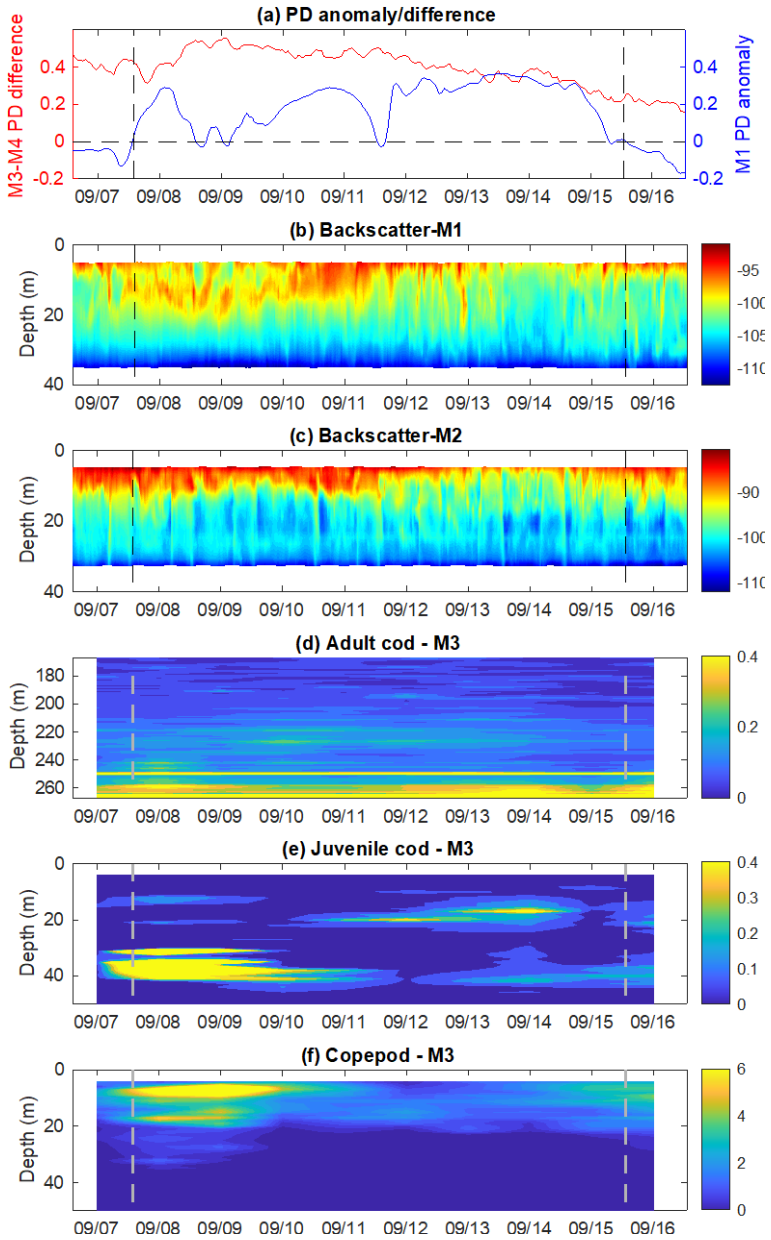

Figure 186. Timeseries of different variables during the September 2017 event
(a) near-bottom potential density (PD) anomaly on the shelf (blue curve) and middepth PD difference on the slope (red curve); (b) relative backscatter (proxy for zooplankton) at M1 and (c) in the upper layer of M2; Nautical area scatter coefficient (NASC, m^2/nmi^2) of (d) adult cod, (e) Juvenile cod, and (f) Copepods at M3. The vertical black dashed lines denote the range of the event.

The NASC of the adult cod (Figure 186d) shows concentrations at the bottom, and only changes slightly during the event. Recall that, during simultaneous coastal and canyon upwelling, the isopycnal tilt in deep water is relatively weak (Figure 183a). This suggests that the adult cod at depth are essentially unaffected by the canyon upwelling.

5.4.4 Conclusions

The timing, frequency, and intensity of episodic wind-driven events in the eastern Beaufort Sea is an important structuring feature of this marine ecosystem, affecting physical, chemical, and biological characteristics and habitat for invertebrates, fish, and marine mammals. The current study has identified some key characteristics of these events not previously described, and the case study hints at the system wide repercussions that changes in these events could have with changing ocean conditions. These insights illustrate the value of integrated synoptic sampling designs such as implemented by MARES. Future analysis of these events and their drivers and consequences will undoubtedly further increase our understanding of this system.

5.5 New Findings

The western portion of the Canadian Beaufort Sea, in the vicinity of the Mackenzie Canyon and the Yukon coastal area, has been studied intensively as part of the MARES program, from 2016 to 2018, some data extending into 2019.

Early studies of the oceanography of this part of the Beaufort Sea have described the "extraordinary spatial and seasonal variations in ice cover, temperature, light, freshwater, turbidity, and currents of the (Canadian) Beaufort Sea (which) define unique places or times critical to marine life" as a setting for marine life (Carmack and Macdonald 2002). Over the past two decades, important changes in physical conditions have taken place, especially such as higher air temperatures, reduction in and earlier clearing of sea ice cover, and changing winds to easterly wind dominance, in most years. These physical regime changes affect the marine biology (plankton, fish, birds, and marine mammals) of the Beaufort Sea.

Key contributions from MARES, which expand the understandings of the biophysical system in the eastern Beaufort Sea, highlight the benefits of conducting integrated synoptic sampling:

- The Mackenzie Canyon has profound effects on the large-scale regional circulation of the Pacific Water Mass and the Atlantic Water Mass. In particular, the Mackenzie Canyon results in a large amplification of the effects of upwelling in bringing nutrient rich waters from deeper waters into the euphotic zone of the upper layer that overcomes the nutrient depletion due to previous phytoplankton blooms. These processes greatly increase marine primary productivity, making the Mackenzie Canyon a biological "hotspot". The extensive MARES mooring array measurements of ocean currents and water properties resulted in new insights into the upwelling processes within, and to the west of, the Mackenzie Canyon. These measurements demonstrated the importance of upwelling to westward transport of deeper nutrient rich waters over the outer continental shelf into Alaska, the recirculation of deep offshore waters into the Mackenzie Canyon, and the episodic eastward transport of the bottom-intensified shelf-break jet to the east of the Canyon.
- The Mackenzie River plume is a unique estuarine feature in the Arctic Ocean, being highly dynamic in response to the winds, varying between the dominant easterly winds as well as the less frequent westerly wind episodes. The plume results in a degree of stratification of the upper layer by comparison to other parts of the Beaufort Sea. Large frontal features within the plume and at its boundaries can also result in the aggregation of suspended objects, including zooplankton, which can enhance biological productivity. The MARES program contributed to direct measurements of the underside of the Mackenzie River plume in the Mackenzie Canyon area and further west through the glider-based observations in August–October 2016 and T/S sensors in the moored arrays especially in 2016-2017. MARES also compiled and analyzed satellite-derived surface expressions of the Mackenzie River plume for the summer–fall of 2016, 2017 and 2018.
- MARES observations elucidated understandings of the movement of the Mackenzie plume westward across the shelf under dominant easterly wind events, entraining the nutrient rich deeper water and bringing them into the upper layer photic zone.
- MARES provided a deeper understanding of the effects of wind and an increased awareness of the importance of this primary driver:
    - Semi-sustained westerlies prior to break up in 2018 led to a shortening of the open water season, potentially resulting in a protracted spring bloom. In turn, this influenced the growth of taxa that feed directly or indirectly on this freshly produced carbon. Spring and summer westerlies also pushed the Mackenzie River plume away from the mooring array into the Canadian archipelago, likely reducing the overall freshwater input to the Beaufort Gyre during this time.

    - Easterly prevailing winds in 2017 created a shorter spring transition, and an earlier and longer open water season. This resulted in greater solar warming of the water, stronger stratification, and potentially supported an earlier, explosive, but shorter-lived phytoplankton bloom that favored juvenile cod but not zooplankton.
- Interannual variability remained high as can be seen with the intrusion of migratory Arctic cyclones into the Western Arctic. The collapse of the Beaufort High during Winter 2016–2017 (e.g., Moore et al. 2018) affected ocean-sea ice dynamic and thermodynamic processes over the study site, particularly with the prevalence of counter-clockwise sea ice motion in the Beaufort Gyre. MARES provided quantitative understandings of this anomalous episode on the sea ice regime and upper layer of the ocean in the Mackenzie Canyon and the adjoining western shelf/slope region.
- Zooplankton abundance estimated by the two acoustic instruments (ADCP, AZFP) showed similar seasonal cycles. The increase in zooplankton abundance that started during the spring transition/ice retreat and peaked during the open water/summer season was expected. However, zooplankton abundance declined over a relatively long period from a peak in mid-summer to minima in spring. The length and gradual rate of this decline was somewhat surprising. It was expected that zooplankton abundance in the water column at the depths above the acoustic instruments would effectively decline due to downwards ontogenetic migration of the large-bodied *Calanus* spp. but this should have been a sharp transition. Based on these data, it is clear that some zooplankton persist in the water column over winter that should be available to support pelagic predators such as fish.
- The effects of easterly winds in 2017 potentially also influenced juvenile cod biomass. The rapid ice clearing, and western transport of the Mackenzie plume, and earlier warming of surface waters may have accelerated the growth of juvenile cod in the summer of 2017, "accelerating" cohort hatching and growth (see Bouchard and Fortier 2011). This "accelerated" cohort may have then more effectively grazed down zooplankton; explaining why we observed a lower zooplankton biomass in summer 2017. Conversely, when westerlies dominate, the cooler icier waters promote a prolonged bloom, delayed hatching and slower growth of cod, but higher zooplankton abundance.
- The MARES mooring data has led to the identification of a persistent recirculation in the canyon that appears to be the result of interaction of the southern limb of Beaufort Gyre and the canyon topography (Lin et al. 2020). The low-frequency variation of the recirculation is correlated with the wind stress curl in the Canada Basin, which drives changes in the Beaufort Gyre.
- An in-depth analysis of episodic upwelling/downwelling events in the MARES data revealed:
    - Over the two-year period, there was more upwelling than downwelling in both the coastal region and canyon, particularly in the second deployment year. Note that both types of events occur throughout the year.
    - Canyon upwelling events were driven by the wind stress curl over the Canada Basin, which varied on longer timescales than the wind stress along the coast that forces the coastal upwelling events. As such, there can be multiple coastal events during the time-period of a single canyon event.
    - Increased negative wind stress curl resulted in stronger westward flow impinging on the canyon, which led to a stronger recirculation and enhanced up-canyon flow.
- A focused analysis of a coastal and canyon upwelling event (September 7–September 15, 2017) revealed:
    - An intensified westward-flowing shelf current and cross-stream Ekman cell with offshore flow in the surface layer and onshore flow at depth, with dynamics becoming more complex during the second half of the event when the flow rotated anticyclonically. The current rotation was potentially associated with the variable wind. The hydrography had a

lagged and prolonged response to the wind and current, showing the presence of upwelled warm and salty water, extending several days beyond the relaxation of the Ekman cell.
    - Measurements of fluorescence, turbidity and dissolved oxygen from M2 identified that fluorescence was very low until Sep 11 when a signal appeared below 50 m and continuously deepened and strengthened until the end of the event. Dissolved oxygen showed a similar signal. We suspect that this pattern is related to the upwelling circulation. During the first part of the event, the secondary circulation advected water towards the surface in the vicinity of the shelfbreak, which tended to keep the water trapped there. This in turn would promote phytoplankton growth, which was probably occurring above the depth we could measure (<50 m). After several days one would expect a signal in fluorescence and oxygen to develop which would deepen in time. The penetration of this signal to depth was likely aided by the collapse of the Ekman cell.
    - The measurements from the ADCP and the AZFP showed that as the upwelling develops, the backscatter signal was enhanced, particularly at M1, and subsequently weakened again towards the end of the event. A similar, although not as pronounced patter was present in the upper layer, at M2. Zooplankton enhancement was also apparent in the data from the AZFP farther offshore at M3. This could be interpreted as either an advection of zooplankton to the mooring sites or possibly some enhanced growth in the zooplankton population in response to the primary production occurring during/after the initial upwelling signal.
    - Information gathered by the AZFP at M3 was probably most strongly influenced by the canyon upwelling. Copepods and juvenile cod showed an enhanced signal in the upper 20 m, and between 30-40 m, immediately after the onset of the event. Inspection of the full timeseries over the duration of the array deployment revealed that such high NASC patches for zooplankton and juvenile cod were generally associated with upwelling, indicating that this one event was not unique. We suggest that during these events the phytoplankton were fluxed offshore, which attracted the copepods and juvenile cod in the upper layer.
- The glider component of the MARES project provided physical, biological, and chemical observations acquired from a moving platform and allowed for collection of fine scale information in the Mackenzie canyon and of the Mackenzie River plume.
    - Provided insights into the flow of the Mackenzie plume, identifying four different plume flow regimes, as well as the temporal and spatial scales at which key processes are occurring. These flow regimes, largely influenced by wind forcing, have significant impacts on the final destination of the plume waters, their retention within Arctic waters, and their influence on biological communities, with implications for potential anthropogenic impacts such as those that may be predicted by regional oil trajectory models.
    - Wind appeared to be the main driver of shelfbreak and Mackenzie canyon circulation.
    - Multi-year variability of summertime winds affected the structure of the Beaufort Gyre, shelfbreak boundary current, and downstream fate of Mackenzie River water.
    - The shelfbreak jet and the coastal current changed strength and direction on event time scales of days to weeks.
    - In years when the average summertime winds were strongly easterly (i.e., 2005–2011), most of the Mackenzie River water flowed westward and eventually ended up in the Beaufort Gyre, adding to the gyre's freshwater supply and potentially being trapped in the Arctic for up to 14 years.

    - During weak wind years, most of the Mackenzie River water was downwelled, flowed eastward into the Canadian Arctic Archipelago, and exited the Arctic much faster (a couple of years).
    - The direction and strength of the summertime Chukchi and Beaufort shelfbreak jet should be assumed to be steady on the inter-annual timescale.
- Sediment samples provided a snapshot of the organic sources and meiobenthic diversity across the Mackenzie shelf (McMahon et al. 2020).
    - Mid-shelf stations received a substantial organic input from marine sources rather than river deposition, and a response was observed with increased benthic meiofaunal abundance.
    - Benthic meiofaunal distribution patterns may vary across years depending on zonal winds causing opposing directional transport of Mackenzie plume material, however our results suggested that the meiofauna were largely dependent on marine carbon for food sources.
    - The largely consistent values seen in total organ carbon across the shelf belie a shift in origin as detailed by source specific organic markers. Terrestrial carbon is supplanted by more labile marine derived organic matter. Measures of total amino acids per unit carbon suggested that mid-shelf stations receive the highest deposition of marine labile organic matter to the sediments and the highest water column production furthest offshore at station M4. Additional markers of algal input such as highly unsaturated fatty acids show that M2 is a particularly rich zone for the deposition of labile marine derived material to surface sediments. These markers are rapidly lost with depth requiring significant annual fluxes from surface production and/or ice.
    - Benthic meiofauna showed highest diversity and abundances at mid-shelf stations. Station M3 has the highest overall abundances and diversity in contrast to labile organic carbon in the sediments, which was greatest at station M2. The majority of the benthic meiofauna identified were surface deposit feeders, who graze on available sources of organic matter near the sediment-water interface (Rhoades and Germano 1982). The mismatch in organic carbon and benthic abundance and diversity can be explained by the fact that the multitude of surface deposit feeders at M3 are quickly taking advantage of available carbon and grazing it down more aggressively when compared to station M2. Station M1 had the lowest abundance, diversity, and organic carbon, which is thought to be a result of ice scouring and coarse sediment texture (mostly gravel and rocks), and less availability of labile carbon. Station M4 had the second greatest abundance among the four stations sampled for meiofauna, with the greatest calculated wet weight biomass but lower dry weight biomass than station M3. This is related to the presence of larger meiofaunal organisms identified in deeper water.
    - Results from the meiofauna community analysis combined with information gathered from amino acids, carbon, and lipid biomarkers strongly suggested that the highest carbon fluxes and available (labile) organic carbon in the sediments occur at mid-shelf stations, and that these are fueled by marine sources. Although we anticipated that inner-shelf stations would show highest labile organic carbon because of the predicted flux of POC associated with the Mackenzie River freshet, it may be that both summer zonal winds and winter ice conditions presented conditions that reduced the influence of freshet organic carbon availability in 2016, during the time when samples were collected. Alternatively, this ecosystem may not routinely depend upon Mackenzie River input of organic carbon as an available food source but for nutrients that subsequently drive water column production. Additional studies are necessary to further evaluate the influence of Mackenzie River freshet on organic carbon dynamics and its link to

meiofaunal communities the abundance and diversity of meiofaunal organism in the Beaufort Sea.

- Marine mammal tagging provided new insights into the use of CTD-fluorometry satellite tags on spotted and bearded seals and foraging activity (Gryba et al. 2019).
    - Our analysis using state-space models illustrated the utility of satellite CTD-fluorometer tags to extend inferences of foraging beyond what was possible with surface movements alone. We identified foraging hot spots based on spatiotemporal overlap of foraging bearded and spotted seals. Some of these areas coincided with high prey density and high use areas by other species (e.g., Grebmeier et al. 2015, Ciatta et al. 2015, Kuletz et al. 2015).
    - Inclusion of dive parameters had little effect on predictions of amount of time spent foraging and in transit, but depth-corrected dive duration helped refine foraging locations. We also demonstrated that dive parameters can provide insights into the probability of switching between foraging and transiting.
    - Our pilot program demonstrated that collecting oceanographic parameters *in situ* at a scale relevant to the diving marine mammals can identify water bodies akin to oceanographic stations occupied by ships (e.g., Danielson et al. 2016). We illustrated that animal-borne oceanographic sensors can provide insights into environmental parameters influencing foraging decisions by spotted and bearded seals. The method revealed that spotted and bearded seals had an affinity to foraging in Bering Sea summer water during their fall and winter movements in the Chukchi and Northern Bering seas.

6 Climate Change Considerations and Next Steps

The physical environment in the eastern Beaufort Sea has been undergoing substantial changes, most of which are predicted to continue through 2050 and beyond. Kavik-Stantec (2020) summarized the main current and projected trends in some of the key physical parameters in this region (Table 51).

Table 51. Summary of Currents Trends and Future Projections of Key Physical Attributes

Physical Attribute	Metric	Unit	Current Condition/Trend	Future Projection
Air temperature	Mean	˚C	Annual mean daily temperature of –10.0°C, increasing at a rate of +0.07 °C/yr over the past 30 years	Expected to increase by 5.2°C by 2050
Wind	Direction (mean/median)	degrees	Mean wind direction of 175° and median of 140° (ESE) at Tuktoyaktuk	Limited projections available for wind direction; there may be more reversals of the surface wind direction as the climate warms, sea ice thins, and the locations of the maximum Sea Level Pressure (SLP) changes
	Speed (mean/ median)	km/h	Mean current wind speed at Tuktoyaktuk of 11.68 km/h, and median of 11.00 km/h. Past mean trends are variable with a slight decrease of -0.12 m/s/decade in recent data.	Winds speeds are projected to increase over the next 30 years by a median of 5% to a maximum of 6.5% for the Beaufort Sea region
	Variability		Variability in wind speed at Tuktoyaktuk is 11.68 ± 11.19 km/h. Variability in wind direction at Tuktoyaktuk is 175 ± 105°.	Complex interactions between climate warming, locations of maximum SLPs, and changes to direction, e.g., the collapse of the Beaufort High in 2017, with change in direction of surface winds, and this may be more frequent in future.
Sea level rise (including frequency and severity of storm surges)	Mean sea level rise (at Tuktoyaktuk, NWT)	mm/yr	+1.9 ± (2.0) mm/yr	+300mm ± 200mm mean increase by 2050
	Frequency of Storm Surges >1.5m at Tuktoyaktuk	Exceedance Probability (0 – 1.0)	0.39	Increased likelihood
	Frequency of Storm Surges >2m at Tuktoyaktuk	Exceedance Probability (0 – 1.0)	0.04	Increased likelihood
Ocean temperature	Near-Bottom Temperatures	˚C	None	Expected to increase marginally, but this is very uncertain.

Physical Attribute	Metric	Unit	Current Condition/Trend	Future Projection
and heat content (including inferences on bottom temperature)	Summer Mixed Layer Temperature	˚C	-0.03 ˚C/yr	Uncertain as this recent trend likely due to changes in the freshwater distribution.
	Summer Sea Surface Temperature (SST)	˚C	>0.05 ˚C/yr in the Southern Beaufort. -0.03 ˚C/yr south of Banks Island.	Mean SST of 3-4 ˚C, 50%-70% of SST observations in excess of the 1976–2005 maxima.
Sea ice (extent, thickness, type, timing, including landfast ice)	Ice Thickness	m	Decreasing as multi-year ice transitions to first year ice; largest reductions are in deep offshore waters of Canada Basin; reduction rate only 0.1 m/decade on slope and shelf	If current trend continues, ice thickness reduction of 0.3 m by 2050 from present values on continental slope and shelf, with larger reductions in the much deeper water of the Canada Basin
	Timing of Ice Freeze-up	weeks	Large inter-annual variability, statistically later by 0.15 wks/yr in most areas; change larger at 0.2 wks/year off Banks Island.	Current trend expected to continue, 2050 freeze-up in coastal areas may be delayed by 4.5 weeks from present conditions
	Timing of Break-up	weeks	Large inter-annual variability, with no significant trend in most areas, except Amundsen Mouth at 0.2 wks/yr.	Possibility of earlier break-up, but magnitude is uncertain.
	Open Water Duration	weeks	Increasing by 0.15 – 0.20 wks/yr except no significant trend in Amundsen. .	Current trend expected to continue; increased open water duration of 4.5 to 6 weeks from present conditions; 50 to >60% chance of ice-free conditions in late summer and early fall by 2050
	Ice Motion	cm/s	Winter mean ice speeds on shelf have increased from 2 to 5 cm/s in last 35 years.	Expected to continue to increase but no projections available as to magnitude
	Landfast Ice Duration	days	Reductions of 2-3 days/yr, varying according to sub-region.	Expected to continue to increase at or near present levels resulting in reductions of 60-90 days from present conditions
Currents and water column structure (physical and chemical)	Near-Bottom Salinity	Practical Salinity Unit (PSU)	None	Uncertain
	Summer Mixed Layer Salinity	PSU	-0.04 PSU/yr	Uncertain – salinification of up to 1.5 PSU in the regional model, freshening of < 1 PSU in the global model.
	Summer Mixed Layer Depth	m	0.11 m/yr (when ice-free)	Increases by 3-8 m

Physical Attribute	Metric	Unit	Current Condition/Trend	Future Projection
	pH and Alkalinity	pH/ Saturation Level	Fastest rate of acidification in Canada	Increased acidity and under saturation (<1) of carbonate expected
	Dissolved Oxygen	T_{mol}	-73 T_{mol}/decade (mean vertically integrated value)	Continued decrease, but the models have had poor skill with this parameter.
Permafrost conditions	Extent of permafrost	Degrees North	Continuous permafrost in Mackenzie Valley 67.5° N, advancing at average of 3 km N per year. Subsea permafrost northern extent decreasing -2 km N over the past 10,000 years.	Predictions for RPC8.5 indicate faster northern encroachment of discontinuous permafrost, possibly up to 9 km per year average, which would mean it would reach the Beaufort coast before 2050. Subsea permafrost northern extent moving shoreward < 0.1 km by 2050.
	Permafrost temperature	°C	Variable, generally increasing at 0.9 °C per decade in south and faster in north.	Increasing trend expected. As permafrost temperatures approach 0°C, permafrost is no longer viable.
	Active layer thickness	m	Variable	For few RPC 8.5 projections available: present day = 0.54 m, 2050 = 0.6 m, 2080 = 0.73 m
Freshwater runoff from Mackenzie River	Mean discharge	m^3/sec	10,000	11,800 ± 1,600 by 2050 (10-20% increase over baseline)
	Maximum discharge	m^3/sec	22,000	25,960 ± 2,000 by 2050 (10-20% increase over baseline)
	Sediment discharge	kg/sec	1715	1,870 (<10% increase over baseline) by 2050
	Freshet Timing	days / decade	+2.7	7–28 days earlier by 2050
	Month of maximum river volumes	Month	June	May (by 2050)
	Water quality (NO_3)	$mmol/m^3$	N/A	−2.3 ± 1 by 2050
Coastal exposure and erosion	Erosion	m/yr	Mean of 1-2 m/yr in Mackenzie Delta area, up to 40 m/yr reported in extreme cases (e.g., Pelly Island). Mean of 1.2 m/yr on Herschel Island. Up to 9 m/yr year along Yukon Coast. .	Coastal exposure and erosion were not variables considered in the RPC8.5 climate models; as a result, there are no projections for coastal exposure from those sources. However, at current average rates coastal retreat would be 30–60 m by 2050 at susceptible locations and hundred of metres or more at particularly exposed locations.

Current and future changes in key physical drivers will continue to stress the biological structure and function of this marine ecosystem and over time reduce the general resiliency of individual species and communities of marine species to human activities and altered ocean temperature, reduced extent and quality of sea ice, increased ocean acidification, and changing pelagic and benthic habitat.

There remains uncertainty about responses of lower trophic levels to changing environmental conditions in the Arctic and the MARES data has shown some of this episodic wind and ice driven complexity. Potential changes could include increases in primary production due to a longer Open Water Season, a new or stronger fall phytoplankton bloom, to a collapse of phytoplankton stocks due to a lack of sea ice edge induced blooms and increased occurrence of fungal parasites. The timing and reproductive strategies for most arctic zooplankton and fish species are linked to the melting of sea ice and the timing and intensity of the phytoplankton bloom. As result, they entire food is susceptible to these changes as was already observed in the northern Bering and Chukchi Seas (Huntington et al. 2020). Additionally, expected changes in contaminant levels in the water column due to climate change and increasing acidification of the Arctic Ocean may also increase sensitivity of zooplankton and fish to potential effects from human activities.

If climate change effects such as increasing light availability (due to less or thinner sea ice or snow cover) and temperature in surface waters benefit primary productivity, bottom-up food web processes may benefit some fish. Conversely, a warming Arctic could drive northward range expansions of species currently limited to more southerly latitudes by ice (e.g., the forage fish capelin (*Mallotus villosus*), or Pacific sand lance (*Ammodytes hexapterus*)), and promote new or more pervasive interspecific interactions with unknown consequences, especially among fish species with similar dietary preferences like capelin and arctic cod, which could favour productivity of some fish species at the expense of others.

The shift in the distribution of sea ice and open water habitat is also likely to affect marine mammals directly by altering the timing of migration and length of time spent in the eastern Beaufort Sea by whales, and the availability of suitable sea ice habitat for seal breathing holes and birthing lairs, and indirectly by changing the distribution of prey species. A longer Open Water Season and increased access to the region via the Bering and Chukchi seas may also lead to more frequent occurrences of southern species like killer whale, grey whale (*Eschrichtius robustus*) or humpback whale (*Megaptera novaeangliae)*, introducing more predation pressure and/or competition for food resources. Marine mammal populations already vulnerable to climate change (e.g., beluga whales, ice seals, polar bear), may become less resilient to effects from human activities, which themselves may increase as the region becomes more accessible.

Ultimately, all these changes will affect people living in the Arctic in fundamental ways, potentially altering their economy and demographics, and directly affecting infrastructure, subsistence activities, cultural vitality, and public health. To better understand these coming changes across the socio-ecological system of the Beaufort Sea, more integrated, multi-disciplinary, multi-year studies like MARES are needed. Ideally, such observations are matched with the development of regional models and scenarios of the future ocean climate so that we may better predict, mitigate, and adapt to what is coming.

7 References

Allen S, Durrieu de Madron X. 2009, A review of the role of submarine canyons in deep ocean exchange with the shelf. Ocean Sci. 5(4):607-620.

Archambault P, Snelgrove PVR, Fisher JAD, Gagnon J-M, Garbary DJ, Harvey M, Kenchington EL, Lesage V, Levesque M, Lovejoy C, Mackas DL, McKindsey CW, Nelson JR, Pepin P, Piché L, Poulin M. 2010. From Sea to Sea: Canada's three oceans of biodiversity. PLoS ONE https://doi.org/10.1371/journal.pone.0012182.

Ardyna M, Babin M, Devred E, Forest A, Gosselin M, Raimbault P, Tremblay J-É. 2017. Shelf-basin gradients shape ecological phytoplankton niches and community composition in the coastal Arctic Ocean (Beaufort Sea). Limnol Oceanogr. 62(5):2113-2132.

Arrigo KR, Perovich DK, Pickart RS, Brown ZW, van Dijken GL, Lowry KE, Mills MM, Palmer MA, Balch WM, Bahr F, Bates NR, Benitez-Nelson C, Bowler B, Brownlee E, Ehn JK, Frey KE, Garley R, Laney SR, Lubelczyk L, Mathis J, Matsuoka A, Mitchell GM, Moore GWK, Ortega-Retuerta E, Pal S, Polashenski CM, Reynolds RA, Schieber B, Sosik HM, Stephens M, Swift JH. 2012. Massive phytoplankton blooms under Arctic sea ice. Science 336(6087):1408.

Ashjian, CJ, Smith SL, Flagg CN, Wilson C. 1998. Patterns and occurrence of diel vertical migration of zooplankton in the Mid-Atlantic Bight measured by the acoustic Doppler current profiler. Cont Shelf Res. 18:831-858.

Ashjian, CJ, Smith SL, Flagg CN, Idrisi N. 2002. Distribution, annual cycle, and vertical migration of acoustically derived biomass across a 900 km transect in the Arabian Sea during 1994-1995. Deep-Sea Res II. 49:2377-2402.

Babb DG, Landy JC, Barber DG, Galley RJ. 2019. Winter sea ice export from the Beaufort Sea as a preconditioning mechanism for enhanced summer melt: A case study of 2016. J Geophys Res Oceans. 124:6575–6600. https://doi. org/10.1029/2019JC015053.

Balzano S, Marie D, Gourvil P, Vaulot D. 2012. Composition of the summer photosynthetic pico and nanoplankton communities in the Beaufort Sea assessed by T-RFLP and sequences of the 18S rRNA gene from flow cytometry sorted samples. ISME J. 6(8):1480-1498. doi: 10.1038/ismej.2011.213.

Barber DG, Asplin MG, Raddatz RL, Candlish LM, Nickels S, Meakin S, Hochheim KP, Lukovich JV, Galley RJ, Prinsenberg SJ .2012. Change and variability in sea ice during the 2007–2008 Canadian IPY program. Clim Change. 115:115-133 DOI 10.1007/s10584-012-0477-6.

Barber DG, Asplin MG, Papakyirakou TN, Miller L, Else BGT, Iacozza J, Mundy CJ, Gosslin M, Asselin NC, Ferguson S, Lukovich JV, Stern GA, Gaden A, Pućko M, Geilfus N-X, Wang F. 2012. Consequences of change and variability in sea ice during the 2007–2008 Canadian IPY program. Clim Change. (2012) 115:135–159 DOI 10.1007/s10584-012-0482-9.

Bates NR, Mathis JT. 2009. The Arctic Ocean marine carbon cycle: evaluation of air-sea CO2 exchanges, ocean acidification impacts, and potential feedbacks. Biogeoscience 6:2433–2459. https://doi.org/10.5194/bg-6-2433-2009.

Benoit D, Simard Y, Fortier L. 2008. Hydroacoustic detection of large winter aggregations of Arctic cod (*Boreogadus saida*) at depth in ice-covered Franklin Bay (Beaufort Sea). J Geophys Res. 113:C06S90. doi:10.1029/2007JC004276.

Benoit D, Simard Y, Fortier L. 2013. Pre-winter distribution and habitat characteristics of polar cod (*Boreogadus saida*) in southeastern Beaufort Sea. Polar Biol. doi:10.1007/s00300-013-1419-0.

Berline L, Spitz YH, Ashjian CJ, Campbell RG, Maslowski W, Moore SE. 2008. Euphausiid transport in the Western Arctic Ocean. Mar Ecol Prog Ser. 360:163-178.

Bradstreet MSW, Cross WE. 1982. Trophic relationships at high Arctic ice edges. Arctic 35(1):1-12.

Braham HW, Krogman BD, Carroll GM. 1984. Bowhead and white whale migration, distribution, and abundance in the Bering, Chukchi, and Beaufort Seas, 1975-78. NOAA Technical Report NMFS SSRF-778. 39+ pg.

Breed GA, Cameron MF, Ver Hoef JM, Boveng PL, Whiting A, Frost KJ. 2018. Seasonal sea ice dynamics drive movement and migration of juvenile bearded seals *Erignathus barbatus*. Mar Ecol Prog Ser. 600:223-237

Burns JJ, Frost KJ. 1979. The natural history and ecology of the bearded seal (*Erignathus barbatus*) and the ringed seal (*Phoca hispida*). Final Report Outer Continental Shelf Environmental Assessment Program: 311-392.

Burns JJ, Frost KJ, Lowry LF. 1985. Marine mammal species accounts. Alaska Department of Fish and Game, Game Technical Bulletin No. 7. 96 p.

Cameron MF, Frost KJ, Ver Hoef JM, Breed GA, Whiting AV, Goodwin J, Boveng PL. 2018. Habitat selection and seasonal movements of young bearded seals (*Erignathus barbatus*) in the Bering Sea. PLoS ONE 13(2):e0192743

Campbell RG, Sherr EB, Ashjian CJ, Plourde S, Sherr BF, Hill V, Stockwell DA. 2009. Mesozooplankton prey preference and grazing impact in the western Arctic Ocean. Deep Sea Res Part II. 56(17):1274-1289.

Canadian Ice Service (CIS). 2018. Government of Canada, Archive Search; [updated: 2020 Feb 01; accessed 2017 Oct 23]. http://iceweb1.cis.ec.gc.ca/Archive.

Carmack EC, Kulikov EA. 1998. Wind-forced upwelling and internal Kelvin wave generation in Mackenzie Canyon, Beaufort Sea. J Geophys Res. 103(C9):18447– 18458. doi:10.1029/98JC00113.

Carmack EC, Macdonald RW. 2002. Oceanography of the Canadian Shelf of the Beaufort Sea: A setting for marine life. Arctic 55:29–45.

Carmack EC, Macdonald RW, Jasper S. 2004. Phytoplankton productivity on the Canadian shelf of the Beaufort Sea. Mar Ecol Prog Ser. 277:37–50. doi:10.3354/meps277037.

Christman CL, Citta JJ, Quakenbush LT, Clarke JT, Rone BK, Shea RA, Ferguson MC, Heide-Jørgensen MP. 2013. Presence and behavior of bowhead whales (*Balaena mysticetus*) in the Alaskan Beaufort Sea in July 2011. Polar Biol. 36:1851-1856.

Cobb D, Fast H, Papst MH, Rosenberg D, Rutherford R, Sareault JE (Editors). 2008. Beaufort Sea Large Ocean Management Area: Ecosystem Overview and Assessment Report. Can Tech Rep Fish Aquat Sci. 2780: ii-ix + 188 p.

Conlan K, Aitken A, Hendrycks E, McClelland C, Melling H. 2008. Distribution patterns of Canadian Beaufort Shelf macrobenthos. J Mar Syst. 74(3-4):864-886.

Conover RJ. 1998. Comparative life histories in the genera *Calanus* and *Neocalanus* in high latitudes of the northern hemisphere. Hydrobiologia 167:127-142.

Cross JN, Mathis JT, Pickart RS, Bates NR. 2018. Formation and transport of corrosive water in the Pacific Arctic region. Deep Sea Res Part II. 152:67-81. https://doi.org/10.1016/j.dsr2.2018.05.020

Cusson M, Archambault P, Aitken A. 2007. Biodiversity of benthic assemblages on the Arctic continental shelf: historical data from Canada. Mar Ecol Prog Ser. 331:291-304.

David C, Lange B, Krumpen T, Schaafsma F, van Franeker JA, Flores H. 2016. Under-ice distribution of polar cod *Boreogadus saida* in the central Arctic Ocean and their association with sea-ice habitat properties. Polar Biol. 39:981–994. https://doi.org/10.1007/s00300-015-1774-0

Dee D, and National Centre for Atmospheric Research Staff (Eds). Last modified 06 Feb 2020. "The Climate Data Guide: ERA5 atmospheric reanalysis." Retrieved from https://climatedataguide.ucar.edu/climate-data/era5-atmospheric-reanalysis.

Deines K. 1999. Backscatter Estimation Using Broadband Acoustic Doppler Current Profilers. In: Proc. Sixth Working Conf. on Current Measurement, San Diego, CA. IEEE, 249-253.

DeRobertis A, Higginbottom I. 2007. A post-processing technique to estimate the signal-to-noise ratio and remove echosounder background noise. ICES J Mar Sci. 64:1282–1291.

Dezutter T, Lalande C, Dufresne C, Darnis G, Fortier L. 2019. Mismatch between microalgae and herbivorous copepods due to the record sea ice minimum extent of 2012 and the late sea ice break-up of 2013 in the Beaufort Sea. Prog Oceanogr. 173:66-77.

Dickson AG, Sabine CL, Christian JR. (Eds.) 2007. Guide to Best Practices for Ocean CO2 Measurements. PICES Special Publication 3:101 pp.

Dmitrenko IA, Kirillov SA, Myers PG, Forest A, Tremblay B, Lukovich JV, Gratton Y, Rysgaard S, Barber DG. 2018. Wind-forced depth-dependent currents over the eastern Beaufort Sea continental slope: Implications for Pacific water transport. Elem Sci Anth 6(1):66.

Emmerton C, Lesack L, Vincent W. 2008. Mackenzie River nutrient delivery to the Arctic Ocean and effects of the Mackenzie Delta during open water conditions. Global Biogeochem Cycles. 22(GB1024). doi: 10.1029/2006GB002856.

Falk-Petersen S, Mayzaud P, Kattner G, Sargent JR. 2009. Lipids and life strategy of Arctic *Calanus*. Mar Biol Res. 5:18-39.

Fellman J, D'Arnore D, Hood E. 2009. An evaluation of freezing as a preservation technique for analyzing dissolved organic C, N and P in surface water samples. Sci Total Environ. 392(2-3):305-312. doi: 10.1016/j.scitotenv.2007.11.027.

Fichot CG, Kaiser K, Hooker SB, Amon RMW, Babin M, Belander S, Walker SA, Benner R. 2013. Pan-Arctic distributions of continental runoff in the Arctic Ocean. Sci Rep. 3:1053. https://doi.org/10.1038/srep01053.

Fissel D, Marko J, Melling H. 2008. Advances in upward looking sonar technology for studying the processes of change in Arctic Ocean ice climate. J Oper Oceanogr. 1(1):9-18. doi: 10.1080/1755876X.2008.11081884.

Fissel DB, Borg K, Asplin MG, Nasonova S, Forest A, Pickart RS, Lin P, Gong D, Melling H, Wiese FK, Gryba RD. 2020. Influence of the wind-driven Mackenzie River plume on the oceanography of the Canadian Beaufort Sea in late spring and summer. CMOS Virtual 54th Congress.

Fissel DB, Borg K, Asplin MG, Lawrence J, Melling H, Forest A, Pickart RS, Lin P, Wiese FK, Gryba RD. 2019. Sea ice velocities in the vicinity of Mackenzie Canyon from a two year-long mooring array, with comparisons to ice velocities obtained off the central Mackenzie Delta. Paper Presented at the ArcticNet Annual Science Meeting, Halifax NS, Dec. 2019.

Forest A, Sampei M, Hattori H, Makabe R, Sasaki H, Fukuchi M, Wassmann P, Fortier L. 2007. Particulate organic carbon fluxes on the slope of the Mackenzie Shelf (Beaufort Sea): Physical biological forcing of shelf-basin exchanges. J Mar Syst. 68(1-2):39-54.

Forest A, Babin M, Stemmann L, Picheral M, Sampei M, Fortier L, Gratton Y, Bélanger SD, Devred E, Sahlin J, Doxaran D, Joux F, Ortega-Retuerta E, Martin J, Jeffrey WH, Gasser B, Miquel J-C. 2013. Ecosystem function and particle flux dynamics across the Mackenzie Shelf (Beaufort Sea, Arctic Ocean): An integrative analysis of spatial variability and biophysical forcings. Biogeosciences 10(5):2833-2866. DOI: 10.5194/bg-10-2833-2013.

Forest A, Osborne PD, Fortier L, Sampei M, Lowings MG. 2015. Physical forcings and intense shelf-slope fluxes of particulate matter in the halocline waters of the Canadian Beaufort Sea during winter. Cont Shelf Res. 101:1-21.

Forest A, Osborne PD, Curtiss G, Lowings MG. 2016. Current surges and seabed erosion near the shelf break in the Canadian Beaufort Sea: A response to wind and ice motion stress. J Mar Syst. 160:1-16.

Foukal NP, Pickart RS, Moore G, Lin P. 2019. Shelfbreak downwelling in the Alaskan Beaufort Sea. J Geophys Res Oceans. 24(10):7201-7225.

Frost KJ, Lowry LF, Pendelton G, Nute HR. 2004. Factors affecting the observed densities of ringed seals, *Phoca hispida*, in the Alaskan Beaufort Sea, 1996-99. Arctic 57(2):115-128.

Gallaway BJ, Griffiths WB, Craig PC, Gazey WJ, Helmericks JW. 1983. An assessment of the Colville River delta stock of arctic cisco - migrants from Canada. Biol Pap Univ Alaska 21:4-23.

Geoffroy M, Majewski A, LeBlanc M, Gauthier S, Walkusz W, Reist JD, Fortier L. 2016. Vertical segregation of age-0 and age-1+ polar cod (*Boreogadus saida*) over the annual cycle in the Canadian Beaufort Sea. Polar Biol. 39**:**1023–1037. https://doi.org/10.1007/s00300-015-1811-z.

George JC, Clark C, Carroll GM, Ellison WT. 1989. Observations on the ice-breaking and ice navigation behavior of migrating bowhead whales (*Balaena mysticetus*) near Point Barrow, Alaska, Spring 1985. Arctic 42(1):24-30.

Gradinger RR, Bluhm BA. 2004. In-situ observations on the distribution and behavior of amphipods and Arctic cod (*Boreogadus saida*) under the sea ice of the High Arctic Canada Basin. Polar Biol. 27:595–603 https://doi.org/10.1007/s00300-004-0630-4.

Graham M, Hop H. 1995. Aspects of reproduction and larval biology of Arctic cod (*Boreogadus saida*). Arctic 48:130–135.

Grebmeier JM, Bluhm BA, Cooper LW, Danielson SL, Arrigo KR, Blanchard AL, Clarke JT, Day RH, Frey KE, Gradinger RR, Kedra M, Konar B, Kuletz KJ, Lee SH, Lovvorn JR, Norcross BL, Okkonen SR. 2015. Ecosystem characteristics and processes facilitating persistent microbenthic biomass hotspots and associated benthivory in the Pacific Arctic. Prog Oceanogr. 136:92-114.

Gryba RD, Wiese FK, Kelly BP, Von Duyke AL, Pickart RS, Stockwell DA. 2019 Inferring foraging locations and water masses preferred by spotted seals *Phoca largha* and bearded seals *Erignathus barbatus*. Mar Ecol Prog Ser. 631:209-224.

Hartwig L. 2009. Mapping traditional knowledge related to the identification of ecologically and biologically significant areas in the Beaufort Sea. Can Manuscript Rep Fish Aquat Sci. 2895: iii+25p.

Harwood LA, Stirling I. 1992. Distribution of ringed seals in the southeastern Beaufort Sea during late summer. Can J Zool. 70(5):891-900.

Harwood LA, Smith TG, Auld JC. 2012. Fall migration of ringed seals (Phoca hispida) through the Beaufort and Chukchi Seas, 2001-02. Arctic 65(1):35-44.

Harwood LA, Smith TG, Melling H, Alikamik J, Kingsley MCS. 2012. Ringed seals and sea ice in Canada's Western Arctic: Harvest-based monitoring 1992-2011. Arctic 65(4):377-390.

Harwood LA, Quakenbush LT, Small RJ, George JC, Pokiak J, Pokiak C, Heide-Jørgensen MP, Lea EV, Brower H. 2017. Movements and inferred foraging by bowhead whales in the Canadian Beaufort Sea during August and September, 2006–12. Arctic 70(2):161-176.

Hauser DDW, Laidre KL, Stern HL, Moore SE, Suydam RS, Richard PR. 2017. Habitat selection by two beluga whale populations in the Chukchi and Beaufort seas. PLoS One 12(2):e0172755.

Hill PR, Blasco SM, Harper JR, Fissel DB. 1991. Sedimentation on the Canadian Beaufort Shelf. Cont Shelf Res. 11(8-10):821-842.

Holmes RM, Shiklomanov AI, Suslova A, Tretiakov M, McClelland JW, Spencer RGM, Tank SE. 2019. River Discharge [in "State of the Climate in 2018"]. Bull. Amer. Meteor. Soc. 100(9):161–163. doi:10.1175/2019BAMSStateoftheClimate.1. ArcticGRO webpage is at https://arcticgreatrivers.org/

Horvat C, Jones DR, Iams S, Schroeder D, Flocco D, Feltham D. 2017. The frequency and extent of sub-ice phytoplankton blooms in the Arctic Ocean. Sci Adv 3:e1601191.

Huntington HP, Danielson SL, Wiese FK, Baker MR, Boveng P, Citta JJ, De Robertis A, Dickson DMS, Farley EV, George JC, Iken K, Kimmel DG, Kuletz K, Ladd C, Levine R, Quakenbush L, Stabeno P, Stafford KM, Stockwell D, Wilson C. 2020. Evidence suggests potential transformation of the Pacific Arctic ecosystem is underway. Nat Clim Change 1–7.

Huntley M, Strong KW, Dengler AT. 1983. Dynamics and community structure of zooplankton in the Davis Strait and Northern Labrador Sea. Arctic 36(2):143-161.

IMG Golder and Golder Associates. 2011. Traditional Knowledge Collection Program, Aklavik Community Report submitted to BP Exploration Operating Company Limited, 240-4 Avenue SW, Calgary Alberta T2P 2H8. Report number 09-1334-1034.

Jones JM, Thayre BJ, Roth EH, Mahoney M, Sia I, Merculief K, Jackson C, Zeller C, Clare M, Bacon A, Weaver S. 2014. Ringed, bearded, and ribbon seal vocalizations north of Barrow, Alaska: seasonal presence and relationship with sea ice. Arctic 67(2):203-22.

Kanamitsu M, Ebisuzaki W, Woollen J, Yang S-K, Hnilo JJ, Fiorino M, Potter GL. 2002. NCEP-DOE AMIP-II Reanalysis (R-2). 1631-1643, Nov 2002, Bulletin of the American Meteorological Society. Data provided by the NOAA/OAR/ESRL PSL, Boulder, Colorado, USA, from their Web site at https://psl.noaa.gov/data/gridded/data.ncep.reanalysis2.html.

Kavik-Stantec. 2020. Beaufort Region Strategic Environmental Assessment Final Report. Appendix C: Climate Change Predictions for the Strategic Assessment. Report prepared for Inuvialuit Regional Corporation, Inuvialuit Game Council and Crown-Indigenous Relations and Northern Affairs Canada. https://rsea.inuvialuit.com/.

Kelly BP, Badajos OH, Kunnasranta M, Moran JR, Martinez-Bakker M, Wartzok D, Boveng P. 2010. Seasonal home ranges and fidelity to breeding sites among ringed seals. Polar Biol. 33:1095-1109.

Kitamura M, Amakasu K, Kikuchi T, Nishino S. 2017. Seasonal dynamics of zooplankton in the southern Chukchi Sea revealed from acoustic backscattering strength. Cont Shelf Res. 133:47–58.

Kirillov S, Dmitrenko I, Tremblay B, Gratton Y, Barber D, Rysgaard S. 2016. Upwelling of Atlantic Water along the Canadian Beaufort Sea continental slope: Favorable atmospheric conditions and seasonal and interannual variations. J Clim. 29(12):4509–4523.

Kjellerup S, Dünweber, Møller EF, Schiedek D, Oskarsson GJ, Rigét F, Johansen KL, Mosbech A. 2014. Vertical and horizontal distribution of zooplankton and polar cod in southern Baffin Bay (66-71˚N) in September 2009. Polar Biol. 38:699-718.

Klinck JM. 1996. Circulation near submarine canyons: A modeling study. J Geophys Res Oceans. 101(C1):1211-1223.

Korneliuss RJ, Ona E. 2002. An operational system for processing and visualizing multi-frequency acoustic data. ICES J Mar Sci. 59:293–313.

Kirillov S, Dmitrenko I, Tremblay B, Gratton Y, Barber D, Rysgaard S. 2016. Upwelling of Atlantic Water along the Canadian Beaufort Sea continental slope: Favorable atmospheric conditions and seasonal and interannual variations. J Clim. 29(12):4509–4523.

Kjellerup S, Dünweber, Møller EF, Schiedek D, Oskarsson GJ, Rigét F, Johansen KL, Mosbech A. 2014. Vertical and horizontal distribution of zooplankton and polar cod in southern Baffin Bay (66-71˚N) in September 2009. Polar Biol. 38:699-718.

Kulikov E, Carmack E, Macdonald R. 1998. Flow variability at the continental shelf break of the Mackenzie Shelf in the Beaufort Sea. J Geophys Res Oceans. 103(C6):12725-12741.

Lavoie D, Macdonald RW, Denman K. 2009. Primary productivity and export fluxes on the Canadian shelf of the Beaufort Sea: a modelling study. J Mar Syst. 75:17-32.

Lavoie D, Denman KL, Macdonald RW. 2010. Effects of future climate change on primary productivity and export fluxes in the Beaufort Sea. J Geophys Res. 115:C04018. doi:10.1029/2009JC005493.

Lin P, Pickart RS, Stafford KM, Moore G, Torres DJ, Bahr F, Hu J. 2016. Seasonal variation of the Beaufort shelfbreak jet and its relationship to Arctic cetacean occurrence. J Geophys Res Oceans 121(12):8434–8454.

Lin P, Pickart RS, Moore GWK, Spall MA, Hu J. 2019. Characteristics and dynamics of wind-driven upwelling in the Alaskan Beaufort Sea based on six years of mooring data. Deep Sea Res Part II doi:10.1016/j.dsr2.2018.01.002.

Lin P, Pickart RS, Fissel D, Ross E, Kasper J, Bahr F, Torres DJ, O'Brien J, Borg K, Melling H, Wiese FK. 2020. Circulation in the vicinity of Mackenzie Canyon from a year-long mooring array. Prog Oceanogr. https://doi.org/10.1016/j.pocean.2020.102396

Lowry LF, Sheffield G, George JC. 2004. Bowhead whale feeding in the Alaskan Beaufort Sea, based on stomach content analyses. J Cetacean Res Manage. 6:215-223.

MacDonald R, McLaughlin F. 1982. The effect of storage by freezing on dissolved inorganic phosphate, nitrate and reactive silicate for samples from coastal and estuarine waters. Water Res. 16(1):95-104. doi: 10.1016/0043-1354(82)90058-6.

Macdonald R, Solomon S, Cranston R, Welch H, Yunker M, Gobeil C. 1998. A sediment and organic carbon budget for the Canadian Beaufort Shelf. Mar Geol. 144:255– 273.

Macdonald R, Wong C, Erickson P. 1987. The distribution of nutrients in the southeastern Beaufort Sea: Implications for water circulation and primary production. J Geophys Res Oceans 92(C3):2939-2952.

Macdonald RW, Carmack EC. 1991. The role of large-scale under-ice topography in separating estuary and ocean on an arctic shelf. Atmosphere-Ocean 29(1):37-53.

Macdonald RW, Paton D, Carmack EC, Omstedt A. 1995. The freshwater budget and under-ice spreading of Mackenzie River water in the Canadian Beaufort Sea based on salinity and 18O/16O measurements in water and ice. J Geophys Res. 100:895 – 919.

MacIntyre KQ, Stafford KM, Berchok CL, Boveng PL. 2013. Year-round acoustic detection of bearded seals (*Erignathus barbatus*) in the Beaufort Sea relative to changing environmental conditions, 2008-2010. Polar Biol. 36:1161–1173. https://doi.org/10.1007/s00300-013-1337-1.

Macdonald R. 2014. How one biogeochemist sees change in the Arctic Ocean. Arctic Signal, Canadian Meteorological and Oceanographic Society. https://cmos.in1touch.org/uploaded/web/ArcticSIG/ArcticSIG%20Newsletter%20Volume%201%20Issue%2004_Dec%202014.pdf

Majewski AR, Walkusz W, Lynn BR, Atchison S, Eert J, Reist JD. 2015. Distribution and diet of demersal Arctic Cod, (*Boreogadus saida*), in relation to habitat characteristics in the Canadian Beaufort Sea. Polar Biol. 39:1087–1098. http://dx.doi.org/10.1007/s00300-015-1857-y.

Majewski AR, Atchison S, MacPhee S, Eert J, Niemi A, Michel C, Reist JD. 2017. Marine fish community structure and habitat associations on the Canadian Beaufort shelf and slope. Deep Sea Res Part II: Oceanographic Research Papers 121:169-182.

Manley TO, Hunkins K. 1985. Mesoscale eddies of the Arctic Ocean. J Geophys Res. 90:4911–4930.

Mate BR. Krutzikowsky GK, Winsor MH. 2000. Satellite-monitored movements of radio-tagged bowhead whales in the Beaufort and Chukchi seas during the late-summer feeding season and fall migration. Can J Zool. 78(7):1168-1181.

Mathis JT, Cross JN, Bates NR. 2011. Coupling primary production and terrestrial runoff to ocean acidification and carbonate mineral suppression in the eastern Bering Sea. J Geophys Res. 116:C02030, doi:10.1029/2010JC006453.

McLaughlin FA, Carmack EC. 2010. Deepening of the nutricline and chlorophyll maximum in the Canada Basin interior, 2003–2009. Geophys Res Lett. 37:L24602. doi:10.1029/2010GL045459.

McMahon R, Taveras A, Neubert P, Harvey HR. 2020. Organic Biomarkers and Meiofauna Diversity Reflect Differential Carbon Inputs Across the Coastal Shelf of the Mackenzie Delta. Limnol Oceanogr. (in press).

Melling H, Johnston P, Riedel D. 1995. Measurements of the underside topography of sea ice by moored subsea sonar. J Atmos Oceanic Technol. 13(3):589-602. doi: 10.1175/1520-0426(1995)012<0589:MOTUTO>2.0.CO;2.

Melling H, Riedel DA. 1995. The underside topography of sea ice over the continental shelf of the Beaufort Sea in the winter of 1990. J Geophys Res. 100(C7):13641-13653.

Melnikov IA, Chernova NV. 2013. Characteristics of under-ice swarming of polar cod *Boreogadus saida (Gadidae)* in the central Arctic Ocean. J Ichthyol. 53:7–15. https://doi.org/10.1134/S0032945213010086

Millero FJ, Graham TB, Huang F, Bustos-Serrano H, Pierrot D. 2006. Dissociation constants of carbonic acid in seawater as a function of salinity and temperature. Mar Chem. 100:80–94. https://doi.org/10.1016/j.marchem.2005.12.001.

Moore SE. 2000. Variability of cetacean distribution and habitat selection in the Alaskan Arctic, Autumn 1982-91. Arctic 53(4):448-460.

Moore SE, deMaster DP, Dayton PK. 2000. Cetacean habitat selection in the Alaskan Arctic during the Summer and Autumn. Arctic 53(4):432-447.

Moore SE, Laidre KL. 2006. Trends in sea ice cover within habitats used by bowhead whales in the western Arctic. Ecol Appl. 16(3):932-944.

Moore GWK, Schweiger A, Zhang J, Steele M. 2018. Collapse of the 2017 winter Beaufort High: A response to thinning sea ice? Geophys Res Lett. 45:2860– 2869. https://doi.org/10.1002/2017GL076446

Mucci A, Forest A, Fortier L, Fukuchi M, Grant J, Hattori H, Hill P, Lintern G, Makabe R, Magen C, Miller L, Sampei M, Sasaki H, Sundby B, Walker T, Wassmann P. 2008. Organic and inorganic fluxes, p. 113-142. *In* Fortier L, Barber D, Michaud J [eds.], On thin ice: A synthesis of the Canadian Arctic Shelf Exchange Study (CASES). Aboriginal Issue Press.

Mucci A, Lansard B, Miller L, Papakyriakou T. 2010. CO2 fluxes across the air-sea interface in the southeastern Beaufort Sea: the ice-free period. J Geophys Res Oceans 115:C04003. doi: 10.1029/2009JC005330.

Muchaca I. Allen S. 2018. Effects of a Dynamically Wide Submarine Canyon on Coastal Currents During an Upwelling Event. Paper presented at the Ocean Sciences Meeting, Portland OR.

Muchaca I. 2019. Circulation and upwelling in Mackenzie Canyon, a dynamically wide submarine canyon in the Beaufort Sea. Ph.D. Thesis, University of British Columbia, https://open.library.ubc.ca/cIRcle/*collec*tions/ubctheses/24/items/1.0378375

Mullison J. 2017. Backscatter Estimation Using Broadband Acoustic Doppler Current Profilers – Updated. Presented at ASCE Hydraulic Measurements & Experimental Methods Conference, Durham, NH.

Mundy CJ, Gosselin M, Ehn J, Gratton Y, Rossnagel A, Barber DG, Martin J, Tremblay J-E, Palmer M, Arrigo KR, Darnis G, Fortier L, Else B, Papakyriakou T. 2009. Contribution of under-ice primary production to an ice-edge upwelling phytoplankton bloom in the Canadian Beaufort Sea. Geophys Res Lett. 36:L17601.

NCEP. 2019. NCEP Reanalysis 2 Surface Winds provided by NOAA/OAR/ESRL PSL, Boulder, Colorado, USA. Retrieved January 31, 2019 from *https://psl.noaa.gov/*.

Nelson RJ. 2013. Development of indicators for Arctic marine biodiversity monitoring in Canada. DFO Canadian Science Advisory Secretariat Research Document. 2012/123, 2013, 35 pp.

Nghiem SV, Hall DK, Rigor IG, Li P, Neumann G. 2014. Effects of Mackenzie River discharge and bathymetry on sea ice in the Beaufort Sea. Geophys Res Lett. 41:873–879. doi:10.1002/2013GL058956.

Ni H-G, Lu F-H, Luo X-L, Tian H-Y, Zeng EY. 2008. Riverine inputs of total organic carbon and suspended particulate matter from the Pearl River Delta to the coastal ocean off South China. Mar Pollut Bull. 56(5):1150-1157.

Niemi A, Ferguson S, Hedges K, Melling H, Michel C, Ayles B, Azetsu-Scott K, Couple P, Deslauriers D, Devred E, Doniol-Valcroze T, Dunmall K, Eert J, Galbraith P, Geoffroy M, Gilchrist G, Hennin H, Howland K, Kendall M, Kohlbach D, Lea E, Loseto L, Majewski A, Marcoux M, Matthews C, McNicholl D, Mosnier A, Mundy CJ, Ogloff W, Perrie W, Richards C, Richardson E, Reist R, Roy

V, Sawatzky C, Scharffenberg K, Tallman R, Tremblay J-É, Tufts T, Watt C, Williams W, Worden E, Yurkowski D, Zimmerman S. 2019. State of Canada's Arctic Seas. Can Tech Rep Fish Aquat Sci. 3344: xv + 189 p.

Nikolopoulos A, Pickart RS, Fratantoni PS, Shimada K, Torres DJ, Jones EP. 2009. The western Arctic boundary current at 152°W: Structure, variability, and transport. Deep Sea Res Part II 56(17):1164-1181. doi:10.1016/j.dsr2.2008.10.014.

Okkonen SR, Ashjian CJ, Campbell RG, Maslowski W, Clement-Kinney JL, Potter R. 2009. Intrusion of warm Bering/Chukchi waters onto the shelf in the western Beaufort Sea. J Geophys Res Oceans 114:C00A11. doi:10.1029/2008JC004870.

Osborne PD, Forest A. 2016. Sediment dynamics from coat to slope – Southern Canadian Beaufort Sea. Coastal Research 75(100075):537-541. doi: 10.2112/SI75-108.1

Ouyang Y. 2003. Simulating dynamic load of naturally occurring TOC from watershed into a river. Water Research 37(4):823-832.

Parker-Stetter SL, Horne JK, Weingartner TJ. 2011. Distribution of polar cod and age-0 fish in the U.S. Beaufort Sea. Polar Biol. 34:1543-1557.

Parsons TR, Webb DG, Dovey H, Haigh R, Lawrence M, Hopky GE. 1988. Production studies in the Mackenzie River — Beaufort Sea estuary. Polar Biol. 8:235–239. https://doi.org/10.1007/BF00443455.

Petty AA, Hutchings JK, Richter-Menge JA, Tschudi MA. 2016. Sea ice circulation around the Beaufort Gyre: The changing role of wind forcing and the sea ice state. J Geophys Res Oceans 121: 3278–3296. https://doi.org/10.1002/2015JC010903.

Pickart RS. 2004. Shelfbreak circulation in the Alaskan Beaufort Sea: Mean structure and variability. J Geophys Res. 109(C4), doi:10.1029/2003jc001912.

Pickart RS, Moore GWK, Torres DJ, Fratantoni PS, Goldsmith RA, Yang J. 2009. Upwelling on the continental slope of the Alaskan Beaufort Sea: Storms, ice, and oceanographic response. J Geophys Res. 114. https://doi.org/10.1029/2008jc005009.

Pickart RS, Spall MA, Moore GWK, Weingartner TJ, Woodgate RA, Aagaard K, Shimada K. 2011. Upwelling in the Alaskan Beaufort Sea: Atmospheric forcing and local versus non-local response. Prog Oceanogr. 88:78-100. doi:10.1016/j.pocean.2010.11.005.

Pickart RS, Schulze LM, Moore GWK, Charette MA, Arrigo KR, van Dijken G, Danielson SL. 2013. Long-term trends of upwelling and impacts on primary productivity in the Alaskan Beaufort Sea. Deep Sea Res Part I 79:106-121. doi:10.1016/j.dsr.2013.05.003.

Pickart RS, Spall MA, Mathis JT. 2013. Dynamics of upwelling in the Alaskan Beaufort Sea and associated shelf–basin fluxes. Deep Sea Res Part I 76:35–51. https:// doi.org/10.1016/j.dsr.2013.01.007.

Proshutinsky A, Krishfield R, Toole JM, Timmermans ML, Williams W, Zimmermann S, Yamamoto-Kawai M, Armitage TWK, Dukhovskoy D, Golubeva E, Manucharyan GE, Platov G, Watanabe E,

Kikuchi T, Nishino S, Itoh M, Kang SH, Cho KH, Tateyama K, Zhao J. 2019. Analysis of the Beaufort Gyre freshwater content in 2003-2018. J Geophys Res Oceans. 124(12): 9658–9689. doi: 10.1029/2019JC015281.

Quakenbush L, Citta J, George JC, Heide-Jørgensen MP, Small R, Brower H, Harwood L, Adams B, Brower L, Tagarook G, Pokiak C, Pokiak J. 2012. Seasonal movements of the Bering-Chukchi-Beaufort stock of bowhead whales: 2006-2011 satellite telemetry results. Report to the International Whaling Commission Scientific Committee SC/64/BRG1. 22p.

Quakenbush LT, Small RJ, Citta JJ. 2013. Satellite tracking of bowhead whales: movements and analysis from 2006 to 2012. U.S. Dept. of the Interior, Bureau of Ocean Energy Management, Alaska Outer Continental Shelf Region, Anchorage, AK. OCS Study BOEM 2013-01110. 60 pp + appendices.

Renaud PE, Riedel A, Michel C, Morata N, Gosselin M, Juul-Pedersen T, Chiuchiolo A. 2007. Seasonal variation in benthic community oxygen demand: A response to an ice algal bloom in the Beaufort Sea, Canadian Arctic? J Mar Syst. 67(1-2):1-12.

Robbins LL, Hansen ME, Kleypas JA, Meylan SC. 2010. CO2calc- a user-friendly seawater carbon calculator for Windows, Mac OS X, and iOS (iPhone). US Geological Survey Open-File Report, 2010–1280, 17 pp. Available at https://pubs.usgs.gov/of/2010/1280/.

Roy V, Iken K, Archambault P. 2014. Environmental drivers of the Canadian Arctic megabenthic communities. PLoS ONE https://doi.org/10.1371/journal.pone.0100900

Rutzen I, Hopcroft RR. 2018. Abundance, biomass and community structure of epipelagic zooplankton in the Canada Basin. J Plankton Res. 40(4):486-499.

Ryan TE, Downie RA, Kloser RJ, Keith G. 2015. Reducing bias due to noise and attenuation in open-ocean echo integration data. ICES J Mar Sci. doi:10.1093/icesjms/fsv121.

Rutzen I, Hopcroft RR. 2018. Abundance, biomass and community structure of epipelagic zooplankton in the Canada Basin. J Plankton Res. 40(4):486-499.

Sepp M., Jaagus J. 2011. Changes in the activity and tracks of Arctic cyclones. Clim Change 105:577–595. https://doi.org/10.1007/s10584-010-9893-7

Serreze MC, Barrett AP, Crawford AD, Woodgate RA. 2019. Monthly variability in Bering Strait oceanic volume and heat transports, links to atmospheric circulation and ocean temperature, and implications for sea ice conditions. J Geophys Res Oceans 124(12):9317–9337. https://doi.org/10.1029/ 2019JC015422.

Simpson K, Tremblay J, Gratton Y, Price N. 2008. An annual study of inorganic and organic nitrogen and phosphorus and silicic acid in the southeastern Beaufort Sea. J Geophys Res. 113(C7): doi: 10.1029/2007JC004462.

Skyllingstad ED, Paulson CA, Pegau WS, McPhee MG, Stanton T. 2003. Effects of keels on ice bottom turbulence exchange. J Geophys Res. 108(C12):3372. doi:10.1029/2002JC001488, 2003.

Smith M, Stammerjohn S, Persson O, Rainville L, Liu G, Perrie W, Robertson R, Jackson J, Thomson J. 2018. Episodic reversal of autumn ice advance caused by release of ocean heat in the Beaufort Sea. J Geophys Res Oceans 123(5):3164-3185.

Smoot CA, Hopcroft RR. 2017. Depth-stratified community structure of Beaufort Sea Slope zooplankton and its relations to water masses. J Plankton Res. 39(1):79-91.

Smoot CA, Hopcroft RR. 2017. Cross-shelf gradients of epipelagic zooplankton communities of the Beaufort Sea and the influence of localized hydrographic features. J Plankton Res. 39:65-78. doi.10.1093/plankt.fbw080

Søreide JE, Lue E, Berge J, Graeve M, Falk-Petersen S. 2010. Timing of blooms, algal food quality, and *Calanus glacialis* reproduction and growth in a changing Arctic. Global Change Biol. 16: 3154-3163. doi: 10.1111/j.1365-2486.2010.02175.x

Spall MA. 2007. Circulation and water mass transformation in a model of the Chukchi Sea. J Geophys Res. 112:C05025. https://doi.org/10.1029/2005jc003364.

Spall MA, Pickart RS, Fratantoni PS, Plueddemann AJ. 2008. Western Arctic shelfbreak eddies: Formation and transport. J Phys Oceanogr. 38:1644–1668.

Stirling I, Archibald R, DeMaster D. 1977. The distribution and abundance of seals in the Eastern Beaufort Sea. J Fish Res Board Can. 34:976-988.

Strickland J, Parsons R. 1960. A manual of sea water analysis. Bulletin No. 125. Nanaimo, BC, Canada: Fisheries Research Board of Canada, Pacific Oceanography Group. 192 pages.

Stroeve JC, Maslanik J, Serreze MC, Rigor I, Meier W, Fowler C. 2011. Sea ice response to an extreme negative phase of the Arctic Oscillation during winter 2009/2010. Geophys Res Lett. 38:L02502. doi:10.1029/2010GL045662.

Thomson DH, Fissel DB, Marko JR, Davis RA, Borstad GA. 1986. Distribution of bowhead whales *Balaena mysticetus* in relation to hydrometeorological events in the southeastern Beaufort Sea, 1980 1983. Environmental Studies Revolving Fund Report No. 028, Ottawa. 119 p.

Treacy SD, Gleason JS, Cowles CJ. 2005. Offshore distances of bowhead whales (Balaena mysticetus) observed during fall in the Beaufort Sea, 1982-2000: An alternative interpretation. Arctic 59(1):83-90.

Tremblay J- É , Bélanger S, Barber DG, Asplin M, Martin J, Darnis G, Fortier L, Gratton Y, Link H, Archambault P, Sallon A, Michel C, Williams WJ, Philippe B, Gosselin M. 2011. Climate forcing multiplies biological productivity in the coastal Arctic Ocean. Geophys Res Lett. 38:L18604.

Tremblay J-É, Anderson, LG, Matrai, P, Couple, P, Bélanger, S, Michel, C, Reigstad, M. 2015. Global and regional drivers of nutrient supply, primary production and CO_2 drawdown in a changing Arctic Ocean. Prog Oceanogr. 139:171-196. http://dx.doi.org/10.1016/j.pocean.2015.08.009

Urban-Malinga B, Wiktor J, Jabłońska, Moens T. 2005. Intertidal meiofauna of a high-latitude glacial Arctic fjord (Kongsfjorden, Svalbard) with emphasis on the structure of free-living nematode communities. Polar Biol. 28:940-950.

Wadhams P. 2000. Ice in the Ocean, Gordon and Breach Science Publ., London, p. 71

Waga H, Hirawake T, Fujiwara A, Grebmeier JM, Saitoh S. 2019. Impact of spatiotemporal variability in phytoplankton size structure on benthic macrofaunal distribution in the Pacific Arctic. Deep Sea Res Part II 162:114-126.

Welch HE, Bergmann MA, Siferd TD, Martin KA, Curtis MF, Crawford RE, Conover RJ, Hop H. 1992. Energy flow through the marine ecosystem of the Lancaster Sound region, Arctic Canada. Arctic 45(4):343-357.

Wiese, FK, Gryba R, Kelly BP. 2017. Marine Arctic Ecosystem Study - Pilot Program: Marine Mammals Tagging and Tracking. US Dept. of the Interior, Bureau of Ocean Energy Management, Alaska Region, Anchorage, AK. OCS Study BOEM 2017-017. 78 pp.

Wiese FK, Harvey HR, McMahon R, Neubert P, Gong D, Wang H, Hudson J, Pickard R, Ross E, Fabijan M, Gryba RD. 2018. Marine Arctic Ecosystem Study—Biophysical and chemical observations from glider and benthic surveys in 2016. Anchorage (AK): US Department of the Interior, Bureau of Ocean Energy Management. OCS Study BOEM 2018-024. 98 p. https://www.boem.gov/BOEM-2018-024/

Wiese FK, Ashjian C, Bahr F, Fabijan M, Fissel DB, Gryba RD, Kasper J, Monacci N, Nelson J, Pickart R, Ross E, Stafford K, Torres D, Turner C. 2019. Marine Arctic Ecosystem Study (MARES): Moorings on the Beaufort Sea shelf, 2016-2017. Anchorage (AK): US Department of the Interior, Bureau of Ocean Energy Management. OCS Study BOEM 2019-009. 163 p.

Williams WJ, Carmack EC. 2008. Combined effect of wind-forcing and isobath divergence on upwelling at Cape Bathurst, Beaufort Sea. J Mar Res. 66(5):645–663.

Williams WJ, Carmack EC. 2015. The 'interior' shelves of the Arctic Ocean: Physical oceanographic setting, climatology and effects of sea ice retreat on cross-shelf exchange. Prog Oceanogr. 139:24-41.

Woodgate RA. 2018. Increases in the Pacific inflow to the Arctic from 1990 to 2015, and insights into seasonal trends and driving mechanisms from year-round Bering Strait mooring data. Prog Oceanogr. 160:124–154. https://doi.org/10.1016/j. pocean.2017.12.007.

Wood KR, Overland JE, Salo SA, Bond NA, Williams WJ, Dong X. 2013. Is there a "new normal" climate in the Beaufort Sea? Polar Res. 32. http://dx.doi.org/10.3402/polar.v32i0.1955.

Yang D, Shi X, Marsh P. 2015. Variability and extreme of Mackenzie River daily discharge during 1973-2011. Quaternary International 380-381:159-168.

Yurkowski DJ, Semeniuk CAD, Harwood LA, Rosing-Asvid A, Dietz R, Brown TM, Clackett S, Grgicak-Mannion A, Fisk AT, Ferguson SH. 2016. Influence of sea ice phenology on the movement ecology of ringed seals across their latitudinal range. Mar Ecol Prog Ser. 562:237-250.

A Appendix A: High Resolution Seasons Figures

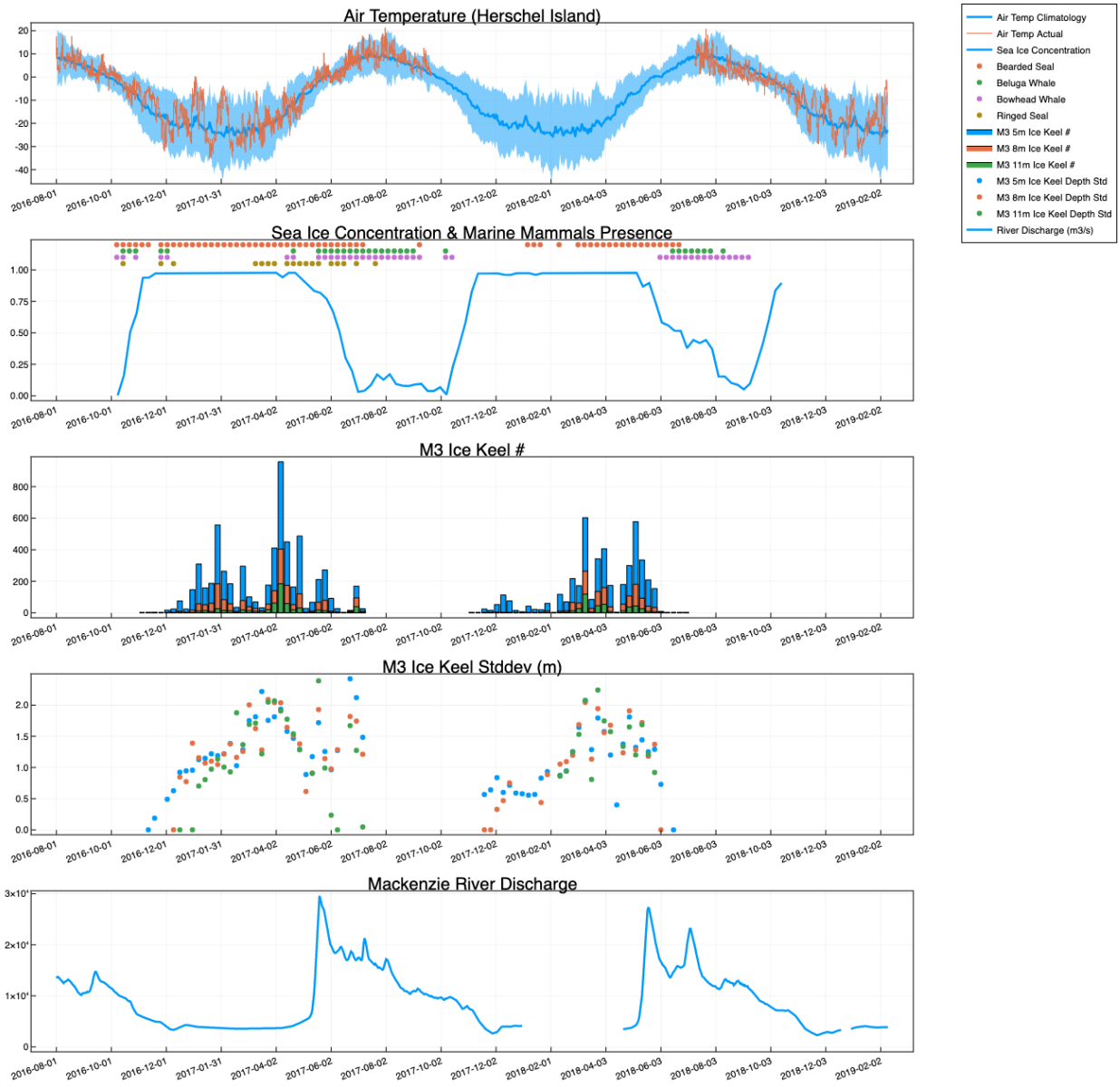

Figure A-1. Time series plots of (from top to bottom) air temperature, sea ice concentration & marine mammal presence, ice keel # & depth standard deviation, and Mackenzie River discharge of the MARES mooring deployment period.

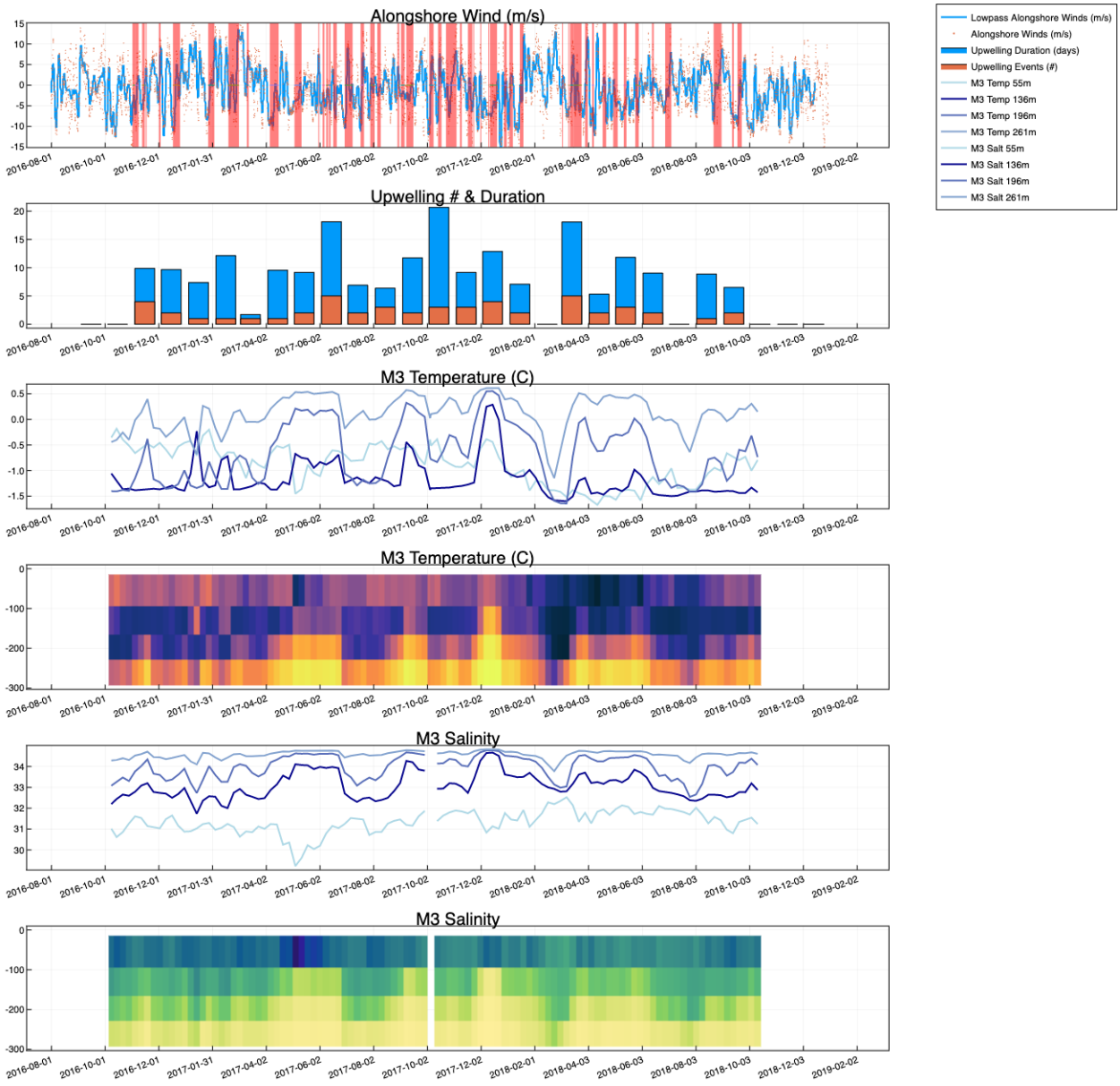

Figure A-2. Time series plot of alongshore winds with upwelling period highlights, monthly upwelling counts and durations, M3 temperature measurements and M3 salinity measurements.

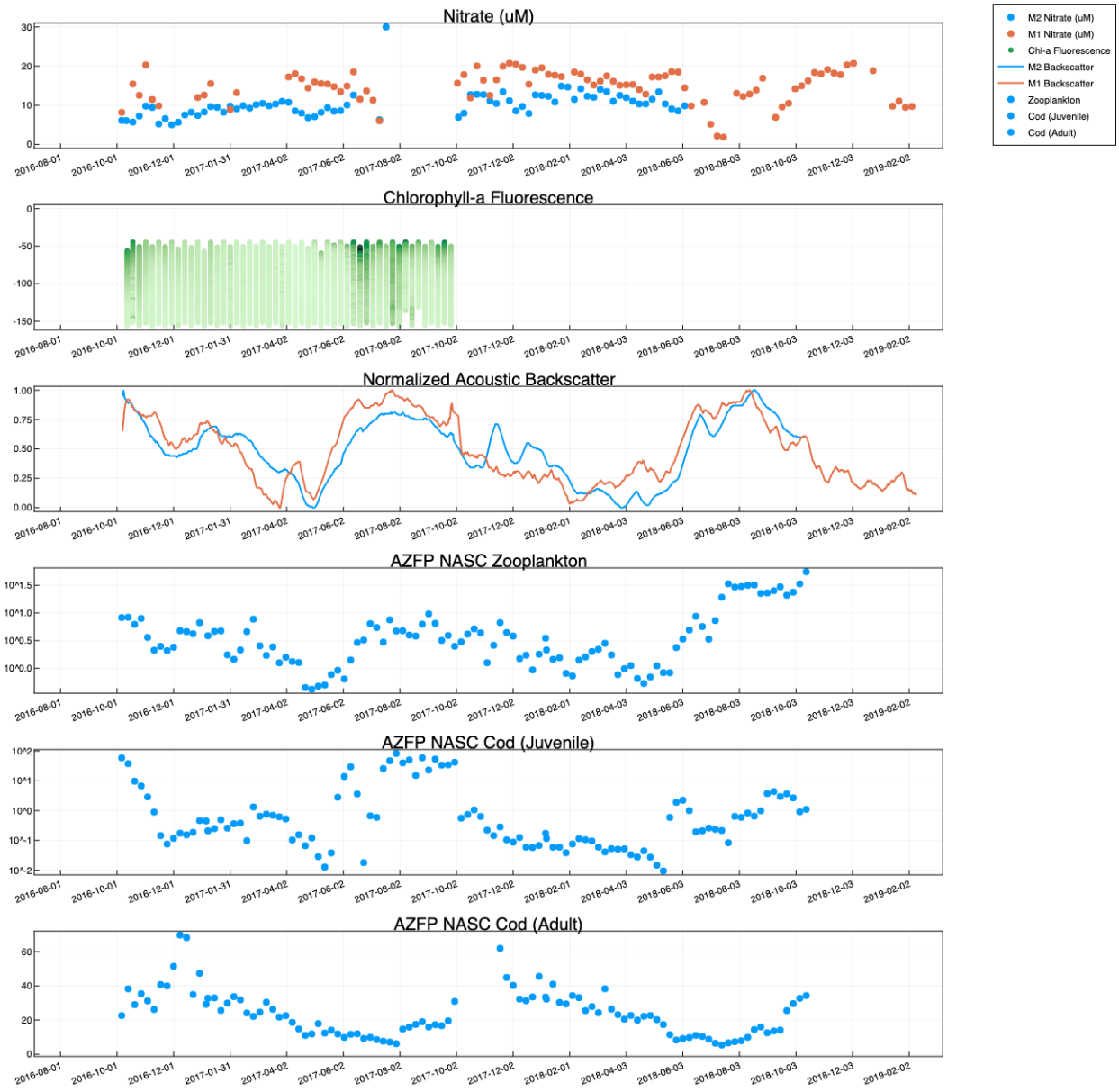

Figure A-3. Time series plots (from top to bottom) of nitrate, chlorophyll-a fluorescence, normalized acoustic backscatter from ADCP, and AZFP NASC zooplankton, juvenile cod, and adult cod.

Department of the Interior (DOI)

The Department of the Interior protects and manages the Nation's natural resources and cultural heritage; provides scientific and other information about those resources; and honors the Nation’s trust responsibilities or special commitments to American Indians, Alaska Natives, and affiliated island communities.

Bureau of Ocean Energy Management (BOEM)

The mission of the Bureau of Ocean Energy Management is to manage development of U.S. Outer Continental Shelf energy and mineral resources in an environmentally and economically responsible way.

BOEM Environmental Studies Program

The mission of the Environmental Studies Program is to provide the information needed to predict, assess, and manage impacts from offshore energy and marine mineral exploration, development, and production activities on human, marine, and coastal environments. The proposal, selection, research, review, collaboration, production, and dissemination of each of BOEM’s Environmental Studies follows the DOI Code of Scientific and Scholarly Conduct, in support of a culture of scientific and professional integrity, as set out in the DOI Departmental Manual (305 DM 3).